BRUSHLESS ASYNCHRONOUS INDUCTION MACHINES WITH LEADING VAR CAPABILITY

By

Stephen Bruce Kuznetsov, B.S.E.E., M.A.Sc.

February 1981

A thesis submitted for the degree of Doctor of Philosophy of the University of London and for the Diploma of Membership of the Imperial College

Department of Electrical Engineering
Imperial College of Science and Technology
London SW7

DEDICATION

To the memory of Professor Leo Aldo Finzi of the

Carnegie Institute of Technology

who had once remarked of the young electrical machine designer

". . . an action-oriented orchestration of innovative inputs

generated by escalation of meaningful indigenous

decision making dialoque . . ."

ABSTRACT

A new technique of continuously generating reactive power from the primary of a brushless induction machine is conceived and tested on a 10 kW short-stator linear machine and on 26 kW and 112 kW rotary cage motors. An auxiliary magnetic wave, travelling at rotor speed is artificially created by the space transient attributable to the asymmetrical primary winding. At least two distinct windings of different wavelength on a common magnetic core have been investigated. This rotor wave drifts in and out of phase repeatedly with the stator MMF wave proper and the resulting modulation of the airgap flux is used to generate reactive VA apart from that required for magnetization or leakage flux. Leading power factor operation has been demonstrated on the 112 kW machine. The VAR generation effect increases with machine size and unity power factor operation of the entire machine is seen to be commercially viable for large brushless induction motors and power systems induction generators.

The initial objective of this study was to improve power factor in high speed linear induction machines which was accomplished largely by eliminating the detrimental effects of the exit-edge power loss and using the same phenomena to generate large quantities of leading volt-amperes especially suited for the machines with high sheet-rotor velocities. The primary objective for extending the work to the rotary machines was to develop a brushless, cage rotor induction motor capable of naturally commutating high power thyristor semiconductor devices in a current-source inverter intended for variable-speed, variable frequency applications such as in a three-phase or DC-link traction drive system ranging from 100 kW to 1000 kW in output.

ACKNOWLEDGEMENTS

To Professor E.R. Laithwaite, my major advisor, I wish to express my gratitude for his support, expertise and genuine interest.

To Dr. H.R. Bolton of Imperial College, Professor M.G. Say of Heriot-Watt College and Professor Gordon Rawcliffe of the University of Bristol I am very thankful for their encouragement and advice.

To Mr. Peter Collins of Newman Industries, England, Mr. Matthew Guarino of the United States Department of Transportation, Mr. C.J. Mole of the Westinghouse Electric Corporation, Mr. Kenneth Phillips of the Eaton Corporation and Dr. Gabor Kalman of the Garrett-AiResearch Corporation of California, I am most grateful for their continued enthusiasm and technical interest.

The financial support of the National Research Development Corporation of the U.K. and the Imperial College of Science and Technology is acknowledged.

TABLE OF CONTENTS

I. INTRODUCTION

1.1 ADVENT OF BRUSHLESS VAR GENERATION

This thesis is concerned with the analysis and exploitation of a new electromagnetic mechanism for generating reactive volt-amperes from the primary of brushless rotary and linear induction machines. The initial discovery of a related technique may be attributed to the research team at the University of Manchester under the direction of Sir Frederic Williams, who had shown analytically and experimentally, that a third source of reactive volt-amperes pertaining to a discontinuous primary excitation and a continuous secondary member, existed in high-speed induction machibes in addition to the conventional magnetizing and leakage flux reactive requirements. [1 - 3]

The distinction lies in the nature of this third source of reactive power. All published literature on the series of discontinuous primaries incorporated in the spherical, phase-mixing, phase-shifting, logarithmic and linear machines built by Williams and his successors, indicates that the primary edge transient was only used in a detrimental fashion in the respect that only lagging reactive volt-amperes were generated [4 - 6]. Rather, the purpose of this thesis is to discuss a few schemes of exclusively using stator control of the airgap flux distribution but generating leading reactive volt-amperes, that is, a negative reactive source, over large segments of the primary excitation.

Over three-quarters of a century of induction machine design have focused on exploiting rotary machines for which only symmetrically excited primaries were developed and it was concluded that all induction machines must have a constant magni-

tude of airgap flux density. Further, history seemed to dictate that such space-transient effects due to either magnetic permeance variations or magneto-motive force irregularities should be minimized as a fundamental design philosophy. However, as early as 1966 Laithwaite pointed out [7] that fundamentally there was little evidence to suggest that the discovery of a positive electrical quantity -- a third source of reactive VA -- as shown to be comparable in magnitude to magnetizing and leakage flux losses, would not exist as a negative quantity and of approximately the same magnitude.

On a macroscopic basis, extensive research and analysis centering around the generalized electrical machine theory originally introduced by R.H. Park in 1929 [8] further suggested that an induction machine with leading power factor at the terminals, analogous to an overexcited synchronous motor, did not violate any basic rules of physics or mathematics. While it was clear that several different rotor current patterns would suffice to give a net negative kVAR consumption at the terminals, the question arose how to establish and maintain any of these patterns purely by electromagnetic induction in an inductive electric rotor circuit. The overwhelming conclusion of this thesis is that the introduction of abrupt space-transients in the airgap flux on a continuous and stable basis is the only practical method known to date to establish the equivalent of an overexcited cage-rotor current distribution. Figure 1.1 shows the basic nature of the induction condenser concept.

None of the designs presented in the thesis should be con-

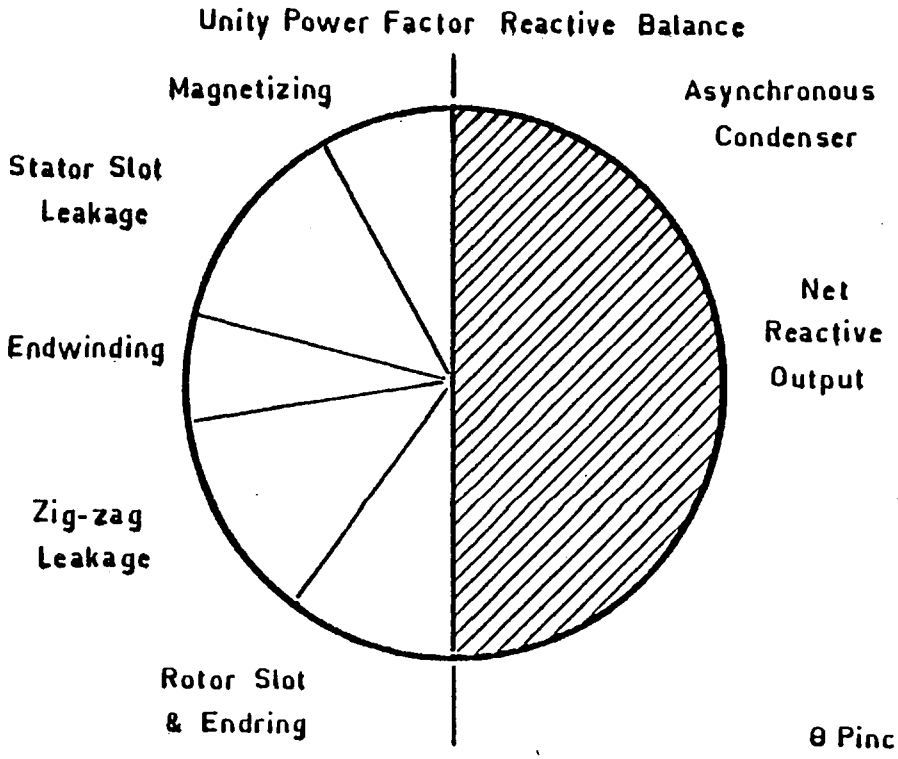

Figure 1.1 General indication of consumed and generated reactive power components in an integral induction motor and asynchronous condenser in medium-size machines.

sidered optimum with the exception of the two-stage, eleven pole linear induction machine (termed the LIM-ASC-II) which formed the major part of the experimental work. Rather the hardware developed during this period is intended to show that foremost, the classic short-primary exit-edge effect that deterred the commercial advantage of the high-speed linear induction machine for over two decades may be entirely neutralized or used to an advantageous purpose such as power factor control. Second, that this same basic edge-effect should necessarily be incorporated in large rotary induction machines for which it is desired to improve the "airgap" power factor to the extent that the terminal power factor may be at a unity or leading value continuously.

The reader, if he so desires, may take the viewpoint that reactive, wattless or "imaginary" power is basically a fictiticious quantity in that it was first conceived by the electric power engineer merely as a mathematical convenience in systems analysis and that it does not quite represent a physical entity such as real power which has a mechanical equivalent -- watts. However, if this is the case, then the reader is asked to examine the test data on the linear machines combining motor and VAR-generating windings, which shows conclusively that power factor improvement is occurring either at a higher or constant efficiency than was the case without reactive control. This is the essence of wattless power, for while it is not dissipative as such, its circulation and transmission is responsible for either excessive real power losses or alternately reduced real power consumption. The overwhelming systems concept paramount to the technology presented here is that power factor compensation should be performed directly at the source of im-

perfection rather than transmitting large quantities of reactive power over long distances between power station and load centers.

The approach underlying the thesis is entirely historical from the conception of the asynchronous condenser principle to the development of a 112 kW rotary machine which befits the title of the thesis. In particular, the entries in this chapter all portray several parallel schools of thought over a period of ninety years, which lead to the development of the Theta-Pinch and J-Jump concepts expounded in Chapters II through V, referring to the rotary and linear machine MMF configurations respectively. Throughout the thesis and the published literature to date [9-11] concerning this brushless VAR generation, the word transient is used frequently and can easily be misunderstood as even "space-transient" connotes an aura of vagueness. Moreover, to classify this phenomena as exploiting another harmonic field of the induction machine is clearly in error because this overlooks the basic mechanism that is novel to this thesis. It must be realized that the rotor-speed traveling wave, lagging behind the primary synchronous traveling wave by the slip, is responsible for generating large quantities of negative reactive volt-amperes. Over a limited section of airgap, the inductively-fed rotor is magnetizing the airgap and in addition inducing image currents in a distinct tertiary winding, on the primary block, at a reduced wavelength. Therefore, it is proper to regard this machine as two separate electromagnetic units, using a common rotor, a common stator core and a common magnetic flux at the transition between these two sections, the value of which is altered above or below a unity ratio according to, fundamen-

tally, a pole number-slip product.

In lieu of using the term space-transient, an alternative approach is to consider the nature of the rotor currents rather than the airgap flux. Over the airgap section whereby the primary is responsible for providing magnetization, the rotor currents are largely conventional slip-frequency, alternating currents the magnitude of which varies as a function of longitudinal position. Yet over the remaining airgap periphery for which the rotor provides magnetization, these rotor currents are direct-currents, of approximately the same peak value as the slip-frequency currents but with the vitally important distinction that these direct currents have a space-modulation distribution, (that is sinusoidal in nature and at exactly the same pole-pitch as the main primary winding) which decays as a function of time but very slowly in large machines (according to the Goodness Factor [12] and the rotor leakage inductance). The mechanism for changing slip-frequency currents to direct-currents is the action of the longitudinal exit-edge. By discontinuing primary excitation abruptly, if the rotor currents directly at this point are any value other than zero and the rotor electric circuit has any inductance, then it is clear that these rotor currents will decay naturally (eventually to zero in the most basic case); this is nothing more than a rotating polyphase switching transient. In effect, it appears that the longitudinal exit-edge is performing in a manner similar to conventional commutator by changing frequency albeit electromagnetically. This explanation is especially illustrative for both linear and rotary machine examples although it should be emphasized that at all times, the primary member or

tertiary winding (on the primary block) cannot distinguish whether the rotor contains slip-frequency alternating currents or space-modulated direct currents because both produce nearly identical field patterns in the airgap; this reconfirms the basis of generalized machine theory and further serves to unify the asynchronous and synchronous types of machines which have heavy current patterns on both sides of the airgap.

In particular, the advent of brushless VAR generation may be traced to one experimental study by Laithwaite in 1964 [13] which concentrated on rotor windings for a six-pole rotary induction machine with an arc-shaped short-primary. Several key points are paraphrased here in summary:

> "The paper describes a method of replacing the squirrel-cage with a wound rotor which is short-circuited but which is so arranged that the undesireable effects at the two edges are made to cancel each other. The system is most favorable to cases in which the pole-pitch of the machine is such that it divides evenly into the complete periphery. ... Even when running at synchronous speed, the transient rotor currents set up by the edges of the stator were present. ... When the machine is on load, the rotor current is a purely magnetizing current for regions outside the stator block and is capable of setting up a considerable flux density outside the block, even though the reluctance of the magnetic circuit be very high."

While the main purpose of this paper was to compare squirrel-cage rotors against wound types and their effect in either attenuating or prolonging transient rotor currents at the primary entry edge (with a view towards achieving a constant-efficiency variable speed machine), the work clearly started the process of evolution towards the asynchronous condenser

induction machine. At this point it was noticed that using the time constants characteristic of conventional machine construction in terms of airgap sizing, rotor leakage inductances and peripheral speed, the transient MMF documented in this arc machine at the primary entry zone would be significantly stronger if a second stator block occupied the inactive periphery immediately following the primary in the direction of rotor motion. Laithwaite then suggested that the airgap be maintained at a uniform dimension around the entire periphery by incorporating a short-circuiting grid in unwound primary slots rather than physically remove the stator iron. Immediately it was realized that instead of a short-circuiting grid, a tertiary winding would constitute a rotating polyphase current transformer if the machine was large enough so that the magnetization current was negligible compared to both load and transferred rotor current. This was the birth of the reactive-current-compensated induction machine.

1.2 OVEREXCITED SYNCHRONOUS CONDENSER

Historically, the over-excited DC-field synchronous condenser is the most common electromagnetic machine exhibiting leading VAR capability with high efficiency; the first large salient-pole synchronous condenser having been built by the Westinghouse Company in 1884 to provide reactive control for the Niagara Falls New York generation and long-distance transmission project. [14] Since that date, essentially no major modifications in the design of synchronous condensers were implemented with the exception that about 1910, industry saw the introduction of the turbogenerator rotor to this synchronous machine and thus two and four pole units became commonplace. As with conventional synchronous machines, design changes in the reactive compensator followed the basic trends of insulation refinement, high voltage primaries and in particular, high temperature rotor windings.

The first Westinghouse synchronous condenser had an apparent power to weight ratio of 0.02kVA/lb. using convection cooling. The state-of-the-art in synchronous condenser technology was achieved in 1973 [15] by the manufacture of a direct liquid (deionized water) cooled stator and turbo-rotor windings in addition to liquid cooling all the bearing, silver-graphite brushes and slip-rings. The voltage rating of the unit was 10, 110 V line-to-line peak and at a shaft speed of 4950 r.p.m., a continuous rating of 7 MVA was achieved yielding an overall specific power density of 1.7 kVA/lb. at an average temperature of 356^{o}F. The machine has a ninety-second overload capability of 10 MVA for which the armature copper current density is 26, 793 A/in^{2}. Other parameters are given in Table 1.1 as

Table 1.1

State of the Art Wound-Field Synchronous Condenser Electrical Characteristics

Output Rating Continuous (MVAR)	6.94
Armature Output Current (A)	560
Frequency (Hz)	165
Armature Voltage (V r.m.s.)	4130
Field Current (A)	1795
Field Voltage (V)	85
Speed (r.p.m.)	4950
Total Weight (lb.)	4202
Outside Diameter (in.)	33
Overall Length (in.)	45.5
Rotor Diameter (in.)	21.46
Active Magnetic Length (in.)	13.6
Radial AirgapLength (in.)	0.40
Total Losses (kW)	495.4
Armature Current Density (A/in^2)	18,667
Field Current Density (A/in^2)	15,885
Phase Resistance at 356°F (ohm)	0.218
Base Impedance (ohm)	7.38
Synchronous Reactance Unsaturated (P.U.)	3.44
Transient Reactance Unsaturated (P.U.)	0.496
Subtransient Reactance Unsaturated (P.U.)	0.316
Stator Leakage Reactance (P.U.)	0.174
Field Leakage Reactance (P.U.)	0.358
Zero Sequence Reactance (P.U.)	0.102
Damper Leakage Reactance (P.U.)	0.142
Specific Volume (cu. ft./kVAR)	0.00537
Peripheral Velocity (ft/sec at 4950 rpm)	465
Gyroscopic Moment (in-lb)	6070
Water Inlet Pressure (PSI)	450
Water Flow Rate (GPM)	36

they also served as a general guideline for which the tertiary windings of the 112 kW machine discussed in Chapter V were dimensioned.

The points in common between conventional synchronous condensers and the asynchronous condenser concept detailed in this thesis are as follows.

i) The rotor MMF, whether injected via slip-rings or induced to form a space-modulated brushless direct-current pattern, must exceed the stator MMF by nearly the same ratio for a given zero power factor terminal condition.

ii) The terminal performance of these two machines concerning the tradeoff between differing values of real power capability and reactive capability is nearly identical once the product of slip and magnetization Goodness factor, G is substituted for the conventional field current parameter as shown in Figure 1.2. This gives a universal indication of the extent to which leading power factor operation is practical for large mechanical power outputs as would typify an overexcited synchronous motor but applied to an eight pole self-compensating induction motor (SCIM) similar to that discussed in Chapter V. This assumes that the tertiary current phase angle has been perfectly adjusted as a function of slip along with specially designed change in pole-pitch stator laminations.

iii) The rather high temperature rises associated with an overexcited rotor windings on a synchronous condenser

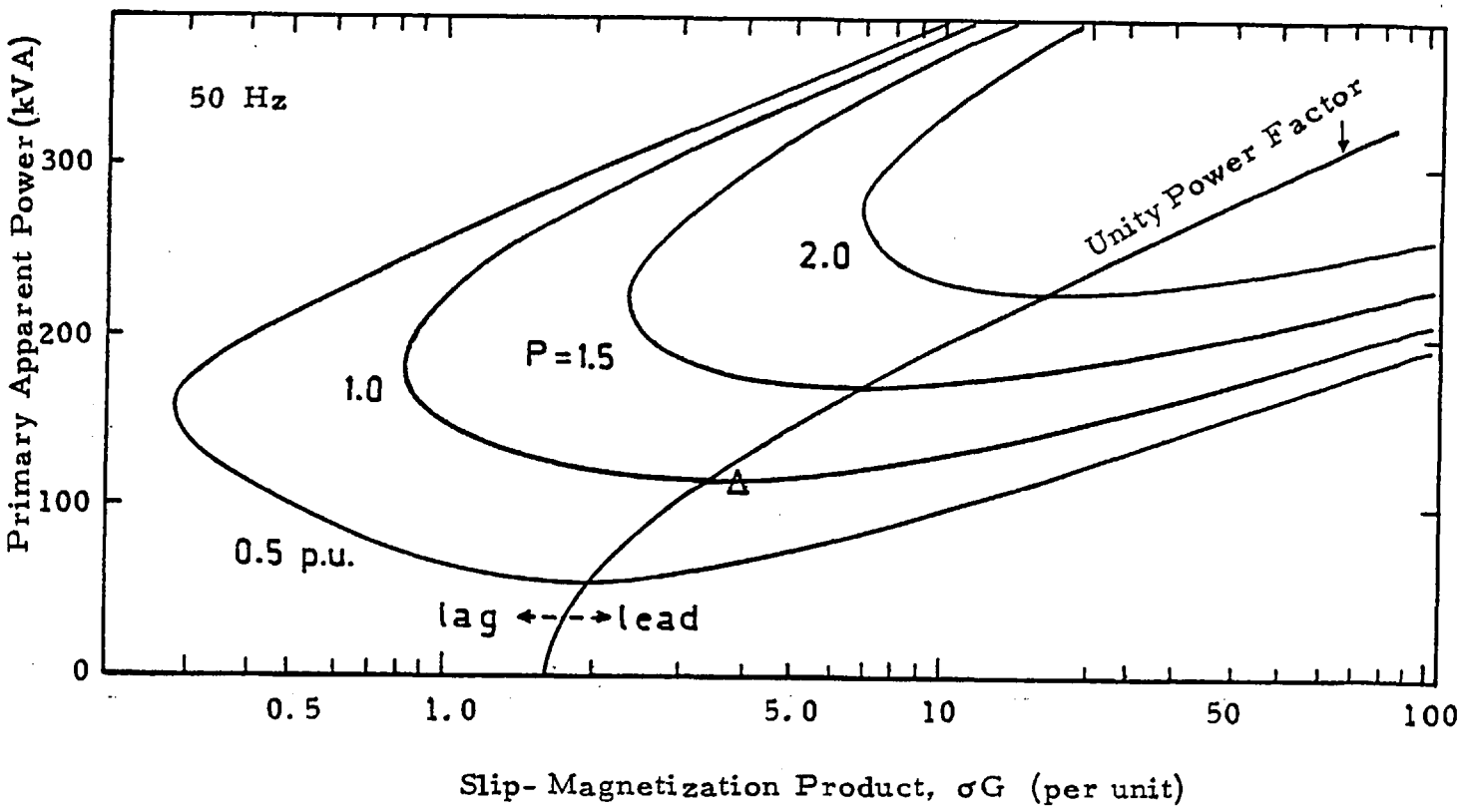

Figure 1.2 Performance of eight-pole self-compensating induction machines for different values of per unit mechanical power.

is well within all typical temperature limitations for cage-rotor constructions.

iv) The armature reaction effect of the tertiary winding on the asynchronous condenser is approximately the same strength as the armature reaction effect in a synchronous machine considering the differences in airgap sizing.

v) Current densities, time-constants and subtransient reactances for both asynchronous and synchronous types may be designed to be equal, simultaneously, assuming that a cylindrical-rotor machine is specified and damper windings are used.

The major differences between an asynchronous and synchronous condenser are of importance only at the final design stage. In essence, the process of technological evolution and evaluation is based on maximizing the similarities between two apparently different mechanisms rather than attempting to keynote only dissimilarities. Nevertheless, some of the more paramount but less general differences are as follows.

i) The ratio of the average rotor MMF to stator MMF in the brushless version will generally be less than the synchronous type for a given total leakage flux requirement because the smaller airgap of the former allows a considerable magnetization saving. However, this apparent advantage is partially offset by the effects of current natural decay which may be prominent in the asynchronous condenser with short rotor-time-constants.

ii) The asynchronous condenser requires an external regulation device such as an induction regulator, phase-shifter or semiconductor switching to maintain the output of the tertiary near a zero power factor condition as a function of slip due to the rotationally-controlled phase angle of induced voltage. This phase control is analogous to the need for magnitude control in the synchronous machine to guarantee a fixed power angle with varying system receptivity, except that in the former, the total working kVAR output must be regulated whereas exciter control is usually under 2% of the armature output.

iii) The asynchronous type will have a larger steady-state and transient reactance per peripheral meter than the synchronous type based on typical designs for dimensioning airgaps but assuming the same rotor volume.

iV) The unsaturated subtransient reactance (X'') of the asynchronous condenser will usually be larger than the negative sequence reactance (X_2); in the synchronous condenser they are generally equal.

v) Both the subtransient reactance and negative sequence reactance of the asynchronous condenser in relation to the positive sequence reactance (X_s) will be larger than the ratios $X_2:X_s$ and $X'':X_s$ characteristic of the synchronous version.

1.3 STATIC DOUBLE INDUCTION REGULATOR

With a few of the characteristics of the asynchronous condenser as mentioned in the previous two sections, early in the evolution of this machine, two issues remained paramount to successful and efficient operation, that were largely solved by considering several of the electromagnetic peculiarities of the moving-coil induction regulator, a relatively new device to heavy current technology. [16] This reactive potential divider is termed a static device despite the fact that it uses a moving coil but this does not have any continuous motion and its setting is only changed according to different load conditions. In particular, both single phase and polyphase versions exhibit three important traits relevant to the rotating induction machine with a tertiary winding that is the subject ofdiscussion.

i) The moving-coil is a short-circuited coil that is inductively fed by the primary winding, carries current loadings comparable to the primary and yet incurs no appreciable braking focus or excess losses on the primary; the overall efficiency of these units for large kVA sizes is typically 97%. This is explained by the fact that all such regulators have the two, identical halves of the main winding (termed primary and secondary) wound in opposite directions which largely neutralizes any mechanical forces on the coil (termed the tertiary).

ii) The regulator exploits a phenomena which is usually considered to be an imperfection and minimized in large electromagnetic designs -- that under certain regulation conditions, the primary and secondary magnetic

fluxes buck each other and instead of exclusively flowing around the high permeability magnetic core, the common magnetic path is the large airgap in the center of the core.

iii) The voltage on either primary or secondary winding may exceed the mains terminal voltage across the two windings, connected in series opposing.

The most well developed treatment of this phenomena was explained by Rawcliffe and Smith [17] who, using only a lumped parameter equivalent circuit approach (without a non-linear magnetic field analysis or a numerical determination of the precise airgap reluctance) correctly predicted the hitherto unsolved problem of low-end and high-end performance. More important, this analysis also pointed to the physical insight that inspired all further development of the asynchronous condenser machine and paraphrasing from [17]

> " . . . on no-load there are two magnetizing currents in the regulator one in the moving coil and one in the main winding; and in many senses the moving coil is more properly regarded as an auxiliary primary inductively fed, rather than as a short-circuited secondary winding. . . . When the moving coil is regarded as an extra primary winding it becomes natural that, on-load, it should provide the additional ampere-turns due to the load current, in the same way as a primary winding normally does. This was confirmed by many tests. Since the main primary winding of the regulator cannot exert any net ampere-turns on the main magnetic circuit, the extra primary does so instead."

A new electromagnetic mechanism had been "discovered" nearly two decades after such devices were first produced commercially, for as Rawcliffe proved, the mains current in ampere-

turns. This was clearly the world of parallel magnetic circuits for which iron and air were equal contenders for providing a main magnetic circuit despite large differences in permeance. Only one question Rawcliffe left unanswered for the next generation of engineers. What would happen if this moving coil were given a continuous, high-speed motion in a polyphase system of such induction regulators?

1.4 POLYPHASE SHUNT COMMUTATION

Concurrent with the widespread application of slip-ring AC machinery such as the synchronous condenser throughout world power systems at the generating end, the utilization of electric power saw the rapid application of the mechanical commutator to AC machinery and its use as a frequency changer. The first pervasive emergence of the AC commutator was to railway traction drives in Europe at 16 Hz about 1906 followed by Lamme's success with series-compensated traction motors in America at a 25 Hz frequency. [18] These were very important advances for the AC machinery because it showed quite conclusively that despite the added high frequency switching transients encountered with the AC traction motors, high efficiencies and high specific power densities were obtainable to the extent that the machine still remains a serious industrial competitor to the DC traction machine.

Within a decade after the introduction of the AC commutator single-phase traction machine, commutation was sufficiently understood that industry was soon building polyphase commutator machines and at 50 Hz frequencies such as the Schrage motor [19], the Type NS (Nebenschluss) discharge-winding with induction regulator speed control [20], and most important the shunt-commutator, adjustable power-factor and adjustable-speed motor with a range of 3:1 [21]. The latter is the main subject of discussion because this machine is first and foremost an induction machine for which the commutator is acting as a frequency changer; both speed and power factor control are obtained by adjusting the brush position and spacing, whereas the Type NS machine relies on external voltage control to the rotating

armature winding. The phasor diagram for the former is shown in Figure 1.3 for sub-synchronous speeds. The key points of interest in this machine are that:

(i) unity power factor will occur at an 80% efficiency in machines as small as 12 kVA at 50 Hz,

(ii) essentially it is an inverted induction machine for the primary is on the rotor and the slip-frequency secondary is stationary,

(iii) the rotor also carries a conventional lap winding (in the same slots as the primary) which is brazed to a DC-type commutator, and

(iv) the primary is fed at mains frequency via slip-rings while the secondary is fed from the commutator using sets of polyphase brushes.

The characteristics of this machine which are of special interest to the asynchronous condenser technology are as follows:

(i) Unity or leading power factor operation up to cos $\emptyset$ = -0.85 of the entire machine is possible with Goodness factors as low as 50.

(ii) The lap winding injects an EMF into the secondary to cause the latter to develop a CEMF of almost equal value; the differences between these two voltages determining the amount of speed control achieveable and the differences in phase between the two allowing power factor adjustment.

(iii) All the rotor slots carry two sets of heavy current windings and yet it is the rotor slotting geometry that demands a smaller slot cross-sectional area in compari-

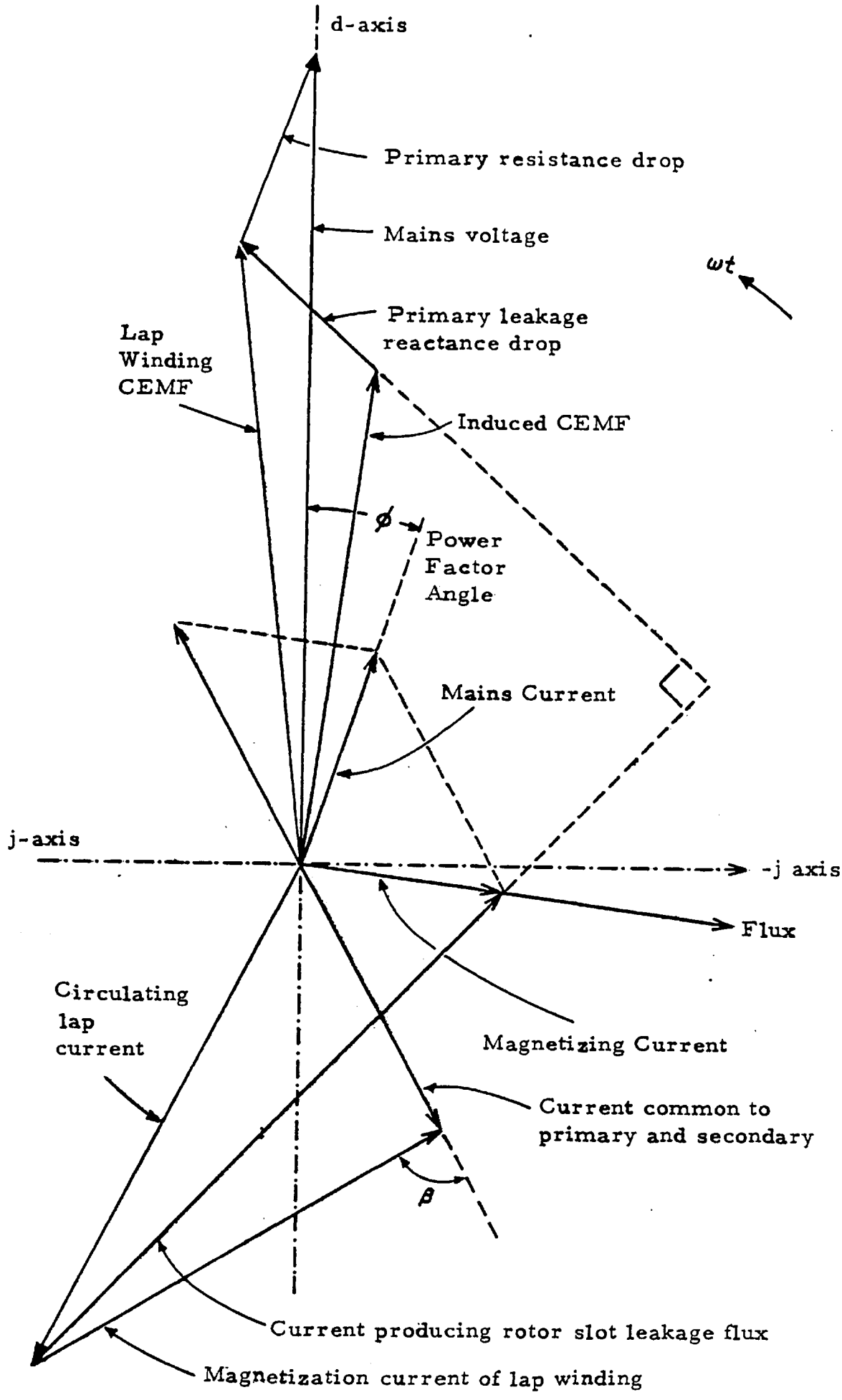

Figure 1.3 Phasor diagram of a shunt AC commutator machine at brush angle β.

son to that available on the stator; whereas in the asynchronous condenser, the slots that carry two sets of windings are the stator slots and this is only present in the overlap region, typically fourteen slots.

With these characteristics of the commutator machine, it was realized that fundamentally there should be no reason why inverting primary and secondary positions would not produce an adjustable power factor device. The point to note is that the commutator is not basic to adjustable speed or reactive control. Rather, the only new major penalty that the asynchronous condenser must accrue is an additional magnetization loss for the tertiary winding (with the rotor setting up this part of the airgap field), a reactive loss that the mechanical commutator circumvents.

1.5 INDUCTION TRANSIENT OVERSPEEDING

A Formal mathematical treatment of this topic is given in Chapter VII with both analytical and numerical techniques, but transient overspeeding is introduced here since the physical understanding surrounding this phenomena was instrumental in explaining the operation of the self-compensation induction machine (SCIM). In essence, if any cage induction machine has any significant rotor inductance and if the accelerating torque is unusually high (due to either sudden, full excitation or a lower than average mechanical load or inertia), then the forced rate of change of load current can exceed the natural decay of load current and an effective time lag of current exists in the secondary circuit; not accounted for by the steady-state equivalent circuit. The process can exist in both the high-slip and low-slip regions, [22] the latter implying that at synchronous speed (and in a symmetrical machine) the secondary is still carrying substantial currents which will persist well into supersynchronous operation. Considerable hunting usually exists around the running-light point which for large machines may last up to three or four cycles. In general, two pole cage machines are the most prone to transient overspeeding as depicted by the larger $X_2:R_2$ ratios (based on equivalent circuit steady-state parameters) they possess as compared to multipolar types. Figure 1.4 gives a general guide to how the open-circuit time constant of cage machines vary according to rating for two, four and twelve pole machines up to the megawatt range [23]. While this does not indicate the number of cycles of hunting, it may be used to determine the relative degree of oscillation among units of equal voltage excitation and inertia constant.

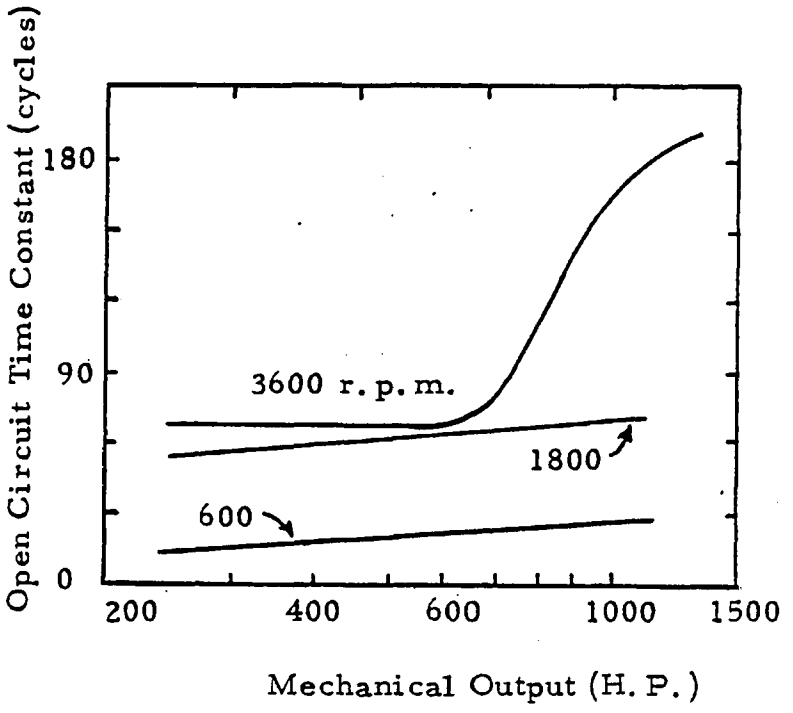

Figure 1.4 Open-circuit time constant for standard cage-rotor induction machines with 2300 Volt primary windings for two, four and twelve pole designs from the same manufacturer.

The initial interest in supersynchronous hunting stemmed from the thought that if all the rotor currents could be instrumented for magnitude and phase during a transient swing, then if the naturally occurring current pattern could be reproduced on a continuous basis along with a small phase-shift, this would serve to be the ideal MMF distribution for a unity power factor induction machine. Recently, there has been renewed interest in transient overspeeding from the analyst's approach since computer calculations are able to simulate the exact effects of rotor and stator slotting (or "grinding") on among other aspects, low-inertia start-up. Figure 1.5 shows the results of a digital simulation based on the serraphile function given in [24] for a no-load acceleration, two different types of slotting geometry and two excitation voltage magnitudes. A cage machine rated at 4 kW, four-poles with 36 stator slots and 10 rotor slots/pole/phase primary had a 7/9 chording. It is seen that one overspeed exists even for the half-voltage excitation irrespective of the slotting refinements (stator and rotor are identically simulated in shape, that is, the same serraphile function is used in each part of Figure 1.5).

At full excitation, the more gradual slotting (labelled A=0.5) goes through synchronous speed three times, while the coarser, open-sided slotted machine (A=1.0) exhibits transient overspeeding twice. Some of the effects especially at high slips are explained mathematically by Section 3.3 Synchronous Rotor Harmonic Interaction, while for the main part, this slotting geometry variation may be understood to alter the rotor leakage inductance significantly.

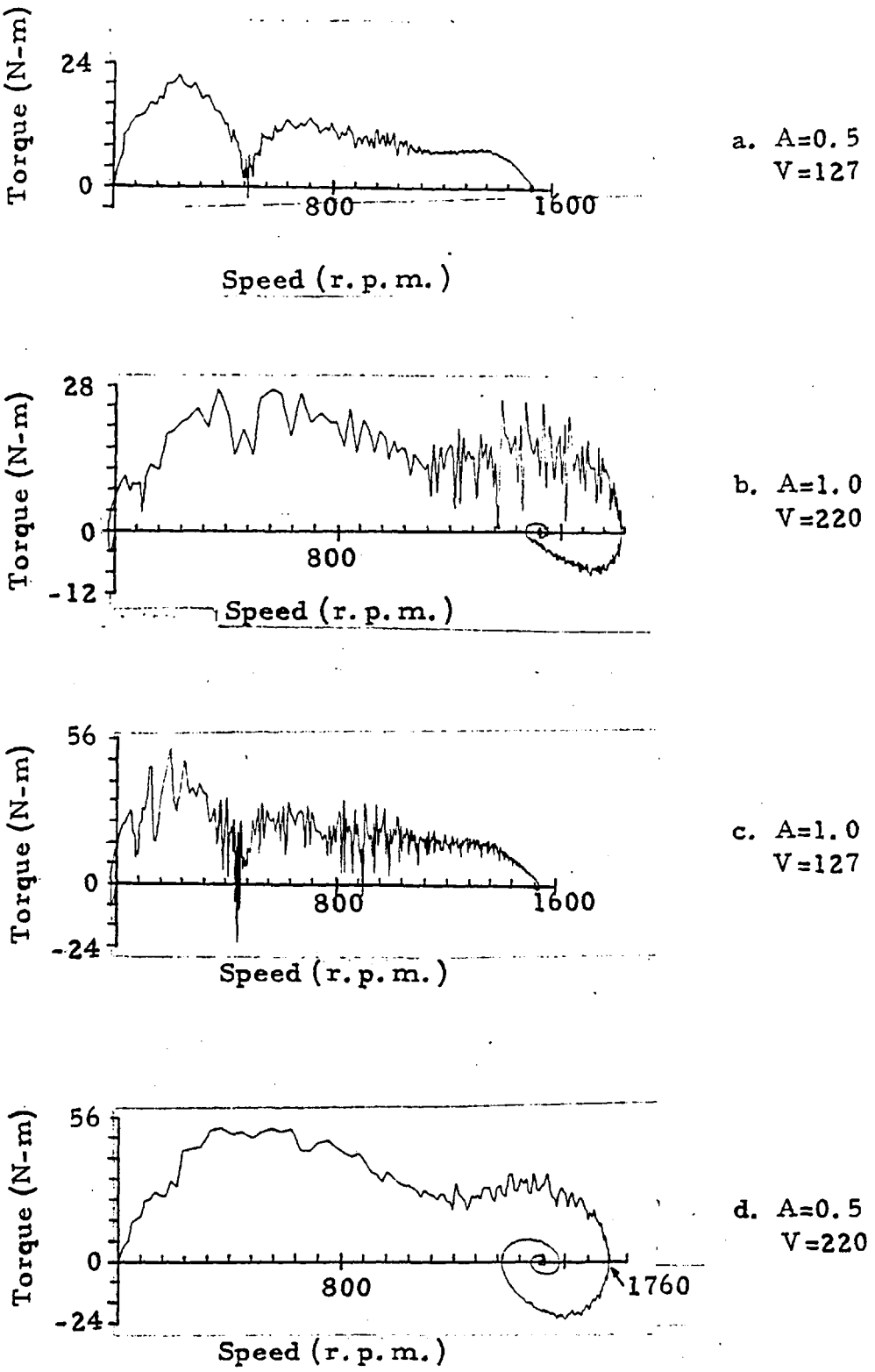

Figure 1.5 Transient overspeeding of a 4 kW, three-phase cage machine suddenly excited with 50 Hz for different values of applied voltage and slot geometry all with no load torque; from [24].

The preceeding section on transient overspeeding should have served to suggest that some mechanism of electromagnetic "memory" of the cage rotor current pattern is desireable, for example large amounts of rotor leakage inductance. Recently, academic research has focused on a "magnetic" machine which utilizes, in effect a current pattern memory by nature of the rotor material which is a hard-magnetic material such as barium-ferrite. [25-26] This is essentially a permanent magnet machine but most important it relies on the continuous remagnetization of this moving high-retentivity magnetic material to produce a new synchronous pole-pattern every revolution according to whatever shaft speed it is driven at. It has been named the Roesel generator and has been designed to produce constant frequency at variable speeds up to a range of 2:1. This is a completely brushless machine with the armature winding being stationary and the barium ferrite material rotating about the outer periphery in a narrow band. As depicted in Figure 1.6 the most novel feature is that the stator laminations have 44 mechanical degrees removed from the polyphase armature winding slotting and wound with a high-current AC exciter coil to effect magnetization.

The concentrated exciter coils use the same frequency as the alternator output rather than direct current. In operation, a magnetic "recording" of the AC exciter field is reproduced in the ferrite layer. When a complete rotor revolution is made within an integral number of alternating polarity periods of the exciter's alternating current, an integral number of magnetic poles of alternating polarity (and negligible constant polarity) are retained by sectors of the ferrite band. The

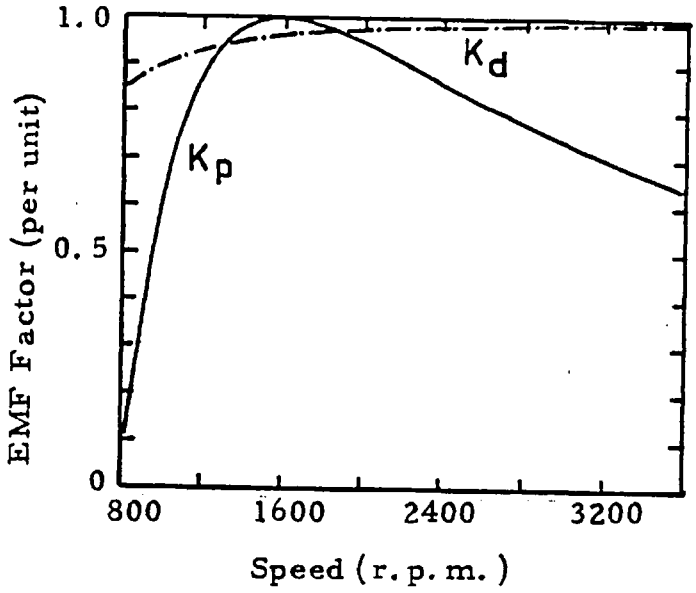

Figure 1.7 Pitch and distribution factors for a constant-frequency, variable-speed 60 Hz Roesel generator from [26].

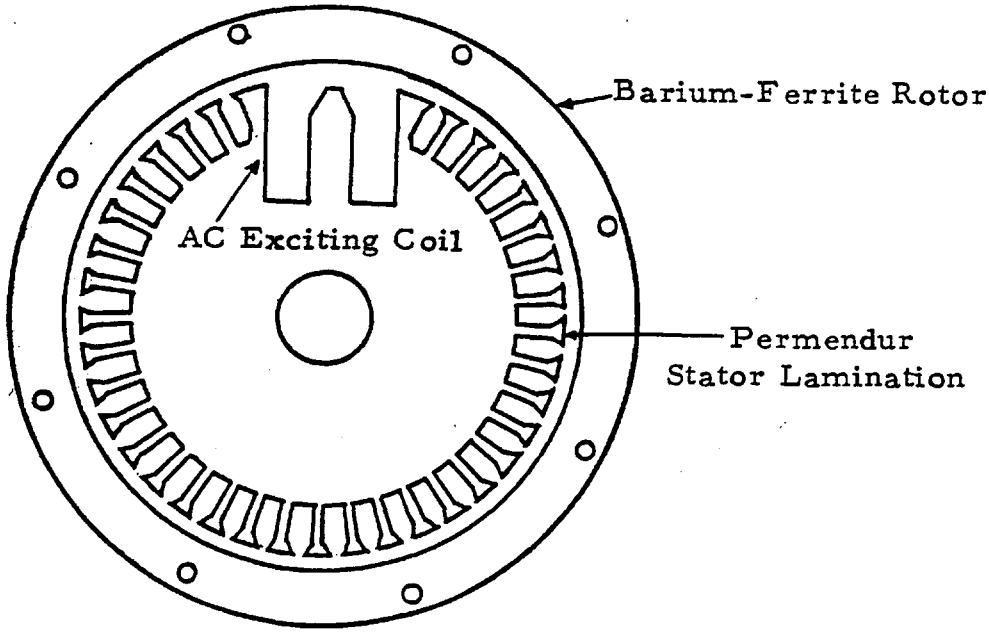

Figure 1.6 Core laminations for a Roesel generator with magnetic rotor.

continuous shifting of the "printed" poles on the rotor appears as slipping the poles backward and increasing their peripheral length, when for example the speed is increasing. The amount of ferrite being remagnetized increases as the speed departs from the preferred synchronous speed (according to the chording and pitch design). In the limit there will exist a speed, at which the narrow sector which is not remagnetized oppositely disappears, so that there is one less pole around the periphery. The inventor has called this critical state an "odd pole synchronous speed".

While the rate of flux cutting the armature remains fixed for any shaft speed, this does not, however, keep the generated terminal voltage constant due to the rather drastic change in pitch factor as shown in Figure 1.7; the distribution factor remains reasonably constant as a function of speed.

Present information on Roesel generators indicates that power densities as high as 0.014 kVA/lb. have been achieved in the 1-10 kVA range for output frequencies of 400 Hz at unity power factor. Unlike the aforementioned synchronous condenser and shunt AC commutator motor technology, this generator constitutes a true-space transient phenomenon. Its emergence and limitations combined with the earlier induction experiments by Laithwaite [13] on arc-shaped primaries and continuous wound-rotors served as the cornerstone for development of the first Theta-Pinch design -- an electromagnetic memory machine.

1.7 STATE OF THE ART

The initial impetus for research on reactive compensation integral to induction machines was aimed at only linear machines but throughout the development it was realized that many of the electromagnetic techniques applied in linear version would be consistent with reactive enhancement in rotating machinery as long as certain reservations on either power to weight ratio or temperature rise limitations could be altered. While the rotating brushless induction machine has been hailed as the workhorse of modern electric utilization due to its robust construction, asynchronous running, self-starting and regulation free operation, one serious limitation has always been evident in that both efficiency and power factor are very sensitive to mechanical load variations assuming a constant voltage supply. These characteristics are shown in Figures 1.8 and 1.9 for a 2kW rotary cage machine and three different excitation voltage magnitudes. Figure 1.10 shows the maximum typical efficiency and power factor of standard cage machines as a function of mechanical output on constant voltage. [27]

A wealth of information now exists on induction motor efficiency and power factor improvement; the most recent concentrate on thyristor phase-chopping of the input excitation to effect a type of voltage (and thus magnetization) control. However, none of these techniques are discussed or used in this thesis for it is felt that they do not focus on fundamental electromagnetic problems but rather minor constructional or operational changes in conventional, symmetrical machine design such as increasing core length, copper volume, change in lamination steel permeability characteristics or slotting geometry.

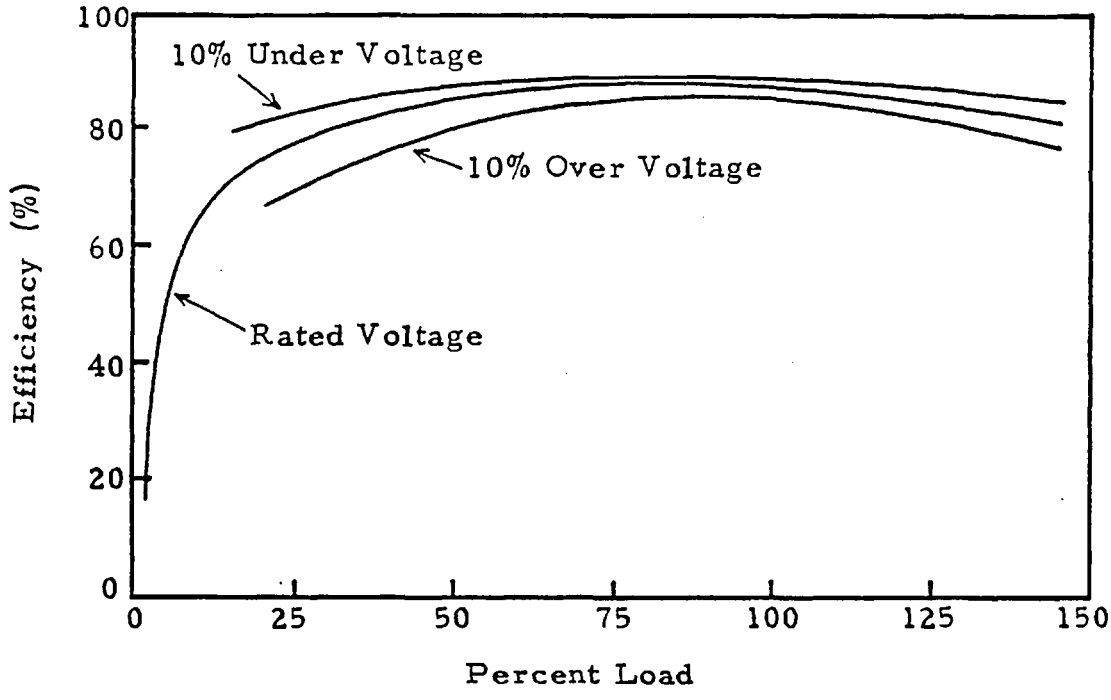

Figure 1.8 Effect of Line Voltage on Efficiency of Standard Unit

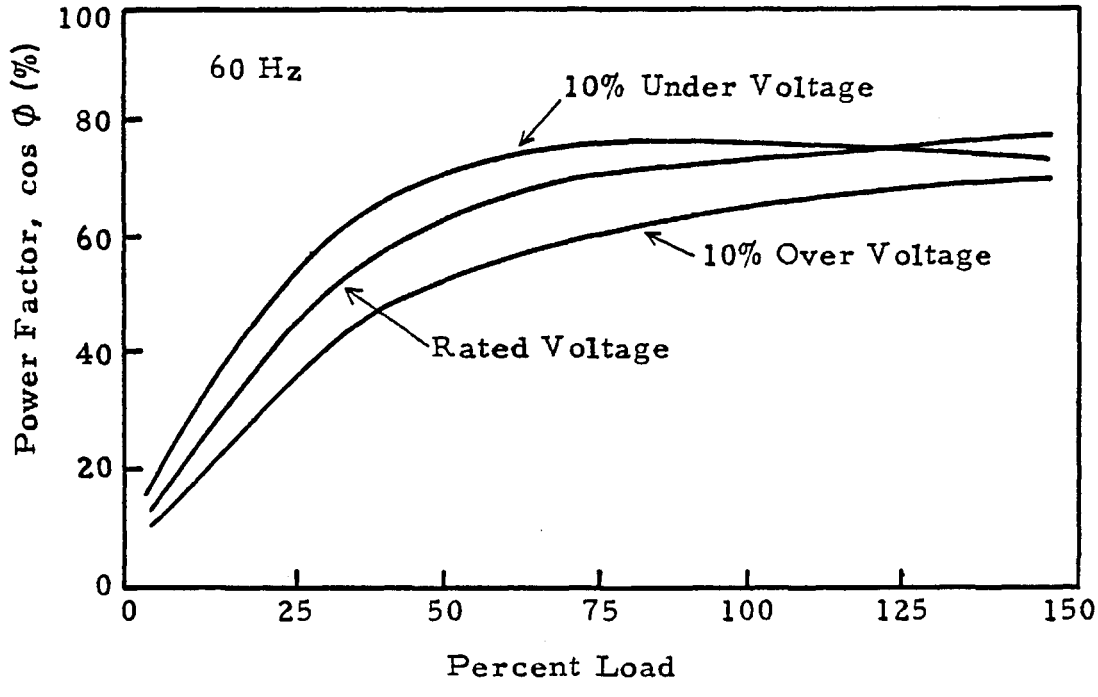

Figure 1.9 Effect of Line Voltage on Power Factor of Standard Unit

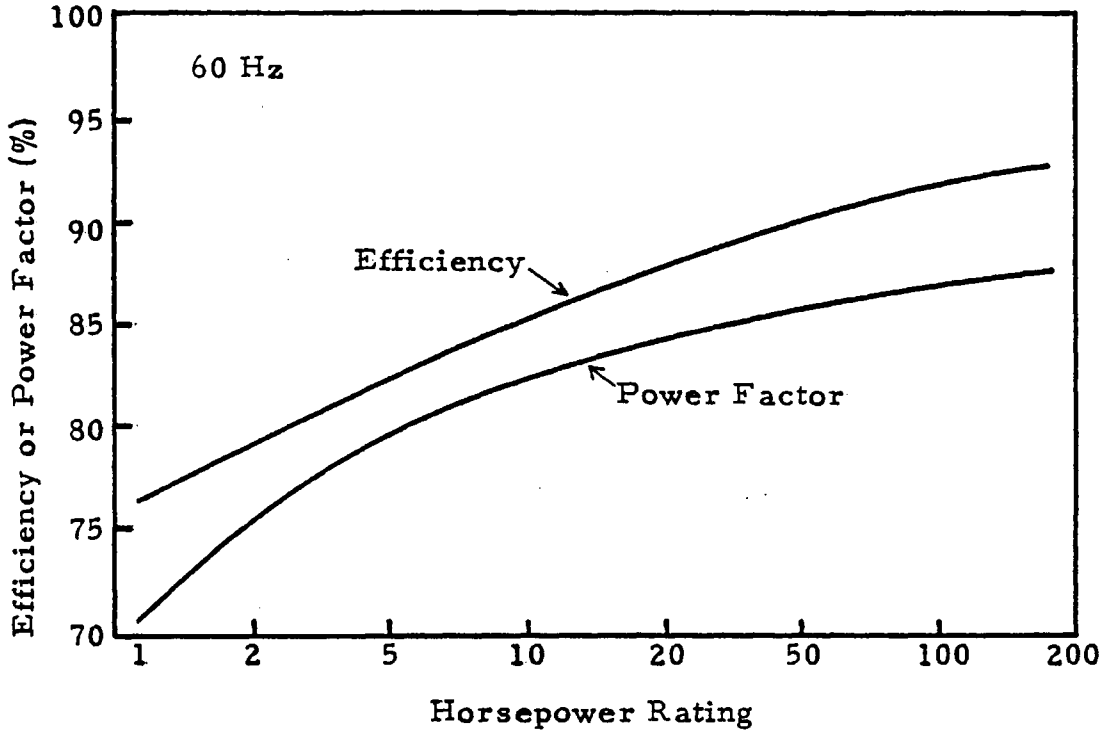

Figure 1.10 Efficiency and Power Factor versus Rating of Standard Units

Based on the experimental work and theoretical framework existing on the self-compensated, dual winding induction machine (SCIM) explored in this thesis, the concept of applying asynchronous condenser windings to rotary machines has yielded an average 15% improvement in terminal power factor for 500 H.P. size units as compared to symmetrically-wound single-primary cage machines. Figure 1.11 shows the envelop of the maximum attainable power factor capability as a function of mechanical loading using the Theta-Pinch method discussed in Chapters IV and V. This presents a four-pole, 60 Hz design concept in one-repeatable section around the entire machine periphery and is based on the results of the 112 kW, 50 Hz, eight-poles in two repeatable sections, SCIM unit developed in the laboratory. The amount of extrapolation for this 500 H.P. prediction is negligible for both machines have a rotor active volume differing by only 12% based on the change in operating speeds and copper temperatures. It has been assumed that new laminations have been specified for the SCIM units.

The only major penalty incurred in the SCIM design is a 3 to 5% loss in efficiency at the 373 kW load point. Utilizing Class F (90^{o}C rise) insulation throughout both machines, the SCIM unit would require the next larger frame size for both the additional spatial core flux and to accommodate the extra stator slots carrying the tertiary winding. This added manufacturing cost is entirely offset by the life-time reactive power penalty saving for which is presently assessed at $150/kVAR for drive motors by the Electric Power Research Institute, USA.

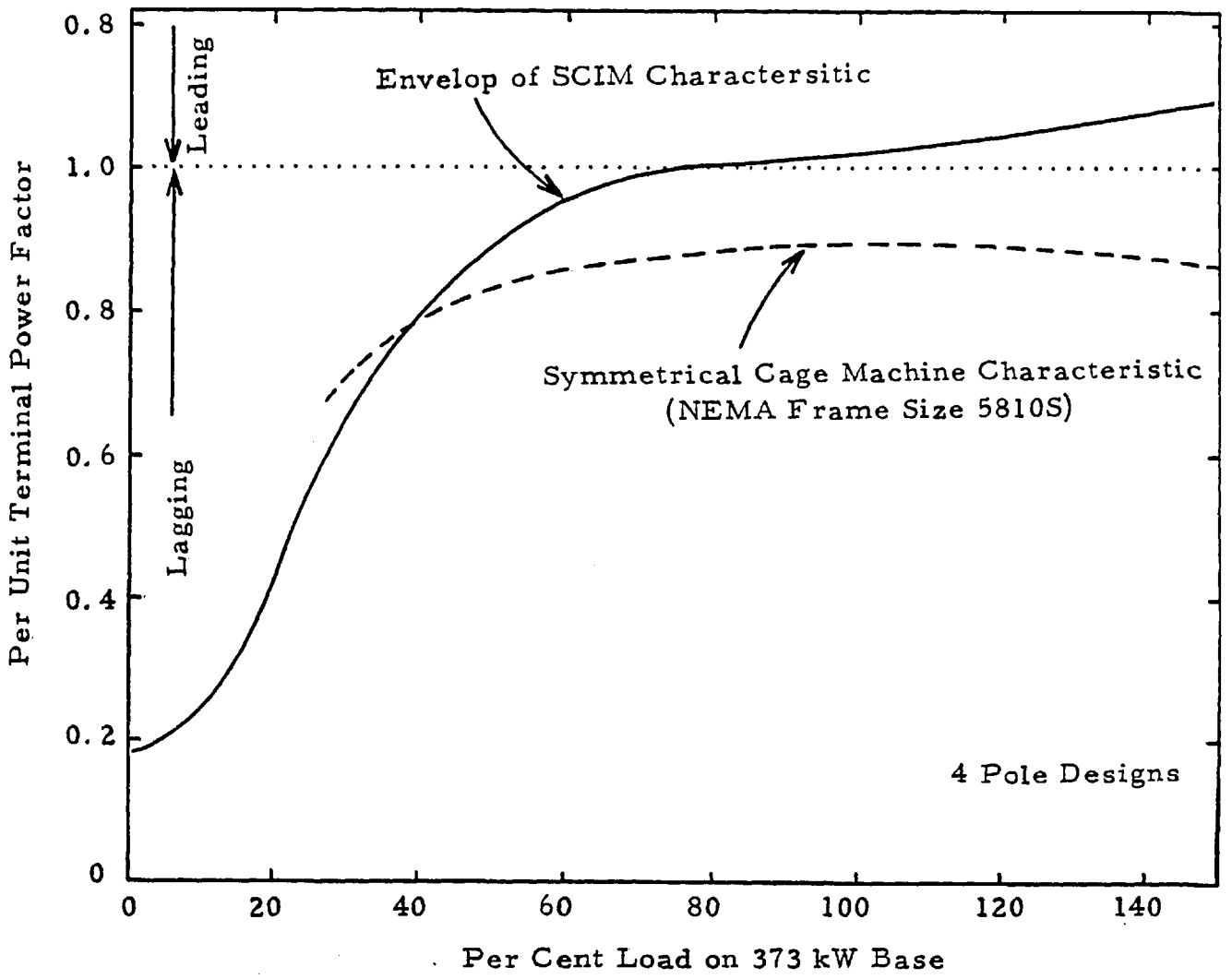

Figure 1.11 Terminal power factor versus mechanical loading for a self-compensated induction motor (SCIM) and a conventional symmetrically-wound single-winding induction motor; both units are three-phase, 60 Hz, 500 H.P. with cage-rotors.

1.8 REFERENCES

[1] F.C. Williams, E.R. Laithwaite and L. Piggott, "Brushless Variable Speed Induction Motors," Proc. IEE, Vol. 104A, pp. 102-118, April 1957.

[2] F.C. Williams, E.R. Laithwaite and J.F. Eastham, "Development and Design of Spherical Induction Motors," Proc. IEE, Vol. 106A, pp. 471-484, December 1959.

[3] E.R. Laithwaite, Development and New Applications of Induction Motors, Ph.D. Thesis, Manchester University, 1956.

[4] D.E. Hesmondhalgh and D. Tipping, "General Method for Prediction of the Characteristics of Induction Motors with Discontinuous Exciting Windings," Proc. IEE, Vol. 112, pp. 1721-1735, September 1965.

[5] F.C. Williams, E.R. Laithwaite, J.F. Eastham and W. Farrer, "Brushless Variable - Speed Induction Motors using Phase Shift Control." Proc. IEE, Vol. 108A, p. 100, 1961.

[6] F.C. Williams, E.R. Laithwaite, J.F. Eastham, and L.W. Piggott, "The Logmotor - A Cylindrical Brushless Variable Speed Induction Motor," Proc. IEE, Vol. 108A, No. 38, pp. 91-99, April 1961.

[7] E.R. Laithwaite, The Engineer in Wonderland, English Universities Press, 1967, p. 170.

[8] R.H. Park, "Two-Reaction Theory of Synchronous Machines - Part I," Trans. AIEE, Vol. 48, pp. 716-730, July 1929.

[9] E.R. Laithwaite and S.B. Kuznetsov, "The Asynchronous Condenser - A Brushless Adjustable Power Factor Induction Machine," IEEE Trans. Power Apparatus and System, Vol. PAS-99, No.6, pp. 2422-2432, 1980.

[10] E.R. Laithwaite and S.B. Kuznetsov, "Reactive Power Generation in High-Speed Induction Machines by Continuously Occurring Space Transients," IEEE Trans. Magnetics, Vol. MAG-16, No. 5, pp. 716-718, 1980.

[11] E.R. Laithwaite and S.B. Kuznetsov, "Development of an Induction Machine Commutated Thyristor Inverter for Traction Drives," IEEE Trans. Ind. Appl., Vol. IA-17, No. 2, March/April 1981.

[12] E.R. Laithwaite, "The Goodness of a Machine," Proc. IEEE, Vol. 112, No. 3, pp. 538-541, March 1965.

[13] E.R. Laithwaite, "Rotor Windings for Induction Motors with Arc Shaped Stators," Proc. IEE, Vol. 111, No. 2, pp. 315-

321, February 1964.

[14] C.F. Scott, "High Voltage Power Transmission," Trans. AIEE, Vol. 15, 1898, pp. 673-718.

[15] T.E. Brown and R.F. Grahl, "Design, Development, Fabrication and Testing of a Synchronous Condenser for a High-Power Three-Phase Traction Drive," Garrett-AiResearch Corporation for U.S. Department of Transportation, NTIS Document FRA-ORD-76-266 or PB284397, December 1976.

[16] E.T. Norris, "The Moving Coil Voltage Regulator," Jour. IEE, Vol. 83, p.1, 1938.

[17] G.H. Rawcliffe and I.R. Smith, "The Moving Coil Regulator: A Treatment from First Principles," Proc. IEE, Vol. 104A, pp. 68-76, February 1957.

[18] B. Lamme, "Different Methods and Systems of Using Alternating Current in Electric Motors," Trans. AIEE, Vol. 21, 1904.

[19] H.K. Schrage, Elektrotechnische Zeitschrift, Vol. 35, p. 89, 1914.

[20] K.K. Schwarz, "Die Neuere Entwicklung des Staendergespeisten Drehstrom-Nebenschluss-Kollektormotors," Elektrotechnik und Maschinenbau, 1953, Vol. 53, p. 85.

[21] F.J. Teago, "Test Results Obtained from a Three-Phase Shunt Commutator Motor," Jour. IEE, Vol. 60, pp. 328-338, 1922.

[22] J. Bendl, "Physical Analysis of Transient Phenomena after Connection of a Braked Induction Machine to Voltage," Acta Technica CSAV, Vol. 21, No. 3, pp. 270-287, 1976.

[23] C.F. Wagner, "Induction Machines," Electrical Transmission and Distribution Reference Book, Westinghouse Electric Corporation: Pittsburgh, 1964, p. 193.

[24] H. Rausch, "Influence of Two-Sided Slotting Upon the Non-Stationary Operating Behavior of Induction Machines," Proc. Intern. Conf. on Electrical Machines, Athens, Greece, September 1980, pp. 1818-1825.

[25] J.F. Roesel, "Electric Power Generator," U.S. Patent 3, 521, 149; July 21, 1970.

[26] L.R. Herman, "The Roesel Generator - Constant Frequency with Variable Speed," Paper No. A76-035-6, IEEE Winter Power Meeting, New York, January 25-30, 1976.

[27] Federal Energy Administration, Energy Efficiency and Electric Motors, Office of Industrial Programs, Report for Contract No. CO-04-50217-00, August 1976, Washington, D.C., pp. 14-71.

II. EXIT EDGE EFFECTS

1. SHORT-PRIMARY MACHINES

The idea of improving the power factor of brushless induction machines has often intrigued the electrical engineer and like any other problem in science two methods of solution appear evident. First, one may choose to rectify the problem by attacking the underlying cause of concern or alternatively, as second best one may devise some novel scheme to circumvent the apparent difficulties experienced by the user without actually attacking the crux of the problem. However, as far as the consumer is concerned, the methodology is unimportant; rather, only the end product is vital--what is the terminal power factor? The approach taken in this first series of tests is the latter for we have allowed the LIM proper to have a notoriously low power factor and continue to have excess rotor copper losses but have made use of this otherwise wasted exit-end magnetic energy and oriented it (i.e., phased properly) so as to improve power factor rather than another parameter such as efficiency which has remained constant.

A. Background of Experimental Apparatus

Conversion of the SLIM to a high Goodness machine (G≈20) with a uniform pole-pitch winding having 7 poles concentrated on the secondary conducting material. The stator block with its 48 coils that was used for the described experimental program had previously undergone testing on the Imperial College High Speed Test Rig as a 4-8 change pole motor [1]. It utilized a 1.58 mm thick aluminium sheet annulus secured to a 19 mm thick solid steel rotor disc. Since the leading power factor SLIM concept prefers a rotor with a long time constant which necessitates a highly conductive rotor, therefore the first major construction work consisted of fabricating in situ, a 9.5 mm thick aluminium annulus, 2.13 m in diameter to replace the 1.58 mm thick annulus. Most important, all of the joints on the new rotor were T.I.G. welded which insured a continuous secondary circuit and thus no extraneous rotor induced transients appeared on the stator voltage and current waveforms.

The stator block of the SLIM, which was shaped in a 90^{o} arc, was first reconnected as a conventional linear motor comprising 7 poles of uniform pitch and having an equivalent synchronous linear speed of 46 mi./hr. with 50 Hz excitation. The High Speed Test Rig is portrayed in Figure 2.1 and the details of the new SLIM experimental machine are given in Table 2.1. A 120 kVA frequency changer set is used for excitation in the range of 25-150 Hz, which in effect allows motoring up to nearly 140 mph with this particular winding connection. For dynamic testing of the SLIM, a 15 k.w. DC dynamometer is attached to the Disc Rig central shaft and thus sypersynchronous (braking) operation as well as plugging of the SLIM was available.

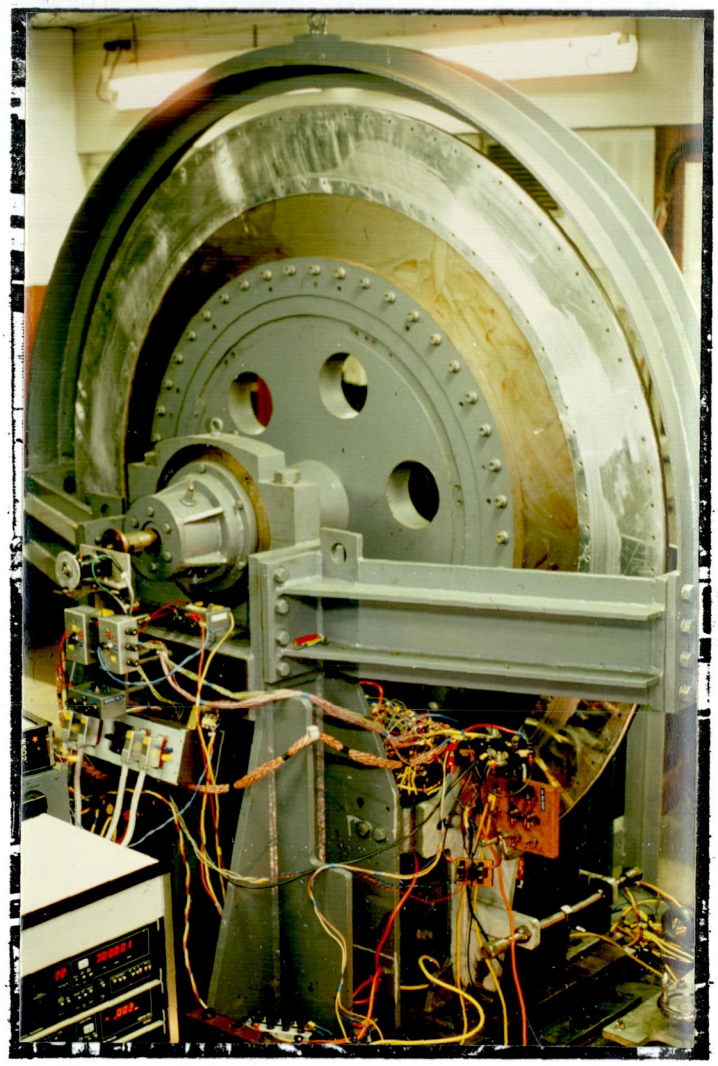

Figure 2. 1 The dynamic test rig used for evaluating short-primary effects in specialized induction machines.

Table 2.1

Characteristic Parameters of the Experimental SLIM Connected as a Uniform Pole Pitch Machine

Longitudinal Core Length	1.46 m
Transverse Core Width	0.157 m
Stator Block Depth	0.120 m
Slot Width	0.0.43 m
Slot Depth	0.0381 m
Slot Pitch	0.0270 m
Aluminium Annulus Thickness	0.0095 m
Aluminium Width	0.229 m
Steel Disc Thickness	0.019 m
Disc Moment of Inertia	510 N-m-sec^2
Operating Entrefer Distance	0.010 m-0.012 m
Number of Poles	7.2
Total Number of Coils	48
Turns/Coil	12
Mean Length of Coil	11.54 m
Slots/Pole/Phase	2.5
Total Number of Slots	54
Pole Pitch	0.2025 m
Coil Span/Pole Pitch	0.80
Aluminium Resistivity (20°C)	3.25x10^{-8} Ω-m
Russell and Norsworthy Factor	1.933
Total Stator Copper Cross Section/Phase	7.88x10^{-6} m^2
Synchronous Speed (50 Hz)	208.3 RPM
Peak Output Torque (50 Hz, 50 A/ϕ)	460 N-m
Moment Arm to Center of Motor	0.9545 m

To correlate experimental results with theoretical predictions more precisely, an extensive system of airgap search coils was installed over every stator slot of the block. This was accomplished by machining search coil wire surface-grooves longitudinally down the center of every stator tooth with a 0.5 mm cutting wheel. In comparison to conventional tooth flux measurement coils, this technique is superior in that any leakage flux pickup is minimized in addition to having the resolution of a slot pitch. Figure 2.2 shows the tooth geometry.

To insure that the stator-to-rotor airgap can be brought down to nearly the same size as in conventional rotary machines, a miniature cutting lathe was specially fabricated and attached to the High Speed Test Rig to allow the aluminium annulus to be skim-machined in situ. This resulted in an airgap of nearly 1.0 mm (mechanical); this remains fixed during all of the very high speed tests.

The first on-line evaluation commenced on April 7, 1978 by evaluating the uniform pole-pitch SLIM performance. The Goodness factor was subsequently substantiated as being between 15 and 20, and in comparison to tests done in 1975 with the very thin aluminium rotor [2], the thrust per ampere saw a remarkable rise of better than fourfold. From the electromagnetic standpoint, the ultra-violet recordings of search coil voltages showed that the airgap flux was almost perfectly free of harmonic fluxes even at the minimum gap setting. Moreover, the SLIM now possessed an overload thrust capability at 50 Hz excitation that was in excess of the loading capacity of the DC Dynamometer at this one speed.

The final tests with this uniform 20.3 cm pole-pitch winding indicated that the machine has a peak power factor-

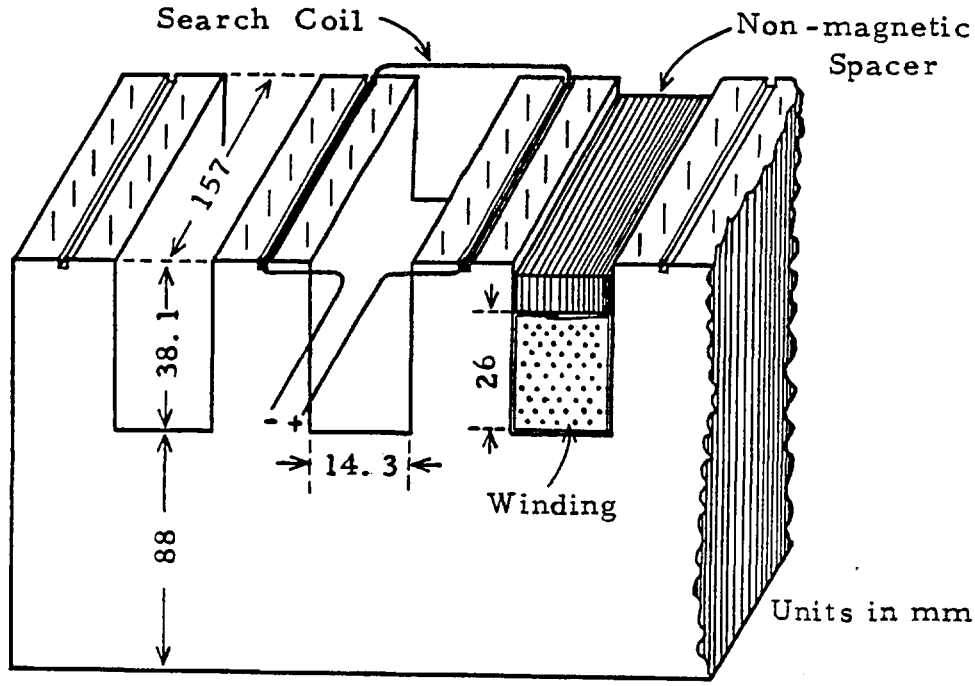

Figure 2. 2 Primary block tooth geometry for the longitudinal-flux, laboratory machine with search coil slotting.

efficiency product (at 50 Hz) of 0.4 and furthermore, the use of an unlaminated steel rotor disc seemed to incur no measureable excess losses. The data from these first series of tests is summarized in Figure 2.3.

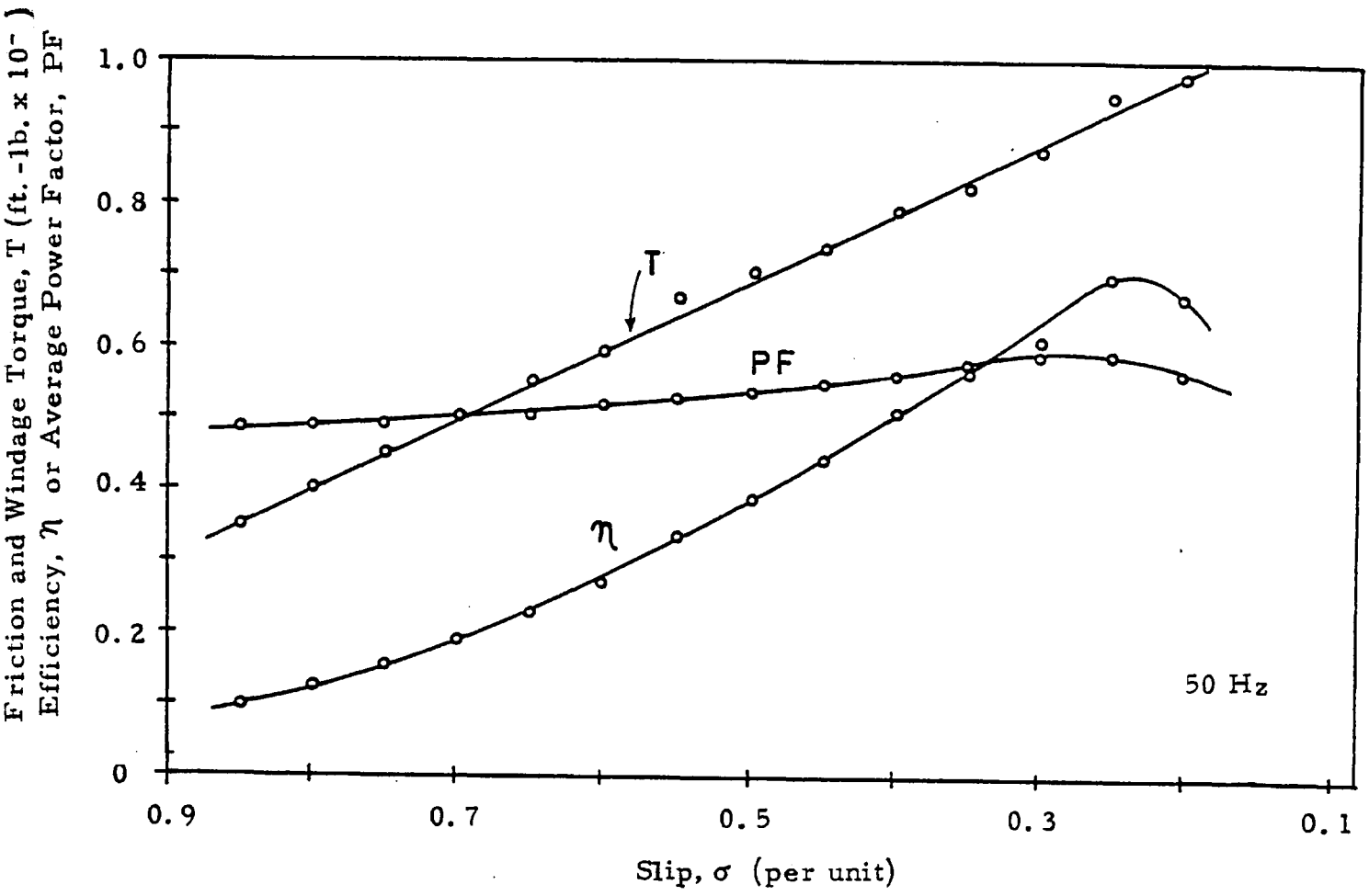

Figure 2.3 Performance characteristics of the six pole, uniform pole-pitch linear machine from a reduced voltage, acceleration test without dynamometer and prior to modification.

B. Experimental Results with Field Deceleration Concept

In an effort to produce three distinct field speeds in tandem on a common stator block and with the stator winding excited at only one frequency, the last 32 coils were reconnected to form two smaller wavelength fields, while the first 16 coils nearest the entry edge of the block remained intact from the previous 7 pole arrangement. Figure 2.4 shows the exact winding layout while Table 2.2 indicates the differences in field speeds. Most important the net effect of this scheme is that a decelerating field pattern is produced in the direction of rotor travel where at medium values of slip (with respect to the winding section 1), all three winding sections are contributing to forward thrust. However, when the slip of the first winding section becomes less than about 0.25 per unit, this is when the leading power factor action starts to take place.

Table 2.2

Winding Field Scheme of Experimental Machine

Winding Section	Pole-Pitch, m	Relative Field Speed	Sample Slips, p.u.	
No. 1-Coils 1-22	0.2025	100%	0.5	0.25
No. 2-Coils 23-40	0.162	80%	0.375	+0.062
No. 3-Coils 41-48	0.108	53.3%	0.062	-0.406

Ideally the section No. 1 winding may be said to provide the propulsion force with coils 1-22 having lagging power factor, while sections 2 and 3 would strictly comprise a volt-ampere-reactive (VAR) generator to compensate for the VARs consumed by section No. 1 without producing any significant braking thrust. The winding arrangement shown in Figure 2.4 was put on test with all coils in series connection and at 50 Hz

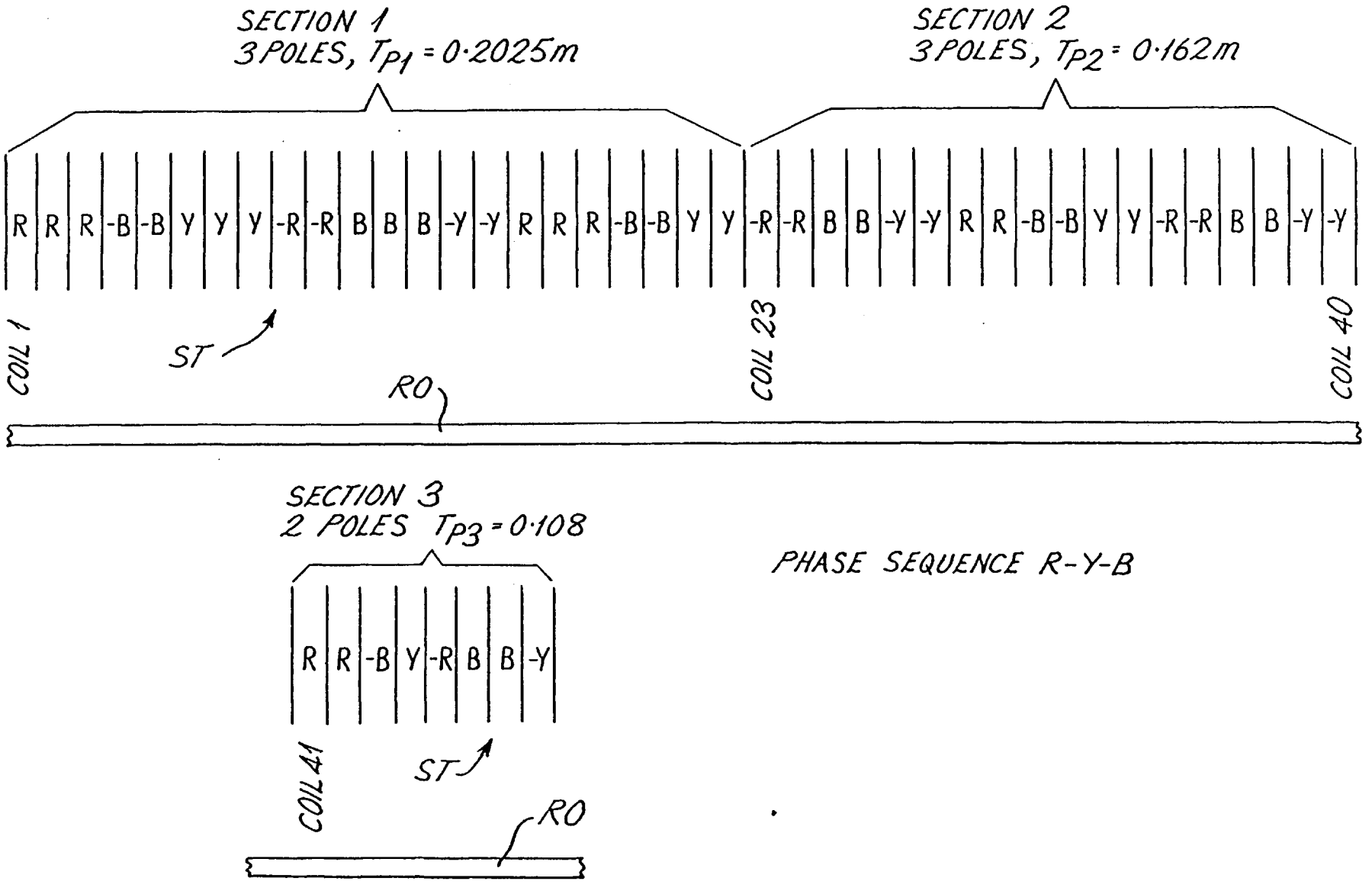

Figure 2.4 Winding layout of the experimental SLIM connected as a combination motor/VAR generator.

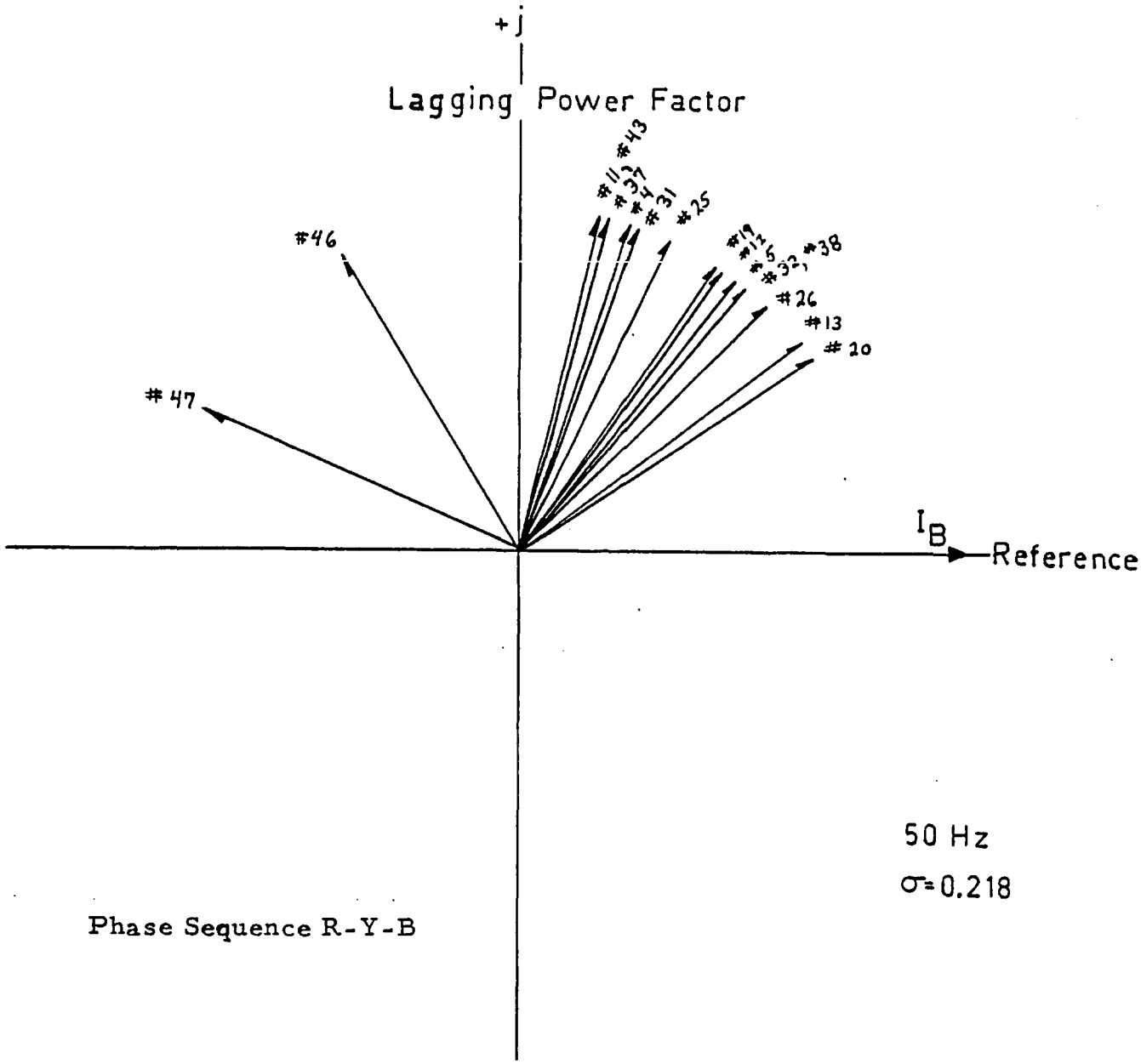

Figure 2.5 Phase plot of the "B" phase set of coil voltage angles for all machine coils connected in series.

excitation. As expected none of the coils showed leading power factor in this one test, which was attributed to the fact that in this one simple connection, all coils had equal ampere turns excitation since the sections 2 and 3 had been reconnected rather than rewound. Nevertheless, there was a considerable range of coil phase angles from 28^{o} to 156^{o} which can be explained by conventional linear motor theory. A representative phase angle plot of the I_b set of coils taken at the running light slip of 0.218 p.u. is shown in Figure 2.5.

A most successful attempt was made to reduce the ampere-turns of the section 2 and 3 coils with respect to the section 1 coils simply by shunting a significant amount of current away from the former two groups and thus avoid rewinding coils for less turns. To expedite trying to empirically find the proper impedance of a shunting loop for the sections 2 and 3 windings and to avoid the excess losses in a shunting connection, it was decided to effectively isolate the sections 2 and 3 windings from the section 1 by using a shunting path of virtually zero impedance. The modified circuit is shown in Figure 2.6.

Using the same excitation and mains current as in the first attempt, the new connection scheme not only permitted the SLIM to run to a higher running light speed but improved the overall power factor by 28% to 0.62 per unit and 9 coils in the section 2 winding clearly registered leading power factor on two independent measuring devices. The first 9 coils after the section 1 to section 2 transition showed these conclusive results. The very first power factor angle plots taken of all of the three phases for sections 2 and 3 are shown in Figure 2.7. The important conclusions of this

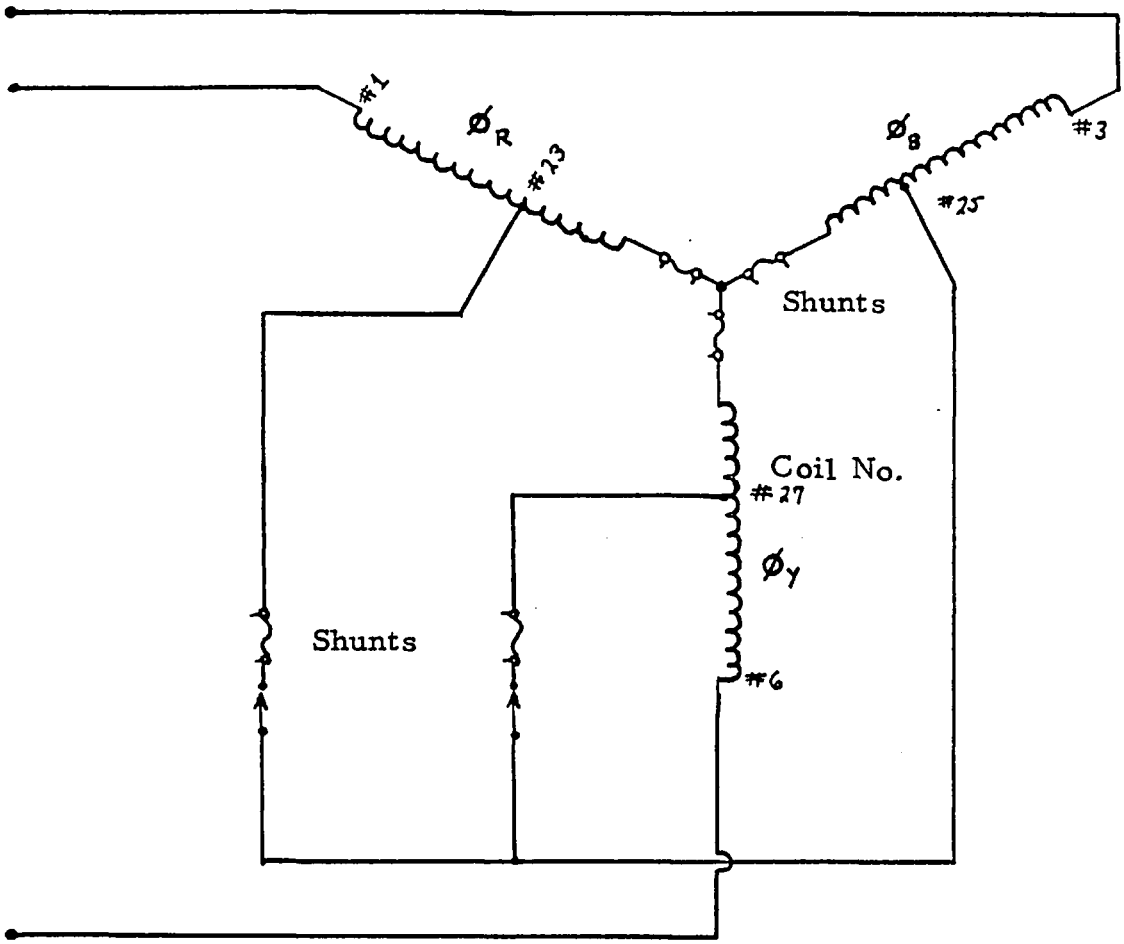

Figure 2.6 Experimental SLIM connection diagram for 3/7/78 tests showing location of current shunts.

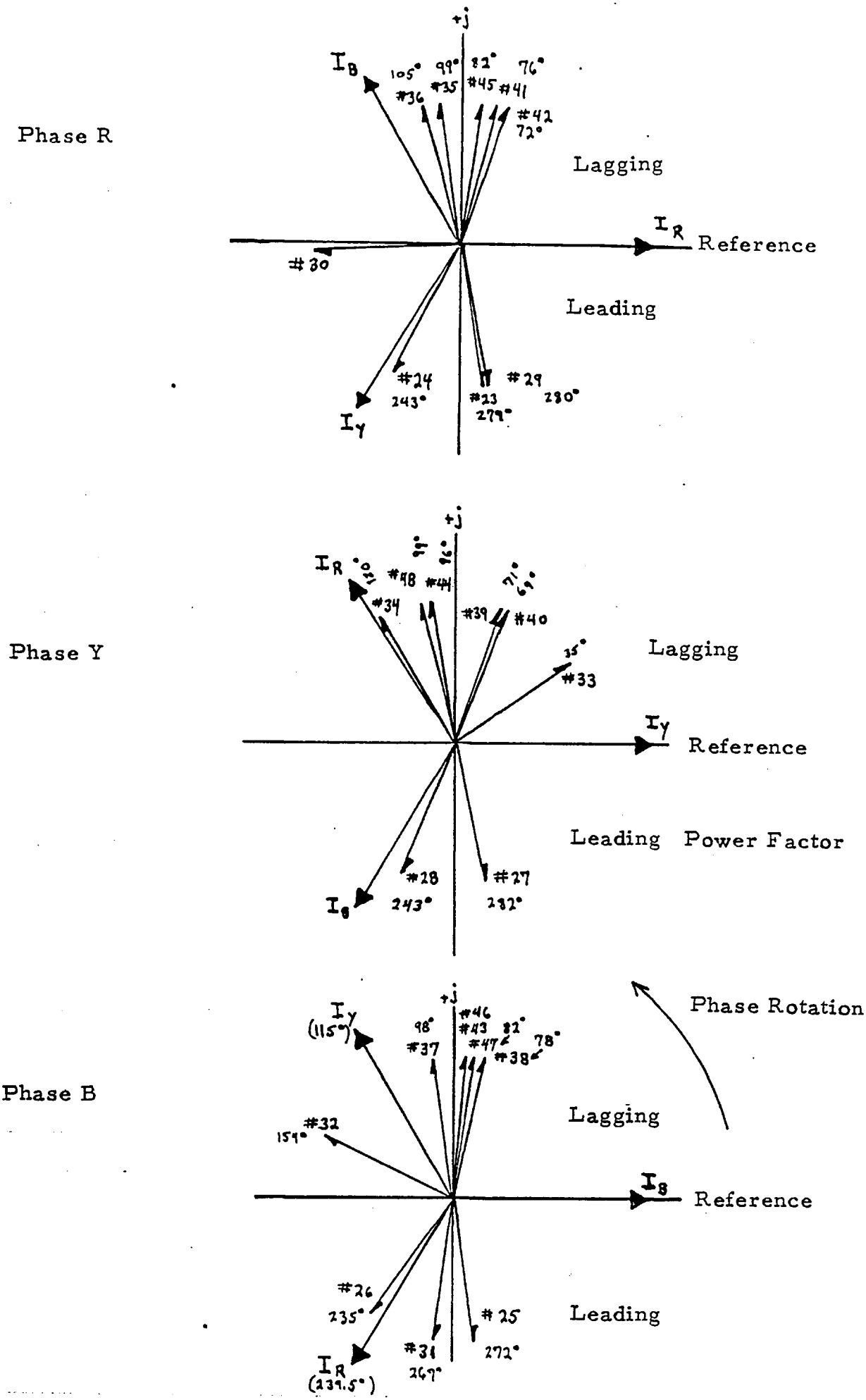

Figure 2.7 First phase angle plots from 3/7/78 tests showing coil voltages in sections 2 and 3 at a slip of 0.205 per unit at 50 Hz frequency.

first successful test were:

1. Five coils in the middle of section 1, although not drawing leading current, showed phase angles of 45^{o} to 48^{o} thus indicating lagging power factors of 0.7 which is about 8% higher than the total power factor for this machine when connected as a uniform section 1 type;
2. coils in 2 of the phases of section-1 spaced 1 pole or less before the section 1-section 2 transition showed phase angles of 30^{o} to 40^{o} indicating that power factors of 0.86 were easily obtainable with the total machine current;
3. leading power factor was recorded for:
   a. both of the 2 coils of phase "Y" in the first pole after the section 1-section 2 transition
   b. all of the 4 coils of phase "R" in the first two poles after the section 1-section 2 transition
   c. three coils of the "B" phase, 2 in the first pole of section 2 and one in the second pole.

Referring to Figure 2.7, note that also the voltage phasors are distributed in all four quadrants, whereas phase plots from a conventional rotary machine would all be confined to one quadrant only. Subsequent experimentation revealed that for increased mains current, i.e., driving the disc at a higher speed, the entire pattern of phasors would start to rotate (in addition to its understood rotation at ωt) as well as an increase in magnitude.

In essence, this one stator block, of equal slot spacing, coil dimensions, and turns, contained two separate machines that were electrically isolated but strongly magnetically

coupled via the sheet rotor secondary circuit. Moreover, this one experimental setup proved that it was possible and practical to magnetize the stator core of the isolated section 2 and 3 windings by rotor currents only, and in doing so produce leading power factor current. This represents the most basic laboratory method of continuously producing leading current in the actual working coils of the stator by using a brushless rotor with currents established purely by electromagnetic induction.

Instead of using a DC field to excite the condenser windings, the magnetization field was provided by the rotor currents established by the LIM. Now it is appropriate to classify these relocated windings as an asynchronous condenser (ASC) although to an electromagnetic purist, the effect could still be considered as synchronous.

On the laboratory SLIM, the problem of directly connecting the section 2 and 3 winding or A.S.C. to the LIM section 1 in parallel was avoided, since the impedance levels of the two windings were not modified. Rather, on the July 3, 1978 runs, the most expedient way of finding a good impedance match was to simply connect the A.S.C. windings to itself and observe the internal balance of reactive power. This is shown diagramatically in Figure 2.8b. Most important, this one arrangement was crucial for verifying that all of the magnetization current was being supplied from the rotor.

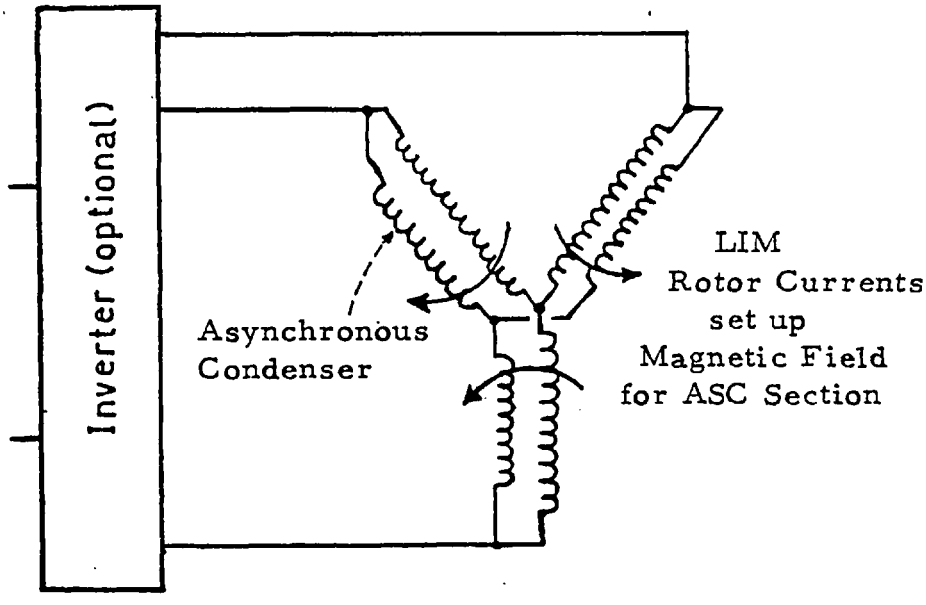

Fig. 2.8a Conceptual arrangement of combining LIM and reactive power generator (ASC) onto one common winding block.

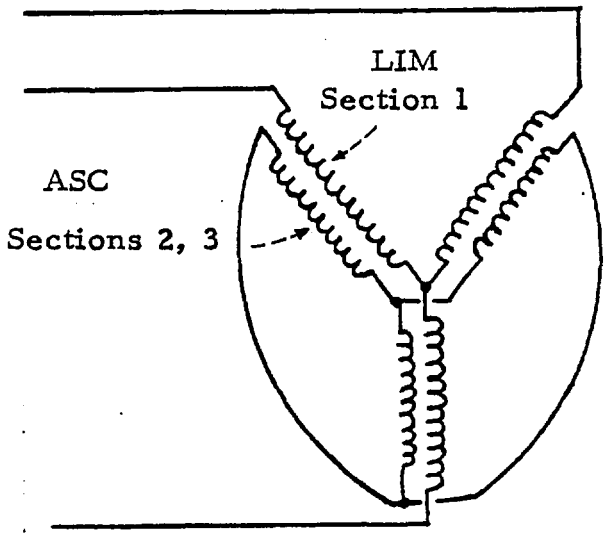

Fig. 2.8b Analogous arrangement used in 3/7/78 tests combining LIM and induction generator on common block with LIM providing the magnetizing current and isolated ASC.

C. Subsequent Experimental Aim

Later the A.S.C. windings were investigated in a variable load impedance mode to determine the proper coil turns changes, the maximum VAR output, and the optimum value of slip for supplying the entire LIM with internally generated reactive power. One specific test is shown in Figure 2.9. It uses a manually adjusted variable complex-impedance shunting loop, which allowed mains current to partially excite the ASC section. This was an intermediate step between the non-successful total series connection and the experimentally proven fully-shunted ASC section.

Subsequent tests have revealed that if a manually-adjusted external complex-load is connected to the ASC windings, a total of 22 coils out of a maximum possible number 26 coils for the whole ASC section, now exhibit the leading power factor-condenser effect at the natural running light speed of the LIM. A plot of the reactive power generated by one phase of the ASC section coils as distributed over a wide speed range (from σ =0.304 to σ =-0.064) is included in Figure 2.10. In particular, at the below running light speed corresponding to about σ =0.20, all 26 coils of the ASC section contribute to positive reactive power generation, although not of equal proportions.

Most important, these series of tests have confirmed the universality of the manually adjusted external load that is primarily inductive in determining the peaking locations and phase differences between individual ASC section coils with respect to the main LIM slip speed. Additionally, these tests have substantiated that the parasitic braking thrust produced by circulating large reactive currents in the ASC section windings is entirely negligible from the input end of

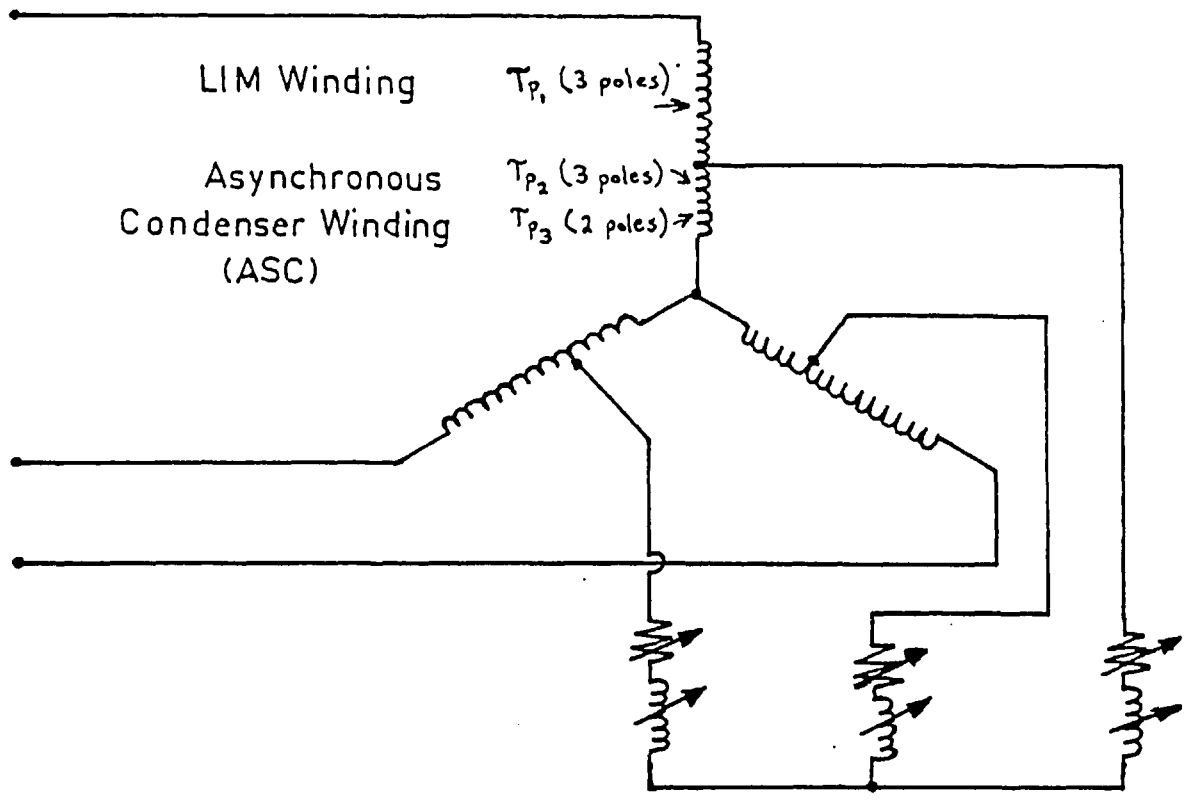

Figure 2.9a Experimental LIM-ASC winding arrangement using a manually-adjusted shunt impedance across ASC.

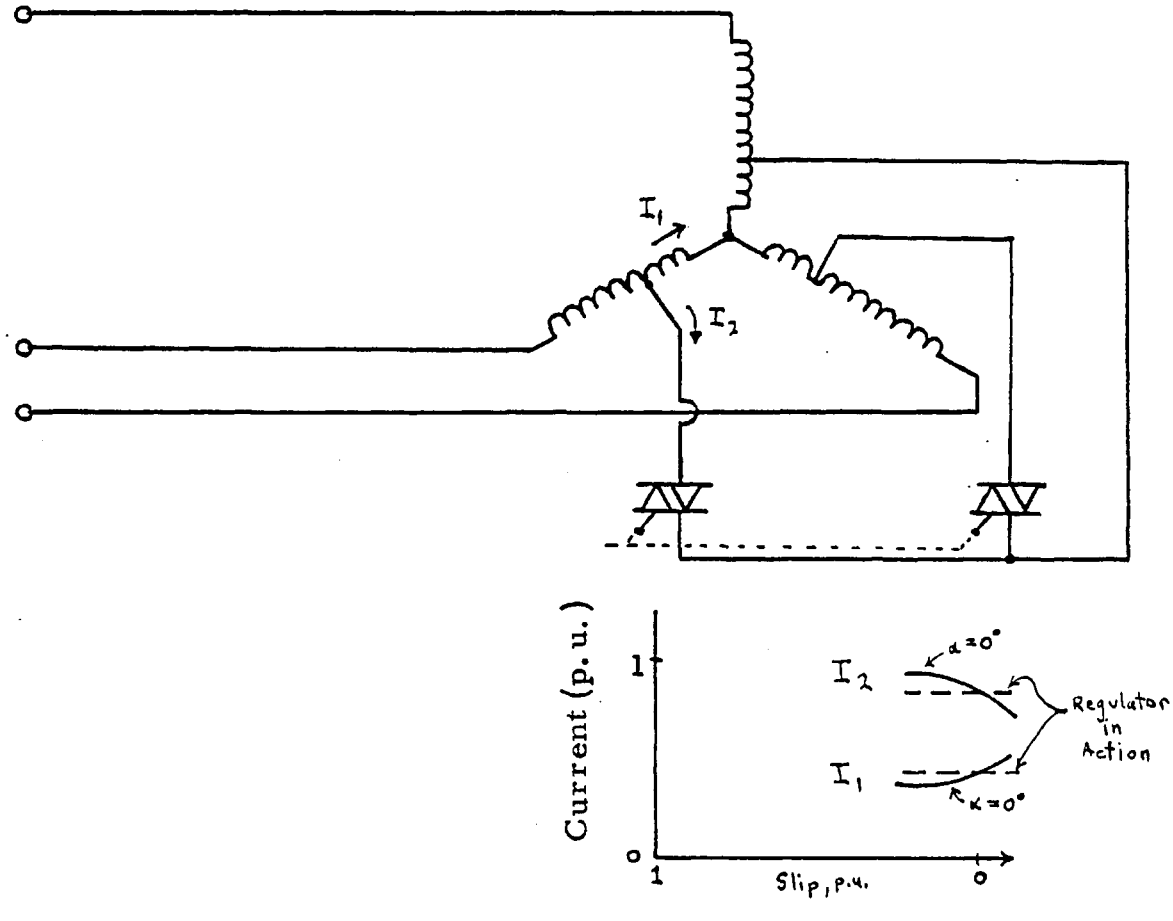

Figure 2.9b Automatic regulation version of setup shown in Fig. 2.9a with a thyristor delayed-gating current shunt.

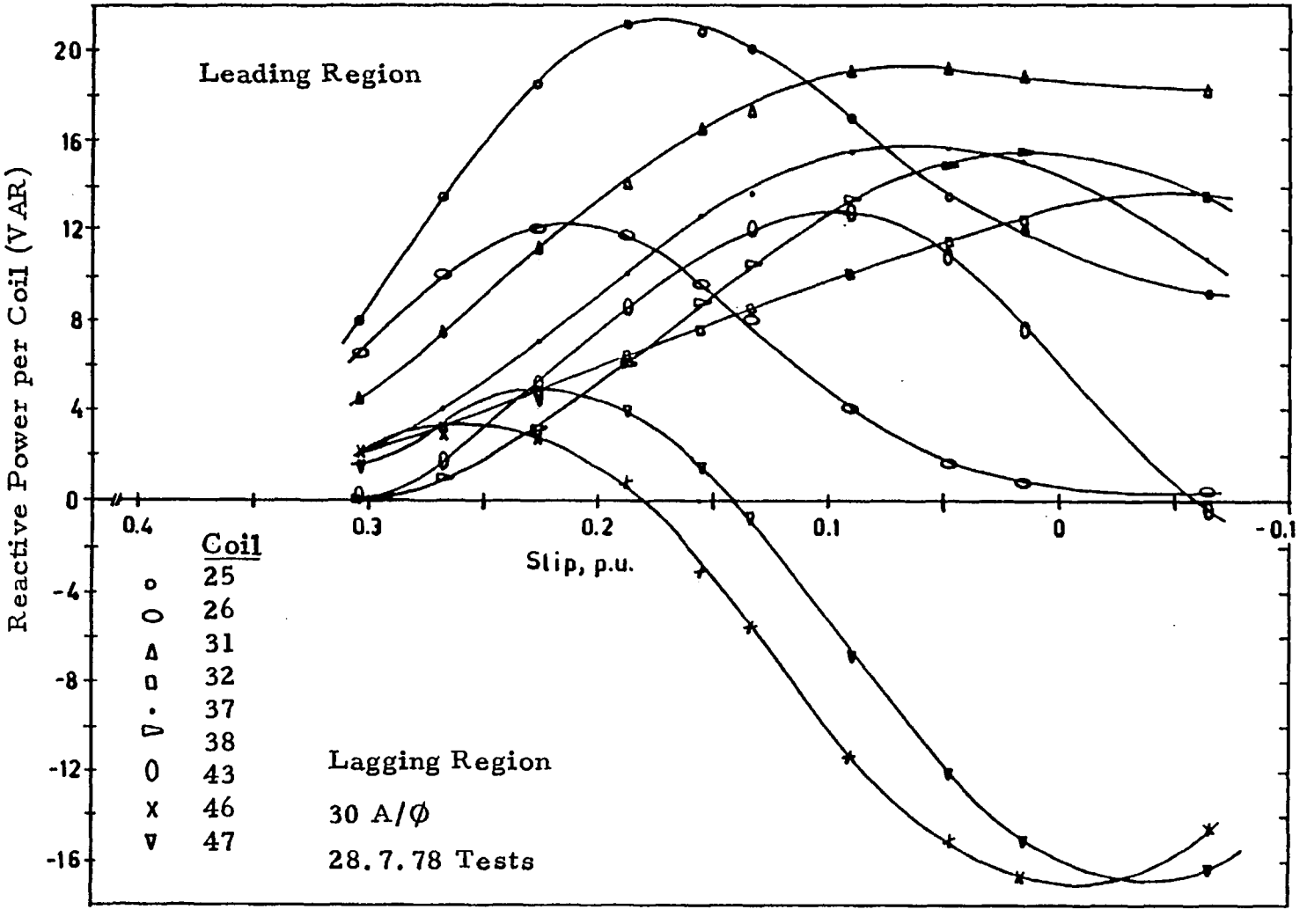

Figure 2.10 Asynchronous Condenser Section Reactive Power Distribution with Load Impedance on Phase B of Z= 0.0813 + j2.51 Ohms using a 3-pole LIM.

the LIM section. The change in input power with and without the ASC connected is nearly the same as the resolution of the LIM wattmeters!

The LIM winding was changed from a 3 pole unit to a 4 pole unit (with the same wavelength) and the ASC section (3 poles total) was rewired to the same wavelength as the LIM winding but with periodic phase jumps. This new configuration yielded a much more uniform reactive power distribution along the ASC section of the block with a consequent increase in the total phase-group leading VARs. Although the total reactive power generated by the ASC is still a strong function of the LIM slip speed, the major advantage of this phase jump technique was that the point of maximum VAR generation occurred at a considerably smaller slip speed of the LIM. For this very purpose, the addition of one more active pole to the LIM changed the running light slip from σ =0.156 to σ =0.125 at the very modest current loading of J_s = 24,500 A/m (which was limited by the mains variac rather than the LIM thermal rating).

Dynamic tests proceeded with the same instrumentation and method of ASC impedance loading as in Section B. The 40-channel data logger was installed on the High Speed Rotary Test Rig to permit instant and continuous measurements of the B_p-B_q flux waveforms from the LIM-ASC search coils. Approximately 8,000 data points are needed to produce a comprehensive set of phase and magnitude plots for all airgap flux sensors, coil voltages, real powers and reactive powers over a broad range of slip speeds for just mains frequency.

It is only anticipated that direct LIM-ASC connection is optimum over a relatively narrow range of operating slip speeds, for instance from σ=0.122 through σ =0.127. In

fact, significantly outside the intended range of VAR compensation, the ASC unit actually starts to consume VARs at nearly the same level as the LIM and consequently the total system power factor would be worse than with only the LIM connected. The answer to this is simply that the ASC must be phased properly at any given slip with respect to the LIM that provides the rotor currents exciting the ASC windings. To accomplish this in the laboratory, a three phase rotary transformer-phase shifter that is continuously variable from -180^{o} to $+180^{o}$ was connected between the LIM and ASC windings as per Figure 2.11.

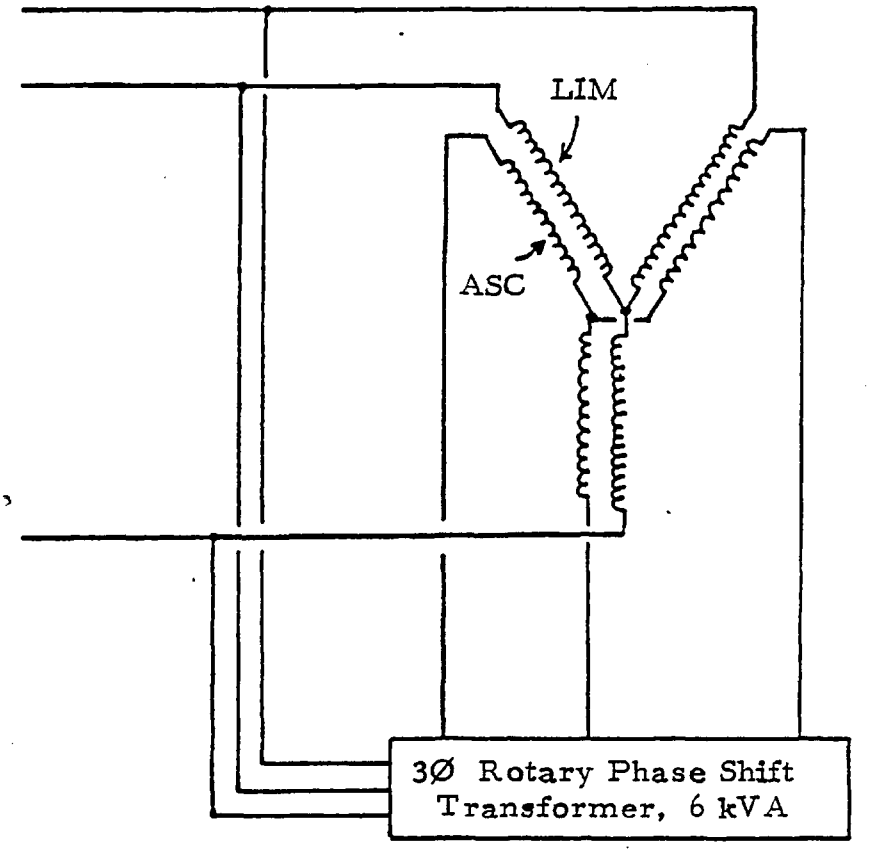

Figure 2.11 Parallel connection of LIM and ASC windings for second series of tests with manually adjusted phase-shifter to maximize ASC reactive output.

D. Future Directions

Although this technique of manually adjusting the magnetic phase shifter to peak the ASC output was acceptable in the laboratory, it is of course too cumbersome for a commercially available variable speed LIM-ASC drive system. Figure 2.12 shows a conceptual automatic system to correct the phase shift between the LIM and ASC windings over a broad speed range. Rather than utilize a servo-motor controlled magnetic phase shifter, a thyristor phase shifter is superior in terms of speed of response and overall cost of construction since no forced commutation circuits are necessary as the entire system is line-load naturally commutated. At first glance, the power circuits of Figure 2.12 appear to resemble that of any ordinary cycloconverter regarding the thyristor connections only. However, in effect the entire operation of the circuit shown is entirely different from a cycloconverter since:

a) the thyristors perform the sole function of phase shifting rather than frequency conversion,
b) the thyristor gating sequence is controlled by the ASC reactive power capability (i.e., the LIM-ASC phase difference) as a function of LIM slip,
c) the thyristors are always gated at a zero delay angle in that there is no phase chopping; optimum performance is gained when there is a transientless direct connection between LIM and ASC.

Although the magnetic phase shifter principle can provide a continuously variable phase shift in contrast to the thyristor phase shifter which obviously can only provide phase corrections in discrete steps, the thyristor version can overcome this difficulty by incorporating the group-gating

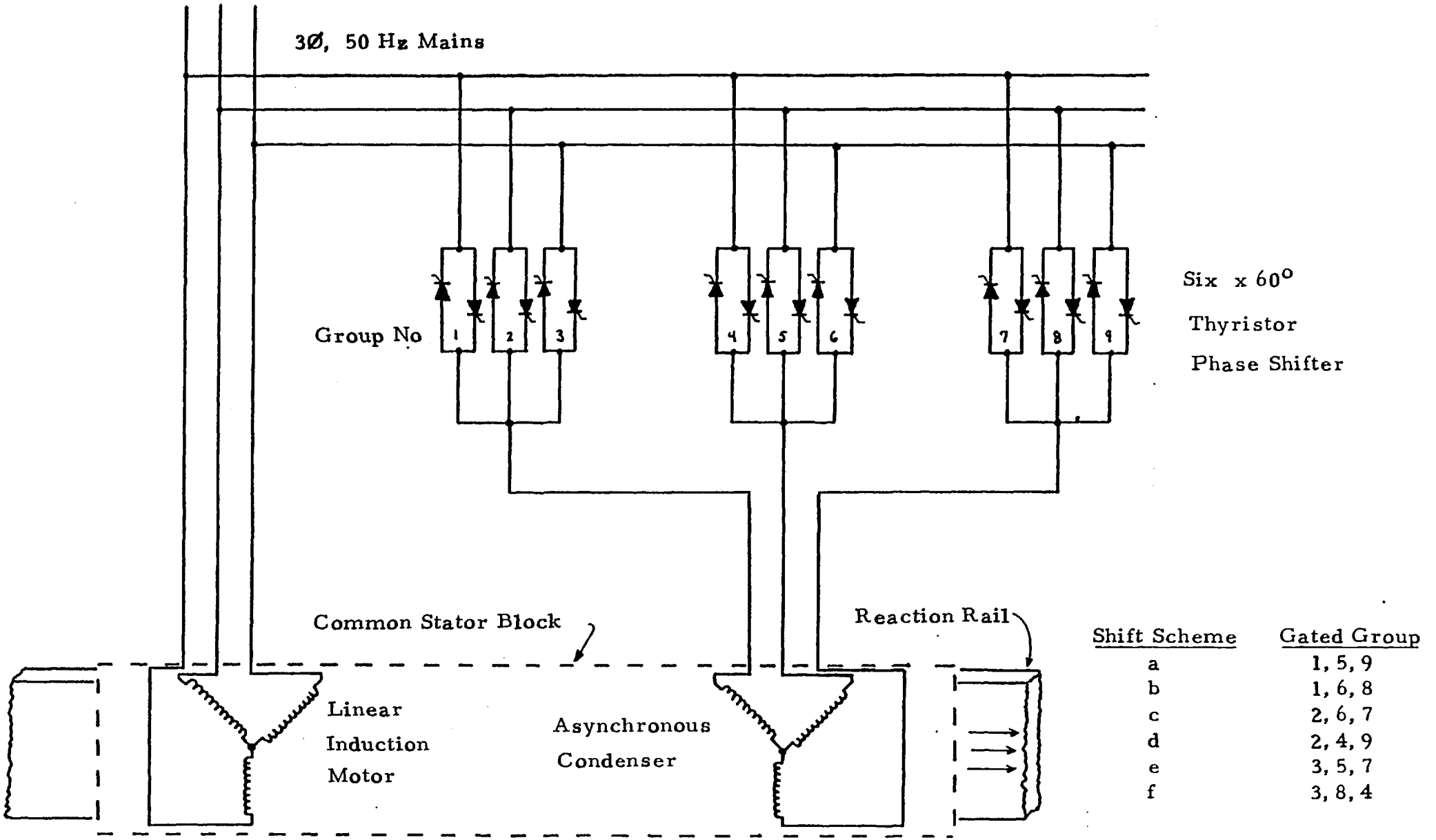

Shift Scheme	Gated Group
a	1, 5, 9
b	1, 6, 8
c	2, 6, 7
d	2, 4, 9
e	3, 5, 7
f	3, 8, 4

Figure 2.12 Power arrangement for automatic static phase shifter between LIM and ASC windings to extend slip range for magnetic power factor improvement at constant efficiency.

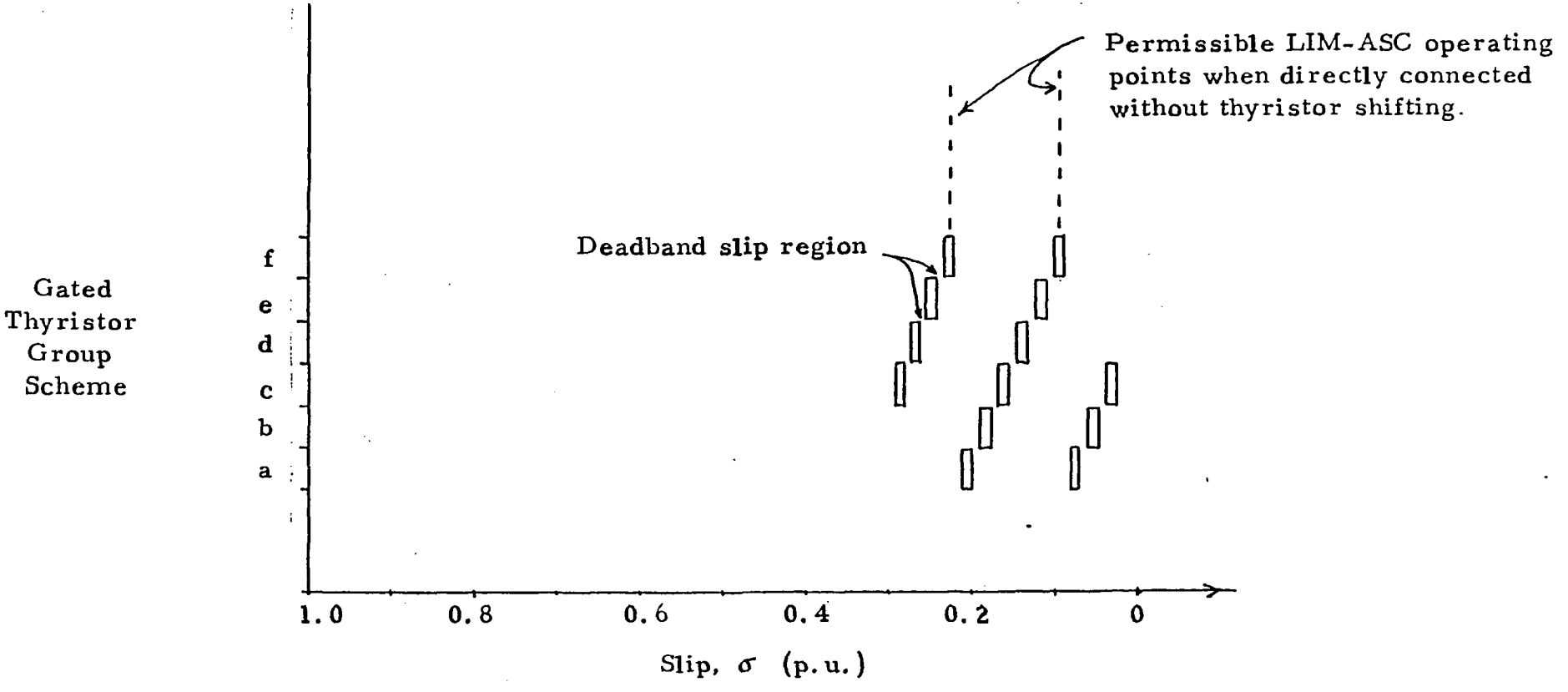

Figure 2.13 General application of discrete step LIM-ASC current phase shifter to extend dynamic range of exit-end VAR compensation for use with thyristor circuitry of Figure 2.12.

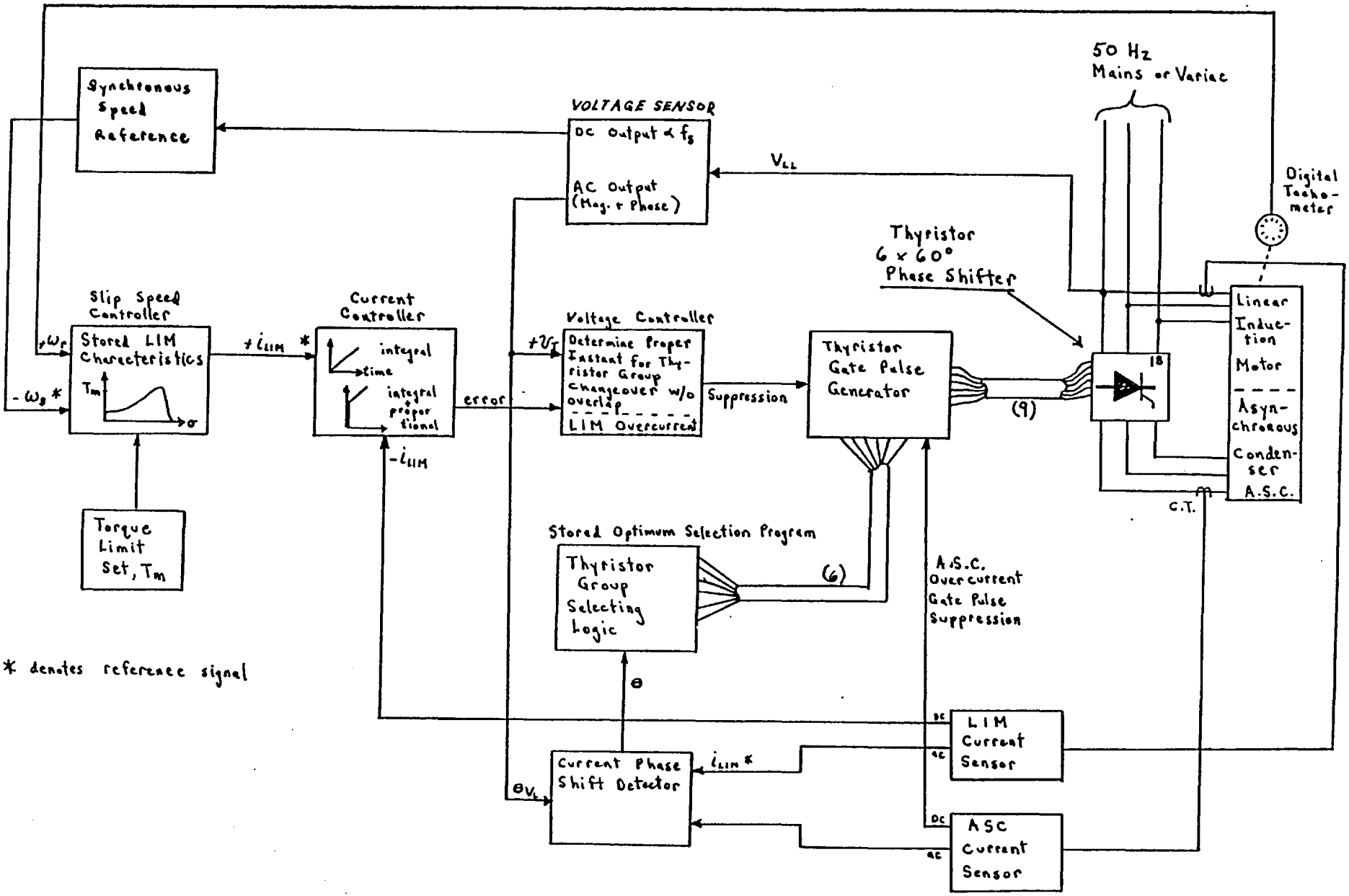

Figure 2.14 Control layout for automatic phase shifter between LIM and ASC windings for power factor regulation.

sequence as shown in Figure 2.13. This indicates that there does exist a series of small slip regions where it is impractical to conduct the LIM and ASC together even through any one of six thyristor controlled phase shifts, but since this "deadband" region is effectively very small in relation to the whole upper speed range, by simply adjusting the LIM applied voltage by a maximum of plus or minus 2%, the consequent change in slip speed now permits the thyristor controller to select one of the six available connection paths between LIM and ASC to permit optimum VAR transfer.

The results of further testing have indicated that it is advantageous to also custom machine cut the slots in the stator block so as to set the characteristic pole lengths by different slot spacing rather than by simple coil reconnection on a uniform tooth-width and slot-pitch block. Thus most likely, a special machine employing the asynchronous condenser concept should be a linear machine. The optimum reduction in field speed between the LIM and ASC windings has been confirmed and the ASC should not contain multiple decelerating field speeds. A final shape of composite SLIM-ASC blocks should take the form shown in Figure 2.15 supposing that a parallel connection is opted for and all new construction is designated rather than retrofitting.

In addition to the promise of improving linear motor power factor, the decelerating field concept offers another equally important application especially in reference to state-of-the-art variable speed industrial and transport drives. Thyristor technology has advanced to the point where variable speed induction motor drives nearly all rely on fixed pole, variable frequency excitation. Yet it is important to note that in almost all economy minded applications

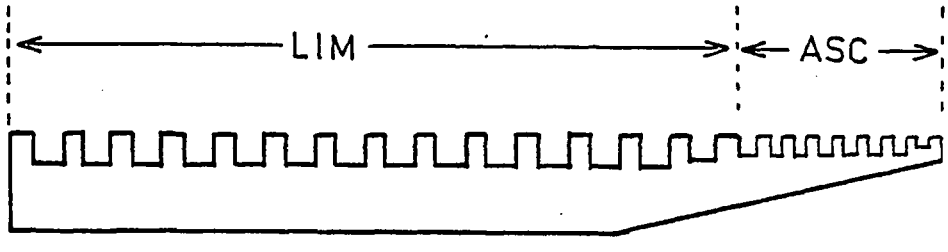

Figure 2.15 Conceptual shape of composite motor and asynchronous condenser for exit-end flux recovery.

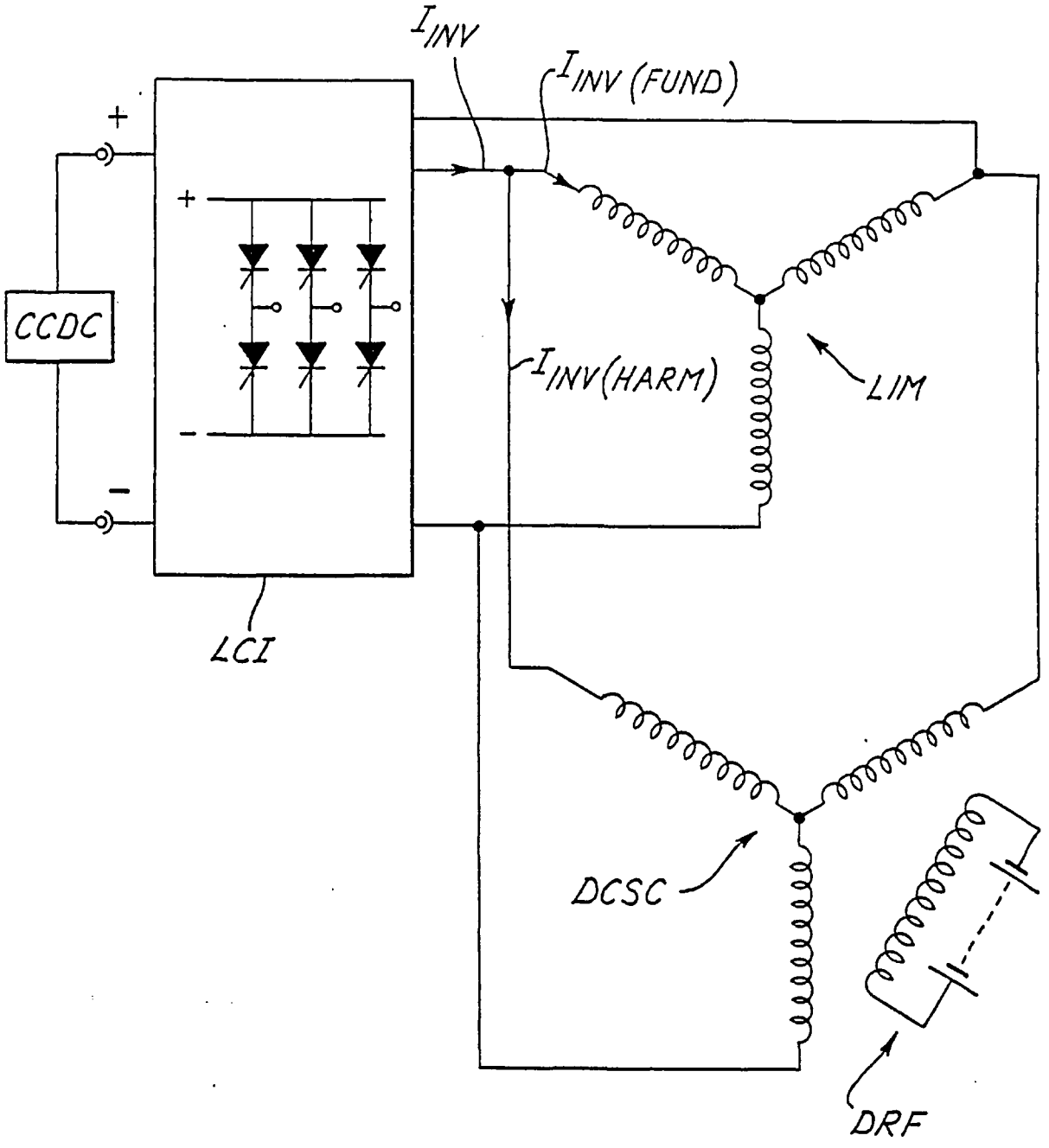

Figure 2.16 State of the art method of providing linear induction motor with reactive power from a DC-field synchronous condenser and real power from a DC-link, variable frequency inverter.

especially in the megawatt range, modern drive systems unfortunately inject square wave current into the induction motor with the consequent excess stator losses, excess rotor losses and unyielding harmonic torques. (The system briefly described in Figure 2.16 avoids these problems but at the expense of having a synchronous machine several times the cost of the induction motor.)

The basic problem lies in the fact that the induction machines used today are electromagnetically only suited for sinusoidal current. To design an induction motor that specifically prefers square wave current is something that has been needed since the advent of the thyristor semiconductor device in 1962 but has not been attempted as of this date. As second best to an induction motor that actually prefers non-sinusoidal currents to set up a rotating magnetic field (harmonic free), the ASC winding additionally serves as a harmonic current filter. This permits the LIM winding proper to only receive the fundamental, sinusoidal component of its terminal current, which is strictly speaking a square wave current. Figure 2.17 applies in this case.

This concept confines both filtering and propulsion equipment to one stator block and does away with the need for either large commutation capacitors or an auxiliary synchronous machine. The comparison between this one machine system and state-of-the-art propulsion schemes with two requisite machines is fully treated in Chapter VI for the case of the leading power factor rotary machine initiating natural commutation of the thyristor inverter system.

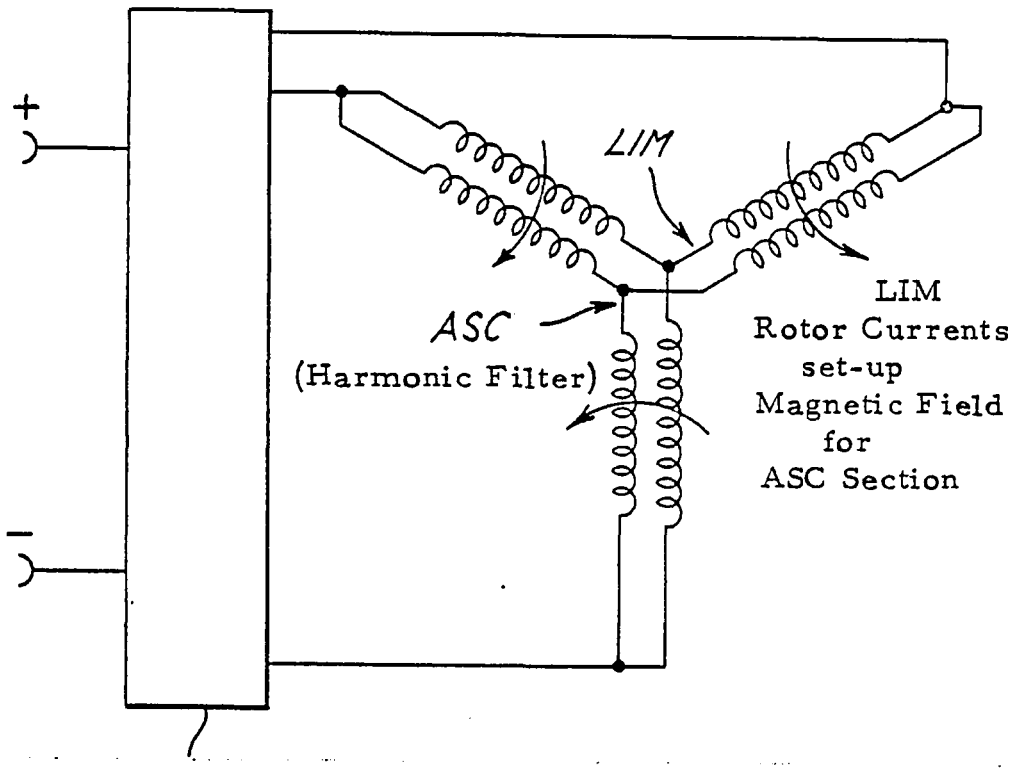

Figure 2.17 Parallel connected version of integral motor/asynchronous condenser machine for square-wave inverter output.

2.2 ENTRY ZONE DYNAMICS

In 1956 Williams et al [5] made a simple analysis of an induction motor in which the primary (s t a t o r) was not continuous around the periphery of a cage rotor but consisted of a sector covering a limited arc of the rotor. In such a situation unmagnetized r o t o r teeth, each surrounded by their own short-circuited loop consisting of a pair of rotor bars and their appropriate end-conductors, enter the active zone of the stator at high speed. The teeth are unable to accept full flux density instantaneously because such a change would demand an infinite emf and current in the rotor bars.

When the coils of the sector of stator are series-connected (as they invariably are in most rotary induction machines) rotor current tends to oppose the stator mmf at the entry point, reducing the flux density just inside that end of the stator virtually to zero. The effect is entirely due to the high speed entry of rotor bars, the rotor current natural time constant and the pattern of current established by the entry edge transient. The slow decay of these transient currents is easily identified as corresponding with a machine of high Goodness Factor.

Williams' analysis treated the phenomenon as being comparable with the "beats" effect of two sound waves of nearly the same frequency. He saw a transient rotor current pattern, printed by the stator coils at the entry edge, travelling at rotor speed $\omega_r = \omega_s (1-\sigma)$ where σ is the fractional slip and ω_s is the stator field speed or synchronous speed. This wave therefore drifts in and out of phase repeatedly with the stator mmf wave proper and the resulting modulaton of the airgap flux density can be represented as in Figure 2.18. These graphs have been

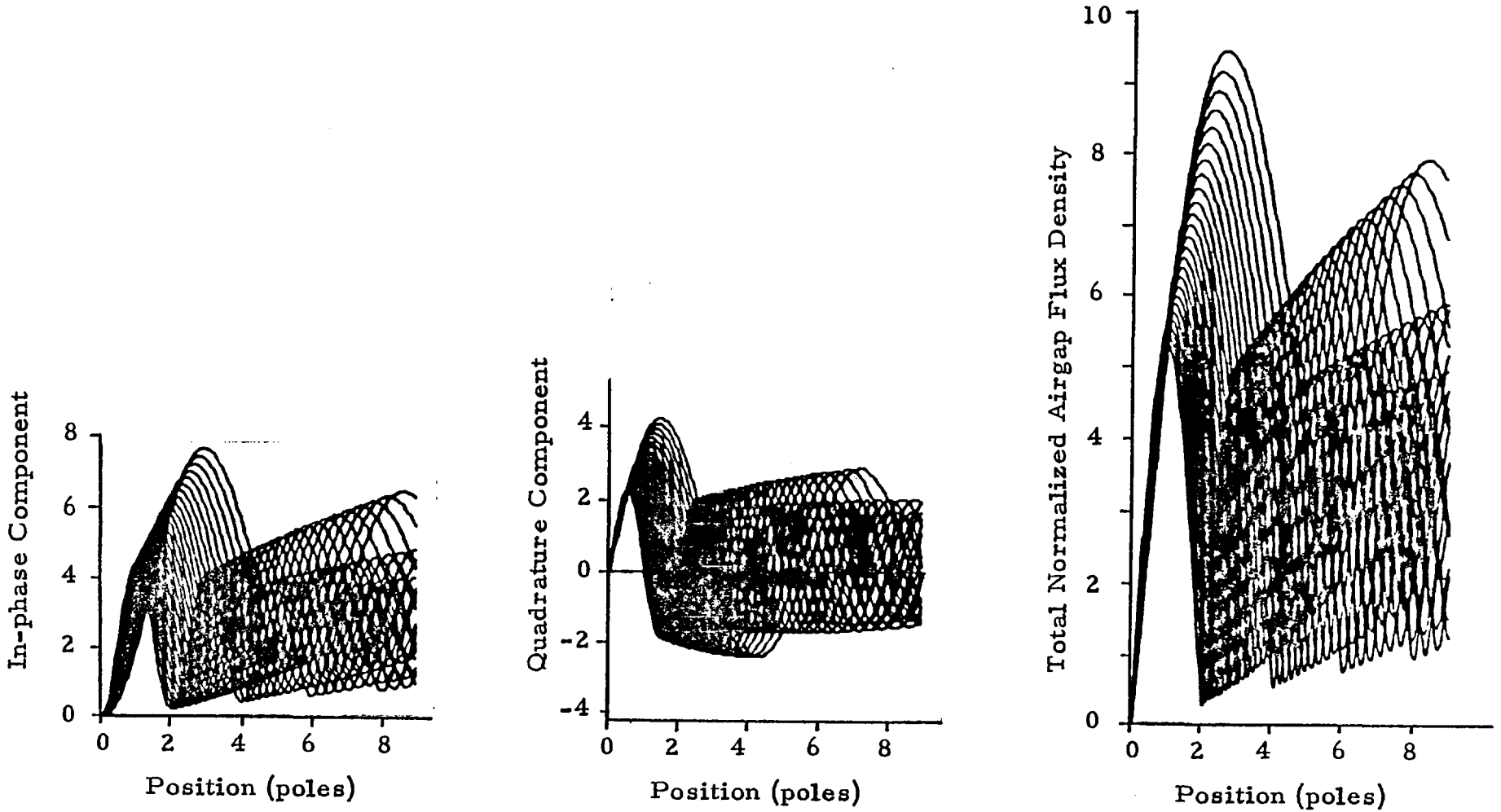

Figure 2.18 Airgap flux density modulation envelopes for a short-primary machine at slip values between 0.50 and 0.26 per unit, a Goodness factor of 30 and a polyphase series winding on the primary.

normalized with respect to the quanitity $\rho_r J_s/\upsilon_s$ where J_s is the stator current loading, ρ_r the effective surface resistivity of the rotor and υ_s is the synchronous field speed.

These theoretical curves of airgap flux density were calculated on a digital computer, the expressions for which were first published by Williams [5] and, in SI units, are

$$B_p = \frac{J_s \rho_r u_s \sigma}{(\sigma u_s)^2 + (u_s/G)^2} \left\{ 1 - \exp\left[-s\pi / \tau_p(1-\sigma)G\right] \cdot \left[\cos \frac{s \pi \sigma}{\tau_p(1-\sigma)} + \frac{1}{\sigma G} \sin \frac{s \pi \sigma}{\tau_p(1-\sigma)} \right] \right\} \tag{2.1}$$

$$B_q = \frac{J_s \rho_r u_s/G}{(\sigma u_s)^2 + (u_s/G)^2} \left\{ 1 - \exp\left[-s\pi / \tau_p(1-\sigma)\, G\right] \cdot \left[\cos \frac{s \pi \sigma}{\tau_p(1-\sigma)} - \sigma G \sin \frac{s \pi \sigma}{\tau_p(1-\sigma)} \right] \right\} \tag{2.2}$$

The major advantage of using a figure of merit such as G, the Goodness Factor is that analytical expressions for both the transient and steady-state flux density at any point "s" along the airgap, or real and reactive power thereof, can be expressed in a closed-form solution.

The total instantaneous flux density in the airgap of a short-primary machine may be represented as

$$b_s = B_p \sin(\omega t) + B_q \cos(\omega t) \tag{2.3}$$

$$= \frac{\rho_r J_s}{u_s \sqrt{\sigma^2 + (1/G)^2}} \left\{ \sin\left[\omega t - \frac{s\pi}{\tau_p} + \tan^{-1}\left(\frac{1}{\sigma G}\right)\right] - \exp\left[\frac{-s\pi}{\tau_p(1-\sigma)G}\right] \sin\left[\omega t - \frac{s\pi}{\tau_p(1-\sigma)} + \tan^{-1}\left(\frac{1}{\sigma G}\right)\right] \right\}$$

where B_p and B_q are the radially-directed flux components at position s from the entry-edge of the primary, in time-phase and time-quadrature with the primary current, J_s in the normal case of zero entry-edge flux.

Williams proceeded to show a rather outstanding correlation between the theoretical expressions for density and data taken from search coil measurements on the surface of a spherically shaped short-primary segment. A polyphase 8-pole winding at 480 Hz was used with only seven search coils positioned every pole-pitch along the block. But, in view of the spherical geometry, accuracy of correlation was maintained by confining measurements to be made at constant synchronous speeds among coils by only allowing such instrumentation to span the center one-third of each pole. A number of magnitude and phase measurements were made at high speed as well as locked rotor; the results for a 12.5% slip test were tabulated in [5] and are shown again in Table 2.3 for columns (i) through (iv). Due to the presence of rotor leakage flux in the measurements, the high speed data cannot be used directly to derive B_p and B_q magnitudes, but a method such as indicated in the phasor diagram of Figure 2.19 is necessary. Let the rotor phase angle be Θ and the leakage component of the locked rotor search coil voltage, V_l be represented as

$$V_L = V_l \sin \Theta \tag{2.4}$$

and its associated phase angle

$$\xi_L = \xi_l - (90^o - \Theta) \tag{2.5}$$

If the phasor V_L is substracted from the high-speed voltage, V_σ, voltages proportional to the in-phase and quadrature components are obtained as

$$k B_p = V_\sigma \sin (\xi_o - \xi_L) \tag{2.6}$$

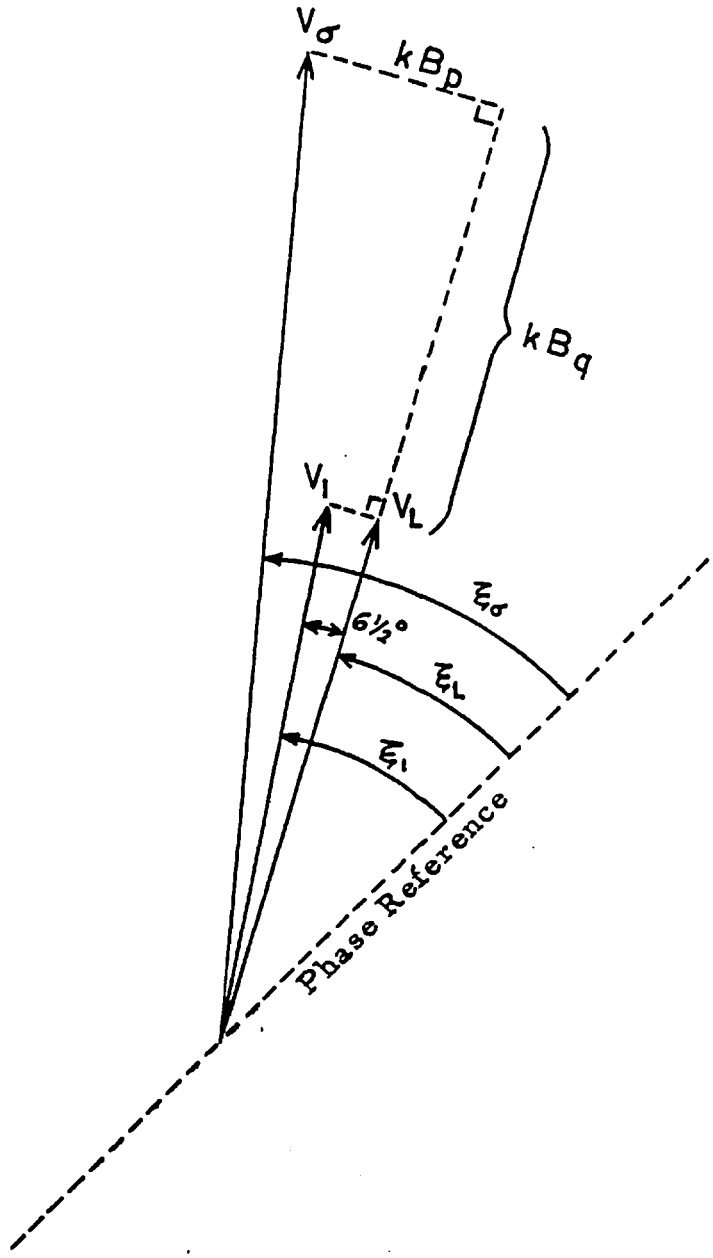

Figure 2.19 Phasor diagram for deriving in-phase and quadrature flux densities from search coil measurements.*

* from Reference 5 , p. 109.

Table 2.3

The Original Data as Published by Williams and Laithwaite for Determining In-phase and Quadrature Components of Flux Density from Measurements on Short-Primary Spherical Induction Motors

Coil No.	Raw Data				Calculations				
	(i)	(ii)	(iii)	(iv)	(v)	(vi)	(vii)	(viii)	(ix)
	V_1 volts	ξ_1 deg	V_σ volts	ξ_σ deg	V_L volts	ξ_L deg	kB_q volts	kB_p volts	$\xi_o - \xi_L$ deg
1	21.6	31.0	25.5	25.	21.4	24.5	4.1	0.2	0.5
2	28.2	26.0	36.0	22.	28.0	19.5	7.9	1.5	2.5
3	31.8	22.5	41.6	22.	31.6	16.0	9.8	4.4	4.0
4	30.0	30.5	40.6	33.	29.8	24.0	10.4	6.4	9.0
5	30.1	17.0	40.7	21.	29.9	10.5	10.2	7.4	10.5
6	29.0	25.0	38.4	34.	28.8	18.5	8.3	10.2	15.5
7	29.8	20.0	36.2	30.	29.6	13.5	5.2	10.3	16.5

$$k\, B_q = V_\sigma \cos(\xi_o - \xi_L) - V_L \qquad (2.7)$$

These last four quantities were also tabulated by Williams (and in Table 2.3) and are graphed in Figure 2.20 to show the rather abrupt changes in phase angles among adjacent search coils such as the sequence 4-5-6. Yet despite this characteristic, as Figure 2.20 reveals the $k \cdot B_q$ piece-wise curve is substantially smooth and the $k \cdot B_p$ has only one major departure from a negative cosine function. The basis for this is that the quantity, $\xi_o - \xi_L$, remains a monotonically increasing function over the whole primary block and this can be attributed to the particular choice of Θ, the rotor phase angle which is unusually large at 480 Hz excitation frequency. From measurements of the total flux density $B_t = [B_p^2 + B_q^2]^{\frac{1}{2}}$, the exponential build-up time constant, $T_r = G/\omega$ of 0.02 sec., and the finite flux at the entry-edge, the rotor phase angle was estimated at 83.5° from the expression

$$\Theta = \tan^{-1}\left\{ \frac{B_t\ (s = o)}{B_t\ (s = s_{max})} \left[\ G\ \right] \right\} \qquad (2.8)$$

where $B_t\ (s = s_{max}) \approx \dfrac{\rho_r\ J_s\ v_s}{G}$ (2.9)

$$\therefore\quad \Theta \approx \tan^{-1}\left[\frac{B_t\ (s = o)\ \ G^2}{\rho_r\ J_s} \right] \qquad (2.10)$$

and it is essential to determine $B_t(s = o)$ from test data of the entry pole search coil. Consequently the angle of 6.5° in Figure 2.19 represents the bracketed quantity in equation (2.5).

Later, and as detailed in Chapter III, the theory was extended to include the rotor leakage constant in a closed-form expression for B_p and B_q. It should be emphasized that the high frequency was chosen not because this yielded $T_2 \approx T_r$ (i.e. Θ approaching 90°) but rather this reduced the "effects of de-

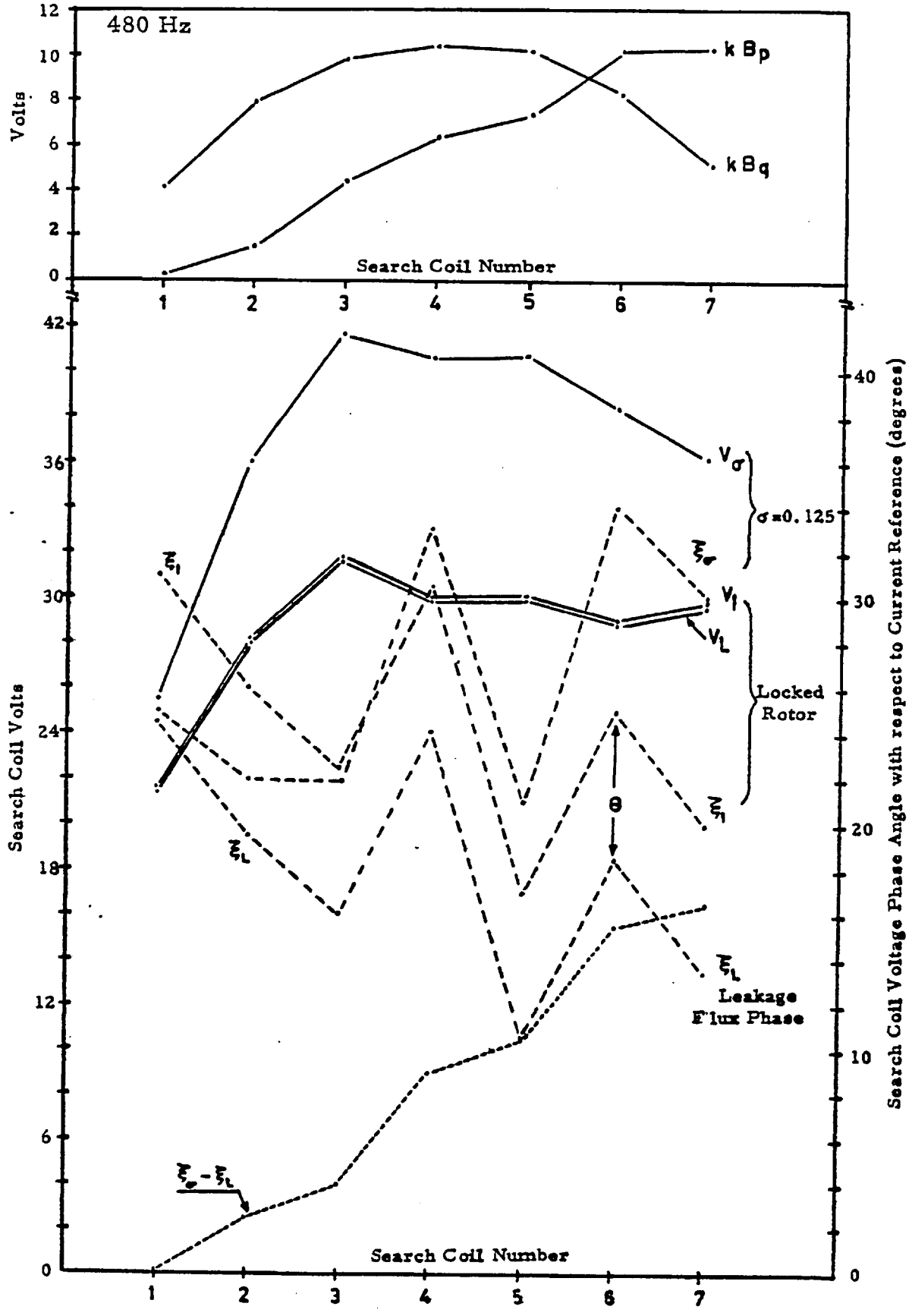

Figure 2.20 Flux measurements from the spherical induction machine of reference 5 by the method of Williams and Laithwaite.

crement" which is the decreasing characteristic of either B_p or B_q towards the end of the primary block. For the first spherical induction motor, one criteria used to classify this was that if

$$T_r \, v_s/s \geq 4.8 \tag{2.11}$$

then decrement is not prominent. This is exactly equivalent to the inequality

$$\frac{G}{s/\tau_p} \geq 15.1 \tag{2.12}$$

the ratio of Goodness to the number of primary poles, n. This general guideline has been followed in both of the rotary machines with asynchronous condenser windings that are discussed in Chapters IV and V. Yet both of the linear machines, LIM-ASC-I and LIM-ASC-II discussed in this chapter do not conform to (2.12); decrement effects for the B_q characteristic commence at slip values greater than 11.6% and 5.5% respectively. From inspection of (2.1) it is evident that oscillations of either B_p or B_q are not to be discernible as long as

$$\frac{\sigma \, p}{1-\sigma} < < 1 \tag{2.13}$$

The airgap flux distribution of the 6 1/3 pole LIM is given in Figure 2.21 for the locked rotor condition and an entrefer of 12 mm. Deviations up to $\pm$ 25% about the mean flux level of 0.0366 milli-Webers/search coil are due to unbalance among phase currents, the use of a fractional slot winding (7.5 slots/pole) and to a minor extent the fully-open slot geometry. The phase

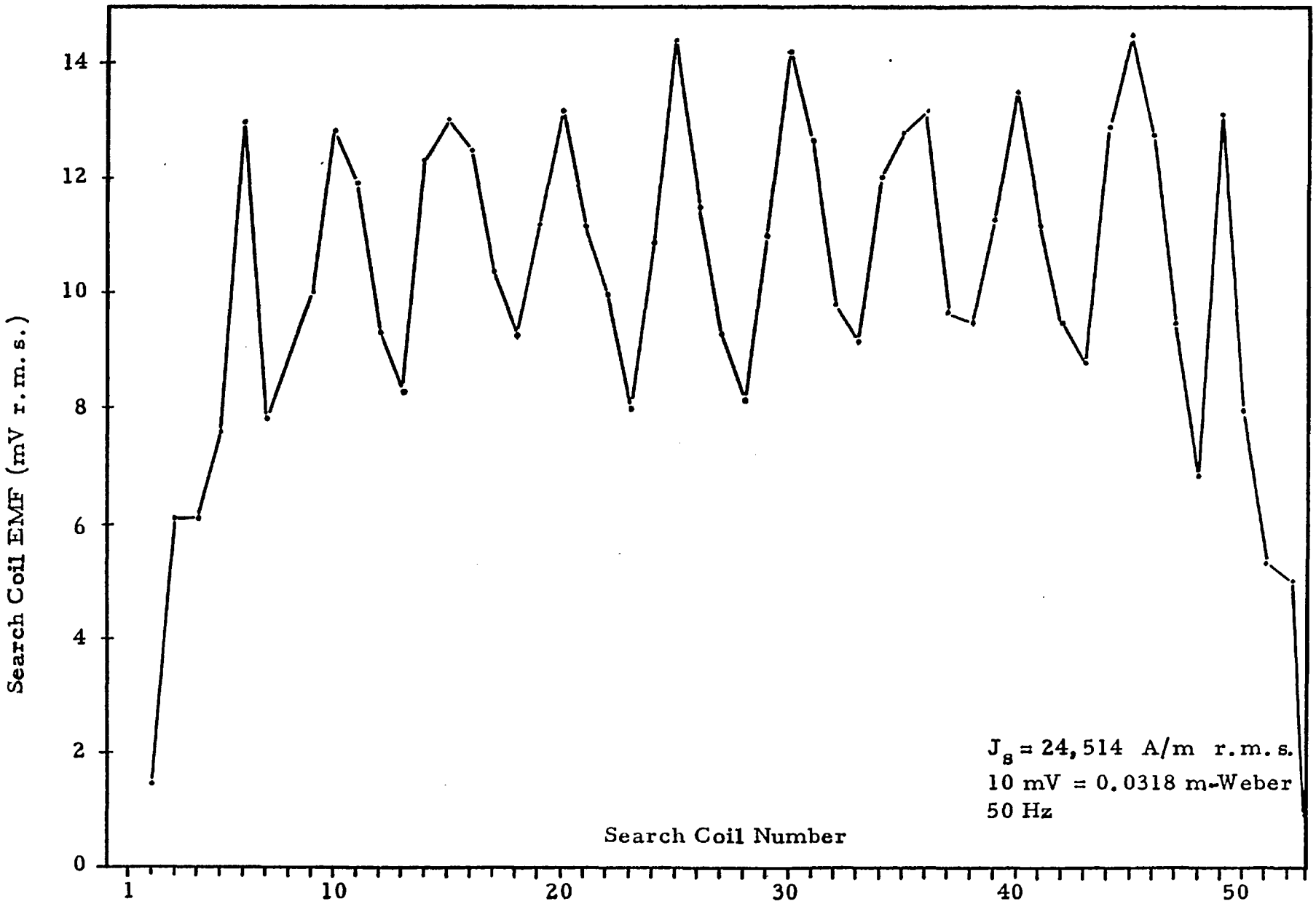

Figure 2.21 Airgap flux distribution at locked rotor for uniform pole-pitch winding with $6\frac{1}{3}$ poles.

plot corresponding to this locked rotor test is given in Figure 2.22 where it is clear that there are no sharp phase changes between slots using the search coils with an area of 4213 mm^2 directly over the core width and one slot pitch longitudinal.

The running light (σ = 0.011) flux distribution for the 6 1/3 pole LIM is presented in Figure 2.23 whereby the fitting of an exponential function to the experimental data indicates that the rotor magnetization time constant is 0.072 seconds and the machine has a Goodness factor of 22.6. This basic characteristic will be retained on all LIM-ASC-I tests and for the LIM-ASC-II, the Goodness will change to approximately $(.2466/.2025)^2$ 22.6 = 33.5. In practice, as most tests for this 11-pole machine used a slightly larger airgap along with a larger secondary overhang resistance, the Goodness factor is taken to be in the range of 28.4 to 30.

Figure 2.23 may also be used to determine the rotor phase angle upper limit while a high frequency test would be needed for a more exact evaluation. At the entry-edge of the machine, the first search coil indicates about 1 mV while the flux distribution shape indicates that for an infinitely-long primary, the last coil would read 167 mV, therefore from (2.8).

$$\theta \leq \tan^{-1}\left[\frac{1}{167}\ (22.6)\right] = 7.7^{o}$$

Based on these tests, Kelvin bridge measurements of the DC resistance, the locked rotor torque and synchronous watts, the elementary equivalent circuit of the 6 1/3 pole LIM prior to power factor improvement is shown in Figure 2.24.

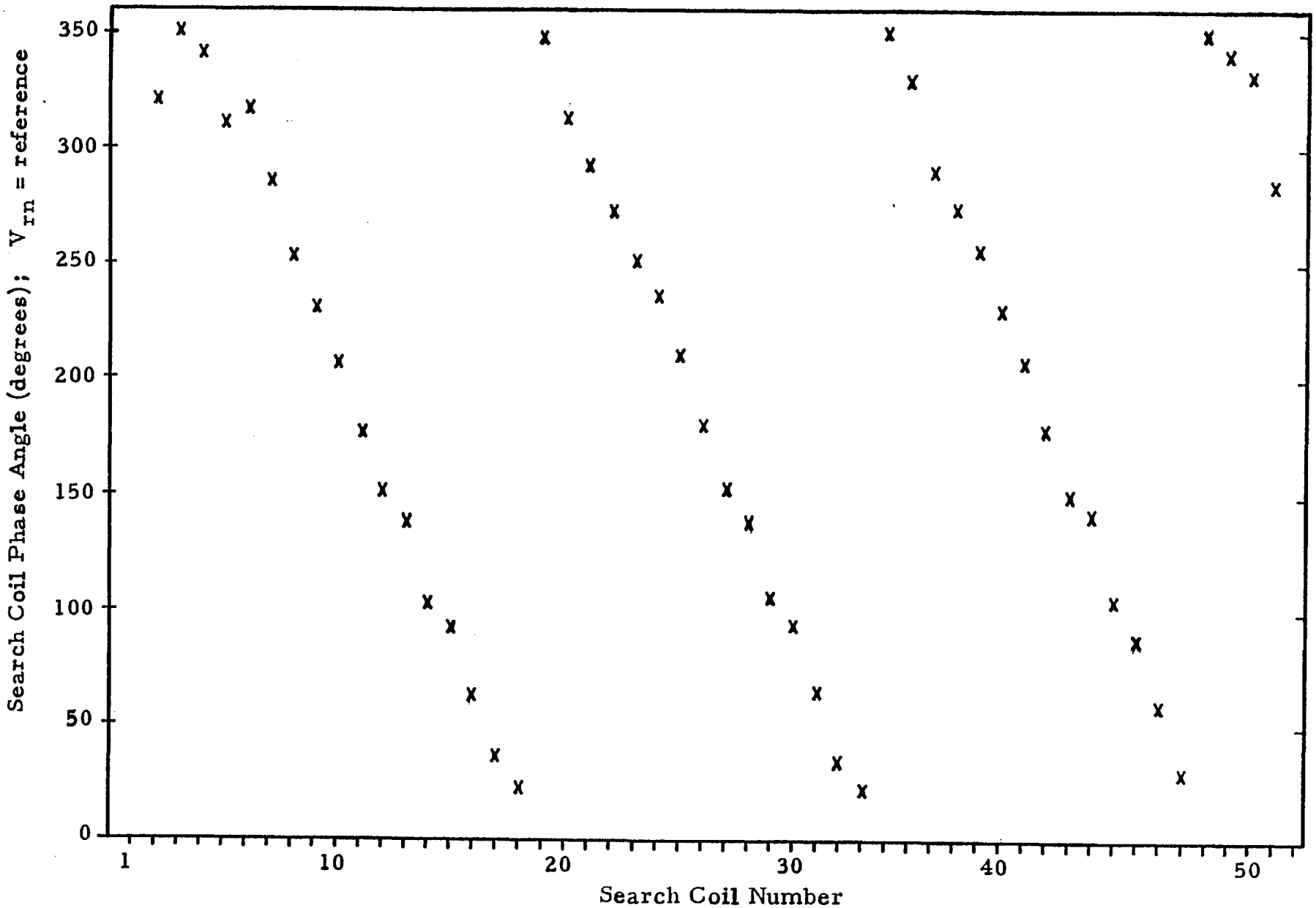

Figure 2.22 Phase distribution of airgap flux at locked rotor for uniform winding with $6\frac{1}{3}$ poles at 50 Hz.

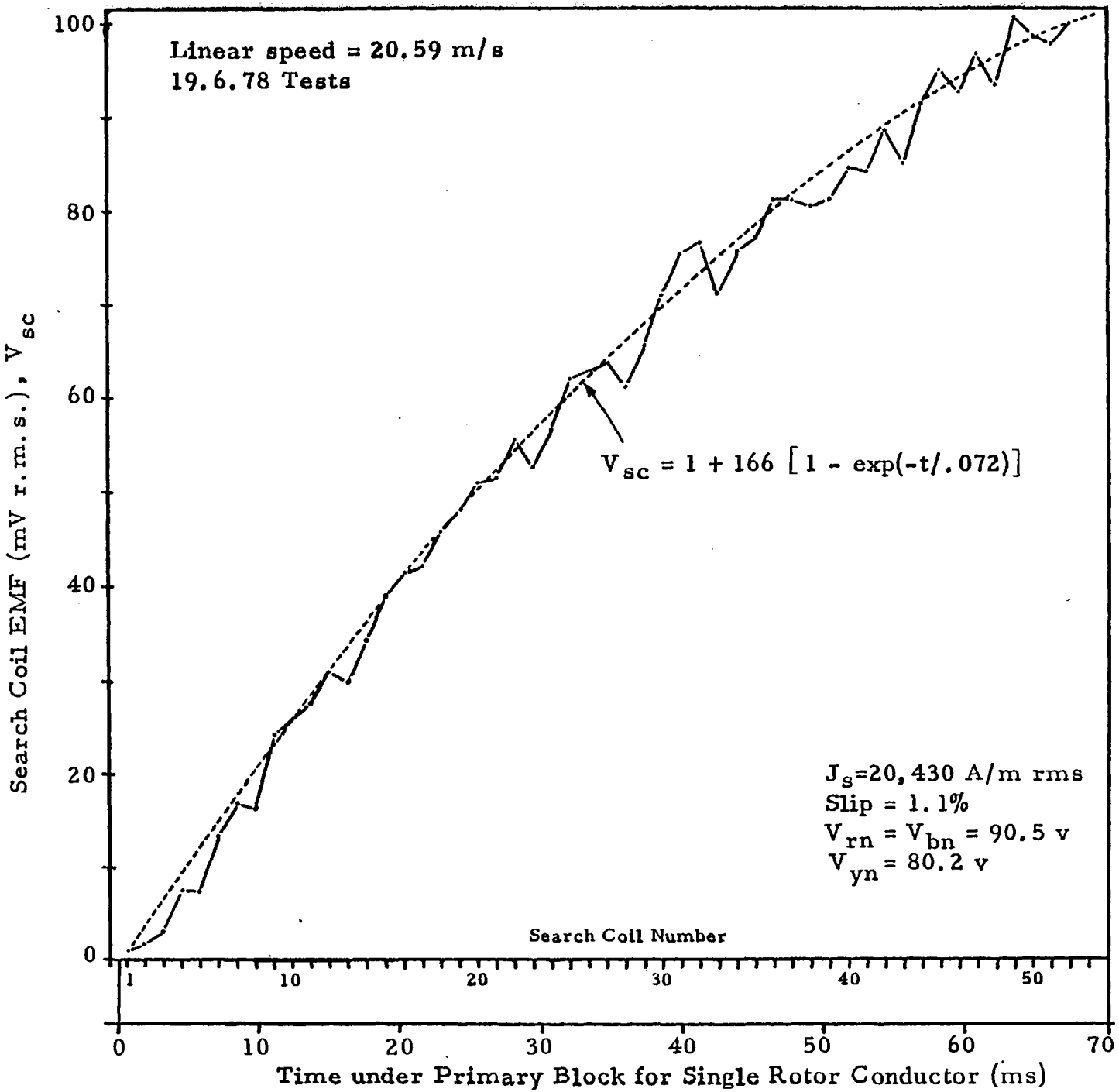

Figure 2.23 Determination of rotor-magnetization time constant on $6\frac{1}{3}$ pole LIM at 50 Hz.

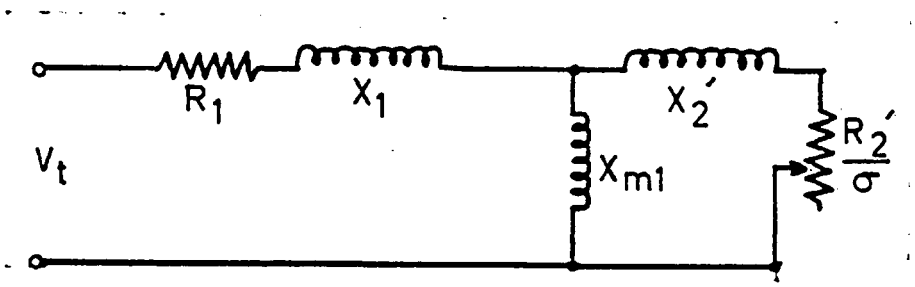

	Phase R	Phase Y & B	
R_1	0.485	0.404	Ohms
X_1	1.416	1.245	
X_m	9.0	7.5	
R_2	0.398	0.332	
X_2	0.054	0.045	

Figure 2.24 Equivalent circuit parameters of the $6\frac{1}{3}$ pole LIM valid for low and medium speeds at 50 Hz.

2.3 IN-PHASE AND QUADRATURE DECOMPOSITION

In Figure 2.25, the flux wave has been resolved into two components, B_p and B_q. The first of these is a flux wave in phase with the stator current loading wave $j_s = J_s \sin(\omega t - \pi s/\tau_p)$ whilst the second is in quadrature with it. The convenience of such a resolution is that the integral $\int B_p J_s$ is the mechanical power developed, and $\int B_q J_s$ represents the reactive power circulating in the machine. The total length of the machine can be measured along the abscissa of Figure 2.25 and the number of waves under the active zone depends on the relationship between the fractional slip σ, and the number of stator poles in the sector, n. Thus for $\sigma = \frac{1}{2}/(n + \frac{1}{2})$ the stator ends at A. For $\sigma = 1/(n + 1)$ the end of the block is at B. The points C and D correspond to slip values of $1\frac{1}{2}/(n + 1\frac{1}{2})$ and $2/(n + 2)$, respectively, and so on.

A conventional rotary machine never entails such phenomena. If its performance were to be shown on a diagram such as Figure 2.25 it is understood that this comparison is made between machines of the same pole-pitch, active length of periphery, fed with the same current loading J_s. Such a machine is referred to as an equivalent conventional machine (ECM). In this comparison the straight line PQ represents the B_p curve, and the baseline OR is the B_q curve. This also assumes that neither machine requires magnetizing current (infinite Goodness) and neither has magnetic leakage.

Several key points emerge from this approach.

(i) For values of σ and n such that $\sigma < 1/(n + 1)$, identified as Quadrant I, $\int B_p ds$ is less for the arc machine than the rectangle PB' BO, i.e rotor losses above those in the equi-

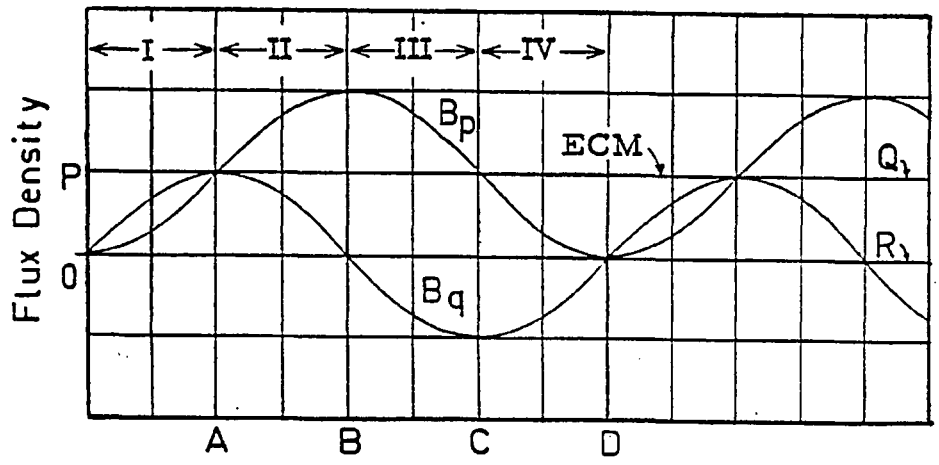

Figure 2.25 Airgap flux distribution in an idealized short-primary induction machine with no leakage flux and zero magnetization requirement; valid for all speeds in general.

valent conventional machine will occur. At precisely $\sigma = 1/(n + 1)$ there will be no difference in the net mechanical output.

(ii) For values such that $1/(n + 1) < \sigma < 1\frac{1}{2}/(n + 1\frac{1}{2})$, labeled Quadrant II, more output per unit current will be obtainable from the transient-ridden arc motor than in the equivalent conventional machine. This does not imply that the efficiency will ever exceed 100%. Rather, in the transient mode an induction motor may have a higher efficiency than predicted by the relation σ = rotor loss/rotor input, as derived from the steady-state equivalent circuit.

At $\sigma = 2/(n + 2)$ the two machines are externally indistinguishable, but internally the arc machine incurs a penalty (as it does for all values of slip between $\sigma = \frac{1}{2}/(n + \frac{1}{2})$ and $1\frac{1}{2}(n + 1\frac{1}{2})$ in that both the core flux and the tooth flux in the central regions of the arc exceed those in the equivalent conventional machine.

(iii) In Quadrant III, the B_q characteristic starts to take on negative values although it is clear that the $\int B_q ds$ will always remain positive and the machine as a whole is operating at a lagging power factor. For all values of slip other than $\sigma = 2/(n + 2)$, $4/(n + 4)$, $6/(n + 6)$ etc. the value of $\int B_q ds > 0$. However, the importance of Quadrant III is that this represents the useful aspect of a third source of reactive kVA and this will be a negative value in certain peripheral locations in contrast to the conventional, positive magnetizing and leakage flux reactive requirements. This is the most preferred quadrant suggesting that power factor improvement will be able to occur at constant efficiency.

(iv) At block positions following the peak of the negative B_q curve, as depicted by Quadrant IV, the B_p wave is reduced to values less than the ECM level yet the mechanical power developed

by the whole machine is still above the conventional rotary machine. It neglects any exit-edge power losses which are not included in the model which has an infinitely long primary block. In general, Quadrant IV represents the second most desirable mode for "artificially" extending the machine's range of operation in this peripheral location.

The ensuing development of the short-primary machine, based on these concepts commenced with one central idea. That, just as easily as transient phenomena caused the airgap density to change from a constant level to oscillating, it ought to be possible to reverse this process and in so doing maintain a constant but negative B_q value at all longitudinal positions beyond point C in particular without affecting the B_p and B_q characteristics from O to point C. This mechanism would therefore continue supplying B_p at the ECM level yet accumulating simultaneously an ever increasing amount of negative B_q. In the two rotary machines that evolve this principle into practical winding configurations the equivalent of point C is referred to as the θ_1 location with the exception that flux density at point O will never be zero due to the "re-entry" flux phenomena at high speed (in the rotary θ-Pinch machines only).

In a majority of short-primary machines, the largest reactive requirement will be the airgap magnetization rather than the leakage flux and is directly accounted for in equations (2.1) and (2.2). Figures 2.26 and 2.27 plot the B_p and B_q waves up to 9 poles for the specific case of G = 30 which represents the basic LIM-ASC-II motoring section design whereby airgap magnetization is appreciable but not excessive. In general, most linear machines even at the megawatt level rarely exceed G = 30; this characteristic is presented as the first illustration of a departure from

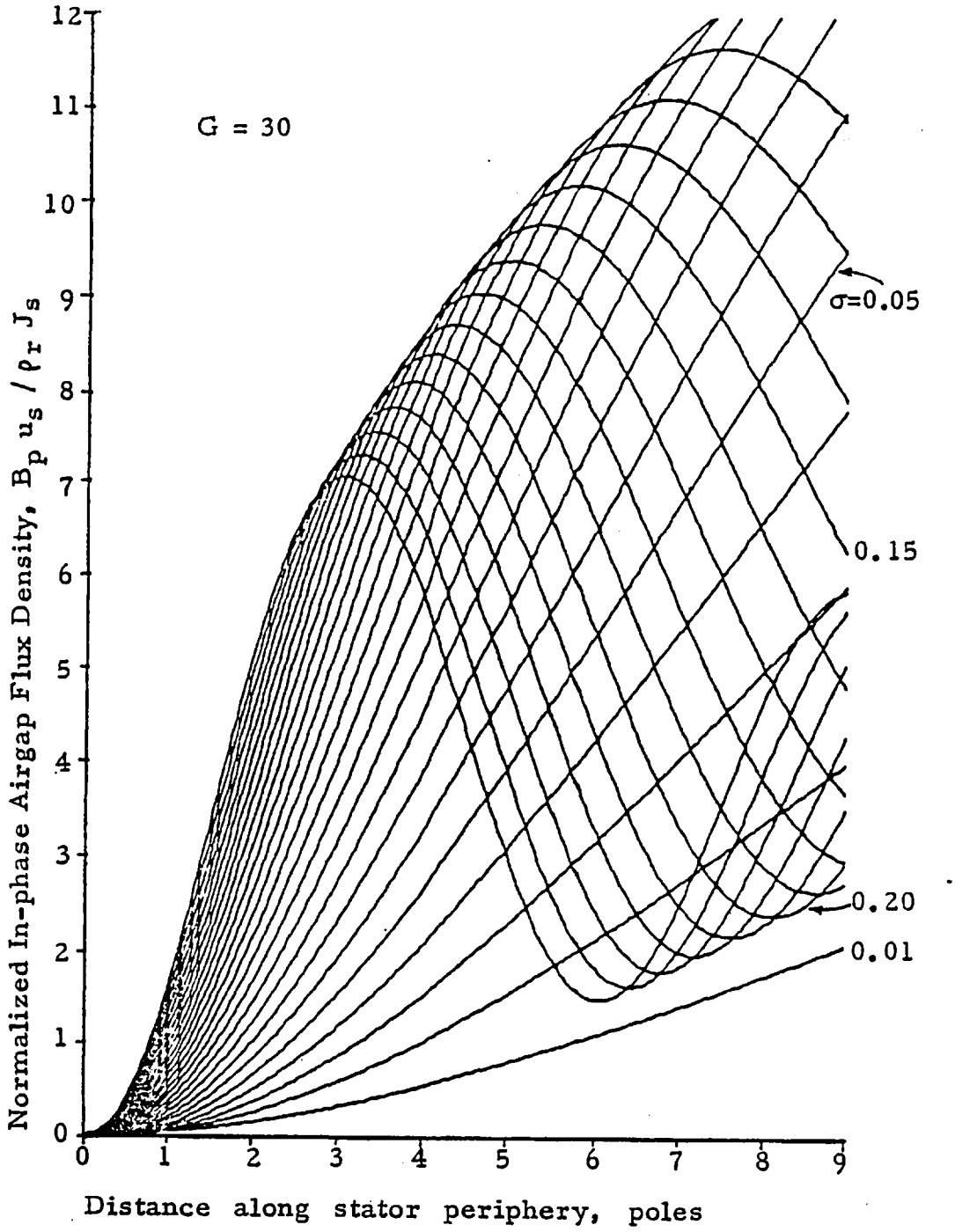

Figure 2.26 In-phase airgap flux density versus longitudinal position for the motoring sector of LIM-ASC-II.

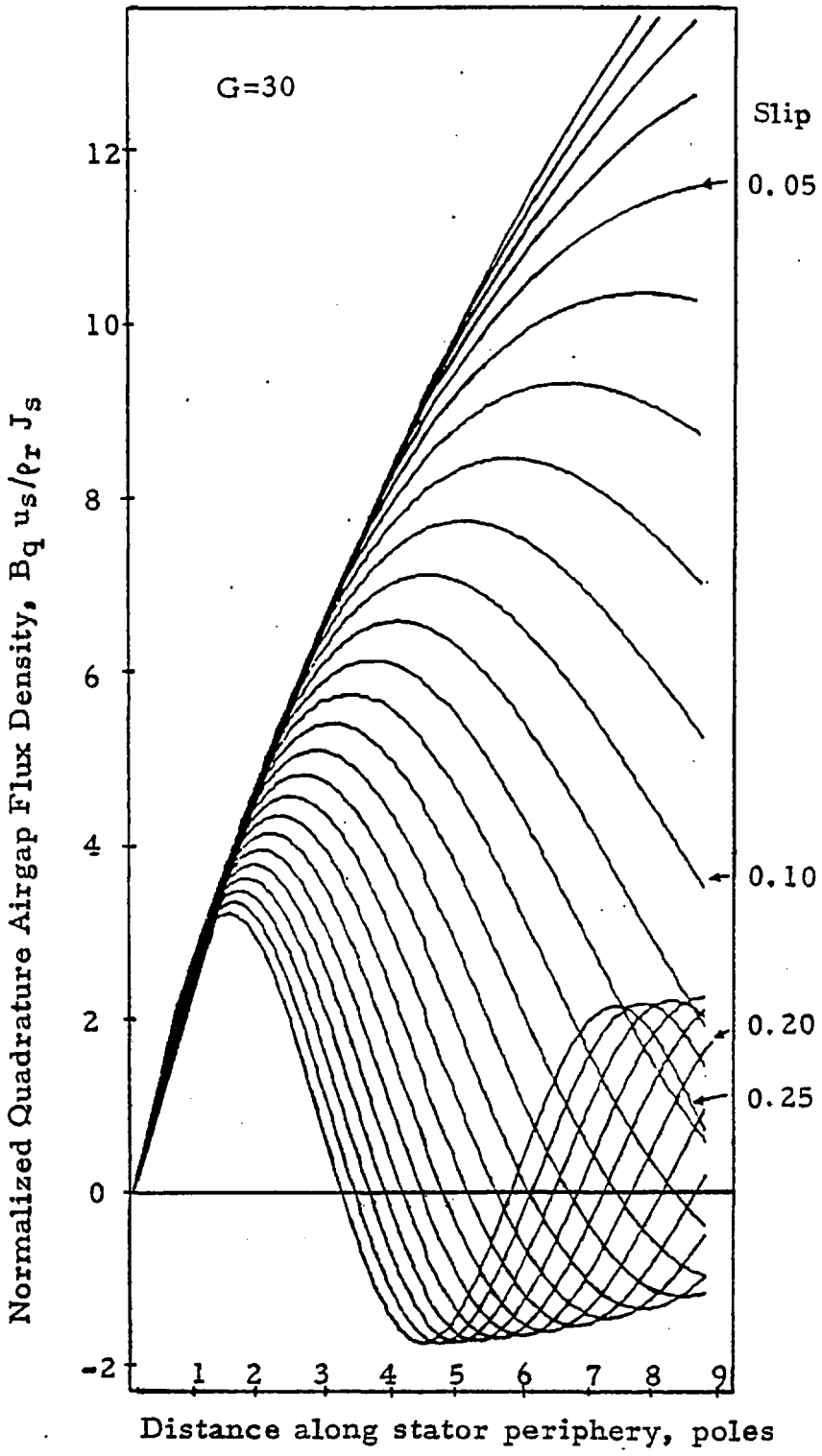

Figure 2.27 Quadrature airgap flux density versus longitudinal position for the motoring sector of LIM-ASC-II.

the non-decaying oscillations of Figure 2.25. With decreasing values of slip the relative magnetization requirement with respect to the B_q characteristic is pronounced enough that, for example at two practical upper ranges for slip values

$$\frac{|B_q\ (s/\tau_p = 4.5,\ \sigma = 0.25)|}{B_q\ (s/\tau_p = 1.5,\ \sigma = 0.25)} = 53.7\%$$

and

$$\frac{|B_q\ (s/\tau_p = 8.5,\ \sigma = 0.15)|}{B_q\ (s/\tau_p = 2.8\bar{3},\ \sigma = 0.15)} = 23.6\%$$

In the case of $G = \infty$, it is clear that both of the above ratios will be unity. From inspection of (2.2) and setting $s = \infty$, the normalized quadrature waves, will attain the steady-state or ECM level of

$$\frac{B_q\ v_s}{J_s\ \rho_r} = \frac{1/G}{\sigma^2 + 1/G^2} \qquad (2.14)$$

In Figure 2.27, a synchronous field speed of 25.3m/s and $G = 30$ was used; by evaluating equation (2.14) at a slip value of 0.25, the ECM level for the B_q component is 0.524 per unit. This may also be graphically determined by extending the Quadrants IV & V modulation envelop past the 9th pole location and measuring the offset above the abscissa.

The ECM level for the in-phase flux density is

$$\frac{B_p\ v_s}{J_s\ \rho_r} = \frac{\sigma}{\sigma^2 + 1/G^2}\Bigg|_{G = 30,\ \sigma = 0.25} = 3.93 \qquad (2.15)$$

and a slip of 0.15 per unit, (2.15) yields a value of 6.35. In the limit of infinite Goodness, it is clear that the ECM level will be equal to $1/\sigma$, so that the magnetization requirement of G=30 represents a 1.75% and a 4.7% reduction in the B_p component for the slip values of 0.25 and 0.15 respectively. As with the quadrature flux evaluation, to assess the effects of decrement between the points "B" and "D" on the B_p wave, now consider the effective reduction in the oscillating component about the ECM level of $1/\sigma$ so that these may be compared with the B_q ratios at points "C" and "A" about the zero ECM level.

$$\left.\frac{1/\sigma \; - B_p(s/\tau_p = \frac{2(1-\sigma)}{\sigma}, \sigma)}{B_p(s/\tau_p = \frac{1-\sigma}{\sigma}, \sigma) - 1/\sigma}\right|_{\sigma = 0.25} = 82.9\%$$

With these effects of magnetization included, the theoretical maximum rate of change of the quadrature flux with respect to peripheral angle, $\theta = s\pi/\tau_p$ along the airgap, motoring sector is, by differentiating (2.2)

$$\frac{d\,B_q}{d\theta} = \frac{\hat{J}_s \; \rho_r \; u_s/G}{(\sigma u_s)^2 + (u_s/G)^2} \; \frac{\pi\sigma}{(1-\sigma)}\left[\frac{1}{\sigma G} + \sigma G\right] \qquad (2.16)$$

The rate of change of B_q over the asynchronous condenser windings is negative and thus the ratio of $\dot{B}_q$ in the first section ($\theta < 3\pi/2$) to that in the second section ($\theta > 3\pi/2$) is

$$\beta = \dot{B}_q(\theta < 3\pi/2) \Big/ \dot{B}_q(\theta > 3\pi/2) = -\pi\left[1 + (\sigma G)^2\right]$$

The transition to machine parameters of value occurs as $\sigma G=1$ in the interests of maximizing β; for practical machines with $\sigma = 0.02$ and G=150, the ratio is $\beta=-31.4$ and consequently the B_q decrement in the ASC region is minimal in large units.

A similar calculation at $\sigma = 0.15$, shows that the magnitude of the B_p oscillation at the Quadrant III-IV boundary has decreased to 76.6% of the value at the Quadrant I-II boundary. Thus, in general the effects of magnetization are most pronounced with the quadrature flux wave both in terms of the magnitude of B_q and the change in the peak component with slip, $d\hat{B}_q/d\sigma$.

Further inspection of (2.1) and (2.2) indicates that it is accurate to express both flux waves as a function of the pole position - slip product $s\sigma/(1-\sigma)\tau_p$ rather than pole position alone. The in-phase and quadrature waves have been replotted in Figure 2.28 for the G = 30 case to illustrate this noting that each curve has its own abscissa. These general curves are only valid over a limited slip range in contrast to Figure 2.25; as the Goodness increases so does the range of validity. On the B_p characteristic, the line PQ represents the ECM level while the line SR represents the ECM level on the B_q graph.

A potential reactive generation scheme is indicated on both graphs by the dashed line commencing at point C, for example at a pole-slip product of $n\sigma/(1-\sigma) = 0.575$ with respect to Curve B. This would allow the in-phase component to maintain a level higher than the ECM value initially and the quadrature to assume the most negative value initially; the horizontal dashed line does not account for the G = 30 case which controls the natural decay rate of such a scheme. Rather, the purpose of these curves is to show one method of implementing a practical winding configuration. Let Curve A represent the flux distribution for one primary coil and the successive 12 characteristics up to Curve B represent 12 successive coils along the primary in the opposite direction of rotor rotation in a 15 slot/pole winding. Then it is clear that as all coils are operating at the same slip (based on a definition

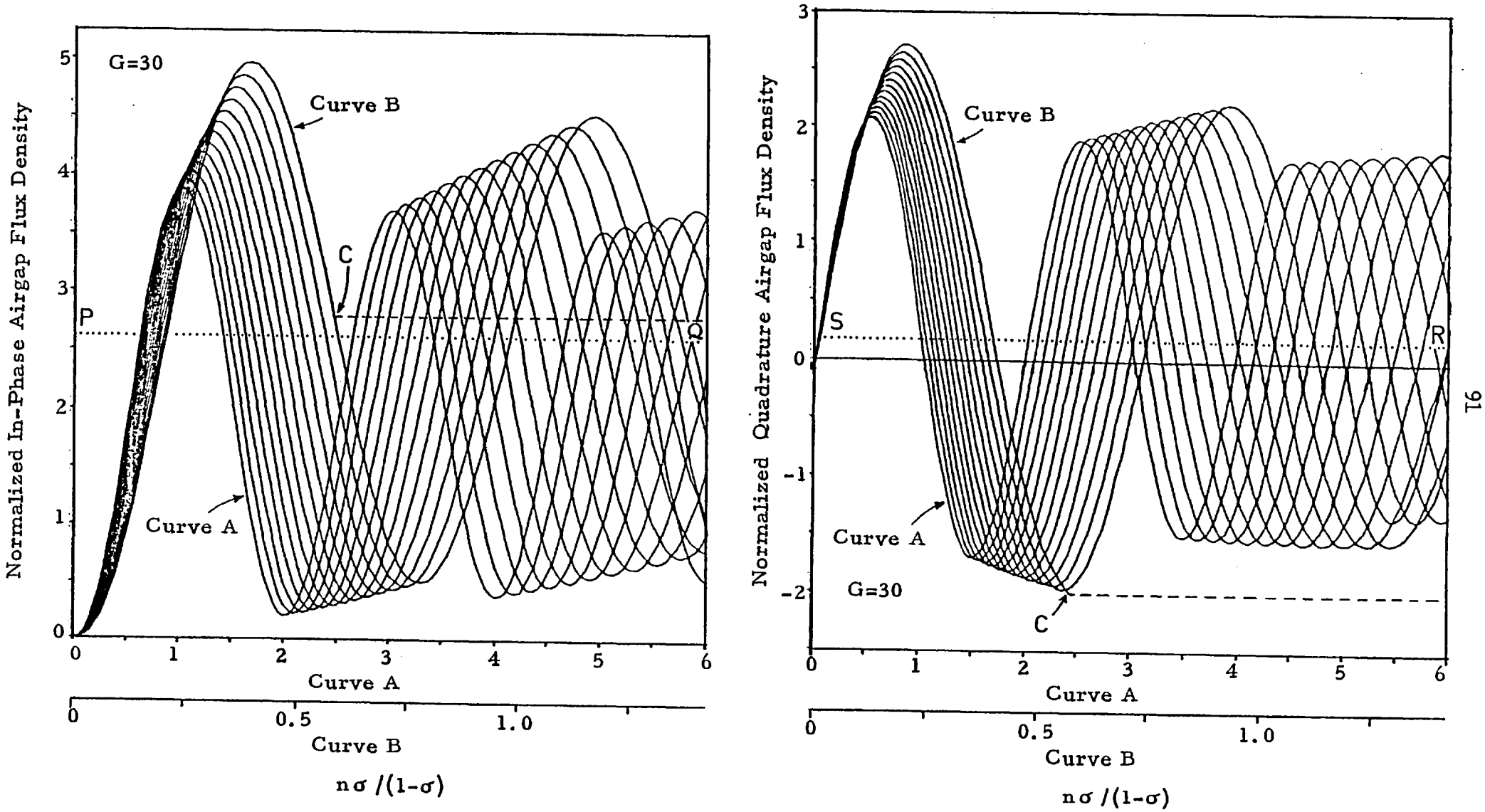

Figure 2.28 General airgap flux distribution at medium speeds as a function of longitudinal position - slip value product.

of fractional rotor speed only), the coils near the Curve A characteristic when at maximum B_q output will only be able to yield B_p values below the ECM level P-Q as occurring at $n\sigma/(1-\sigma) = 1.5$. This is a direct result of having a Goodness factor approximately equal to $n\pi/(1-\sigma)$.

The method for ensuring that a quasi-constant B_p or B_q level could be maintained after point C, first evolved by supposing that a second, current-forced winding on the primary block (referred to as the tertiary winding) was wound starting at point C on top of the primary winding (which starts at O). In effect, a constant-magnitude $B_p - B_q$ distribution would result as the superposition of two oscillating excitations, in both time axes. The one block would thus contain the "ramped" linear motor characteristic at the front end and a conventional rotary machine distribution (but having a negative B_q) over the bulk of the remaining sector. The only drawback appeared to be that ideally, for perfect neutralization, both primary and tertiary would have to be operated at equivalent surface currents which posed a problem either in terms of construction or utilization.

Since the first laboratory tests that produced a negative B_q characteristic did not have the facility of new machine construction, the modification of a single winding linear machine into two distinct but non-overlapping windings proved that it was not necessary to superimpose distinct flux waves by physically overlaying currents in the exit-end poles. Rather, the rotor current wave itself over the last poles sufficed as the other oscillating excitation; as experimentation later confirmed, the rotor is magnetizing the airgap past the point C. However, once this was established five key observations were noted.

(i) The pole-pitch in the tertiary winding, τ_{p3} should be

different from the primary pole-pitch, τ_{p1} according to the relation

$$\tau_{p3} = \tau_{p1} (1 - \sigma) \qquad (2.16)$$

this is not a necessary condition for reactive generation but important for full utilization of the rotor currents; all of the results in this chapter do not allow for this except by coil reconnection -- a stepped phase change.

(ii) It is not necessary for the tertiary surface current loading to equal or exceed the secondary current loading to generate leading kVAR in the tertiary; the tertiary loading can be treated as the equivalent of an armature reaction effect in a DC-field synchronous condenser.

(iii) Despite the differences in magnitude between j_{s3} and j_{s2}, a whole variety of power factor improvement options are available because a multiple of tertiary poles may either be connected in series or parallel to give at the terminals an effective $j_{s3} > j_{s2} \approx j_{s1}$ without any reduction of basic efficiency; the basic rotor loss is only incurred once -- under the primary sector.

(iv) The combination of a Goodness-dominated natural decay of rotor flux and a forced decay due to the tertiary reaction effect mean that these machines can have zero exit-effect power losses; if the tertiary sector is as long or longer than the primary sector than the exit-edge flux can be reduced to zero for all values of slip whereas the conventional LIM will only allow this condition when $\sigma = \frac{2}{n+2}$, $\frac{4}{n+4}$, etc. (which are the slip points whereby

reactive generation is always zero by the new scheme).

(v) The maximum value of negative B_q at the start of the tertiary winding, point C^+ would not have to be limited to the maximum negative B_q value at point C^- but that an "amplification" of flux occurs at the boundary depending on the change in surface current loading and on the exact mode (phase) of operation for the tertiary. For example if the B_p characteristic is of negligible importance beyond Quadrant III, then

$$\hat{B_q}(s = C^+) \approx \sqrt{\hat{B_q}(s = C^-)^2 + \hat{B_p}(s=C^-)^2} \qquad (2.17)$$

The limit on the tertiary reactive flux is simply the maximum total flux, B_t at the transition point but in general $B_t(s=C^+) \approx B_t(s=C^-)$. The mechanism for reactive generation really makes use of a basic VA source rather than a VAR source with the choice of use entirely up to the designer; if this edge apparent-power is consumed as real power then speed control is possible at the expense of power factor control. This basic apparent power transfer offered by a 4 pole LIM, a 2 pole tertiary and a phase-shift induction regulator was documented early in the experimentation and is shown in Figure 2.29 noting that the magnitudes at $\theta = 90^o$ and $\theta = 180^o$ are nearly identical. The instrumentation for this test is shown in Figure 2.44.

The modulation of the airgap flux density for the case of infinite Goodness results in certain locations along the periphery having zero flux at all times for a given slip $\sigma = \frac{2}{n+2}$; this is not the case for the G = 30 example because the decrement of the B_p wave never reached a zero level. However, in large rotary

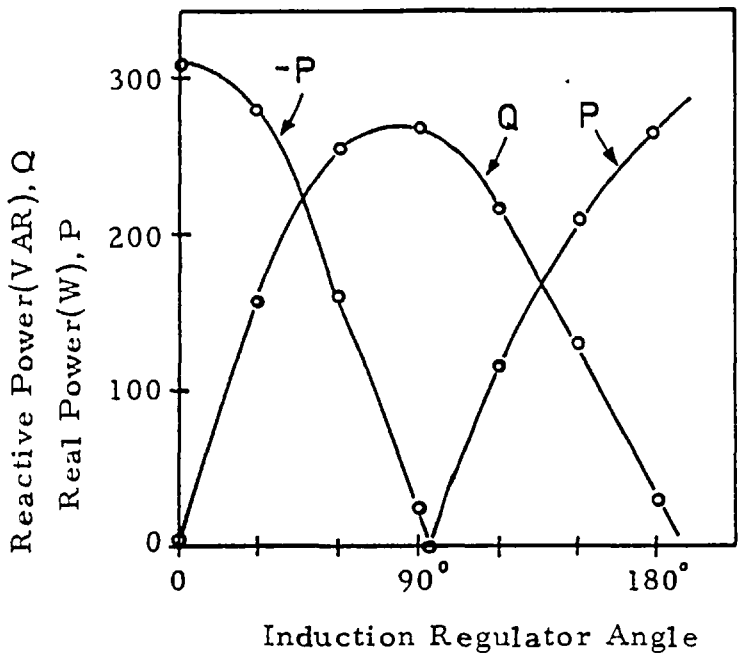

Fig. 2.29 a Net tertiary leading reactive power, Q, real power generated, P and real power absorbed, -P at 54 V_{ln}, 50 Hz primary excitation.

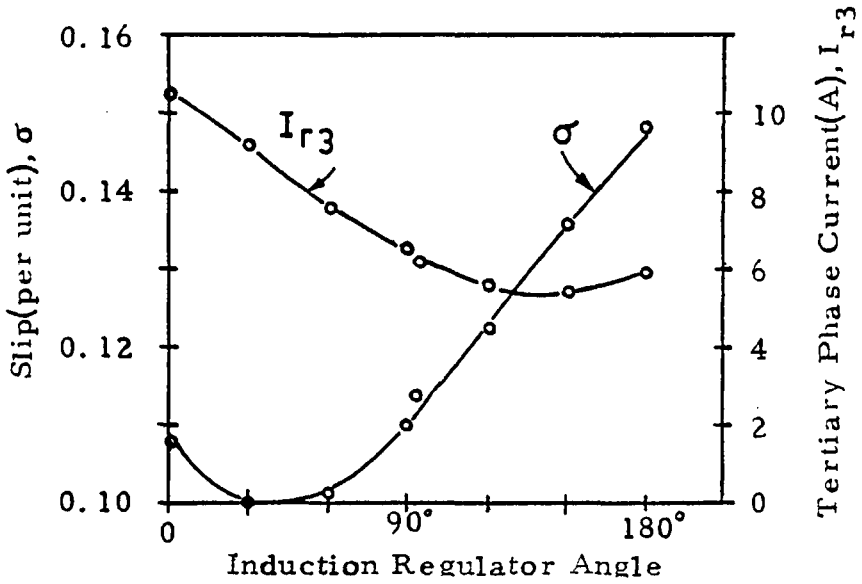

Fig. 2.29b Slip and tertiary current corresponding to Fig. 2.29a and without DC dynamometer loading; friction loss=280 W at σ =0.11.

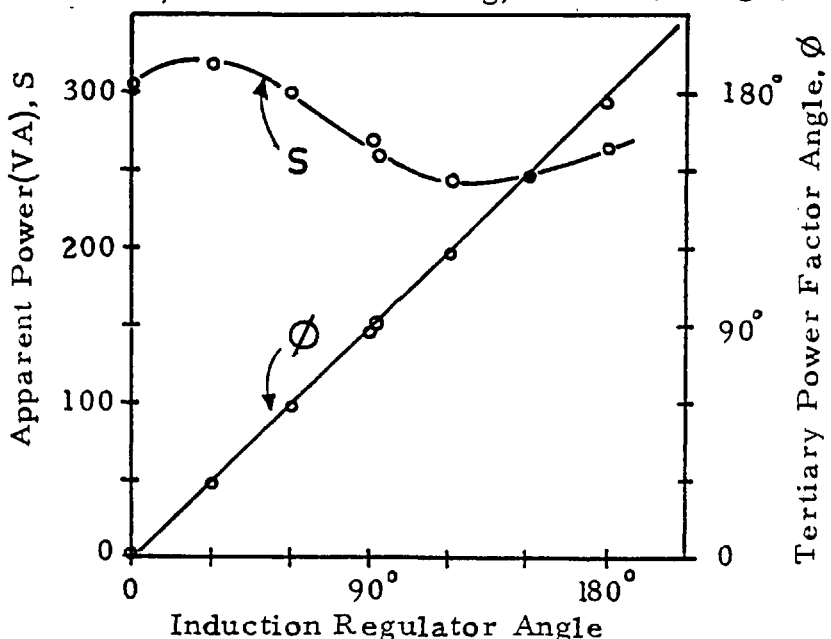

Fig. 2.29c Tertiary net apparent power and phase angle $\emptyset = \tan^{-1}(Q/-P)$

machines, such as the SCIM-MK.II, a Goodness of 212 is essentially the same as G = ∞ as regards the null flux locations. Furthermore, the concept of overlapping primary and tertiary windings was first simulated on the digital computer with both sections having G = 212, equal pole-pitches but a variable-phase, variable magnitude tertiary current loading. Each computerized flux plot maintains a constant, negative ratio J_{s3}/J_{s1} and by virtue of the large number of slips calculated a variable-phasing between the two sections is derived. Figures 2.30 through 2.32 consider the arbitrary case of J_{s3}/J_{s1} = -0.50 for all peripheral locations between three and seven poles and J_{s3} = 0 for n $\leq$ 3. Figure 2.30 is the most illustrative as it depicts the total component of airgap flux for σ = 0 to σ = 0.09 and then in the range σ = 0.50 to 0.37. In general, the low slip curves are relatively phase insensitive; the effect of J_{s3} is primarily to reduce the $\partial B_t/\partial s$ incremental slope as well as shifting the location of peak B_t to smaller s values. Obviously, these curves are the most important for high efficiency operation, but all high speed curves are relatively close to peaking at the s/τ_p=3 boundary and thus the effect of J_{s3} is limited to a single reduction mode. However, for medium slip values, at the s/τ_p=3 transition, there is a wide spread of B_t values from zero to over 50% of the peak value and thus a J_{s3} wave may be superimposed with a phase shift between the values of 0^o (corresponding to the σ= 0.50 wave) and 32.4^o (corresponding to the σ= 0.37 wave).

To appreciate the significance of the superposition technique, it should be emphasized that in the 0.50 to 0.37 range of slips, without the J_{s3} wave, B_t would continue oscillating in almost exactly the same manner for $s/\tau_p > 3$ (shown in Figure 2.30) as for $s/\tau_p < 3$ due to the high Goodness. The most useful superposi-

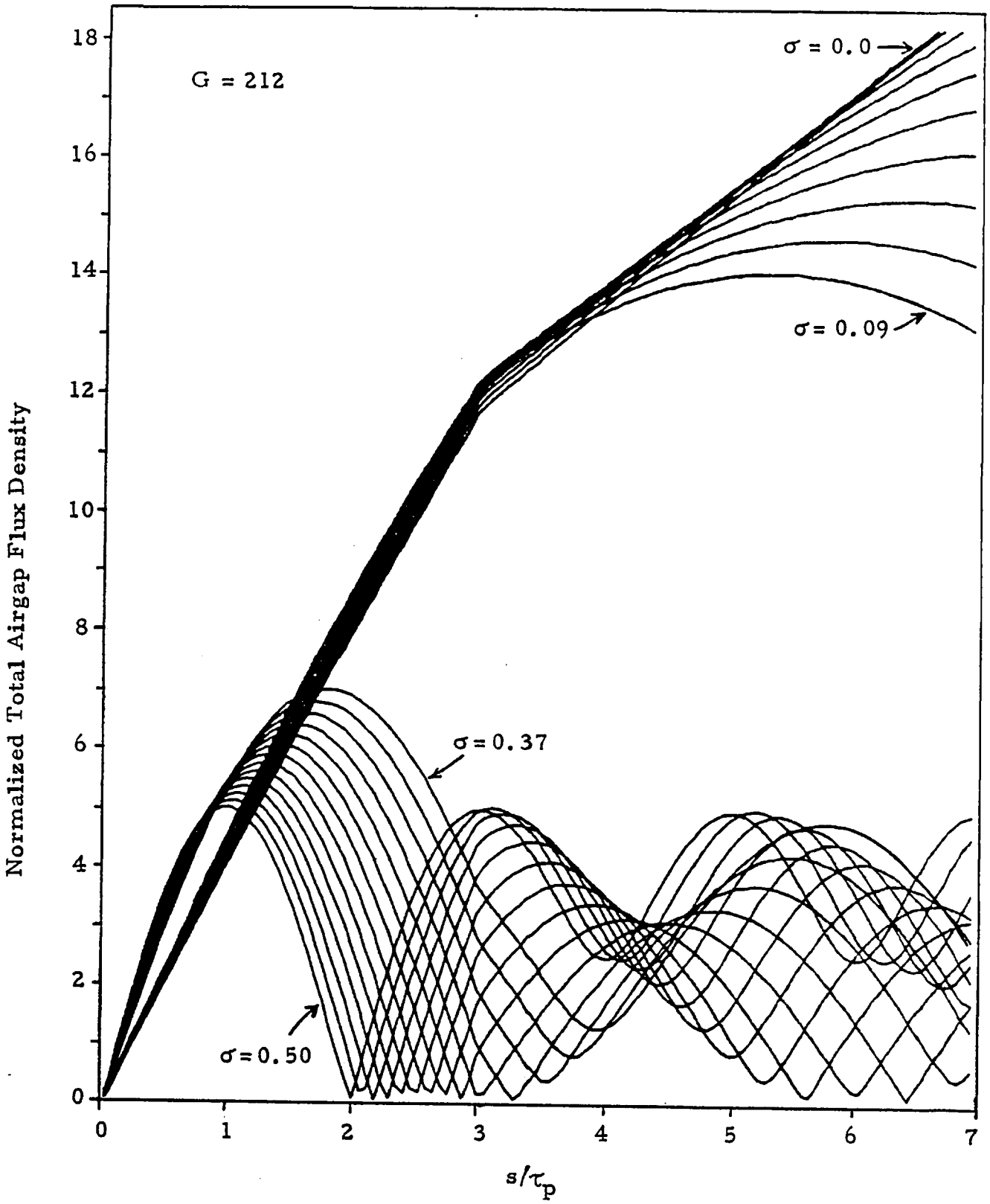

Figure 2.30 Total airgap flux density for primary winding from 0 to 3 poles and tertiary winding from 3 to 7 poles with high and low range of slip values with steps of 1%.

tion mode is the zero phase shift type initiated for the $\sigma = 0.50$ characteristic which appears to be "critically-damped". The magnitude of the B_t wave for $s/\tau_p > 3$ is exactly equal to $|J_{s3}/J_{s1}| \cdot B_t(s/\tau_p < 3)$ without <u>any</u> exponential decay in magnitude for the entire length of the block.

Figure 2.31 shows the in-phase airgap distribution with $J_{s3} = -0.5\ J_{s1}$ for slip values from 0.14 through 0.50 per unit. In general, the effect of the tertiary winding is to extend the negative B_p region for low values of slip. For slip values such as 0.41 the response for $s/\tau_p > 3$ is a 50% reduction in magnitude for which the oscillations never become negative as a consequence of initiating the J_{s3} wave at the point where the 0.41 slip curve is zero. To account for "carry-over" flux as in a practical rotary machine, two such identical sets of curves for B_p must be overlayed and a finite entry flux determined if the following expression of periodicity is not a whole number.

$$s/\tau_p = 2\left(\frac{1+\sigma}{\sigma}\right) \qquad (2.18)$$

For example, in the SCIM-MK.II machine, the total number of poles is four per repeatable section and a J_{s3} wave is introduced at $s/\tau_p = 3$. Then, Figure 2.31 indicates that the re-entry flux at $s = 0$ can be nulled naturally at a slip value of 0.388 but this should be avoided. (Equation (2.18) indicates that with a 4 pole block, normally periodicity will occur at $\sigma = 0.333$). The overwhelming conclusion is that in the range of $\sigma = 0.03$ to $\sigma = 0.10$ the J_{s3} wave will be ineffectual at pole numbers even as high as seven (similar to the $\sigma = 0.14$ curve which does not even appear to change slope at $s/\tau_p = 3$) and this is precisely what is de-

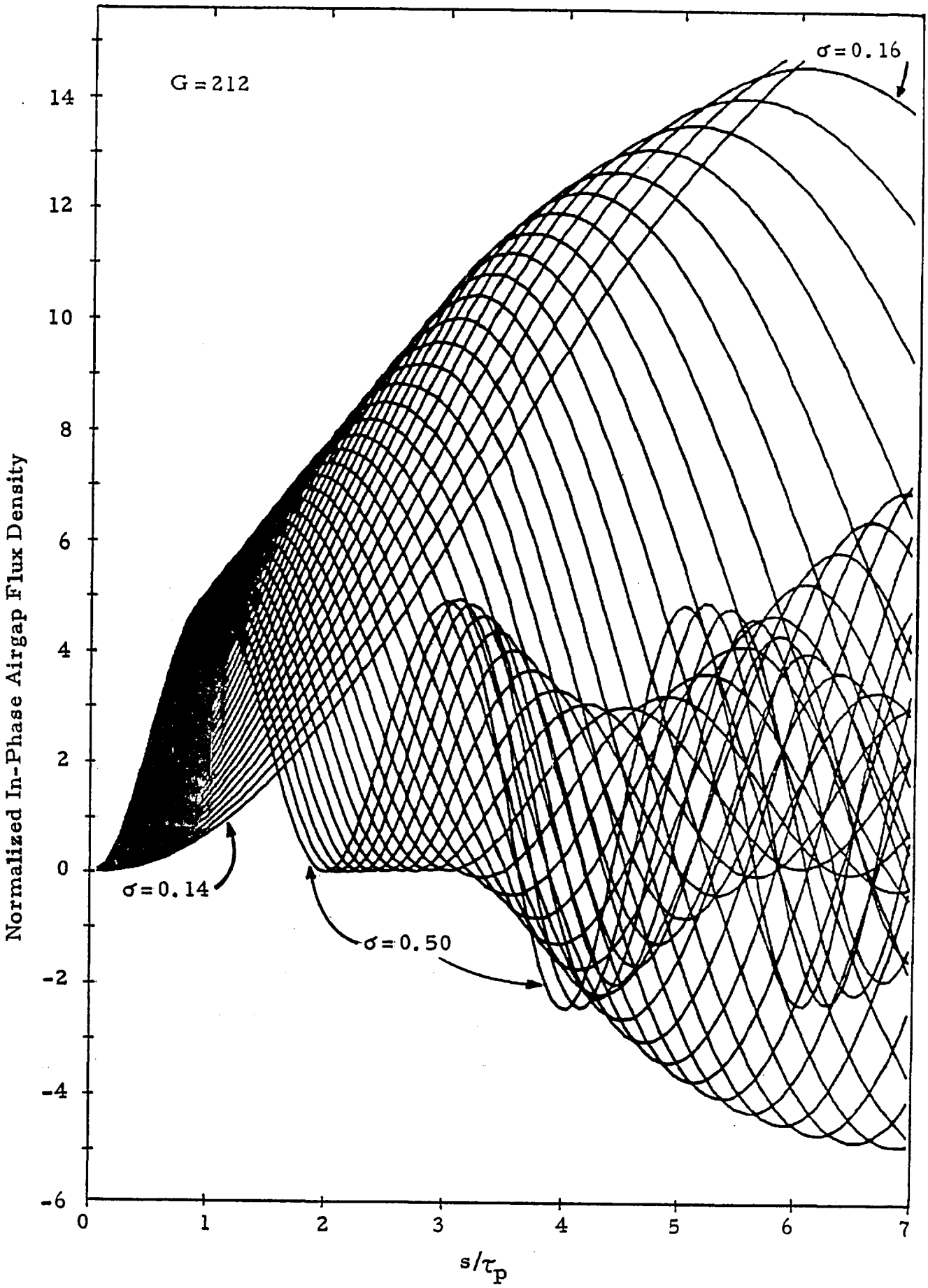

Figure 2.31 In-phase airgap flux density for primary winding from 0 to 3 poles and tertiary winding from 3 to 7 poles with different values of per unit slip.

sired for the B_p characteristic in a power producing machine. Starting performance has been altered by the drastic modulation attributed to the series-connected tertiary winding but in the laboratory machine one particular parallel-series winding has been tried which circumvents harmonic speeds.

Figure 2.32 depicts the quadrature airgap distribution with $J_{s3} = -0.5\ J_{s1}$ for slip values from $\sigma = 0.50$ through $\sigma = 0.29$ and a $s/\tau_p = 3$ transition point "C". Of the curves shown in the tertiary overlap region the $\sigma = 0.29$ response is the most valuable since B_q peaks at about -6.25 as a consequence of this wave being closest to zero at the $s/\tau_p = 3$ point. (The wave which actually yields the maximum negative B_q occurs at $\sigma = 0.28 \geq \frac{1}{3+1}$ as seen by Figure 2.36). It is clear that once this B_q wave has peaked at $s/\tau_p = 4$, the in-phase nature of J_{s3} with B_q causes the latter to rise to an equally large but positive value. Therefore the most desirable technique is to either cut-off the block between $s/\tau_p = 4$ and $s/\tau_p = 5$ or else at exactly $s/\tau_p = 4.1$ reconnect the last coils in the tertiary winding to give J_{s3} a 180° phase shift. The latter is the preferred method of solution because it reduces the positive rate $d\bar{B}_q/dn$ from a value of 7.5 per unit/pole to 3.75 per unit/pole where it is understood that one unit = $B_q\ v_s/\rho_r\ J_{s1}$. The net result is that the $\sigma = 0.29$ curve will not cross the abscissa until $s/\tau_p > 6.1$ and even by visual inspection it is clear that $\int_0^{6\tau_p} B_q ds < 0$. This one particular mode is shown in Figure 2.33 and compared against the $\sigma = 0.29$ characteristic with $J_{s3} = 0$ which yields $\int B_q ds \approx 0$ at G = 212.

The high speed plot of B_q with tertiary stator excitation is shown in Figure 2.34 for $\sigma = 0$ through $\sigma = 0.28$; note that for

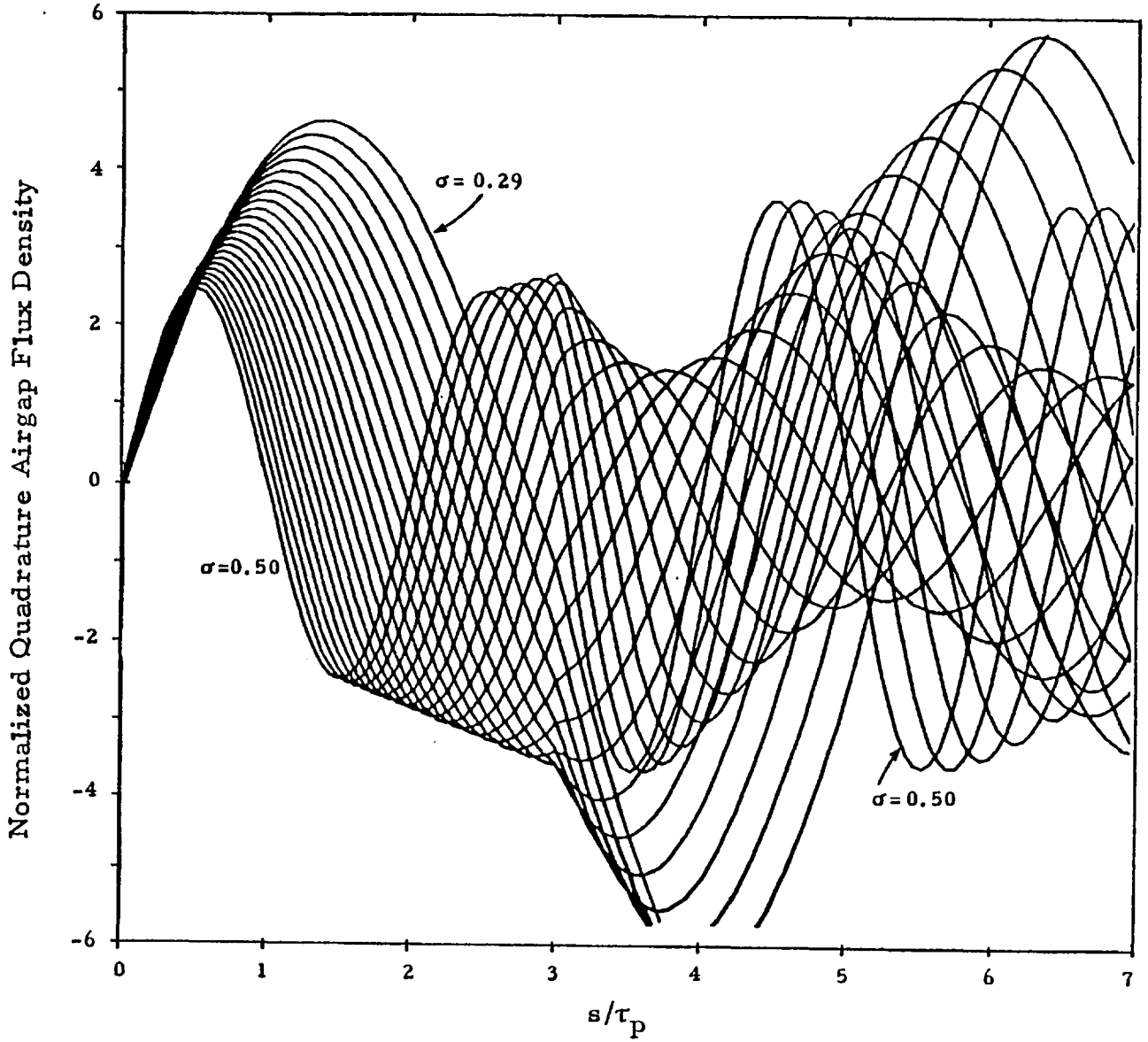

Figure 2.32 Quadrature airgap flux density for primary winding from 0 to 3 poles and tertiary winding from 3 to 7 poles at medium slip values in per unit.

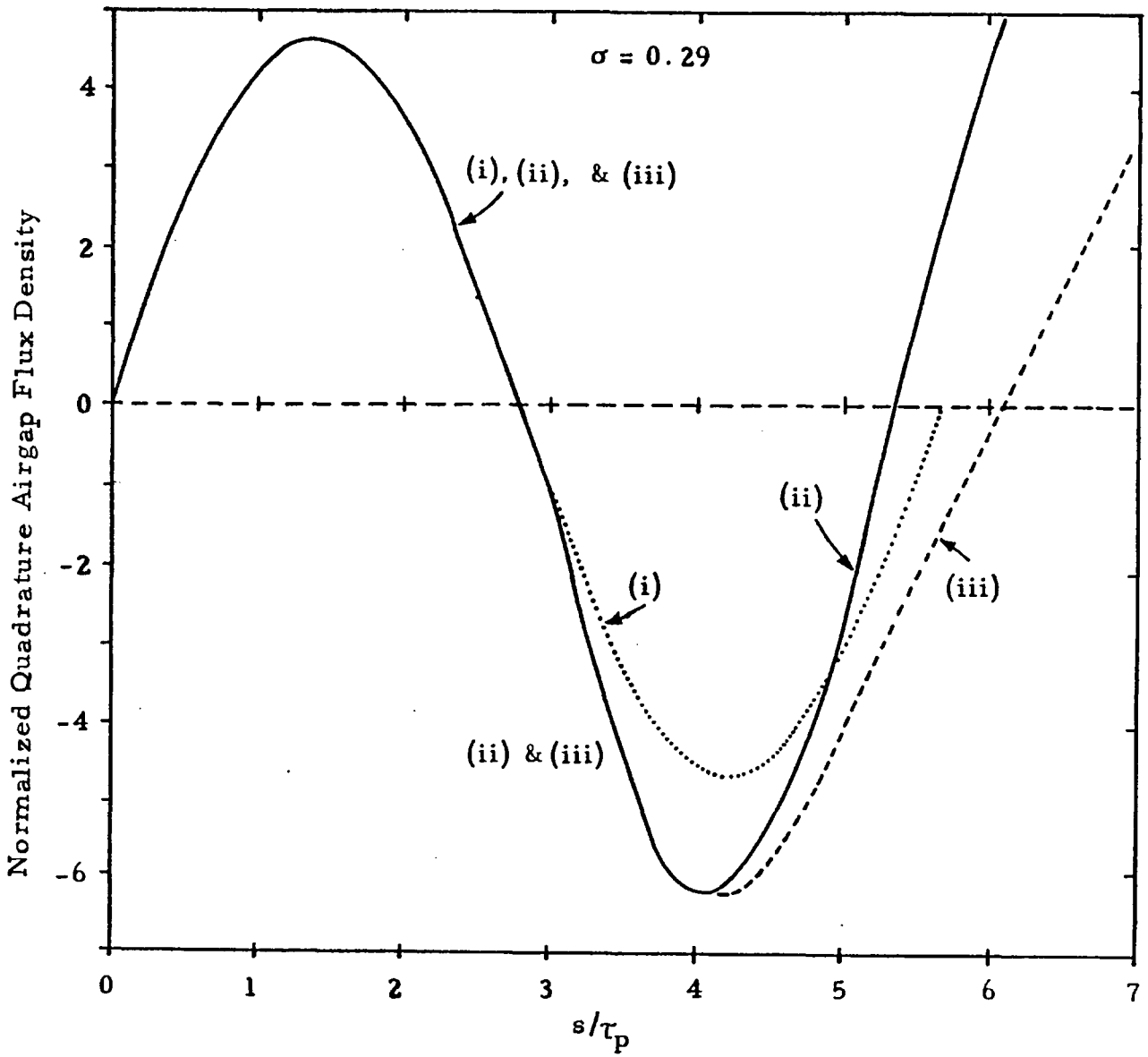

Figure 2.33 Quadrature airgap flux density at 29% slip for (i) uniform primary winding, (ii) primary with superimposed tertiary $J_{s3}=-0.5\ J_{s1}$ and (iii) tertiary with 180° phase change at $s/\tau_p=4.1$

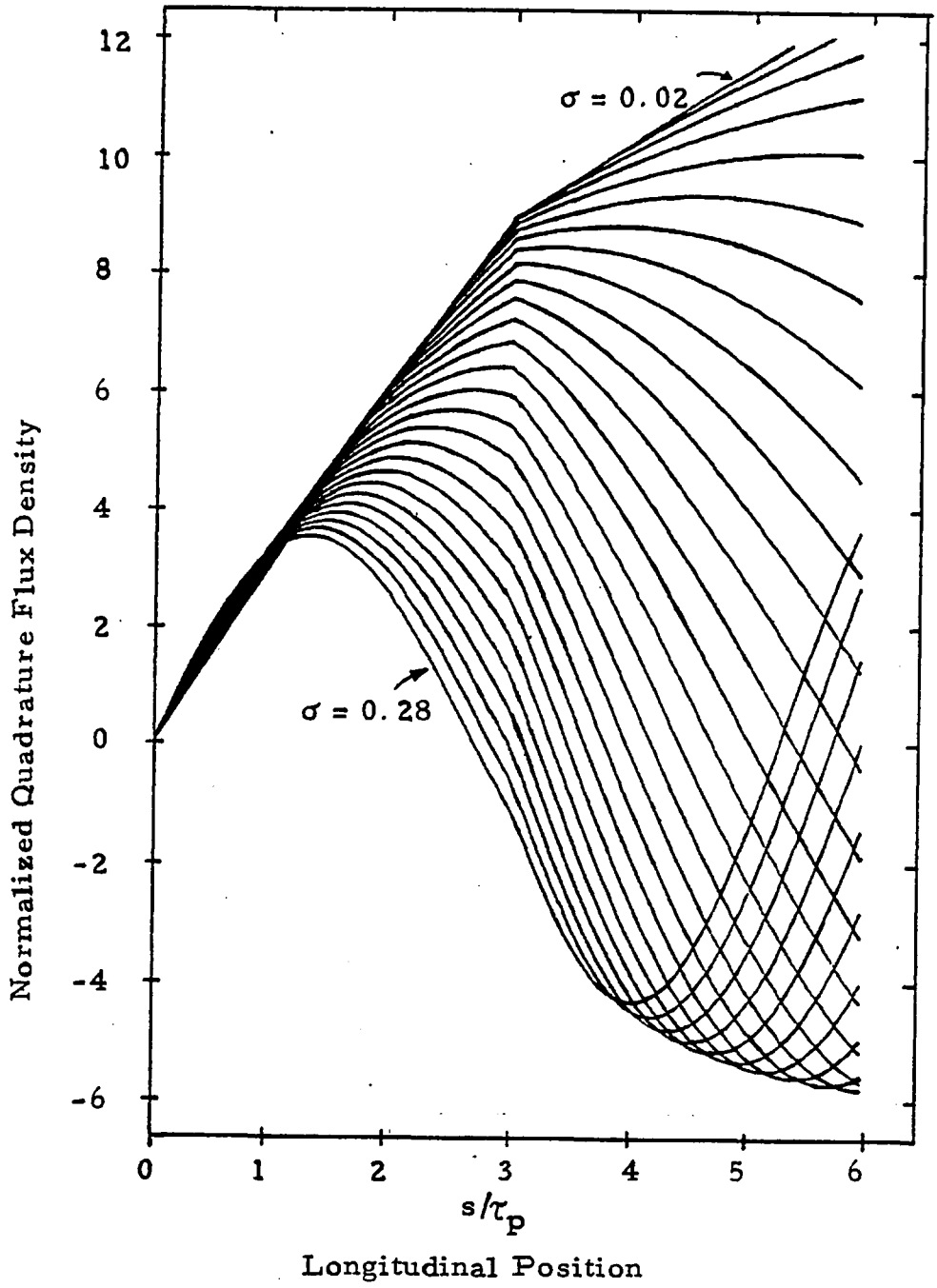

Figure 2.34 Quadrature airgap flux density at high speed for primary winding from 0 to s/τ_p=6 and tertiary winding from s/τ_p=3 to s/τ_p=6 with $J_{s3} = -0.5\ J_{s1}$; G = 212 magnetization.

$s/\tau_p > 3$ the effect of $J_{s3} = -0.5\, J_{s1}$ is approximately the same as in the high speed B_t plots since it causes decrement to occur for $3 < s/\tau_p < 7$ rather than at $s/\tau_p > 7$. Figures 2.35 to 2.37 are the B_q, B_p and B_t plots starting at $\sigma = 0.50$ for $J_{s3} = -0.5\, J_{s1}$ with a change in the tertiary winding to the region $s/\tau_p = 4$ through $s/\tau_p = 7$.

The basic efficiency of the LIM-ASC-I machine ($G = 20$) corresponding to the equivalent circuit parameters of Figure 2.24 is shown in Figure 2.38 as a function of the R_1/R_2 ratio according to the well known expression

$$\eta = \frac{1 - \sigma}{1 + (1/\sigma)\cdot[(R_1/R_2)(\sigma^2 + 1/G^2)]} \qquad (2.19)$$

which is generally valid for the steady-state model of the induction motor without reactive compensation. To include the loss of the asynchronous condenser winding which is only an $I_3^2R_3$ dissipation in the tertiary branch, the R_1 value in (2.19) may be modified to $R_1' = R_1 + R_3/\sigma G$ under the assumption that the phase angle of the tertiary is always adjusted to only peak reactive output.

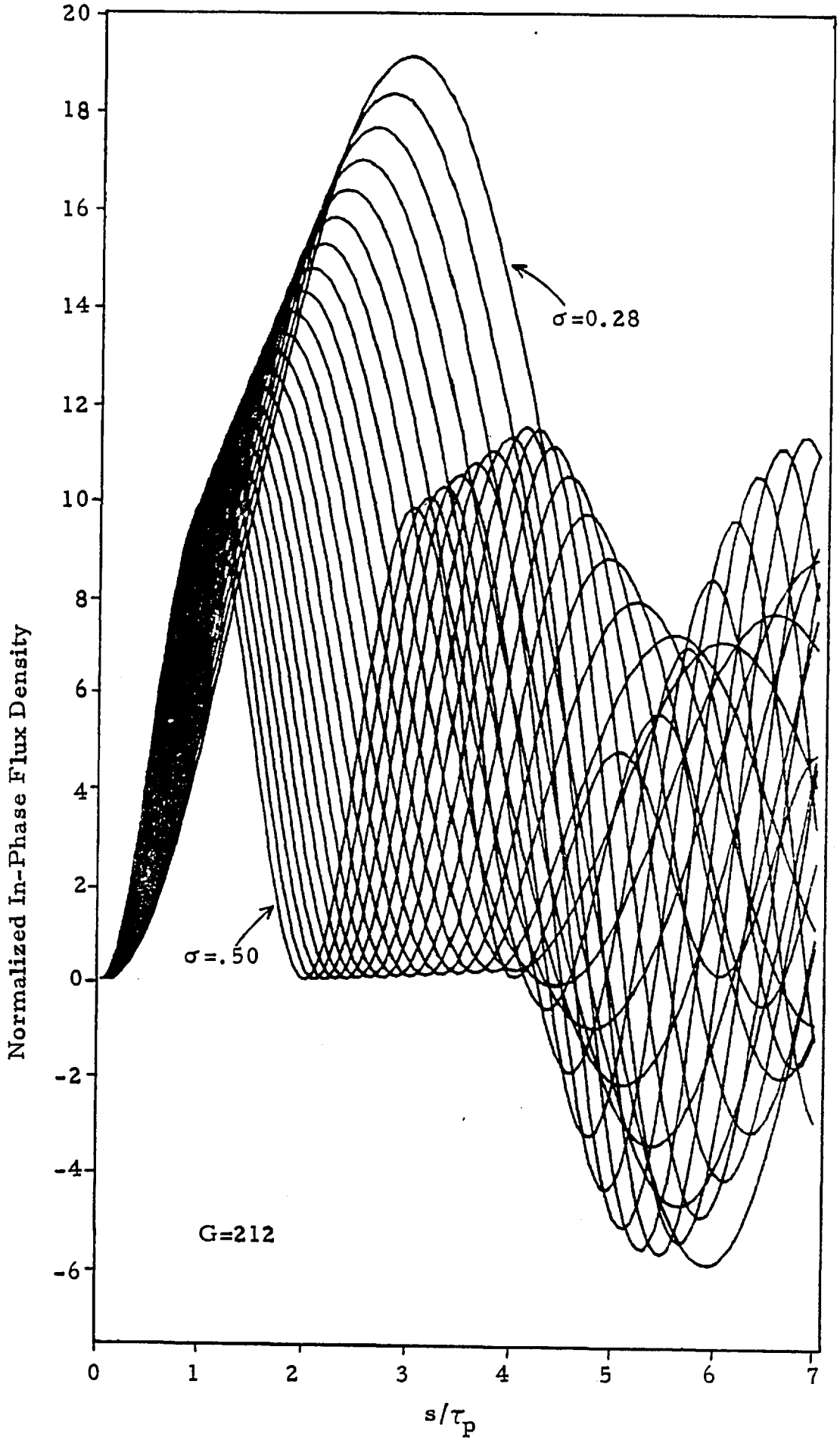

Figure 2.35 In-phase airgap flux density for primary from 0 to 4 poles and tertiary winding from 4 to 7 poles.

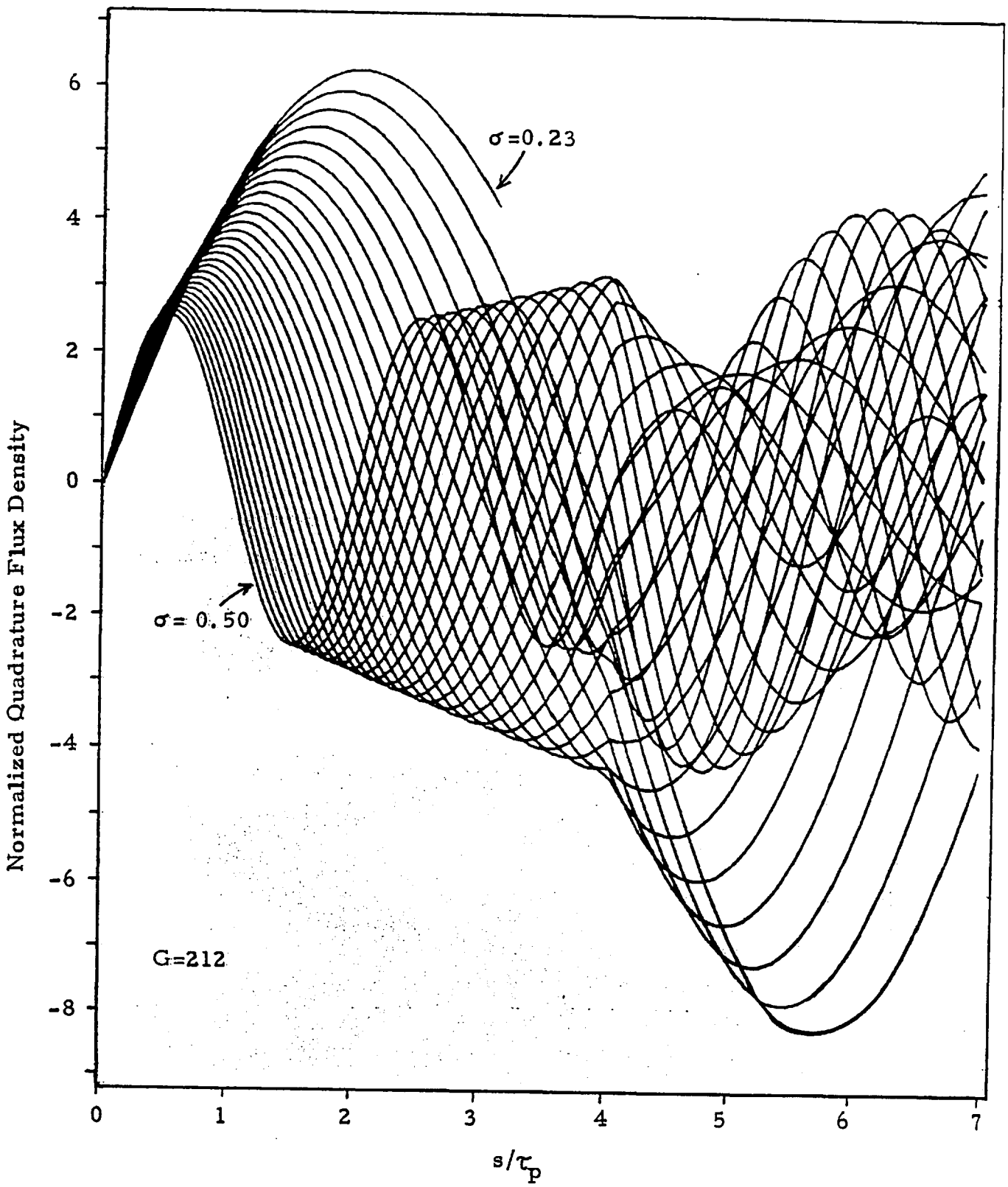

Figure 2.36 Quadrature airgap flux density for primary winding from 0 to 4 poles and tertiary winding from 4 to 7 poles with different values of per unit slip.

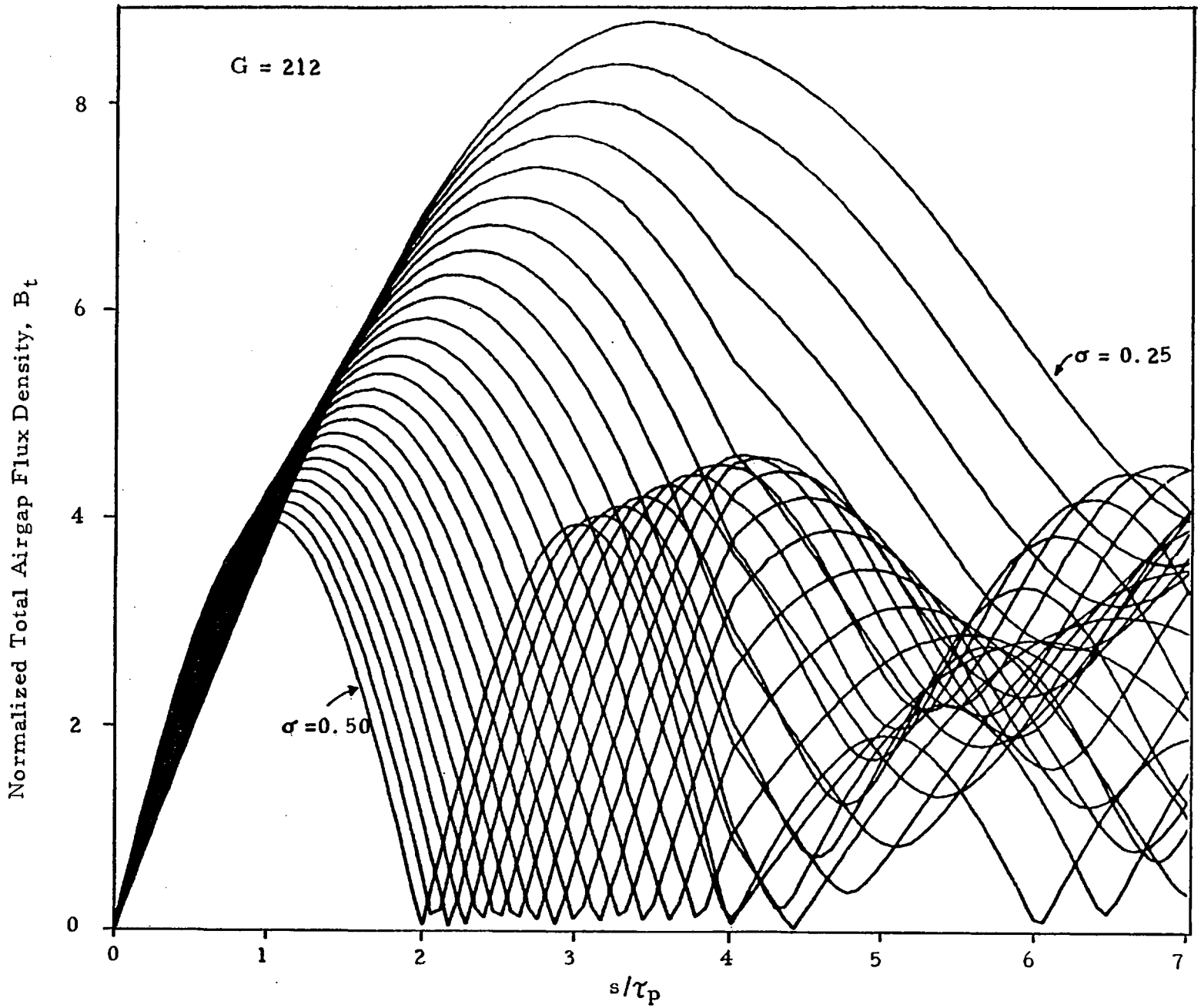

Figure 2.37 Total airgap flux density for primary from 0 to 4 poles and tertiary winding from 4 to 7 poles with $J_{s3} = -0.5\ J_{s1}$

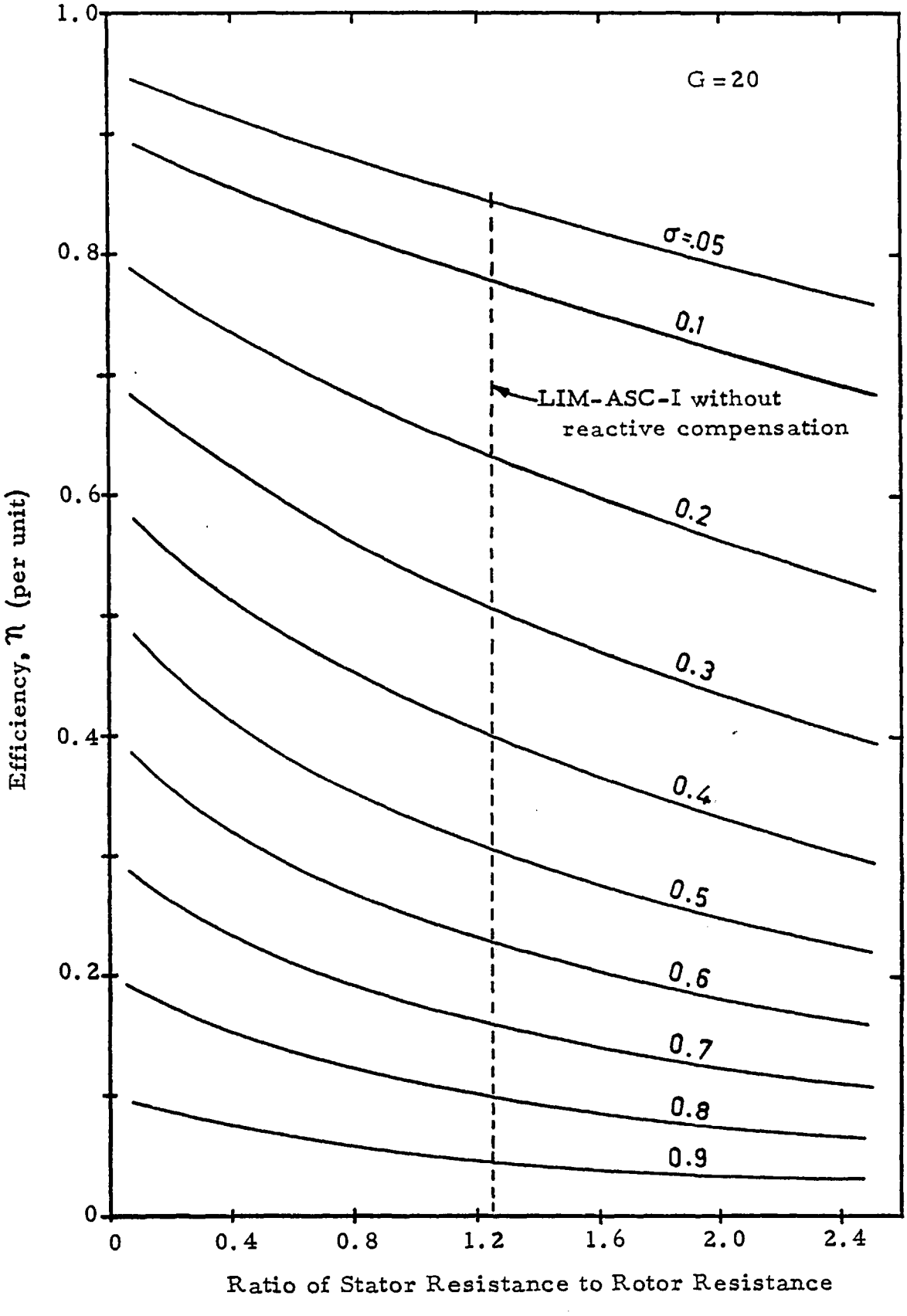

Figure 2.38 Steady-state efficiency of general induction machines without end-effect losses and for a G=20 magnetization.

A. Preliminary Considerations

The optimum solution to the LIM power factor problem is to simultaneously remedy the internal LIM power factor distribution as well as possible while still retaining the ASC reactive generator at the LIM exit-end to make use of the inevitable (if not desirable) exponential build up of airgap flux under the propulsion windings; this is precisely what "LIM-ASC-II" the final outcome of this research project has done.

As far as the ASC winding is concerned, there is one general precaution that was adhered to -- the stator current loading of the first of two ASC sections did not exceed the stator current loading of the LIM by a margin depending on the sum of the leakage reactances of the ASC coils for the leading power factor current desired. This design constraint on operation means that the experimental arrangement is relatively easy to implement, but a strict series connection is cumbersome for research because it demands that the LIM phase current be passed through two distinct groups of series windings comprising the ASC.

To demonstrate the "J-jump" winding concept on the first machine LIM-ASC-I, a two-stage change in the stator current loading was produced at two places for the experimental arrangement immediately after the LIM proper and exactly in the middle of the ASC winding. Most important, the first step change in J_s was continously variable in magnitude (normally downward) and phase due to the external phase shifter, while the second step change in J_s was fixed in magnitude and necessarily an upward jump in current loading

by 3 per unit. To investigate the transient phenomena that was continuously occurring at the second "jump" spot, the change from low impedance to high impedance coils was made in the middle of a two slot per pole per phase group in order that the irregular phase shift between successive coils here would not be unduly affected by unbalance in phase currents. Refer to Figure 2.39 for the distribution of the magnitude of J_s in the experimental machine LIM-ASC-I.

The other justification for using the series/parallel combination is based on the particulars of the research equipment; namely the induction regulator. In short, the world of parallel interconnections allows this type of phase shifter to be operated as a current transformer (instead of a voltage transformer) which makes best use of the device's characteristics, as well as that of the LIM. The classification of the induction regulator as a current transformer is largely due to the rather poor magnetic coupling between rotor and stator circuits which causes the ratios X_1/X_m and X_2/X_m to be higher than normal; as a consequence the overall current transformation ratio is more nearly constant than would be in a conventional transformer under varying terminal voltages and load power factor angles. In effect, this permits load tests on the ASC winding to take place nearly independent of the LIM current loading and thus the apparent "armature reaction" effect exhibited by the ASC on the rotor currents can be ascertained as a single variable.

For information purposes, Figure 2.40 shows a possible but less desirable series connection of the induction regulator output with the LIM winding which constitutes the experimental version of an exclusive series connection with four quadrant control on regenerated power from the ASC winding.

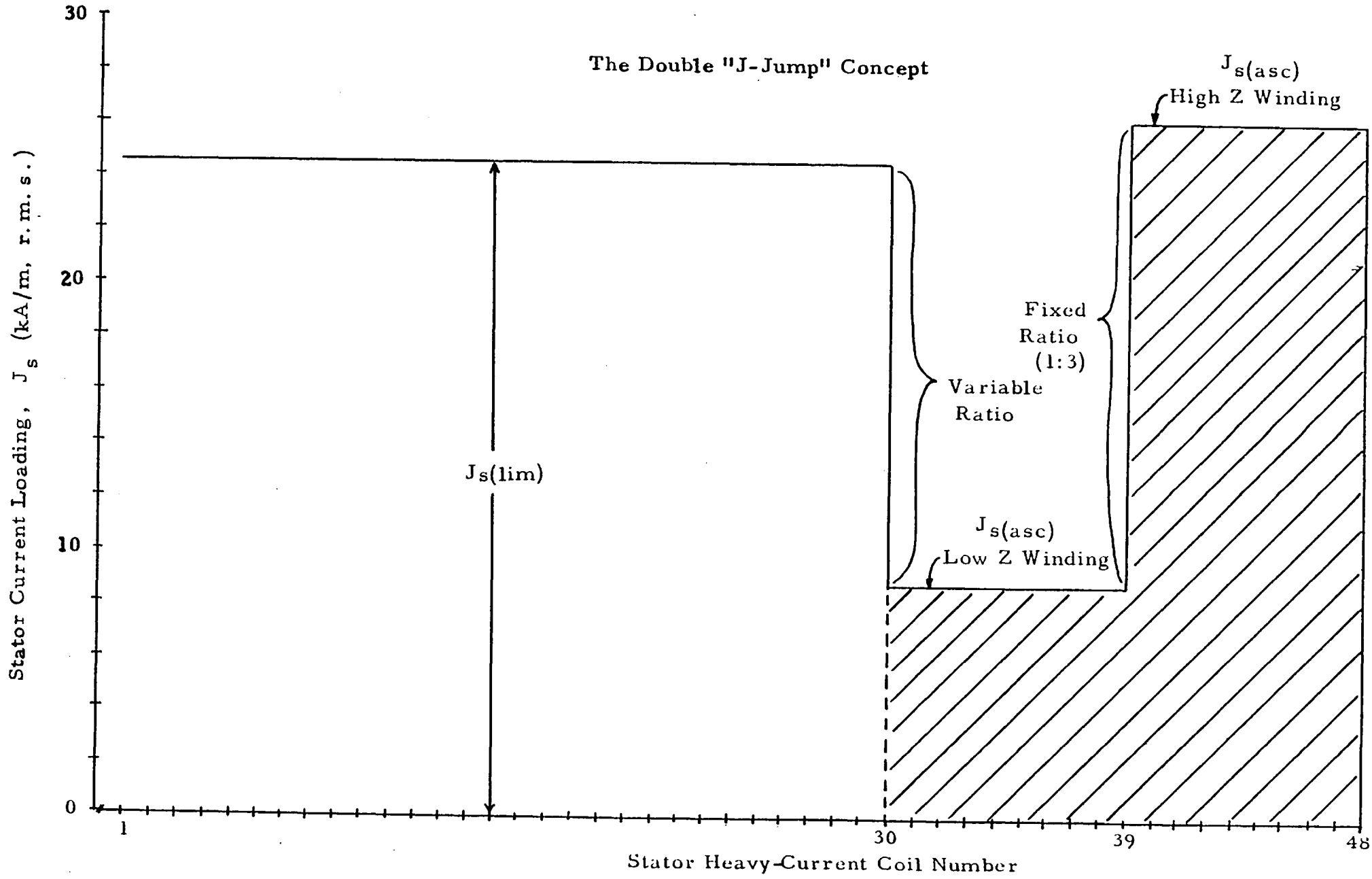

Figure 2.39 Distribution of Stator Current, Linear Motor and Asynchronous Condenser(ASC) Sections

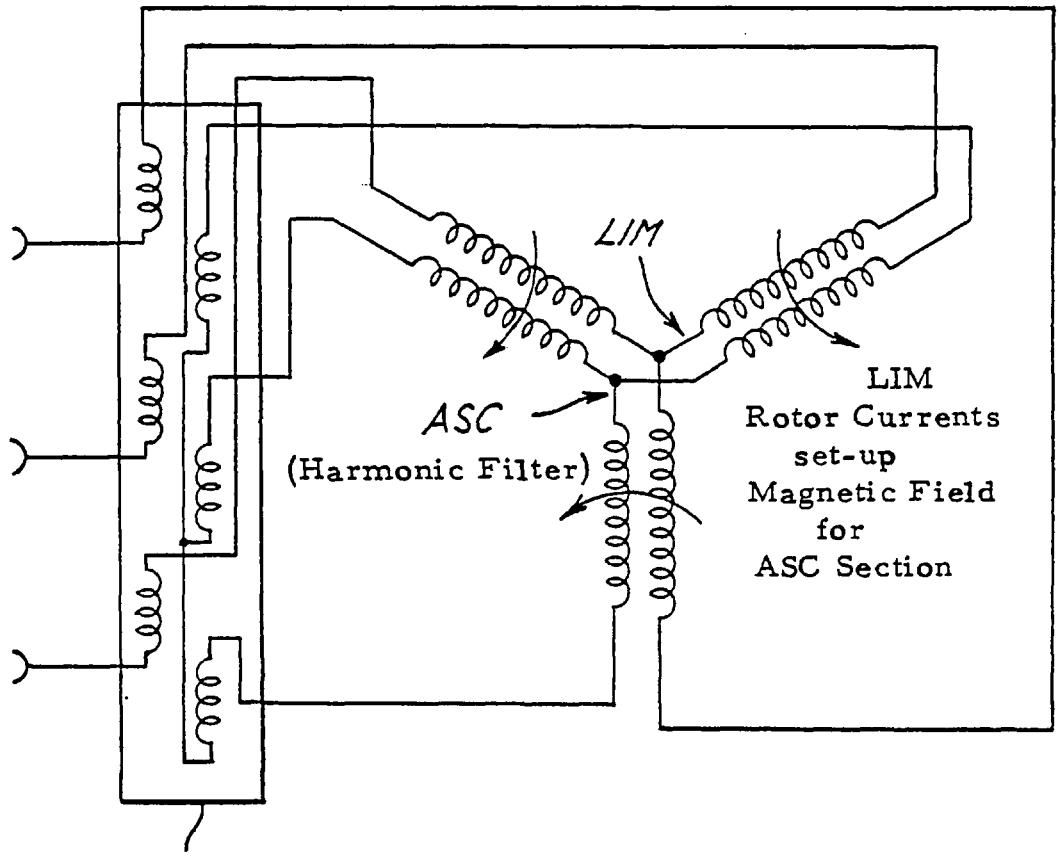

Rotary Phase Shifter Current Transformer

Figure 2.40 Series connection of asynchronous condenser windings with primary LIM winding with adjustable phasing setup.

The most practical implementation of the test machine is shown in Figure 2.41, where the induction regulator is entirely eliminated and the output of the ASC was paralleled with the LIM but internally, e.g., after the first entry-end pole pitch rather than at the terminals. Both the LIM and ASC were individually series connected in a star winding with floating neutrals. This hybrid connection between windings was most promising because it allowed better load matching for the ASC than would be possible otherwise with machine terminal connections and winding the ASC coils with more series turns/coil.

Most important, the last scheme is commercially viable without the induction regulator or thyristor pole shifting as long as the load is relatively constant such as a blower or pump whereby an exact operating speed can be calculated and the ASC operated at maximum leading current flow. During induction motor start-up to the maximum efficiency speed, the direct connection of the ASC to the motor windings would detract from the terminal power factor of the machine at large slips, but this is only momentary assuming that the machine is not to be used in an accelerating/decelerating duty cycle.

Figure 242 is included at this point to define the general shape of the phase shift versus slip curve for the experimental machine LIM-ASC-I and is also applicable, with minor modifications, to all machines with 50 Hz excitation independent of whether power factor correction takes the form of series or parallel inter-connection of the two windings.

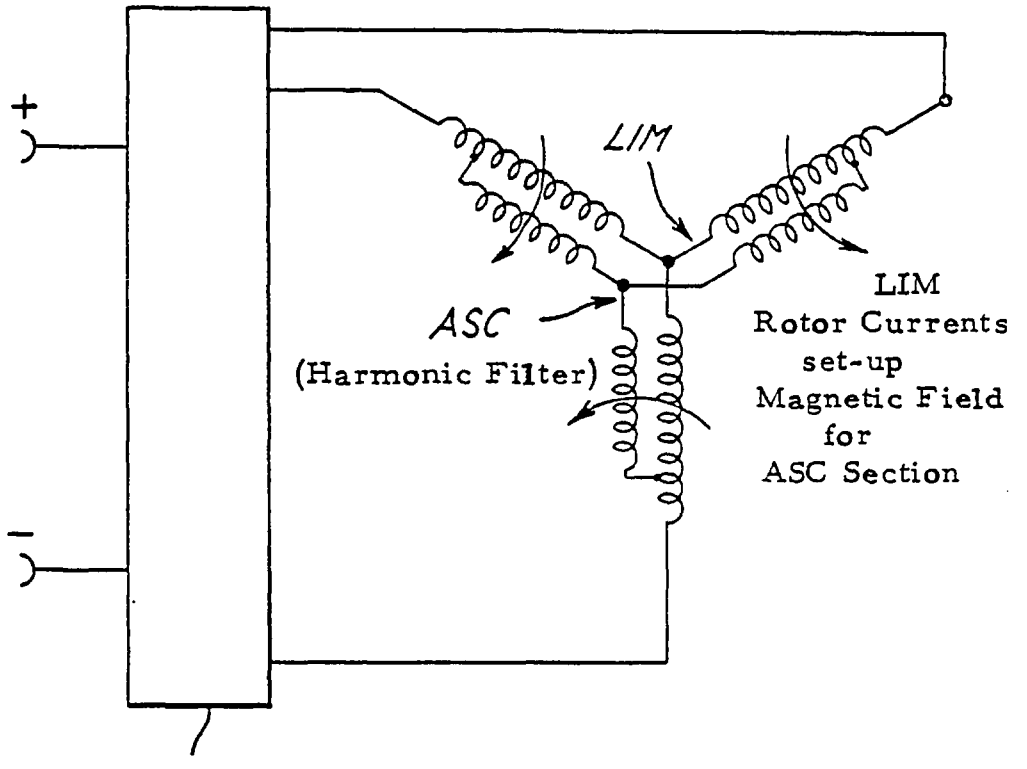

Figure 2.41 Parallel connected version of integral motor/asynchronous condenser machine for square-wave inverter output with impedance matching provided by tap after first pole of LIM winding.

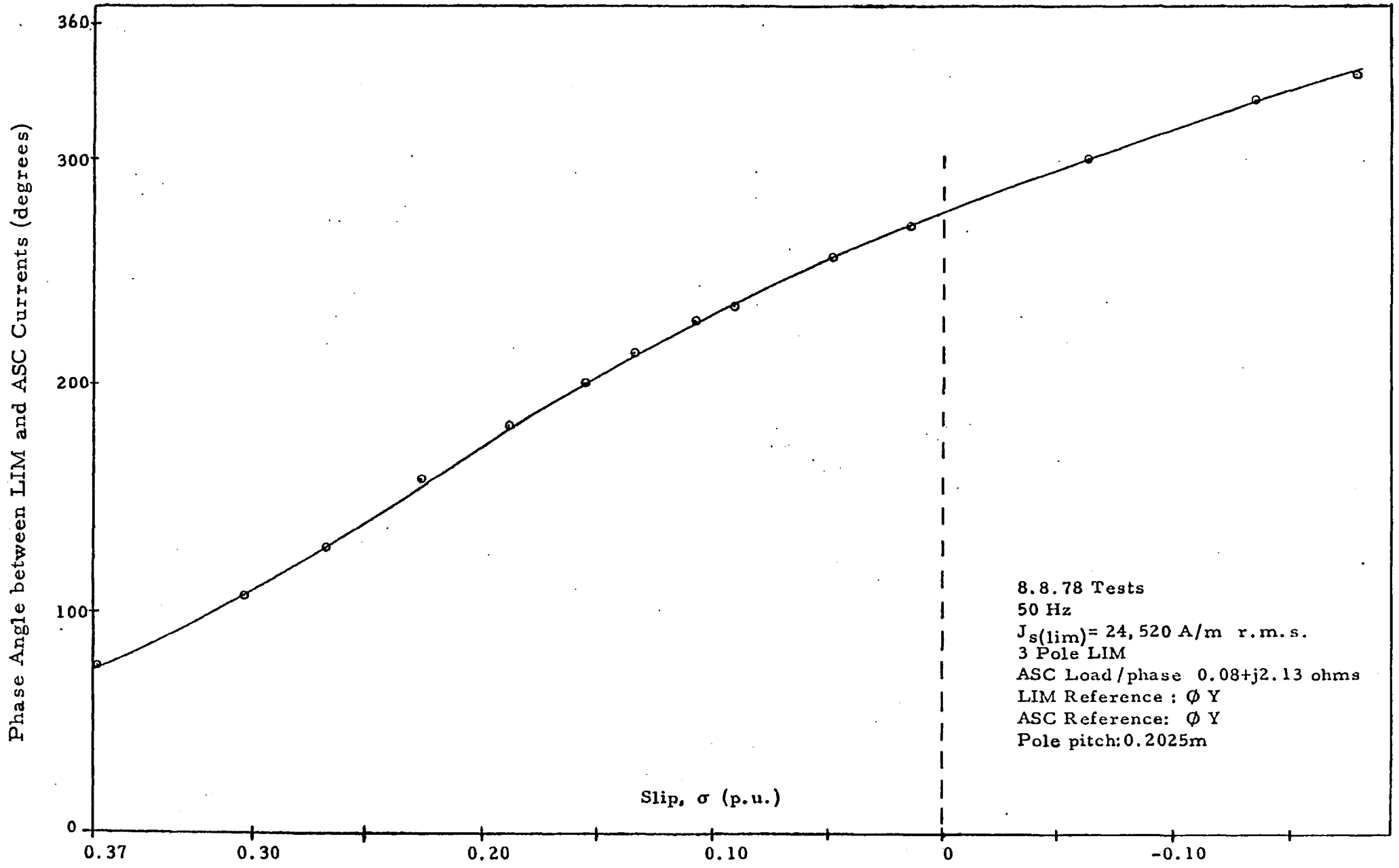

Figure 2.42 LIM to ASC Current Phase Shift at Constant LIM Current Loading

B. Primary Research Objective:

This section summarizes the evaluation of a brushless linear induction motor with an integral asynchronous condenser (ASC) winding on the same stator block as the LIM. The experiements show that the reactive generator section of the motor is capable of recovering at least 11.7% of the reactive power input to the conventional LIM winding. The specific purpose of this concept is to effect an improvement in the terminal power factor of the entire machine by feeding the recovered reactive power back into the mains to compensate for the typically low power factor of the LIM alone. It should be emphasized that all of these tests have opted to operate the ASC in a purely reactive generator or leading power factor mode (with the exception of stator winding I^2R losses) and thus it may be said that power factor improvement is taking place at constant efficiency. In practice, power factor improvement is manifested by a reduction in mains current to the LIM-ASC machine while at constant voltage.

The subsequent section is concerned with a brief theoretical analysis of the phenomena underlying induction condensers, pole-shrinking in the ASC section, four-quadrant control of the ASC and limitations on "J-jump" (step change in stator current loading) windings. Special reference is made to the two-axis theory of brushless induction machines as developed for spherical motors for the purpose of confirming the experimental machine's Goodness factor, airgap flux build-up and decay, and operating constraints. The results obtained are used to dimension the second and larger LIM-ASC machine being demonstrated with both an increased Goodness factor and number of poles; the latter being considered the most significant improvement over the machine tested in the

initial experimental setup.

The bulk of the tests described are performed on a 4 pole LIM with the ASC section winding comprising 2.4 poles of the same pole pitch as the LIM. Extensive testing of this arrangement with LIM and ASC windings connected in parallel at the terminals only, has been completed at 50 Hz and at 75 Hz in an effort to correlate experimental data with theoretical predictions. Since the purpose of the ASC winding is to recover the otherwise wasted LIM exit-end magnetic airgap energy, all of the tests concentrated on uni-directional operation. Fundamentally the difference between the LIM and ASC is that the former must always magnetise the airgap and jointly establish rotor currents (to act as either motor or dynamic braking generator) while the ASC should "demagnetise" the airgap magnetic field setup by the transient rotor currents at the exit-end of the LIM. Thus, the inductively fed ASC can supply either a passive or active load, of any power factor, at the discretion of the operator. In the tests described, the ASC output is confined to the zero power factor (i.e., maximum leading kVAR) mode by manually adjusting a rotary phase shift transformer connected to the mains.

The only practical way to effect condenser action in any set of coils situated at the exit end of a high Goodness machine at small slips, is to reduce the stator MMF with respect to the rotor MMF; this demands either a drastic increase in coil chording or a reduction in series turns/coil supposing all coils carry equal phase currents and are arranged in a winding with equal pole pitch as the LIM. Alternately, as an experimental convenience, the first series of LIM-induction condenser machines have equal chording factors with both winding sections incorporating series

connected coils exclusively. Condenser action occurs since the current loading of the ASC can be reduced independently of the LIM. The peculiar and highly successful feature of the described test machine is that the first 1.2 poles of the ASC winding following the LIM retain the same series turns/coil as the LIM, while the last 1.2 poles of the machine comprise the high impedance section as these coils have been reconnected with three times the series turns per coil. In operation these two groups are in series and thus, this step change in stator current loading, J_s allows the machine to be classified as a "J-jump" winding.

On a broad basis, the alternative to the "J-jump" concept is a winding with uniform pole pitch, nearly uniform stator current loading, and most likely a varying chording factor but most important a specific phase shift will be introduced between successive poles or non-integral multiples thereof. The justification for this arrangement is based on changing the electromagnetic mechanism from a discrete or lumped winding at the exit-end of a high speed linear machine into a distributed winding interspersed among the main working coils. In effect, this will mean that not only the LIM proper will require less reactive kVA input, rather this permits the phase shift concept of power factor improvement to be applied to squirrel cage induction motors, where there is no "exit-end effect" per se. Throughout the text, the phase shift reactive control method is referred to as the "θ-Pinch" concept.

From an academic point of view, both the "J-jump" and "θ Pinch" schemes of reactive power regeneration are quite similar in making use of the two axes of the induction machine for effecting power factor improvement with little effect at

all on the efficiency; moreover both schemes necessarily rely on brushless rotors with high ratios of magnetizing (or demagnetizing) inductance to rotor resistance for, in essence, it is desirable for the rotor to have an electromagnetic memory.

C. The Experimental Machine

The basic sheet rotor LIM reported in this section is the same as that described in section 1 with the exception that the winding connections are different and the coil series turns have been changed in nine coils. The major difference in testing has been that now an active load (i.e., the mains) is used to evaluate the ASC section whereas previously, only a passive load was on test since no induction regulator was available. The changes in instrumentation are outlined in section 4D .

The bulk of the experimental work centered around the winding layout shown in Figure 2.43 comprising a 4 pole LIM and a 2.4 pole ASC of equal pole pitch and chording. The details of each winding are included in Table 2.4 along with updated dimensions and operational parameters. As before, the air-gap of the machine was kept at the minimum position for all tests and variable frequency excitation was used to substantiate different values of Goodness factor.

In summary, the advantages of this machine over the previous winding arrangement are:

1. Best possible use of the available block space for proportioning between LIM and ASC windings bearing in mind that the ASC winding spans more slots in an experimental machine than in a commercially designed machine.

2. Two ASC stator current loadings can be investigated simultaneously due to the aforementioned "J-jump" winding; likewise two different armature reaction effects on the rotor currents and airgap field are tested simultaneously.

3. The ASC stator I^2R losses can now be supplied by the mains rather than by the rotor currents due to the four quadrant capability of the induction regulator in use;

Table 2.4

Characteristic Parameters of the Experimental Single-Sided Machine LIM-ASC-I

Longitudinal Core Length	1.49 m
Transverse Core Width	0.157 m
Stator Block Depth	0.120 m
Slot Width (uniform)	0.01428 m
Slot Depth (uniform)	0.0381 m
Slot Pitch (mean)	0.0274 m
Aluminium Annulus Thickness	0.0095 m
Aluminium Width	0.229 m
Steel Disc Thickness	0.019 m
Disc Moment of Inertia	510 N-m-sec^2
Typical Operating Entrefer	0.010 - 0.012 m
Aluminium Resistivity (20°C)	3.25 x 10^{-8} Ω-m
Theoretical Russell and Norsworthy Factor	1.933
Synchronous Speed @ 50 Hz	207 RPM (20.5 m/s)
Moment Arm to Center of Motor	0.949 m
Total Number of Coils	48
Total Number of Slots	54
Pole-pitch (uniform)	0.205 m
Chording Factor (uniform)	0.80
Slots.Pole.Phase	2.5
Calculated Distribution Factor (3Ø, fundamental)	0.962
Total Stator Copper Cross Section/Slot	189 mm^2

Features Particular to the LIM (Coils 1 through 30)

Series Turns/Coil	12
Mean Length of Coil	11.54 m
Half-filled or Mixed Type Slots	1 -6 incl., 31-36 incl.
Fully-filled Slots of One Type	7-29 incl.
Winding Sequence (1 Pole)	R R R -Y -Y B B B
Slot Fill Factor	35%
Ratio Active Conductor/Total Conductor Length	32.6%

Features Particular to the ASC Section for Coils 31-39 incl.

Series Turns/Coil	12
Mean Length of Coil	11.54 m
Resistance/Coil (20°C)	0.0205 Ω
Reactance/Coil (50 Hz, 1Ø uncoupled)	0.065 Ω
Half-filled or Mixed Type Slot Numbers	31-36, 40-45

Features Particular to the ASC Section for Coils 31-39 incl.

(continued)

Current Density at 10A/Phase	1.27 A/mm^2
Stator Current Loading at 10A Phase	8,173 A/m

Features Particular to the ASC Section for Coils 40-48 incl.

Series Turns/Coil	36
Mean Length of Coil	3.46 m
Resistance.Coil (20°C)	0.185 Ω
Reactance/Coil (50 Hz, 1Ø uncoupled)	0.54Ω
Half-filled or Mixed Type Slot Numbers	40-45, 49-54
Fully-filled Slots of One Type	46-48 incl.
Current Density at 10A/Phase	3.81 A/mm^2
Stator Current Loading at 10A/Phase	24,520 A/m

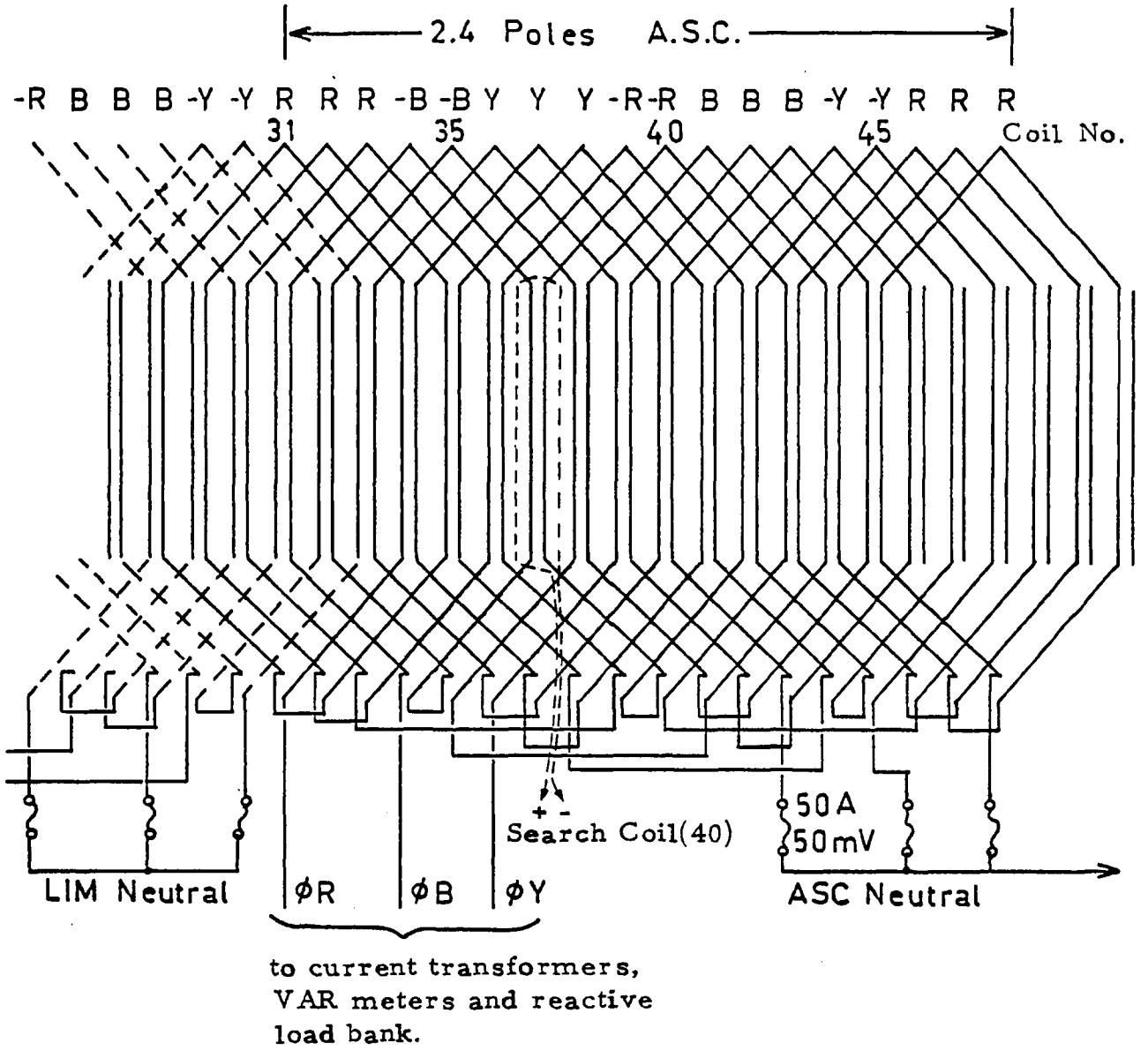

Figure 2.43 Winding connections for asynchronous condenser section of LIM-ASC-I with 4-pole LIM section from coil 1 to 31.

leaving the rotor currents exclusively for reactive excitation.

The disadvantages of this one-block "LIM-ASC-I" (which were rectified in the design of the two block "LIM-ASC-II") are:

1. To yield a Goodness factor of about 20 at 50 Hz for LIM-ASC-I, the pole pitch was made large with a corresponding reduction in the number of poles that can be accommodated on the 54-slot block; only 4 poles of excitation are available with the present scheme.

2. As a consequence of having only 4 poles, the maximum theoretical rotor efficiency that can be obtained is 78.5% (at a slip of 0.215 p.u.) neglecting stray rotor losses; in practice the overall efficiency for the LIM alone will be less than 55%.

3. Both the stator slot leakage reactance (at 50 Hz) and winding resistance are unnecessarily high due to the poor utilization of paralleled circular wire embedded deep in the slot.

4. The ratio of the airgap flux density to the magnetizing current at 50 Hz is not as high as would be desirable in an experimental machine for the explicit purpose of confirming B_p -B_q airgap flux densities versus longitudinal block position curves as done with spherical motors at 480 Hz; additionally the use of a fractional slot pitch winding is a major experimental inconvenience for both phase and magnitude measurements.

D. Instrumentation

The crux of the instrumentation problem is to measure both phase and magnitude of 48 coil voltages, 52 search coils, and six phase currents simultaneously along with 5 wattmeter and 1 VAR meter readings--an exercise involving about 220 data points for each frequency, slip, stator current and induction regulator phasing desired. This has not been attempted to date for it requires a rather elaborate computer data acquisition system. However, as second best, the data logger in use in Lab 002C has accomplished 98% of these measurements in a period less than 45 seconds with direct printing of the results; thus leaving only the wattmeter readings to be taken by hand. The general layout of the instrumentation is shown in Figure 2.44; noting that both a digital phase meter and a Magslip resolver are simultaneously in operation to check electronic measurements against manually adjusted Lissajous "in-phase" lines on the oscilloscope. The current in phase Y of the LIM is used as the reference in all phase tests.

The purpose of taking both phase and magnitude information is twofold. First, from a fundamental point of view, this allows the Maxwell stress vector to be calculated anywhere in the airgap and thus assess the machine's distribution of real and reactive power independent of the actual coil voltages and currents. Second, to evaluate how well each individual coil in the machine is absorbing or giving power, the induced voltage for each coil must be known (and since shadow coils were not wound with the working coils, the best alternative is to use the airgap located search coils to estimate induced flux) in addition to the coil terminal voltage. As shown later, a three to one difference in coil

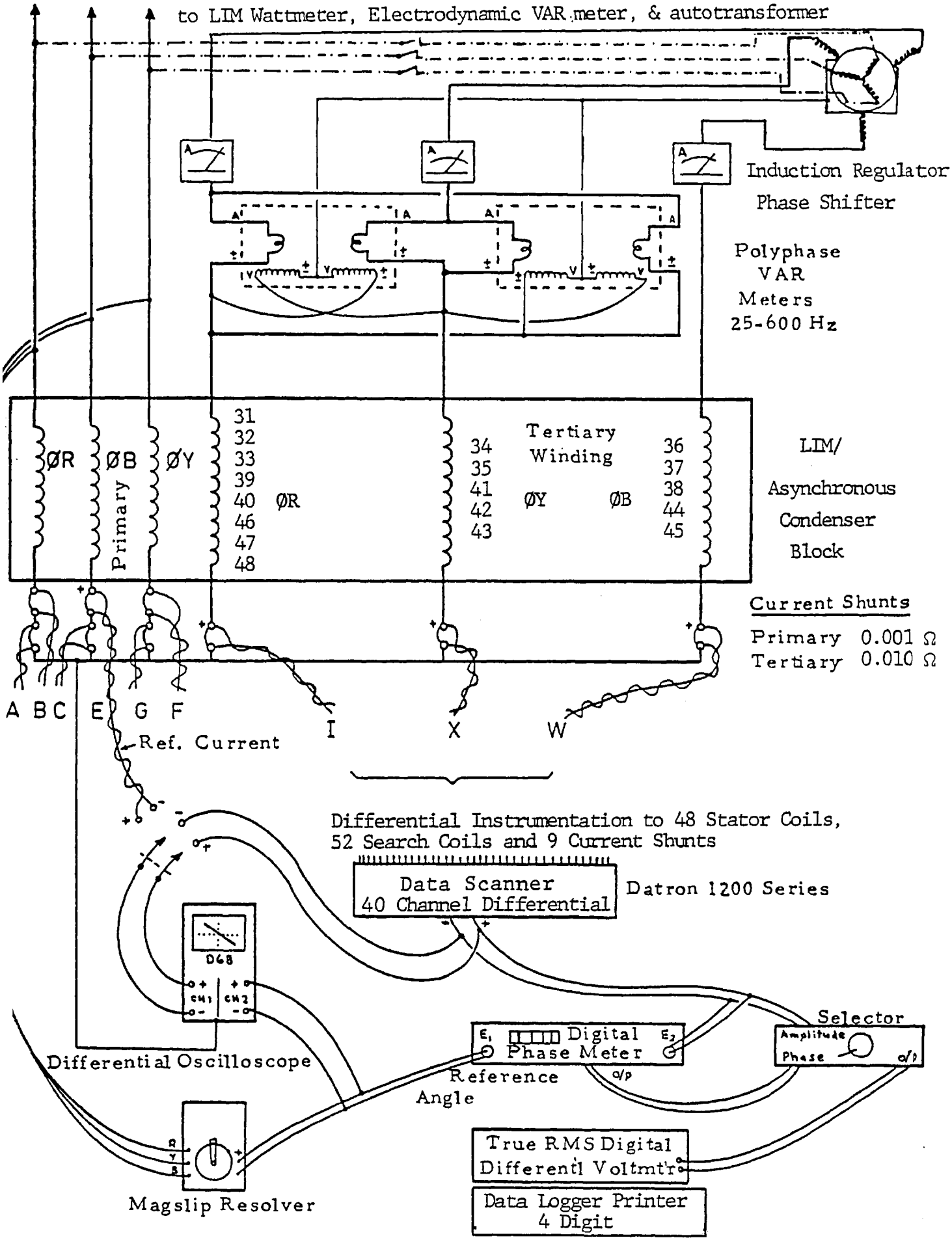

Figure 2.44 Instrumentation of LIM and Asynchronous Condenser Windings.

power factor for adjacent coils in the LIM is typical in all phases which constitutes the prime area for concern and correction for all high speed longitudinal-flux, short-stator machines.

E. Experimental Results

The overall power factor for the entire machine connected as a 48 coil, 6.4 pole linear induction motor is given in Figure 2.45 to be compared with the power factor versus slip curves of machines with fewer poles but with equivalent Goodness factors and frequency. The test pertaining to Figure 2.45 is taken at a constant stator current loading of 20,400 A/m which in effect seems to guarantee that no magnetic saturation of the iron core is prominent because it was experimentally verified that the propulsion force of this machine scaled up as the square of the current loading for small changes in phase current at a constant slip. Also note that in using the two wattmeter method (i.e., line to line voltage measurements only) for determining overall power factor, the characteristic "sin $(\frac{n\pi\sigma}{1-\sigma})$" oscillation in component power factor is evident, where n is the number of poles and σ is the per unit slip. In practice, the correlation between theory and experimental results is not exact but this is primarily due to the large values of "R_1 and X_1" equivalent circuit parameters which tend to obscure the true airgap power factor. Most important, the maximum overall power factor of 0.63 per unit occurs at the slip of 0.225 per unit, while the maximum efficiency of 0.68 occurs at a slip of about 0.22 or less.

Before showing the results of the combined 4 pole LIM and ASC on-line with the double "J-jump" winding, consider the most basic arrangement of a 4 pole LIM and 2.4 pole ASC winding all with uniform pitch and series turns per coil; the particular choice of inductive load on the ASC has caused one step change in current loading from $J_s(\text{lim})$ = 24,500 A/m to $J_{s(\text{asc})}$ = 5,300 A/m. Figure 2.46 summarizes the results of the first tests of this nature for it shows the three most

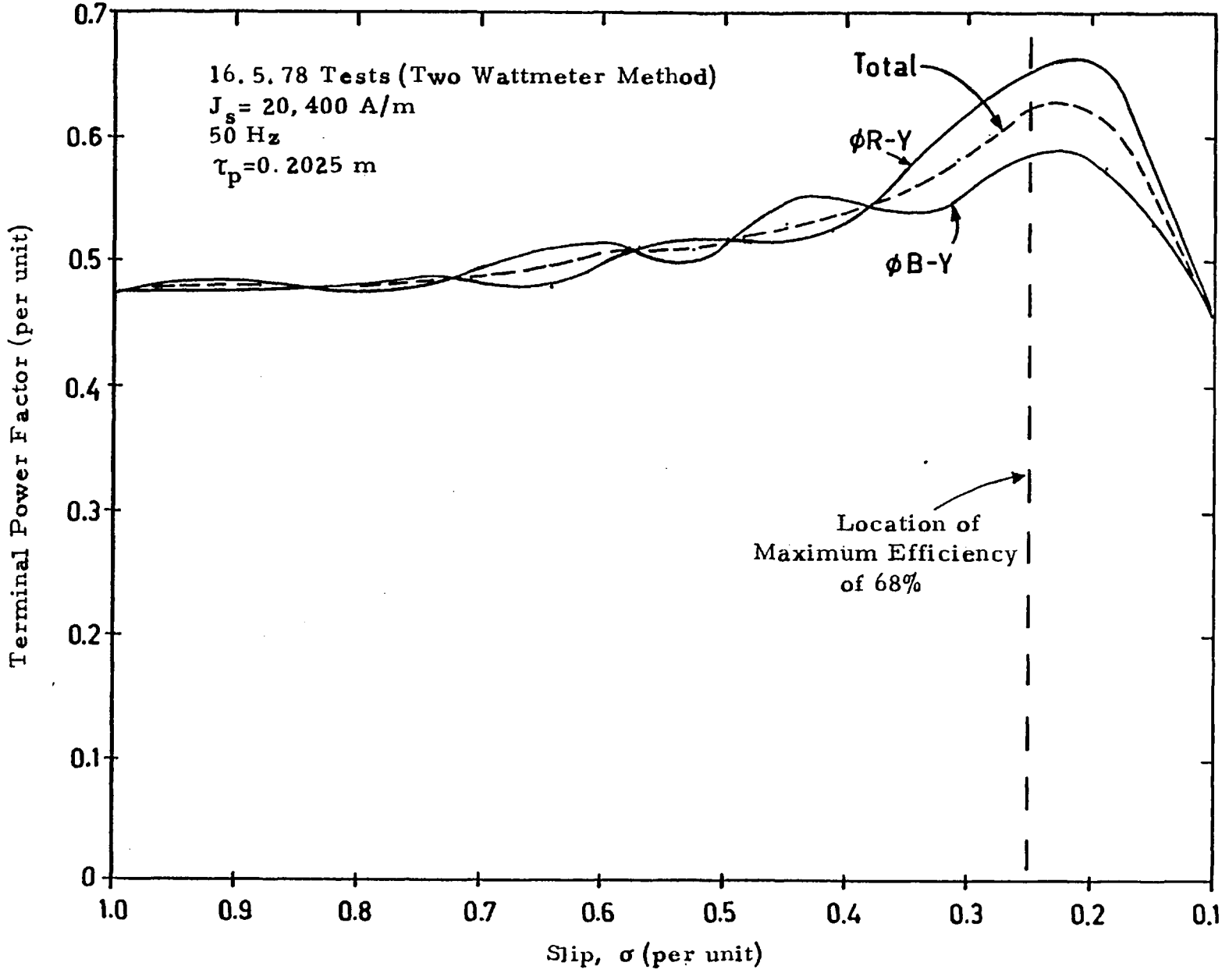

Figure 2. 45 Power Factor of 6. 4 pole , 48 coil LIM without ASC correction.

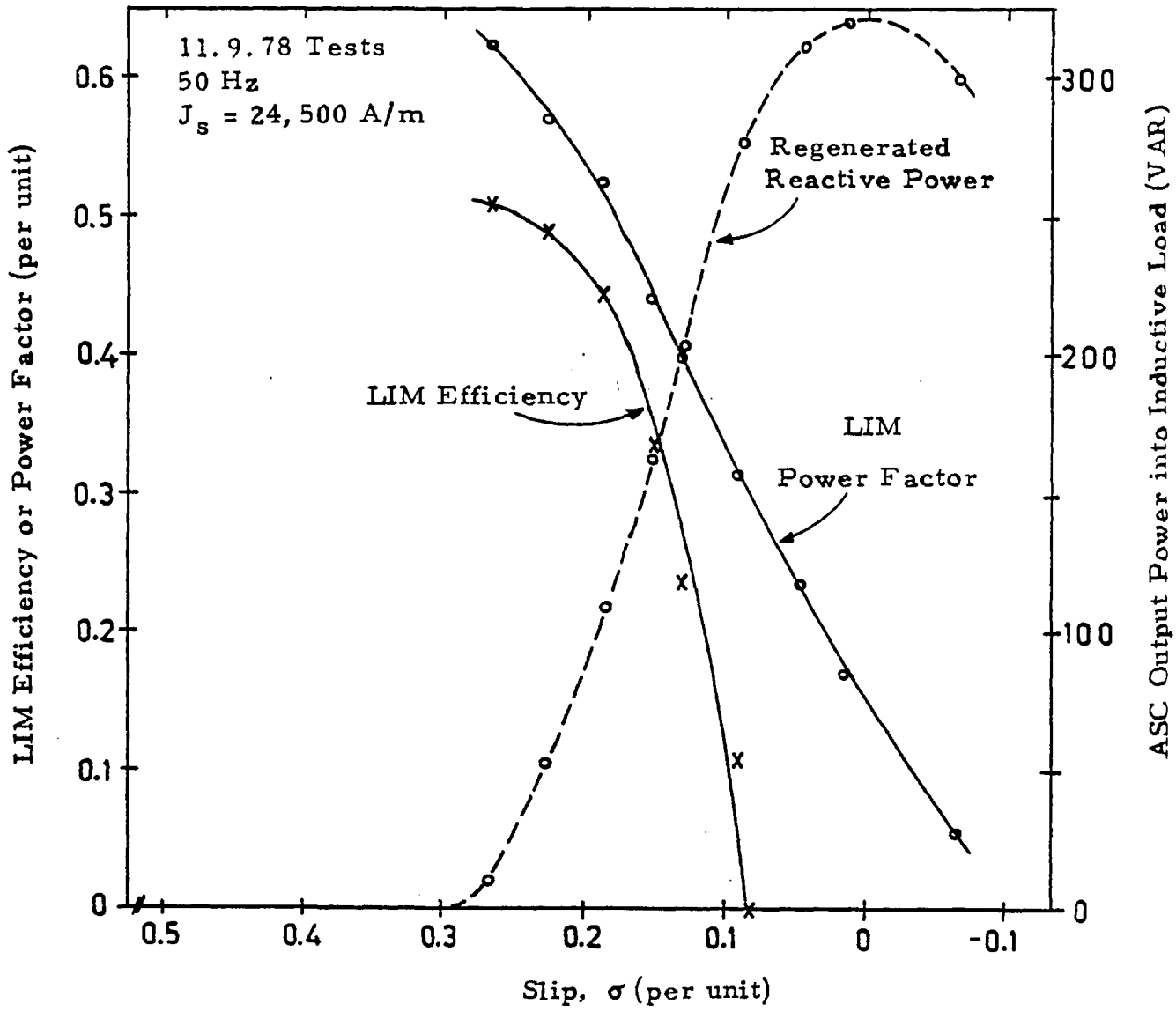

Figure 2.46 LIM efficiency and power factor without correction on a 4-pole section and ASC net reactive output supplying an isolated inductive load.

important performance characteristics, the LIM efficiency, the LIM-only power factor, and the regenerated reactive power at the ASC terminals (supplying the inductive load) all as a function of slip. The most outstanding conclusions from the one graph are:

1. The LIM efficiency peaks at a slip of about 0.27 p.u. indicating that the 4 poles of active excitation appear to perform more like a 3 pole, short stator machine in terms of location of peak efficiency. However, the maximum efficiency of 0.50 p.u. is typical of a 4 pole machine.

2. The power factor of the LIM alone peaks at a slip greater than 0.27 p.u. and attains the value of at least 0.625 p.u. As expected, the slope of the LIM power factor curve is nearly constant at the value $\delta(\text{kW/kVA})/\delta\sigma = 1.95$ in a range from the maximum efficiency location to well past the running light slip of 0.083 p.u.

3. There is no discernible change in these LIM power factor or efficiency curves whether the ASC winding is carrying a leading load current or not. (If the ASC were connected to a resistive load, there would be a significant decrement in the efficiency of the LIM.)

4. The regenerated reactive power from the ASC winding rises from milli-VARs at slips greater than 0.30 p.u. to a maximum of 0.35 kVAR at zero slip for the tests at 50 Hz. Separate tests carried out on the ASC leakage reactance indicate the total generated reactive power including the ASC consumption amounts to 0.58 kVAR for the Figure 2.46 conditions. The reactive power consumption of the LIM alone, at its peak power factor, is 2.82 kVAR.

5. The distributions of the LIM power factor and the ASC output as a function of slip seem to indicate that it is

difficult to effectively utilize the ASC output for LIM kVAR correction (independent of the connection scheme adopted) since the LIM has an intrinsically low power factor-efficiency product of 0.046 per unit at, for example, slip= 0.10 p.u.

The last conclusion is especially noteworthy because it underlines the major problem in trying to use too short a stator block for both the LIM and ASC windings--simply there are not enough poles of LIM excitation to allow the LIM to have both peak efficiency and power factor at a slip of 0.10 per unit or less. However, it is relatively easy to shift both the efficiency and power factor curves horizontally to the right (in addition to an increase in peak performance) so that the maxima of the three curves occur at nearly the same slip, say, at σ =0.075 p.u.

Moreover, there also exists the possibility of shifting the ASC output curve horizontally to the left so that its output may be peaked at a slightly larger slip than 0.01 p.u. This may be accomplished by reducing the excitation frequency below 50 Hz or alternately by enlarging the airgap; the two most practical methods of increasing the ratio of rotor element time spent under the ASC block section to the rotor current decay time constant. However, if the machine designer has a choice between these two adjustable options, it would be desirable to keep the rotor time constant the same (i.e., at 64 milliseconds) and reduce the frequency to about 46.5 Hz to peak the ASC output at σ =0.075 p.u.

Now that the major issues affecting future development work on a macroscopic scale have been brought out, it is instructive to look at the internal dynamics of the machine electromagnetics. In this respect, the most basic concern

is simply, what is the "armature reaction" effect of the ASC current loading on the continuously decaying transient rotor currents? It is a straightforward task to calculate the natural decay of the rotor currents over an unexcited stator block section, but to estimate the forced decay caused by a bucking flux from the ASC winding requires an exact empirical determination of the mutual coupling between rotor and stator; this is of course complicated by the fact that the path of rotor current changes shape as a function of slip.

Still referring to the most basic LIM-ASC winding with a uniform series turns per coil, Figure 2.47 shows the variation of the total airgap flux (magnitude) over the entire machine for slips between σ =0.134 p.u.; which corresponds to the indicated data points in Figure 2.46. The conclusions to be drawn from this plot of the normal component of density $\sqrt{B_p^2+B_q^2}$ are:

1. With the exception of the σ =0.268 data, the reduction in airgap flux commences at search coil number 31 location, which as expected is the slot-pitch-wide coil directly centered over the first slot containing conductors of the ASC winding.

2. The flux distribution for slips between 0.188 and 0.268 p.u. indicates that there is a reduction in the positive rate of rise, i.e., a leveling off of the total magnitude approximately one pole-pitch prior to the first slot containing the ASC conductors, independent of the ASC current loading. The major concern here is that the ASC stator block is acting like a magnetic shunt so as to spread the core flux for the last pole of the LIM over a much wider airgap surface area.

3. At slips of less than 0.227, the current loading of

the ASC has nil effect on the airgap flux over the LIM proper. Most important, the "armature reaction" effect of the ASC is an integral effect on the decrement of airgap flux and to a first approximation, the linear superposition of ASC current loading on opposing and naturally decaying rotor currents is a viable model.

To appreciate the shape of the experimental curves in Figure 2.47 and to contrast them against theoretical predictions of the in-phase and quadrature flux density distribution for the LIM alone, reference Figure 2.48. First, comparing the dashed curves representing the total magnitude of flux density with the experimental curves, the correlation is surprisingly excellent in that the divergence of the flux distribution (for slips between 0.10 and 0.27) commences at a distance along the LIM block of $s/\tau_\rho = 2\frac{1}{4}$ in practice, and at $s/\tau_\rho = 2.0$ in theory. Moreover, to substantiate the oscillations of the direct and quadrature axes fluxes, the ratio of the total flux at $\sigma = 0.134$ to the total flux at $\sigma = 0.268$ at the specific location $s/\tau_\rho = 4$ (i.e., the end of the LIM excitation) is 1.63 p.u. by experiment and 1.78 p.u. in theory, a 9% difference.

The last question that arises is how to account for the exact flux shunting caused by the ASC block; this requires an especially accurate method of "calibrating" the normalized curves of Figure 2.48. Fundamentally, the absolute magnitude of the flux density is derived from the synchronous field speed, the effective rotor resistivity and the stator surface current density. However, in practice the presence of harmonics in a fractional slot pitch winding along with the uncertainty of the effective conductor cross section in the slot tend to limit the accuracy on straightforward calculations of J_s; additionally the major error actually occurs in trying

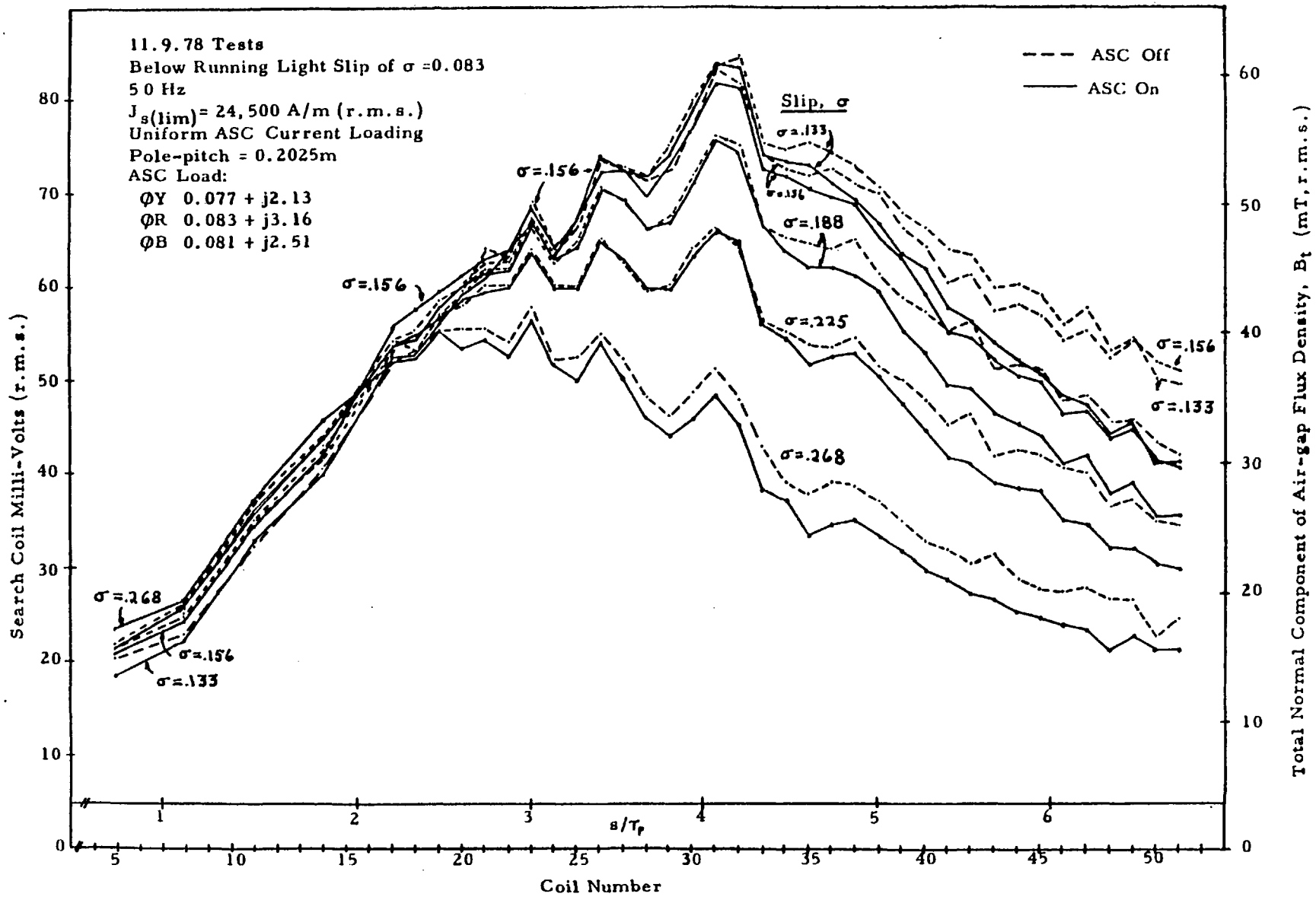

Figure 2.47 Total Air-gap Flux Density as a Function of Longitudinal Block Location

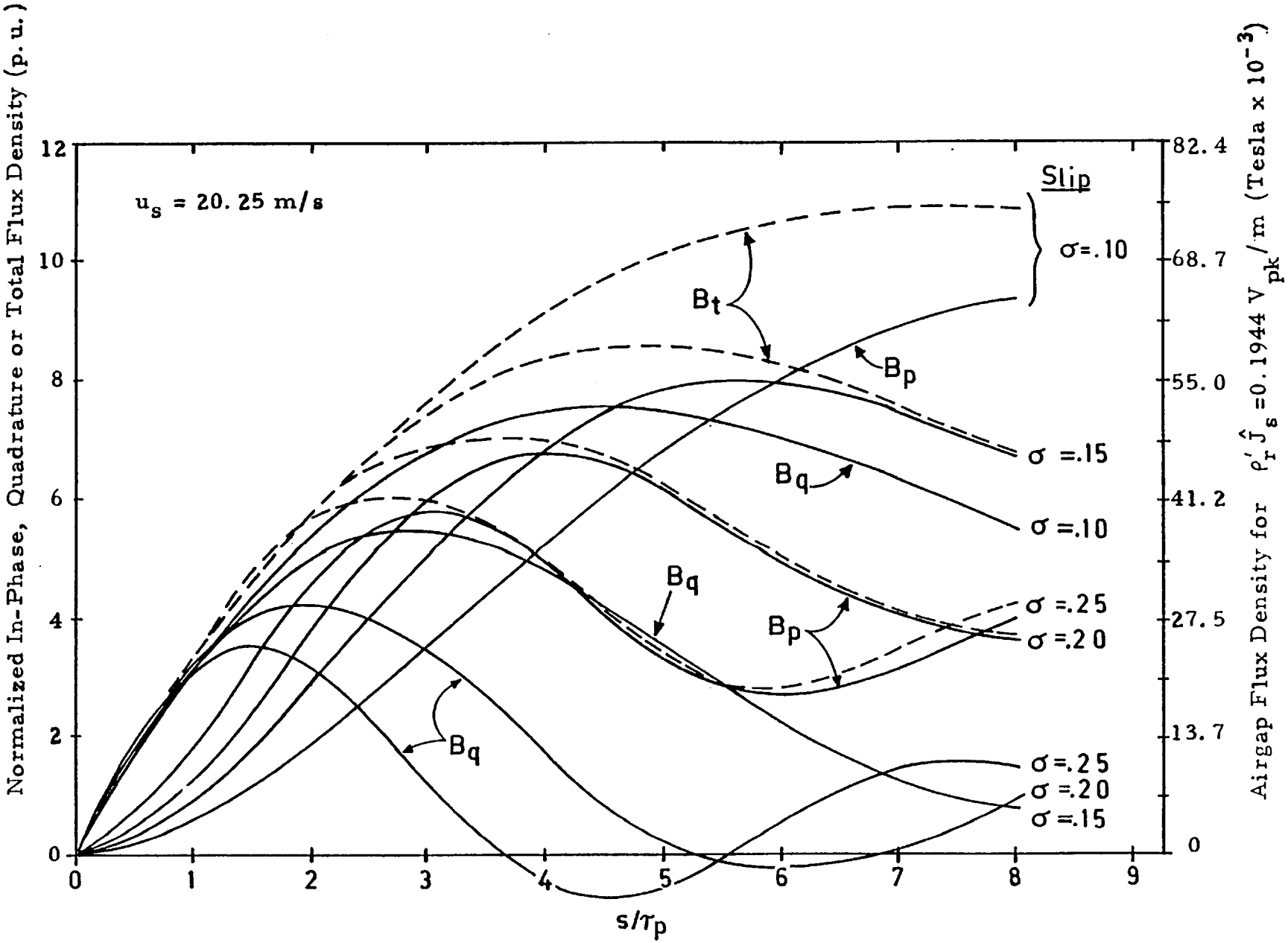

Figure 2.48 Theoretical component and total flux density for G=20 magnetization versus position.

to calculate the rotor resistivity, ρ_r due to temperature effects and differing rotor frequencies. Yet, the experimental solution to this problem is exact because it is possible to determine the lumped product $\rho_r \cdot J_s$ from a separate test.

If a running light test is performed on the LIM alone (perferably the 6.4 pole version), the experimental results of the total airgap flux distribution may be summarized as

$$B_t = K\left[1 - \exp\ (-t/T)\right] \qquad (2.20)$$

where T, the rotor time constant and K are the "best fit" describing parameters. However, at the slip, $\sigma = o$, it is accurate to say that $B_t = B_q$ and thus

$$K = \frac{\rho_r\ J_s\ \ T\ \ \pi}{\tau_\rho} \qquad (2.21)$$

Using 50 Hz test data from June 19, 1978 at a phase current of I_{ph} = 25 A.r.m.s., the lumped product for rotor voltage drop is taken to be

$$\rho_r\ \hat{J}_s = \frac{(.2025\ \text{m})(.128\ \text{Tesla})\ \sqrt{2}}{(.072\ \text{sec})\ \cdot\ \pi} = 0.162\ \text{pk V/m}$$

This empirical value is 15% lower than the straightforward calculation of the same quantity, and with the former utilized in Figure 2.48 (scaled to I_{ph}=30) the value of total flux density of a uniform LIM block is within a 3.5% error of the experimental density on a LIM block with extended iron beyond the winding (i.e., an unexcited ASC). This correlation, based on an exact tooth+slot surface area of the search coils without any fringing-flux compensations, is tabulated in Table 2.5.

Table 2.5

Correlation of total LIM airgap flux between infinitely-long stator block model with magnetization current and 4-pole-excitation experimental machine with 3 poles extended iron at exit end.

Conditions: 50 Hz, J_s=24,520 A/m (I_{ph}=30 A), Location s/τ_p=3.0

Slip,σ	Experimental B_{te}(mT,rms)	Theoretical B_{tt}(mT)	B_{te}/B_{tt}
0.268	40.95	39.6	1.034
0.227	46.07	45.0	1.021
0.188	49.10	49.2	0.999
0.156	50.2	50.4	0.996
0.134	50.2	51.6	0.973
0.089	51.2	53.0	0.966

The overwhelming conclusion to be drawn about the presence of the ASC block integral with the LIM block is that influence of the former on the LIM core flux is negligible in light of the previous evidence; furthermore, any corrections to the experiemental data for fringing flux or semi-filled LIM slots 1-6, 31-36 would be very marginal in comparison to the large flux distributed between s/τ_p=4 and s/τ_p=7 in Figure 2.47 and Figure 2.49 the high speed and supersynchronous flux plot. In essence, this forms the most basic proof that the ASC block is indeed being magnetized by the transient rotor currents and not by the LIM currents directly.

The results plotted in Figure 2.49 for the B_t distribution

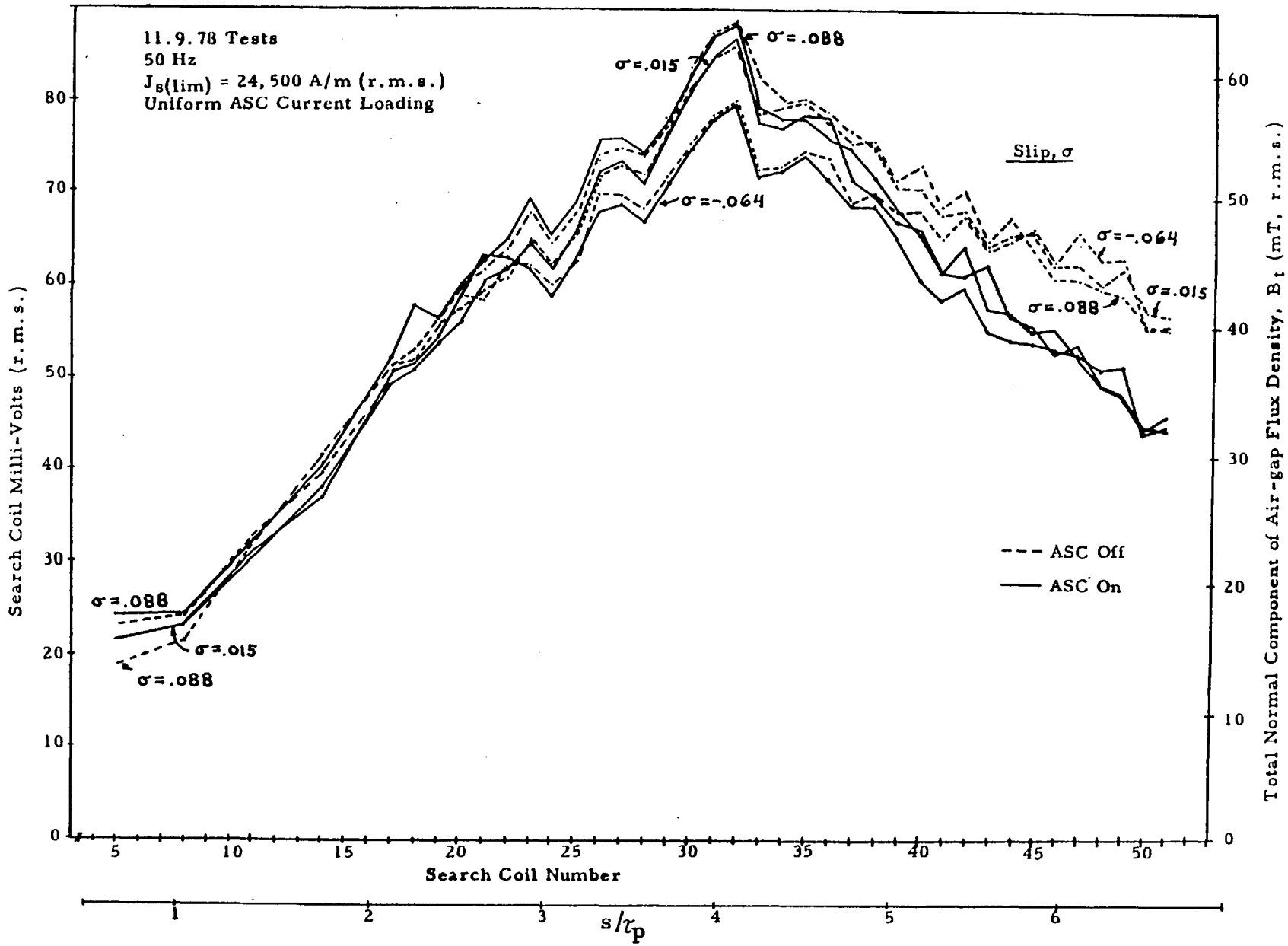

Figure 2.49 Total Air-gap Flux Density as a Function of Block Location at High Speed & Supersynchronous

between slips of 0.089 and 0.015 are especially valuable because in this practical operating range of slips, the decrement of ASC magnetizing flux is nearly independent (in contrast to Figure 2.47) of slip and only space dependent. A first order expression of the armature reaction attributable to the ASC loading is given, for the particular case that the LIM to ASC "J-jump" transition occurs at s^*

$$J_{sp(asc)}=J_{s(lim)}\left[1-\exp\left(\frac{-s^*\pi}{(1-\sigma)\tau_p G}\right)\right]\left[\exp\frac{-(s-s^*)\pi}{(1-\sigma)\tau_p G}\right]-\frac{g\pi\ B'_q}{\tau_p \mu_o} \tag{2.22}$$

where $J_{sp(asc)}$ is the magnitude of the surface current density of the ASC winding beginning at $s/\tau_p=4$ and in-phase with the LIM stator current density $J_{s(lim)}$, g is the airgap length, and B_q, is the flux density in space quadrature with $J_{sp(asc)}$ and is heavily dependent on the complex impedance of the ASC external load. Fundamentally, the instantaneous in-phase component of the ASC current loading can be expressed:

$$j_{sp(asc)}=j_{s(lim)}-j_{mp}=J_{sp(asc)}\ \sin\left[\frac{(s-s^*)\pi}{\tau_p}\right] \tag{2.23}$$

where j_{mp} is the normal magnetization component of current and by definition this is an in-phase quantity for this sets up the flux density B_q' over the ASC section. The instantaneous quadrature component of the ASC current loading is

$$j_{sq(asc)}=\frac{\pi g\ B_p}{\tau_p \mu_o}\ \cos\left[\frac{(s-s^*)\pi}{\tau_p}\right] \tag{2.24}$$

To simplify the analysis, suppose that the ASC load is purely reactive rather than a complex impedance so that

the direct axis induction-rotor load equation is

$$\sigma u_s B_p' \sin \frac{(s-s^*)\pi}{\tau_p} = X_{asc}\, j_{sq(asc)} \qquad (2.25)$$

$$= X_{asc} \frac{\pi g B_p'}{\tau_p \mu_o} \cos\left[\frac{(s-s^*)\pi}{\tau_p}\right]$$

and the quadrature axis flux cutting-rotor load balance is expressed as

$$\sigma u_s B_q' \cos \frac{(s-s^*)\pi}{\tau_p} = -X_{asc}\, j_{sp(asc)} \qquad (2.26)$$

$$= -X_{asc}\, J_{s(lim)}\left[1-e^{-\frac{s^*\pi}{(1-\sigma)\tau_p G}}\right]\left[e^{-\frac{(s-s^*)\pi}{(1-\sigma)\tau_p G}}\right] - \frac{\pi g B_q'}{\tau_p \mu_o} \sin\left[\frac{(s-s^*)\pi}{\tau_p}\right]$$

where X_{asc} is the total load reactance referred to the air-gap, i.e.

$$X_{asc} = \frac{X_{leakage} + X_{external}}{(\text{No. of series coils/phase})(\text{Series turns/coil})}$$

The solution of the previous two equations yields

$$B_p' = 0$$

$$B_q' = -\frac{X_{asc}\, J_{s(lim)}\left[1-e^{\frac{-s^*\pi}{(1-\sigma)G\tau_p}}\right]\left[e^{\frac{-(s-s^*)\pi}{(1-\sigma)G\tau_p}}\right]}{\sigma u_s \cot\left[\frac{(s-s^*)\pi}{\tau_p}\right] - \frac{X_{asc}\, g\, \pi}{\tau_p \mu_o}} \qquad (2.27)$$

which are valid only in the region that "s" is greater than "s*". This is not a complete analysis because the B_q' wave from the LIM has not been included in the last equation, however to confirm the basic assumptions with the experimental data of Figure 2.49 suppose that the important information from the slip = 0.015 plots is represented as in Figure 2.50 .

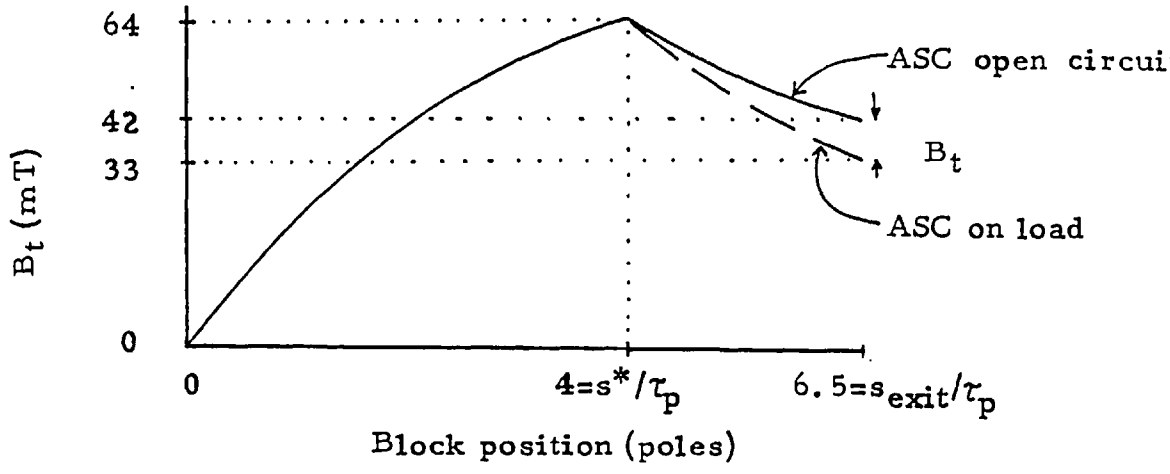

Figure 2.50 Summary of Figure 2.49 for a slip value of 15%.

If the peak total airgap flux density is expressed as

$$B_t = K_1 J_{s(lim)} \left[1 - e^{- s^*\pi/(1-\sigma)G\tau_p} \right] \qquad (2.28)$$

and substituting the values from Figure 2.50.

$J_{s(lim)}$ = 24,520 A/m and B_t = 64 mT,

the empirical constant K_1 is thus

K_1 = 0.00553 mT/(A/meter)

and if this same constant is used in the equation describing the decay of flux in the ASC section, where the effect of the ASC armature reaction amounts to a final reduction in flux at the end of the block of ΔB_t = 9 mT,

$$\Delta B_t = K_1 J_{s(asc)} \left[1 - e^{- \frac{(s_{exit} - s^*)\pi}{(1-\sigma)G\tau_p}} \right] \qquad (2.29)$$

the estimated value of ASC current loading is:

$$J_{s(asc)} = \frac{9 \text{ mT}}{(.00553)\left[1 - e^{-(2.5)\pi/(1-.015)\cdot(20)}\right]} = 4,950 \text{ A/m}$$

Since $J_{s(lim)} = 24,520$ r.m.s. A/m corresponds to 30A/phase, this estimated $J_{s(asc)} = 4,950$ A/m corresponds to 6.06A/phase exactly as the two windings are identical in this conversion. In practice, it was found that the ASC phase current measured was an average of 6.24 A.

Now that the airgap induction has been verified by the surface mounted search coils, the open circuit voltage of the ASC heavy-current coils will be investigated to show that stray effects such as tooth-tip and zig-zag leakage are not discernible but that non-uniform phase changes in flux are present, as expected. Referring to Figure 2.51 the open circuit coil voltages are plotted for the 18 ASC coils, each spanning 6 slots, all with uniform series turns per coil, $N_t = 12$. In theory and in practice, the results of Figure 2.51 are related to search coil voltages, V_{sc} of Figures 2.47 and 2.49 by

$$V_{oc(n)} = N_t K_d \left[\frac{V_{sc(n)}}{2} + \sum_{i=n+1}^{n+5} V_{sc(i)} + \frac{V_{sc(n+6)}}{2} \right] \qquad (2.30)$$

where the fundamental distribution factor for the search coils is

$$K_d = \frac{\sin(90^o)}{6 \sin(\alpha/2)}\Big|_{\alpha = 26.5^o} = 0.727 \qquad (2.31)$$

and "α" is the average and nearly constant phase angle between adjacent search coils over the ASC section block, and n is the classification number of the search and working coils as indicated in Figure 2.43.

However, a rather astonishing experimental treasure was revealed when the average "α" angle for the LIM search coils

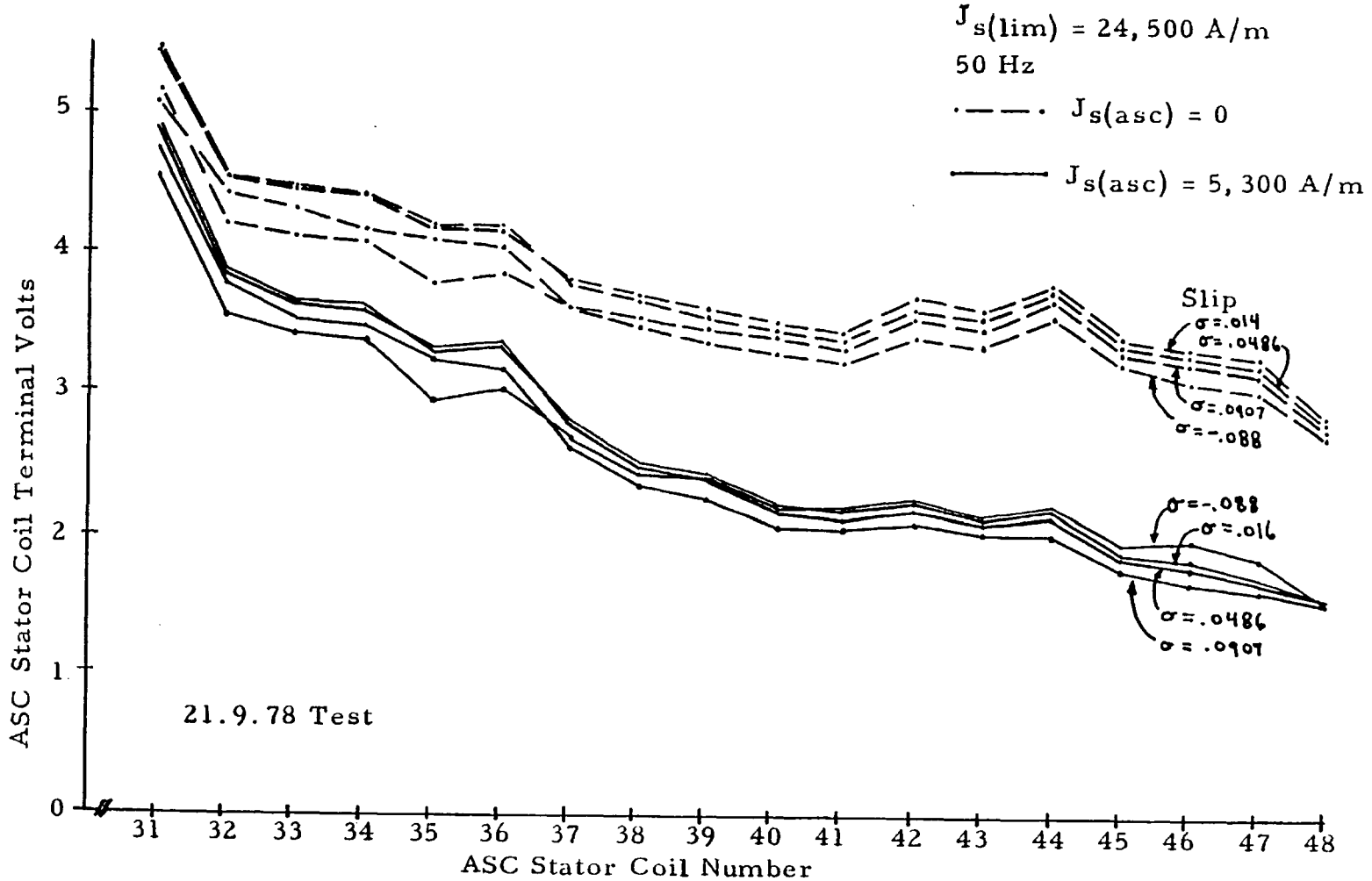

Figure 2.51 ASC Terminal Coil Voltage Magnitude near Running Light Slip, σ=.083

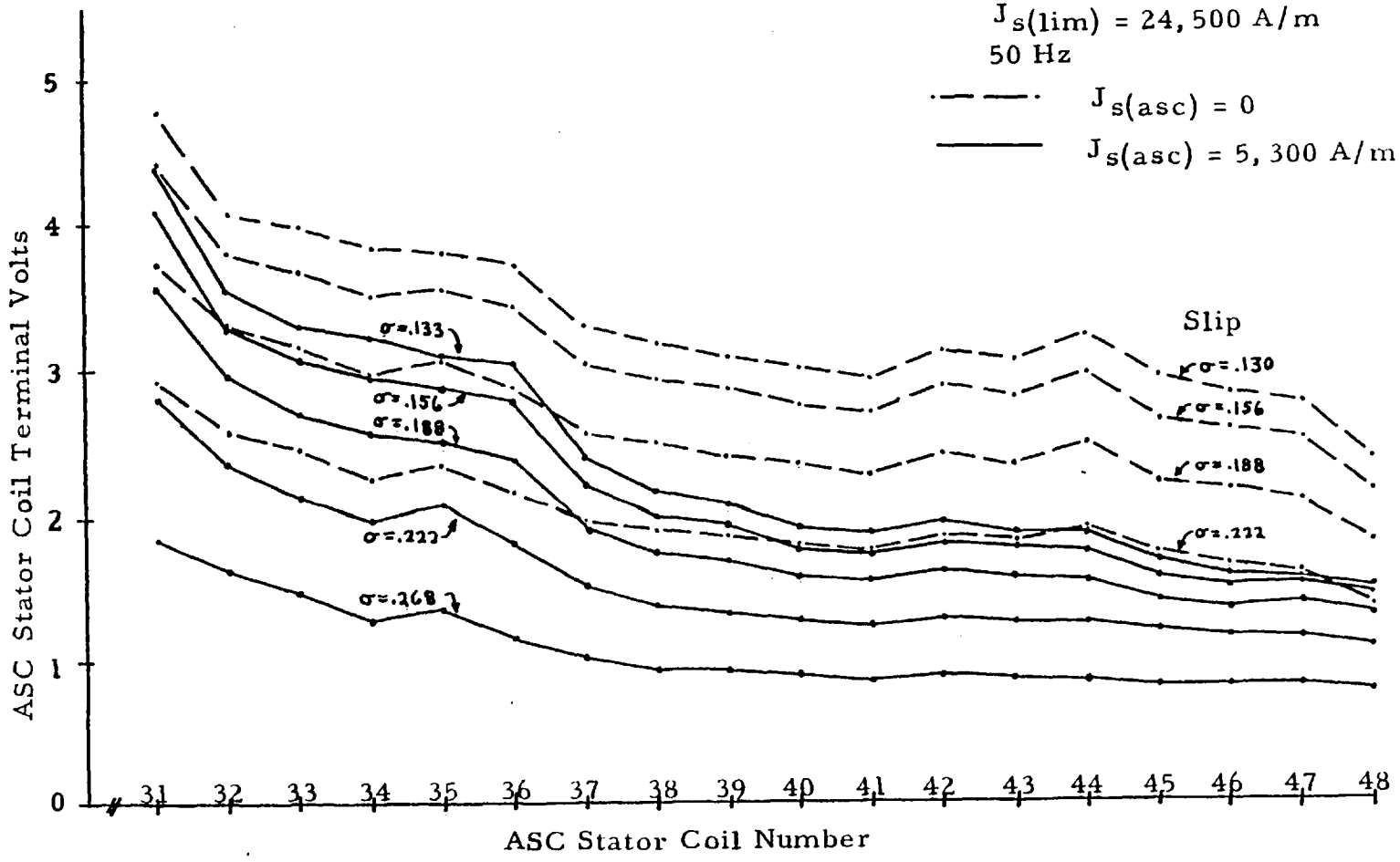

Figure 2.52 ASC Terminal Voltage Magnitude below Running Light Slip, σ=0.083

was compared with the "α" angle for the ASC search coils, as the former, on an average, agreed with theory but the α_{asc} was unquestionably larger---in other words, the effective pole pitch of the airgap flux over the ASC had shrunk in comparison to the LIM airgap pole pitch. This was substantiated with both the ASC being loaded or on open circuit. The amount of "pole-shrinkage" may be calculated as

$$\frac{\text{Avg. LIM slot-slot phase angle}}{\text{Avg. ASC slot-slot phase angle}}$$

$$= \frac{(180^{\circ}/\ 7.5 \text{ slots per pole})}{\text{Experimental } \alpha_{asc}} \qquad = 24^{\circ}/\ 26.5^{\circ}$$

$$= 90.6\%$$

In real terms, this means that the ASC field will go through one pole in (0.906) 7.5 = 6.8 slots which amounts to a phase error of about 17°/pole. This effect is of course accummulative and thus, with an 18 coil ASC winding the phase error is 17 $(26.5^{\circ}-24^{\circ}) = 42.5^{\circ}$ at the last ASC coil. It should be emphasized that this effect is not prominent in the working-coil voltage plot of Figure 2.52 whether on or off load, but it is apparent in the reactive power distribution/coil plot shown in Figure 2.53.

To explain the sharp differences between adjacent coil VARs in Figure 2.53, there are three simultaneously occuring sources, which are in order of increasing importance, the constant offset of the airgap flux by 17°/pole, the unbalance in phase currents, and the modulation of the airgap B_q wave as a function $\sin(s\pi/\tau_p^*)$ where τ_p^* is a pole pitch smaller

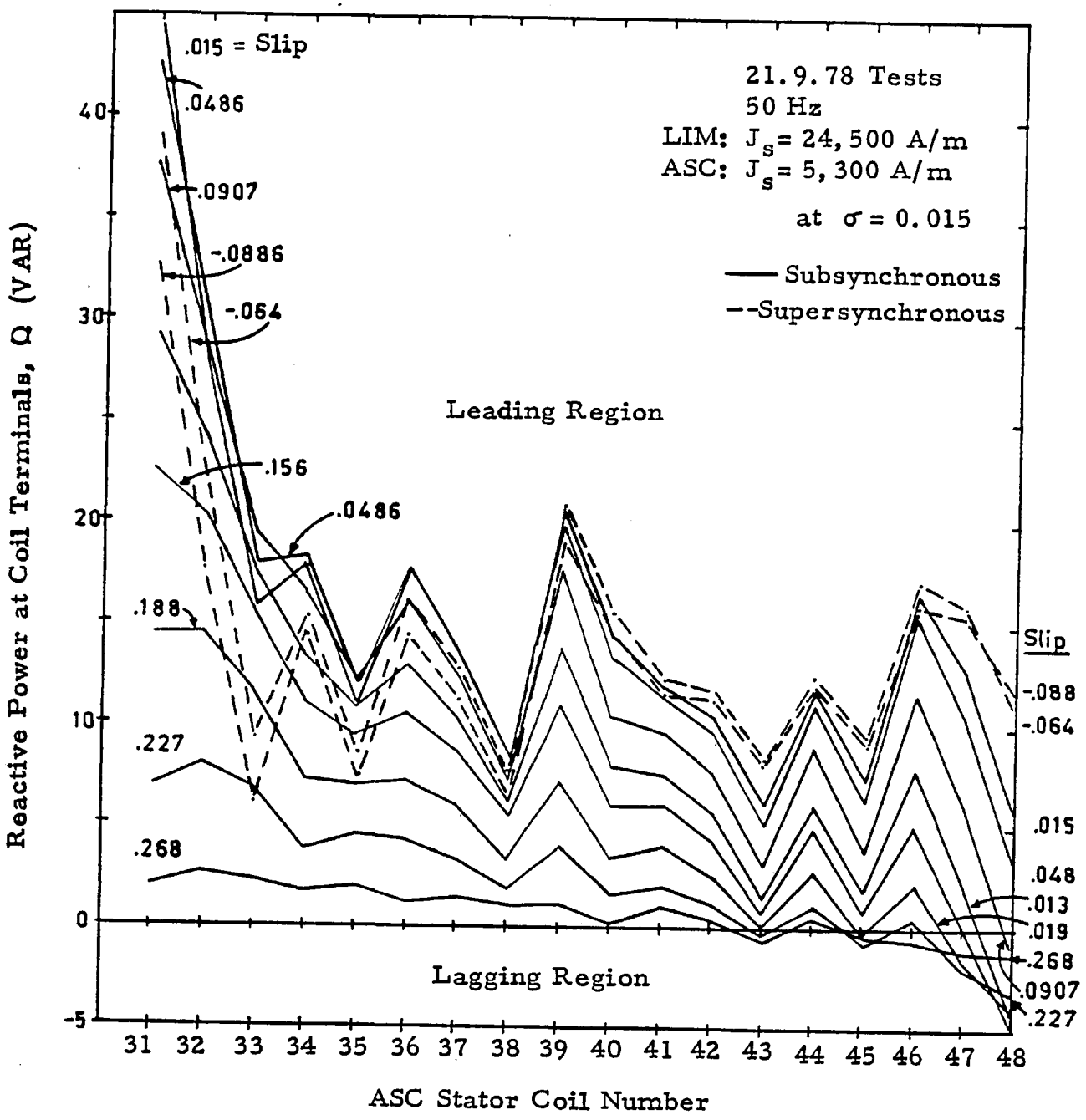

Figure 2.53 Asynchronous Condenser Reactive Power Distribution

than the winding pitch. The current unbalance is nearly constant throughout the range of slips in the per unit ratio $I_r:I_y:I_b = 1.0:0.984:0.876$. Since the plotted quantity is coil terminal VARs, the algebraic summation of these for all 18 coils accurately gives the total reactive power circulated in the Y-connected inductive load. Even when the data of Figure 2.53 is corrected to balanced phase currents, the overall picture is the largely unchanged because the crux of the problem is due to the seemingly random variation of the phase angle between coil terminal voltage and phase current. The total ASC reactive power output corresponding to the test data of Figure 2.53 , is shown in Figure 2.54 along with the ASC current loading as a function of slip.

The next series of tests combined the modification of a high impedance connection for the last 9 coils of the ASC, the inclusion of the induction regulator phase shifter at the ASC output and coupling the phase shifter to the LIM at the mains terminals. The effect of increasing the number of turns per coil from 12 to 36 is to yield in practice a 2:1 increase in coil terminal output reactive power (rather than a 3:1 increase) due to the change in leakage reactance from 0.065 ohms to 0.54Ω/coil (uncoupled 1 Ø value at 50 Hz). Most important, as Figure 2.55 indicates, this impedance change amounts to maintaining the reactive power output from low-Z and high-Z winding sections nearly constant despite the rotor pole shrinkage that is still occuring. This winding in conjunction with the LIM constitutes a double "J-jump" winding in that the

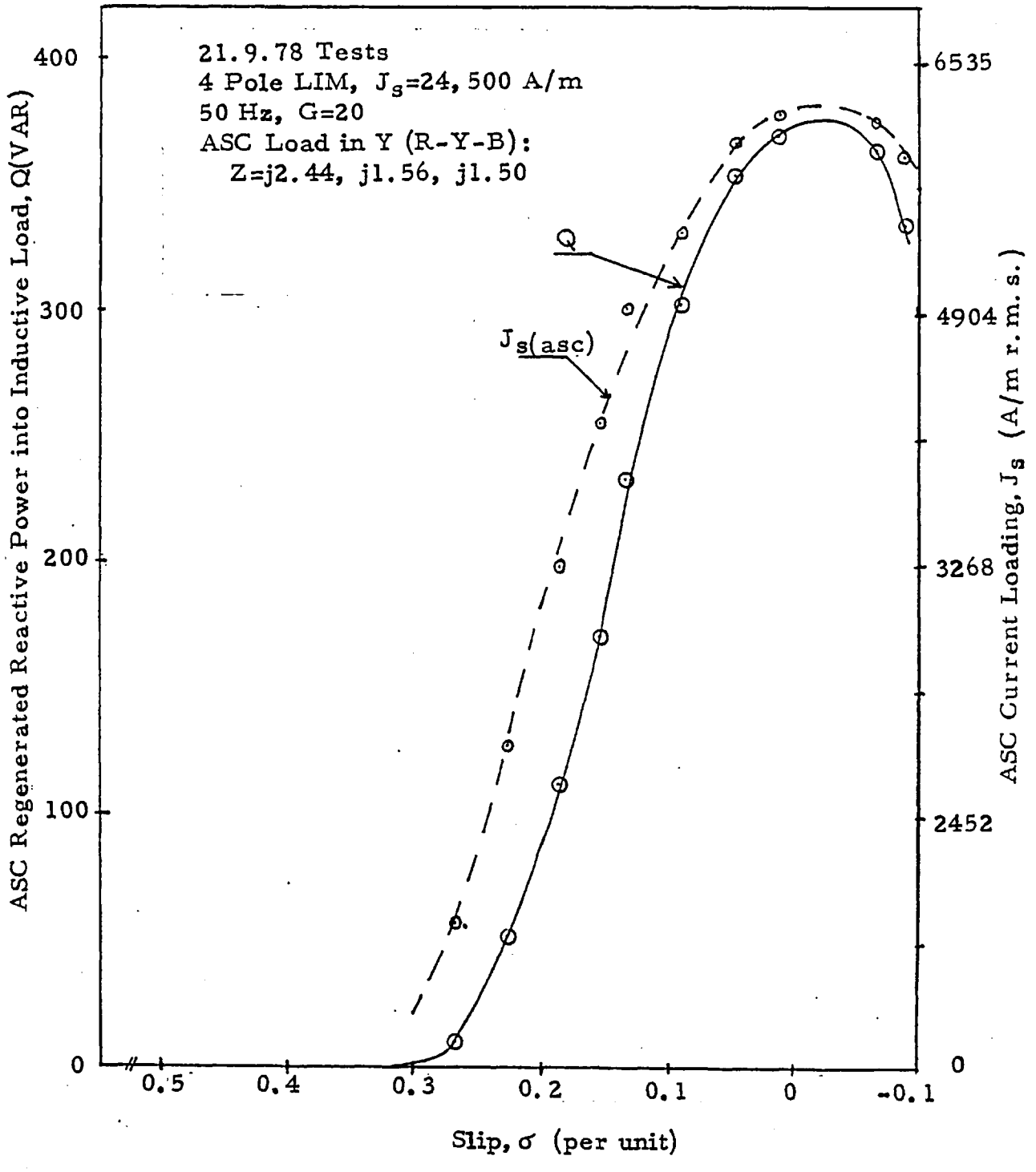

Figure 2.54 Asynchronous condenser terminal output and current loading with uniform impedance stator winding and load matching to balance ASC phase currents.

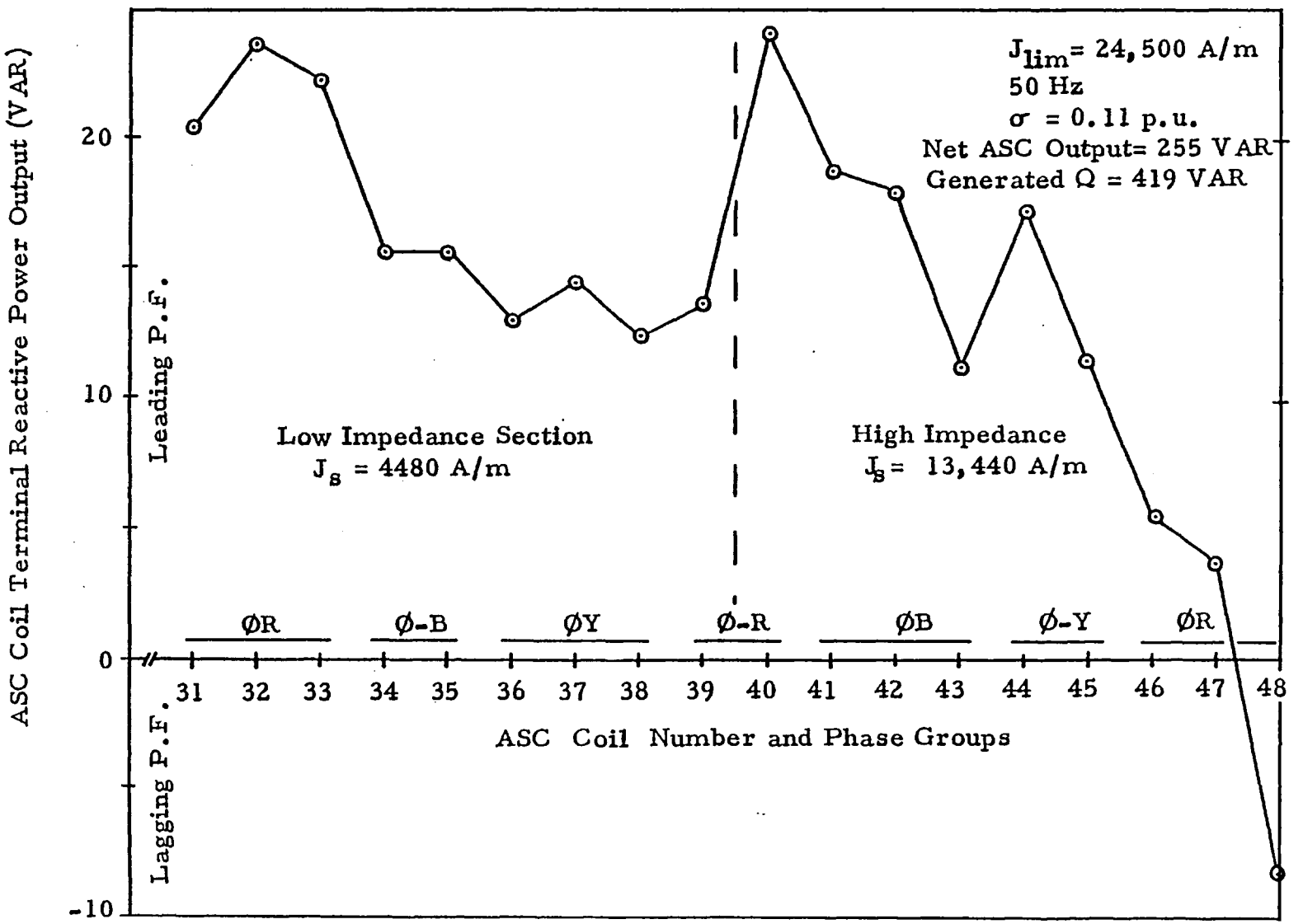

Figure 2.55 ASC coil terminal reactive power output with 4 pole LIM for 16.11.78 tests.

stator current loading of Figure 2.55 changes from LIM entry to exit-end as 1.0:0.183: 0.548 per unit.

To indicate how well each coil is acting as a reactive generator, Figure 2.56 plots a relative utilization factor which is called the reactive power factor and is defined as the sine of phase angle between coil terminal voltage and phase current. In particular, note that at the winding impedance transition between coils No. 39 and 40 (of the same phase), the utilization is approximately the same. However, there appears to be a characteristic modulation of coil phase angles, e.g. at coils 31, 36, 43, 46, 47, the phase angle departs rather markedly from 90^{o} including coil 48 which actually appears to be reversed as it absorbs reactive power. The immediate solution to cases such as coil number 48 is to disconnect it from ØR and connect it to ØY.

For the special case of the tests supporting Figures 2.55 and 2.56 the major cause of poor utilization was a combination of having only a three-phase winding (whereby 3 slots per wavelength had no change in stator current phase for 7.5 slots/pole at 0.8 chording) and the pole shrinkage rather than a core flux modulation problem. Inspection of Figure 2.56 reveals that invariably, there is a positive phase change in all of the 7 coil phase groupings, e.g. in the first group: 42^{o} - 74^{o} - 100^{o}, which means that any B_q modulation of the phase angles is swamped-out by load current forcing due to the series connection. Moreover, the indicated phase angles differ from an average angle of 90^{o} in any 2 or 3 coil group principally because a

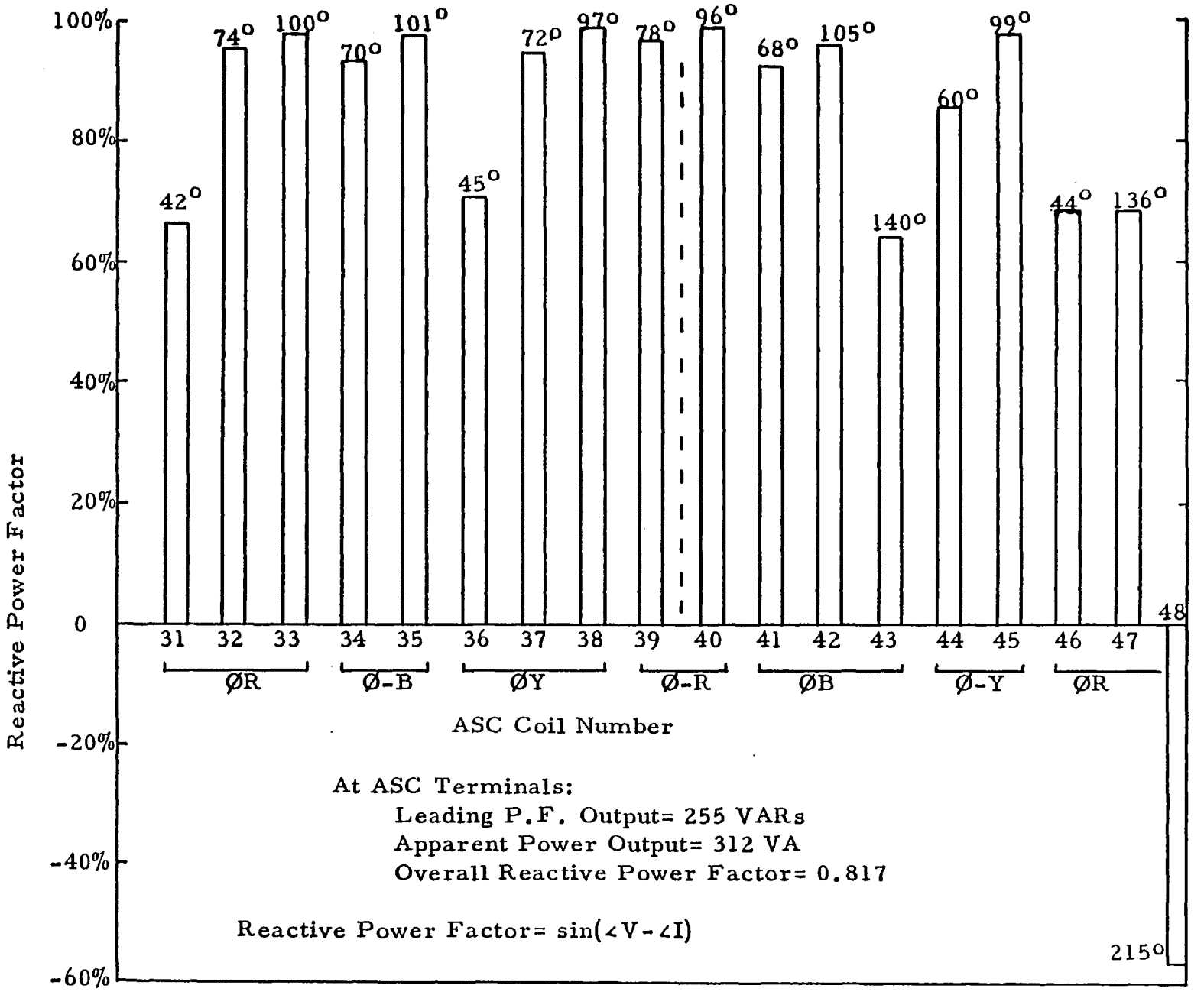

Figure 2.56 Utilization of reactive power in linear motor condenser windings, $\sigma = 0.11$ p.u.

small amount of real power must be transferred, e.g. coils 31 and 32 are motoring while coil 33 is generating. However, for the particular angles involved, too much real power is being unnecessarily circulated since each coil only requires about one watt I^2R loss in the low impedance section at J_s=5000 A/m and thus a terminal angle of 88° would be sufficient for a 30 VAR output/coil. Table 2.6 presents the terminal characteristics.

Table 2.6

Summary of 16.11.78 Tests

Four Pole LIM Running Lights Slip = 0.083 p.u.

Operating Slip, σ = 0.11 p.u. (50 Hz)

LIM Apparent Power = 4.64 kVA

LIM Loading = 24,520 A/m rms

LIM Power Factor = 0.402 uncompensated

ASC Loading = 4480 A/m and 13,440 A/m

Net ASC Output = 0.255 kVAR

Gross Generated Reactive Power from ASC = 0.503 kVAR

Gross ASC Output/Input LIM Reactive Power = 0.503/4.28=11.7%

Maximum ASC "Armature Reaction" (at end of machine) = 26.2%

Net LIM-ASC Terminal Power Factor = 0.437

Gross ASC Output Scaled to 40% Armature Reaction (σ=0.05)= 1.08 kVAR

Up until this point, the experimental results have centered on the utilization of the asynchronous condenser winding only, but equally as important the internal power distribution of the coils in the LIM proper will be discussed. The outstanding conclusion to emerge is that the fundamental reason underlying poor utilization of the ASC winding (i.e. sin $\emptyset \neq 1.$) is the same mechanism that causes the LIM coils to depart severely from cos $\emptyset = 1.$ operation. From basic LIM theory, it is well known that the airgap power factor problem is <u>not</u> due to the large iron-iron airgap present in linear machines, per say but stems from the presence of two traveling waves in the airgap. One wave has the same pole pitch, τ_p as the LIM windings, while the end-effect wave has a pole pitch equal to $\tau_p(1-\sigma)$ where σ is the per unit slip. It is the interaction of this latter wave with the LIM stator winding that is responsible for the bulk of the correctable power factor problem and this is the area where the research is directed to at present.

The other causes of poor power factor in longitudinal flux LIMs should be mentioned; the remedies are fairly conventional although sometimes rather expensive to implement. High speed machines with 50 Hz supplies necessitate large pole pitches, which means a large number of slots/pole/phase if only a three phase supply is available. The larger the number of slots/pole/phase, q the more difficult if not impossible it becomes to produce a polyphase winding with both uniform tooth-tooth phase angles and uniform resultant slot currents, assuming balanced phases, etc. for a given

number of phases. For example, even with a fractional slot pitch winding of $q=4\frac{4}{5}$, a uniform phase change of $12\frac{1}{2}^{o}$ is practical with a three phase supply but the resultant current magnitudes oscillate between $\sqrt{3}$ and 2. The problem is further complicated by the fact that there is a minimum number of teeth per pole (a direct function of the airgap sizing) which must be adhered to, i.e. the phase differences between teeth must be reasonably small. The first design guideline that should be followed in respect of improving power factor, is simply that 50 Hz high-speed machines with large airgaps utilizing double layer windings and standard 50%-50% phase mixing, is to limit $q \leq 2$ by increasing the number of supply phases. It's a practical suggestion considering the large number of LIM installations to date for high speed ground transportation that have used on-board alternators but have failed to use any system other than 3Ø. [6]

The experimental machine LIM-ASC-I uses a q=2.5 slots/pole/phase winding with the rather unusual phase and magnitude distribution shown in Figure 2.57 for the fully filled slots.

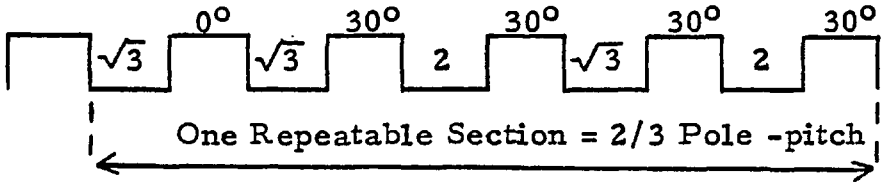

Figure 2.57. Phase change between adjacent slots and the resultant magnitude of slot MMF.

The above diagram is helpful only in assessing coil power factors when the machine is at standstill. The experimental

results of the LIM coil power factor tests are listed in Table 2. for the slip of 0.11 p.u.; this clearly brings to light the aforementioned problem of using only a 3 phase supply with relatively small airgap induction in comparison with current loading. For the two types of phase groups, the experimental results follow the pattern:

Coil No.	cos Ø = P.F.		Coil No.	cos Ø = P.F.	
21	0.035		24	0.191	
22	0.407	q=3	25	0.602	q=2
23	0.67				

Additionally, this test represents not only poor utilization of the first or entrance-end coil(s) in each phase group, but simultaneously, above average performance for the last coil in most of the phase groups, such as No. 23, 25, 18, 28. In fact, the use of a 3Ø supply with a low number of slots/pole/phase has inadvertantly and favorably phase-advanced these last coils which was a task that hitherto had been thought only possible by special experimental reconnections.

The measured LIM terminal power factor corresponding to Table 2.7 was 0.39 p.u. (which is about 65% of the maximum) and this is derivable from the individual power factors and VA/coil. The important conclusion is that in all cases except coil 11, the power factors are below unity because the airgap flux (or induced voltage thereof) leads the phase current by too large a margin but this is correctable due to the travelling magnetic fields. By applying this pole-

Table 2.7

LIM Power Factor and Apparent Power at 50 Hz, Slip=0.11 p.u., J_s = 24,520 A/m r.m.s.

Phase Y				Phase R				Phase B			
Coil	V.A.	Ø	P.F.	Coil	V.A.	Ø	P.F.	Coil	V.A.	Ø	P.F.
7	124	110°	0.34	9	161	100°	0.174	11	146	88°	-0.035
8	141	126°	0.588	10	161	120°	0.500	12	165	108°	0.309
14	163	95°	0.087	16	178	90°	0.	13	167	126°	0.588
15	179	124°	0.560	17	185	109°	0.325	19	185	98°	0.132
21	190	92°	0.035	18	198	129°	0.630	20	195	126°	0.588
22	194	114°	0.407	24	207	101°	0.191	26	194	97°	0.122
23	206	132°	0.670	25	207	127°	0.602	27	200	119°	0.485
29	196	106°	0.275					28	201	136°	0.719
30	191	127°	0.602								

phase modulation (PPM) technique to advance the current angle by δ, the coils in each sub-group can have uniform power factors, e.g.

Coil No.	Total Angle	Correction Angle to Yield 0.67 P.F.
21	$92^\circ + \delta_1$	$\delta_1 = 40^\circ (.70 \text{ rad})$
22	$114^\circ + \delta_2$	$\delta_2 = 18^\circ (.314 \text{ rad})$
23	132°	

The solution is to phase shift whole groups of coils (by diminishing angles) until the new rotor current pattern is established as a steady-state phenomenon, and then it is appropriate to commence the phase modulation sequence again. Note that the angles δ_1, and δ_2 chosen above are only optimum at the one slip of 0.11 and a Goodness factor of about 20. If the Goodness factor of the machine were smaller, the ratio δ_1/δ_2 would be smaller. In theory, the PPM angles approximately scale as:

$$\delta \approx \tan^{-1}\left(\frac{1}{\sigma G}\right)$$

F. Conclusions

1. The region of maximum reactive output as a function of slip, the LIM to ASC phase shift and the effective armature reaction of the ASC loading have been verified.

2. Consequently, the winding dimensions for the machine "LIM-ASC-II" were calculated to peak the ASC output and LIM power factor at nearly the same slip speed.

3. The power factor of individual LIM coils is heavily dependent on the current forcing of the series connection in addition to the offset caused by the end-effect traveling wave.

4. Based on the experimental results up to December 1, 1978, LIM-ASC-II was designed with a pole pitch of 0.260 m, a Goodness factor of 28 at 50 Hz, and facilities for independent measurements to be made of the core flux shunting by the ASC block. The LIM was finalized with nine poles and the ASC section with two poles, a total of 99 coils of high and low impedance in 108 slots. The LIM power factor was designated to peak at slip $\sigma = 0.115$ per unit, but to be operated at $\sigma = 0.08$ p.u.

5. LINEAR OVEREXCITATION

A. Two Stage Exit Regeneration

The concept of linear overexcitation was first conceived as a completely analogous mechanism to overexcitation in a rotary synchronous condenser with DC excitation with the one major exception that in the linear version, overexcitation would only occur over a limited airgap section rather than with a uniform distribution. As machines become larger and the airgaps relatively smaller, rotor and stator currents tend to be mirror images. Yet when such a machine has an abrupt change in stator current loading and the rotor has significant inductance, then it is possible to only match stator and rotor currents over a first section with the result that in the second, this mismatch of rotor to stator manifests itself as a genuine form of continuously occurring overexcitation using entirely induced currents.

The most outstanding characteristic of this development has been that the two-stage concept first initiates a phase change in the condenser section while the latter stage relies on an abrupt change in MMF magnitude as well as a physically different winding. Based on the 80.35% terminal power factor attained with this approach, the "two-stage J-jump" appears to be preferrable to similar flux-recovery schemes with a continuously graded-MMF condenser section at the exit end of a high speed LIM.

This section summarizes the construction and development effort devoted towards the first electrical machine specifically designed to be a brushless induction machine with an in-

tegral asynchronous condenser (ASC) winding. The machine designated for this purpose is termed "LIM-ASC-II" and is comprised of a two-block arch-shaped stator unit retrofitted onto the existing high-speed linear induction machine test rig in place of the single block stator described as LIM-ASC-I.

The series of experiments ascertained exactly the capability of a brushless induction machine to generate reactive kVA at 50 Hz (principally) along with the relative merits of using new winding construction methods aimed specifically at reducing slot leakage kVAR. As with the LIM-ASC-I machine, the LIM-ASC-II machine relies on the same basic electromagnetic concepts to effect an improvement in terminal power factor of the entire unit by feeding the recovered reactive power back into the mains. For these series of short-stator machines, power factor improvement is occurring at the same or a higher overall efficiency than without end-effect neutralization.

B. Dimensioning the LIM-ASC-II

The completed stator arch block for the entry-end of LIM-ASC-II is shown in Figure 2.58 prior to being impregnated with a two-stage, high-temperature araldite resin. An identical unmachined stator block is also shown in the same figure to give an indication of the size of the original laminated torus from which four identical 90° arcs were cut prior to slotting. Since all slotting was performed prior to the power factor improvement project, the LIM-ASC-II slots were effectively made shallower by the addition of paxolin non-magnetic packing material in the bottom of all slots as shown in Figure 2.59 . The subsequent section shows the calculations discerning the change from deep-slot circular windings incorporated in the LIM-ASC-I design to top-of-slot rectangular cross-section windings inherent throughout the LIM-ASC-II design. This one modification alone lowered the per unit slot leakage kVAR for the second machine to 16% of the value for the first prototype. A separate set of computer calculations are included as Appendix I to ascertain the marginal increase in end-winding leakage reactance that was accrued by changing the pole-pitch from 0.202 m to 0.247 m for the LIM-ASC-II unit. The coil layout used to wind this machine is shown to scale in Figure 2.60 with insulation between turns rated at 180°C and 2000V strength. The characteristic parameters and construction dimensions of the 99 coil LIM-ASC-II are given in Table 2.8.

LIM-ASC-II was specified and wound with uniform slot width and slot pitch dimensions throughout both stator cores

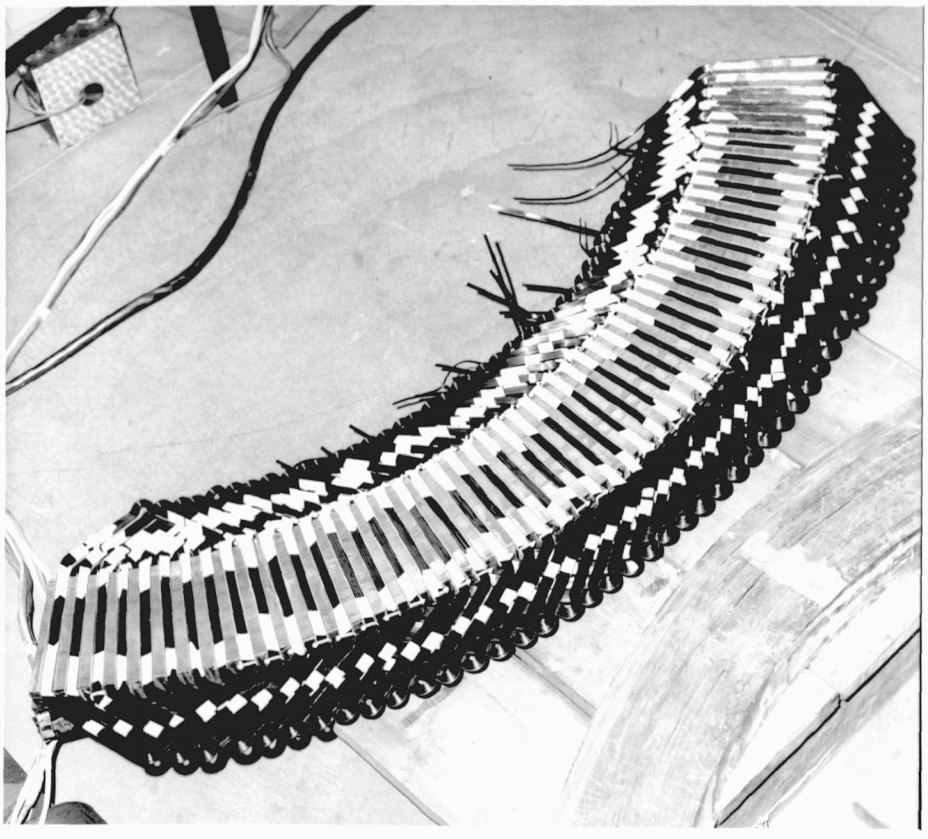

Figure 2.58 The entry-end stator segment for LIM-ASC-II prior to being impregnated and joined to the exit-end segment; an unmilled stator core is also shown.

Table 2.8

Dimensions and Operating Conditions for the LIM-ASC-II Machine

Longitudinal Core Length, mean	3.01 m
Transverse Core Width	157 mm
Stator Block Depth	120 mm
Slot Width (uniform)	14.3 mm
Slot Depth (uniform)	38.1 mm
Slot Pitch (mean)	27.4 mm
Aluminium Annulus Thickness	9.3 mm
Aluminium Width	229 mm
Steel Disc Thickness	19.05 mm
Aluminium Resistivity (20°C)	3.25×10^{-8} Ω-m
Steel Disc Resistivity	1.498×10^{-7} Ω-m
Disc Moment of Inertia	510 N-m-sec^2
Theoretical Russell and Norsworthy Factor	1.96
Synchronous Speed @ 50 Hz	247.2 RPM
Moment Arm to Center of Motor	0.9545 m
Typical Operating Entrefer	12 mm
Goodness Factor (X_m/R_2) @ 50 Hz	28.4
Total Number of Coils	99
Total Number of Slots	108
Pole-pitch (uniform)	0.2466 m
Coil Span/Pole-pitch	0.888
Slots/Pole/Phase	1
Phases	9
Distribution Factor (9Ø)	1.0

1. Features Particular to the LIM (Coils 1-81) and First ASC Section (Coils 82-90)

Series Turns/Coils (1 layer)	6
Mean Length of Coil	5.568 m
Resistance/Coil (20°C, D.C. Kelvin Bridge)	0.011 Ω
Reactance/Coil @ 50 Hz (in air)	0.00754 Ω
Reactance/Coil @ 50 Hz (1Ø, in block, no secondary)	0.014 Ω
Conductor Type (180°C insulation, 2000V)	5 mm x 2 mm
Mean Depth of Conductor in Slot, upper layer (lower)	3.5 mm (8.5 mm)

2. Features Particular to the ASC Section (Coils 91 through 99)

Series Turns/Coil (2 layers)	14
Mean Length of Coil	13.0 m
Resistance/Coil (20°C)	0.0315 Ω
Reactance/Coil @ 50 Hz (in block, 1Ø uncoupled)	0.076 Ω
Conductor Type (150°C insulation, 1500 V)	4.57 mm x 1.78 mm
Current Density at 20A/Phase	2.46 A/mm^2
Stator Current Loading at 20A/Phase	19,200 A/m r.m.s.
Mean Depth of Conductor in Slot, upper (lower)	5.6 mm (10.2 mm)
Chording Factor	0.939

in the interests of minimizing construction costs. It represents an important milestone in linear machine development for having both a high Goodness Factor and a high ratio of Goodness Factor: excitation poles with the windings nearly resembling the proverbial "current sheet" top-of-core winding. The connection diagram is given in Figure 2.61.

Theoretical calculation of the quadrature, in-phase and total normal-directed airgap flux densities peculiar to the geometry of the LIM-ASC-II for the 9 poles of exitation that characterize the flux build up section are shown in Figure 2.26 for 50 Hz excitation and in Appendix III for 150 Hz excitation.

C. Calculation of Slot Leakage Inductance for Stator Top Coil Layer

The slot leakage due to the field of the top conductor alone is given by the formula

$$L_t = \frac{\mu_o N^2 L}{b_s}\left[h_2 + \frac{1}{3}(h_1)\right] \quad \text{Henries}$$

where N= number of turns

L= stator core width (m)

b_s= slot opening rectangular slot (m)

h_2= depth from top-of-slot to top of conductor (m)

h_1= depth of conductor of one coil or layer (m)

$\mu_o = 4\pi \times 10^{-7}$ H/m

a. Original LIM-ASC-I Machine with circular wire

N = 12

L = 0.157 m

b_s= 0.0143 m

h_2= 0.012 m

h_1= 0.013 m

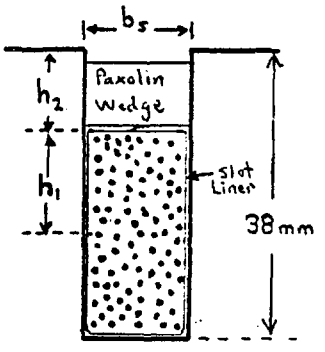

L_t = 32.4 μH

b. New LIM-ASC-II Machine with top-of-slot rectangular conductor

N = 6

L = 0.157 m

b_s= 0.0143 m

$h_2 \leq$ 0.001 m

h_1= 0.005 m

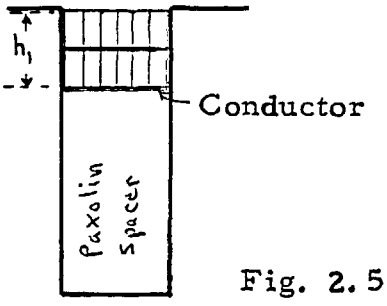

Fig. 2.59

L_t = 1.32 μH

Thus the overall reduction in slot leakage reactance amounts to

$$\frac{L_{t(II)}}{L_{t(I)}} = 0.0407 \text{ p.u.}$$

i.e. the top layer of the new machine has less than 5% of the leakage as the top layer of the original design. Although a good deal of this reduction is due to the change in series turns, even if the turns were the same, the per unit reduction in slot leakage is exceptionally impressive.

$$\frac{L_{t(II)}}{L_{t(I)}} = 0.163 \text{ p.u.} \quad \text{assuming } N_{II} = N_{I}.$$

In terms of calculating the slot leakage reactive kVA for an equivalent current loading density, the number of turns is immaterial to a first order and thus LIM-ASC-II has about 16% of the slot kVAR as LIM-ASC-I.

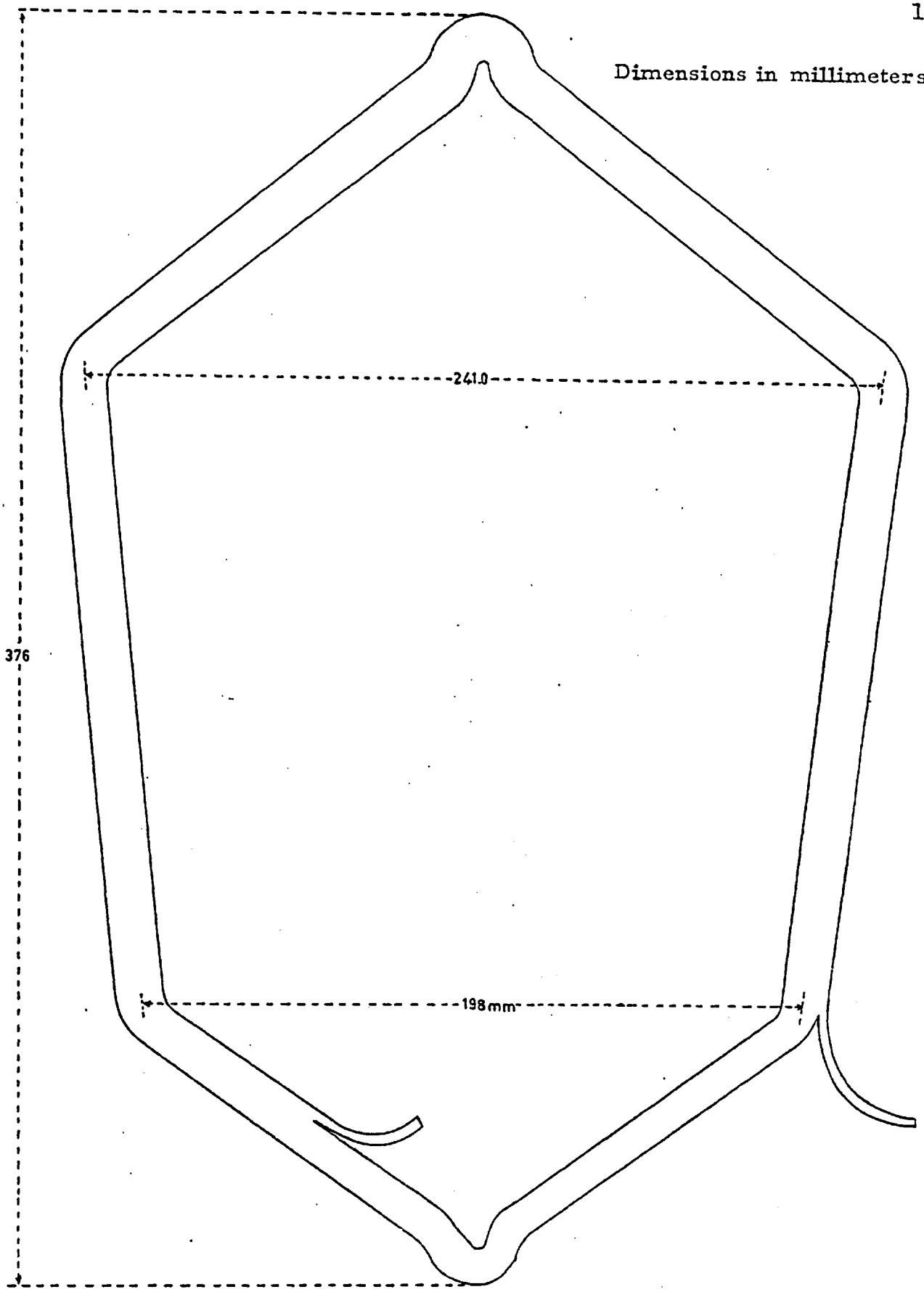

Fig. 2.60 Outline of the stator coils for the LIM-ASC-II with 2 mm/5 mm wire.

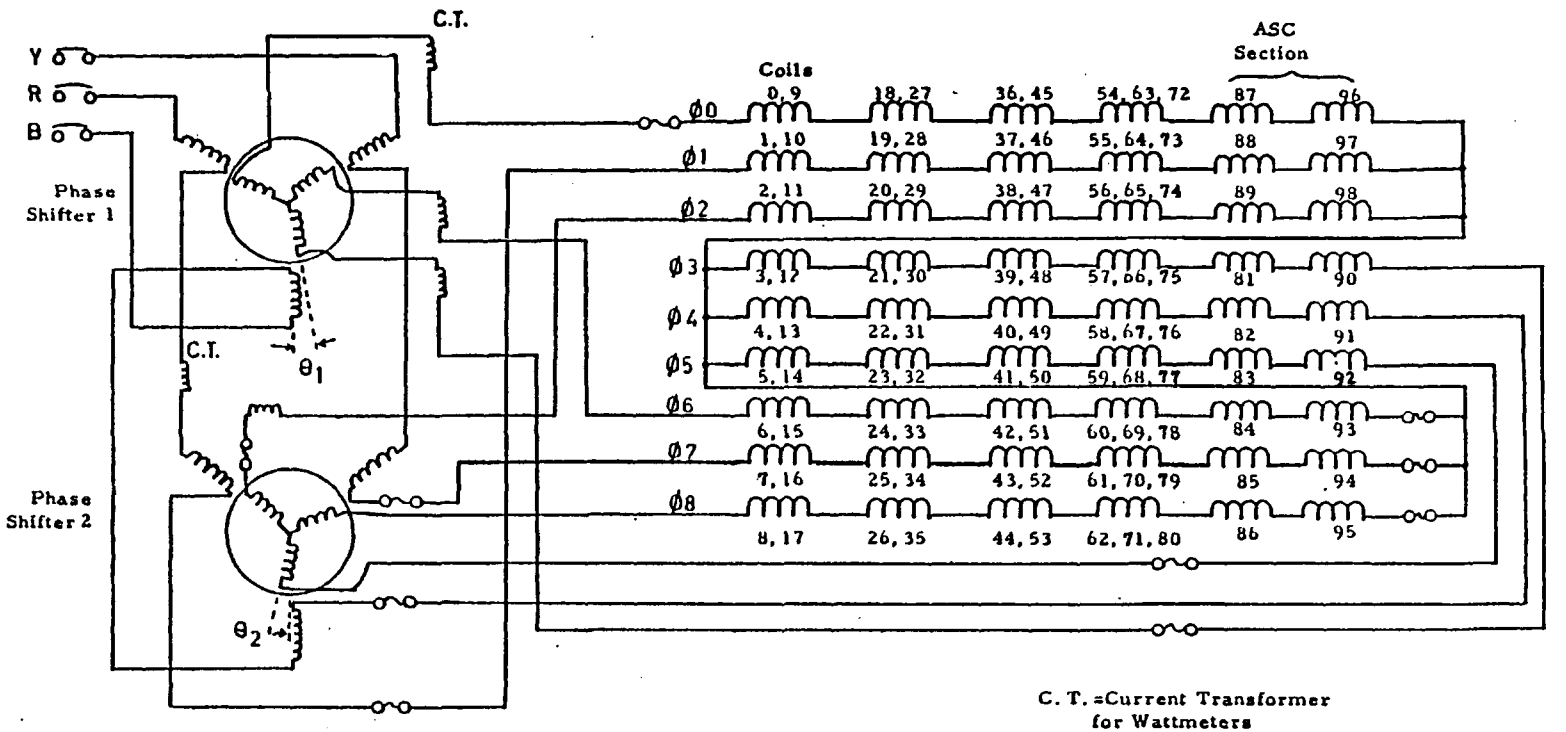

ASC and Motoring Coils

Figure 2.61 Heavy current connections for the 9-phase, 1 slot/pole/phase LIM-ASC-II machine.

E. J-Jump Machine Test Results

A series of acceleration tests were performed with the LIM operating at the designed rated current loading of 57,600 A/m r.m.s. in addition to steady-state, reduced current tests with the dynamometer in action. Specifically, for the LIM-ASC-II with nine poles of excitation, the basic theory predicts that the best "airgap efficiency" is obtained at a slip of $\sigma=1/(n+1)$ per unit where n is the number of poles and $\sigma=$ 10% for this case; the power factor for just the motor section should be optimum around a slip of $2/(n+2)$ which is 18%. The most spectacular test result was that very close to the theoretical maximum power factor slip value of $2/(n+2)$, the total LIM-ASC terminal power factor peaked at 80.3% with 50 Hz excitation and current loadings in the range of 19,200 A/m to 24,000 A/m. This was in contrast to the earliest design criterion for LIM-ASC-II because originally the ASC was to function in shifting, significantly, the peak of the cos ϕ characteristic to coincide with the efficiency characteristic w.r.s.t. slip; the tests indicated that a 3% change in slip values was practical whereas an 8% shift in slip values was too optimistic for the "9+2" pole configuration.

The tests immediately established that the condenser winding alone peaked in output at a slip less than 2%; at 18% slip, the ASC output was considerably too small to effect a major change in the overall power-factor-optimum slip value. Yet this was found to be entirely acceptable

since the basic LIM power factor was inherently, extraordinarily high, over 73%. Throughout the analysis, it was realized that if only the LIM had two or three more excitation poles, for example 12, then the ASC windings could effect a major change in the optimum-power-factor-slip as unquestionably the basic LIM would peak at 14% slip or less. However, inspection of Figure 2.62 reveals that this suggestion was unnecessary for only one major reason--the ASC winding performed in the slip region where it was exactly needed the most, the region where the LIM power factor traditionally becomes poor. Fortunately, for LIM-ASC-II, even at the peak-efficiency-slip of 11%, the motoring section power factor remained as high as 63% which is directly attributable to the very low slot leakage kVAR requirement inherent in the rectangular wire windings. The composite machine had a terminal power factor of 78.3% at this 11% slip which represents a power factor-efficiency product (simultaneous values) of 60.3%, the highest attained for this machine. Table 2.9 presents a summary of a test run.

At the anticipated stable operating point, at a slip less than the peak efficiency slip, for example an 8% slip, the basic LIM power factor has decreased to 56% but this is effectively compensated for by the ASC which is now operating at about 90% of its maximum capability, raising the terminal power factor to about 73%.

In short, LIM-ASC-II represents a new class of single-sided linear machines for which integral, magnetic power

Table 2.9

Maximum Power Factor Test Summary for 14/12/79

LIM-ASC-II

Frequency: 50 Hz, Connection: Y-series, Airgap Setting: 14-15 mm

Phase	Terminal Volts (r.m.s.)	Current (A)	VA	Watts	Phase Power Factor
1	12.2	19.68	240.1	189.6	0.789
2	11.4	22.89	260.9	203.5	0.779
3	12.1	19.68	238.1	192.8	0.809
4	12.3	19.44	239.1	194.8	0.815
5	11.9	22.89	272.4	209.7	0.769
6	12.4	20.54	254.7	205.0	0.804
7	11.2	19.68	220.4	179.8	0.815
8	10.8	22.89	247.2	198.3	0.802
9	10.6	19.98	211.7	180.3	0.851
			2184.0	1754.0	

Overall Net Power Factor = 1754 W / 2184 VA = 0.8035 p.u.

Stator I^2R Loss = 385 W

Windage and Friction Loss = 330 W

Rotor Field Speed = 20.64 rad/sec

Disc Acceleration = 0.08716 rad/sec^2

Accelerating Torque = 40.35 N-m

Accelerating Power = 833 W

Calculated Rotor Loss = 206 W

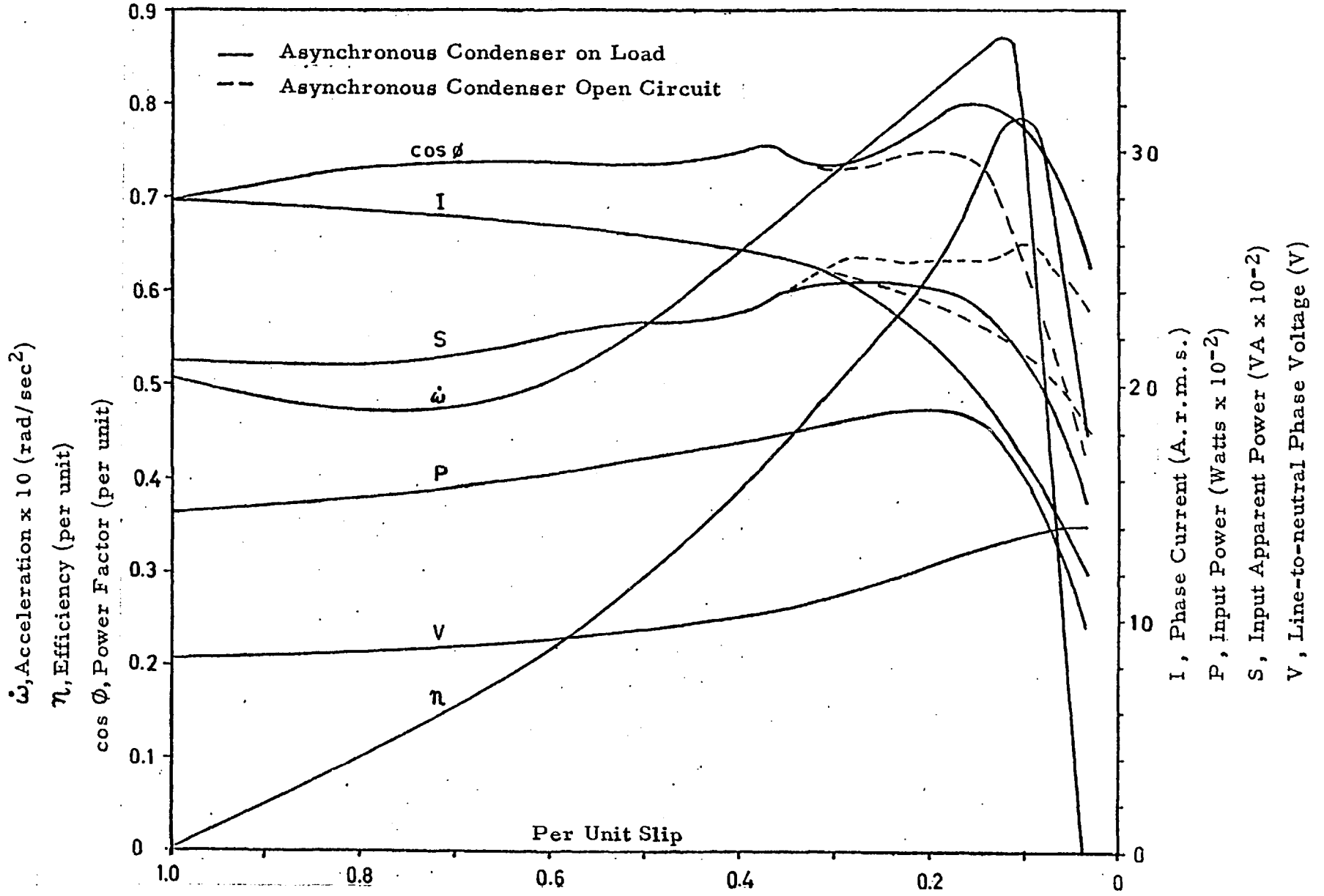

Figure 2.62 Performance of the LIM-ASC-II during an acceleration test with 50 Hz excitation.

factor correction complements efficient operation in neutralizing the hitherto unsolved problem of exit-edge losses, seemingly inherent to high surface-velocity machines. LIM-ASC-II as tested on 50 Hz has a peripheral synchronous speed of 58.9 m.p.h. and it is believed that this machine has the highest documented power factor [7] of any single-sided or double-sided LIM, irrespective of size, built to date with published results. In contrast, the maximum power factor ever attained for the 10-pole LIM used on the Linear Induction Motor Research Vehicle (LIMRV) of the U.S. Department of Transportation was 68% at a sinusoidal-waveform frequency of 94.3 Hz [6] . Figure 2.63 compares the major terminal characteristic of LIM-ASC-II against the LIMRV machine at different frequencies corresponding to the optimum power factor in each case. For LIM-ASC-II this frequency is taken as 50 Hz since low frequency tests were not performed in this region on the basis that power factor would only increase marginally at the expense of total efficiency. Table 2.10 compares the major dimensions and winding data between the two machines.

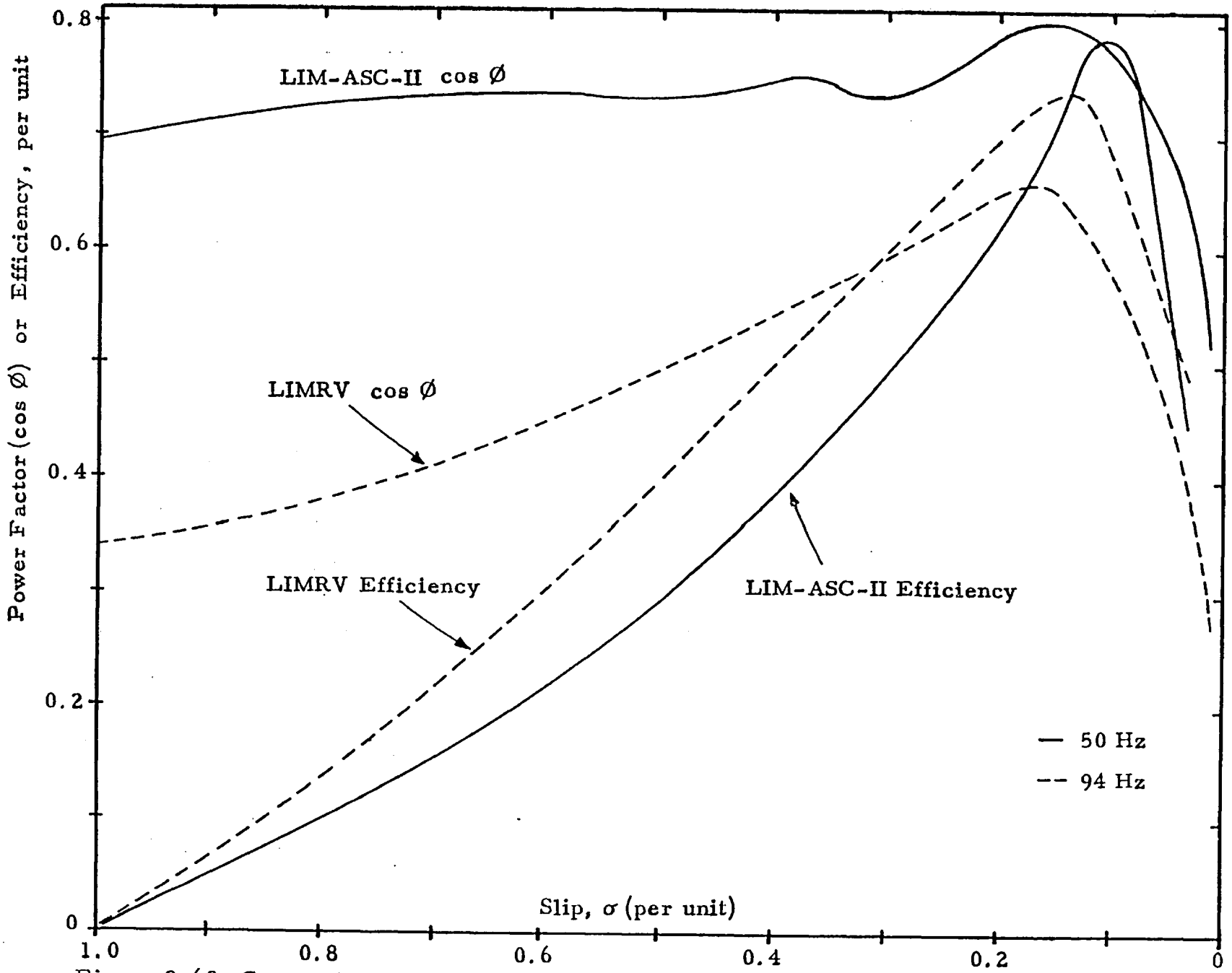

Figure 2.63 Comparison of performance parameters between LIM-ASC-II and LIMRV units.

Table 2.10

Comparison Between High-Speed, Single-Sided, Short-Primary LIMs

	LIMRV	LIM-ASC-II
Poles	9	9
Pole-pitch(m)	0.356	0.247
Primary Stack Width (mm)	254	157
Goodness Factor (50 Hz)	16.5	28.4
Phases	3	9
Coil Span/Pole-pitch	0.666	0.888
Slots/pole/phase	5	1
Operating Entrefer (mm)	19	12
Carter's Coefficient	1.156	1.02
Secondary Aluminium Thickness(mm)	3.3	9.3
Russell-Norsworthy Factor	1.50	1.86
Secondary Conductivity (% of Cu)	47.25	61.5
D^2L equivalent (m^3)	0.37	0.144
Airgap Flux Density (T r.m.s.)	0.18	0.158
Maximum Efficiency (%)	74	77.5
Frequency for Max. Efficiency(Hz)	94.3	50
Maximum Power Factor (%)	66	80
Slip for Max. Power Factor (%)	17	16
Maximum Thrust (kN)	6.48	2.1
Stator Current Loading (kA/m r.m.s)	91	57

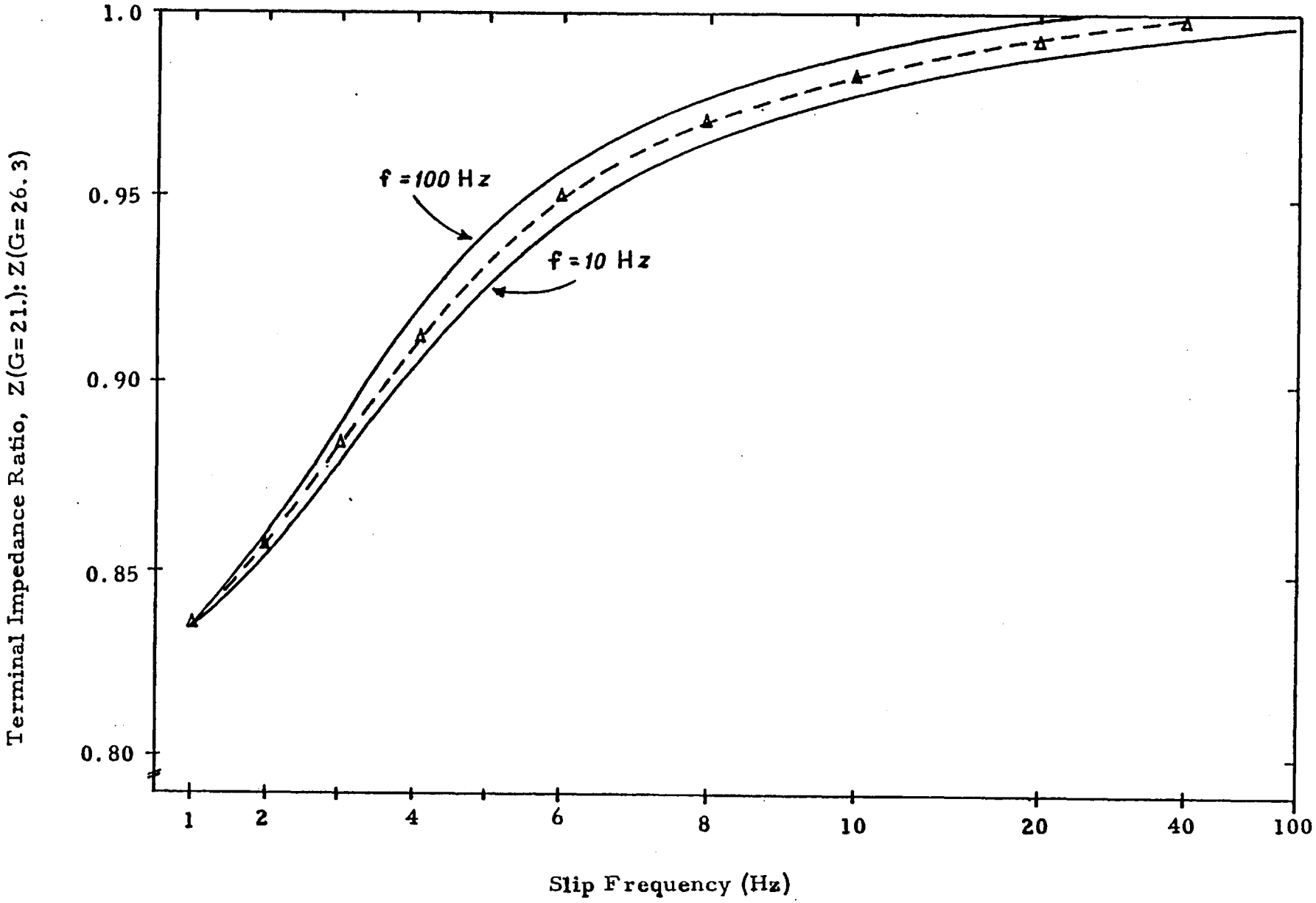

Figure 2.64 Terminal impedance ratio for the LIM-ASC-II machine with two different airgap settings.

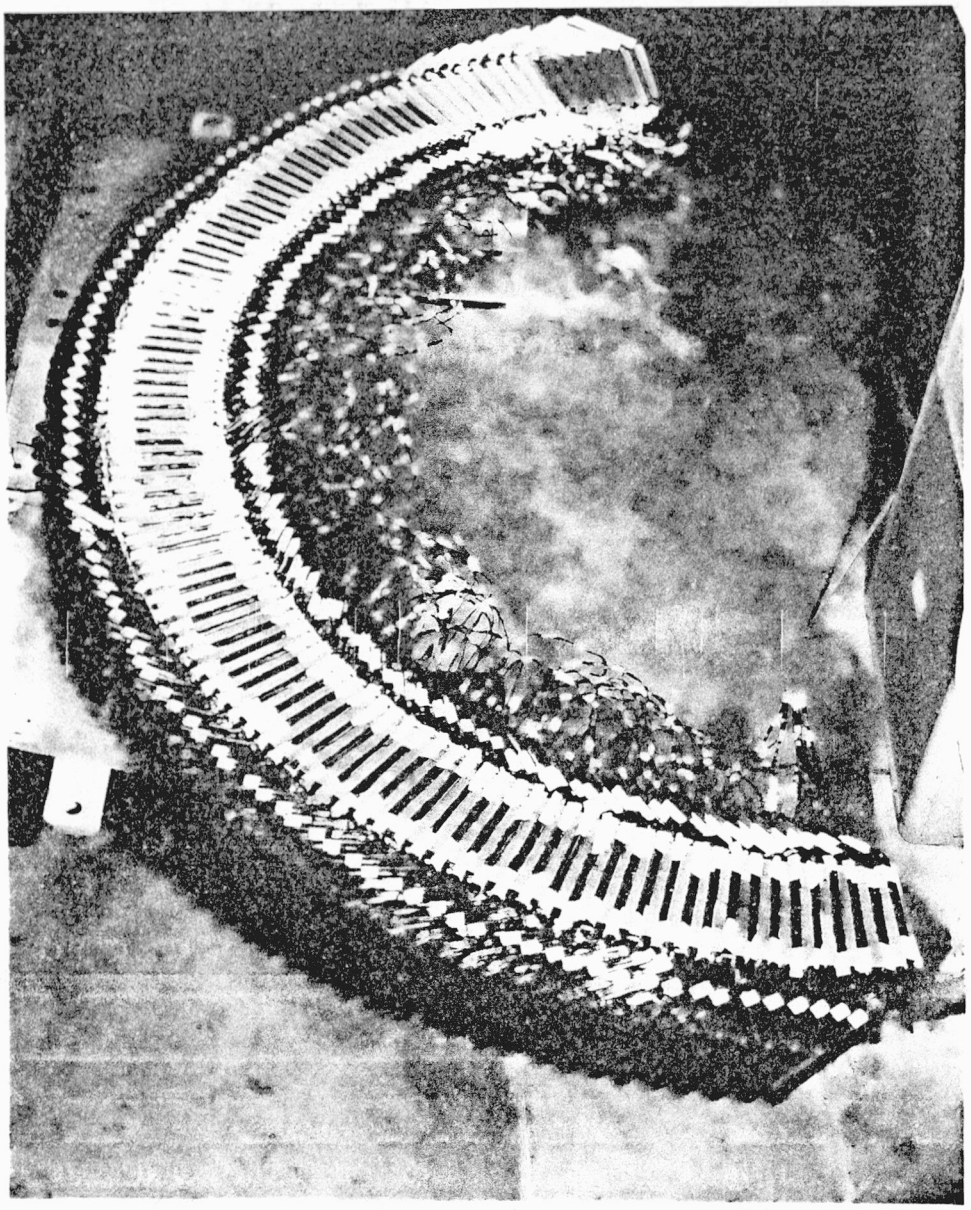

Figure 2.65 View of the completed LIM-ASC-II machine.

2.7 RECOMMENDATIONS FOR HIGH SPEED LINEAR MOTOR DESIGN

A. Longitudinal Flux Machines

1. Series connection of phase coils in both motoring and condenser sections of machine is essential, however the choice between voltage feedback (LIM and ASC in series) or current feedback (parallel connection) types of power factor compensation are optional depending if fixed speed or variable speed operation is anticipated, respectively.

2. Irrespective of the exact division between motor and condenser section, the flux density at the exit-edge of the entire machine should not exceed 30 mT, independent of the airgap, if the efficiency is not to be sacrificed.

3. The ratio of the electrical airgap to the main pole-pitch generally follows the theoretical relationship

$$\frac{g}{\tau_p} = \frac{\mu_o}{\pi} \frac{J_s}{B_t} k\ (\sigma)$$

where J_s is the stator current loading, B_t is the total normal component of airgap flux "over" the stator block at just the transition point between LIM and ASC windings (i.e. the shrink point), and $k(\sigma)$ is a correction factor to allow for variance in the operating slip value at which this ratio is determined. The point to remark is that the designer should always attempt to have the pole-pitch slightly higher than predicted by this formula because the effective stator current

loading is always significantly less than given by standard design formulas. In general, nearly all high speed linear motor designs to date [4,6] have been built with too small a pole-pitch with the resultant lower-than-anticipated air gap flux density.

4. The number of motoring poles should be greater than eight without exception. There is no attractive alternative to this criterion as the only tradeoff to number of poles is the operating slip; while the product of poles times slip gives an indication of the rotor flux decrement, the slip must be a minimum for all continuously operating machines. Power and force machines are a permissible exception. The overwhelming conclusion is that the speed machines must have a large pole pitch combined with many poles; a long machine is in order irrespective of supply frequency. The choice of supply frequency in the event that 50 Hz excitation may be departed from, is actually a rather crucial matter because the linear machine's performance does not increase linearly with frequency (as often assumed in the literature describing inverter applications to LIMs). Most important, the designer has to make certain that rotor flux decrement does not occur at the highest frequency or at an intermediate frequency. Should the excitation frequency be, for example, too high, one finds that the airgap flux peaks along the stator block at a position considerably before the end of the block, i.e. the end of the block occurs after the "90 degrees" mark on the sinusoid representing the B_t space wave. For instance if LIM-ASC-II is operated at 75 Hz rather than 50 Hz, in fact this condition ensues and the efficiency drops noticeably.

On the other side of the spectrum, if care is not excercised the frequency may be too low to obtain the high efficiency simultaneously with high power factor. This is a result of not allowing the airgap flux to peak at all and thus the end of the motoring section occurs before the crest of the B_t flux distribution. In fact this type of problem may arise at 50 Hz, when the number of motor poles are too small, the operating slip is too low, or possibly the rotor magnetization time constant is too small, say on the order of 30 ms. It should be emphasized that these effects must be considered independently of the changes that occur with leakage reactance requirements and magnetization as frequency is altered.

5. The width of the stator should never be less than about 2/3 the pole-pitch if power factor is not to be sacrificed. Generally this guideline has been followed in the past designs along with avoiding transverse-edge-effects as it has always been clear that the sheet-rotor secondary width, in excess of the stator width, is a strong function of pole-pitch on an efficiency basis. The one area in which LIM-ASC-II did not exceed the state-of-the art was in having a very wide stator; however construction details would demand that a machine with a stator width of 0.32 m (or twice that of LIM-ASC-II) would require a rotor at least 4m in diameter to accommodate the endwinding.

6. The longitudinal flux machine, burdened with the massive endwinding, has often been the subject of controvery due to its hitherto poor power factor which many scientific personnel have explained by the endwinding leakage-reactance require-

ment. However, the major outcome of this research has shown that the bulk of the power-factor problem takes place in the phase of the slot-conductor induced voltage rather than singling the problem to the endwinding. However, notwithstanding, it should be pointed out that end-windings are generally too massive since designers follow rotary machine guidelines and are very conservative about the amount of chording. In general the designer should note that the amount of chording permissible with a high speed LIM increases when the ratio of stator width: pole pitch becomes significantly less than one. For example, LIM-ASC-II could have been favorably chorded down to 6/9 rather than its present 8/9 without a noticeable loss in efficiency; this particular decision to only use a small amount of chording was based entirely on the manufacturing constraints of using rectangular cross-section wire whereby the coil "knuckle" had to be confined to a 10mm space.

7. New to the one-dimensional machine designer, the results of LIM-ASC-I and LIM-ASC-II have permitted a unique guideline to emerge for "airgap winding" machines or just machines with large airgaps. In particular, the maximum permissible (i.e. suggested) slot depth filled with conductor (considering both cases of ferromagnetic or non-ferromagnetic stator teeth) bears a strong dependence on the electrical airgap encountered, if power factor is important. Based on experimental results, it is now fair to state that if the slot depth, to the bottom of the stator conductor is more than 50% greater than the electrical airgap spacing, then the machine will accrue appreciable slot leakage reactance in terms of what is presently achieveable and commercially practical. This is

by no means a method by which to size-up the slot of a linear machine, rather it is intended as an upper limit. Specifically, if a high speed longitudinal flux SLIM is designed with a pole-pitch:airgap ratio of at least 20, with an alumimium sheet rotor (filling 80% of the airgap or better) then as a general rule, the maximum slot depth on a core with a 1:1 tooth width:slot width ratio may be as small as 70% of the airgap without a stator resistance (copper) exceeding the rotor resistance. Thus power factor improvement is evident without trading off efficiency.

8. The question has often been asked, of both longitudinal and transverse flux designs, how many stator teeth per linear meter are necessary, or what should be the ratio of iron contributing a magnetizing or working MMF in contrast to those absorbing or shunting MMF? Fortunately, in the longitudinal flux machine the answer is easy to surmise because the problem is less complex once a criterion for number of electrical degrees per linear meter is established. Here it is important that very small linear increments be used in evaluating a design, even fractional tooth pitches, because the average number of electrical degrees per meter obviously overlooks phenomena such as local backward traveling fields and forward traveling harmonics. For the commercial designer rather than the academic, this concern appears in the form of usually one parameter -- the number of slots/pole/phase. Using only this one guideline, it is nevertheless the single most important parameter dominating the power factor characteristic, assuming the machine size has already been established. The overwhelming problem is clearly understood .... the LIM de-

signer is always striving to implement a large pole-pitch (0.5m is the baseline) but at the same time each tooth should show a regular and pronounced, positive change in phase, over eight poles or more! The constraints are that a three phase system (i.e. 60^{o} phase jumps) only is available and techniques such as disproportionate-phase-mixing are out of the question because of their larger kVAR requirement. The one alternative that emerges incessantly is to have 3 slots/pole/phase, 4 slots/pole/phase, or even 5 slots/pole/phase as common practice. The degree of merit for multiple slots/pole/phase is simply based on how closely the rotor and stator are coupled at high speed. In a machine with a high Goodness factor, a 5 slot/pole/phase winding would be expected, in this rotor flux dominated case, to yield an incremental phase error per slot of 12^{o} from the slot centered by each phase group, so that if the third slot has a coil terminal power factor angle of 35^{o} ($\cos \phi = .819$) the first slot can be expected, at the very best, to have a terminal voltage angle of $35^{o} + 24^{o}$ for which the cosine is 0.515, a 37% reduction in utilization! This assumes that zig-zag leakage flux is minimal and this is always the case in sheet rotor machines; the presence of zig-zag leakage flux in rotary induction machines helps to explain why it is more practical to use multiple slots/pole/phase without severe penalties in power factor. Moreover, the poor utilization attributable to multiple slots/pole/phase in linear machines is only prominent at high speed because on starting speeds, the phase of the airgap flux largely follows the harmonic content of the stator MMF so that the angle of the induced voltage is fairly uniform among coils in the same phase group.

The solution to the problem was demonstrated in LIM-ASC-II for which the LIM and ASC windings had only 1 slot/pole/phase by using the external phase shifters to yield the 9Ø system (20^{o} phase jumps between adjacent coils). Although one cannot expect most commercial installations to incorporate phase shifters, it does stand on record that a large number of high speed LIM demonstration programs to date [8 - 14] have made use of on board turbo-alternators for supplying the LIM, for which a 9Ø or 15Ø supply system would bear no additional cost above the 3 phase systems used (in fact the alternator efficiency would be improved simultaneously). Yet, there is a way of ensuring a 1 slot/pole/phase LIM winding when only 3 phases are available. This is accomplished by having single ASC coils in parallel with segregated groups of LIM coils, i.e. phase shift afforded by the ASC increases the number of differently phased slot currents. The first application of this technique has been devised for the rewinding of a 20 kW, 8 pole induction motor because it eliminates any need for thyristors; the winding schematic is included in Appendix VI.

9. For longitudinal-flux linear induction machines intended for high speed operation, an entry-edge flux shunt is beneficial for both efficiency and power factor criteria. There is insufficient data available at this time to attempt an optimization of additional stator iron to be included before the first pole of the block containing the windings, but simple calculations reveal that due to the low flux density anticipated in the entry flux shunt, the added performance is obtained with a negligible increase in core weight. Moreover, any manufacturing costs attributable to this flux shunt are abso-

lutely nil because no winding is included and it may be said that the intended improvement is merely a new way of shaping the leading edge stator tooth, albeit it may end up being a pole-pitch long in the designs of the future. An unanswered question is, in addition to what type of "surface impedance" should this flux shunt offer, but also, is there an advantage to having small, unexcited teeth at the shunt surface rather than smooth surface? It is assumed that all flux shunts will be included as an integral part of the stator core, and punched on the same long laminations that enclose the LIM and ASC windings, the latter being a form of exit-edge flux shunt. The operation of the entry edge shunt is basic for it allows the first LIM pole to receive about the same magnitude of flux that the first generation, series connected LIMs would have under the second pole, assuming equivalent Goodness factors and slip! It should come as no surprise, that despite the lack of windings or shading rings in the flux shunt, the phase of the core flux with respect to longitudinal distance, that leaves the flux shunt is properly phased at high speed to effect an improvement. This is primarily explained by the well known integral conditon $\int J_r . d_s = 0$ which demands that the rotor sheet current density is continuous across boundaries and likewise, the airgap flux density is continuous. Moreover, the phase changes in the flux shunt are consistent because nowhere in this machine is there a change in the magnetization time constant nor in the rotor leakage flux path; the slow, quasi-linear buildup of airgap flux from the entry edge (now the flux shunt edge) continues as in the first generation LIMs. In general whenever the change in magnitude is increasing and gradual, the phase of the airgap flux changes at a uniform rate.

The last remaining question that will only be solved by experimentation is whether the choice of odd or even numbers of excitation poles for the LIM is most suitable for use with, say an entry flux shunt one pole pitch long. Based on the existing knowledge of LIM-ASC-II, the 9 pole LIM could very well turn out to be the most favorable combination because published literature [12, 14] from industrial organizations operating 8 and 10 pole LIMs with some type of entry "nose" have concluded that this extended stator iron made no difference to their machines ... possibly they passed over the effect by only testing even pole number motors! In retrospect, Laithwaite has shown [16], that careful shaping of exit-end iron could be used as an accurate way of controlling the exit losses and thus the top operating speed of large, power-type LIMs. Now, the shaping of the entry-end iron is seen as another method of speed control for it was in this manner that the effect was first noticed. LIM-ASC-II operated up to a balancing slip of 0.08 p.u in the forward direction, while for the same input conditions but reversing the phase sequence and disconnecting the ASC, the machine stabilized at a slip of 0.034 p.u. by virtue of using the ASC iron as an entry nose. Both slips are much lower than in conventional LIMs of the same length, but the 0.034 slip (providing 486 Watts for windage & friction) is phenomenal.

10. The last guideline is based on the selection of rotor conducting and ferromagnetic material. As has always been the case, there is no need to laminate the rotor backing iron for if one finds that eddy current losses in solid steel unacceptable, then this is undoubtedly a direct result of operating

the machine at too high a slip and nothing more (probably Guide-line No.4 was not followed). If high frequency is to be used, in excess of 250 Hz, as a general rule the slot leakage reactive losses will be so large, that the stray eddy current losses in the rotor solid steel will not be a problem partially because the conducting sheet is a rather effective screen for the backing iron and partially as the Watts consumed by the rotor solid steel will still be under 20% of the core loss of the laminated stator.

Looking at previous SLIM designs, the one conclusion that emerges is that most designers have calculated the thickness of the rotor steel (as well as the stator core) based on a much larger flux density than was ever obtained in practice. For at least a decade, industrial designs indicated a considerable safety margin in steel thickness to avoid the seemingly colossal fear of "saturation". To say the least, most machines ever built did not even come close to saturation, especially with respect to the rotor steel for the airgap flux rarely made it above 0.3 Tesla and backing iron was always ½ inch or greater in old designs. [13, 14, 15]. This is explained by the fact that most applications ran with airgaps larger than first quoted to the designer; secondly there has always been a trend to overestimate the quantity J_s in calculating the resultant airgap flux density, and third the uncertainty that existed about the exact shielding effect offered by the conductor sheet. The latter is due to the manufacturer's failure to ensure uniform conductivity of the T6-6061 Aluminium used for reaction rails and partially because the designers have always used the Russell & Norsworthy Factor for calculating effective rotor resistance which has been found to yield too

high a resistance, especially as the airgap is increased and the rotor field pattern less well defined.

In future SLIM designs, it would thus be fair to say that if the rotor backing steel exceeds 10 mm in most designs, then something is clearly wrong. The only exceptions are applications such as the I.C. High Speed Test Rig whereby the steel rotor thickness is 9.5 mm but was designed this thick due to the tight mechanical tolerances that the disc must withstand especially with respect to the maximum axial bending deflection when subjected to SLIMs with high attractive forces. The present disc will only deflect 1.3 mm axially when LIM-ASC-II is started at locked rotor with a current loading of 40,000 A/m r.m.s.

Concerning the thickness of the rotor disc or reaction rail, to generalize, most previous designs have used to too thin a conductor (in contrast to the steel thickness). The result has been that the peak-torque operating slip has usually been much too high with the ensuing larger rotor losses. While it is clearly understood that extra conducting material is a direct factor in escalating track costs, the additional energy costs typically outweigh the capital investment in 15-20 years. Additionally, some designers have justified high rotor resistances because of a high starting torque criterion but the point remains that a good low speed motor will never succeed as a high speed machine. The alternatives might be to include a change pole winding or even a line-commutated cycloconverter to yield 15 Hz operation followed by a step change to 50 Hz mains. In conclusion a low starting torque machine should never be objectionable if a continuous, long run at high speed is to be anticipated and optimized for...i.e. keep the secondary resistance as low as possible.

2.8 REFERENCES

[1] D.A. Lowther and E.M. Freeman, "Normal Force in Single-Sided Linear Induction Motors," Proc. IEE, Vol. 120, 1973, pp. 1499-1506.

[2] M. Balchin, The Analysis and Design of Windings for Linear Induction Machines, Ph.D. Thesis, Imperial College, 1975.

[3] E.R. Laithwaite and S.B. Kuznetsov, "The Asynchronous Condenser: A Brushless Adjustable Power Factor Induction Machine," IEEE Trans. Power Apparatus and Systems, Vol. PAS-99, No.6, No./Dec. 1980, pp. 2398-2408.

[4] R. Weakley and S.B. Kuntz, "Static Testing Report-Tracked Levitated Research Vehicle Propulsion System," U.S. Department of Transportation, NTIS Document FRA-74-10650, August 1974.

[5] F.C. Williams, E.R. Laithwaite, and L.S. Piggott, "Brushless Variable Speed Induction Motors," Proc. IEE, Vol. 104A, June 1956, pp. 102-122.

[6] R. Bevan and S.B. Kuntz, "Effect of Machine Length on the Performance of Linear Induction Motors: An Experimental Investigation," U.S. Department of Transportation, NTIS Document, FRA-77-14572, December 1977.

[7] E.R. Laithwaite and S.B. Kuznetsov, "The Development of a Stator-Controlled Brushless Induction Machine with Leading VAR Capability," Electric Machines and Electromechanics International Quarterly, Vol. 6, No. 3, May-June 1981, pp. 1-18.

[8] D.C. Coho, G.B. Kliman, J.I. Robinson, "Experimental Evaluation of a High-Speed Double Sided Linear Induction Motor," IEEE Transactions on Power Apparatus and Systems, Vol. PAS 94, pp. 10-17, 1975.

[9] R.B. Powell, "Linear Induction Motor Electrical Performance Test," U.S. Dept. of Transportation, NTIS Document FRA/ORD-76-265, June 1976.

[10] R.B. Powell, "Linear Induction Motor Electrical Braking Test," U.S. Dept. of Transportation, NTIS Document FRA/ORD-76-264, April 1976.

[11] R.B. Powell, "Linear Induction Motor Research Vehicle Reaction Rail Edge Effect Investigation," U.S. Dept. of Transportation, NTIS Document, FRA/ORD-76-263, April 1976.

[12] R.J. Bevan, and G.P. Kalman, "Non-Uniform Power Distribution in Linear Induction Motors due to End-Effects," IEEE Transactions on Power Apparatus and Systems, Vol.PAS-98, No.5, pp. 1516-1521, 1979.

[13] T.A. Nondahl, and T.A. Lipo, "Transient Analysis of a Linear Induction Motor Using the d,q Pole-by-Pole Model," IEEE Transactions on Power Apparatus and Systems, Vol. PAS 98, No. 4, pp. 1366-1374, July 1979.

[14] G.B. Kliman, W.R. Mischler, and W.R. Oney, "Performance of a Single-sided Linear Induction Motor with Solid Back Iron and with Various Misalignments," FRA/ORD-78-36, U.S. Dept. of Transportation, May 1978.

[15] R.B. Powell, and G.P. Kalman, Feasibility Study of a 15,000 kVA Capacitor Assisted Power Unit for Induction Motor Propulsion, U.S. Dept. of Transportation, FRA/ORD-77-43, January 1977.

[16] E.R. Laithwaite, Induction Machines for Special Purposes, London: Newnes, 1966.

[17] F.C. Williams, E.R. Laithwaite and J.F.Eastham,"Development and Design of Spherical Induction Motors," Proc. IEE, Vol. 106A, No. 30, December 1959, pp. 471-484.

III. TRANSIENT ANALYSIS

3.1 SURFACE LAYER APPROACH TO FINITE AIRGAP MODEL

A. Analytical Solution of Discontinuous Primary Excitation and Continuous Scondary.

The representation of an induction machine with a finite airgap, narrow stator teeth and deep rotor slots by a travelling wave model has been expanded for over 25 years by Mishkin [1], Cullen and Barton [2], and Tipping [3]. The principal components of the magnetic and electric structure comprise a system of concentric layers with different permeabilities and different conductivities, with no specific limits on relative dimensions or frequency range. The outcome of their work showed that despite the rather complicated layout of the tooth tip and slot shape, the basic nature of torque production in the machine is more concerned with the propagation of an electromagnetic wave in an airgap rather than the "saliency" or "reluctance" effects which appear to dominate the literature on induction machines. In essence, this approach to accurately describe the fundamental and harmonic EM wave propagation is termed the "layer" approach. In contrast, slot geometry calculations are only crucial when the exact value of leakage inductance must be known for terminal power factor characteristics.

The use of finite element computer analysis for the magnetic structures is crucial for exactly determining slot

inductance and zig-zag flux components, but in terms of calculating wave propagation it will yield no better results than an analytical layer model which represents the machine elements as equivalent parameters in an electric transmission line to determine power flow, disspation, circulating power, etc. The crossover point when a finite element analysis is clearly superior is when the induction machine has a very large airgap but this is rarely the case with rotary mahines, and thus the 1-dimensional, radially directed layer model is generally valid.

Several methods have been devised to allow the 1-dimensional layer model to have greater accuracy while still retaining a simple, analytical, closed-form solution. For example, while a layer may theoretically represent any electric or magnetic shape in the actual machine, it has been found convenient to assume that all conductive materials are homogeneous and isotropic, while selected magnetic materials should have an anisotropic representation. Typically, the magnetic permeability in the radial direction is infinite while the tangentially directed permeability is usually considered to be finite.

The impetus for using the layer approach is based on:

(i) Analytical solutions are possible even with discontinuous excitations and this gives the designer a tool with which to see how rapidly magnetic and electric dimensions change performance. To some

extent, the finite element numerical solution, either 1-dimensional or 2-dimensional, does not offer this facility because it is largely experimental in nature and thus the designer of an entirely new machine has to run a series of finite element programs until the desired conditions are found on an empirical basis.

ii) The layer model is readily adaptable to high frequency operation without any modifications, while in general finite-element analysis cannot handle harmonic response although it is clear that the latter yields the total airgap waveform. The layer approach will handle machine response to, for example, a non-sinusoidal inverter waveform by establishing a series of equivalent circuits, each with its own distinct values of the R_2, X_2 and X_m parameters which do not necessarily scale linearly with frequency. The parameters R_1 and L_1 are usually considered to be frequency independent.

The layer model is at a disadvantage when the following information is desired:

i) Stray loss cannot be calculated directly since it is assumed all laminations are continuous in any one place and thus joints or magnetic gaps do not exist.

ii) Hysterisis loss or unusual core materials cannot be considered.

iii) Tooth-tip ripple is not present and thus cogging torques cannot be determined analytically by a wave approach.

iv) The tooth frequency e.m.f. induced in the rotor cage bars cannot be directly solved for; these results in rotor circulating current paths at about 1kHz in a practical machine unless either the rotor or stator laminations are skewed.

v) The deviation of the rotor current paths from uniform axial flow under the active stator region cannot be calculated in the 1-dimensional model; this is an entirely different problem from iv) in that the path of the fundamental rotor current is of concern and the controlling parameter is the ratio L_m/R_2 for if this is less than $1/\omega_s$ there is usually a significant component of tangential rotor flow under the stator length [4]. The problem is solved by generally increasing the pole-pitch, reducing the airgap, or incorporating more, narrower rotor bars along the periphery. In a sheet rotor machine, the sheet should be slitted axially in the absence of a cage construction.

B. A Method for Analysing the θ-Pinch Rotary Machine

Any "θ-Pinch" machine or similar type of induction machines with discontinuous stator excitation such as the "Induction Excited Alternator" as developed by Williams and Tipping in [5], may be analyzed from a one-dimensional layer model. The convenience of such an example as the θ-Pinch machine is that the rotor structure is absolutely continuous- a conventional cage design, while the induction excited alternator requires a more complicated one-dimensional formulation since the rotor is wound and has isolated, closed loops. Both machines are entirely brushless and use ordinary magnetic steels. A general layer model is presented here based on a continuous rotor but an infinite number of differing stator excitations may be present as long as each excitation is confined to a distinct region around the periphery, e.g. in the machine under discussion, the region from $\theta=0$ to θ_1 is the excitation or main winding and the region from θ_1 to θ_2 is the asynchronous condenser or tertiary winding.

For machines such as the two-speed pole-amplitude-modulation (PAM) induction machines, whereby the stator does not have distinct regions but the windings are interleaved around the entire periphery, the only fast method for analysis is to use "winding functions" as described in [6] or [7]. The θ-Pinch layer model cannot in general be used for PAM because this necessitates solving for new boundary conditions every few slots rather than at two positions per repeatable section of two poles or greater. It is important to note that pole-amplitude-modulation is based on higher harmonics (although the actual fundamental speed is often

ambiguous) while the θ-Pinch is mainly a sub-harmonic machine and there is only one subharmonic to be concerned with in the latter--the "α_1" wave (this rotor speed wave is supersynchronous during generator operation).

The plan of approach is to model any induction device of the θ-Pinch type (this includes arch motors [8], shorting-grid machines [3], or self-compensating induction motors (SCIM) [9]) as comprising a series of repeatable sections. The formulation of equations for one repeatable section covers the entire machine, with each section having as many distinct stator excitations as desired although the differences in excitation usually appear as a change in either pole-pitch, current loading or phase rather than a frequency change between sections.

The applications of layer theory have always tended to model the stator excitation and rotor current path by an infinitely small current sheet with a linear current density

$$j_s = \hat{J}_s \sin(\omega_s t - \theta) \qquad (3.1)$$

in Amperes/meter periphery (also termed the current loading). The advances in this theory have placed this current sheet at a radial location which is sandwiched by two magnetic layers to more accurately simulate the primary or secondary leakage flux paths than by simply placing the currents sheets exactly at the airgap boundaries. In the former configuration, a third-order linear differential equation accurately describes the distribution of the airgap flux and the total flux surrounding the current sheet [10]. If this model is simplified by placing the current sheet right

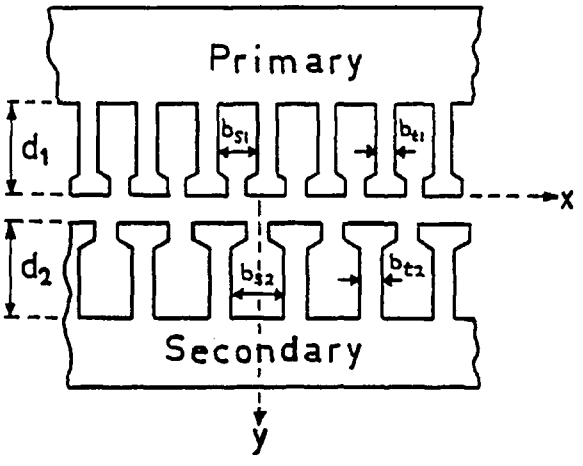

Fig. 3.1a Identification of dimensional terms for a cage or wound rotor induction machine.

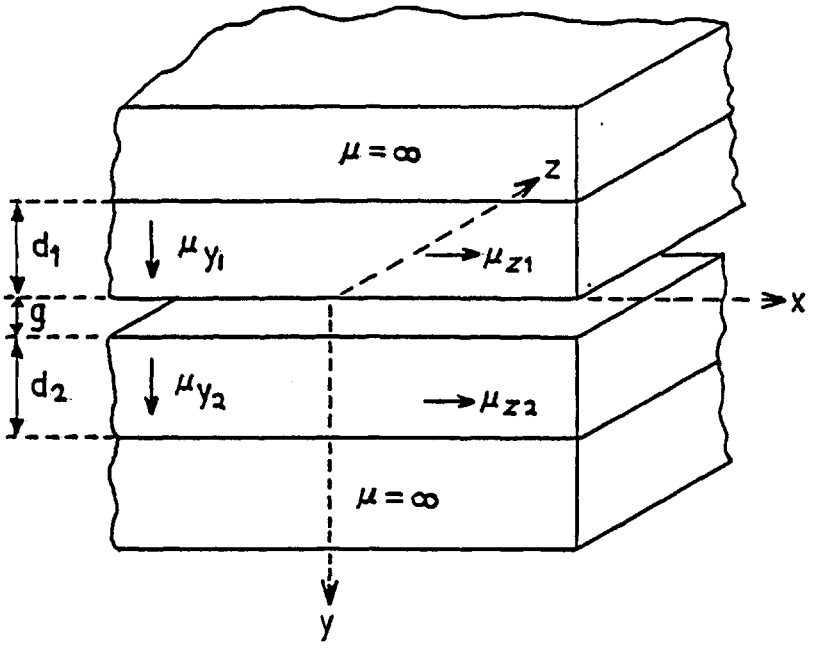

Fig. 3.1b The Mishkin layer model corresponding to Fig. 3.1a

at the airgap surface for the secondary current distribution, then the complexity of the system is reduced to a second order model, without the effect of secondary leakage inductance [11]. In all of these concepts, the effects of magnetic saturation cannot be taken into account directly although the relative permeability in the anisotropic materials may be modified later as an iterative process once the B field has been determined [12].

The Mishkin model of the induction machine is based on Figure 3.1 where the tooth magnetic material is anisotropic while the core material of both primary and secondary is isotropic. In the most general model, both current sheets are sandwiched by magnetic steel of zero conductivity and the technqiue can be readily applied to one repeatable section of a θ-Pinch motor which has two windings per section. Figure 3.2 is a developed layout of a slice in the radial-tangential plane of one repeatable winding section with two independent stator windings of zero overlap longitudinally (tangentially) and a continuous, conductive secondary. This is the basic model and if desired the number of primary windings in any repeatable section may be infinite if the order of the system of equations is not a constraint. To be shown, most applications will require the solution of either 7 or 13 simultaneous equations.

In order to limit the system equations for a general θ-Pinch configuration, as exemplified by Figure 3.2, to be third order, the following assumptions must be adhered to:

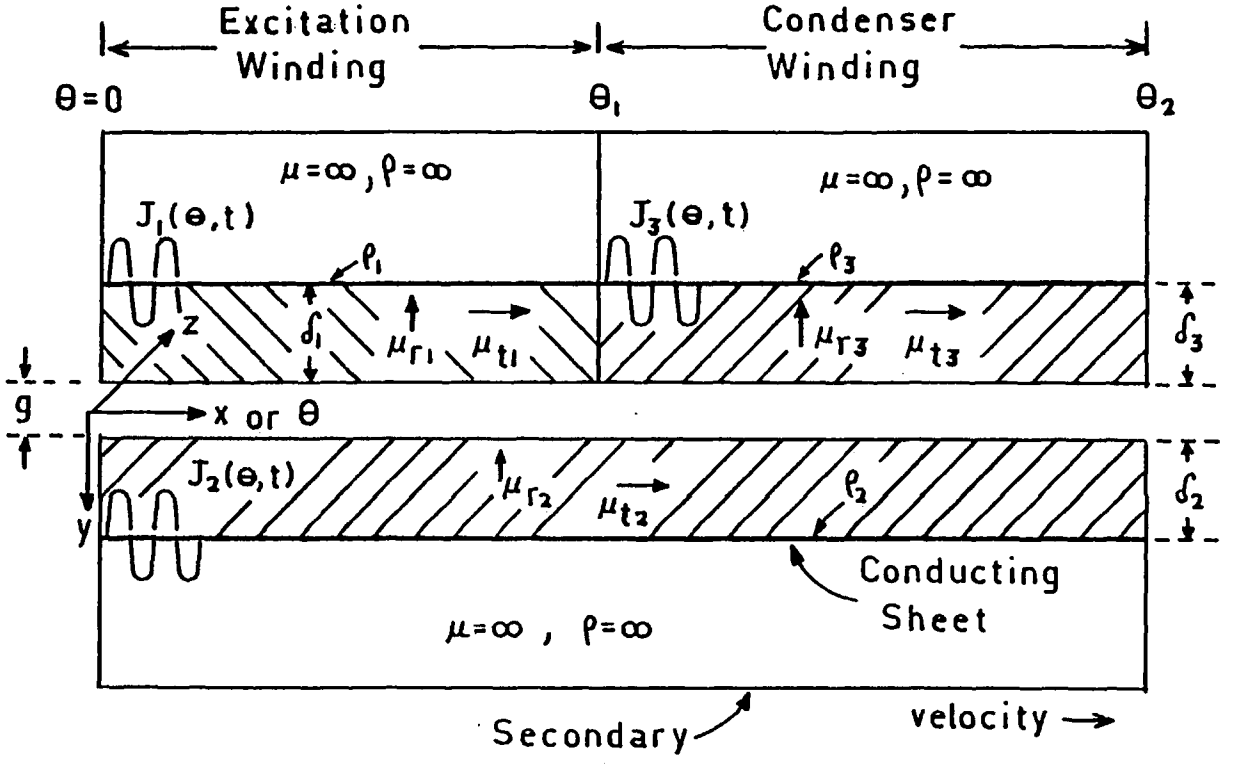

Fig. 3.2 General layer model of an induction machine, one repeatable section, with two independent windings on the primary block with zero overlap and a continuous cage or sheet rotor secondary.

i) The radial permeability in all the tooth sections is infinite, i.e.

$$\mu_{r1} = \infty, \quad \mu_{r2} = \infty, \quad \text{and } \mu_{r3} = \infty$$

ii) The excitation current sheet for section $\theta=0$ to $\theta = \theta_1$ must be moved to the airgap and therefore $\delta_1=0$. In doing so, none of the significant effects of wave propagation are lost because $J_s = J_1$ must be a series winding to avoid circulating currents and thus it is always current forced whereby $J_s(\theta,t) = J_s$ is the amplitude of the stator current wave.

Although $\delta_1 = 0$, the current loading is still calculated as

$$\hat{J}_s = \frac{2\sqrt{2}\ N\ I_\phi\ K_{dp1}}{\tau_s} \qquad \text{A/m periphery} \qquad (3.2)$$

where N=series turns/coil (assuming double layer winding)

I_ϕ=phase current (r.m.s.)

τ_s=slot pitch (m)

K_{dp1}=fundamental chording and distribution factor

As far as VAR generation is concerned, the inclusion of the δ_2 and δ_3 parameters are crucial (in contrast to δ_1) as the current $J_r=J_2$ and $J_{asc}=J_3$ need to be determined. Of these two, J_{asc} is less difficult to obtain by solution because this comprises a balanced, polyphase winding preferrably series connected in which case J_{asc} is a constant amplitude whereas J_r is a cage current for which the spatial

distribution is not singly defined for the amplitude is a function of peripheral distance (and axial location in small machines). In short, two of the three currents are confined to known paths but in the determination of the corresponding magnetic field densities, all of these solutions will have a space-modulated amplitude for the B field.

With these simplifications, a final working model for a practical θ-Pinch machine is shown in Figure 3.3. The quantity of major interests is the radial component of airgap flux density, B_g in both sections 1 and 2. The incorporation of the leakage layers δ_2 and δ_3 allow the rotor current J_r and the stator condenser current J_{asc} to be surrounded by their own leakage flux B_1 in addition to linking the common airgap flux; these comprise the total conductor flux density, B_r

$$B_{r2} = B_{g2} + B_{12} \tag{3.3}$$

$$B_{r3} = B_{g3} + B_{13} \tag{3.4}$$

where all of these are complex quantities. By applying Ampere's Law to the rotor leakage layer of radial thickness δ and enclosing the axial component of rotor current, J_r

$$B_1 = -\mu_r \delta \overset{o}{J}_r \tag{3.5}$$

where the derivative denotes the space rate of change of J_r with respect to the tangential direction, a basic expression of inductance is established. Similarly, by applying Ampere's Law to both the airgap and leakage layers

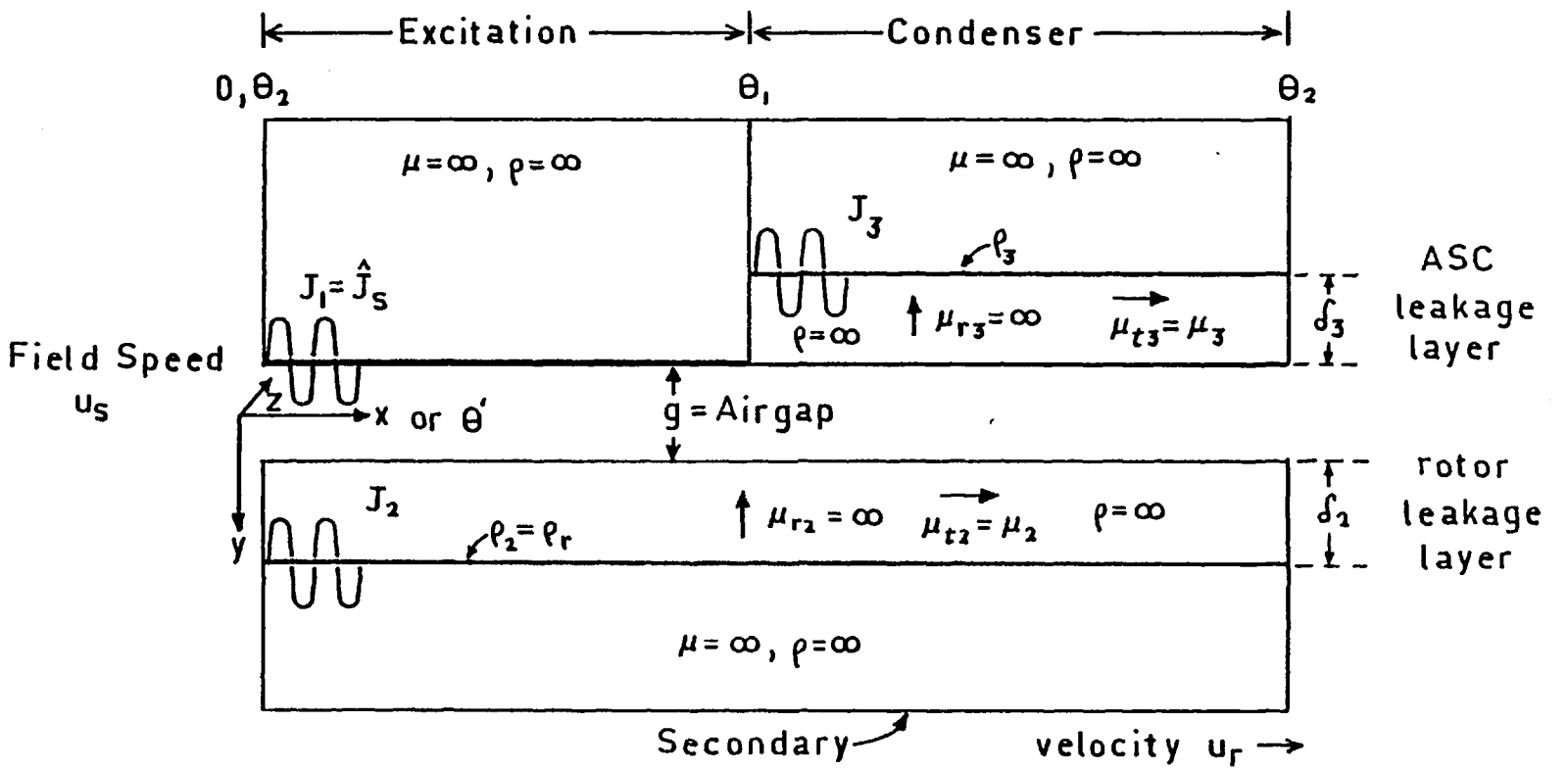

Fig. 3.3 Simplified model of an induction machine whereby current J_1 is known and and currents J_2 and J_3 are unknown in regions containing radially-ideal laminations but of tangential total permeability μ_2 and μ_3.

simultaneously

$$\overset{o}{B}_g = \frac{\mu_o}{g} (J_s + J_r) \qquad (3.6)$$

the space rate of change of the radial airgap flux density is expressed in terms of the current available for magnetization of the finite airgap g.

Suppose that the rotor is moving at a constant velocity v_r (peripheral speed) and that the synchronous field speed is

$$v_s = 2 \tau_p f \qquad (3.7)$$

where τ_p is the stator pole-pitch and f is the supply frequency. The difference between the rotor speed and the synchronous field speed is denoted by σ and on a per unit basis this slip appears as

$$v_r = (1-\sigma)v_s \qquad (3.8)$$

Application of Faraday's Law to the rotor sheet current path by using the total flux composed of the airgap and leakage components, yields the motional and time dependence nature of the induced rotor current as

$$\rho_r \overset{o}{J}_r = v_r \overset{o}{B}_r + j\omega B_r \qquad (3.9)$$

The stator excitation is assumed to be sinusoidal or composed of a series of sinusoidal waveforms of harmonic number h, and at the instant of time $t=\pi/2\omega_s$ the spatial

distribution of the current may be represented as the real part of (3.1) or

$$J_s = \hat{J}_s e^{-j\pi x/\tau_p} = \hat{J}_s e^{-j\theta} \tag{3.10}$$

The characteristic equation for the airgap is derived by substituting (3.6) into (3.9), (3.5) into (3.9) through the use of (3.2) to yield the third order system

$$\rho_r \frac{g}{\mu_o} \overset{\circ\circ}{B}_g - \overset{\circ}{J}_s = v_r \overset{\circ}{B}_g - \frac{\mu_r g \delta}{\mu_o} \overset{\circ\circ\circ}{B}_g - \mu_r \delta \overset{\circ\circ}{J}_s + j\omega\left[B_g - \mu_r \delta \overset{\circ}{J}_r\right] \tag{3.11}$$

This may be rearranged to show a complex impedance for the rotor conducting material as

$$\frac{v_r \mu_r \delta g}{\mu_o} \overset{\circ\circ\circ}{B}_g + \frac{g}{\mu_o}\left[\rho_r + j\omega\mu_r\delta\right]\overset{\circ\circ}{B}_g - v_r \overset{\circ}{B}_g - j\omega B_g = \overset{\circ}{J}_s(\rho_r + j\omega\mu_r\delta) - v_r\mu_r\delta\overset{\circ\circ}{J}_s \tag{3.12}$$

The space rate of change of J_s is

$$\overset{\circ}{J}_s = -j\frac{\pi}{\tau_p}\hat{J}_s e^{-j\theta} \tag{3.13}$$

and

$$\overset{\circ\circ}{J}_s = \frac{-\pi^2}{\tau_p^2}\hat{J}_s e^{-j\theta} \tag{3.14}$$

The magnetization Goodness factor is defined as

$$G = \frac{\tau_p^2 \mu_o \omega}{\rho_r g \pi^2} \tag{3.15}$$

The use of the last three equations in (3.12) permits the characteristic equation for the airgap to be expressed in final form with the non-dimensional parameters G and σ

$$(1-\sigma)\frac{\tau_p^3\,\omega\mu_r\delta}{\pi^3\,\rho_r}\dddot{B}_g + \frac{\tau_p^2}{\pi^2}\left[1+j\frac{\omega\mu_r\delta}{\rho_r}\right]\ddot{B}_g - (1-\sigma)G\frac{\tau_p}{\pi}\dot{B}_g - jG\,B_g =$$

$$-jG\,\hat{J}_s\,\rho_r\,\frac{1}{v_s}\left[1+j\frac{\sigma\omega\mu_r\delta}{\rho_r}\right]e^{-j\theta} \qquad (3.16)$$

Therefore, for the first section, $\theta=0$ to $\theta=\theta_1$, the airgap equation is of the general form

$$C_3\dddot{B}_g + C_2\ddot{B}_g + C_1\dot{B}_g + C_0B_g = F\,e^{-j\theta} \qquad (3.17)$$

The general solution to (3.17) will yield 3 terms, all of which may be classified as electromagnetic transients and their attenuation constants may be found by solving the auxiliary equation

$$\omega T_2\lambda^3(1-\sigma)\alpha^3 + \lambda^2(1+j\omega T_2)\alpha^2 - G\lambda(1-\sigma)\alpha - jG = 0 \qquad (3.18)$$

for the roots α_1, α_2, and α_3. The rotor leakage time constant is defined as the ratio of the leakage inductance per axial-by-tangential square to the rotor surface resistivity

$$T_2 = \frac{\mu_r\delta_r}{\rho_r} \qquad (3.19)$$

To determine the attenuation constants for the condenser section, the only major modification to the homogeneous equation is to increase the linear (C_1) and constant (C_o) terms according to the increase in surface impedance between

the rotor sheet and the ASC linear current sheet. Therefore, (3.17) is now of the form for $\theta=\theta_1$ to $\theta=\theta_2$

$$C_3 \dddot{B}_g + C_2 \ddot{B}_g + C_1' \dot{B}_g + C_0' B_g = F' e^{-j\Theta} \tag{3.20}$$

where the primed quantities denote the changed variables. The space attenuation constants for the condenser section are the roots of

$$\omega T_2 \lambda^3(1-\sigma)\alpha^3 + \lambda^2(1+j\omega T_2)\alpha^2 - G\lambda(1-\sigma)\left[1 + \frac{j\omega \delta_2 \mu_2}{\rho_3 + j\omega \delta_3 \mu_3}\right]\alpha - j\,G\left[1 + \frac{\rho_2 + j\omega \delta_2 \mu_2}{\rho_3 + j\omega \delta_3 \mu_3}\right] = 0 \tag{3.21}$$

To complete the general solution of (3.17), the entire representation requires that the airgap flux density be separated into steady-state (forced response) and transient (natural response) components, and moreover, from the aspect of determining real and reactive power flow, it is convenient at this point to further separate the radial airgap flux into in-phase and quadrature components with the stator current serving as the time-phase reference.

$$\text{In-Phase Component} \quad B_p = B_{pss} + \text{Real} \sum_{n=1}^{3} A_n e^{\alpha_n \theta'} \tag{3.22}$$

$$\text{Quadrature Component} \quad B_q = B_{qss} + \text{Imag} \sum_{n=1}^{3} A_n e^{\alpha_n \theta'} \tag{3.23}$$

where $$\theta' = \theta\, \tau_{p1}/\pi \tag{3.24}$$

$$B_{pss} = \frac{\rho_r \hat{J}_s}{\sigma v_s \epsilon} \left\{ \cos(\Theta) + \left[\sigma\omega T_2 + \sigma(\omega T_2)^2_G + \frac{1}{\sigma G} \right] \sin(\Theta) \right\} \quad (3.25)$$

$$B_{qss} = \frac{\rho_r \hat{J}_s}{\sigma v_s \epsilon} \left\{ \left[\sigma \omega T_2 + \frac{\sigma(\omega T_2)^2}{G} + \frac{1}{\sigma G} \right] \cos(\Theta) - \sin(\Theta) \right\} \quad (3.26)$$

and the non-dimensional decrement factor is

$$\epsilon = (1 + \omega T_2/G)^2 + (1/\sigma G)^2 \quad (3.27)$$

The steady-state equation for the condenser section is of the same form as (3.25), (3.26), and (3.27) except that the rotor surface resistivity must be replaced by the ASC surface resistivity, the rotor magnetic depth δ_2 is replaced by the ASC magnetic layer δ_3 and the Goodness factor is modified for a limited section of airgap periphery to

$$G' = G \left[1 + \frac{\rho_2 + j\omega\delta_2\mu_2}{\rho_3 + j\omega\delta_3\mu_3} \right] \quad (3.28)$$

and the ASC leakage time constant may be expressed as

$$T_3 = \frac{\mu_3 \delta_3}{\rho_3} \quad (3.29)$$

Without restriction on the numerical value of θ_1, the steady-state airgap flux density for the periphery at a location greater than θ_1 is

$$B_{pss} = \frac{\rho_3 K_1 (1-\sigma)}{v_s \epsilon'} \left\{ \left[\frac{1}{\omega T_2''} - \omega T_3 \right] \sin(\Theta) - \left[1 + T_3/T_2'' \right] \cos(\Theta) \right\} \quad (3.30)$$

$$B_{qss} = \frac{\rho_3 K_1 (1-\sigma)}{v_s \epsilon'} \left\{ \left[1 + T_3/T_2'' \right] \sin(\Theta) + \left[\frac{1}{\omega T_2''} - \omega T_3 \right] \cos(\Theta) \right\} \quad (3.31)$$

where K_1 is not a scalar constant (as $\hat{J}_s$ was in the excitation section equations) but a complex number that depends on the rotor speed, phase of the rotor current and loading of the ASC electric circuit.

All of the exponential attenuation constants are known at this stage, but the amplitudes of the transients A_1, A_2, and A_3 remain to be found for both sections as well as the airgap flux "steady-state" component over the ASC section, a total of 7 terms. There are two rules for determining these transient component coefficients. Fundamentally, the θ-Pinch machine must satisfy boundary point conditions at two points in the machine, θ_1 and θ_2. At each boundary point there are three quantities that must be matched at all times; they are

a) the total rotor sheet flux density is continuous,

b) the airgap flux density is continuous, and

c) the total rotor sheet current is continuous.

The meaning of continuous is that with respect to the boundary position shown in Figure 3.3, the normal component (radial) of the flux density must not experience any abrupt, stepped transitions if the α_1, α_2 and α_3 transients are all considered; the same is also true of the axially directed rotor current. The leakage flux at the boundary may not experience abrupt jumps but this is already implied by conditions a) and b).

Therefore three independent boundary conditions have been established at each boundary which results in six of the seven remaining coefficients capable of being evaluated.

Implicit in the one-dimensional representation of the airgap flux and currents, the integral of B_r, B_g, J_s, J_{asc} or J_r must be zero around the circumference on a continuous basis, i.e. at every point in the cycle (under the assumption of balanced polyphase windings)

$$\int_{\theta_1}^{\theta_2} J_s e^{-j\theta} \, d\theta = 0 \qquad (3.32)$$

$$\int_{\theta_1}^{\theta_2} J_{asc} e^{-j\theta} \, d\theta = 0 \qquad (3.33)$$

$$\int_{\theta_1}^{\theta_2} J_r e^{-j\theta} \, d\theta = 0 \qquad (3.34)$$

By application of Ampere's Law it follows that

$$\int_{\theta_1}^{\theta_2} B_r \, d\theta = 0 \qquad (3.35)$$

$$\int_{\theta_1}^{\theta_2} B_g \, d\theta = 0 \qquad (3.36)$$

In particular, the most valuable integral condition is that the asynchronous condenser current loading is a net zero value because this is an independent condition and consequently the system of seven simultaneous equations

may be solved and finally the coefficient B_{gss} in the condenser section is determined.

C. Approximate Solutions

If the sharp transients α_2 and α_3 are neglected and the rotor current is assumed to consist only of the slowly decaying α_1 transient and the steady-state current, this total rotor current, J_r bears a rather distinct relationship with the stator current loading under the assumption that

i) $G >> 1$

ii) $\omega \delta_2 \mu_2/\rho_2 \geq 1$

iii) $\sigma G \geq 1$

and at a location such that $\theta > \pi/\alpha_2 \tau_{p1}$ this rotor to stator relationship is

$$J_r \approx - \frac{\hat{J}_s}{1 + \omega T_2/G} \tag{3.37}$$

while for a location such that $\theta < \pi/\alpha_2 \tau_{p1}$

$$J_r \approx - \frac{\hat{J}_s}{1 - j/G} \tag{3.38}$$

To express the transient amplitudes of the airgap flux density over region $\theta = 0$ to $\theta = \theta_1$, this may be accomplished in terms of the transient component of the rotor current. From Faraday's Law applied to a cage rotor

$$\rho_r \dot{J}_r = u_r \dot{B}_g + j\omega B_g \tag{3.39}$$

and integrating the general expression for B from (3.17), the transient amplitudes of B_g are

$$A_{(n)} = \frac{\rho_2 \ J_{r(n)}}{u_r + j\omega/\alpha_{(n)}} \tag{3.40}$$

The approximate value of B_g at just the point where it may be said that the α_2 transient is insignificant, is for $\theta \approx \pi/\alpha_2 \ \tau_{p1}$

$$B_g = \frac{-\rho_2 \hat{J}_s}{u_r} \left[\frac{1}{1 + \omega T_2/G} \right] \tag{3.41}$$

Here it is assumed that G>>1 but with no slip restriction because the term u_r rather than u_s is included in (3.41). However, at locked rotor a better approximation is

$$B_g = \frac{-\rho_2 \hat{J}_s}{u_s} \left[\frac{1}{(1 + \omega T_2/G) - j/G} \right] \tag{3.42}$$

D. Exact Solutions

The exact solution for the airgap flux density at all points along the airgap gives the desired output of this machine after simply one integration of the in-phase B_g component with the rotor current to yield the mechanical power developed

$$P_m = \frac{u_r}{2} \int_0^{\Theta_1} B_p(\Theta) \hat{J}_s \, d\Theta \qquad \text{Watts} \qquad (3.43)$$

This differs from the generalized machine theory approach [13] because the latter requires that the amplitude of the airgap flux density is constant around the machine periphery; thus the equivalent of the synchronous machine power angle does not exist in the space-transient induction machine unless such a model defines separate power angles for each pole, or better for each slot pitch.

The reactive power circulating about the motoring winding is given by

$$Q_m = \frac{u_s}{2} \int_0^{\Theta_1} B_q(\Theta) \hat{J}_s \, d\Theta \qquad \text{VARs} \qquad (3.44)$$

where the total airgap flux may be expressed in complex form as

$$B_t(\Theta) = B_p(\Theta) + j B_q(\Theta) \qquad (3.45)$$

In practical "θ-Pinch" machines, the total flux at θ_2 must be matched to the total flux at $\theta=0$ and this is called the re-entry or carry-over flux for it exists at the exit end of the condenser windings which is the start of the motoring winding. To simplify the functional dependence of the re-entry flux, suppose that the only function of the α_2 and α_3 transients is to match boundary conditions perfectly right at the transition point. Here it is assumed that the main and ASC windings do not overlap but that the transition is abrupt and finite. However, in terms of affecting gross quantities of reactive VA, mechanical power output or terminal voltages, the α_2 and α_3 transients are negligible. This has been confirmed experimentally as discussed in Chapter IV. Thus it may be concluded that the usefulness of these quickly decaying transients lies in matching boundary conditions as demanded by one type of mathematical approach.

For performance calculations, the airgap flux density may be accurately represented as

$$\theta<\theta<\theta_1 \qquad B_g(\theta) = B_{gss} + B_1 e^{\alpha_1 \theta'} \tag{3.46}$$

$$\theta_1<\theta<\theta_2 \qquad B_g(\theta) = B_2 e^{\alpha_1'(\theta'-\theta_1')} \tag{3.47}$$

$$B_{gss} = \frac{\rho_r \hat{J}_s}{\sigma u_s \epsilon} \tag{3.48}$$

and all other quantities are complex. In the motoring region, corresponding to (3.46), the principal transient attenuation coefficient is (from Appendix IV)

$$\alpha_1 = -\frac{1}{\lambda}\left[\frac{1}{G(1-\sigma)^3 + \omega T_2(1-\sigma)} + j\,\frac{1}{1-\sigma}\right] \tag{3.49}$$

$$\approx -\left[\frac{1}{u_r T_2} + j\,\frac{\omega}{u_r}\right] \tag{3.50}$$

In the motoring region, the fast α_2 and α_3 transients are

$$\alpha_2 = \frac{-\pi}{\tau_{p1}}\sqrt{\frac{G}{\omega T_2}}\left[1 + \frac{1}{2\left[(1-\sigma)\sqrt{G\,\omega T_2} - j\,\omega T_2\right]}\right] \tag{3.51}$$

$$\alpha_3 = \frac{\pi}{\tau_{p1}}\sqrt{\frac{G}{\omega T_2}}\left[1 - \frac{1}{2\left[(1-\sigma)\sqrt{G\omega T_2} + j\,\omega T_2\right]}\right] \tag{3.52}$$

In the condenser region, the last two transients effectively have either their rate of decay speeded up by the (1 + X) term.

$$\alpha_2 = -\frac{1}{\lambda_2}\sqrt{\frac{G}{\omega T_2}(1+X)}\left\{1 + \frac{1}{2(1+X)\left[(1-\sigma)\sqrt{G\omega T_2(1+X)} - j\omega T_2\right]}\right\} \tag{3.53}$$

$$\alpha_3 = \frac{1}{\lambda_2}\sqrt{\frac{G}{\omega T_2}(1+X)}\left\{1 - \frac{1}{2(1+X)\left[(1-\sigma)\sqrt{G\omega T_2(1+X)} + j\omega T_2\right]}\right\} \tag{3.54}$$

$$\text{where } X = \frac{\mu_3\,\delta_3}{\mu_2\,\delta_2} = \frac{L_3}{L_2} \tag{3.55}$$

$$\lambda_2 = \text{Rotor pole pitch}/\pi = \frac{\tau_{p1}(1-\sigma)}{\pi}$$

The airgap flux density inside the condenser region, B_2 may now be exactly calculated after defining the terms

$$G' = G(1 + X)^2 \tag{3.56}$$

$$T_2' = T_2(1 + X) \tag{3.57}$$

$$\lambda' = \lambda(1-\sigma) \tag{3.58}$$

and utilizing six auxiliary component terms as

$$B_2 = \frac{\text{Term A} \cdot \text{Term B}}{\text{Term C} - (\text{Term D}/\text{Term E}) \cdot \text{Term F}} \cdot \frac{\rho_r \hat{J}_s}{\sigma u_r \epsilon} = \frac{B_2' \rho_r \hat{J}_s}{\sigma u_r \epsilon} \tag{3.59}$$

where $\text{Re [Term A]} = 1. - e^{-\theta_1/u_r T_2'} \cos(\omega\theta_1/u_r)$ (3.60)

$\text{Im [Term A]} = - e^{-\theta_1/u_r T_2'} \sin(-\omega\theta_1/u_r)$ (3.61)

$\text{Re [Term B]} = 1.0$

$\text{Im [Term B]} = - 1/(\omega T_2')$

$\text{Re [Term C]} = 1 - e^{-\theta_2/u_r T_2'} \cos(\omega\theta_2/u_r)$ (3.62)

$\text{Im [Term C]} = - e^{-\theta_2/u_r T_2'} \sin(-\omega\theta_2/u_r)$ (3.63)

$\text{Re [Term D]} = 1 - e^{-(\theta_2-\theta_1)/u_r T_2'} \cos(\omega(\theta_2-\theta_1)/u_r)$ (3.64)

$\text{Im [Term D]} = - e^{-(\theta_2-\theta_1)/u_r T_2'} \sin(-\omega(\theta_2-\theta_1)/u_r)$ (3.65)

$\text{Re [Term E]} = \omega^2 T_2' (\theta_2-\theta_1)/u_r$ (3.66)

$\text{Im [Term E]} = - \omega(\theta_2-\theta_1)/u_r$ (3.67)

$\text{Re [Term F]} = 1 - e^{-\theta_1/u_r T_2'} \cos(\omega\theta_1/u_r)$ (3.68)

$\text{Im [Term F]} = - e^{-\theta_1/u_r T_2'} \sin(-\omega\theta_1/u_r)$ (3.69)

The excitation transient flux amplitude may be expressed as a function of the condenser transient flux amplitude since "carry-over" is crucial

$$B_1 = -\left[1 + \frac{\text{Term G}}{\text{Term H}} \cdot B_2'\right] \frac{\rho_r J_s}{\sigma u_s \epsilon} \qquad (3.70)$$

$$\text{Re [Term G]} = 1 - e^{-1/u_r T_2} [\gamma \cos(\psi) + \psi \sin(-\psi)] \qquad (3.71)$$

$$\text{Im [Term G]} = -e^{-1/u_r T_2} [\gamma \sin(-\psi) - \psi \cos(\psi)] \qquad (3.72)$$

$$\text{Im [Term H]} = -2\omega(\Theta_2 - \Theta_1)/u_r \qquad (3.73)$$

$$\text{Re [Term H]} = (\Theta_2 - \Theta_1)\cdot(\omega^2 T_2' - 1/T_2')/u_r \qquad (3.74)$$

$$\text{where } \gamma = 1 + \omega^2 T_2 (\Theta_2 - \Theta_1)/u_r \qquad (3.75)$$

$$\psi = \omega(\Theta_2 - \Theta_1)/u_r \qquad (3.76)$$

and again Θ is in units of meters airgap periphery for all equations (3.60) through (3.76) as expressed by (3.24). The external load placed onthe asynchronous condenser, (e.g. the main excitation winding) must be referred to the airgap so that an effective $\mu_3\delta_3$ and an effective ρ_3' may be used to represent the complex load on the ASC electric circuit. The condenser leakage time constant as originally expressed in (3.29) may be expanded to

$$T_3 = \frac{\mu_3\delta_3 + Q_{asc}/3\cdot J_{asc}^2\omega}{\rho_3 + P_{asc}/3\cdot J_{asc}^2} = \frac{L_3}{\rho_3'} \text{ (sec.)} \qquad (3.77)$$

Q_{asc} is the total VAR generation which must supply leakage and magnetizing requirements of the main winding and

P_{asc} is the power extracted from or feed into the rotor in excess of that required to supply the I^2R losses of the condenser winding. Both the individual magnitude and phase of Q_{asc} and P_{asc} can be varied by the (slip-controlled phase angle difference between the internal generated condenser emf, E_q and the terminal voltage V_t of the entire machine. However, the total apparent power $S = \sqrt{Q_{asc}^2 + P_{asc}^2}$ of the condenser output is substantially constant and the approximate analytic expression of S_{max} per unit strip length is

$$S_{max} = \frac{g_e B_t^2 v_r}{4 \mu_o} = \frac{g_e B_{2(\theta_1)}^2 v_r}{4 \mu_o} \qquad (3.78)$$

The exact way to find the limit on

$$Q_{asc} = Q_{asc(output)} + Q_{asc(internal)}$$

is by performing the integrations

$$Q_{asc} = Im\left[\frac{u_s}{2}\int_{\theta_1}^{\theta_2} B_2(\theta)\ \hat{J}_{asc}\ d\theta\right] \qquad (3.79)$$

and $$P_{asc} = Re\left[\frac{u_s}{2}\int_{\theta_1}^{\theta_2} B_2(\theta)\ \hat{J}_{asc}\ d\theta\right] \qquad (3.80)$$

The purpose of digital calculations are to maximize the ratio Q_{asc}/P_{asc} which are done by

a) changing the relative length $\theta_2-\theta_1$ with respect to θ_1.

b) changing the rotor resistivity ρ_2 and layer depth

δ_2 in relation to the effective surface resistivity ρ_3' and inductance of the ASC referred to the airgap.

If the total airgap flux density in the tertiary section as expressed by (3.59) is evaluated at Θ_2 and Θ_1 transition points, the ratio of these is

$$\frac{B_2(\Theta_2)}{B_2(\Theta_1)} = \frac{1 - [1 + j\omega\alpha_1(\Theta_2-\Theta_1)T_2']\ e^{\alpha_1(\Theta_2-\Theta_1)}}{[1 - e^{\alpha_1(\Theta_2-\Theta_1)}] - j\omega\alpha_1(\Theta_2-\Theta_1)T_2'} \qquad (3.81)$$

In the limit that T_2' approaches zero in (3.81) as would be the case for a resistance-limited rotor and the tertiary winding used for speed control (real power) applications, then (3.81) reduces to $B_2(\Theta_2)/B_2(\Theta_1) = 1.0$.

Figure 3.4 is the 1Ø voltage-source equivalent circuit valid for low-Goodness SCIM units and Figure 3.5 is the 3Ø current-source equivalent circuit valid for high-Goodness factor SCIMs. Preferably, P_{asc} to supply the $\rho_3(R_3)$ loss should be supplied entirely by the mains rather than by the rotor. The condenser internal voltage E_q (peak value) is a straightforward integration after $B_2(\theta)$ is found numerically.

$$E_q = \left[v_s \int_{\Theta_1}^{\Theta_2} B_2(\theta)\ d\theta \right] \text{ x turns \& winding factors} \qquad (3.82)$$

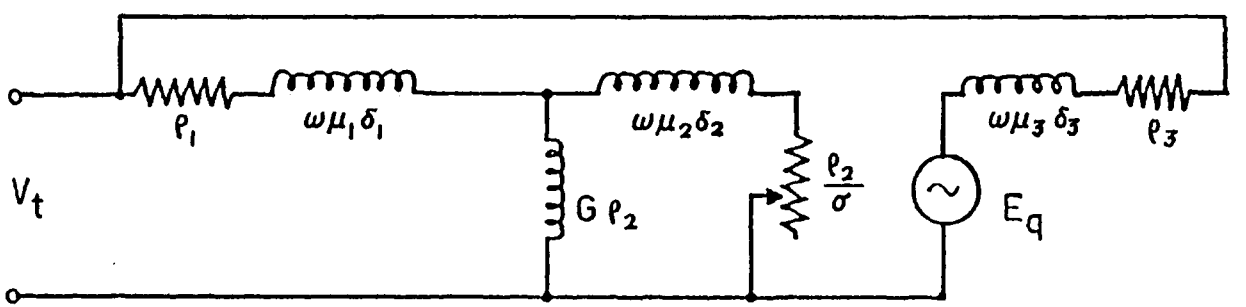

Fig.3.4 Equivalent circuit of integral induction motor-asynchronous condenser with voltage source tertiary model; valid for low Goodness machines.

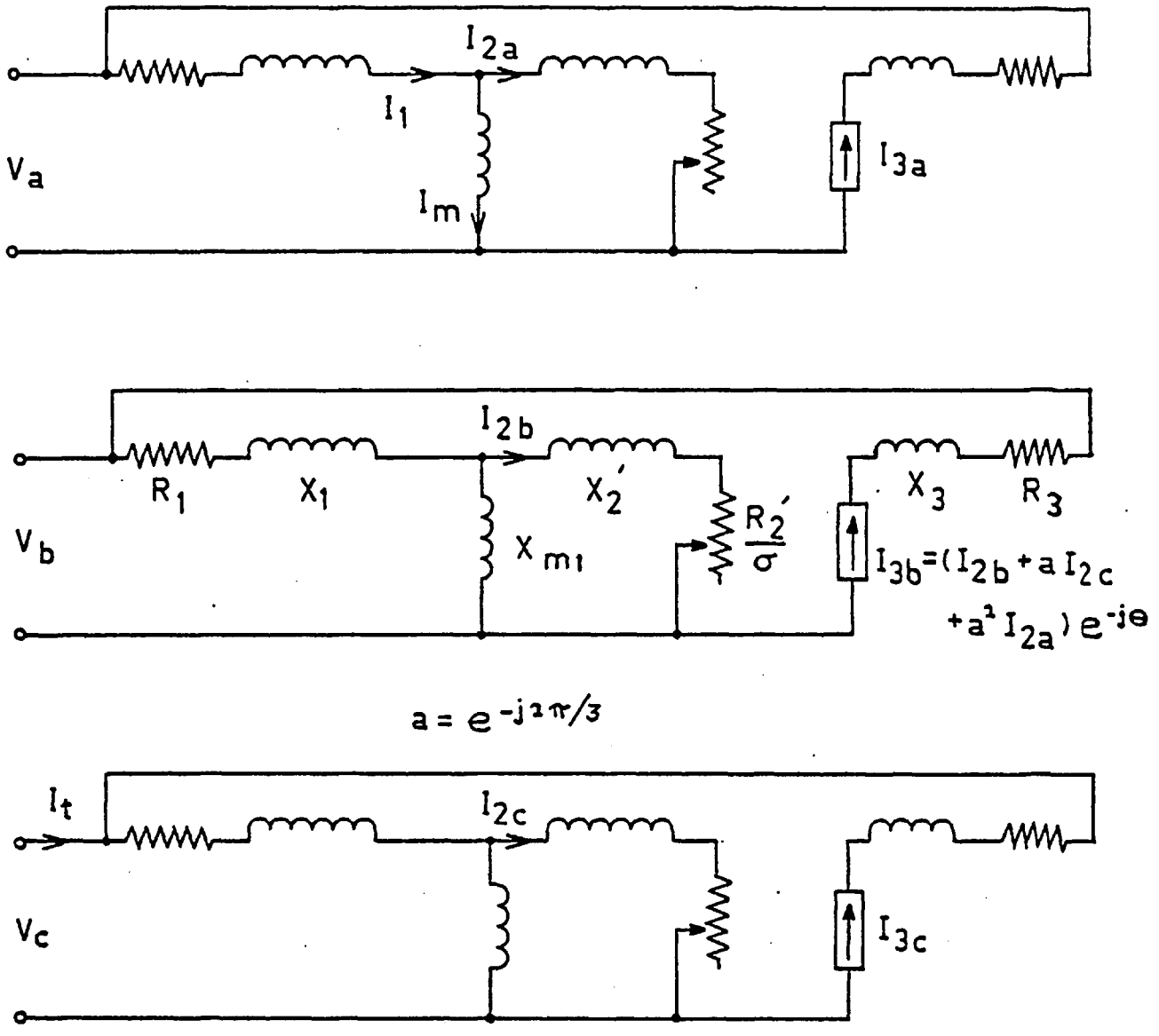

Fig. 3.5 Three-phase current-source equivalent circuit of the integral induction motor/asynchronous condenser; valid for high-Goodness machines and slips less than 10%.

E. Computational Results

The most basic expression of the apparent power transferred from the primary to the tertiary section is based on the $B_t^2 u_r$ energy of the airgap at exit-edge (θ_1) per unit of stator width as given in (3.78). This is based on the earlier work of Williams and Laithwaite [13] who explained real power losses in spherical induction machines at the exit-edge of the primary block by the same formulation as in (3.78) except that all power that was transferred only produced back-torques since no tertiary windings were incorporated in the early short-primary machines. Nevertheless their generalized expressions have served as the basic guide for estimating the performance of both the rotary and linear asynchronous condenser concepts; Figure 3.6 shows the effect of magnetizing current on the normalized exit-edge reactive power transfer as a function of slip and for values of G from $\pi/2$ to infinity. The base quentity is the steady-state secondary real power loss in an equivalent electrical machine which is

$$P_2 = \tfrac{1}{2}\, \rho_2\, J_s^2\, n\tau_{p1} \qquad (3.83)$$

Figure 3.6 is specific to the case of n = 4 poles of primary per repeatable section; it neglects rotor leakage inductance ($L_2 = 0$, $T_2 = 0$) and thus the non-dimensional decrement factor is $\varepsilon = 1 + (1/\sigma\, G)^2$ in the expressions for the total radial (normal) airgap flux density $B_g(\theta_1) = B_t$. For Figures 3.6 - 3.8, the expression for B_t given in (2.3) has been used rather than (3.46) or (3.47). Figure 3.7 shows the normalized exit-edge power transfer for the case of G = 212 and n = 1 through n = 4 poles per primary; the addi-

tional four curves with dashed notation are not for design purposes but show the result of evaluating (3.78) using only the B_q^2 component as given by (2.2) to indicate the relative contribution of the time quadrature flux which is most considerable. The n = 3 curve (based on B_t^2) is the most general design curve appropriate to the G = 212 SCIM-Mk.II machine when using one tertiary (ASC) pole per repeatable section in an eight pole machine with two repeatable sections. These characteristics all assume zero entry-edge flux so that they are only exactly appropriate for sheet-rotor linear motors with condenser windings; the next set of curves do account for the carry-over flux peculiar to the rotary machines. Figure 3.8 is the normalized exit-edge reactive power transfer for the case of G = 212 but for the less practical pole numbers of n = 5 through n = 8.

The radial airgap flux density over the tertiary winding has been calculated from (3.59) through (3.69) with the time constants and speeds as listed in Table 3.1. This specifically considers the case of re-entry flux present over the primary winding section; the only two major assumptions are

(i) that the primary is sufficiently long with respect to the tertiary length that all re-entry transients have decayed completely over the length of the primary so that there are no extraneous effects at the main exit-edge, θ_1,

(ii) that both primary and tertiary have zero overlap although in double layer windings, a six to eight slot overlap region is common; the analysis has an abrupt transition at θ_1 and θ_2.

Table 3.1

Parameters used in Computer Contour Plots of Transient Airgap Flux Density

Figures 3.9 and 3.10

Frequency (rad/sec), ω	314
Effective Rotor Time Constant, (sec), T_2'	0.002 → 0.04
Exponential Decay Argument, $\alpha_1 (\Theta_2-\Theta_1)$	0.025 → 31.0
Tertiary Poles, $(\Theta_2-\Theta_1)/\tau_{p3}$	0.10 → 6.198
Slip, (per unit), σ	0.033

Figures 3.11 - 3.14

Frequency (rad/sec), ω	314
Rotor Coupled Time Constant, (sec), T_2'	0.002 → 0.04
Attenuation Coefficient, Real Comp., (m^{-1}), α_1	1.33 → 26.6
Attenuation Coefficient, Imag. Comp. (m^{-1}), α_1	-16.7
Rotor Speed (m/s), u_r	18.79
Rotor Resistivity, (Ohm), ρ_r	5.46×10^{-6}
Primary Current Loading, (A/m pk), $\hat{J}_s$	45.4×10^3
Primary Section: Tertiary Section Length	4.0 Constant ratio
Tertiary Length at 3.3% slip, (m), $\Theta_2'-\Theta_1'$	0.0194 → 1.164

To show the effectiveness with which the tertiary absorbs power and attenuates the B field over this section before re-entry, (3.59) has been evaluated at θ_1 and θ_2 with the ratio of these two values plotted as a two-dimensional contour map of $B_2(\theta_2)/B_2(\theta_1)$ for the separate real and imaginary components as shown in Figures 3.9 and 3.10 respectively. The ordinate represents the rotor plus tertiary coupled time constant, $T_2 + T_3 = T_2'$ and is plotted to the value of $T_2' = 0.04$ seconds which is appropriate for megawatt size machines. The 112 KW, 8 pole laboratory unit has a T_2' value of about 0.0 35s. The abscissa represents the number of tertiary poles at a 3.3% slip (the preferred value for the 112 kW unit) that are incorporated according to the relation $\tau_{p3} = \tau_{p1}(1-\sigma)$; this parameter should not be considered to be the same as longitudinal position in the tertiary section since the abscissa is the total number of poles. These two figures conclude that for very large machines and for example, one tertiary pole, the B_p component of flux at re-entry will not fall below 68% of the "exit" value and that the B_q component will not be above 5% of the exit value exactly at the entry-edge of the primary. These may be considered to be the master design graphs for the asynchronous condenser θ-Pinch technology. It should be emphasized that the T_2' parameter is a strong funciton of the phase angle of the tertiary current with respect to the primary current as depicted by Figure 2.42. Both Figures 3.9 and 3.10 may also be calculated directly from the closed-form expression (3.81) if only the boundary ratios are required.

The transient component of airgap flux density that is present at the entry boundary of the primary and as calculated from (3.70) through (3.76) is shown in Figures 3.11 - 3.13

for the real and imaginary parts. This B_1 flux decays throughout the entire primary region with the exponential constant as given by (3.61); the steady-state value of flux density (superimposed on the transient) is the standard expression for B_g as given by (3.48). In addition to the parameters given in Table 3.1, the only major assumption is that the decrement factor ε from (3.27) is unity since these contour plots consider $G \geq 200$.

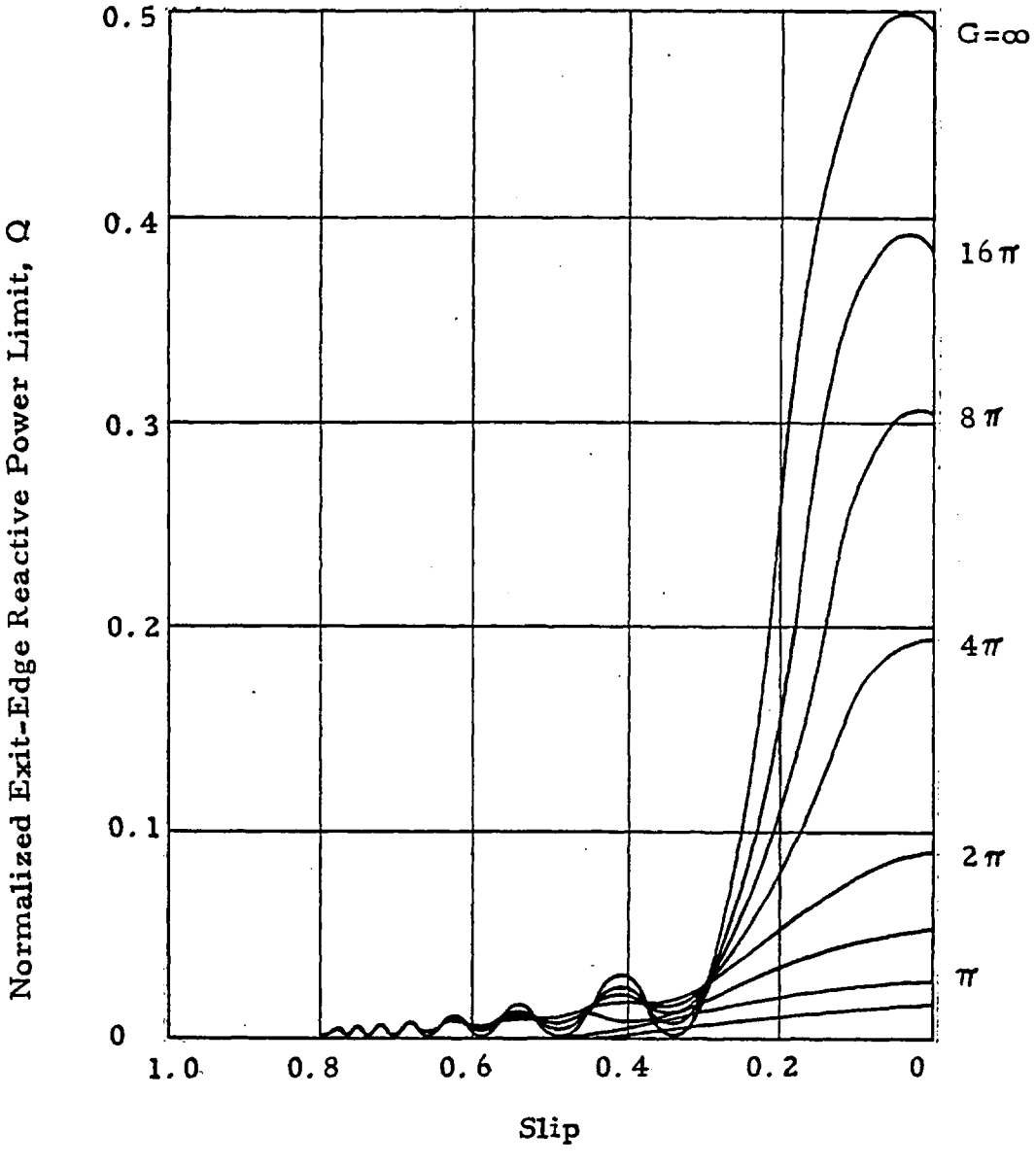

Figure 3.6 Effect of magnetizing current on exit-edge reactive power transfer for short-primary machines with no rotor leakage inductance; originally presented in Reference 13 for exit-edge real power losses.

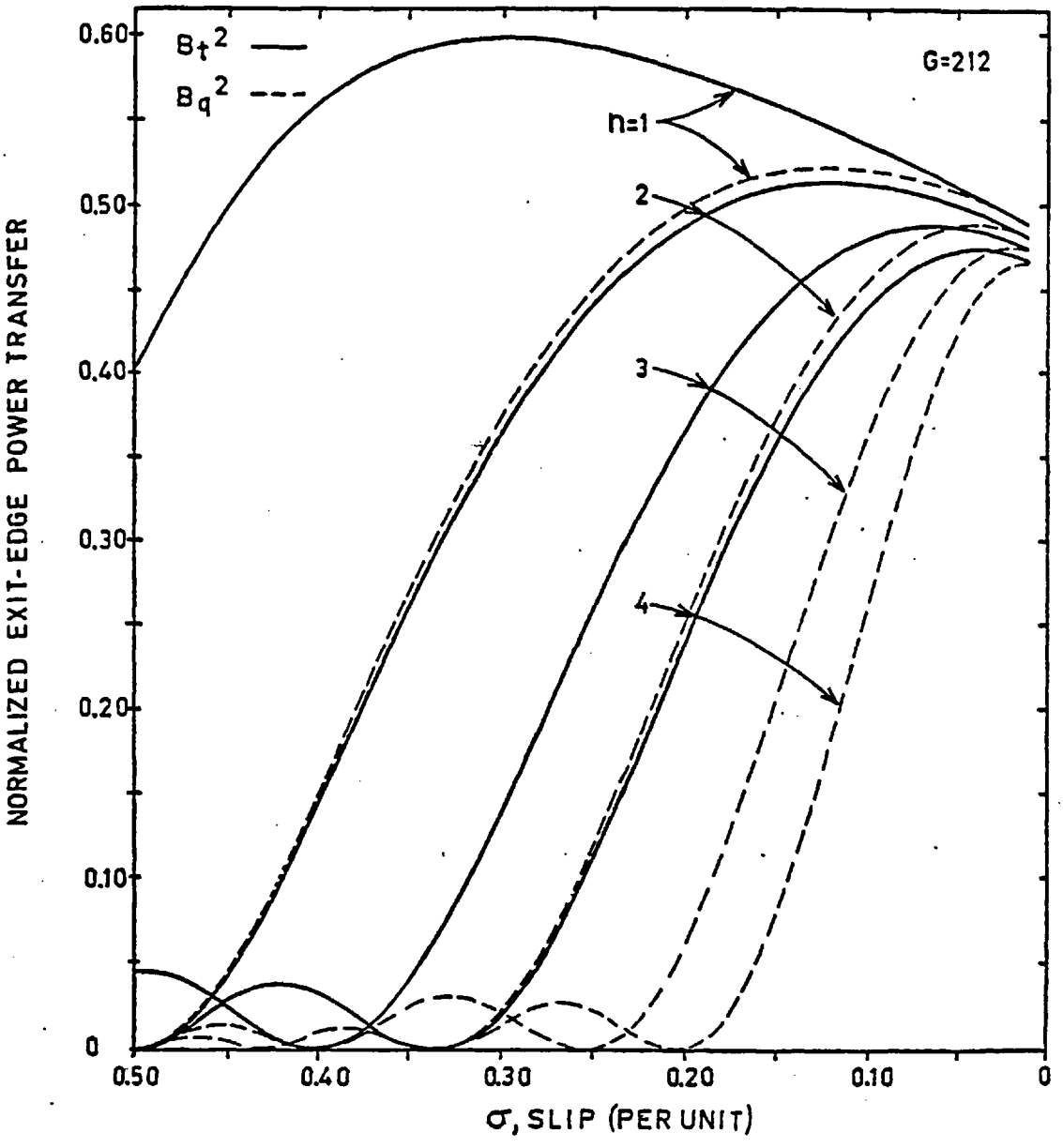

Figure 3.7 Effect of the number of primary poles on the exit-edge apparent power transfer with a very low magnetization requirement and no rotor leakage inductance.

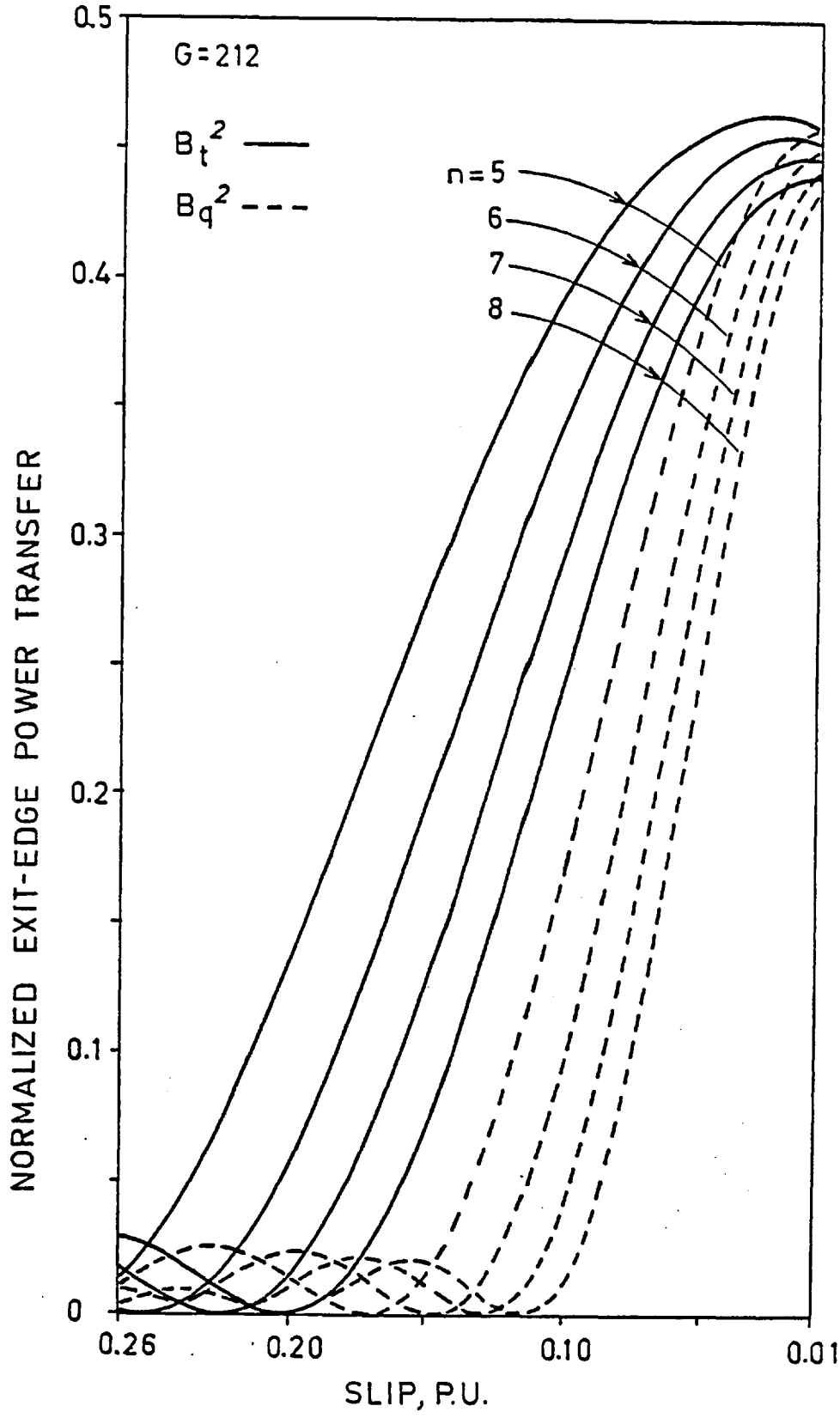

Figure 3.8 Effect of the number of primary poles on the exit-edge apparent power transfer with a very low magnetization requirement and without rotor leakage inductance.

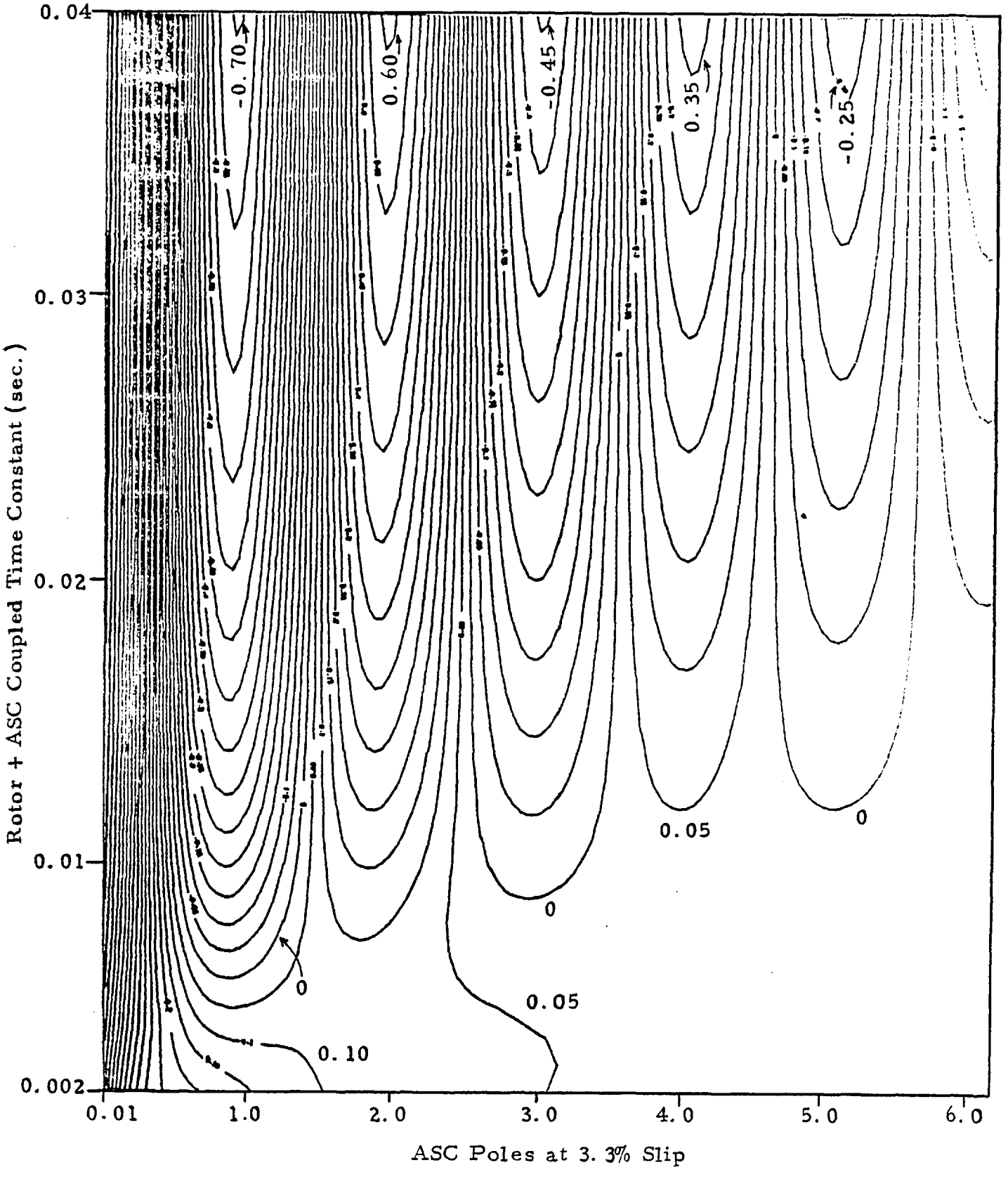

Fig. 3.9 Contour lines of constant ratio of the real component of airgap flux density $B_2(\Theta_2)/B_2(\Theta_1)$ inside the condenser region; calculated from (3.59) -(3.69).

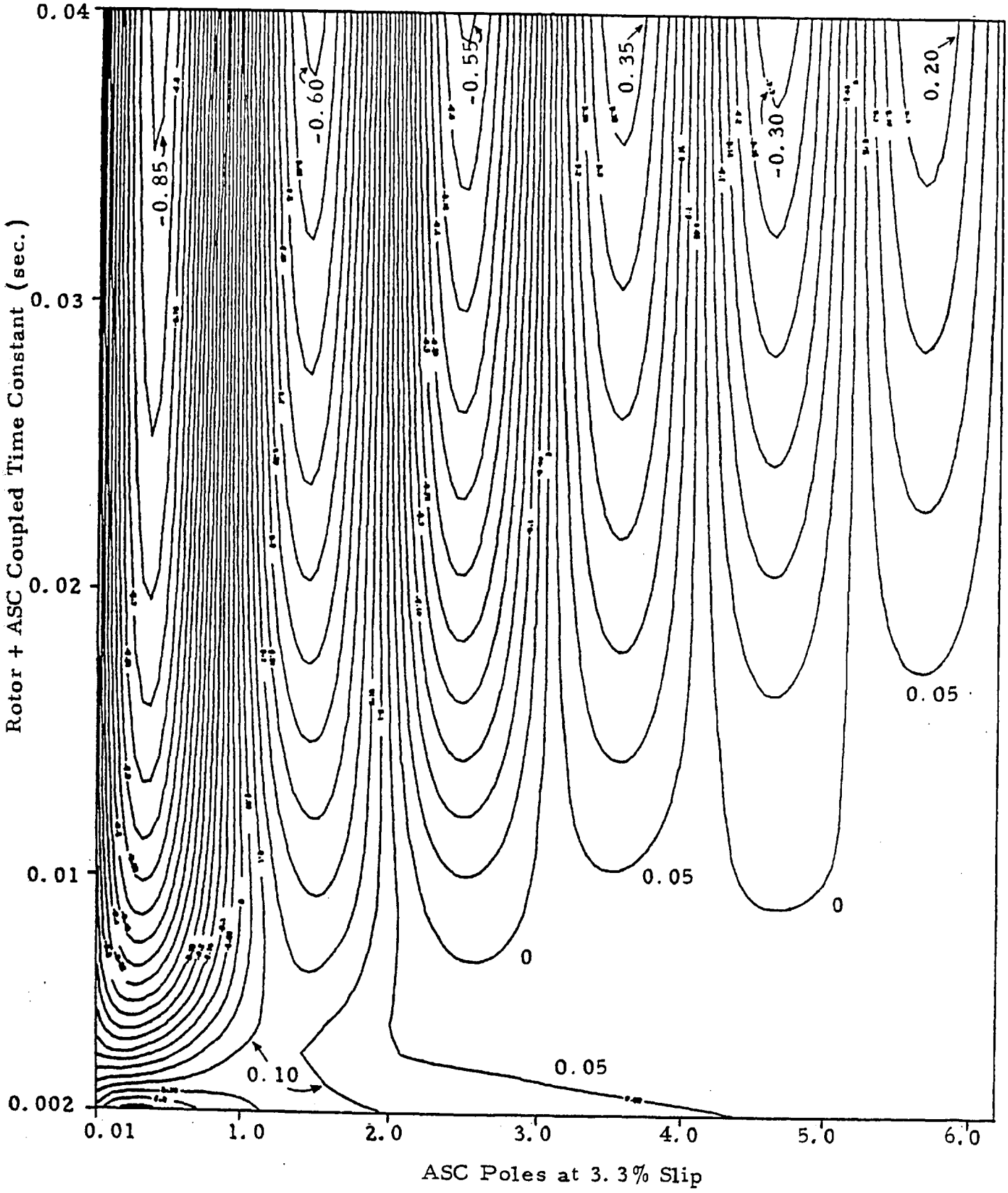

Fig. 3.10 Contour lines of constant ratio of imaginary component of airgap flux density inside the condenser region; calculated from (3.59) -(3.69), $B_2(\Theta_2) / B_2(\Theta_1)$.

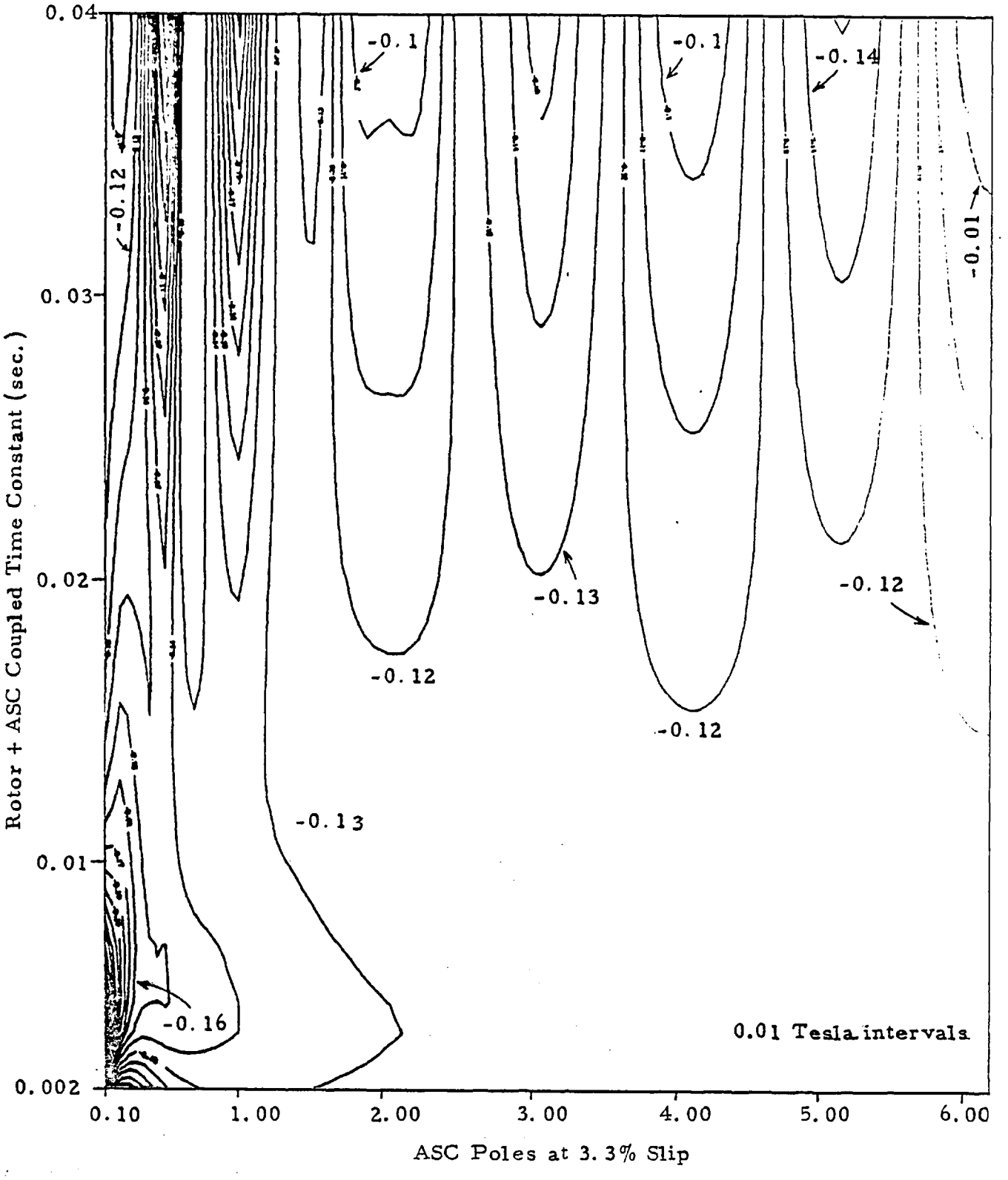

Fig. 3.11 Lines of constant real component of the transient airgap flux density at the entry boundary of the primary region versus tertiary region length.

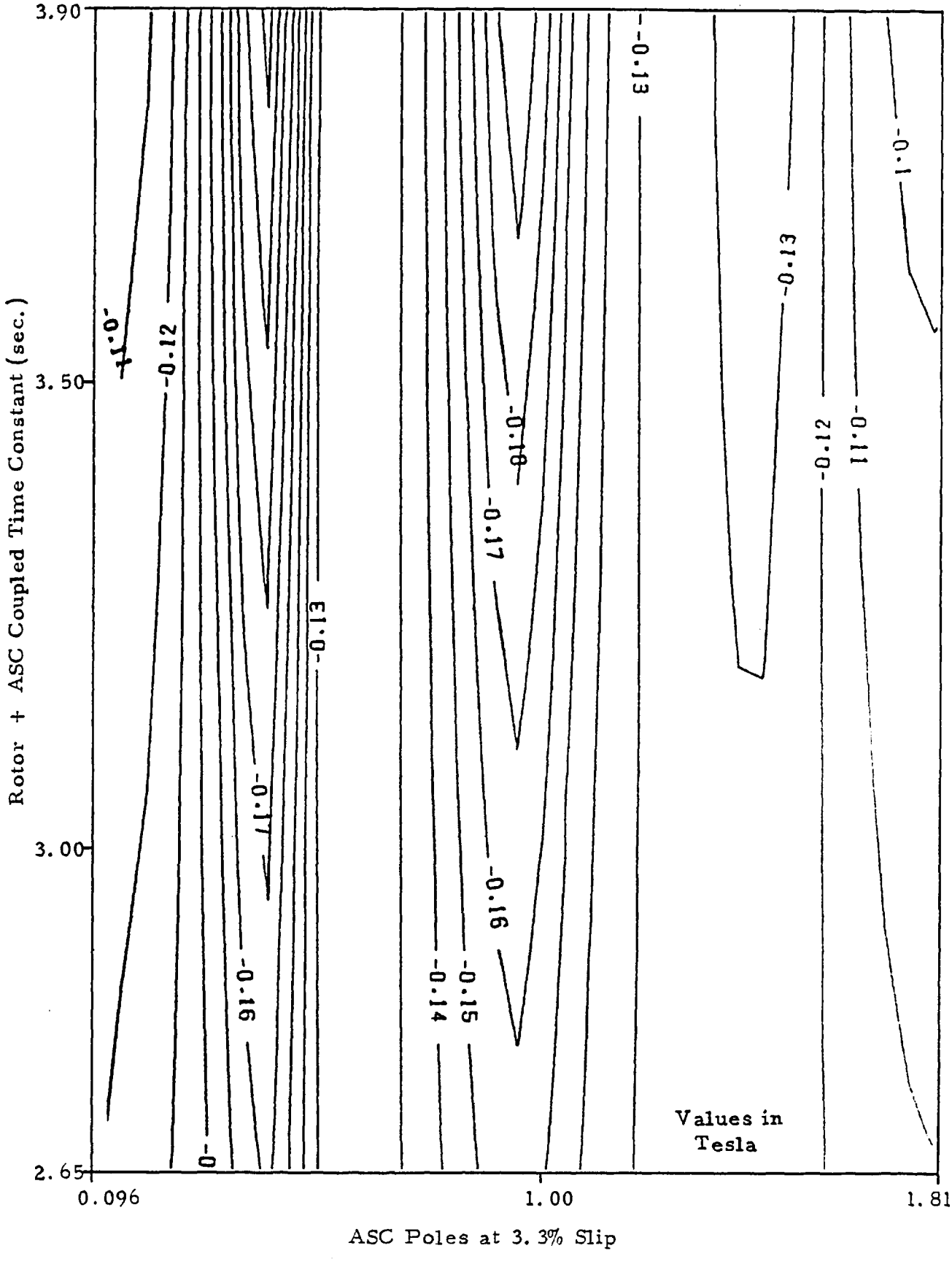

Fig. 3.12 Expanded scale view of Fig. 3.11 for the contour lines of constant real component, transient airgap flux density at the entry to the primary winding(Θ_2) versus total ASC section length & optimum slip.

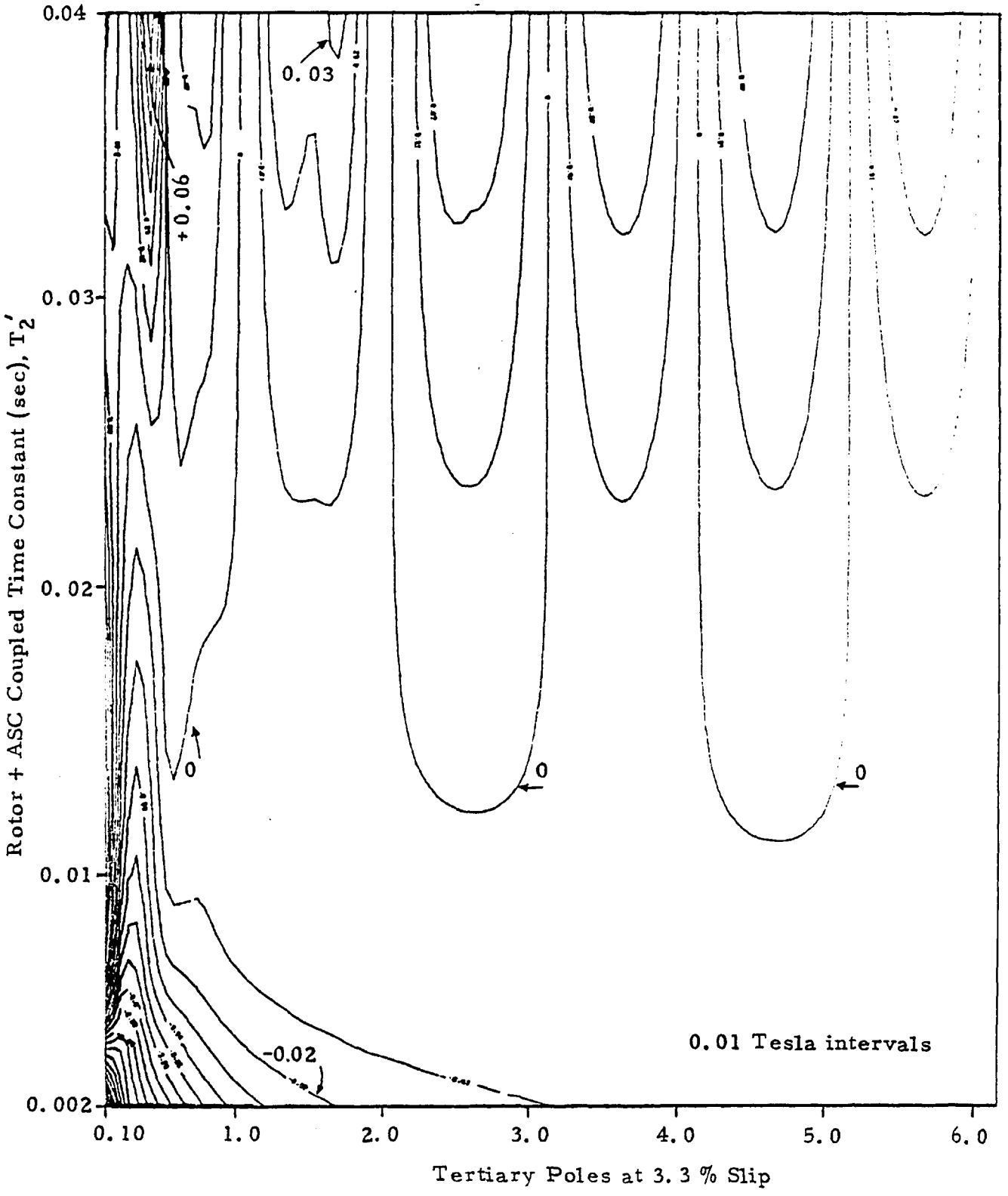

Fig. 3.13 Contour lines of constant imaginary component of the B_1 transient radial-directed airgap density at the entry to the primary section.

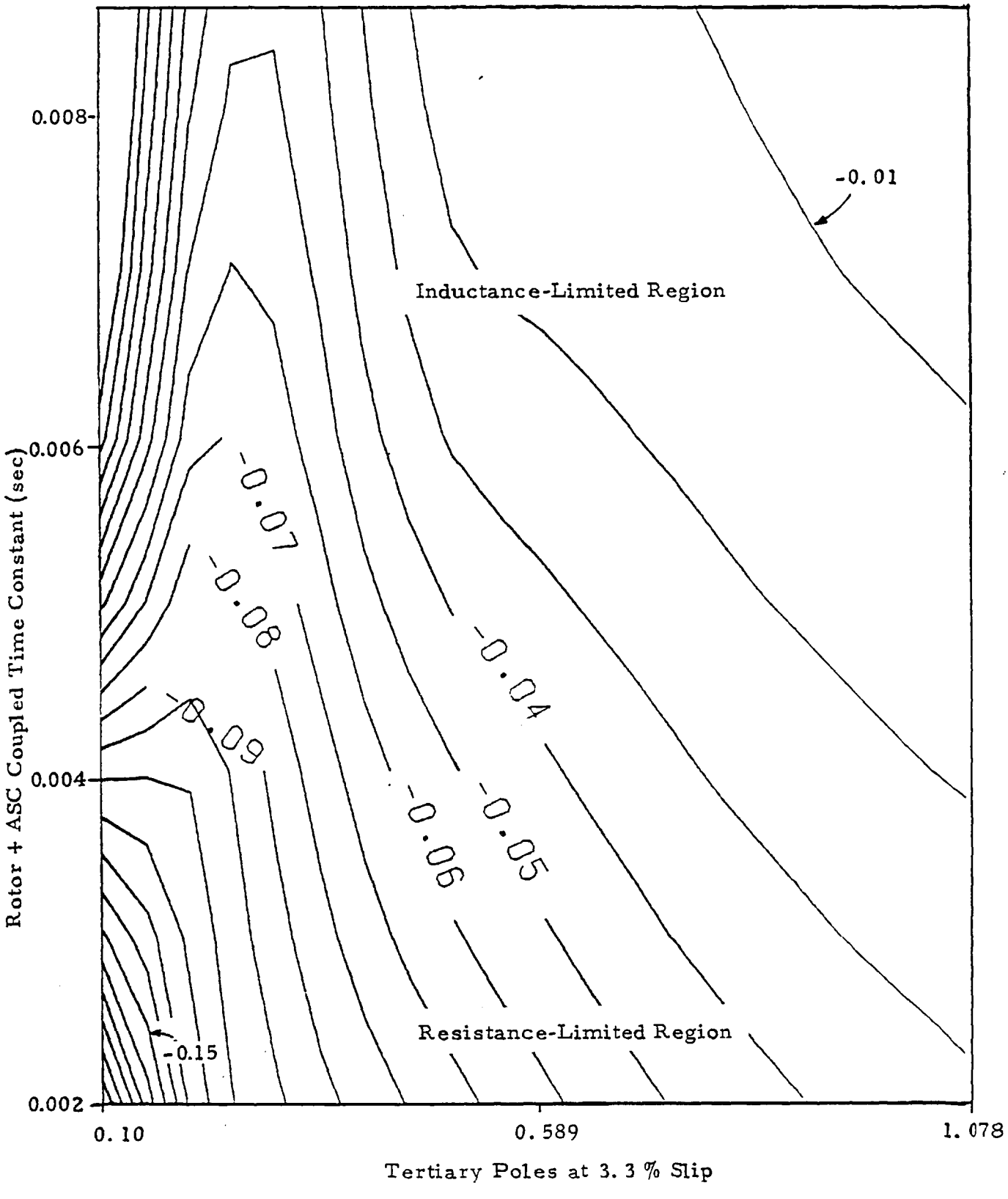

Fig. 3.14 Contour lines of constant imaginary component of B_1 transient radial directed, airgap flux density (in Tesla) at entry point of primary and focusing on region from resistance-limited to inductance-limited rotor + tertiary characteristics using parameters given in Table 3.1

3.2 SPACE HARMONIC REPRESENTATION OF PRIMARY MMF

This section describes a first-order mathematical analysis of the primary magnetomotive force space distribution peculiar to the non-integral wavelength winding configuration of the LIM-ASC machines. The method presented makes use of linear superposition of active and image primary currents and does not consider the contribution of the reaction rail MMF. In modelling the primary MMF, identical LIM-ASC machines are situated adjacent to the central machine along the direction of the travelling field and are periodically spaced at the next integral wavelength beyond each non-integral wavelength winding. This allows the excitation to be represented by discrete steps and the Fourier components are directly synthesized (without transformation) into a series of travelling waves to model the MMF distribution.

Figure 3.15a depicts the winding configuration of the central LIM-ASC primary and sections of two primaries that are included in the infinite series of longitudinally adjacent machines. It is assumed that the primary currents are sinusoidal, the fundamental wavelength is that of a phase belt, and consequently the adjacent primaries are spaced at a pitch of exactly six wavelengths.

Figure 3.15b shows the discrete representation of the phase A MMF for a continuous winding that includes the actual

MMF as shown in Figure 3.15a with the addition of the MMF contribution if the windings were extended to occupy the unfilled slots. The stator core iron is shown to be extended between the windings although this serves to graphically separate the adjacent machines. If all three phases of a continuous winding are excited such that each has an MMF magnitude of $\sqrt{2}$ NI/p over a period of 120° per pole, the fundamental MMF component per phase is $2\sqrt{2}$ NI/πp and the harmonic representation of the resultant travelling wave is

$$F(y,\ n = 1,\ 5,\ 7 \ldots \infty) = \frac{3\sqrt{2}}{\pi} \cdot \frac{NI}{p} \cdot \frac{K_{dp(n)}}{n} \left[\sum_{n=7,13,19\ldots}^{\infty} e^{j\left(\frac{n\pi x}{\tau_p} - \omega t\right)} + \sum_{n=5,11,17\ldots}^{\infty} e^{j\left(\frac{n\pi x}{\tau_p} + \omega t\right)} \right] \tag{3.84}$$

where n = order of harmonic

N = number of turns/pole/phase

I = primary current (r.m.s.)

x = longitudinal distance in direction of forward travelling wave

p = number of pole-pairs

$K_{dp(n)}$ = winding distribution factor and pitch factor

$$= \sin\left(n\pi/3\right) \frac{\sin\left(n\pi/6\right)}{5 \sin\left(n\pi/30\right)} \tag{3.85}$$

Figures 3.15c, 3.15d and 3.15e show the MMF distribution for the individual phases comprising the image MMFs which are directed opposite to that produced if conductors of a

⊗ Denotes 3 slots/pole/phase
Phase A peaks at t=0

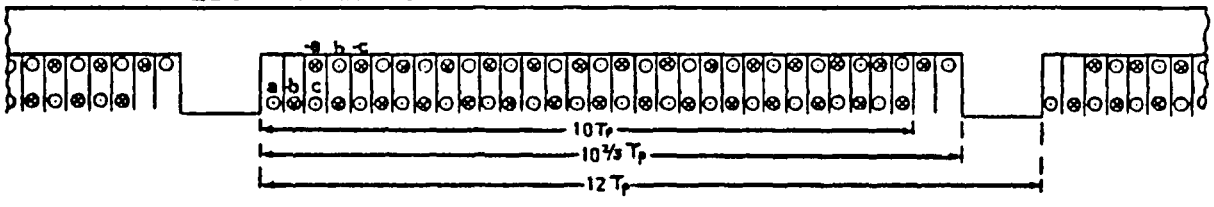

a. Periodic spacing of primary windings for analysis

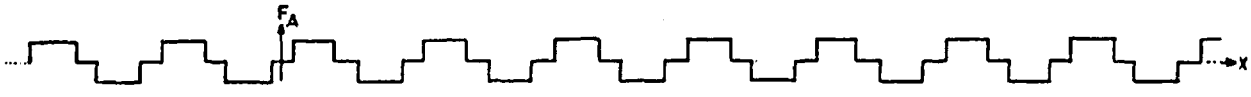

b. Phase A MMF at t=0 for a continuous winding

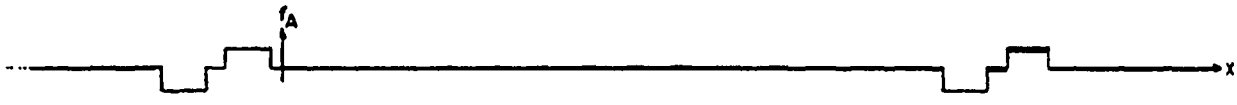

c. Phase A MMF due to entrance/exit region image currents

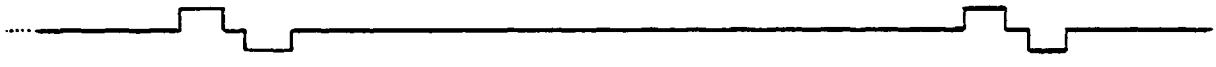

d. Phase B MMF due to entrance/exit region image currents

e. Phase C MMF due to entrance/exit region image currents

f. Total phase A MMF at t=0 for Fourier model of a.

Figure 3.15 Travelling wave representation of magnetomotive force space harmonics

continuous winding occupy the unfilled slots in the entrance/exit regions of the machines. The adjacent machines are spaced at a pitch of six wavelengths, resulting in an image MMF per phase of only one wavelength/machine for which the general harmonic analysis of the standing wave, as shown in Figure 3.16 is

Fig. 3.16 Arbitrary MMF standing wave due to entry/exit region image currents.

$$f_1(y,n,t)=\sum_{\substack{n=2\\(\text{even})}}^{\infty} \frac{2}{n\pi}\left[\cos(n\pi/36)-\cos(5n\pi/36)\right]\sin(n\pi\frac{x}{6\tau_p})\sin(\omega t) \qquad (3.86)$$

To change the zero-sequence standing waves to be compatible with the continuous winding representation by the travelling waves, (3.86) can be transformed into positive and negative-sequence travelling waves as

$$f_1(y,n,t)=\sum_{\substack{n=2\\(\text{even})}}^{\infty} \frac{1}{n\pi}\left[\cos(n\pi/36)-\cos(5n\pi/36)\right]\left[e^{j(n\pi\frac{x}{6\tau_p}-\omega t)}-e^{j(n\pi\frac{x}{6\tau_p}+\omega t)}\right] \qquad (3.87)$$

The summation of all travelling wave components due to entrance/exit region image MMF distribution of all three phases is

$$f_A+f_B+f_C=\frac{NI}{\pi p}\sum_{n=2}^{\infty}\frac{K_{dp(n)}}{n}\left[\cos(n\pi/36)-\cos(5n\pi/36)\right]$$

$$\left\{e^{j(n\pi\frac{x}{6\tau_p}-\omega t)}\left[e^{-j\theta_A}-e^{-j(\theta_B+2\pi/3)}+e^{-j(\theta_C-2\pi/3)}\right]\right.$$

$$+e^{j(n\pi\frac{x}{6\tau_p}+\omega t)}\left[\, e^{-j\theta_A} - e^{-j(\theta_B-2\pi/3)} + e^{-j(\theta_C+2\pi/3)}\right]\Big\}$$

for $\theta_A=33\pi/18$, $\theta_B=34\pi/18$, $\theta_C=35\pi/18$ (3.88)

Alternately, the positive and negative sequence components of image MMF are

$$f_A + f_B + f_c = \frac{NI}{\sqrt{2}p}\sum_{n=2}^{\infty}\frac{K_{dp(n)}}{n\,\pi}\left[\cos(n\pi/36)-\cos(5n\pi/36)\right]$$

$$\left[\, A_f\, e^{j(\alpha_f+\frac{n\pi x}{6\tau_p}-\omega t)} + A_b\, e^{j(\alpha_b+\frac{n\pi x}{6\tau_p}+\omega t)}\right] \quad (3.89)$$

where $\alpha_f=1.396$, $\alpha_b=-0.698$, $A_f=2.285$, $A_b=-1.684$

Figure 3.15f shows the superposition of the continuous wave MMF and the image MMF for phase A when the current is peaking. The summation of equations (3.84) and (3.89) yields the total space distribution of MMF for the non-integral wavelength LIM-ASC primary. The relative harmonic amplitudes of this waveform with respect to the fundamental MMF components is defined as

$$\frac{\text{Total MMF space distribution - Continuous wave fundamental component}}{\text{Continuous wave fundamental component}} =$$

$$\frac{F(y,n=5,7,11,\ldots\infty;t) + f_A + f_B + f_C}{F(y,n=1,t)} =$$

$$\frac{3\sqrt{2}\left\{\sum_{n=7,13,19}^{\infty}\frac{K_{dp(n)}}{n}\, e^{+j(n\pi\frac{x}{\tau_p}-\omega t)} + \sum_{n=5,11,17\ldots}^{\infty}\frac{K_{dp(n)}}{n}\, e^{+j(n\pi\frac{x}{\tau_p}+\omega t)}\right\}}{\Delta}$$

$$+\frac{\sum_{n=2\,(\text{even})}^{\infty}\left[\cos(n\pi/36)-\cos(5n\pi/36)\right]K_{dp(n)}\left[\frac{A_f}{n}e^{j(\alpha_f+\frac{n\pi x}{6\tau_p}-\omega t)}+\frac{A_b}{n}\, e^{j(\alpha_b+\frac{n\pi x}{6\tau_p}+\omega t)}\right]}{\Delta}$$

where $\Delta = 3\sqrt{2}\sin(\pi/3)\,\dfrac{\sin(\pi/6)}{5\,\sin(\pi/30)}$ (3.90)

3.3 SYNCHRONOUS ROTOR-HARMONIC INTERACTION.

This section presents a brief theoretical analysis of the synchronous crawling phenomena exhibited by cage-rotor induction machines when either

a) the MMF pattern created by the particular rotor slotting interacts synchronously with the stator MMF harmonics to produce a primary electromagnetic torque exceeding the fundamental induction torque. It should be emphasized that this is not an induction nor a reluctance torque, occurs with symmetrical wound primaries, is a function of the rotor slot skewing angle, and is most prominent at speeds less than 50% of the fundamental synchronous speed.

b) the MMF pattern created by a space-transient ridden symmetrically-constructed cage rotor interacts synchronously with stator MMF harmonics to produce a primary electromagnetic torque exceeding the fundamental induction torque. This is not an induction torque nor a reluctance torque, principally occurs with asymmetrically wound primaries, is largely dependent on rotor slot skewing and is most prominent at speeds greater than 50% of the fundamental synchronous speed.

The nature of torque production may be clarified, when at any motional speed, the flux distribution of rotor and stator currents have the same number of poles and are traveling at equal field speeds in the same direction and consequently either positive or negative sequence torque will be developed. This depends on the relative MMF posi-

tions in the airgap, irrespective of whether these component MMFs are positive or negative sequence. The torque so created could either be an induction or synchronous type; the distinction depending entirely on how the rotor flux density is established. To be an induction torque, the rotor flux must be initiated by an MMF that is induced by a stator flux of the same number of poles. The two component fields always travel at the same speed regardless of rotor speed, ω_r because the field speed produced by rotor currents at frequency $\sigma\omega_s$ as seen by a stationary observer is

$$\sigma\omega_s + \omega_r = \sigma\omega_s + \omega_s(1-\sigma) = \omega_s \tag{3.91}$$

where σ= per unit slip and ω_s is the synchronous field speed. Conversely, the synchronous type demands that the rotor flux is established by a current that is induced by a stator flux of a different number of poles. Here two field components propagate at the same velocity and develop a constant amplitude torque only at distinct rotor speeds. Yet, when these fluxes interact it is understood that a steady resultant torque demands equal harmonic wavelengths of both MMF distributions.

In short, the difference between induction and synchronous phenomena is entirely dependent on whether it is a harmonic primary MMF that induces the harmonic secondary current (as in the former) or if it is a fundamental primary MMF that induces a harmonic secondary current which reacts with other then fundamental primary fluxes as in the latter case. Numerous literature exists on subsynchronous harmonics but all of this is devoted to the induction type. Notwithstanding,

a common misrepresentation that has been used is that harmonic torques may be modeled by superimposing a harmonic speed-torque curve over a fundamental torque characteristic - both of these assumed constant primary excitation. Yet inspection of all experimental data on this subject reveals that the overall response is best represented by a constant-voltage fundamental torque characteristic overlayed with a constant-current harmonic speed-torque curve. This can be confirmed theoretically by the following analysis which concentrates on the synchronous phenomena; which is so pertinent to the Θ-Pinch technology.

Suppose that a symmetrical cage rotor is modeled by a system of identical coils instead of a continuous surface-layer current sheet such that a single current path in adjacent slots establishes an equivalent current loading of

$$j = J \sin (\pi/2\, n_b)\, e^{j(\theta-\omega_s t)} \qquad A/m \tag{3.92}$$

where it is understood that each rotor bar carries a total current

$$\frac{2}{\sqrt{2}}\, J\, \tau_s\, e^{j k\pi/n_b} \qquad \text{where } k = 1 \ldots n_b \tag{3.93}$$

The MMF distribution due to just one coil of such an array may be represented as in Figure 3.17 over two full poles. Here it is assumed that positive and negative MMF integrals are equal and thus the ratio of these two is

$$MMF(-) \cdot [2\pi - 2\pi/k_- J] = MMF(+) \cdot [2\pi/k_+ J] \tag{3.94}$$

$$k_- J\, [2\pi - 2\pi/n_b P] = k_+ J\, [2\pi/n_b P] \tag{3.95}$$

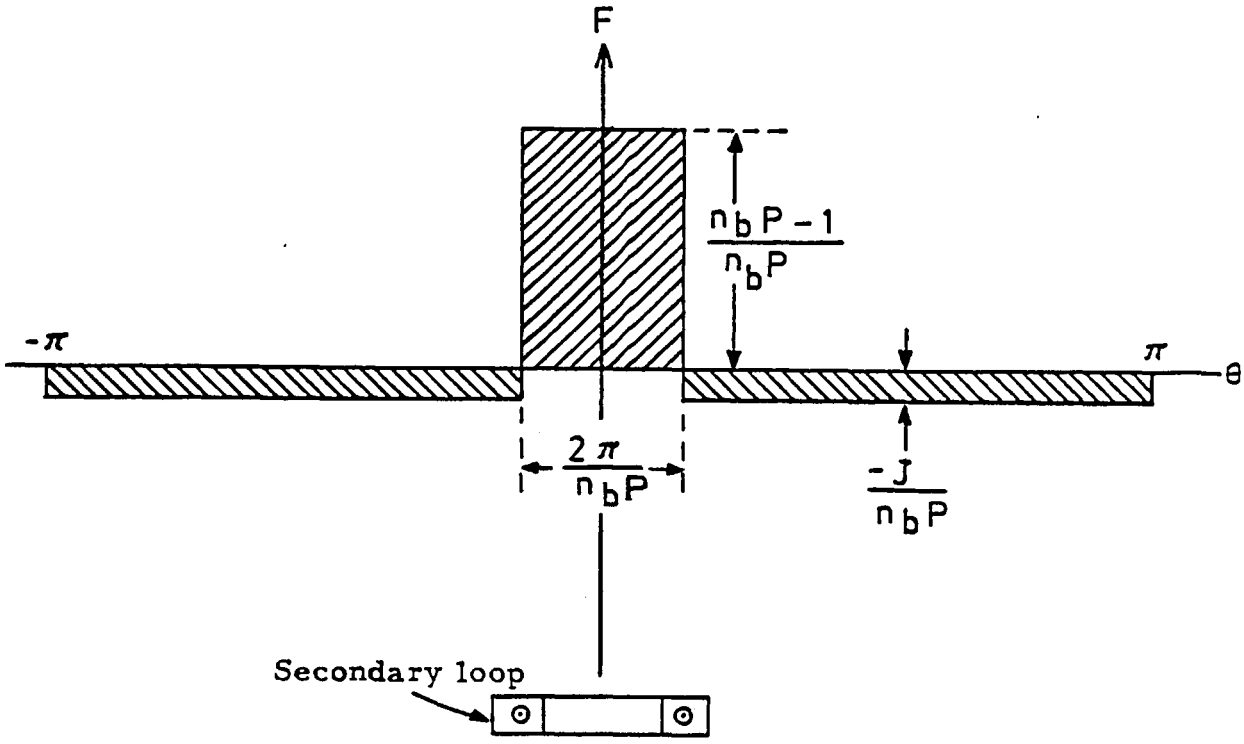

Figure 3.17 Rotor current-loop model for magnetomotive force distribution as a function of airgap peripheral location.

$$\therefore \quad \frac{k_-}{k_+} = n_b P - 1 \tag{3.96}$$

The Fourier series representation of the partial MMF wave may be reduced to a cosine series without a DC component as

$$F = \sum_{k=1}^{\infty} a_k \cos(k\theta) \tag{3.97}$$

where $$a_k = \frac{2}{\pi}\left[\int_0^{\frac{\pi}{n_b P}} (n_b P) J \cos k\theta \, d\theta - \int_{\frac{\pi}{n_b P}}^{\pi} J \cos k\theta \, d\theta\right]$$

$$= \frac{2}{\pi}\left[\frac{J\, n_b P}{k} \cdot \sin \frac{k\pi}{n_b P}\right] \tag{3.98}$$

Therefore the total MMF contribution of an isolated rotor current path is

$$F = \sum_{k=1}^{\infty} \frac{J}{\pi k} \cdot \sin\left(\frac{k\pi}{n_b P}\right) \left[\cos(k\theta - \omega t) + \cos(k\theta + \omega t)\right] \tag{3.99}$$

under the assumption that current is arbitrarily zero at $t=0$ and positive sequence waves propagate in the positive θ direction. In general, the other component currents may be included as

$$F = \sum_{n=1}^{n_b P} \left\{ \sum_{k=1}^{\infty} \frac{J_n}{\pi k} \sin\left(\frac{k\pi}{n_b P}\right) \left[\cos\left(k\theta - \omega t + \frac{2(n-1)k\pi}{n_b P} - \frac{(n-1)\pi}{n_b}\right) + \cos\left(k\theta + \omega t + \frac{2(n-1)k\pi}{n_b P} + \frac{(n-1)\pi}{n_b}\right)\right]\right\} \tag{3.100}$$

Note that the positive sequence waves differ in phase by

$$\left(\frac{2k}{n_b P} - \frac{1}{n_b}\right) \pi \qquad \text{radians} \tag{3.101}$$

while the negative sequence waves differ in phase by

$$\left(\frac{2k}{n_b P} + \frac{1}{n_b}\right) \pi \qquad \text{radians} \tag{3.102}$$

This is nothing especially new in machine theory, the phasor sum of all rotor harmonics will always be zero assuming integral k and P values until either (3.101) or (3.102) is zero or an integral value of 2π , as is standard in modulation theory. Both waves now have 2k poles and thus (3.100) is simplified to

$$F = \frac{1}{\pi} \frac{J}{k} \sin\left(\frac{k\pi}{n_b P}\right) \left[\cos(k\theta - \omega t) + \cos(k\theta + \omega t)\right] \tag{3.103}$$

To illustrate the magnitude of the synchronous crawling effect, the slotting details of a 112 kW, 8 pole cage machine (the SCIM-MK II unit) have been used to evaluate the above expressions as well as substantiating these predictions with observed locking torques. The rotor has 94 slots and the stator is wound in 72 slots. Table 3.2 presents the synchronous MMF poles for the 1st, 5th, 7th, 11th and 13th harmonics for both positive and negative sequence fields.

For the case of 80 rotor slots, the 152 pole field or 19th harmonic is synchronously locked when these fields have zero relative speed which occurs at a speed $2\omega_r/152$

Table 3.2

Harmonic Pole Numbers for Synchronous Crawling Effect

Constant Stator Slotting (72) with Variable Rotor Slotting

Rotor Slots = 94

P = 8		40		56		88		104		136	
+	-	+	-	+	-	+	-	+	-	+	-
8	180	40	148	56	132	88	100	104	84	136	52
196	368	228	336	244	320	276	288	292	272	324	240
384	556	416	524	432	508	464	476	480	460		

Rotor Slots = 92

P = 8		40		56		88		104		136	
+	-	+	-	+	-	+	-	+	-	+	-
8	176	40	144	56	128	88	96	104	80	136	48
192	360	224	328	240	312	272	280	288	264	320	232

Rotor Slots = 88

P = 8		40		56		88		104		136	
+	-	+	-	+	-	+	-	+	-	+	-
8	168	40	136	56	120	88	88	104	72	136	40
184	344	216	312	232	296	264	264	280	248	312	216

Rotor Slots = 84

P = 8		40		56		88		104		136	
+	-	+	-	+	-	+	-	+	-	+	-
8	160	40	128	56	112	88	80	104	64	136	32
176		208		224		256		272		304	

Rotor Slots = 80

P = 8		40		56		88		104		136		152	
+	-	+	-	+	-	+	-	+	-	+	-	+	-
8	152	40	120	56	104	88	72	104	56	136	24	152	8
168	312	200	280	216	264	248	232	264	216	296	184	312	168
328	472	360	440	376	424	408	392	424	376	456	344	472	328

above or below that of the rotor. Equating the negative sequence harmonic due to fundamental stator flux with the positive-sequence rotor flux harmonic

$$\frac{\omega_s}{k} = \omega_s(1-\sigma) - \frac{\omega_s\sigma}{k} \tag{3.104}$$

where the right side term represents the speed of the kP rotor harmonic relative to the primary. The solution of (3.104) is

$$\sigma^* = \frac{k-1}{k+1} \tag{3.105}$$

and if k=19 then σ^*, the synchronous locking slip is 0.90 per unit. This is the primary locking slip for this 80 slot rotor.

On first inspection of columns 1 and 7, it might appear that the higher harmonics of the stator flux as denoted by the pole number sequence 168, 328, 488, 648 reacts with corresponding pole number of rotor flux to produce multiple synchronous locking at rotor speeds that are further harmonics of the basic 19th for example at $\sigma^* = (2k-1)/(2k+1)$ evaluated at k = 19 to yield $\sigma^* = 0.9487$. Unquestionably a series of synchronous locking speeds will be produced but this obscures the major point of interest. Rather, all of these harmonic pole numbers 168, 328, 488, 648 resulting from positive sequence stator harmonics as well as the pole numbers 152, 312, 472, 632 arising out of negative sequence stator flux distributions contribute jointly to producing a very stiff synchronous locking torque at the <u>single</u> slip value of 0.90. There is an infinite series of harmonic pole

numbers at each synchronous locking slip, the only basic condition that must be satisfied is

$$k = n_b' + h_s P \tag{3.106}$$

where n_b' is an even integral multiple of the total number of rotor bars and h_s is a stator harmonic number. Suppose that h_{so} is a stator harmonic which specifically causes the terms

$$\frac{2(n-1)k\pi}{n_b P} \pm \frac{(n-1)\pi}{n_b} \tag{3.107}$$

in (3.100) to be zero, that is $k = h_{so}P$ for which

$$h_{so} - h_s - n_b'/P = 0 \tag{3.108}$$

If the primary contains any two such harmonics, h_{so} and an arbitrary h_s that will solve (3.108), the primary and secondary harmonic pole numbers will be matched. An auxiliary physical constraint is that these harmonic fields must propagate at the same velocity. Clearly the absolute speed of the arbitrary primary harmonic is ω_s/h_s and the speed difference of this harmonic with respect to the rotor motion is $\omega_s/h_s - \omega_s(1-\sigma)$. The velocity of the k^{th} field with respect to rotation is

$$\left[\frac{\omega_s}{h_s} - \omega_s(1-\sigma)\right]\frac{h_s P}{2k} \tag{3.109}$$

and by (3.106) this is equivalent to

$$\left[\frac{\omega_s}{h_s} - \omega_s (1-\sigma)\right] \frac{h_s P}{n_b' h_s P} \tag{3.110}$$

Similiarly the h_{so} propagates past the rotor at $\omega_s/h_{so} - \omega_s \cdot (1-\sigma)$ and consequently at one particular velocity, these two primary harmonics are related as

$$\frac{\omega_s}{h_{so}} - \omega_s (1-\sigma) = \left[\frac{\omega_s}{h_s} - \omega_s (1-\sigma)\right] \frac{h_s P}{n_b' + h_s P} \tag{3.111}$$

and by (3.108)

$$\omega_s \left[\frac{1}{h_{so}} - (1-\sigma)\right] = \frac{\omega_s \left[1-h_s \cdot (1-\sigma)\right]}{h_{so}} \tag{3.112}$$

$$\therefore \quad \omega_s (1-\sigma) = \omega_s (1-\sigma) \left| h_s \right| / h_{so} \tag{3.113}$$

Therefore if it is assumed that both stator fields are positive sequence, clearly (3.113) is the only solution and this demands $h_s = h_{so}$. This represents the induction phenomena, for these two components always propagate at the same velocity regardless of rotor speed. However, consider the effect of having a positive and negative sequence harmonic of the same number of poles and this can be seen by substituting a negative h_{so} value in the right side term of (3.112) as

$$\omega_s \left[\frac{1}{h_{so}} - (1-\sigma)\right] = \omega_s \frac{\left[1 - h_s (1-\sigma)\right]}{-h_{so}} \tag{3.114}$$

$$\therefore \quad h_{so} = \frac{2-h_s (1-\sigma)}{1-\sigma} \tag{3.115}$$

Equivalently

$$\frac{\omega_{s(1-\sigma)}}{2}\left[h_{so} + h_s\right] - 1 = 0 \qquad (3.116)$$

If this expression is satisfied (by operating at a speed of $2/(h_{so} + h_s)$ of synchronous) then this constitutes a synchronous locking torque. The reason that this indicates an infinite number of harmonics is due to the fact that only the summation, $h_{so} + h_s$ is involved rather than a product, the former having an infinite series of pairs.

Referring to Table 3.2 the positive sequence 168, 328, 488, ... arises out of the basic 19th harmonic ($h_s = 19$ and $h_{so} = 1$) but other contributors are listed in Table 3.3.

Table 3.3

h_s	h_{so}	Pole-numbers
25	-5	40
31	-11	88
37	-17	136
43	-23	184
45	-25	200
49	-29	232

3.4 REFERENCES

[1]Mishkin, E., "Theory of the Squirrel-Cage Induction Machine Derived Directly from Maxwell's Field Equations," Journ. Mech. and Applied Math., Vol. VII, Pt. 4, 1954, pp. 472-487.

[2]Cullen, A.L., Barton, T.H., "A Simplified Electromagnetic Theory of the Induction Motor, Using the Concept of Wave Impedance," Proc. IEE, 105C, 1958, p. 331.

[3]Tipping, D., The Analysis of Some Special Purpose Electrical Machines, Ph.D. Thesis, Victorian University of Manchester, June 1964.

[4]Powell, R.B., "Linear Induction Motor Research Vehicle Reaction Rail Edge-Effect Investigation," U.S. Dept. of Transportation, NTIS Document FRA- /ORD-76-263, April 1976.

[5]Williams, F.C., McLean, G.W., Tipping, D., "Induction Excited Alternator," Proc. IEE., Vol. 116, No. 8, Aug. 1969, pp. 1412-1418.

[6]Nondahl, T.A., Novotny, D.W., "Pole-by-Pole Model of a Linear Induction Machine Using Conformal Mapping Coefficients," IEEE Trans. Power Apparatus and Systems, Vol. PAS-98, No. 4, 1979, pp. 1345-1353.

[7]Rawcliffe, G.H., Fong, W., "Speed Changing Induction Motors: Further Developments in Pole Amplitude Modulation," Proc. IEE., Paper No. 3306U, Dec. 1960, pp. 513-528.

[8]Shturman, G.I., "Induction Machines with Open Magnetic Circuits," Elektrichestvo, 1946, No. 10, p. 43.

[9]Laithwaite, E.R., Kuznetsov, S.B., "The Development of a Stator Controlled Brushless Induction Machine with Leading VAR Capability," Electric Machines and Electromechanics Intern. Quarterly, Vol. 6, No. 3, May 1981, pp. 1-18.

[10]Carpenter, C.J., "A Network Approach to the Numerical Soluction of Eddy-Current Problems," IEEE Trans. on Magnetics, Vol. MAG-11, No. 5, Sept. 1975, pp. 1517-1522.

[11]Freeman, E.M., "Travelling Waves in Induction Machines: Input Impedance and Equivalent Circuits," Proc. IEE, Vol. 115, No. 12, 1968, pp. 1772-1776.

[12]Carpenter, C.J., "Numerical Solution of Magnetic Fields in the Vicinity of Current-Carrying Conductors," Proc. IEE, 1967, Vol. 114-11, pp. 1793-1800.

[13]Williams, F.C., Laithwaite, E.R. and Eastham, J.F., "Development and Design of Spherical Induction Motors," Proc. IEE, Vol. 106A, No. 30, December 1959, pp. 471-484.

IV. THETA PINCH CONCEPTS

4.1 THE QUEST FOR THE ROTARY EDGE

One marked distinction between the rotary and linear machines should be evident, in that it is fundamentally an easier task to effect power factor improvement at constant efficiency in the latter. This conclusion is largely independent of the differences in absolute P.F. and efficiency between the two types. Rather, this is the result of utilizing the seemingly imperfect magnetic structure of the linear machines, which has no exact counterpart in the rotary machine.

The crux of the design problem for a practical rotary θ-Pinch machine focused on artificially creating a transient edge as powerful as the physical exist-edge of a longitudinal flux LIM but in the confines of a constant peripheral airgap. It is well known from basic theory that the concept of magnetic flux may be expressed as

$$\text{Flux} = \frac{\text{Magnetomotive Force}}{\text{Magnetic Reluctance}}$$

and if it assumed that by transient, a transient change in flux is desired, then clearly two possibilities exist - either an abrupt change in MMF or reluctance will suffice. Clearly the conventional high speed LIM technology illustrates an abrupt airgap reluctance change yet when combined with the asynchronous condenses principle, both MMF and reluctance effects coexist in harmony as the main flux is gradually tapered off or "demagnetized". From the inception, it was paramount that the rotary counterpart must

only make use of MMF control since reluctance permeations in the airgap would entail unnecessary magnetization or magnetic noise penalties. Despite the fact that the θ-Pinch machines would only rely on one central electromagnetic mechanism, MMF (magnitude and phase) control, the implementation of this scheme is more complicated than the dual mechanism LIM-ASC machines. The reason is simply that in the rotary units, one MMF pattern must both initiate the flux transients as well as utilize them. On the surface this appears to be contradictory - analogous to literally "pulling itself up by its own bootlaces". Yet here lies the beauty of the induction machine, for the polyphase θ-Pinch machine along with the single-phase induction motor performs in just this fashion.

The development of θ-Pinch in the research labs was essentially a quest to find a rotor transient that decays as slowly as possible for a given physical size and to perpetuate such transient phenomena.

The primary purposes for which the 35 H.P. test facility was built were to:

a. validate the asynchronous condenser calculations on a multi-polar machine;

b. experimentally measure rotor time constants for medium size cage machines;

c. determine the amount of ASC armature reaction under differing current loadings and relative ASC section lengths.

The single most valuable outcome of the Theta-Pinch research has been to ascertain the exact amount of "pole-shrinking" that exists over the inductively-fed ASC windings. The effect was first reported in [1] and while the theory behind pole-

shrinking was clear, test results did show some discrepancy. For example, basic short-stator theory predicts that the amount of pole-shrinking is directly related to σ, the fractional slip, but in practice, from both LIM and θ-Pinch tests, it appeared that ASC wavelength was also a function of the machine Goodness factor. Further theoretical work suggested that the ASC phase change per pole was simply related by the function $\tan^{-1}(1/\sigma G)$, but the θ-Pinch testing revealed that this function is too simplistic for serious design reliability. The importance of this one parameter lies in the fact that if the ASC wavelength is not perfectly specified, then every coil in the ASC has a progressively larger phase error (in the direction of rotor rotation) meaning that the ASC utilization/coil could vary from 100% reactive lending to being an induction brake with lagging current.

To give some idea of the value that the laboratory machine served, before the machine had gone on test, calculations were made (based on a combination of theory and scaling of the LIM-ASC-I test results of ASC wavelength) to estimate the exact reduction in pitch for the ASC coils that should then be specified supposing the 35 H.P. unit were to be completely rewound with two distinct pole-pitch windings. The first tests of the Theta-Pinch machine proved that actually the best estimates of pole-shrinking were too conservative, the influence of the Goodness factor had been overestimated (for the two experimental machines under comparison had Goodness factors differing by a ratio of 1:3). The final tests on the θ-Pinch machine showed that at 50 Hz excitation, operating at 105% rated current, 73% of the airgap flux density of the original P.A.M. specification, the dynamometer was at full load at the motor slip of 6% for which the phase readings indicated that the pole-shrinkage was 11.1%--about 100% larger

than expected for this slip setting. For the last winding configuration that had been investigated, this amount of pole shrinkage amounts to a phase error of 59 degrees at the last ASC coil. Had this 35 H.P. machine been rewound with two different pitches of 0.0989m and 0.0879m, then the ASC section would be operating at 100% utilization, i.e., no braking effect or circulating real power.

The last θ-Pinch winding configuration under study and test is shown in Figure 4.1.

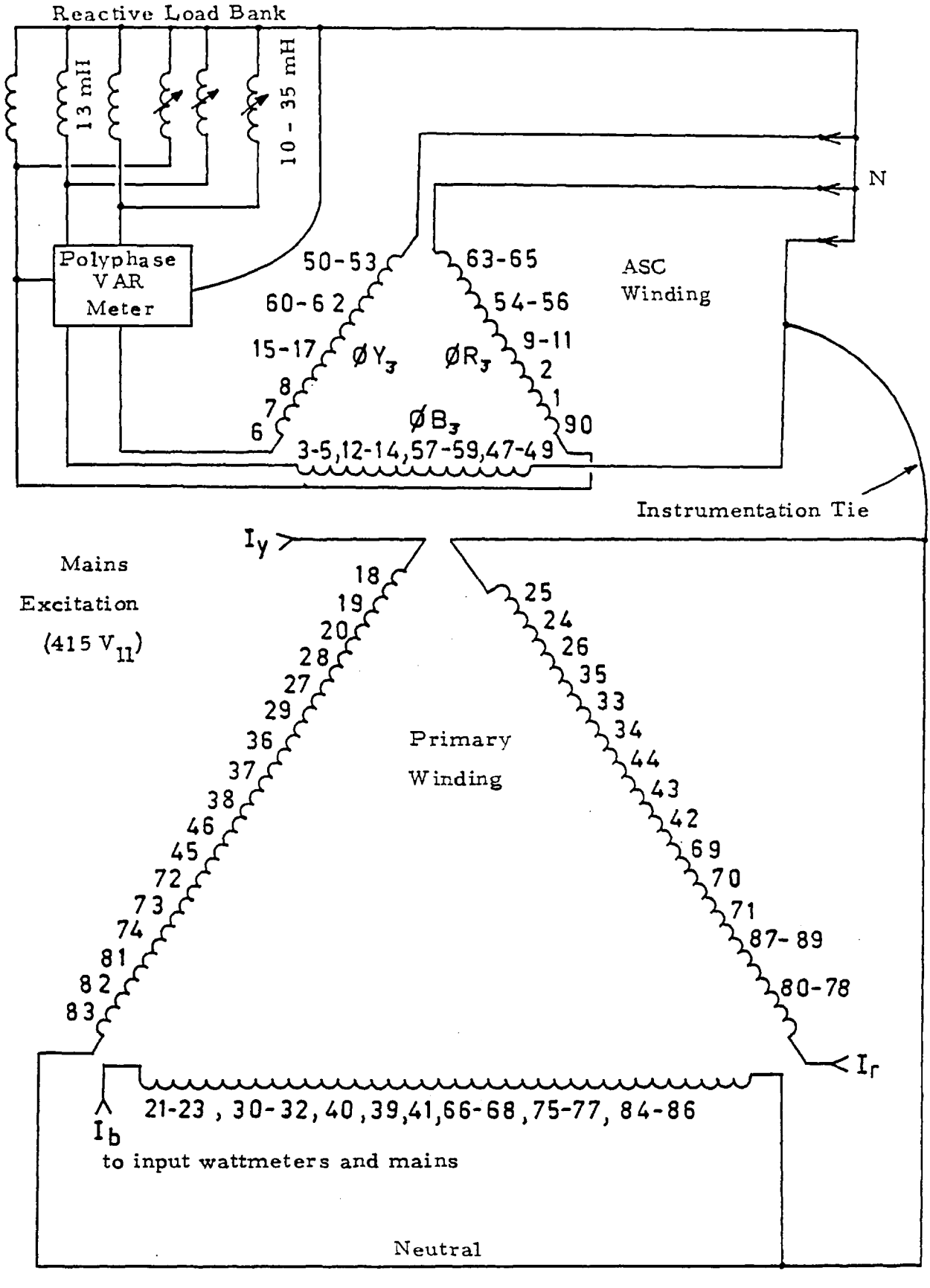

Figure 4.1 Winding layout for the 26 kW, ten-pole machine without pole-amplitude modulation of either primary or tertiary (ASC) sections for harmonic speeds verification and reactive VA generation.

4.2 ROTARY MACHINE CONVERSION

The experimental program for the first SCIM rotary machine modification commenced with the installation of a 35 H.P. Lancashire Dynamo squirrel cage P.A.M. motor directly coupled to a 17 H.P. DC dynamometer. A digital, optical tachometer was fitted to the shaft to allow very accurate slip measurements to be recorded every 8 ms. The original equipment manufacture specifications for the PAM motor are included in Table 4.1. The winding diagram for this 10/12 pole machine as originally connected is shown in Figure 4.2 for one-repeatable winding section which is one-half of the machine's periphery.

The state of the modification work is depicted by Figure 4.3 where the PAM unit has its end cover removed and 180 coil terminal connections are exposed for attachment to instrumentation leads. It was decided to concentrate on coil terminal voltage measurements without recourse to fitting a set of 90 "top-of-tooth and slot" search coils. This was justified on the basis that the working room in the stator bore of this machine is simply too small to permit hand machining of search coil slots (approximately ¼mm deep) axially down the center of every tooth. If in industry, the preliminary test results appear promising then an automated machining jig is essential since the search coil information is vital in the last stages of machine modification and optimization.

Table 4.1

Characteristic Parameters of the "θ-Pinch" Rotary Machine

Stator

Bore diameter, mm	316
Number of slots	90
Conductors in parallel/coil	2
Copper cross section/parallel, mm^2	5.25
Coil throw slots	1-11 incl.
Core length, mm	235
Slot depth, mm	34
Slot width, mm	6.0
Slot pitch, mm	11.1
Coil span, m	0.111
Pole-pitch, m (as 10 pole)	0.0989
Number of turns per coil	6
Pole-pitch/air-gap ratio	164
Chording factor (10 pole)	1.115

Rotor-Squirrel cage

Number of bars (copper)	80
Bar width, mm	5.0
Bar depth, mm	8.0
Copper end ring, mm	6.5x25.4
Slot pitch at bottom of slot, mm	10.9
Tooth top width, mm	10.0
Ratio slot opening/airgap	1.5
Moment of inertia with DC Dynamometer, $N\text{-}m\text{-}sec^2$	7.98

Nameplate Data with Original Pole Amplitude Modulation

Class E insulation, 50 Hz, Lancashire Dynamo & Crypto, 1964

	10 Pole Winding	12 Pole Connection
Voltage, 1-1	400 (440)	400 (440)
Connection	Star	Delta
Horsepower	35	20
Speed, rpm	575	480
Current, A	54.5 (49.5)	35.9 (32.7)
Complex Power, S	37.76 kVA	24.87 kVA
Output Power, P_o	26.11 kW	14.92 k W
Power Factor-Efficiency Product	0.691	0.598
Power Factor (max.)	0.78	0.67

- denotes reverse phasing

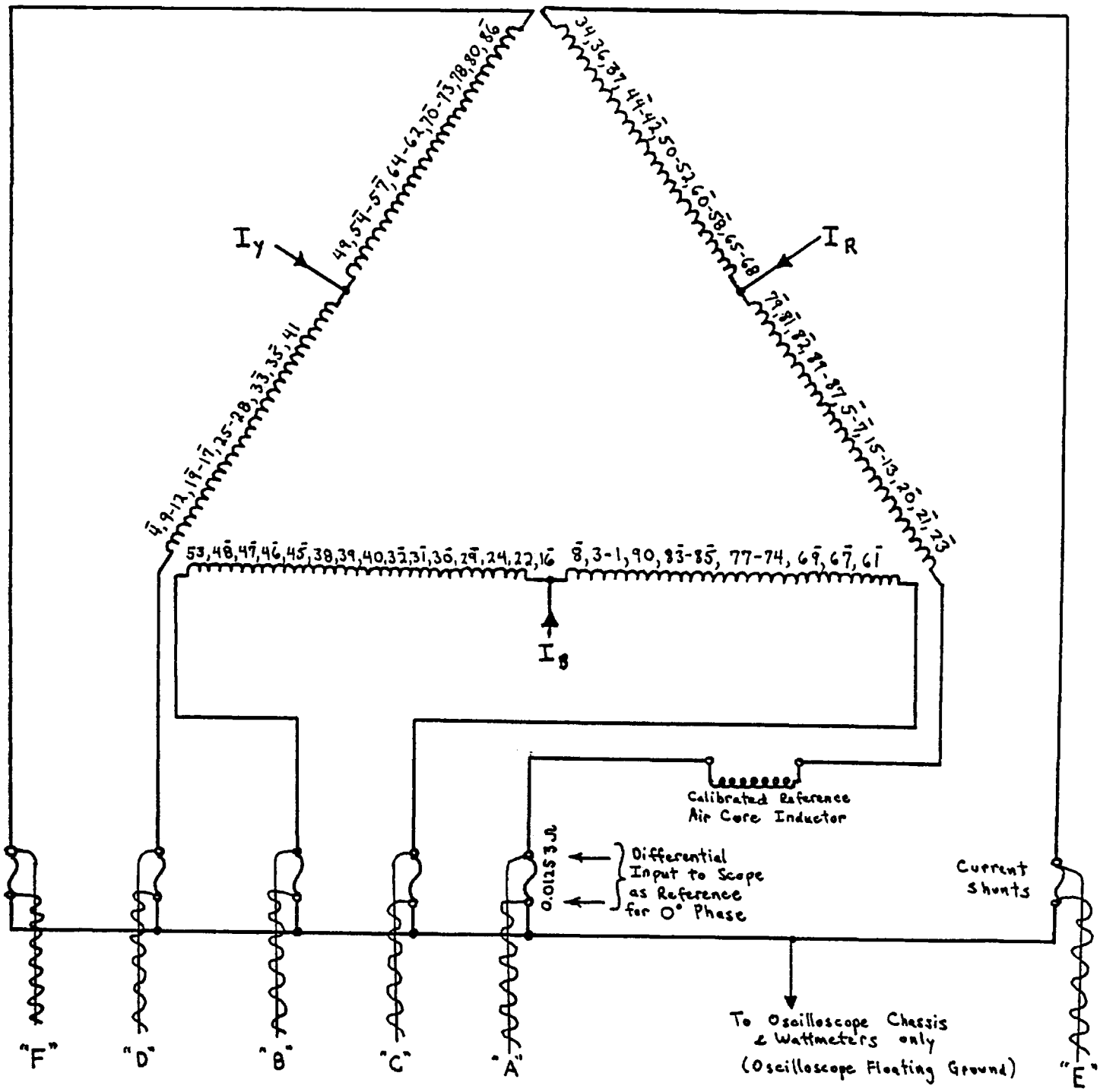

Fig. 4.2 Coil connections and instrumentation references for the 35 H.P. PAM motor, normally connected in a 10-pole mode. Differential (2 wire) instrumentation leads fitted to all 90 coils.

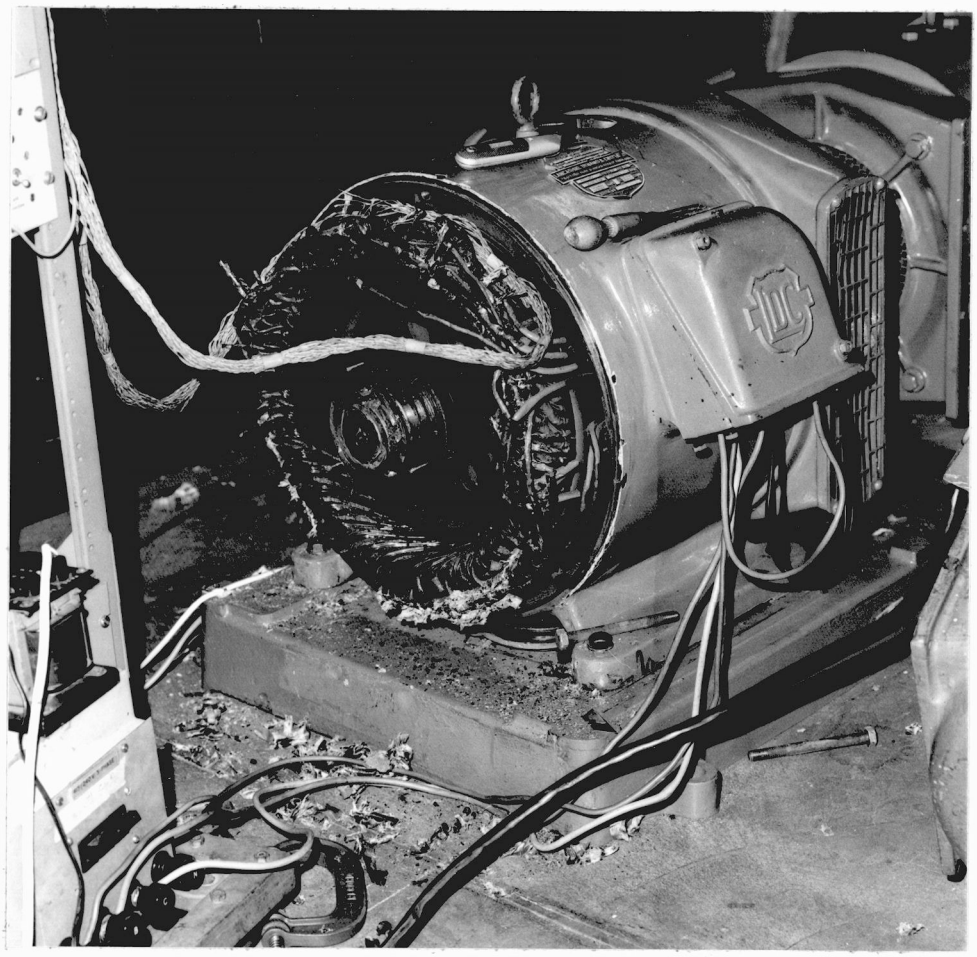

Figure 4. 3 Modification of the 26 kW pole-amplitude-modulation machine for Θ-Pinch tests and coil instrumentation.

4.3 POWER DISTRIBUTION WITH POLE AMPLITUDE MODULATION

The instrumentation of the 35 H.P. 10/12 Pole PAM motor (built by Lancashire Dynamo and Crypto, circa 1964) as an initial check on the reactive power flow and balance between parallel phases in the Y connection, revealed several astonishing problem areas with this first type of PAM. In general there was excellent balance between parallel paths in both magnitude and phase, moderate balance between dissimilar phases for the total phase current, but the most prominent effect was that at small slips when running as a 10 pole machine, the real power distribution between coils of the same phase group was widely divergent and predictable. For example, at 40% of rated voltage and running light at exactly synchronous speed (DC dynamometer acting only as additional windage and friction), the distribution of real power for groups of 3 and 4 slots/pole/phase resembles that of a high Goodness linear machine (at, say 5% slip) in that the "leading" coil in each group will have the worst power factor and the last coil in the group will always have the best power factor.

As expected with a high Goodness machine, such as the test machine, the variations of the induced coil voltages in both magnitude and phase step among coils of any group or between groups are minimal. That is, the cage is very effective in damping out MMF harmonics. The original stator MMF distribution of the 10 pole configuration is given in Table 4.2 for positive, negative and

Table 4.2

MMF Harmonics of the 35 H.P., 10 Pole Machine Connected as PAM[1]

Calculation: 90 Coils, Coil Throw 1-11, 15 coils per phase group in series

Harmonic Number	Positive Sequence	Negative Sequence	Zero Sequence
1	27.1%	5.8%	9.5%
3	6.1	5.0	17.0
5*	100.	0.0	0.0
7	0.1	1.0	35.5
9	0.0	0.0	0.0
11	1.8	1.4	2.9
13	3.8	0.4	1.5

* Base Wavelength

1 Y-Connection

zero-sequence fields, at both supersynchronous and subsynchronous speeds. Even when the leakage reactance drop of each coil is considered (at 12% of rated current), the phase of the coil terminal voltage will always change in 18 to 22 degree steps, for an average flux step of 20 degrees per slot. In short, the PAM machine has balanced phase currents, uniform induced stator voltages, uniform phase changes per coil but only one major discrepancy remains....the phase angle between the rotor flux and the stator current is rarely perfect for either optimization of efficiency or power factor. Examining the PAM's four phase groups of each repeatable section (5 poles) which contain 4 slots/pole/phase, four distinct categories arise which may be characterized as:

a. the net real power transferred by the group is negative (generating mode).
b. all coils in the group have positive real power flow.
c. the net power transferred by the group is zero.
d. the net power transferred by the groups is positive.

A plot of the real powers per coil measured at the individual coil terminals is shown in Figure 4.4 for the four categories listed above, the average real power absorbed per coil should be about 4.4 W/coil, although the degree of circulating power in the machine has allowed some coils to absorb as much as 30 W/coil and others to generate as much as 28 W/coil. As illustrated in Figure 4.5 , the first group of 4 slots/pole/phase, being the most unusual, has power factor angles ranging from 82^{o} to 140^{o}; two

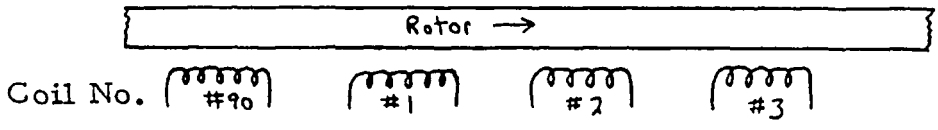

Power	-22.6	-15.5	-6.6	4.19	Watts

a. Net power is negative (generating)

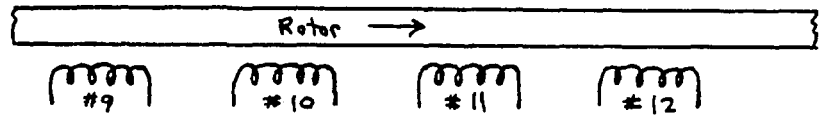

4.67	13.9	22.1	27.4	Watts

b. All coils have positive power

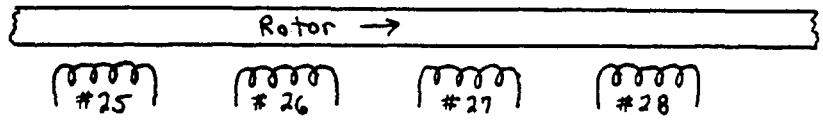

-14.2	-5.1	4.64	14.2	Watts

c. Net power ≈ 0

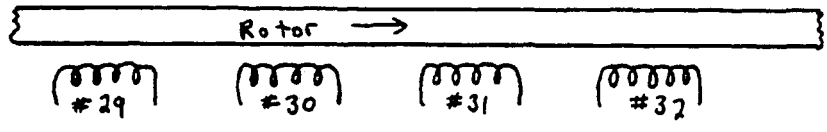

-5.34	4.83	15.2	23.4	Watts

d. Net power is positive

All coil volts ≈ 8.5 V, all coil currents ≈ 3.5 A r.m.s., 50 Hz

Fig. 4.4 Variation of real power transfer depicting four distinct categories for coil groups of 4 slots/pole/phase in the original 10-pole PAM winding at 40% rated voltage and running light, average power/coil is 4.44 Watts.

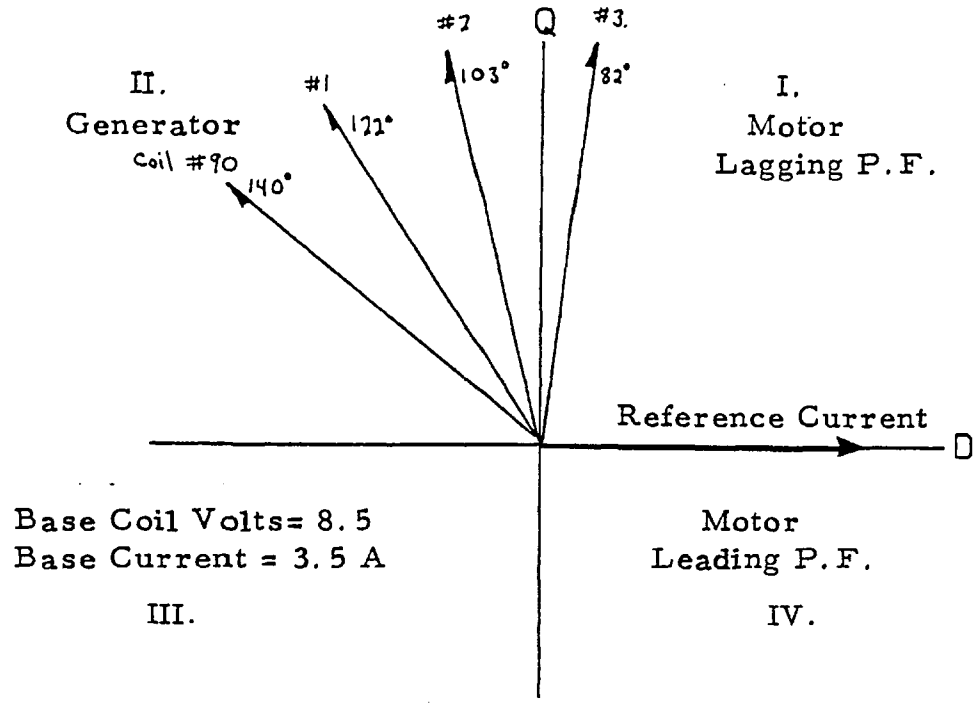

Figure 4.5a Phasor diagram of least favorable coil group of 4 slots/pole/phase at 40% rated voltage, original 10 pole PAM, σ=0.005

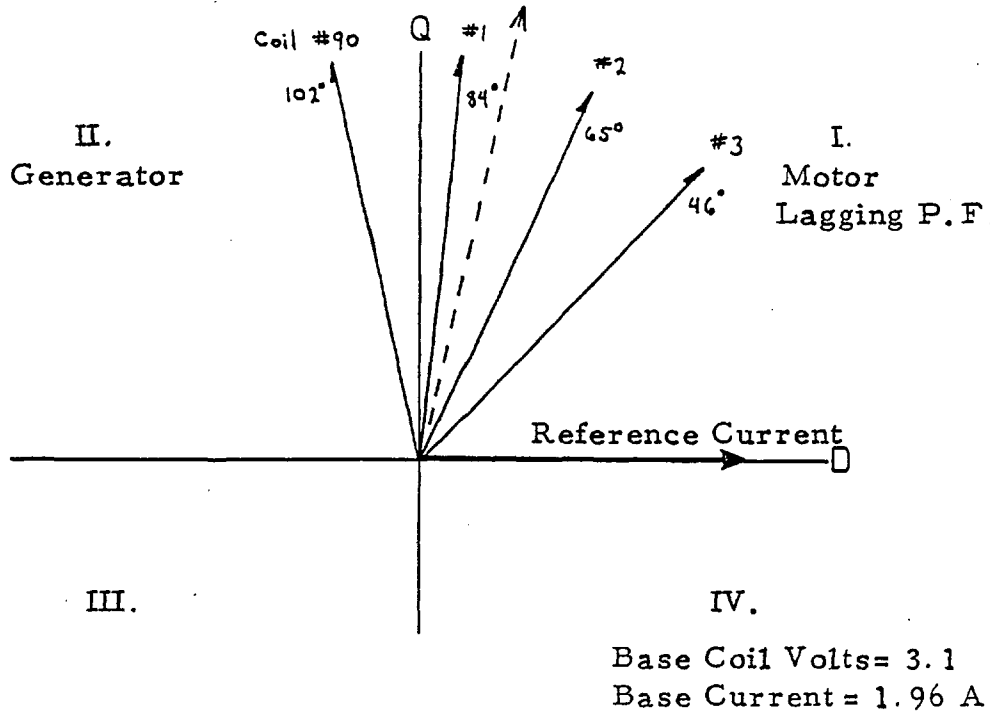

Figure 4.5b Phasor diagram of least favorable coil group of 4 slots/pole/phase at 15% rated voltage and running light on 50 Hz.

isolated machine coils have angles of 164° and six isolated coils have power factor angles of 3 to 5° (i.e. nearly unity power factor). The overall power factor angle for this machine at 40% of rated voltage, running light is 78°.

In essence, operation of the machine in this manner with its associated very poor overall power factor of 0.20 is a direct result of "overfluxing" the airgap by impressing too high a terminal voltage in this case. The apparent power consumed by the machine is to a first approximation simply proportional to the square of the applied terminal voltage, and thus the only way that the machine can supply its running light losses with such a high VA input, is to have, as expected, very large phase angles between coil voltages and currents. However, the situation is complicated by the fact that, unfortunately, the power factor of the overall machine cannot be the same for each coil primarily due to use of stator windings with greater than 1 slot/pole/phase. Thus practical phase groups of 4 slots/pole/phase must necessarily have widely divergent power factors; in a conventional induction machine the average power factor for each group will generally match that of the entire machine, while in the PAM induction motor this will no longer be the case due to the MMF harmonics. The result is that there is a larger degree of real power variation in the PAM stator coils for a given net power transfer, the consequence of this being excess rotor copper losses at any speed. This effect has been experimentally verified.

The two important conclusions to be deduced from Figures 4.4 and 4.5a are that first, even in the "over-fluxed" state, the 10 Pole PAM has no coils at all that show leading power factor. Moreover, though there is excellent phase balance this is accomplished at the expense of having numerous coils contribute nothing to the in-phase flux component of the machine (and this continues to be the case even at 35 H.P. rating, although less severe).

However, the benefit of this first study of PAM came after an inspection of the "underfluxed" phase plots of the machine when running light, i.e. the applied terminal voltage was 15% of rated 415v, which represents an airgap forced VA loading of only 2.25% of the maximum rated apparent power occuring at about 4% slip. Comparing Figure 4.5b, the phasor plot for coil group 90-1-2-3 for the 15% voltage case with the 40% voltage test runs shown in Figure 4.5a, one immediately notices that the "under-fluxed" phasors as a group have been phase retarded by a constant 38^{o}, i.e. a greatly improved overall power factor. The six coils which were formerly operating near unity power factor now were well within the leading power factor region and an additional six coils shifted back into the leading region, at about $10\text{-}15^{o}$. The major point of interest is, only isolated coils or at best groups of two slots/pole/phase will operate in the leading region.... these are the so-called "phase balancing coils" discussed previously which are generally undesirable in terms of MMF harmonics. The phasor plot for the twelve coils operat-

ing in the leading power factor region is included as Figure 4.6.

While the PAM motor was not specially fitted with airgap search coils as had been the case with LIM-ASC-I, the theoretical calculations of the PAM machine slot-leakage reactance indicate that if the voltage behind the slot leakage reactance is taken into consideration rather than coil terminal voltage, the one underfluxed case examined above has at least a total of 16 coils out of 90 with capacitive VAR output. Nevertheless, the point remains that the underfluxed PAM tests are of relatively minor significance since the VA rating of the machine is too far below the rated 37.7 kVA. The next step forward is, obviously, to maximize the number of coils operating in the leading power factor region, and seemingly a full kW load will cause the locus of all phasors to rotate backwards by a nearly equal amount; substantially improving the Quadrant I power factors and allowing the Quadrant IV phasors to more nearly approach the maximum capacitive kVAR position. But in reality and despite the fact that we have a very "stiff" (i.e. low resistance) rotor, the law of diminishing returns takes hold because by increasing the number of coils in the leading region (say by change in slip, load torque, or reconnection), the amount of leading VAR per coil drops off since the rotor flux increasingly tends to shift back in phase in proportion to the integral of the quadrature component of the stator MMF. Subsequently the θ-Pinch mechanism was found to be a viable solution.

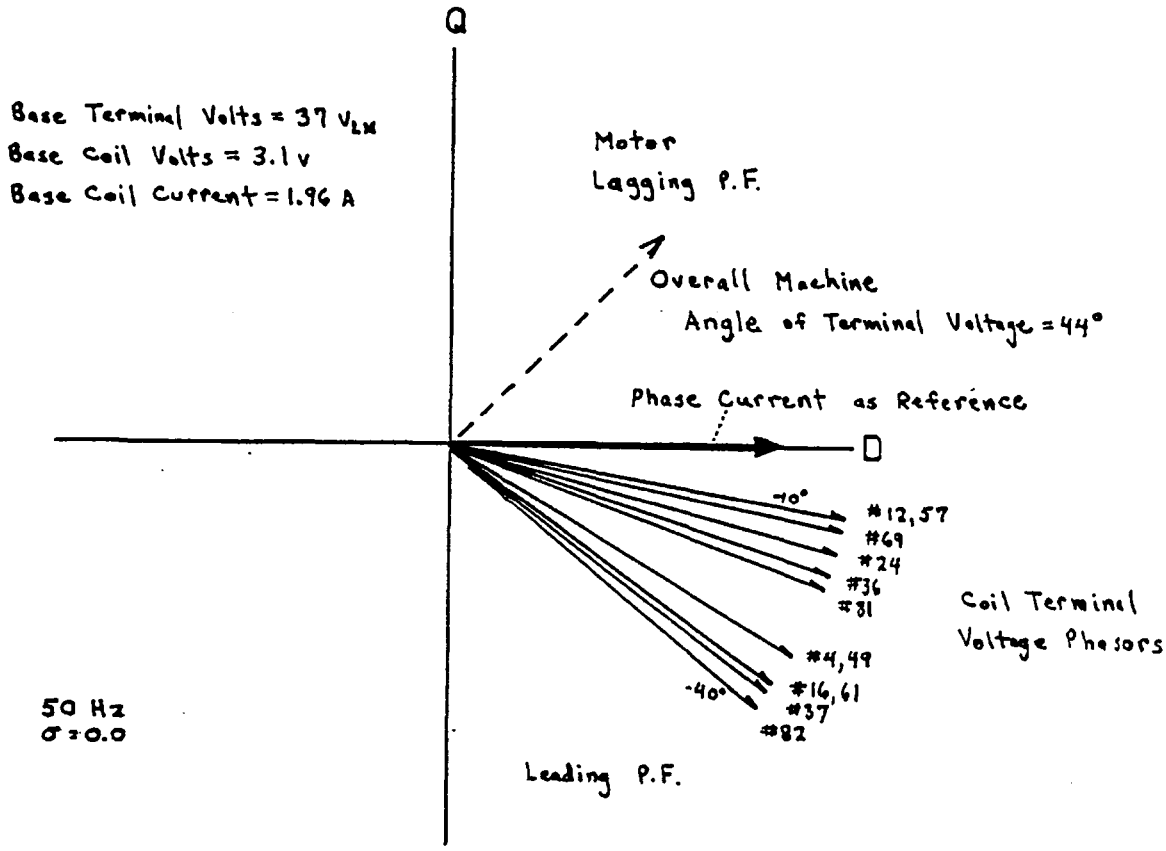

Figure 4.6 Distribution of twelve leading-power-factor coils in the original PAM winding at 15% rated voltage.

Physically, the mature distinction between rotary and linear versions of the ASC concept is that in the latter, a discrete section length of the machine is strictly devoted to reactive power generation (i.e. an induction generator with cos ϕ=0) whereas the former will have to incorporate a continuously mixed space distribution of real and reactive power roles. This is shown diagramatically in Figure 4.7 . It is easier to effect P.F. improvement in the linear machine since the nearly independent kW and kVAR windings are physically isolated in space (as well as in time). Air gap efficiency of a conventional rotary cage induction machine is nearly unity in all cases and is computed as, neglecting iron, stator I^2R, windage and friction losses,

$$\eta = \frac{P_o}{P_o+P_r} \leq 1-\sigma \qquad (4.1)$$

where P_o is the mechanical power output, P_r is the rotor copper loss including excess or "missing" watts, and σ is the per unit slip. Simply, the experimental objective is to ensure that the inequality expressed in (4.1) is as near unity as possible. The efficiency of these induction machines need not approach the maximum efficiency of 1-σ for symmetrically wound stators. The B_p-B_q theory can predict efficiencies above or under 1-σ for short stator or discontinuous winding machines and this is covered in section 2.3 .

A more exacting way to view the challenge between dividing the rotary machine into "territories" of real

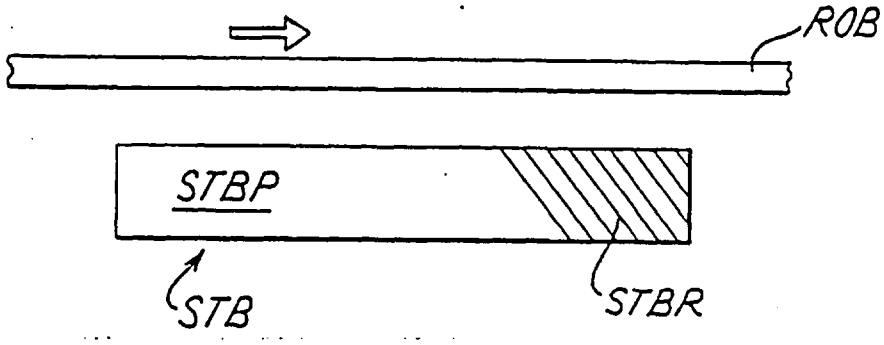

Figure 4.7a Unidirectional application of reactive recovery windings (STBR) to linear machines with propulsive section (STBP).

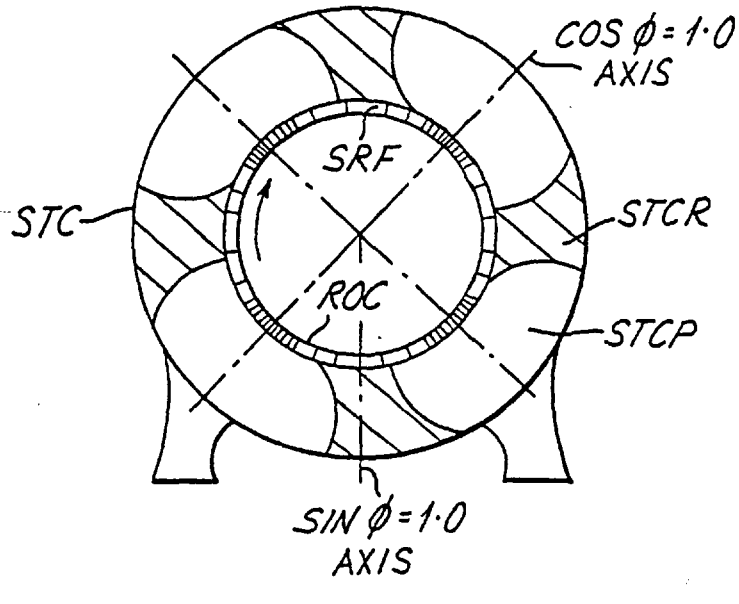

Figure 4.7b Unidirectional application of reactive recovery windings (STCR) to rotary machines with propulsive sector (STCP).

and reactive power flow is to compare the relative difference between two figures of merit applicable to either conventional or "ASC-assisted" machines.

$$\frac{B_q}{J_s} = k_1\sqrt{Q_{gen}} \qquad (4.2)$$

$$B_p x\ J_s = k_2\ P_o \qquad (4.3)$$

where J_s is the stator current loading, B_q is the airgap flux density in time quadrature with J_s, B_p is the in-phase airgap density, P_o is the output power and Q_{gen} is the generated (or absorbed) reactive power.

The important conclusion to be drawn is that unlike large-airgap linear machines which tend to have low values of both B_p/J_s and B_q/J_s, the rotary experimental ASC motor must necessarily have much higher B_q/J_s ratios; for example the 35 H.P. PAM lab machine has a B_q/J_s ratio better than 7 times that of "LIM-ASC-I". Over a broad range of electrical machines there is rarely more than a 2:1 variation in J_s for air-cooled stators, in contrast to the typical 10:1 difference in airgap flux between low speed and high speed machines, if not between rotary and linear types. Moreover, the operating scheme for the ASC-SCIM units is consistent with the requirement that the B x J product integrated around the machine periphery remains the same as before--although the space distribution of B_p is sparser than before, this is compensated for by the increase in magnitude.

Lastly, it should be emphasized that the rotary SCIM

retains the squirrel-cage rotor intact, maintains the airgap at the previous value of 1 mm, and utilizes symmetrically spaced slots of equal width.

4.4 THE INITIAL θ-PINCH EXPERIMENTS

The modification of the 35 H.P. PAM motor to a full fledged θ-Pinch universal test machine was carried out in two steps. First, after a series of exacting phase measurements on the 10 pole PAM were performed at 50 Hz with dynamometer loading, two groups of coils were identified, those that exhibited capacitive kVAR at any operating point in the tests and those coils that repeatedly were classified as Quadrant II (current the D-axis reference) implying real power generation, i.e. braking at a lagging power factor. In all cases, the machine showed nearly perfect half-periphery electromagnetic symmetry, and for the former coil types, six distinct pairs were immediately identified with predictable kVAR output. Interestingly enough, in reference to the latter group, the total number of pairs of coils with phase angles around 140-160^{o} was also found to be six.

With the goal of power factor improvement to take place at constant efficiency, the next logical development was to reconnect the twelve coils from the second group either in another phase path (10 alternatives exist, only one of which may be correct) or else reverse the coil connections, as was the case with one pair. The characteristic parameters of the θ-Pinch motor are tabulated in Table 4.1 and the details of the coil reconnection and the associated new phase angles are shown in Table 4.3 . Reference Figure 4.2 for the original connections. The experiment was a success; at a slip of about 2%, 24 coils out of 90 simultaneously drew leading power factor current

Table 4.3

Summation of Real and Reactive Powers for the 24 Leading Power Factor Coils at 15% rated voltage, running light.

	Original PAM Connections					With Reconnection of 6 Pairs			
Coil Pair Numbers	Group Type	∠Voltage	Θ_{rf}	Watts	VARs	Group Type	Θ_{rf}	Watts	VARs
4,49	D-	284°	-31°	10.35	-6.22	D-	-31°	10.35	-6.22
8,53	C-	6.7°	125°	-6.92	9.89	B+	-58.9°	6.26	-10.3
12,57	D+	83°	-10°	11.89	-2.09	D+	-10°	11.89	-2.09
16,61	B-	164°	-36°	9.77	-7.10	B-	-36°	9.77	-7.11
20,65	A-	250°	116°	-5.30	10.85	A+	-64.1°	5.32	-10.85
21,66	A-	269°	97°	-1.47	11.99	A+	-83.2°	1.47	-11.99
24,69	B+	323°	-15°	11.67	-3.13	B+	-15°	11.67	-3.13
33,78	D-	149°	104°	-2.92	11.72	F+	-73°	3.53	-11.55
36,81	E+	206°	-18°	11.48	-3.73	E+	-18°	11.48	-3.73
37,82	E+	225°	-37°	9.64	-7.26	E+	-37°	9.64	-7.26
41,86	C-	130°	126°	-7.10	9.77	F+	-54°	7.13	-9.77
45,90	C+	210°	102°	-2.50	11.81	B-	-82°	1.68	-11.96
				38.59W	36.5 VAR			90.22W	-95.98 VAR

Base Coil Volts = 3.01 v
Base Coil Current = 1.96 A
Base Group VA = 11.80 VA/pair x 12 = 141.6 VA

Utilization Factor = $\frac{\sqrt{P^2 + Q^2}}{\text{Base Group VA}}$

PAM Utilization = 37%
(24 coils only)

Reconnection Utilization = 100%
(for these 24 coils only)

For Group Types see Figure 4.2

with no readily discernible loss of efficiency. The only problem was that the reconnections resulted in unbalanced phases which had to be compensated for by uncoupling the individual auto-transformers from the ganged operating shaft to ensure equal currents at the expense of different phase voltages.

In contrast to the LIM-phase shifter experiments with current feedback into the mains, the method first tried on the Θ-Pinch motor manifest a power factor improvement by means of voltage reduction. In short, the major reason why no externally adjustable phase shifter was needed with these experiments was because the rotor flux is so much stiffer in the rotary machine as a direct consequence of having a Goodness Factor nearly six times that of LIM-ASC-I; therefore the rotor flux phase can be accurately estimated and virtually no trial-and-error phase tracking need be performed. This particular convenience changed however, when later experiments lumped more leading current coils directly adjacent rather than the quasi-random distribution found in the first tests.

The initial modifications performed on the rotary machine improved the power factor of the machine when connected as a 10 pole unit at the expense of derating the same machine when run as a change pole machine for 12 poles, i.e. the true Pole-Amplitude-Modulation characteristic effected by a simple contactor changeover has been sacrificed in the experimental machine. However, in general, the Θ-Pinch method is applicable to PAM motors as long as

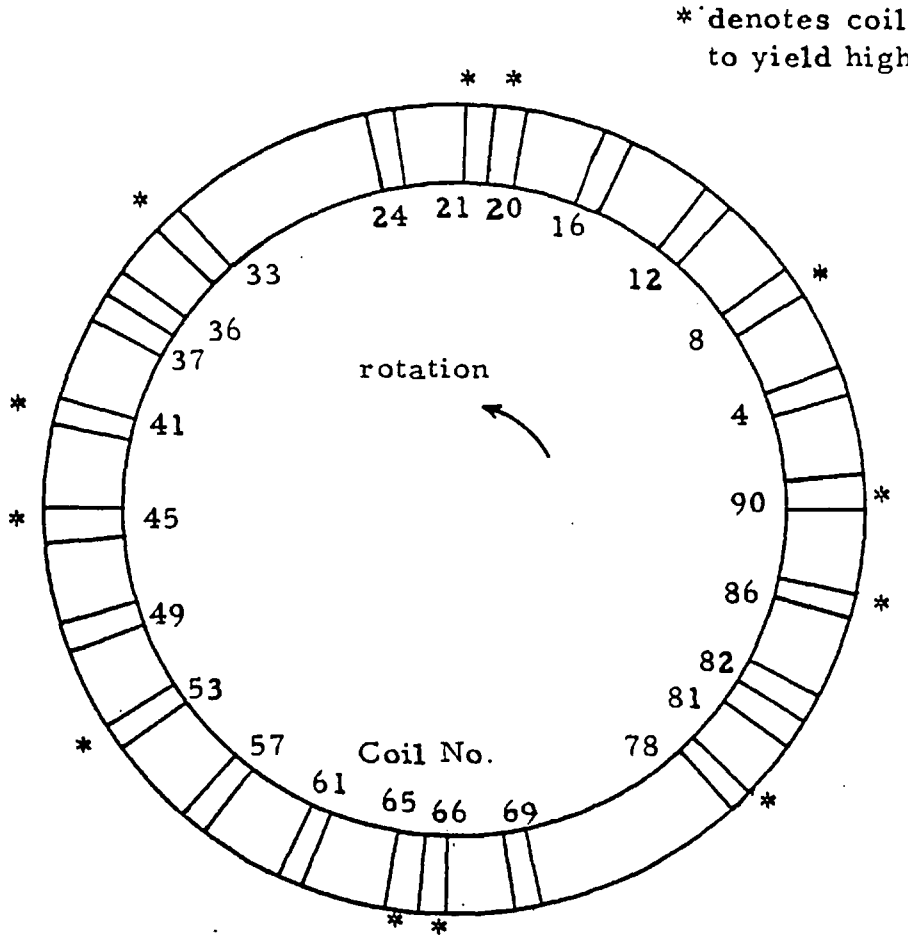

Fig. 4.8a Experimental, distributed winding with 24 leading P.F. coils, $\sigma = 0.005$

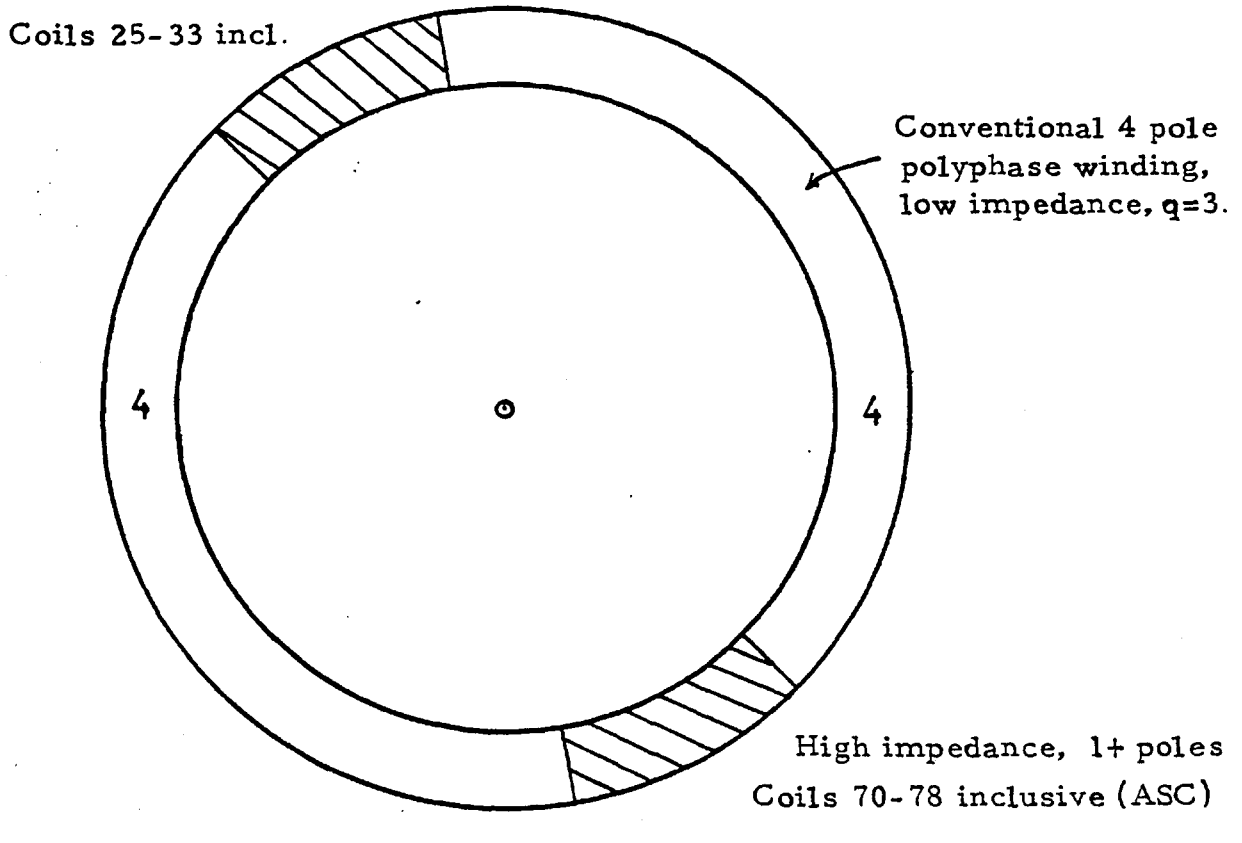

Fig. 4.8b Conceptual diagram of the lumped-winding, Θ-Pinch method.

they are of the "close-ratio" type. [2] The 10-pole speed was selected in preference to the 12-pole speed on the basis that the former had a significantly higher power factor-efficiency product (0.69 versus 0.60) as original equipment manufacture. Secondary reasons for choosing the 10-pole speed are based on the Y-connection (preferable for instrumentation), higher power output, better matching to the high speed dynamometer, and reduced MMF harmonics.

The location of the 24 leading power factor coils is shown diagrammatically in Figure 4.8a for the distributed coil method in contrast to Figure 4.8b which represents a full fledged example of a lumped θ-Pinch approach, the one used in the next series of tests; composed of 8 poles of main winding and 2-plus poles of asynchronous condenser windings spaced as $4\text{-}1^{+} - 4 - 1^{+}$. Note that here we say 2-plus poles of condenser because the first tests had the condenser sections supplying a passive inductive load (as was done with LIM-ASC-I) which substantiated the "natural" pole pitch of an inductively-fed stator to be less than the main pole pitch by approximately $(1-\sigma)$ where σ =per unit slip. The reason that the asynchronous condenser concept is so appealing is because its performance naturally peaks at synchronous speed and in rotary machines, the on-load operating speed is so close to synchronism that the reduction in peak condenser output is only 4% at 2% slip, as shown in Figure 2.54.

Throughout, the primary research objective is to ensure the phase displacement between condenser and motor

windings is perfect for reactive power compensation with nil braking torque inside the machine. If the designer is given only one frequency, one voltage, one mechanical load and slip to work at, then the exact phase displacement translated into coil connections has a unique value and this is what has been done in Figure 4.9.

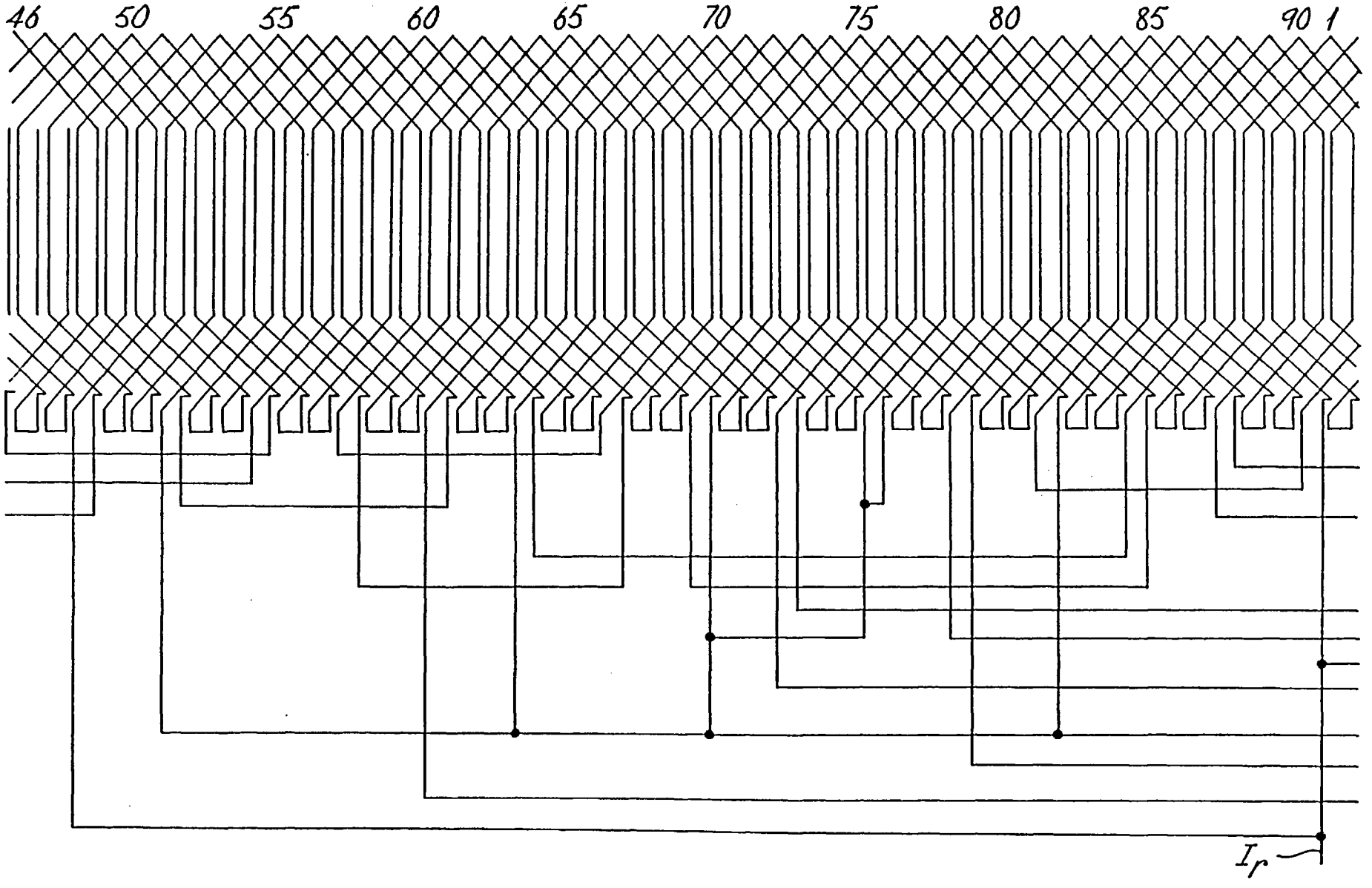

Figure 4.9 Developed diagram of connection sequence for a fully-rated, 10-pole cage induction motor using the Θ-Pinch power factor improvement method and valid for machines with Goodness factors of 75-100 and at a slip of 0.02 per unit on 50 Hz.

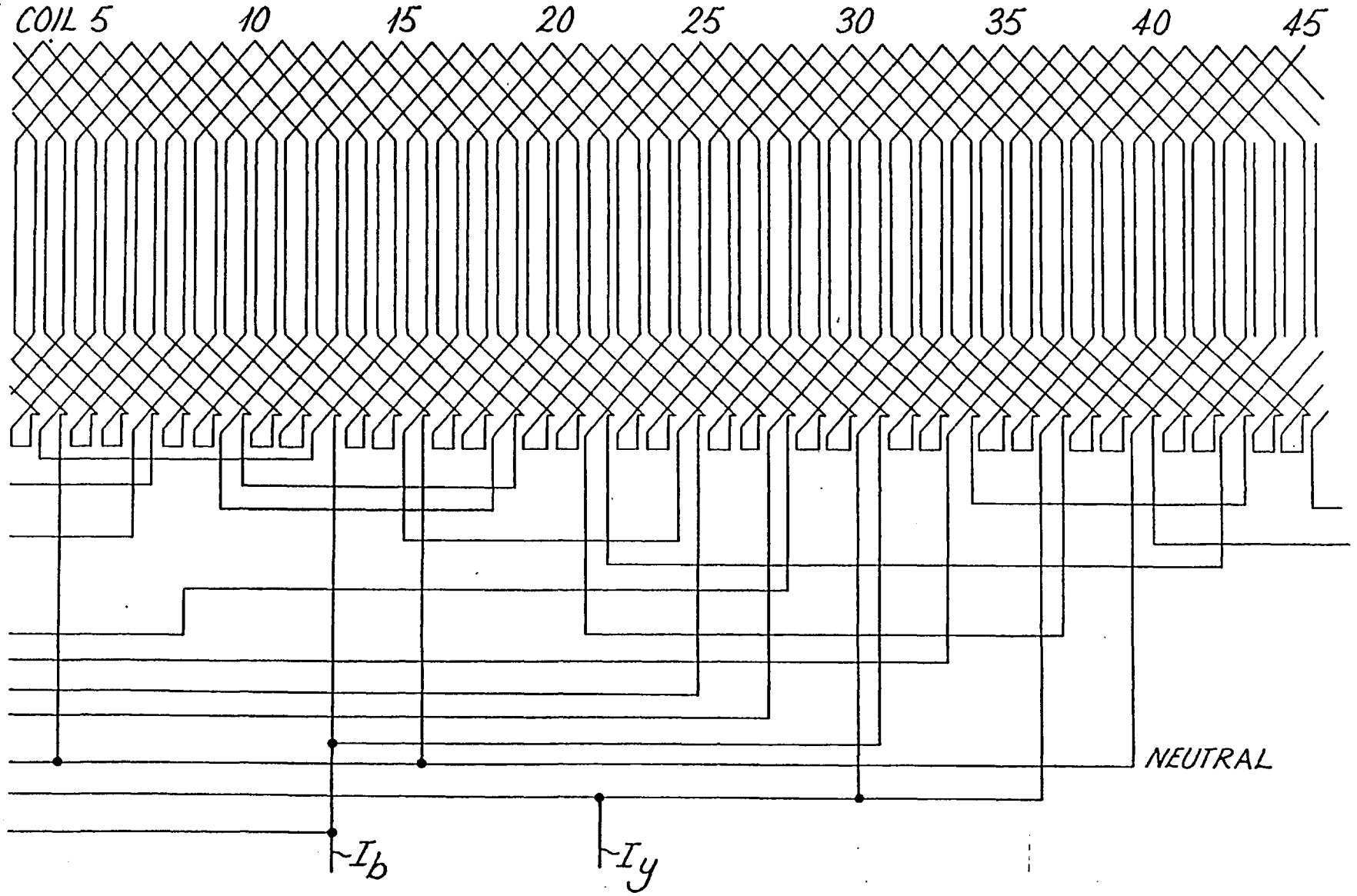

Figure 4.9 continued

4.5 REACTIVE BALANCE MACHINE

Figure 4.10 shows the distribution of the windings in the 35 H.P. rotary machine with symmetrically spaced slots of a conventional ten-pole frame. Each repeatable section of power winding, STDP is a four-pole, three-phase over-chorded winding with pole-amplitude-modulation coil connections. The reactive recovery stator section, STDR has "1+" poles using the same coils as STDP but are so connected to yield a different current density and phasing than the STDP configuration. The "1+" indicates that there is greater than one asynchronous condenser pole in the original one pole-space due to the former's reduced wavelength, which is proportional to rotor speed. Thus a particular primary-tertiary layout is only exactly appropriate for one load and slip value at which nil braking torque exists despite recovery of reactive power. The winding diagram for this machine is given in Figure 4.11 and the operational details are given in Table 4.4.

The first 50 Hz tests of this rotary induction condenser were conducted with the tertiary recovery windings feeding an isolated inductive load. Strictly speaking this does not constitute a unity power factor machine since the recovered reactive energy is not circulated at mains potential but in a closed loop and hence the term "reactive balance machine". The rotor had a magnetization time constant of T=250 ms. A slip value slightly larger than one percent was found such that the reactive power generated by the recovery winding exceeded the reactive power supplied by the mains to the motoring section, that is, the machine consumed a net negative kVAR as indicated in Figure 4.12. This was subtantiated on both an electronic phase meter and an electrodynamic VAR meter

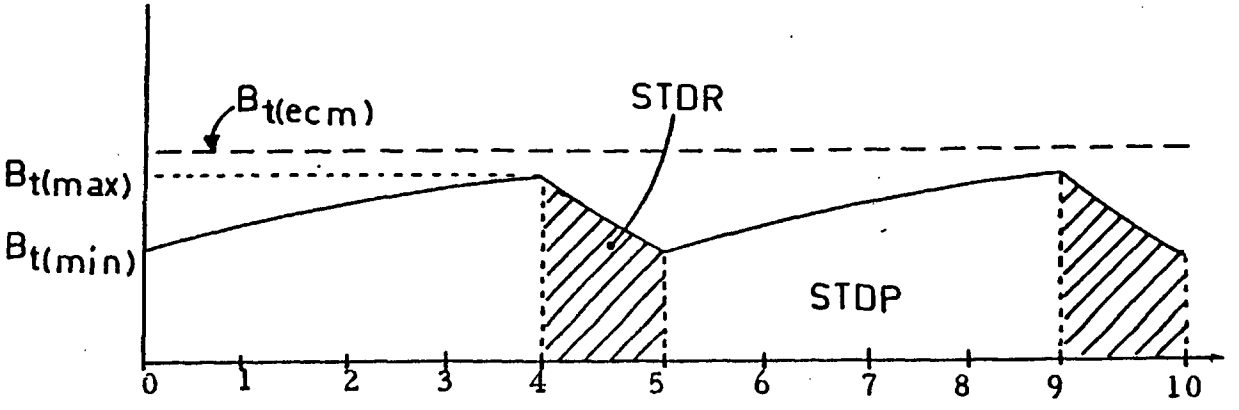

Distance along stator periphery in units of propulsive pitch, τ_p

Figure 4.10 Distribution envelope of total airgap flux density for a general Θ-Pinch machine.

Table 4.4

Characteristics of the 35 H.P. Machine at Reactive Balance Condition

Motoring Section

Torque producing coils	66
Pole-pitch, τ_p	0.0989
Core length (m)	0.222
Airgap (mm)	0.65
Current loading, J_s (A/m)	33,400
Airgap flux density (T)	0.62
Winding Factor	0.756
Core loss (kW)	0.34
Copper loss (kW)	2.76
Stray load loss (kW)	0.19
Reactive input, 1% slip (kVAR)	22
Power input, total (kW)	17.2
Shaft output power (kW)	12.6

Condenser Section

Total leading P.F. coils	24
Induced pole-pitch (m)	0.097
Slot depth (mm)	34
Airgap (mm)	0.65
Current loading (A/m)	29,750
Slot pitch (mm)	11.1
Chording Factor	0.95
Total rotor bars	80
ASC copper loss (kW)	0.78
Turns/coil	6
Reactive output (kVAR)	23
Core outer diameter (m)	0.42
Overall efficiency (%)	73

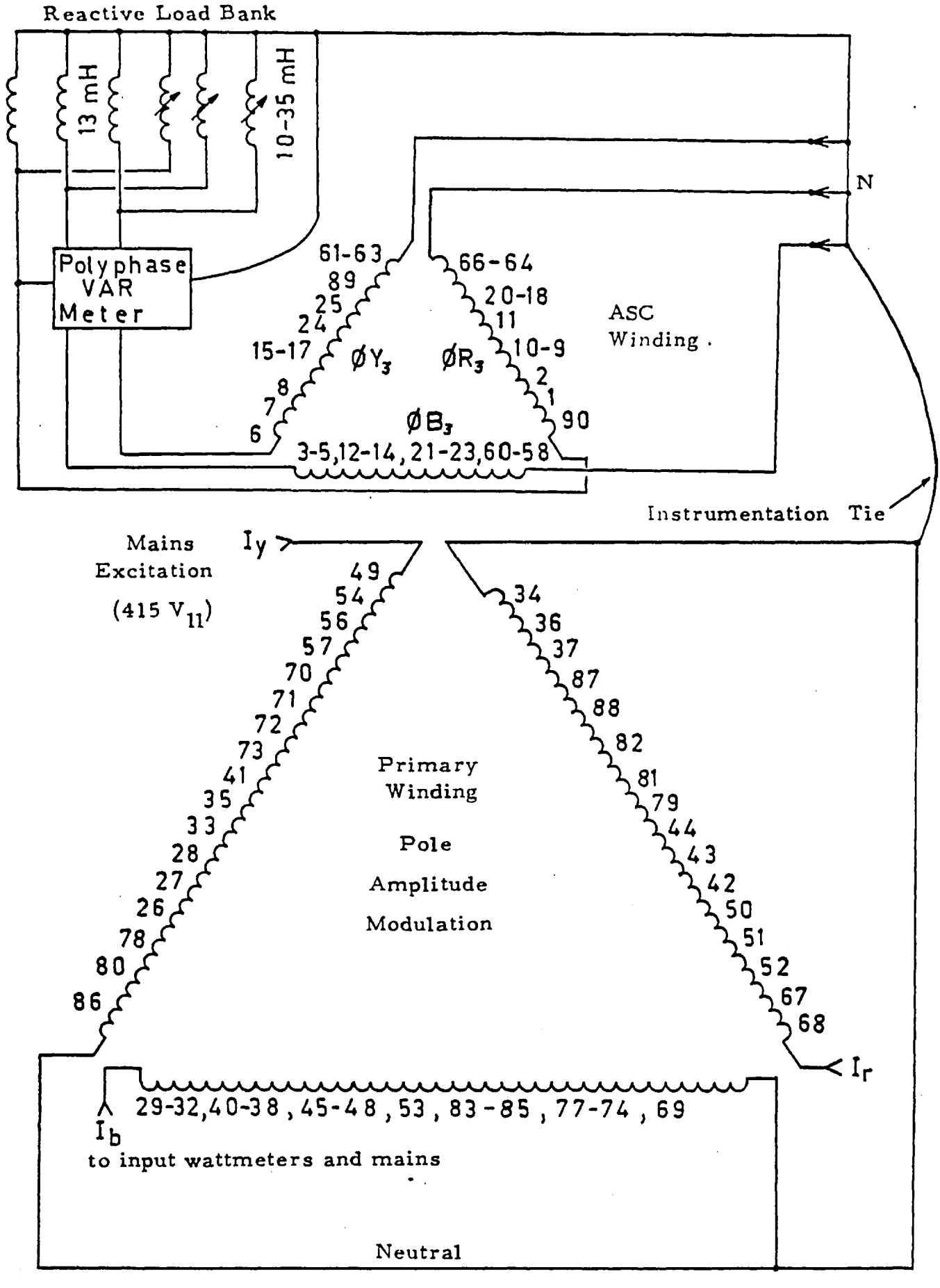

Fig. 4.11 Arrangement for the 26 kW, ten-pole machine with pole-amplitude-modulation of primary sector and conventional 3 slots/pole/phase ASC sector that yielded a zero net reactive power balance between input and ASC load bank.

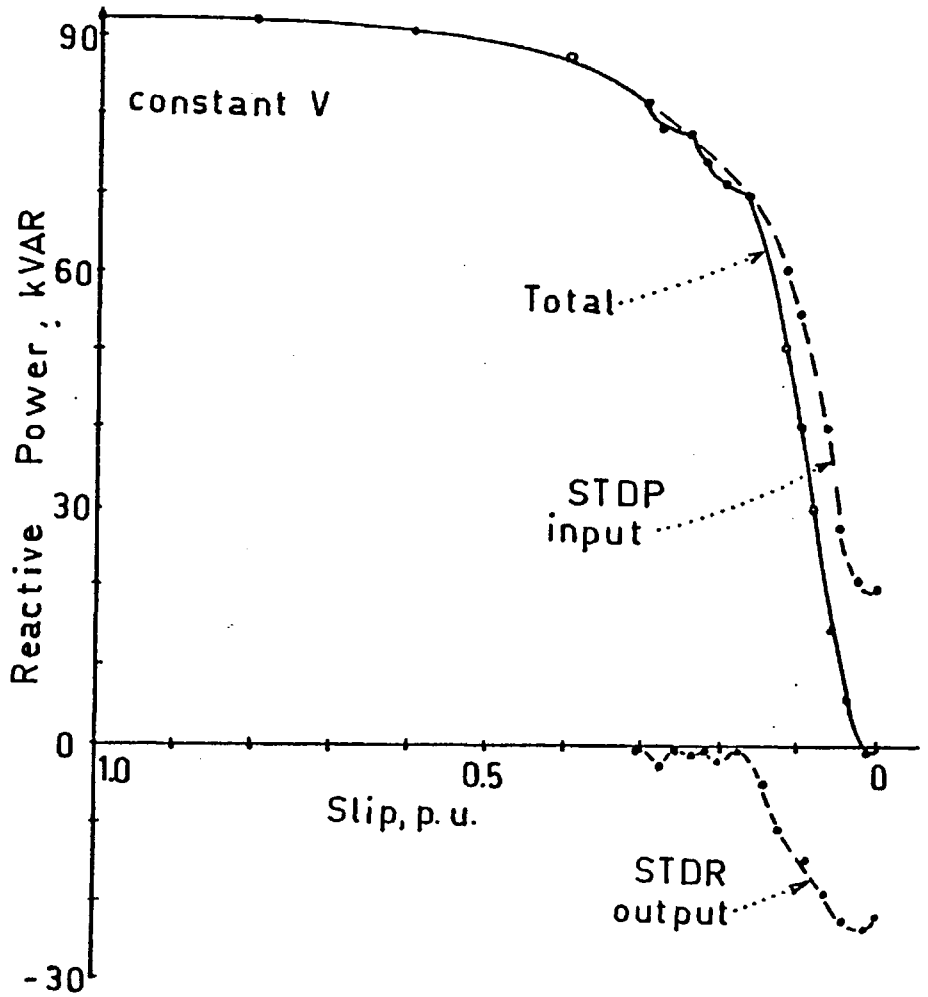

Figure 4.12 Experimentally-obtained input (STDP) and generated (STDR) reactive powers for the ten-pole Theta-Pinch machine in the reactive-balance test of 26/11/79 on 50 Hz.

and electrodynamic meters are given in Appendix VII. The laboratory instrumentation is detailed in Figure 4.13 for these tests. The laboratory facility is shown in Figure 4.14.

These characteristics were obtained on November 26, 1979; after submission of the first published paper [1] concerning the Θ-Pinch principle, but these results appear in the formal discussion of [1] and in [3] . These last series of tests succeeded in their objective due to the extension of the ASC section from 18 coils to 24 coils at the expense of reducing the motoring section length per repeatable section to less than 4 poles; however the configuration is still classified as the "4 - 1+ - 4- 1+" type. The total power input to the machine was 17.2 kW and the shaft was loaded to 12.6 kW by a DC compound-field dynamometer, thus indicating an overall efficiency of 73% at the reactive balance point. This rather drastic drop in efficiency from that appearing in Table 4.1 is attributed to the use of an overchorded winding by 11/9 for both primary and tertiary coils and a uniform slot-pitch around the periphery. In general, the machine has excess stator losses rather than excess rotor losses, approximately 2% of the stator loss arises from the additional resistance drop in the 180 interconnections peculiar to the laboratory machine; the core loss of this machine is 0.34 kW and the stray load loss is 0.19 kW. It should be emphasized that in normal applications, two operating modes for the asynchronous condenser windings are apparent. First, assuming a rewound tertiary (ASC) section, the machine's terminal power factor may be raised to unity at the rated load and slightly above since the motoring section power factor alone is 80% in this machine. Alternately, the ASC winding may be designed to peak at a slip value very close

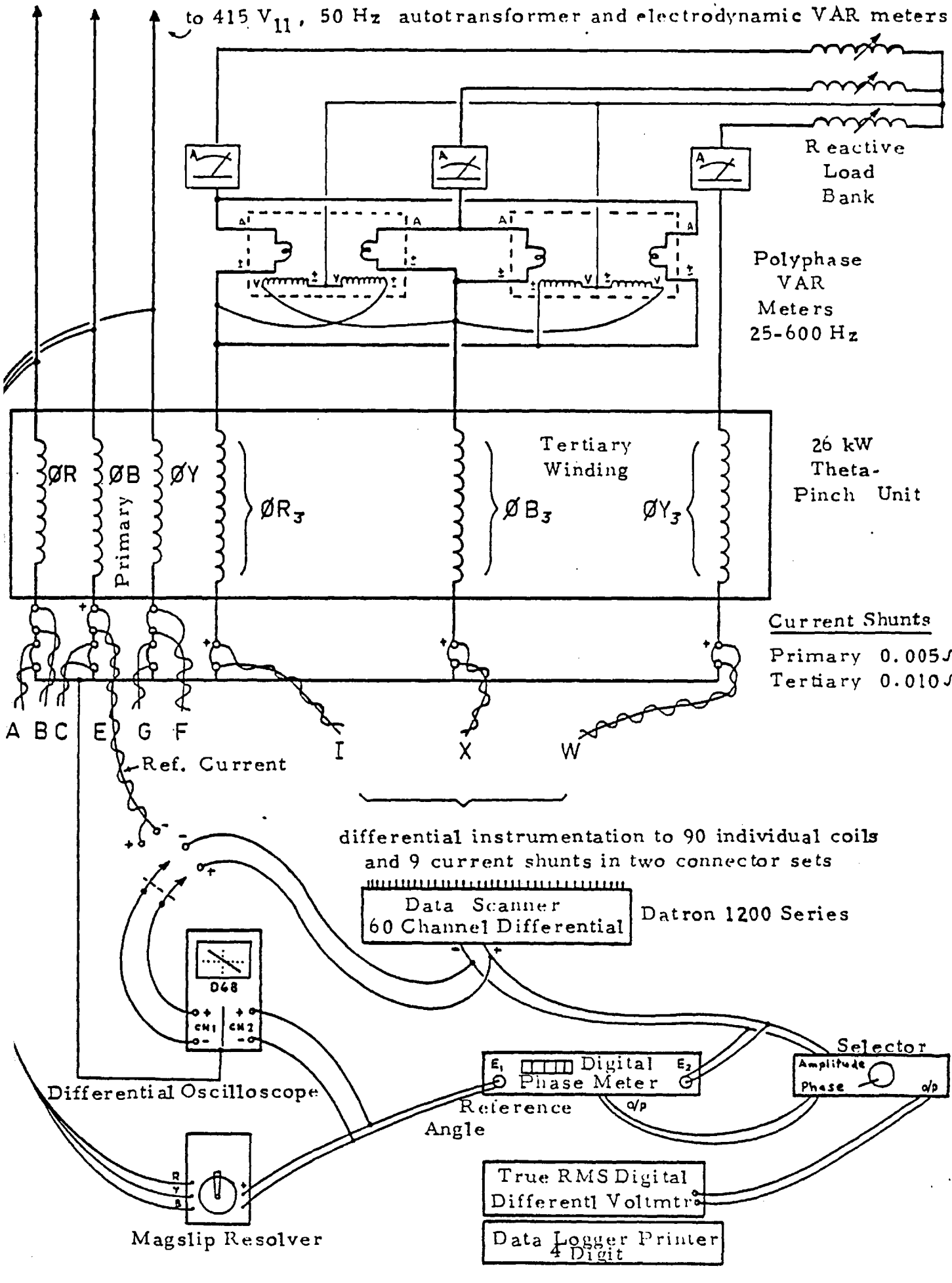

Figure 4.13 Instrumentation of ten-pole machine for reactive-balance tests.

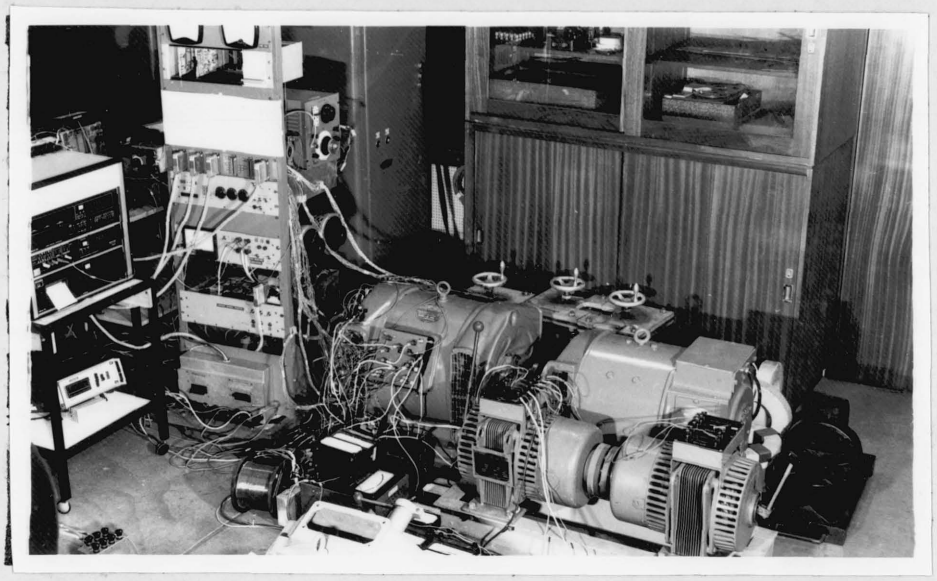

Figure 4.14 The laboratory experimental facility for the first reactive balance tests with the 26 kW Theta-Pinch machine in the center, phase-shifter in the foreground and inductor banks in the backround and right side of dynamometer.

to or at zero, whereby the motor is running lightly loaded and the motoring winding power factor could be as low as 30%. Although it would be impractical to raise the terminal power factor to unity in the latter case, the option of maintaining a reasonable power factor such as 80% under light load is very attractive on a systems basis considering the extraordinary number of lightly loaded machines on the grid at any one time.

The rotary machine with 10 poles (denoted 4-1+-4-1+) followed as a natural development of the first linear machine of 8 poles with power factor correction windings. The choice of the number of motoring poles/repeatable section is a crucial parameter because the rate of rise or demagnetization of the airgap magnetic field for a given rotor time constant, is dependent on the combination of slip, σ and the exciting pole numbers. The concept of using space transients to affect appreciable reactive power generation at the exit-edge of the excited section is restricted to pole number-slip value products lying in the range

$$n^* R_2' < \frac{n^*\sigma}{1-\sigma} < 1.0 \qquad (4.4)$$

where R_2', the referred rotor resistance is equal to 0.037 per unit for the 35 H.P. machine. The basis of this general guideline is that appreciable reactive power generation, Q denotes that the exit-edge power is greater than 0.25 per unit of the equivalent conventional machine rotor copper loss, $\frac{1}{2}P_r J_s^2 n \tau_p$. This value of Q has a limiting value of 0.47 per unit for machines with a large Goodness factor when the rotor speed is at or near synchronous, as exemplified in Figure 3.7. Yet, prior to building up the maximum exit-edge

energy, efficiency constraints demand that such a small slip never be used and hence, the inclusion of R_2' in (4.4). If the total number of poles around the periphery in the equivalent rotary machine is n, the effective number of motoring poles n* never exceeds n/k since an even number of repeatable sections, k are mandatory so as to neutralize the effects of unbalanced magnetic pull. Therefore, it would be possible to produce an efficient unity-power-factor four pole machine at a low slip if only one repeatable section is attempted, but should two repeatable sections be used in practice, then the high-power-factor slip would have to be greater than 33% for which excess rotor losses would be incurred. Conversely, if the total number of poles is greater than 8, then operating slip values can always be between 20% and 3% (the latter being a typical per unit value of R_2) because of the greater freedom in choosing repeatable section lengths.

The fields created by the two sets of stator windings do not induce any significant transformer voltages in each other by virtue of their particular space separation. These windings are ideally, exclusively rotor motion coupled as evidenced by $J_{s(asc)}$ curve in Figure 2.54. With new slotting construction no stray voltages will be induced provided that the ASC winding comprises a speed-dependent pole-pitch which obviously has to be fixed depending on whether power factor correction is to be employed at either full load or running light.

The torque varies with speed as in a convention cage rotor machine with low resistance bars. Using the conventional steady-state equivalent circuit and neglecting the magnetizing reactance, the torque of the Θ-Pinch machine may be described under constant voltage excitation, V_t as

$$T = \frac{9.54\ V_t^2}{\dot{\theta}} \quad \frac{3\ R_2/(\sigma-\sigma_o)}{[R_1 + R_2/(\sigma-\sigma_o)]^2 + [X_1 + X_2]^2} \text{ N-m} \quad (4.5)$$

where $\dot{\theta}$ is the synchronous speed in r.p.m. The only departure of this from an equivalent machine is the introduction of the quantity σ_o which is the per unit difference in slip from zero at which zero torque occurs. The effect of producing torque either above or below synchronism has been well documented for linear and spherical induction machines [4] and with respect to the Θ-Pinch machine the functional relationship of this slip offset is

$$\sigma_o = f(G,\ J_s/J_{s(asc)})$$

For the 35 H.P. machine with the parameters of Table 4.4, σ_o has been measured at -0.008 per unit. In general if the Goodness is low or if the ratio of the main stator current loading to the ASC stator loading is near unity, the magnitude of σ_o will be negligible and zero torque occurs at synchronism.

The only important consideration during startup under constant voltage is that asynchronous crawling can occur and this is dependent on the exact division between motoring and ASC poles. (This is treated in detail in section 5.5) There is one significant harmonic synchronous speed in the basic Θ-Pinch configuration which can occur at a slip

$$\sigma = 1 - \frac{k\ n^* + (n - k\ n^*)/1 - \sigma^*}{n + 2} \quad (4.6)$$

This was not a problem in the 35 H.P. unit because pole-amplitude-modulation was used on the motoring winding; specifi-

cally the ten-pole MMF was originally optimized by the manufacturer to avoid the twelve-pole speed which is the most likely Θ-Pinch harmonic.

For space transients to be of use, their attenuation must be in the same direction as the main travelling field. Physically, the primary type (α_1) follows this criterion and is attributable to the entry edge of the excitation section, i.e. the transition from the ASC to the STDP regions as located by Θ_2 in Fig. 4.10. The secondary type (α_2) occurs here and also as rotor bars exit from the excitation region to the condenser region as located by Θ_1. Fundamentally, both components of the α_2 are equal in magnitude but they propagate in opposing directions at much greater than rotor speed (e.g. 30 times in the 35 H.P. unit). Since this type is attenuated quickly it is of minor importance, but the α_1 transient has a wavelength longer than any conceivable peripheral length of the condenser region, $(\Theta_2 - \Theta_1)\ \tau_p/\pi = 0.13m$. It travels at exactly rotor speed in the hypothetical case of zero airgap and slightly slower (2%) than rotor speed, u_r in the case of airgaps typical of rotary induction machines.

The α_1 is the subject of exploitation. If

$$\frac{1}{G(1-\sigma)^2 + \omega T_2} = \frac{R_2}{X_m(1-\sigma)^2 + X_2} << 1 \qquad (4.7)$$

holds, which is generally true when close to synchronous speed, the α_1 transient may be approximated as [5]

$$\alpha_1 = -\frac{1}{\lambda}\left[\frac{1}{G(1-\sigma)^3 + \omega T_2(1-\sigma)} + j\,\frac{1}{1-\sigma}\right] \qquad (4.8)$$

$$\approx -j\omega/u_r$$

For the machine under discussion, $\alpha_1 \approx -j\ 32.07\ m^{-1}$. Under conditions, such that $G >> 1$ and $G > \omega T_2$, the α_2 inverse-of-wavelength as given by (3.53 and 3.54) is too large at normal operating speeds to affect the power or var transfer across the airgap or the induced condenser voltage. With $G=70$ and $\omega T_2 = 4.3$ only the real part of the secondary transient coefficient is prominent or

$$\alpha_2 \approx -129.7\sqrt{1 + L_3'/L_2}\quad m^{-1} \qquad (4.9)$$

where L_3' is the tertiary winding leakage inductance, L_3 plus the isolated inductive-load inductance. Under maximum VAR transfer conditions, $L_3' = 2\,L_3$ and for the 35 H.P. laboratory machine, $L_3 \approx \frac{n_3}{n_1} L_1 = \frac{24}{66}[.00082]$ p.u. and $L_2 = .00042$ p.u. which yields $\sqrt{1+L_3'/L_2} = 1.55$. Consequently, $\alpha_2 \approx -201\ m^{-1}$ which may be utilized in (3.22) and (3.23) to give the (steady-state and) transient airgap flux propagation; the same exponential coefficients are applicable to both in-phase and quadrature components.

The α_2 and its complementary coefficient, $\alpha_3 \approx -\alpha_2$ are confined to the 4 transition regions of the machine (with 2 repeatable sections) and thus only function to match boundary requirements.

The condenser winding as seen by the rotor current is acting in a similar manner as the rotor is seen to behave

by the main stator excitation. Thus, over a limited airgap angle, the rotor is acting as a second primary, inductively fed from the first (STDP). To complete the analogy, the equivalent of the rotor leakage layer as applied to the condenser winding is merely the sum of the internal leakage fluxes (due to slot, end-winding and zig-zag components) with the external reactive load placed on the ASC winding (as referred to the airgap). Similarly, the equivalent surface resistivity of the ASC section is the total of the windings and the real component of the ASC load; this also allows $p'_{3(asc)}$ to be a negative resistance if an active load is substituted for the passive tertiary load. Consequently, the condenser leakage time constant has been defined as

$$T_3 = \frac{\mu_3 \delta_3 + Q_{asc}/3\ J_s^2 \omega}{\rho_3/t_3 + P_{in}/3J_s^2} = \frac{L_3}{p_3} \qquad (4.10)$$

Since the stator is the reference frame, no speed term is introduced in describing the induced voltage in the condenser winding. The ASC current of the 35 H.P. machine generally follows the theoretical relationship

$$J_{s(asc)} = \frac{J_s}{[(1+\omega_s T_2/G) - j/(\sigma G)]\cdot[(1+\omega_s T_3/G_3) - j/(\sigma G_3)]} \qquad (4.11)$$

where the Goodness factor of the ASC section + passive load is $G_3 = X_m/P'_3$. In the "reactive-balance" laboratory tests, $G_3 \approx 0$. At both the θ_1 and θ_2 transitions, the rotor current density, J_r, the airgap flux density, B_g and the total rotor sheet flux density must be continuous. The excitation field is described by a third-order system while the ASC requires a fourth-order representation as in [3]; a total

of seven integration constants are necessary. The last integration constant can be met by the integral of the induced ASC current which is always finite, and assuming a balanced polyphase load on the ASC

$$\int_{\theta_1}^{\theta_2} J_{s(asc)}\, d\theta = \left[1 - \cos\left(\frac{\theta_2 - \theta_1}{1-\sigma}\right) \right] \hat{J}_s \qquad (4.12)$$

This implies that the constants of integration for all airgap and rotor field parameters are jointly dependent on the proportion of a rotor wavelength(s) occupied by one condenser winding, as obviously odd or fractional number of poles are possible.

Irrespective of the value obtained in (4.12), the integral of B_g or J_r around the entire machine must always be zero based on a 1-dimensional analysis. Normally, a double layer polyphase excitation winding with balanced currents will have a zero net surface current around the periphery, however should the value of (4.12) be significant then the result is that while $\int J_r d\theta$ will remain zero, the condenser section will initiate a large zero-sequence component of current in the other statorwinding STDP by way of the coupled rotor currents.

For machines with a high Goodness factor, G but not necessarily a small slip, it is generally true that when rotor current experiences an increase in amplitude (without large phase changes) this occurs in inverse-proportion to the ratio of the inductances into which the rotor currents must establish flux in the regions surrounding the "artificial" edges of the stator. Moreover, if the amplitude of J_r is increased at the boundary, then it follows that its decay rate will be similar-

ly increased. The converse is also valid, and this was demonstrated on the first linear version of the induction condenser principle as described in Section 2.4 whereby an abrupt change in stator current loading between motoring and condenser sections was practical because of the low G value.

To characterize the rotor current when it is being maintained by the agency of slip, it is only marginally "stiff" despite its inductance-limited impedance; J_r will exhibit sharp changes in both the in-phase and quadrature components so as to maintain gradual phase and magnitude changes in the airgap flux. However, over the ASC section, the added stator-inductance coupled to the rotor circuit as well as a possible reduction in the apparent rotor resistance mean that the rotor current is less susceptible to sharp changes.

In contrast, the airgap flux has a strong dependence on rotor velocity; principally the in-phase component will tend toward zero as synchronous speed is approached while the quadrature compoent rises in concert with the rotor speed for the excitation section. The exact division between B_p and B_q in the condenser section is strictly dependent on the ASC load phase angle rather than on speed.

The single most important criterion for the generation of reactive volt-amps by maintaining a large value of negative B_q, is to ensure that at the transition from excitation to ASC windings, the total airgap flux density, $B_t = (B_p^2 + B_q^2)^{\frac{1}{2}}$ is as large as possible. In the reactive-balance test, the maximum value of 0.62 T r.m.s. was attained at θ_1.

Since there are no sharp changes in airgap length at the θ_1 boundary, in practice the maximum reactive power available at this edge is $Q_{max} \approx 22$ kVAR gross output per repeatable section. The phase angle of the ASC load current is 79^{o}.

Commensurate with the desired VAR characteristics of both stator windings in a high speed mode of operation, the quadrature flux density is always decreasing gradually from its peak at θ_1 in the 35 H.P. machine. Should B_q peak at a location other than this, such as midway along the excitation section, it is clear that the slip-excitation-pole-number product is above the value

$$\frac{n\sigma}{1-\sigma} = 2 \qquad (4.13)$$

Conversely, if B_q peaks at a location greater than θ_1 (in the direction of rotor travel), then clearly the ASC winding is consuming positive reactive power beyond that required for the leakage flux field.

The real and reactive power distribution per coil of one repeatable section at the reactive balance condition, depicted by Figure 4.10 at the terminals is given in Figures 4.15 and 4.16; refer to Figure 4.11 for the phase distribution.

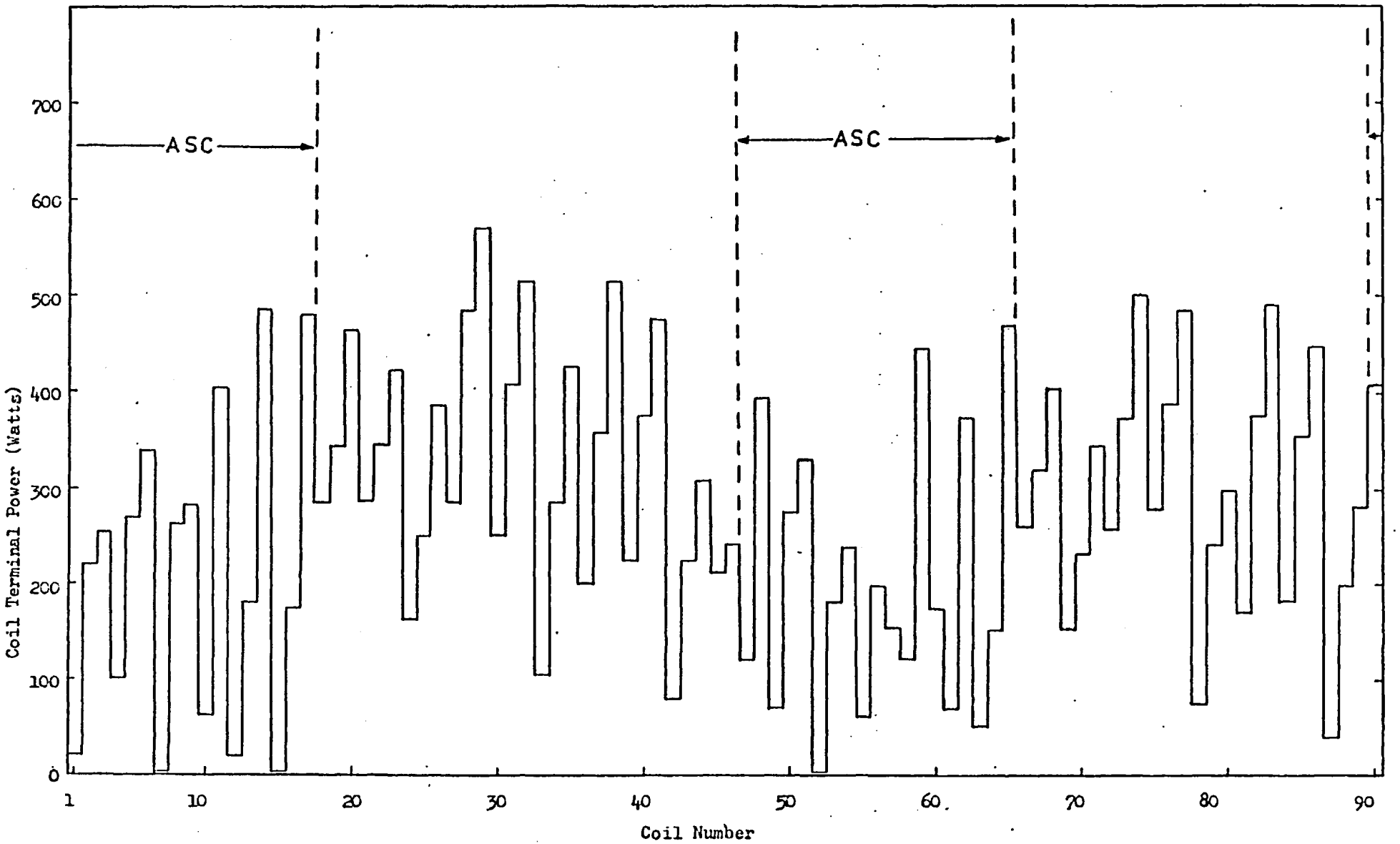

Fig. 4.15 Measured real power distribution in the 26 kW machine during the reactive balance condition, 26/11/79. Test.

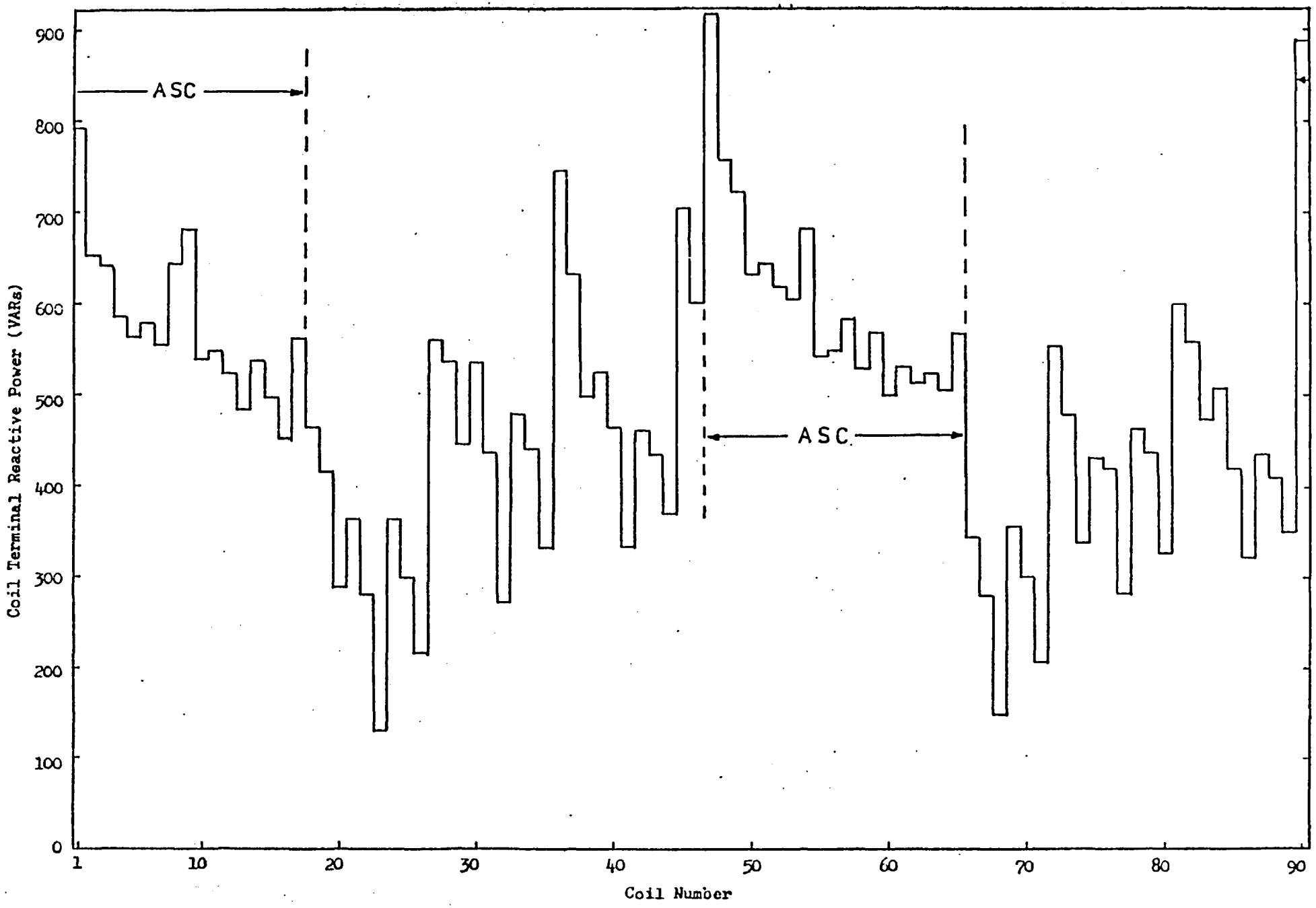

Fig. 4.16 Measured reactive power distribution in the 26 kW machine during reactive balance condition, 26/11/79 Test.

4.6 HARMONIC PHENOMENA WITHOUT POLE AMPLITUDE MODULATION (SCIM-I)

This section is mainly intended as a reference document to explain experimentally why the use of a conventional 3 slots/pole/phase main winding for the 26 kW rotary machine results in a harmonic speed at 83.7% of synchronous speed or 442.5 RPM on 50 Hz. The theory for this is presented in Section 5.3 and here all of the measured angles, coil terminal VARs and Watts are presented in Table 4.5 in a list form for the 90 coils as well as a per phase summary in Table 4.6. The individual coil phase angles are plotted in Figure 4.17, as measured directly by the instrumentation and Figure 4.18 presents the same basic information but with phase angle plotted with respect to individual phase references.

Figure 4.19 shows the VARs per coil at the harmonic speed where one should note that 8 coils are generating leading VARs in the ASC section even at this harmonic speed, although the net reactive consumption of the ASC is still a positive value but small. Figure 4.20 shows the real power consumed by individual coils along the entire periphery where the cross hatched blocks represent the coils producing a braking torque of the rotor; there are 28 of these coils out of 90. This should be considered the most important of the graphs presented in this section.

All the first tests of this machine used the original equipment manufacturer's pole-amplitude modulation winding for the motoring winding only and no harmonic speeds were encountered at all. Then the machine was reconnected with a standard series winding (even both repeatable sections in series) and this major harmonic condition was documented in full.

Table 4.5

Θ-Pinch Mk. I Coil Terminal Power Factor Angles at Asynchronous Crawling, 50% Input Voltage, Slip=26.3% 50 Hz, Inertia J=8.0 N-m-sec^2, No Shaft Load

Coil	Volts	P.F. Angle	Watts	VARs	Coil	Volts	P.F. Angle	Watts	VARs
1	4.31	53.6°	13.9	18.9	32	7.63	60.6	80.2	141.4
2	3.73	76.0	4.91	19.7	33	7.43	93.0	-7.5	143.8
3	3.30	51.3	11.4	14.2	34	8.21	71.9	49.1	151.2
4	3.22	86.0	1.20	17.6	35	8.30	52.2	99.1	126.8
5	2.80	112.	-5.7	14.3	36	8.53	83.0	22.4	182.3
6	2.53	69.0	4.91	12.8	37	8.39	66.3	72.6	165.5
7	2.65	99.0	2.25	14.2	38	8.11	53.1	105.	139.5
8	3.05	117.	-7.5	14.7	39	7.74	77.9	34.3	161.4
9	2.41	59.6	6.60	11.3	40	8.38	57.4	96.2	150.4
10	1.92	115	-4.37	9.54	41	7.87	42.3	123.5	112.4
11	2.45	152	-11.8	6.37	42	7.38	74.9	37.0	142.1
12	1.97	130	-6.8	8.33	43	7.98	57.0	84.2	122.9
13	1.77	172	-9.6	1.35	44	7.45	36.1	117.	86.2
14	2.47	194	13.2	-3.3	45	7.58	68.9	58.4	152.0
15	1.83	152	-8.75	4.65	46	7.77	45.2	118.	118.3
16	1.63	198	8.4	-2.73	47	4.20	23.1	21.1	9.0
17	1.81	201	9.21	-3.51	48	4.24	44.3	16.8	16.1
18	2.66	39.1	44.5	36.1	49	3.52	83.9	2.0	19.3
19	2.31	62.1	23.4	43.9	50	2.67	44.2	10.4	10.2
20	2.28	59.5	24.9	42.3	51	2.68	64.1	6.5	13.1
21	2.62	71.4	17.8	52.9	52	2.73	81.9	2.0	14.5
22	3.13	85.2	5.61	66.5	53	2.15	126	-6.8	9.47
23	3.19	64.4	29.3	61.2	54	1.80	93.0	-0.6	10.2
24	3.16	87.5	2.67	61.2	55	1.84	113.6	-4.0	9.16
25	3.94	87.0	4.0	76.3	56	1.88	133.1	-6.9	7.30
26	4.13	68.1	30.0	74.3	57	1.66	118.0	-4.3	8.0
27	4.43	89.0	1.72	95.4	58	1.68	174.0	-9.2	0.9
28	6.68	79.1	27.4	141.3	59	2.29	193.8	-12.2	-3.1
29	6.93	64.2	65.4	134.2	60	1.41	150.0	-6.6	3.8
30	6.85	94.5	-11.5	145.5	61	1.56	199.2	-8.0	-2.75
31	7.58	78.5	32.1	157.7	62	1.92	211.0	-8.9	-5.40

Table 4.5 continued

Coil	Volts	P.F. Angle	Watts	VARs
63	1.49	176.6°	-8.1	0.5
64	1.77	219.6	-7.4	-6.1
65	1.60	221.9	-6.5	-5.8
66	1.84	57.5	21.1	33.1
67	2.53	90.1	0	54.0
68	2.71	77.5	12.5	56.3
69	2.66	93.0	-2.7	51.5
70	3.63	93.4	-4.2	70.3
71	3.98	72.1	23.8	73.4
72	4.59	93.4	-5.8	98.6
73	5.20	87.1	5.8	111.8
74	5.36	70.0	39.5	108.4
75	5.58	92.7	-5.6	118.8
76	7.38	81.0	24.6	155.1
77	7.52	62.6	73.6	142.0
78	7.21	98.3	-12.9	138.5
79	8.17	77.0	35.5	153.9
80	7.57	64.0	64.4	132.1
81	7.36	90.2	0.50	158.5
82	8.11	70.2	59.8	164.1
83	8.26	55.3	102.	145.7
84	7.85	80.4	27.6	164.7
85	8.25	61.5	83.8	154.4
86	8.14	45.5	121.5	123.7
87	7.68	77.0	33.5	145.2
88	8.00	56.2	86.7	128.5
89	7.37	40.1	109.5	91.9
90	4.61	19.9	23.6	8.61

Table 4.6

Summary of Reduced Voltage, Asynchronous Crawling Test Without Pole-Amplitude Modulation Windings
Positive Sequence, 102 V line-neutral, 50 Hz, 442.5 R.P.M. , Slip = 26.3%, No Shaft Load
10 Pole "Θ-Pinch" Mk. I

Motoring Winding				
	Input	Real Power	Reactive Power	
	Coils 18-46	66-89	18-46	66-89
Phase A	413.4	333.6	983.4	985.3
Phase B	559.4	201.3	1245.5	787.1
Phase C	407.3	359.1	1049.4	1002.

Total Input Power: 2274 Watts, 6053 VARs

Condenser (ASC) Winding			
Input Real Power		Output Reactive Power	
Coils 90 & 1-17	47-65	90 & 1-17	47-65
32.8	-33.4	74.4	14.7
8.5	-11.0	40.1	42.3
3.7	13.0	52.5	50.3

Total Real Power Input: 13.6 Watts
Total Reactive Power Output: 274.3 VARs

Overall Input Power: 2288 Watts, 5779 VARs
Overall Input Power Factor: 0.368
442.5 R.P.M. referred to 12 pole speed: 11.5% slip

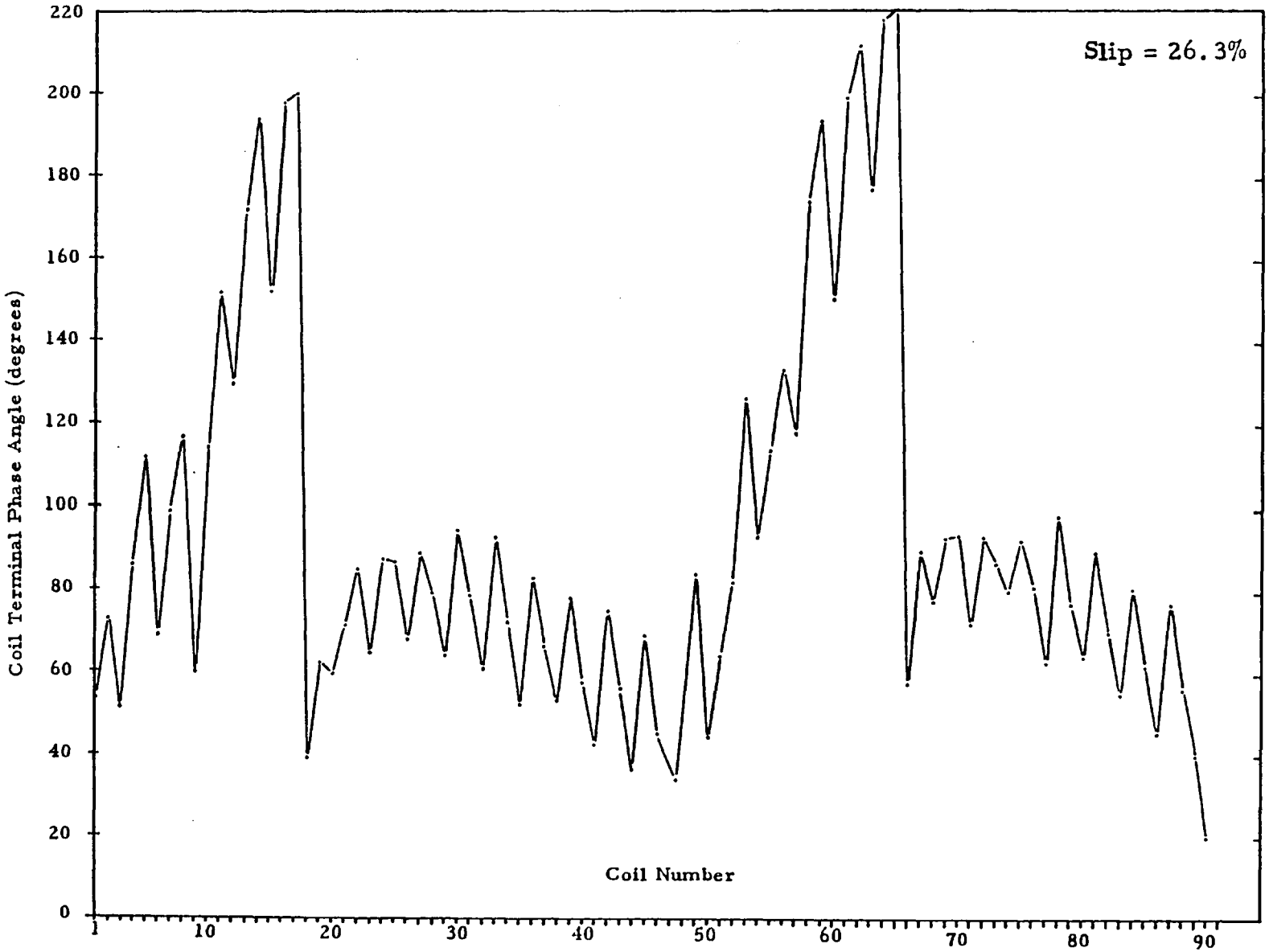

Figure 4.17 Coil terminal phase measurements direct from instrumentation; common reference.

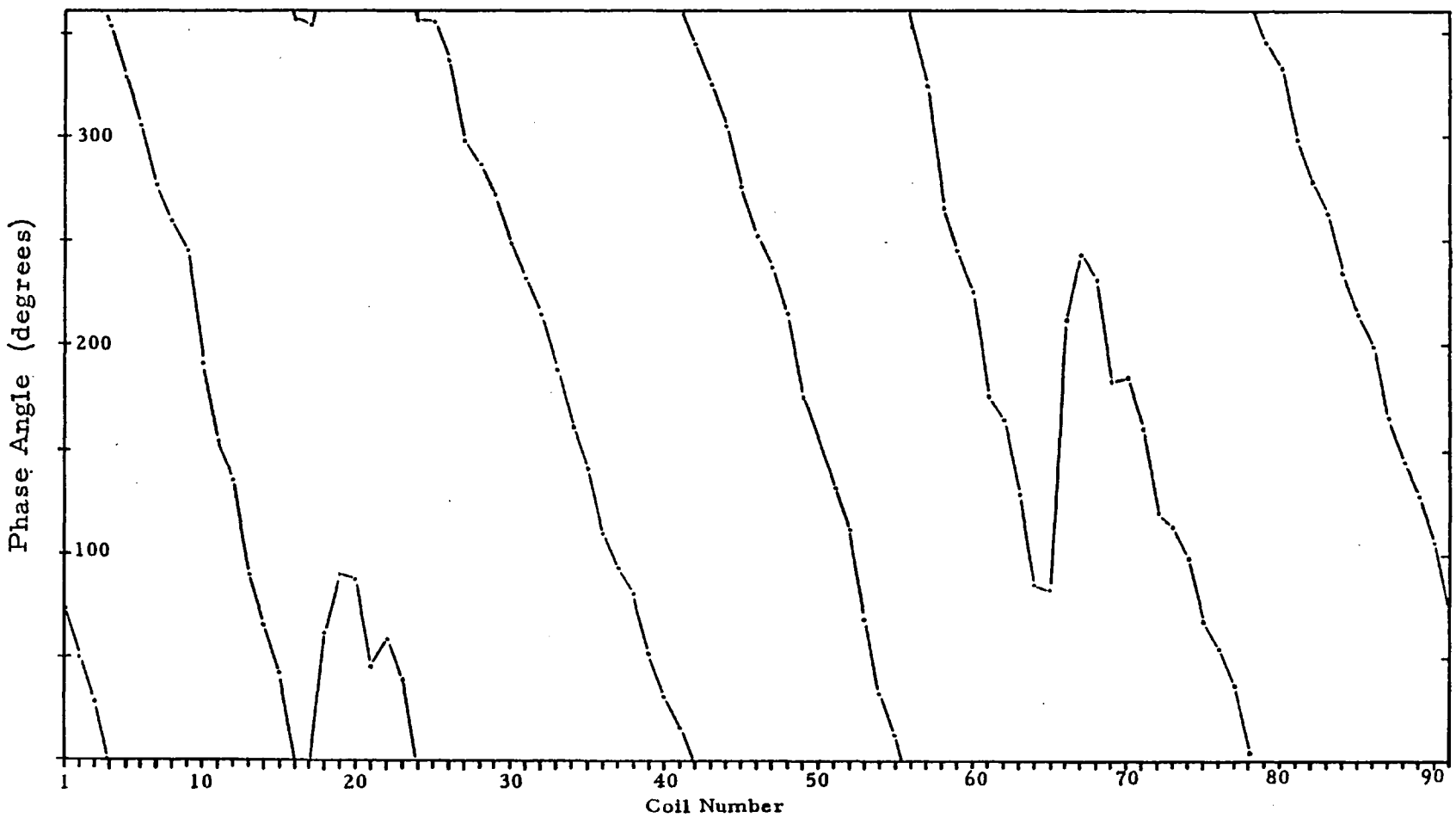

Figure 4.18 Coil terminal voltage phase angles with respect to a constant phase reference at slip of $\sigma = 0.263$ p.u., 50 Hz.

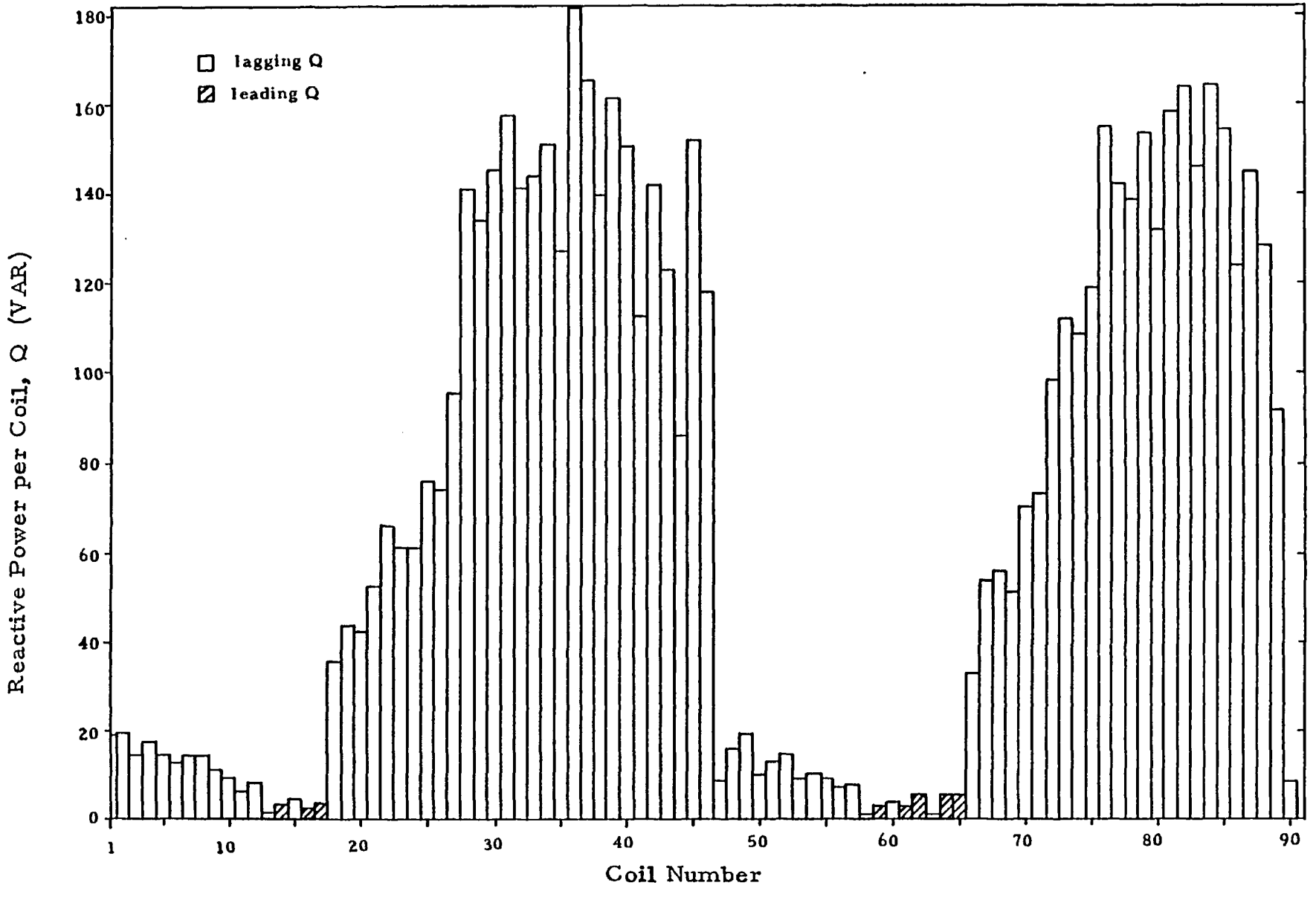

Fig. 4.19 Coil terminal reactive power distribution at harmonic speed of 442.5 RPM, 50 Hz, σ=0.263

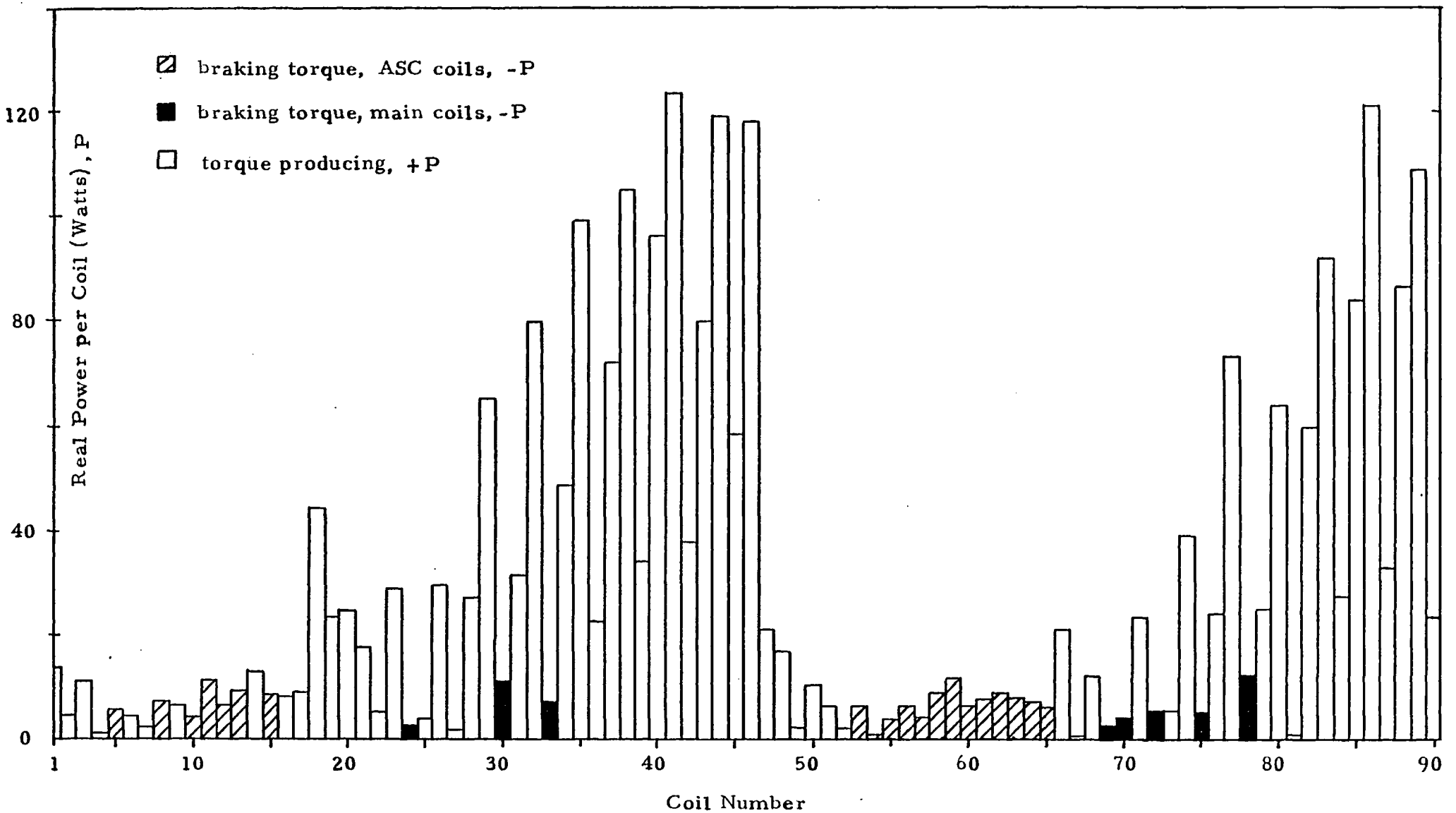

Fig. 4.20 Coil terminal real power distribution at harmonic speed of 442.5 RPM, 50 Hz, $\sigma = 0.263$

4.7 REFERENCES

[1] E.R. Laithwaite and S.B. Kuznetsov, "The Asynchronous Condenser: A Brushless, Adjustable Power Factor Induction Machine," IEEE Trans. Power Apparatus and Systems, Vol. PAS-99, No. 6, Nov/Dec 1980, pp. 2422-2432.

[2] G.H. Rawcliffe, and W. Fong, "Close-Ratio Two-Speed Single Winding Induction Motors," Proc. IEE, 1963, Vol. 110, p. 916.

[3] E.R. Laithwaite, and S.B. Kuznetsov, "Reactive Power Generation in High Speed Induction Machines by Continuously Occurring Space Transients," IEEE Magnetics, Vol. MAG-16, Sept. 1980, pp. 716-718.

[4] E.R. Laithwaite, Induction Machines for Special Purposes. London: Newnes, 1966, p.

[5] Ibid., p. 86.

[6] L.S. Piggott, "A Theory of the Operation of Cylindrical Induction Motors with Squirrel-Cage Rotors," Proc. IEE, Vol. 109c, 1962, pp. 270-282.

V. A LARGE ROTARY INDUCTION CONDENSER

5.1 REACTIVE POWER FLOW

This section examines the real and reactive power transfer between two active elements by describing the interaction between the Theta-Pinch machine and the constant terminal voltage supply network. In this context, an "active" element may be defined as a source or sink of apparent power which is capable of maintaining either its terminal voltage or current capacity independent of the power transferred. The Theta-Pinch machine, which may be briefly described as a variable-phase, rotary current transformer, has been designed specifically for use with an infinite bus, which will be defined to be a constant-voltage, constant-frequency source or sink of infinite apparent power in contrast to a constant-current-mode bus. Clearly the infinite bus is an active element as well as the asynchronous condenser winding of the Theta-Pinch machine once high speed operation is reached.

Conventional rotating synchronous condensers are actively controlled by the injection of a field current in direct response to the terminal voltage magnitude, phase or rate of rise. Alternately, the asynchronous induction condenser under discussion incorporates an analogous field current control by the agency of rotor slip variation and most important this is a stable, compensation mechanism. The asynchronous condenser machine only contains high power windings but this does not preclude this device from being classified as an active element despite the fact

that no low power control windings are used. The self-compensation capability of the asynchronous condenser is best illustrated by supposing that initially the machine is running at a constant terminal power factor, e.g. unity at rated load. If the load is suddenly increased as evidenced by an increase in primary current, this increase is reflected in the slip frequency rotor current and a corresponding increase in the magnitude of the transient DC rotor current component initiated at the transition region in the machine. If this is a large machine with a relatively low magnetization requirement, the tertiary current induced in the stator asynchronous condenser winding will always be a mirror image of the transient DC rotor current and this is the effective compensation current. The following section details the exact operating range for the ratios of tertiary: primary current and tertiary: line current for maintaining unity terminal power factor under differing real power transfer.

The main purpose of the reactive power flow analysis is to establish the proper phase angle criteria not only for the equivalent voltage or current source representing the condenser winding but rather each coil of this tertiary section must be regarded as an individual generator since no two stator coils have either identical induced voltages or phase angles. Conventional machine theory assumes uniform flux distribution throughout the airgap periphery and conveniently assigns a "distribution" factor to avoid the complexity of summing a multitude of phasors since all

voltage phasors should be equal. The phase distribution of the airgap flux throughout the transient region of the asynchronous condenser is given in Chapter III, Section 1 and here it is shown how well the induced voltage so generated may be utilized in light of the constraints placed on power transfer by the magnetic leakage and electric resistance paths.

The apparent power absorbed by the airgap magnetic field may be assigned on a point by point basis to individual stator, tertiary coils as represented in Figure 5.1 where V_1 is the equivalent induced EMF and V_t is the coil terminal voltage. For convenience, it is assumed that V_1 will always be at a zero phase angle, V_t will be at a variable phase angle δ, and I is positive flowing into the internal source.

From conventional analysis [1], the airgap apparent power may be represented as

$$\vec{S} = \vec{V}\,\vec{I}^{*} = (V_1 \angle 0^{o}) \left[\frac{V_t \angle \delta - V_1 \angle 0^{o}}{R + jX} \right]^{*} \qquad (5.1)$$

where R and X are passive elements, representing the per coil resistance and leakage reactance and are assumed to be constant values. By ordinary trigonometric relations, (5.1) may be expressed as

$$S = \left\{ \frac{-V_1^{2}\left(\frac{R}{Z} - j\,\frac{X}{Z}\right) + V_1\,V_t\left[\cos\left(\delta + \tan^{-1}\left(\frac{X}{R}\right)\right) + j\,\sin\left(\delta + \tan^{-1}\left(\frac{X}{R}\right)\right)\right]}{Z} \right\}^{*}$$

for $Z = \sqrt{R^2 + X^2}$. Implementing the complex conjugate oper-

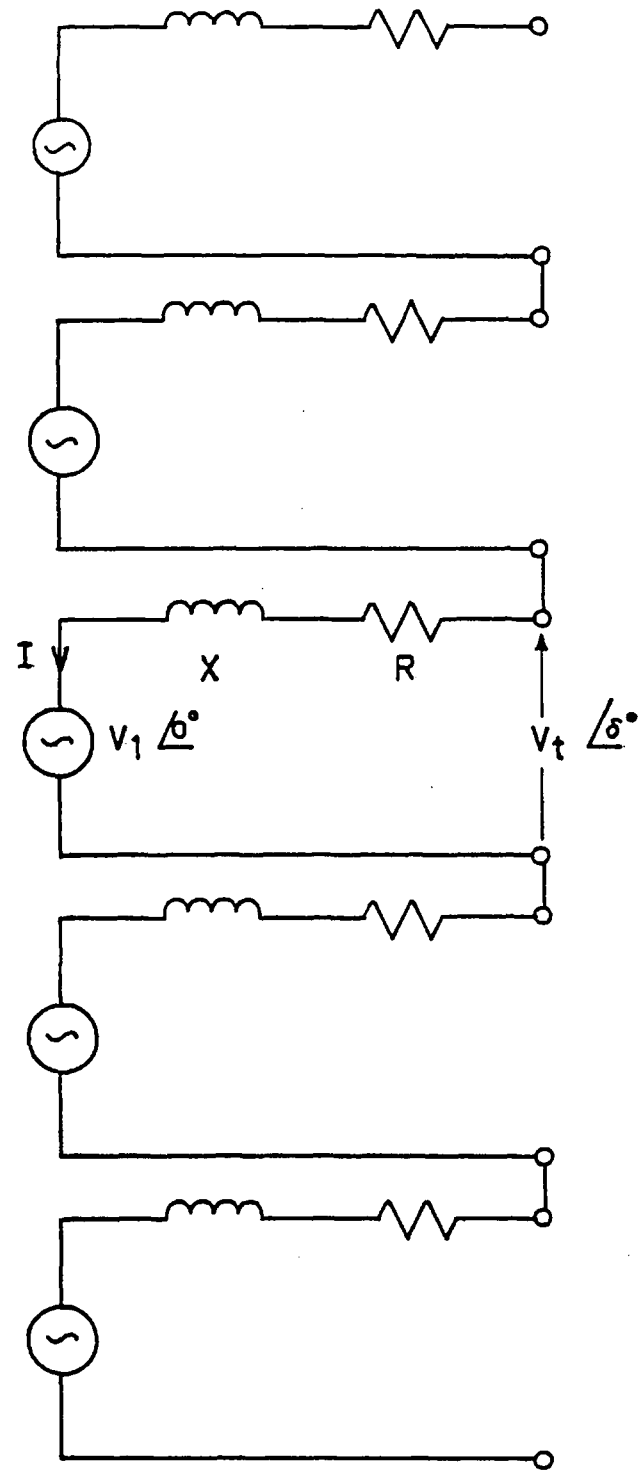

Figure 5.1 Coil-by-coil model of the tertiary winding for representing the airgap induced voltage, V_1.

ation

$$\vec{S} = P + j\,Q$$

where
$$P = -V_1^2 \frac{R}{R^2 + X^2} + \frac{V_1\,V_t \cos\left(\delta + \tan^{-1}\left(\frac{X}{R}\right)\right)}{\sqrt{R^2 + X^2}} \qquad (5.3)$$

$$Q = -V_1^2 \frac{X}{R^2 + X^2} - \frac{V_1\,V_t \sin\left(\delta + \tan^{-1}\left(\frac{X}{R}\right)\right)}{\sqrt{R^2 + X^2}} \qquad (5.4)$$

Consider a large machine model for which it is assumed $R = 0$

$$P = \frac{V_1\,V_t}{X} \cos\left(\delta - 90^o\right) = \frac{V_1\,V_t}{X} \sin\left(\delta\right) \qquad (5.5)$$

$$Q = \frac{-V_1^2}{X} - \frac{V_1\,V_t}{X} \sin\left(\delta - 90^o\right) = \frac{-V_1^2}{X} + \frac{V_1\,V_t}{X} \cos\left(\delta\right) \qquad (5.6)$$

By combining (5.5) and (5.6), it is possible to obtain a expression for the total reactive power transferred in terms of only the real power absorbed, the power angle δ, the leakage reactance and the internal voltage.

$$Q = \frac{P}{\tan(\delta)} - \frac{V_1^2}{X} \qquad (5.7)$$

In the most basic case, suppose that the coil terminal is connected to a passive load represented by an ideal induction motor equivalent circuit for which the total impedance is only the secondary resistance R_2. Then, if it can be assumed that $X >> R_2$, which is a fair approximation at locked rotor conditions, it is clear that the power angle $\delta \approx -90^o$ and

$$Q \approx -\frac{V_1^2}{X} \qquad (5.8)$$

$$P \approx \frac{-V_1 V_t}{X} \approx \frac{-V_1^2 R_2}{X} \qquad (5.9)$$

This serves to define the directions of flow so that negative Q corresponds to reactive power being generated by the condenser voltage source and negative P indicates real power generated by the same source. Conversely, the criterion for Q to be positive, which means that the airgap field will be absorbing reactive power (and valid for speed control applications of the condenser winding), is that

$$V_t \cos(\delta) > V_1 \qquad (5.10)$$

Under the assumption that the tertiary winding resistance is negligible or R = 0, it is clear that the power angle is

$$\delta = \tan^{-1}\left[\frac{P}{Q + V_1^2/X}\right] \qquad (5.11)$$

In general, this power angle must be kept as small as possible in direct contrast to synchronous generator operating angles, and this implies that for condenser utilization

$$Q > P - V_1^2/X \qquad (5.12)$$

and the airgap-power factor is

$$\cos \phi = \frac{P}{\sqrt{P^2 + Q^2}} \qquad (5.13)$$

Suppose that the equivalent load on the condenser winding is represented by a passive impedance

$$\vec{Z}_t = R_t \pm jX_t \tag{5.14}$$

where the terminal power factor is clearly

$$\zeta = \tan^{-1}\left[\frac{\pm X}{R}\right] \tag{5.15}$$

$o < \zeta < \pi/2$ — "overexcited"

$-\pi/2 < \zeta < o$ — "underexcited"

For each case, let the terminal voltage be per unitized as

$$V_t = 1.0 < 0^o$$

and the load apparent power is

$$\vec{S}_t \triangleq \frac{V_t \cdot V_t^*}{\vec{Z}_t} = P_t + j\ Q_t$$

$$= 1.0 < -\zeta \tag{5.16}$$

In general, $P_t = |\vec{S}| \cdot \cos(\zeta)$ and the rated load power is equal to the rated load power factor,

$$P_{tr} = \cos(\zeta_r) \tag{5.17}$$

If the load departs from unity to some per unit factor k_s

$$|\vec{S}_t| = \frac{k_s P_{tr}}{\cos \zeta} \tag{5.18}$$

$$\vec{Z}_t = \frac{\cos \zeta}{k_s P_{tr}} \cdot (\cos \zeta + j \sin \zeta) \tag{5.19}$$

The condenser internal voltage source is

$$\vec{V}_1 = \vec{V}_t\left[\frac{\vec{Z}_t + jX}{\vec{Z}_t}\right] \tag{5.20}$$

$$= V_t \angle\delta \left[\frac{\cos\zeta + k(\sin\zeta + \frac{X.k_s P_{tr}}{\cos\zeta})}{\cos\zeta + j\sin} \right] \quad (5.21)$$

$$|\vec{V}_1| = \sqrt{\cos^2\zeta + (\sin\zeta + X k_s P_{tr}/\cos\zeta)^2} \quad (5.22)$$

$$\angle\vec{V}_t \triangleq \delta = \zeta - \tan^{-1}\left[\frac{\sin\zeta + X\, k_s P_{tr}/\cos\zeta}{\cos\zeta} \right] \quad (5.23)$$

The effects of magnetic saturation may now be included by either calculating the B-H curve from a mathematical function or else directly inputing point-by-point data from an experimentally obtained open-circuit tertiary winding test; the latter being the preferred method. Therefore the MMF F_{v1} as shown in Figure 5.2 corresponding to the condenser source voltage V_1 is obtained. When required interpolation between the points on the open-circuit characteristic is a standard procedure. The phasor representing the resultant of the actual DC component of rotor current and the equivalent armature reaction effect of tertiary current is

$$\vec{I}_{v1} = F_{v1} \angle\delta \quad (5.24)$$

The angle of the tertiary reaction MMF corresponding to phasor $\vec{I}_{ar}$ is

$$\upsilon = -\pi/2 - \zeta \quad (5.25)$$

The magnitude of this reaction effect at rated load is defined as

$$F_{3r}(\text{p.u.}) \triangleq \frac{F_3'(\text{A.T.})}{F_o'(\text{A.T.})} \quad (5.26)$$

For every other loading

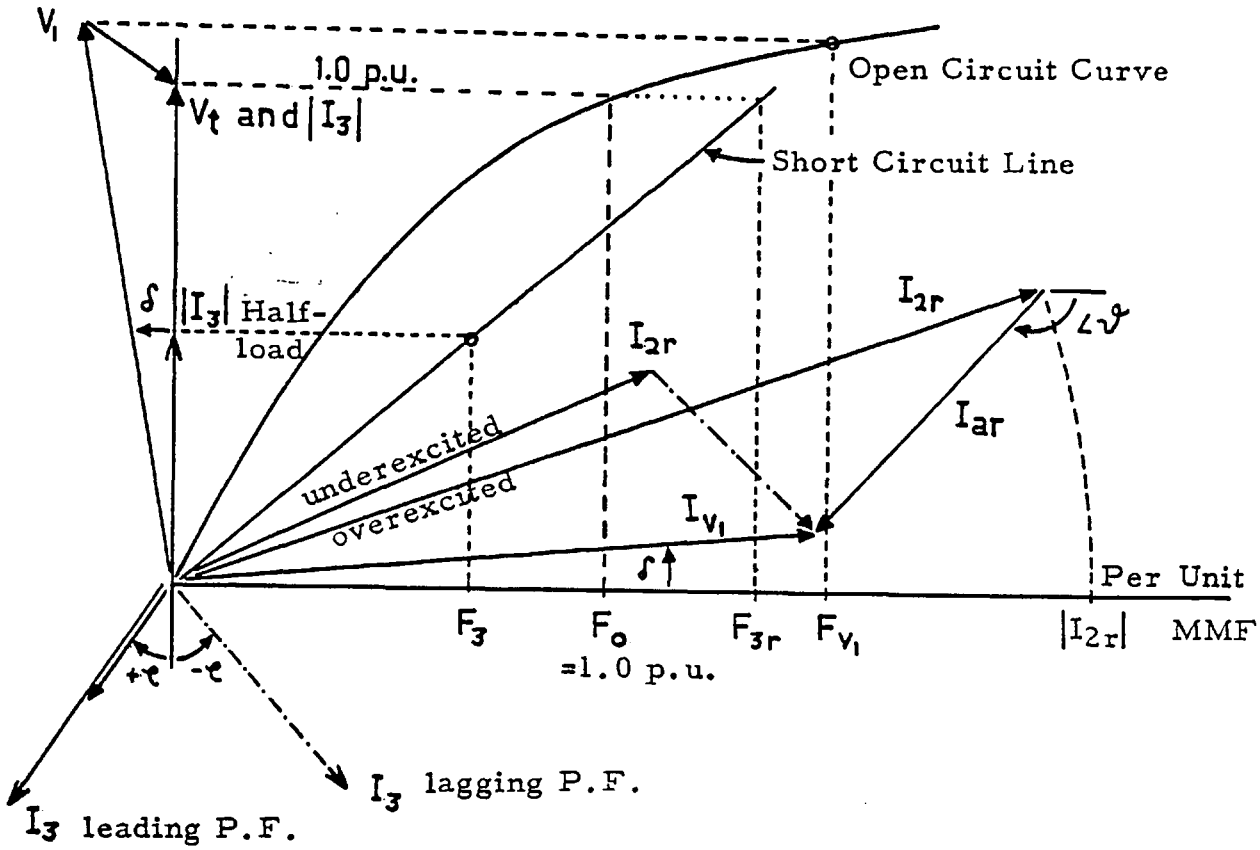

Fig. 5.2 Phasor Diagram for Asynchronous Condenser Characteristics

$$F_3(\text{p.u.}) = \frac{|\vec{I}_3|}{|\vec{I}_3(\text{rated})|} F_{3r}(\text{p.u.}) \tag{5.27}$$

$$= |\vec{S}_t| \; F_{3r}(\text{p.u.}) \tag{5.28}$$

$$\therefore \quad \vec{I}_{ar} = |\vec{S}_t| \; F_{3r} \angle \upsilon \tag{5.29}$$

The resultant equivalent excitation is

$$\vec{I}_{2r} = \vec{I}_{v1} - \vec{I}_{ar} \tag{5.30}$$

where it is clear that $|\vec{I}_{2r}|$ is the per unit requisite rotor current. To be converted into amp-turns, the rotor current producing open-circuit rated mains voltage should be used as the base. This voltage is found by integrating equation (3.79) and incorporating (3.59) for the condenser section flux distribution.

A convenient way of expressing the resultant transient rotor current in terms of dimensionless quantities is to use the logarithmic function of a product of slip and Goodness factor as

$$\frac{\text{Log}_{10} \; (\sigma \; G)}{\text{Log}_{10}(\sigma_o \; G_o)} = |\vec{I}_{2r}| \tag{5.31}$$

where $\sigma_o \; G_o = 1.0$ corresponds to the basic conditions in the composite machine for which the primary is operating at one half rated load and a conventional lagging power factor. In general, a minimum condition for total leading KVAR operation is that

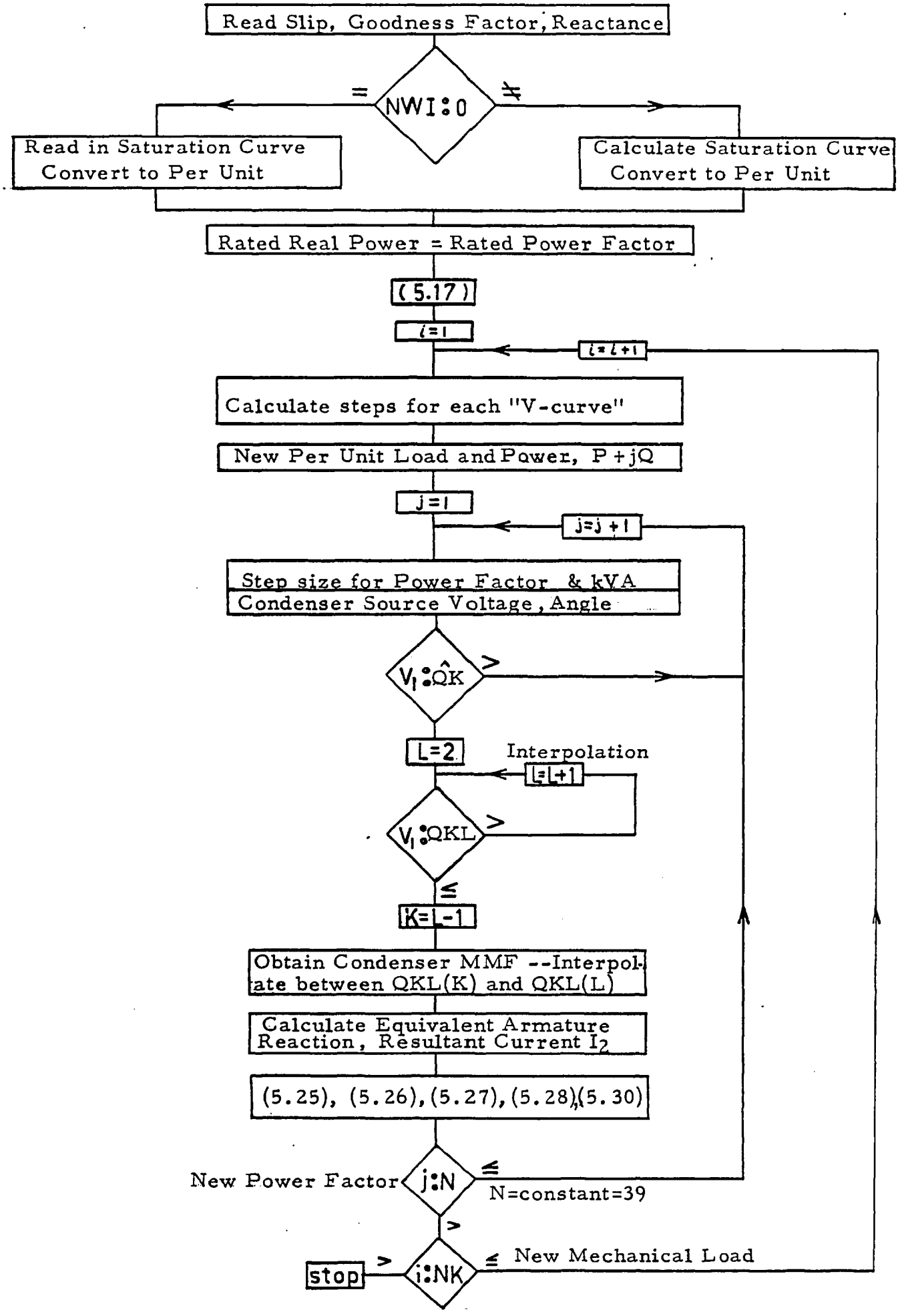

Fig. 5.3 Digital Computer Flow Diagram for Asynchronous Condensers

$$\sigma G > 2 \qquad (5.32)$$

This has been substantiated by operational experience with the SCIM-MK.II machine but the inequality in (5.32) is dependent on the saturation characteristics. Figure 5.3 shows the digital computer flow diagram for simulating the entire machine performance and it uses a point by point saturation curve to plot stator input kVA versus the σG product for differing families of per unit mechanical loading. The saturation curve used is given in Figure 5.4 based on the tertiary V-I characteristics of the SCIM-II machine rather than the lamination B-H curve. The equivalent "V-curves" for the SCIM are plotted in Figure 5.5 for 6 different values of tertiary leakage reactance; the only assumptions that is incorporated is that $R_3 = 0$.

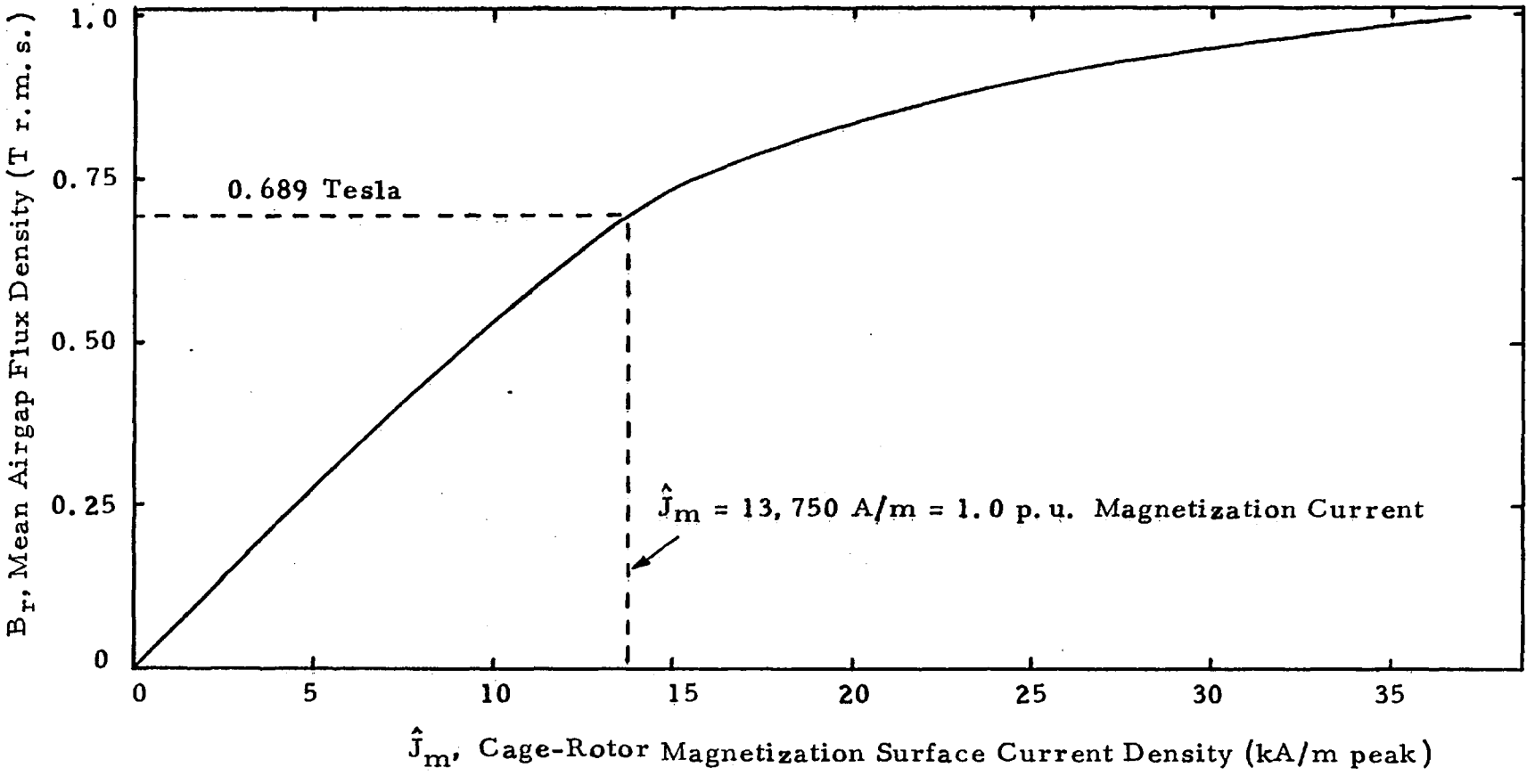

Figure 5.4 Open primary-and-tertiary circuit saturation characteristics for the 112 kW SCIM unit based on magnetic equivalent circuit calculation of total machine magnetic reluctance circuit of rotor, stator core, teeth and 1.31 mm effective airgap.

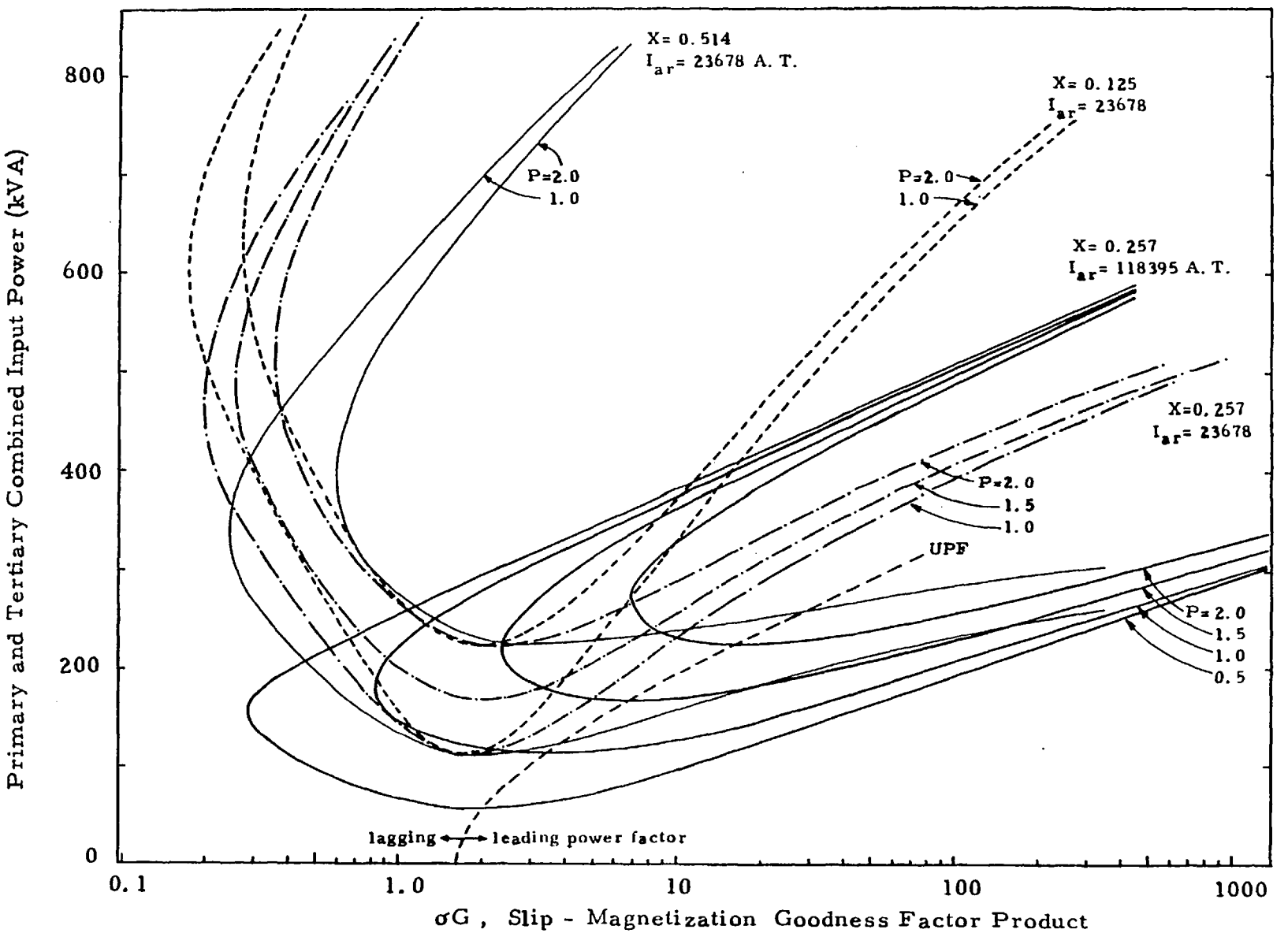

Figure 5.5 Apparent power input of four and eight pole SCIM units for different values of per unit mechanical power grouped according to total leakage reactance, X and tertiary MMF, I_{ar}.

The industrial application of the integral induction motor/asynchronous condenser brings to light a primary consideration concerning any apparent design tradeoff of power to-weight ratio and percentage power factor enhancement. Therefore, consider the example of reactive compensation occuring with the two primary windings individually optimized to peak their respective real and reactive power modes, where specifically the primary current of the former, I_1 along with the condenser primary current, I_3, are fed from the mains, in parallel and a terminal voltage V_t and the total, compensated current is I_t per phase. The power factor angles of the two branch primary currents are ϕ_{asc} and ϕ_1 and the total system power factor angle is ϕ as indicated in Figure 5.1 . By ordinary trigonometric relations, it is clear that

$$I_1^2 = I_t^2 + I_3^2 - 2\, I_3\, I_t \cos(\phi_3 - \phi) \qquad (5.33)$$

and under the assumption that only power absorbed by the ASC section is dissipated as a primary I^2R loss (and consequently no speed control mechanism is available). This power, per phase, is

$$p_1 = V_t\, I_1 \cos \phi_1 \qquad (5.34)$$

and consequently

$$I_t = \frac{p_1 + V_t\, I_3 \cos \phi_3}{V_t \cos \phi} \qquad (5.35)$$

By combining (5.33) and (5.35) it follows

$$I_1 = \left\{ \left[\frac{V_t\, I_3 \cos \phi_3 + p_1}{V_t \cos \phi} \right]^2 + I_3^2 - \frac{2\, V_t\, I_3^2 \cos \phi_3 + p_1\, I_3}{V_t \cos \phi} \cos(\phi_3 - \phi) \right\}^{\frac{1}{2}} \tag{5.36}$$

and the apparent power capacity of the main primary winding on a three-phase system is

$$3S_1 = \left\{ \left[\frac{3V_t\, I_3 \cos \phi_3 + 3p_1}{\cos \phi} \right]^2 + \left[3V_t\, I_3 \right]^2 - 18 \left[\frac{V_t^2\, I_3^2 \cos \phi_3 + p_1\, I_3\, V_t}{\cos \phi} \right] \cos (\phi_3 - \phi) \right\}^{\frac{1}{2}} \tag{5.37}$$

At unity terminal power factors, (5.37) simplifies to

$$3S_1 = \left\{ \left[3V_t\, I_3 \cos \phi_3 + 3\, p_1 \right]^2 + \left[3V_t\, I_3 \right]^2 - 18 \left[V_t^2\, I_3^2 \cos \phi_3 + p_1\, I_3\, V_t \right] \cos (\phi_3) \right\}^{\frac{1}{2}} \tag{5.38}$$

Clearly, the ratio p_1/S_1 is the power factor of the main primary winding, $\cos \phi_1$. The single most important parameter for the large machine model (current-forced) to predict reactive compensation capability is the requisite ratio $I_3 : I_1$ at unity terminal power factor.

$$\frac{I_3}{I_1} = \frac{I_3\, V_t}{\left\{ \left[V_t\, I_3 \cos \phi_3 + p_1 \right]^2 + \left[V_t\, I_3 \right]^2 - 2 \left[V_t^2\, I_3^2 \cos \phi_3 + p_1\, I_3\, V_t \right] \cos \phi_3 \right\}^{\frac{1}{2}}} \tag{5.39}$$

To further simplify this criterion, suppose that at unity terminal power factor, less than one per unit real power, p_1 is being delivered to the primary at one per unit terminal voltage, V_t

$$\frac{I_3}{I_1} = \frac{1}{\left\{\left[\cos \phi_3 + p_1/I_3\right]^2 + 1 - 2\left[\cos \phi_3 + p_1/I_3\right] \cos \phi_3\right\}^{\frac{1}{2}}} \tag{5.40}$$

Rather than solving (5.40) as a singular function of p_1, it is necessary to characterize this by a family of curves according to the ratio of tertiary active power input to primary active power input as

$$\frac{p_3}{p_1} = \frac{V_t\ I_3 \cos \phi_3}{p_1} = \frac{I_3 \cos \phi_3}{p_1} = \frac{1}{k_p} \tag{5.41}$$

$$\frac{I_3}{I_1} = \beta = \sqrt{\frac{1 - \cos^2(\phi_1)}{1 - \cos^2(\phi_3)}} = \left\{1 + \cos^2(\phi_3)\left[k_p^2 - 1\right]\right\}^{-\frac{1}{2}} \tag{5.42}$$

where normally k_p is significantly larger than unity and may be negative. Figure 5.6 plots the tertiary to primary current ratio as a function of the tertiary section power

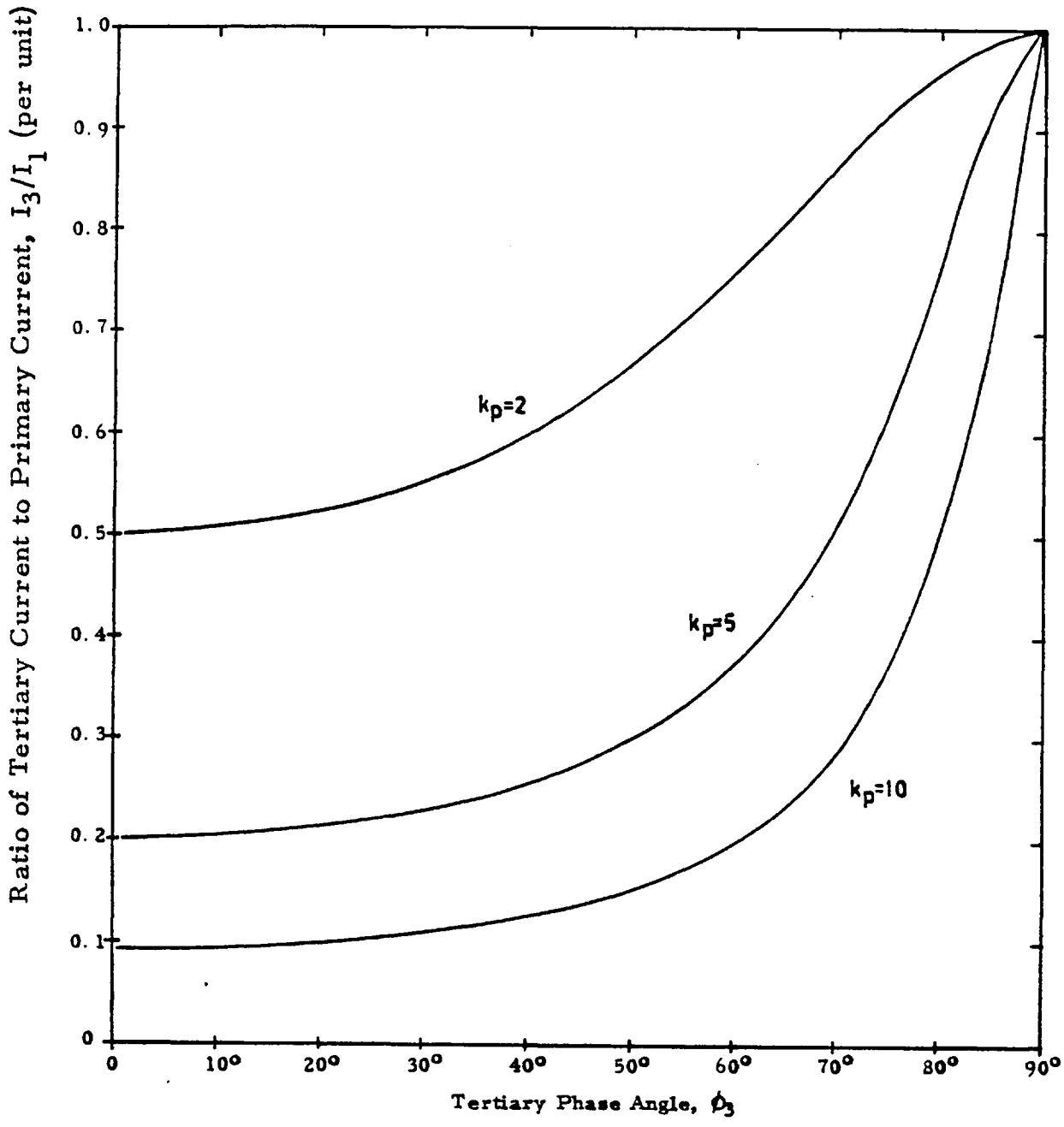

Fig. 5.6 Ratio of tertiary current to primary current at unity power factor

factor angle for values of k_p from 2 through 10; the latter value corresponding to large induction condenser machines such as the Θ-Pinch MK.II design.

Similarly, it is convenient to characterize the composite machine by a family of curves according to the ratio of the tertiary reactive power output to the primary active power input as

$$\frac{Q_3}{P_1} = \frac{V_t\ I_3\ \sin \phi_3}{P_1} = \frac{I_3\ \sin \phi_3}{P_1} = \frac{1}{k_q} \qquad (5.43)$$

and consequently the branch current ratio is a singular function of the I_3 current angle ϕ_3 as

$$\frac{I_3}{I_1} = \left\{ 1 - 2\left[\cos \phi_3 + k_q \sin \phi_3\right] \cos \phi_3 + \left[\cos \phi_3 + k_q \sin \phi_3\right]^2 \right\}^{-\frac{1}{2}} \qquad (5.44)$$

This expression is plotted in Figure 5.7 for values of k_q ranging from 20 through 1.5; the latter value corresponding to the larger induction machines at unity power factor and constant terminal voltage conditions.

An equally important criterion as (5.42) and (5.44), is the ratio of tertiary current to total line current as a function of ϕ_3.

$$\frac{I_3}{I_t} = \left\{ 1 + \beta^2 + 2\beta \cdot \cos\left[\phi_3 - \cos^{-1}(K_p \beta \cos \phi_3)\right] \right\}^{-\frac{1}{2}} \qquad (5.45)$$

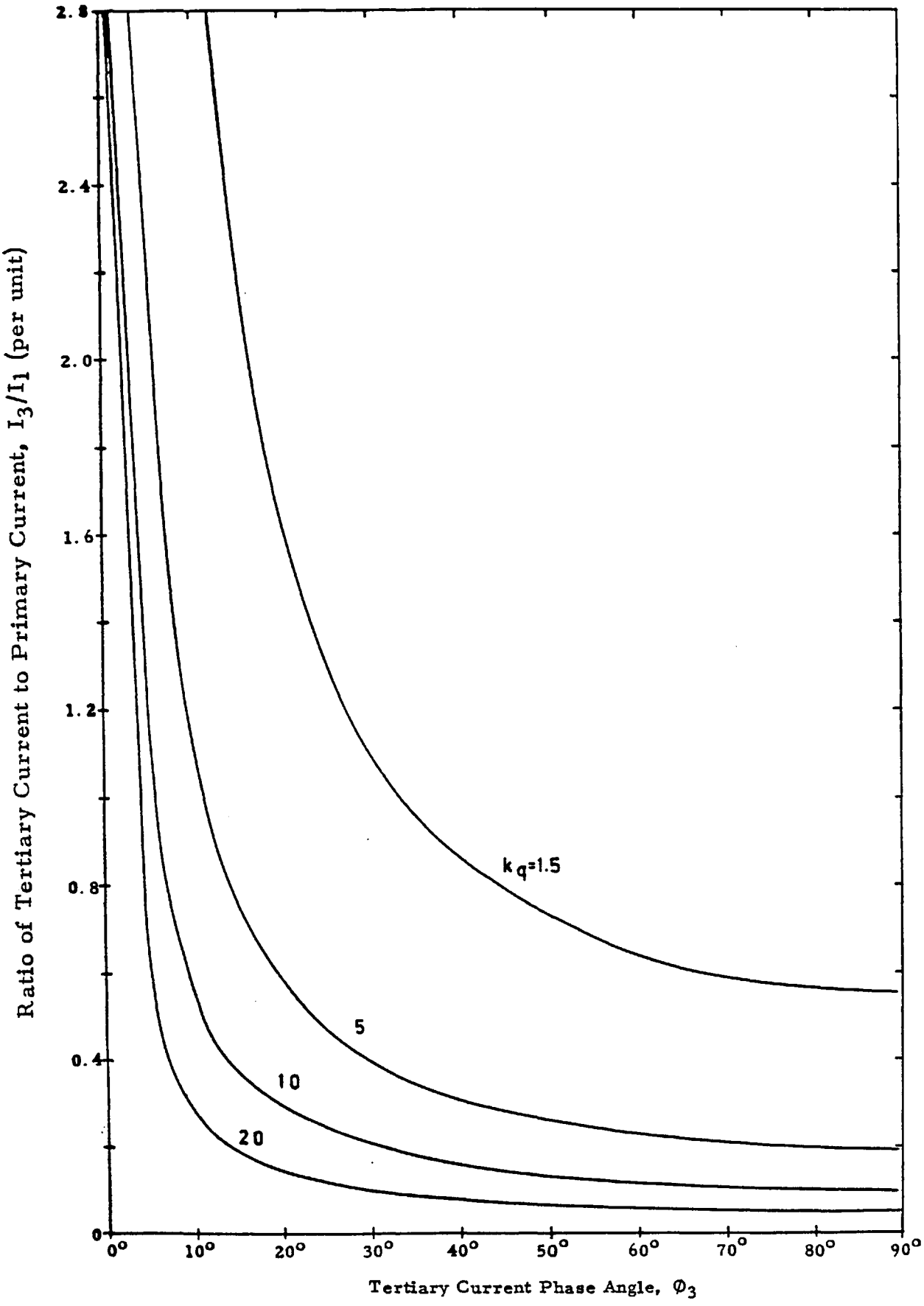

Fig. 5.7 Ratio of tertiary current to primary current at unity power factor

This is plotted in Figure 5.8 for k_p=2 and k_p=20 to indicate active power absorbed by the tertiary power with respect to the primary. On a first order, k_p may be used to express the utilization of the machine, as in the large machine model it is approximately

$$k_p = \frac{p_1}{p_3}\left[\frac{p_m/\eta}{p_m(1-\eta)/\eta}\right]\cdot\frac{(I_1/I_3)^2}{n_3/n_1} = \frac{(AT_1/AT_3)^2}{(1-\eta)\ n_3/n_1} \qquad (5.46)$$

where p_m is the mechanical output per phase, η is the conversion efficiency, $n_{1,3}$ are the primary or tertiary poles and AT is the ampere-turns per phase since primary and tertiary windings necessarily have different turns/phase. In general, the current-forced Θ-Pinch machines satisfy the inequality that

$$n_3\ T_3 > n_1\ T_1 \qquad (5.47)$$

under the assumption of either uniform peripheral slot filling or the tertiary conductor exceeding the primary conductor volume per slot up to 20%.

The ratio of the tertiary current to the total line current may also be expressed in relation to the reactive output of the tertiary, using the parameter k_q, as

$$\frac{I_3}{I_t} = \frac{\beta}{\left\{1 + \beta^2 + 2\beta\ \cos\left[\phi_3 - \cos^{-1}(\beta\ k_q \sin\phi_3)\right]\right\}^{\frac{1}{2}}} \qquad (5.48)$$

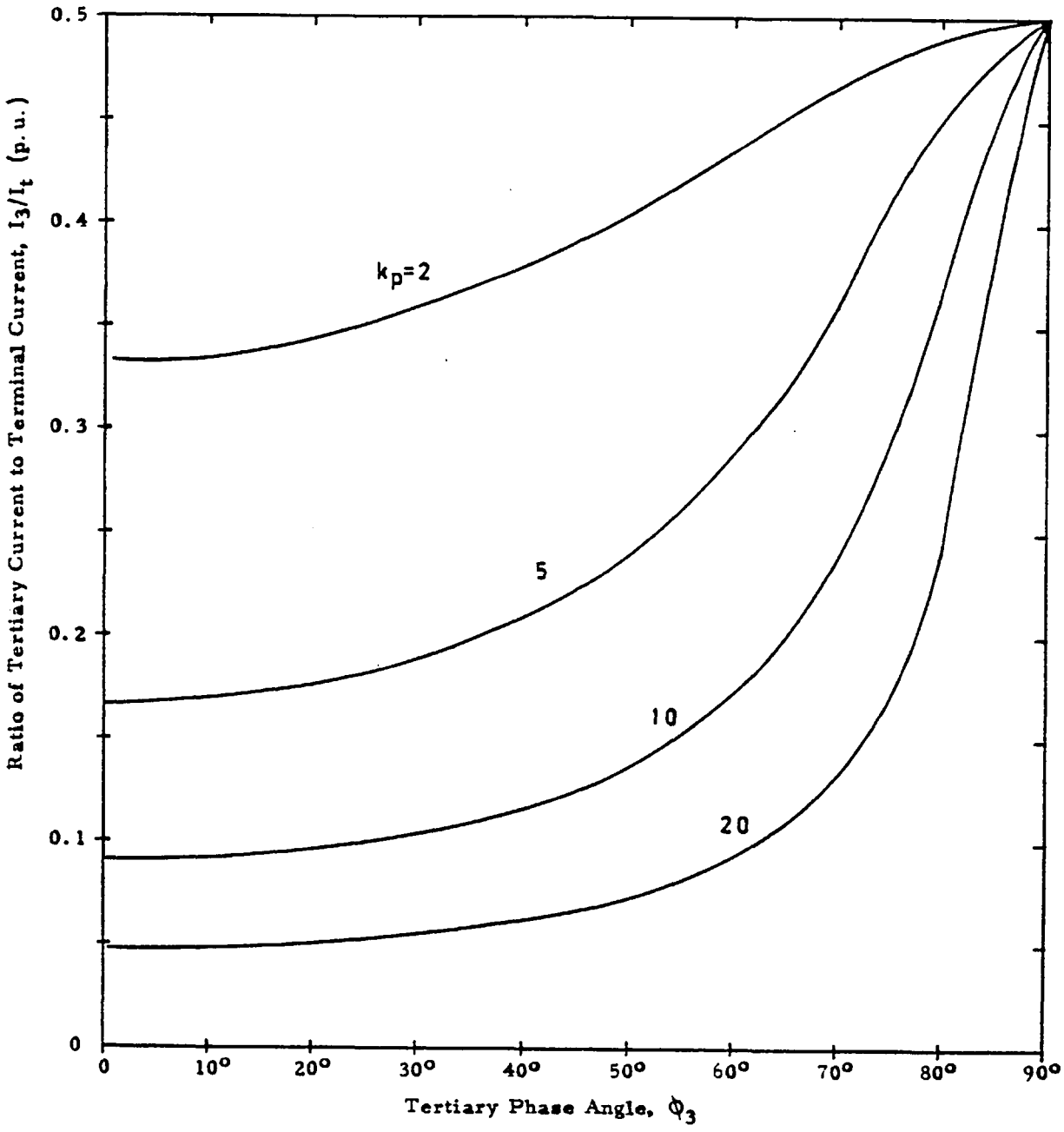

Figure 5.8 Ratio of tertiary current to total current at unity power factor.

This is plotted in Figure 5.9 and should be compared with Figure 5.7 to evaluate terminal performance at constant k_q values.

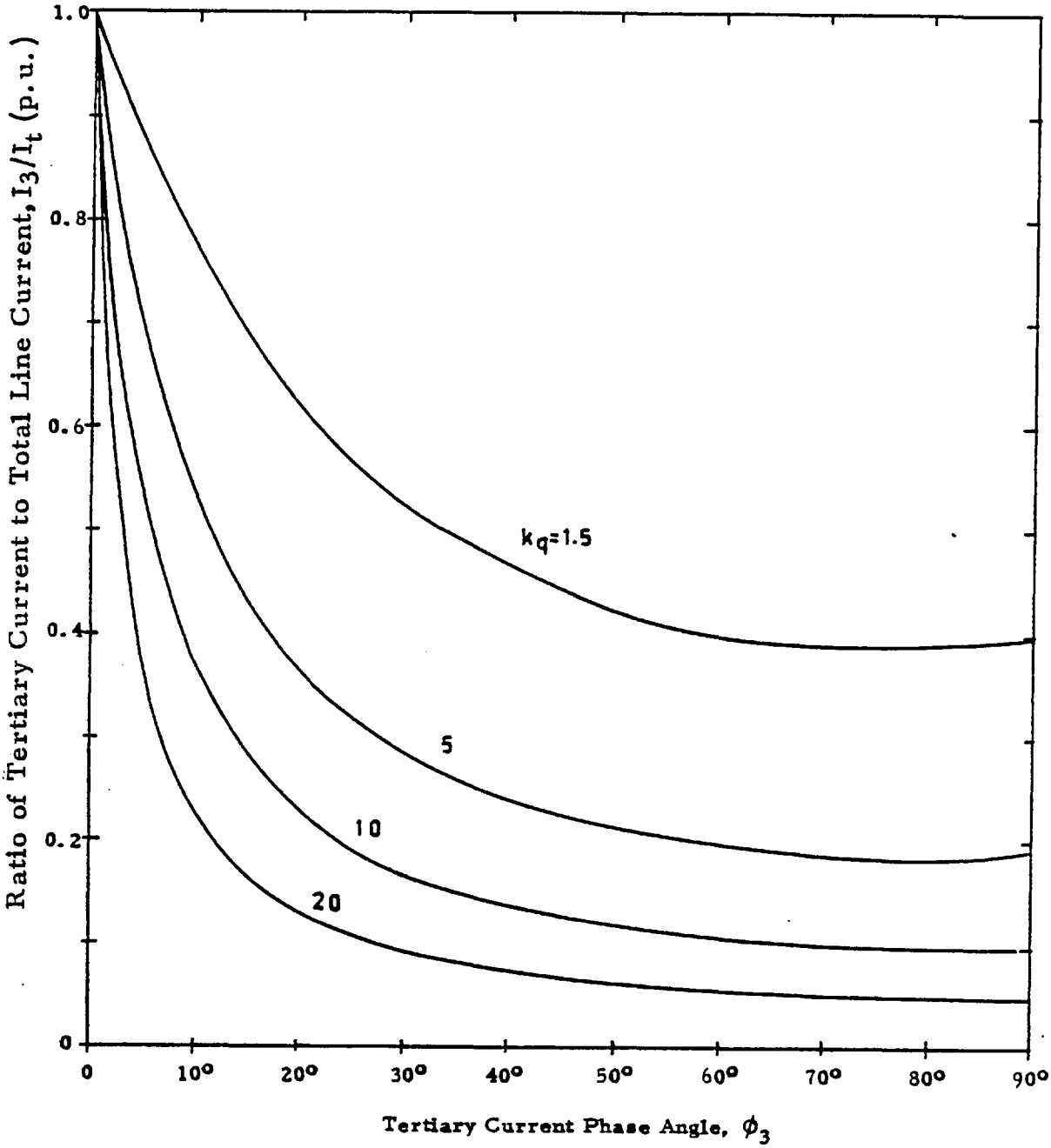

Fig 5.9 Ratio of Tertiary to Total Line Current at Unity Terminal Power Factor

5.2 THE SCIM-II MACHINE

In 1975 it was first suggested that continuous, unity power factor operation of a cage-rotor motor might be achieved by winding design alone if the stator MMF was so configured to produce a progressively decelerating airgap field speed in the direction of rotor motion [2] . This was superseded by the "Theta-Pinch" design whereby instead of having a continuously changing system of field speeds, each repeatable section of the stator periphery contained only one or two abrupt changes in pole-pitch and MMF simultaneously. The 112 kW Theta-Pinch motor is shown in Figure 5.10.

One requirement is that each repeatable section contain at least 4 poles (with respect to the original single pole-pitch winding) to establish the proper flux level; the first machine of this type had a total of 10 poles with pole-amplitude-modulation windings used for the 8 poles of excitation for torque production and the remainder were used as a reactive current generator.

In all of these space-transient machines, referred to in the literature as induction condensers, it is understood that these units still accrue the conventional reactive losses due to leakage flux paths and magnetization as in a lagging power factor machine. The purpose of the second polyphase stator winding is to compensate entirely for the reactive losses by phasing it for maximum leading current without producing any significant braking forces on the rotor.

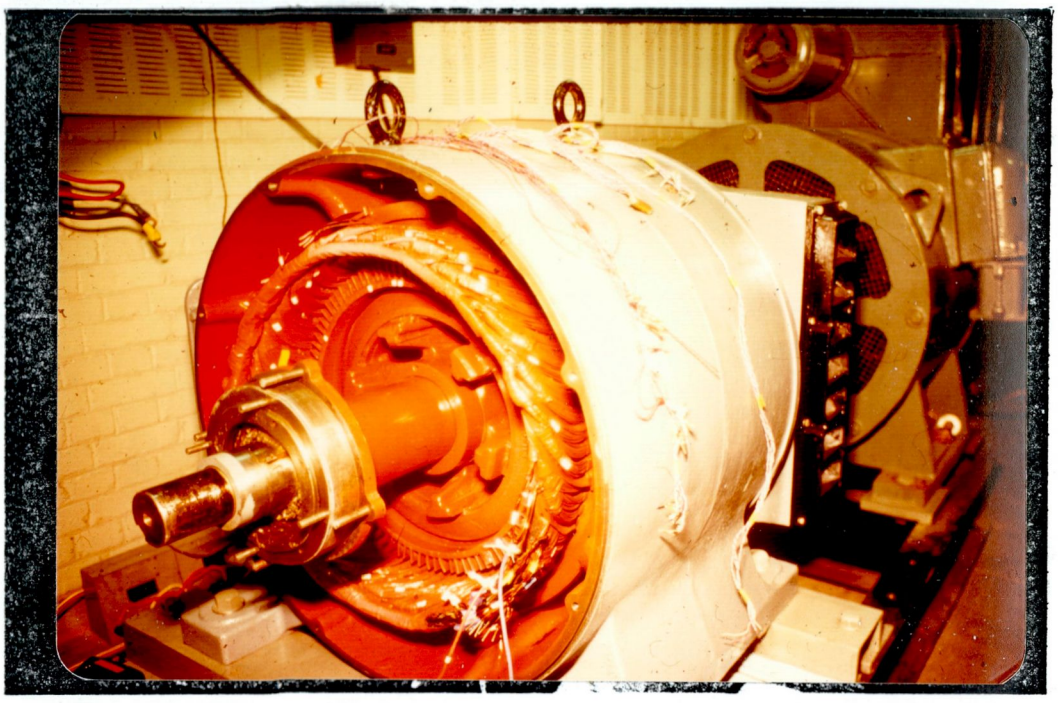

Fig. 5.10 View of the 150 H. P. SCIM unit during the reconnection commencing with one ASC group that is separately-excited as shown in the lower right side of the endwinding. The 150 kVA Type NS AC-commutator dynamometer is in the backround.

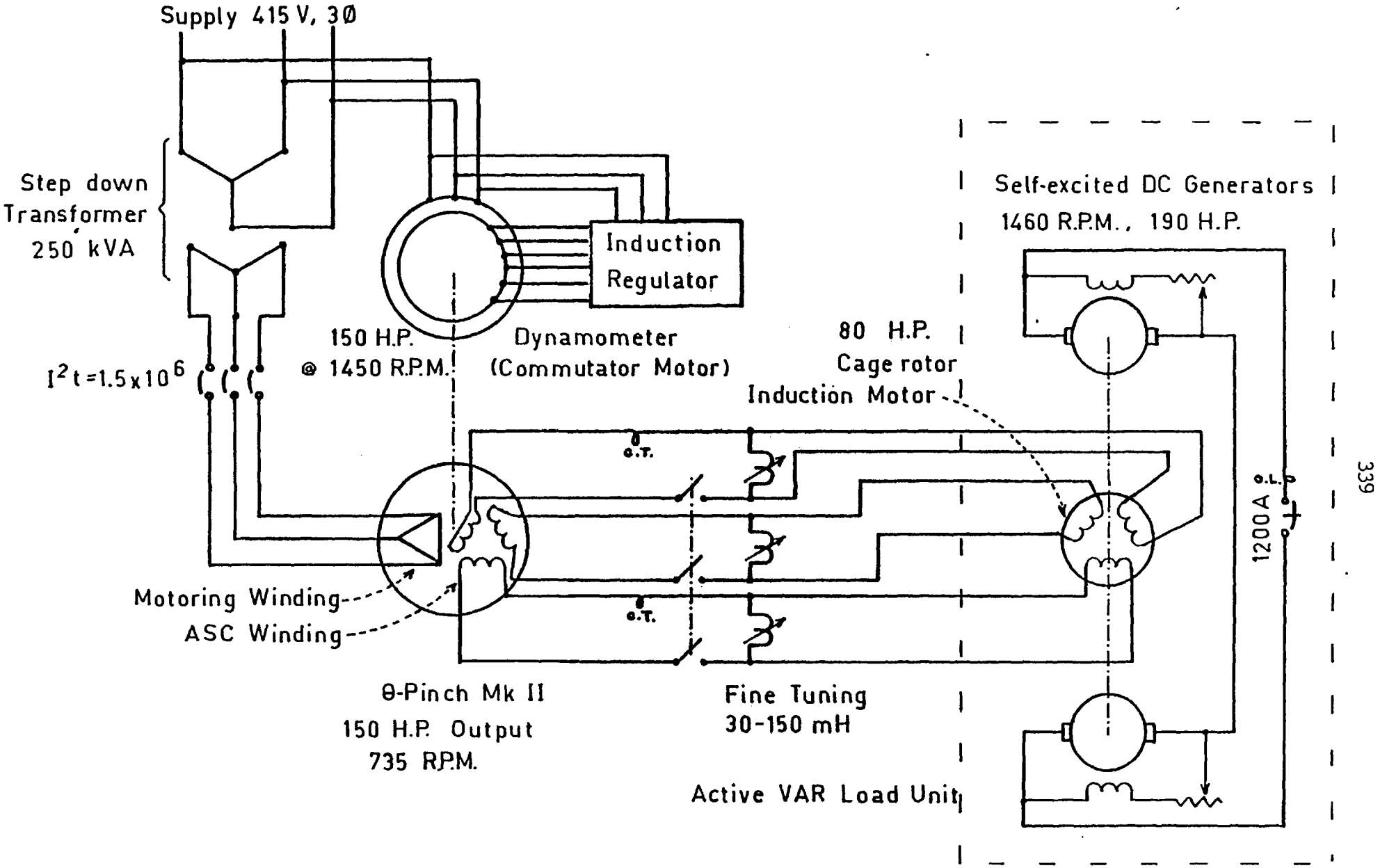

Fig. 5.11 Lab 002C Test Facility for θ-Pinch Reactive Power Balance prior to rewind

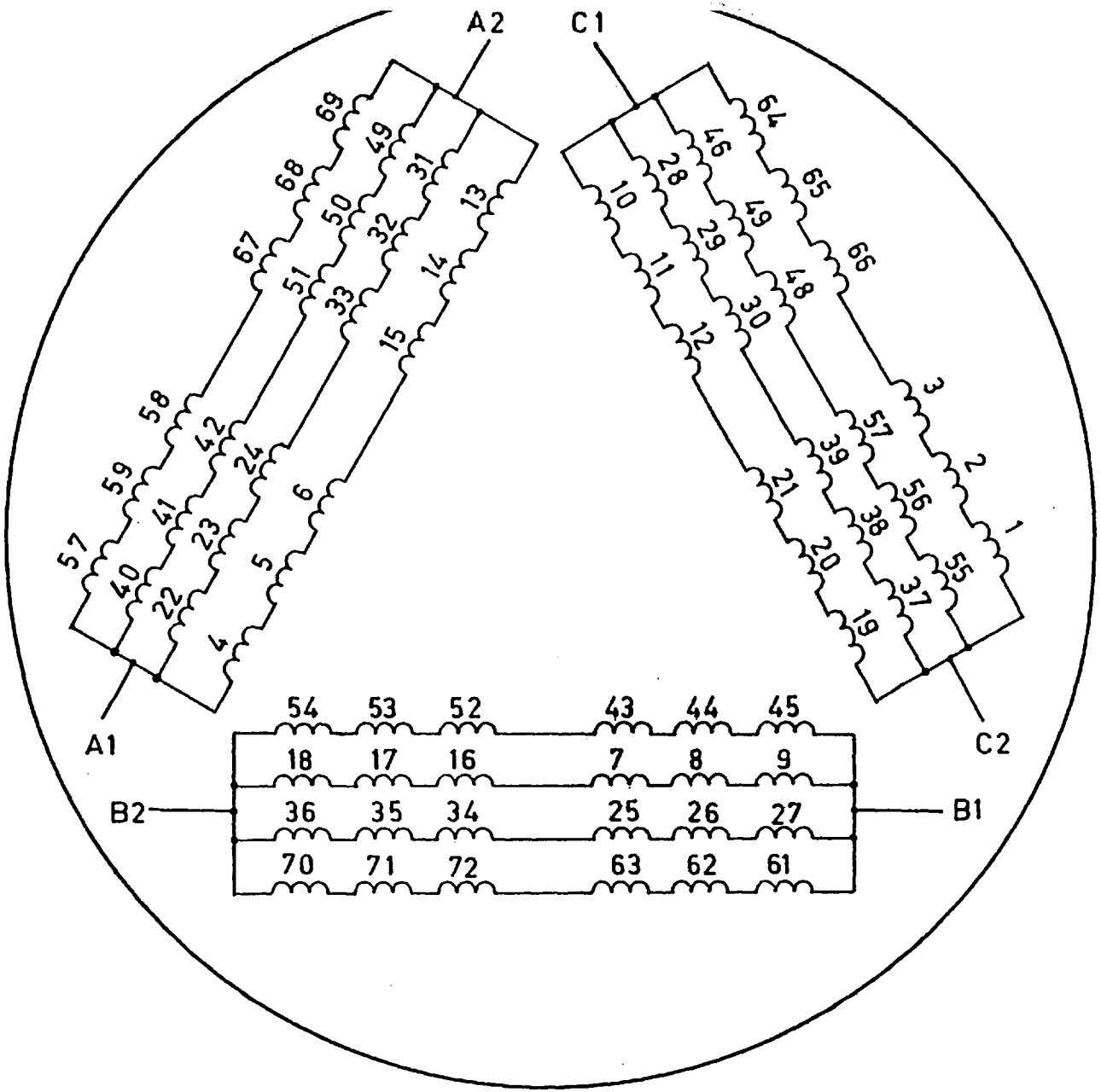

Figure 5.12 Original Equipment Manufacture (Newman) Coil Layout in the 150 H.P. Cage Rotor Induction Motor

Table 5.1

Characteristics of the 150 H.P. 8 Pole Induction Machine Θ-Pinch II with O.E.M. Newman Stator Winding (50 Hz)

Stator

Pole pitch, mm	194
Coil throw slots	1-8
Conductors in parallel/coil	3
Conductor wire size, O.D., mm	1.828
Copper cross section/parallel, mm^2	7.88
Total copper cross section in one slot, mm^2	204.8
Number of turns/coil	13
Weight/set of 72 coils, kg	82.7
Chording factor	0.940
Distribution factor	0.959
Number of coils in series across 415	6
Slot utilization factor, per cent	36.9
Slots/pole/phase	3
Insulation class	A/B
Core-iron loss	710
Teeth-iron loss	480
Tooth surface -iron loss	360
Current density at rated load, A/mm^2	3.58
Total copper cross section in 72 slots, cm^2	147
Mean length of turn, cm	119
Terminal voltage, (Delta connection)	420
Line Current, A	202
Full load slip, %	2.0
Maximum temperature rise, °C	75
Copper loss, kW(stator)	2.39
Starting Current, A	1130
Starting Torque, N-m	1807
Maximum Torque, N-m	5010
Rated Torque, N-m	1205
Slip at maximum torque, %	11.2
Total losses at rated load, kW	9.085
Efficiency at rated load , %	92
Power Factor at rated load, %	91
Maximum airgap flux/pole, running light, Wb	0.0259
Current loading/periphery at rated load, J_s (peak) A/m	44,850

Equivalent Circuit Parameters (Ohms)

R1	0.0620
R2 (locked rotor)	0.1379
R2 (at 2% slip)	0.0692
X1	0.282
X2 (locked rotor)	0.271
X2 (at 2% slip)	0.323
Xm	13.2
Ri - iron loss	316
Goodness Factor	192

Table 5.1 Continued

Characteristics of the 150 H.P., 8 Pole S.C.R. Induction Motor Θ-Pinch II

Stator

Number of slots	72
Conductors in parallel/coil	3
Copper cross section/parallel, mm^2	7.87
Coil throw slots	1-8
Core length incl. 3 ducts, mm	292.1
Number of turns/coil	13
Weight / set of 72 coils, kg	82.7
Ohms/phase @ 20°C	0.0501
Wire size, O.D., mm	1.828
Chording factor	0.939
Distribution factor	0.959
Overall slot area, mm^2	555
Number of coils in series across 415v	6
Insulation class	A

Performance as Original Equipment Manufacture

High speed connection	Delta
Rated load speed, rpm	735
Rated phase current, A	202
Locked rotor torque, per cent	150
Locked rotor current, A	1130
Locked rotor input power, kW	243
Locked rotor power factor, per cent	31
Full load power factor-efficiency product	0.761
Estimated full load mean airgap flux density, T	0.545
Full load slip, per cent	2.0
Full load rotor loss, kW	2.238
Full load stator copper loss, kW @ 20°C	1.533
No-load power input, kW	4.2
No-load phase current, A	68
No-load power factor, per cent	8.9

In all previous tests of the rotary lab machines with asynchronous condenser windings, either an external inductor bank or a phase shifter had to be used to load the ASC windings. For the SCIM - II unit, a three-phase auto-transformer has been used in between the ASC windings and the mains to allow some kind of experimental optimization, since the internal leakage flux penalty of using a phase shifter to vary VARs was avoided. In particular, the use of a variac to control the forcing of VARs into the mains allowed tests to substantiate what fractional turns on the ASC coils would give the highest output; ideally there should be e.g. 8.6 turns/coil. In a commercially built machine, there would be no reason to even include an auto-transformer albeit brazed-connections internally would be very specific to a particular slip, plus or minus about 0.6%, which is actually a rather large margin for 200-500 H.P. size machines. The purpose of the rewind was to obviate the need for any such external devices and consequently, feed the leading VARs directly back into the mains.

The experimental facility and instrumentation for these tests are shown in Figure 5.11. The original winding layout of the 150 H.P. machine with a symmetrically-wound primary is shown in Figure 5.12 with characteristics listed in Table 5.1 including the equivalent circuit parameters. Figure 5.13 shows the computed performance of this machine from the steady-state model and including the deep-bar rotor effect but neglecting stray-load loss, magnetic stauration and hysterisis. Figure 5.14 depicts the computed efficiency based on synchronous watts and the rotor power factor which is taken to be $\cos^{-1}(R_2/\sigma Z_2)$ with both R_2 and X_2 having a slip dependence according to (6.18).

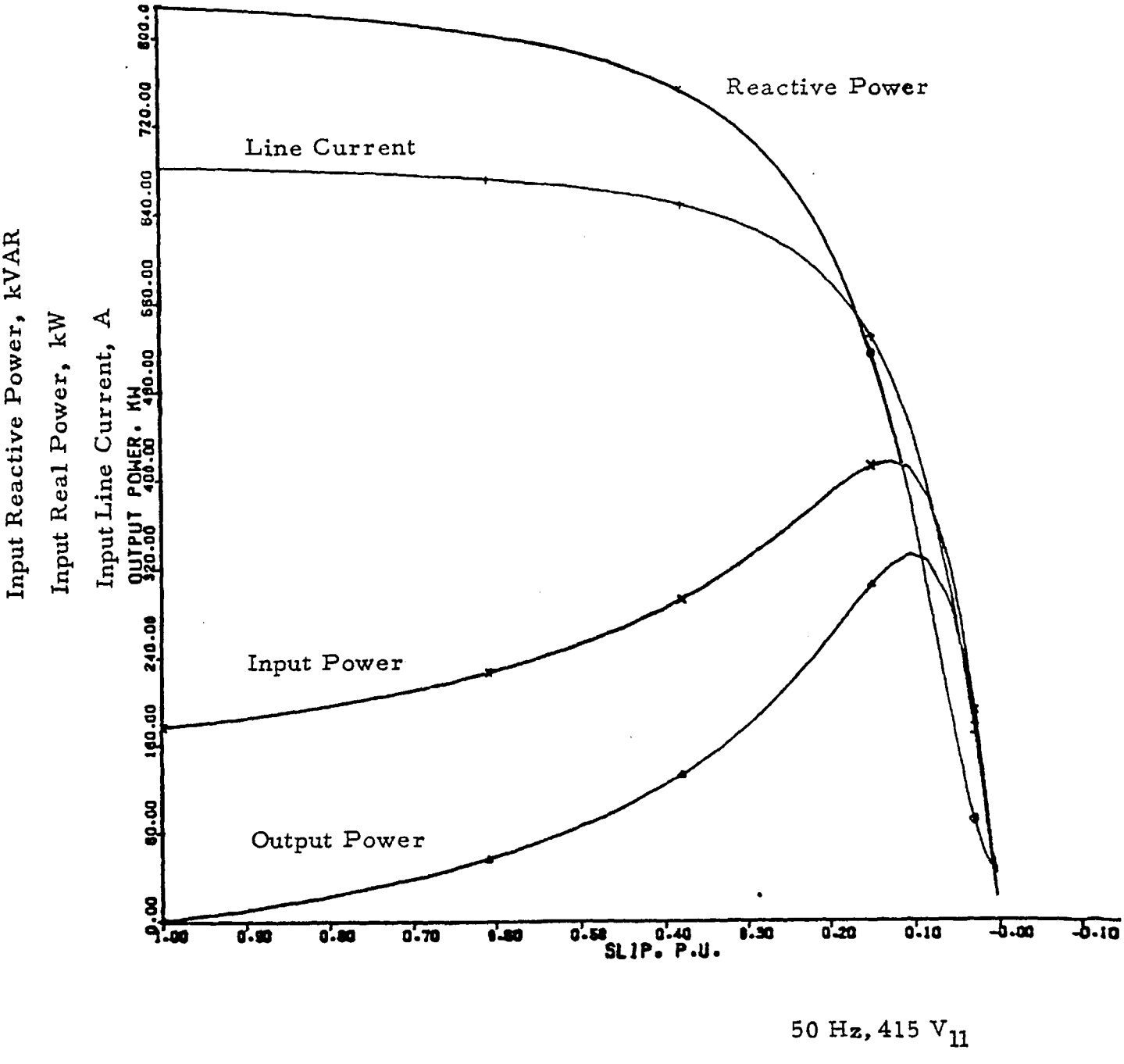

Fig. 5.13 Computed Performance Characteristics of the 150 H.P. Machine as Original Equipment Manufacture, neglecting core loss, stray-load loss, friction and windage loss and magnetic saturation. Deep bar effect included.

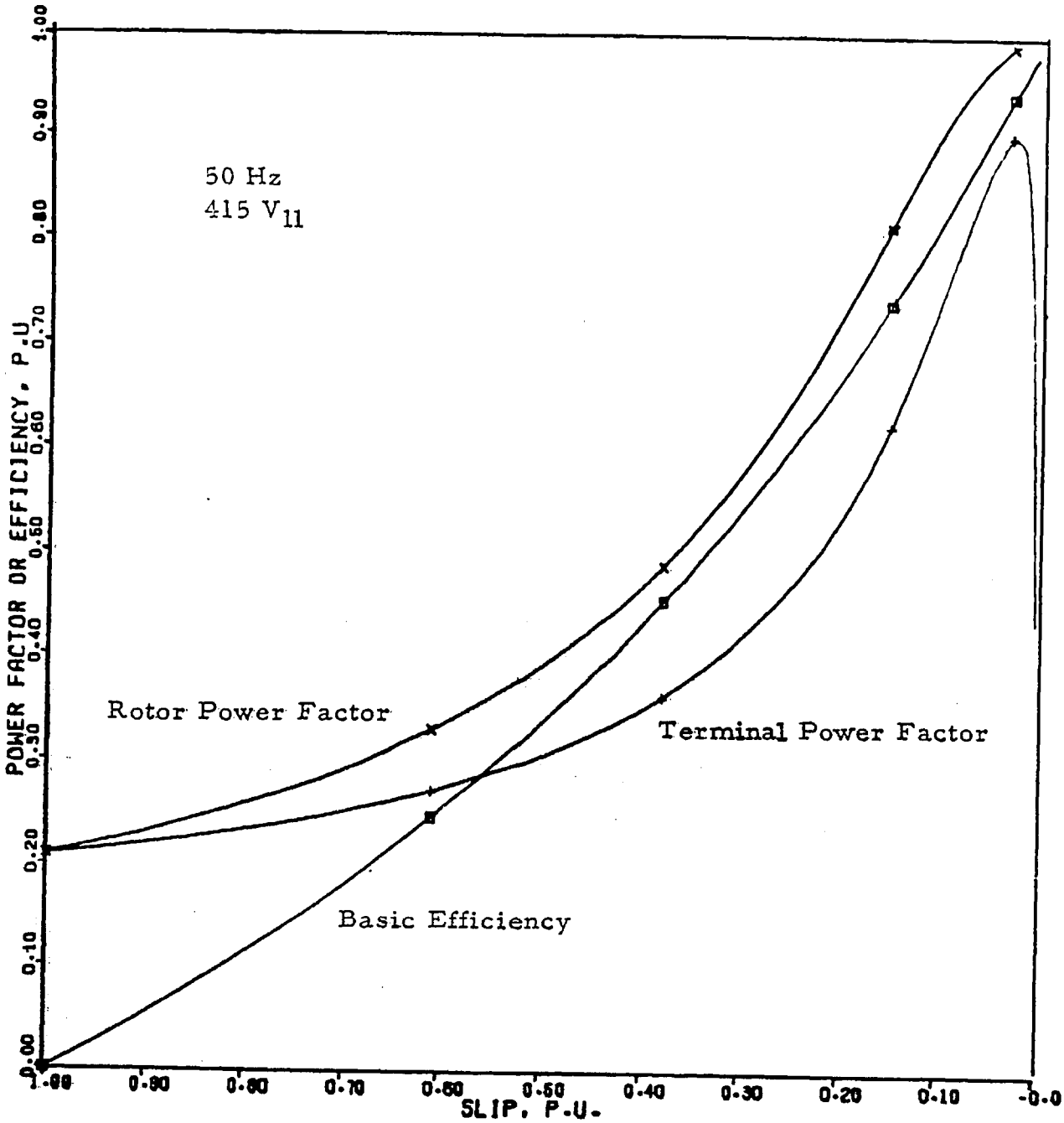

Fig. 5.14 Computed Performance Characteristics of the 150 H.P. Machine as Original Equipment Manufacture, neglecting core loss, stray load loss, friction, windage and magnetic circuit saturation. Deep bar effect included.

5.3 UNITY POWER FACTOR TESTS

The purpose of the reconnection testing was to substantiate computer calculations and previous experimental evidence existing on:

a) Starting torque and current
b) Phase balance (interphase and intraphase)
c) Harmonic speeds
d) Reactive output
e) Relative phase change of ASC induced voltage versus slip
f) Decrement of ASC induced voltage along ASC poles
g) Excess rotor real-power loss
h) Phase angle error per coil as a function of slip due to uniform pitch

A. Starting Currents and Torques

Figure 5.15 shows the starting current of the 150 H.P. machine in the most preferable connection arrangement from the aspect of passing through any harmonic speeds before running light at 744.8 R.P.M. This connection of the main winding was a standard delta type at the terminals with three phase groups per leg in parallel as shown in Figure 5.16 . However, the important aspect of this is not especially the delta, but since each leg is composed of 6 coils in series, it is essential that the spacing of these individual coils around the periphery effect a rather specific MMF shape. The optimum MMF for the start-up mode was found largely by trial and error before the machine was rewound and the location of the coils is shown in Figure 5.17 in schematic form, to complement Figure 5.16 . In general, designers are careful to avoid any delta connections in special circumstances as this might lead to unequal phase currents, but yet this is what precisely makes the SCIM-Mk.II machine at 150 H.P. practical

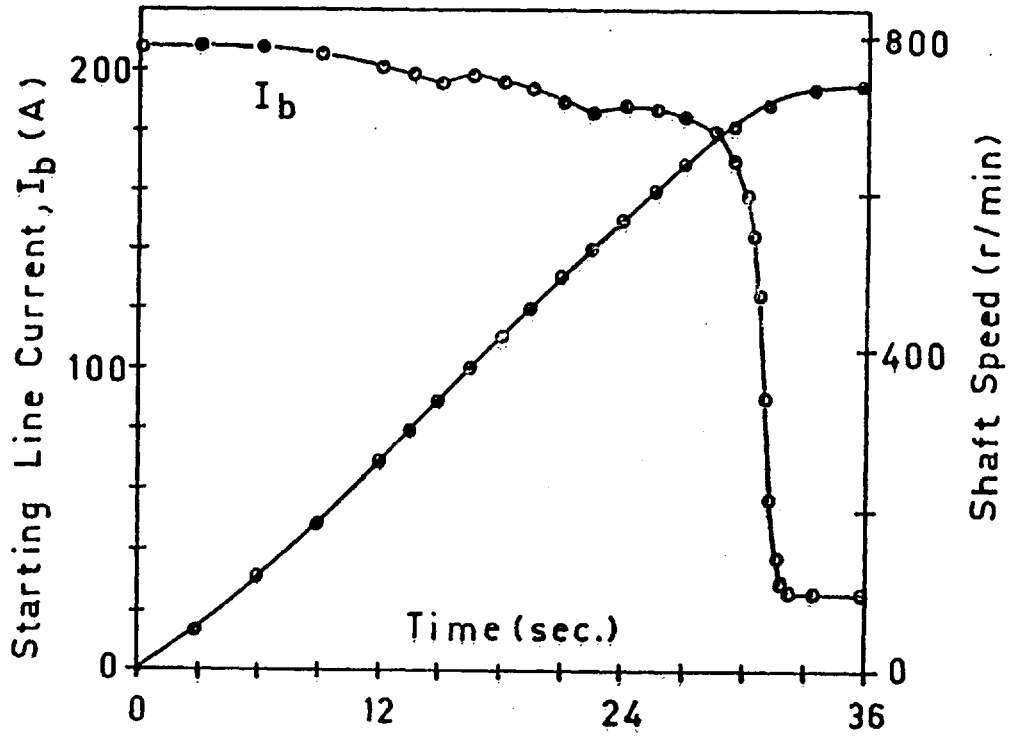

Figure 5.15 Line current and shaft speed during reduced voltage starting with J_{s3}=0 for the tertiary winding and inertia of 67.5 N-m-sec^2.

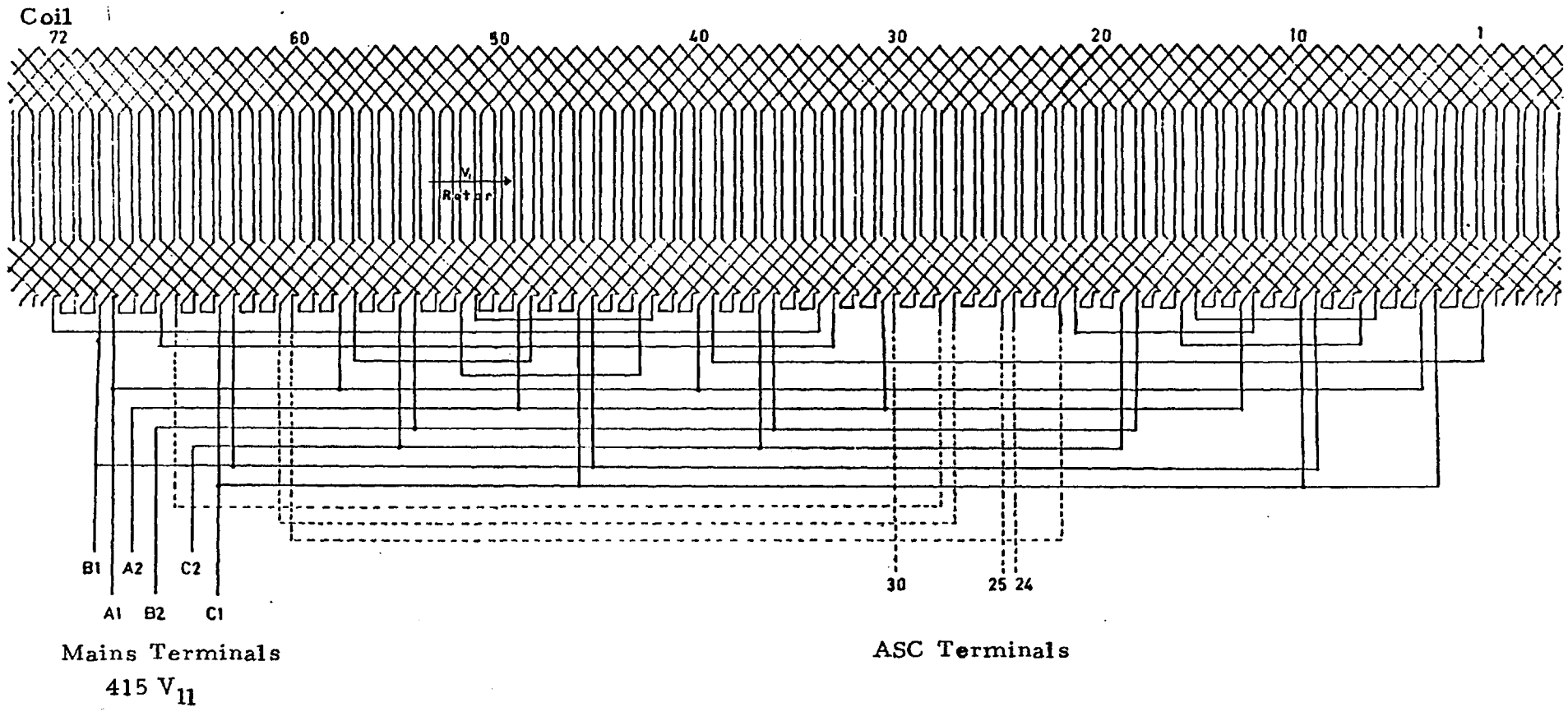

Figure 5.16 Final reconnection diagram for the 112 kW, 8-pole machine using a combination series-parallel primary winding and series-connected tertiary(ASC) winding that yielded a net zero reactive power balance between input and output VARS.

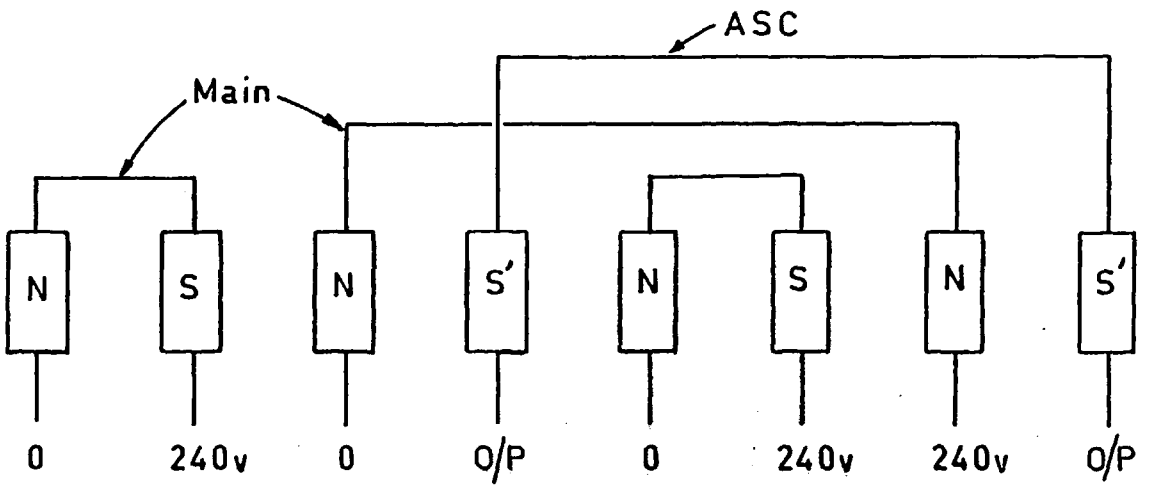

Fig. 5.17 Preferred pole grouping of 112 kW machine used in reconnection testing as detailed in Figure 5.16

to start. Figures 5.16 and 5.17 thus depict a case whereby individual coil currents will differ by at most a factor of 2 (all motoring coils having the same number of turns) at speeds of 66% or higher of synchronous, when harmonics could potentially be a problem. At locked rotor, it is understood that all coils carry substantially the same current as determined by the zig-zag leakage inductance and other non-rotational parameters. The essence of this special connection is that all coils of the first entry pole (of the same phase) among repeatable sections must be series connected before being placed in parallel across the mains as in the delta. Equally important, all of the coils of the middle poles in the motoring section must be series connected within each repeatable section only.

In this particular winding for the 150 H.P. unit, the motoring winding consists of 3 poles where it has been found advantageous to have poles 2 and 3 in each repeatable section in series, with pole 3 being the exit pole preceding the ASC types. (Possibly for other designs which make use of 4 motoring poles per repeatable section, it may be advantageous to have pole number 4 cross connected among repeatable sections, although to a large extent the best arrangement for this exit pole is entirely dependent on the loading of the ASC windings.) The connections so far suggested for the entry and middle poles are largely independent of the ASC loading. Essentially the same starting characteristics could be obtained with a pole-amplitude modulation winding by incorporating interspersed coils in the phase groups whereas the present arrangement uses exclusively 3 slots/pole/phase.

As an alternative to simply avoiding the use of the ASC windings in the starting mode, the inclusion of one star-delta

changeover contactor (nine terminals) with the machine connects the ASC windings to the mains during start to provide exactly the same torque-speed characteristics as a conventionally wound machine. At a slip value less than 15%, the contactor changeover simultaneously effects an ASC impedance level change as well as giving this winding a 120 degree phase shift so that VARs are generated rather than consumed. This is illustrated in Figure 5.18 and the only special requirement is that the ASC winding have two separate conductor paths/coil; in start the ASC is in series with the STDP winding while, for unity power factor operation, the ASC is in parallel-star with STDP.

B. Phase Balance

Phase balance has in general been a problem for equalizing the current among phases although intraphase current or voltage balancing has been very good, owing mainly to the use of two repeatable sections. The interphase balancing is primarily controlled by the use of unequal numbers of coils/phase coupled with the fact that each coil is operating at a slightly different flux level albeit each coil has the same number of turns. The terminal phase balance situation may be cumbersome in large industrial applications, but as far as the airgap of the machine is concerned, it makes no difference per se. Conversely intraphase unbalance can be detrimental to the electromagnetic conditions for VAR generation while this might remain undetectable from terminal measurements. Table 5.2 gives typical figures for the 150 H.P. machine.

C. Harmonic Speeds

In this section, all harmonic speed conditions are based entirely on MMF harmonics and stator-rotor slotting harmonics

Table 5.2

Phase Balance of 150 H.P. Machine with P.F. Correction
Test Results from 30.6.80 Data
Two Parallel Groups per Phase of Motoring Winding

1) Speed: 739.2 RPM (approx. 1/2 load)

I_R = 80.1 I_Y = 60.3 I_B = 78.5 A

V_R = 91.2 V_Y = 89.3 V_B = 86.25 V

2) Speed: 733.1 RPM (approx. 3/4 load)

I_R = 128.3 I_Y = 114.4 I_B = 125.8 A

V_R = 90.0 V_Y = 88.9 V_B 87.2 V

in these machines are exactly the same as in conventional machines. In general, the inclusion of an ASC pole(s) in a rotary machine means that there exists the potentiality that the unit will run at a harmonic speed corresponding to either the next even number of motoring poles or the second higher number of poles. For instance, the basic 8 pole machine comprised of 3-1+ - 3 - 1+ poles could run at either a 10 pole speed or a 12 pole speed depending entirely on the loading of the ASC 1+ pole.

If as in SCIM-II the stator is wound with a uniform 3 slots/pole/phase or the like, where the number of motoring poles are n_1 around the entire periphery, and the number of condenser poles are n_3, then in general the harmonic synchronous speeds occur at

$$\omega_{s(h)} = \frac{n_1 + n_3}{2h} \omega_{s(1)} \qquad (5.49)$$

where $\omega_{s(1)}$ is the fundamental speed and h is the order of the harmonic, any integer larger than the sum $(n_1 + n_3)/2$. This implies that the relative length of the ASC section is not important in determining harmonic speeds. Table 5.3a gives the harmonic slips for the case of 8 and 10 pole peripheries.

Table 5.3a

Harmonic No.	Slip with $n_1 + n_3 = 8$	Slip with $n_1 + n_3 = 10$
5	* 20%	0
6	* 33%	* 16%
7	42.8%	28.5%
8	50.0%	37.5%

However, while the above expression accounts for any serious harmonic effects, some minor torque oscillations exist as a consequence of the relative length of the ASC winding, i.e., the gap in the main excitation. These are due to the combined

modulation of the airgap by the synchronous travelling field and the rotor speed travelling field. The synchronous slip at which these beats occur about are given by

$$\sigma = \frac{h}{h + n_1} \quad \text{per unit} \qquad (5.50)$$

Table 5.3b gives these harmonic slips for the 35 H.P. (n_1=4) and 150 H.P. (n_1=3) units. Note that the pole numbers in (5.49) refer to total poles whereas in (5.50) the poles per repeatable section are used.

Table 5.3 b

Harmonic No.	Slip at n_1=3	Slip at n_1=4
1	25%	20%
2	40%	33.3%
3	50%	42.8%

In practice none of the harmonics given by 5.50 caused any noticeable torque ripples independent of connections, while the three cases in Table 5.3a indicated by an asterisk could be considered serious if only a simple integral slot/pole winding is used. Notwithstanding, the basis of using these machines in a speed control application (as an alternative to P.F. correction) is the combination of effects explained by (5.49) and (5.50) since several of these harmonic speeds are very close, which is an advantage. In general, no steady-state hunting at the harmonic slip speed will occur because both effects produce additional torque subsynchronously of the harmonic and the loss in torque usually occurs at a super-synchronous speed of the harmonic, for example at 502 RPM with respect to Table 5.3b, Column 2.

Figure 5.18 shows a practical speed control connection

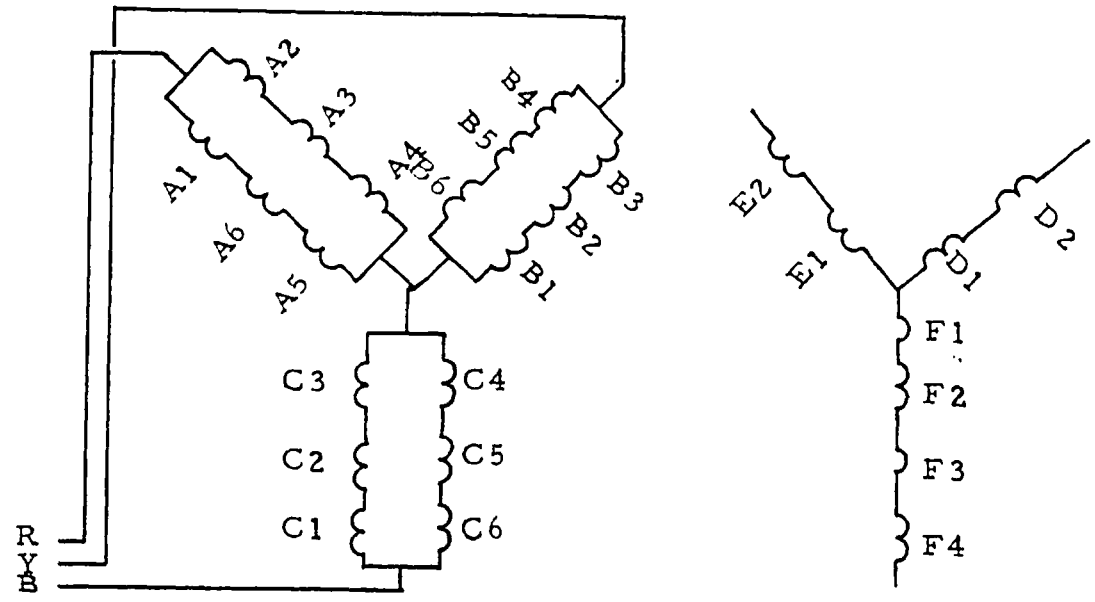

Fig. 5.18a Speed control SC IM connection which yi elds 500 r.p.m. spe ed

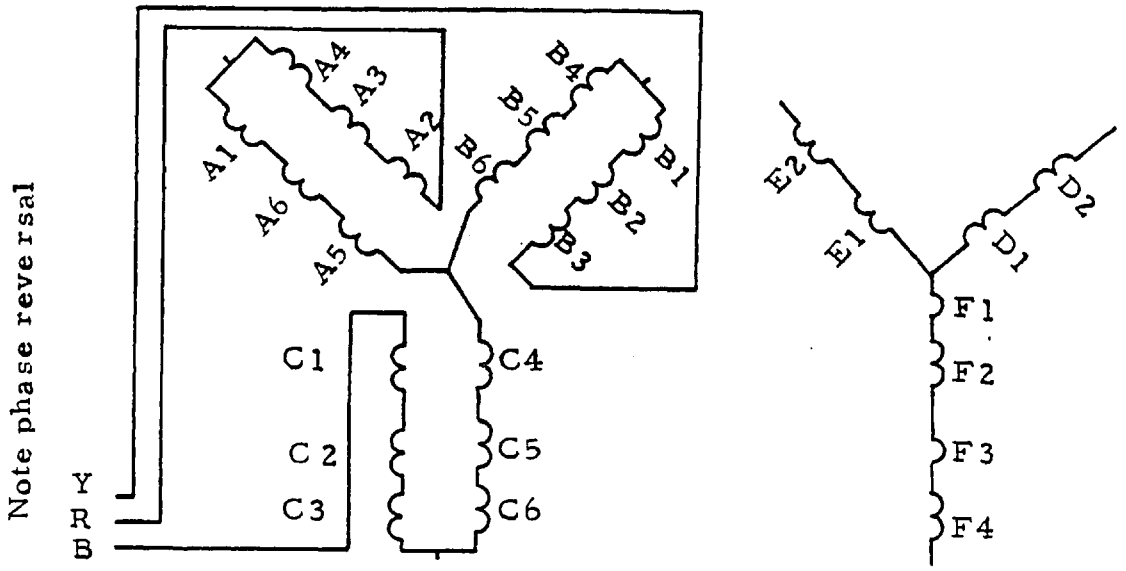

Fig. 5.18b Speed con trol SCIM connection which yields 600 r.p.m. spe ed

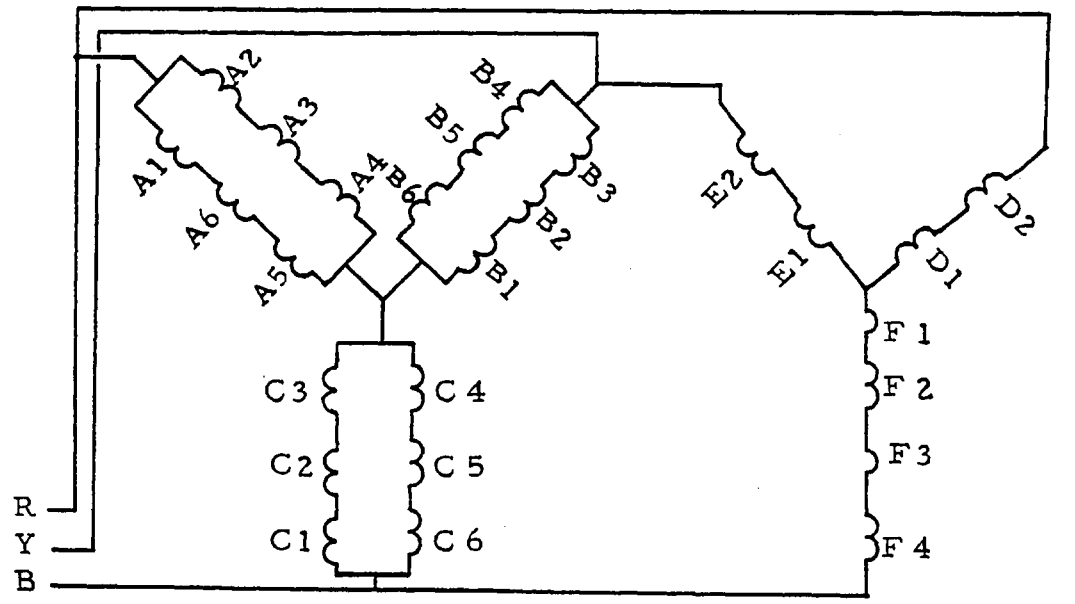

Fig. 5.18c Speed control conne cti on yieldi ng 750 r.p. m.; no P.F. correction.

diagram of the SCIM machine assuming the machine is wound with 3 slots/pole/phase in a type 3-1+ -3 -1+ sequence. The important point is that in having an external contactor, three distinct synchronous speeds are possible; it's similar to pole-amplitude modulation except that three speeds are practical instead of two. All these schemes provide an output in excess of 80 kW although the high speed connection (750 RPM) has the highest efficiency.

Pole-amplitude-modulation has several coils per pole that either have excessive reactive power inputs or else several coils around the periphery (averaging less than 1 coil per pole) that actually produce braking forces on the rotor in the high speed (most preferred) connection.

D. Phase of ASC Induced Voltage

Over a narrow range of slip it is accurate to describe the ASC operation as a rotating current transformer, the phase of a particular ASC phase current being determined by the combined effect of all phases of the main winding, rather than being dependent on single main phase currents. The important aspect of this is that even if the magnitude of the ASC current stays fairly constant, the effective utilization of the ASC winding depends entirely on the proper phase matching and in this respect a multiple of main phases are advantageous over a three-phase system. Conversely, suppose that no external switching is to be used and that a three-phase supply is mandatory, then solid connection of all terminals demands that the phase change of the ASC current with slip remain constant for a given load. In general rotary machines have very little change with slip as compared with linear machines incorporating

condenser winding. (A phase plot of the LIM-ASC-I machine as shown in Figure 2.42 should be referenced for comparison purposes.) For the last two rotary machines, phase plots versus slip of the ASC induced voltage on open circuit of the ASC have been taken and Figure 5.19 is the plot for the SCIM-II machine after being rewound. Ideally, this measurement should be taken at a constant stator current loading over all slips but the range of current variation with respect to Figure 5.19 is not significant. This information tells the designer the maximum speed range which can tolerate a given utilization factor of the maximum reactive power (at a given slip for the number of phases fed from the supply). For the SCIM-II machine, the rate of change of airgap flux phase with slip is 8.8 degrees/1% slip at slip equals 2% and 50 Hz.

E. Decrement of ASC Flux along the ASC Poles

This is a measure of the armature reaction of the condenser windings combined with the Goodness factor of the ASC section which may be considered to be the equivalent of forced and natural response in a linear system, respectively. Measurements are taken of individual coil voltages in the ASC section on open circuit to give the natural flux decrement along, for example, 1+ pole and this is presented for the SCIM-II machine in Figure 5.20 . Then the measurements were repeated on load by monitoring the magnitude of the coil terminal voltages. This is an accurate measurement (despite the resistance and leakage impedance drop which was subtracted in the absence of search coils) because all ASC coils carried the same phase current and saturation of the leakage path was always insignificant in the ASC poles. The SCIM-II machine has an ASC open circuit decrement less than 5% over the 1+pole/repeatable

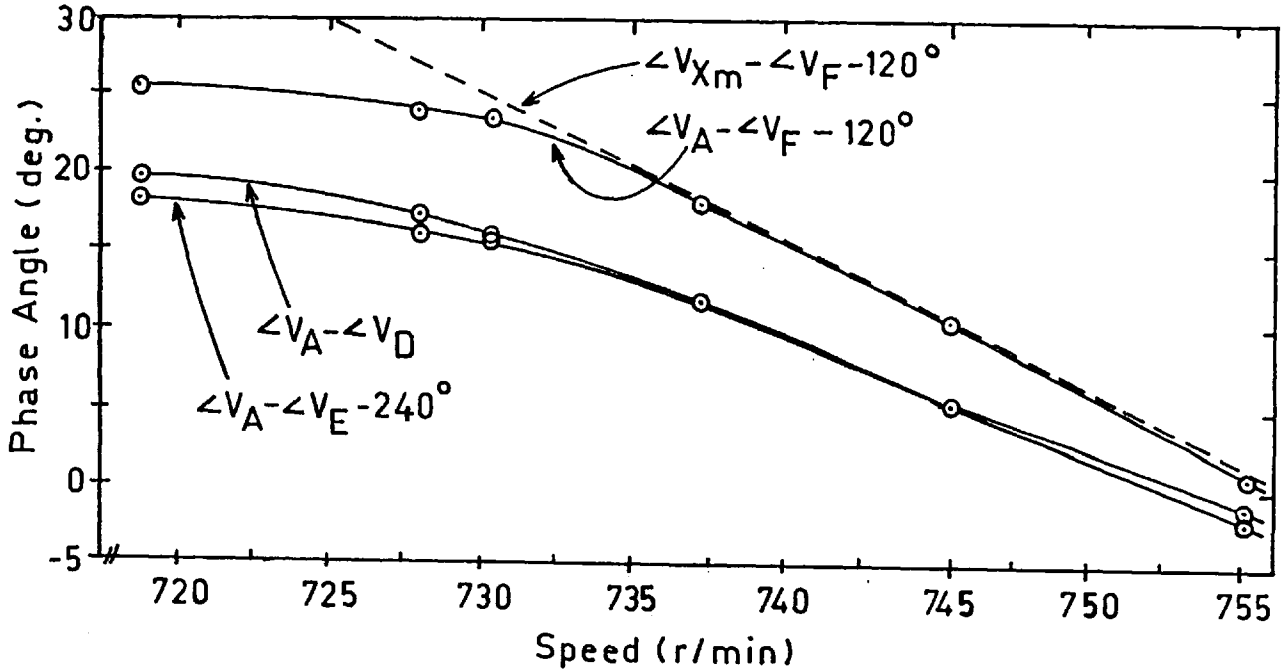

Figure 5.19 Phase angle of tertiary induced voltage with respect to primary input voltage, 50 Hz.

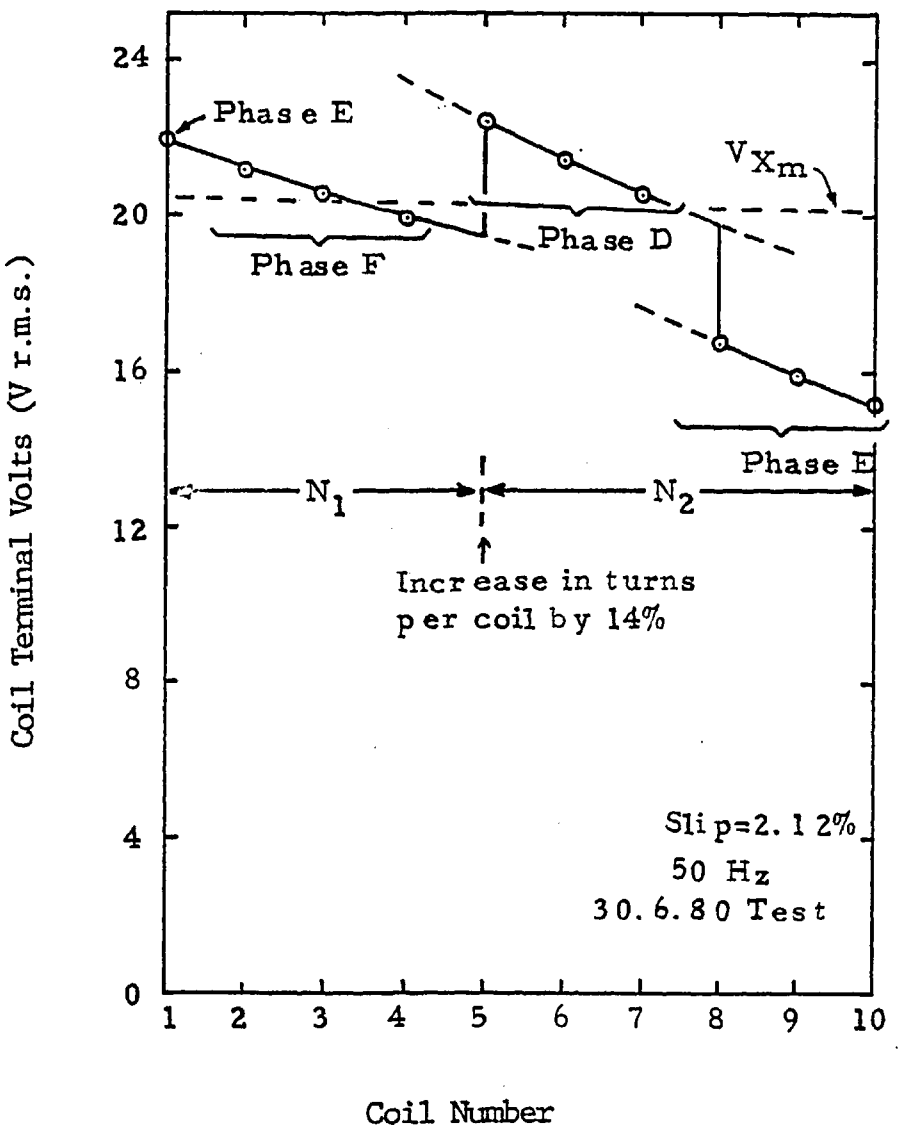

Fig. 5.20 Magnitude of tertiary coil voltages on-load and magnetizing E.M.F. of the coils in the last primary pole-group.

section; on load the voltage decrement is less than 10% proving that, as mentioned in [17], Chapter II, "rotor leakage inductance must be an advantage."

G. Excess Rotor Real Power Loss

The SCIM-II unit does incur additional rotor losses when operating at unity power factor operation, but this is strictly a consequence of running at a 3% slip instead of a 2% slip on full load. The vast majority of rotor losses are directly calculable from the difference in slip rather than from some stray loss as was the case with spherical induction motors. If there is an additional loss in rotor efficiency other than indicated in Table 5.5 , the described dual system of measurement was not able to detect this and the matter was not pursued further. In conclusion, the 112 kW (output) SCIM unit at $\cos\phi=1.0$ experiences about 6.7 kW additional real power losses; this is directly attributed to the use of uniformly slotted stator laminations and the ASC winding I^2R loss.

5.4 STEADY-STATE OPERATING CONSTRAINTS

The machine under discussion is a second version of the "Theta-Pinch" type with 180^{o} mechanical symmetry by using two repeatable sections totalling 8 poles. At unity power factor, the composite machine should be regarded as a poly-phase rotary current transformer to explain the circulation of reactive power within the machine while the output mechanical power can be calculated from existing formulas [3] based on conventional rotor slip loss. The operation of this machine at the rated point of 112 kW is presented as a sequel to the classic paper written by F.J. Teago in 1922 describing the operation of an adjustable power factor shunt-commutator motor [4] . The two should be read in parallel to appreciate the similarities between the commutator and brushless machines; both contain high frequency transients, the former has time transients while the latter relies on space transients yet it is still accurate to represent their operation with phasor diagrams.

The motor, on which tests refer to in this section is described by the manufacturer in Table 5.4 as of original equipment manufacture (1955) prior to the instrumentation and rewind of the stator in 1980.

The tests were made in the Heavy Electrical Engineering Laboratories of Imperial College.

The motor is rated at 150 H.P. continuously when operating at 735 R.P.M. and 91% power factor with the original stator winding and when rewound runs at a speed of 725 R.P.M. at 150 H.P with unity power factor at the terminals.

The motor has the usual stator and rotor laminations;

Table 5.4

Characteristics of the 150 H.P., 8 Pole Induction Machine Θ-Pinch II which are independent of stator winding arrangement.

Stator	
Number of slots	72
Core outer diameter, mm	660.4
Bore diameter, mm	495.3
Slot pitch, mm	21.6
Core length incl. 3 ducts, mm	292.1
Effective iron length, mm	237
Core depth, mm	43.4
Tooth mean width, mm	9.47
Slot bottom width, mm	15.5
Tooth tip width, mm	16.5
Slot opening, mm	5.08
Carter Coefficient	1.125
Maximum slot area below wedge for winding, mm^2	555
Tooth depth, mm	38.1
Rotor - Squirrel Cage	
Number of slots	94
Core outer diameter, mm	493
Core length, mm	292
Slot pitch at periphery, mm	16.48
Core depth, mm	64
Tooth mean width, mm	11.5
Slot bottom width, mm	3.68
Tooth tip width, mm	15.2
Slot opening, mm	1.27
Carter Coefficient	1.02
Bar depth, mm	25.4
Bar width, mm	3.175
Mean length of bar, mm	330
Ratio bar width/slot width	0.862
Total copper cross section area in slots, mm^2	7535
Endring cross section area, mm^2	363
Mean endring diameter, mm	428
Resistance skin-effect factor bar only (50 Hz)	2.21
Resistance skin-effect factor overall (50 Hz)	1.99
Reactance skin-effect factor bar only (50 Hz)	0.66
Reactance skin-effect factor overall(50 Hz)	0.838
Airgap	
Mechanical gap length, mm	1.14
Effective gap length, mm	1.31

the stator, however, carries a tertiary winding, and the rotor is acting as both a secondary and as an inductively-fed primary capable of magnetizing the airgap over a limited section. Herein lies one difference between this motor and an ordinary machine where only the stator primary provides the magnetization. Another and fundamental difference is that the stator also carries an ordinary lap winding in slots distinct from those which contain the primary, motoring winding. This reduced pole-pitch, tertiary winding is termed the asynchronous condenser winding (ASC) and is connected to a three-phase variac (or a phase-shifter if experimentation is desired) in the usual manner associated with polyphase machinery. In order that three phase current may be taken from the ASC winding without producing braking forces on the rotor, it is necessary to ensure that the phase of the rotor flux at high speed exactly corresponds to the reduction in pole-pitch of the ASC coil connections. This requires that all of the ASC stator teeth have slot-wide search coils directly on the stator surface as in [5] or else all of the main current coils must be instrumented for the phase of the terminal voltages and the leakage inductance accurately calculated to arrive at the phase of the airgap flux.

The function of this ASC winding is to inject into the primary winding a positive-sequence current nearly in time-quadrature with the uncompensated line current and of approximately one-half magnitude. This causes the secondary cage currents over the ASC section to attain a value slightly larger than the ASC reactive currents by the value needed to magnetize the airgap. Obviously, the magnitude of the tran-

sient rotor currents is a function of the speed of the rotor which shifts the airgap flux established by the stator primary winding into the ASC section. Hence, if the magnitude of the circulating ASC current can be varied, the resultant change in the airgap flux allows the speed of the motor to be controlled in addition to power factor.

In general, the rotor current is always composed of a space-transient component, J_{rt} and a steady state component, J_{rss} both of which will induce sinusoidally varying currents in the stator windings. Typically, the primary winding has a uniform MMF distribution unless pole-amplitude modulation is used and thus it is accurate to express the current loading as a surface line current, $\hat{J}_s$ in Amps (peak) per meter periphery. Therefore, the relationship between the rotor and stator currents may be expressed in a complex form for the total rotor current as

$$J_{rt} + J_{rss} = \frac{-\hat{J}_s}{(1 + \omega_s T_2/G) - j/(\sigma G)} \qquad (5.51)$$

where T_2 is the rotor leakage time constant being the ratio L_2/R_2 of the leakage inductance to the rotor resistance based on conventional equivalent circuit calculations. Parameter L_2 should ideally be the sum of the rotor inductance plus the reflected tertiary leakage inductance comprising the internal slot, differential, zig-zag and endwinding leakage flux as well as the effective inductance of the external electric load connected to the tertiary which has an angle of about 80^o for power factor control.

The significance of (5.51) is that for very large induction machines, $G > 100$ and the rotor current is nearly a mirror image of the stator current, i.e. $J_{rt} + J_{rss} = -\hat{J}_s$

over the excitation section. Over the ASC section of the machine, equation(5.51)is approximately correct if the effective inductance of the ASC circulating current is coupled to the rotor inductance to yield a larger T_2 value. Additionally, the ASC referred surface-resistance will decrease G in this region, although this is not critical.

The machine operates as an induction motor with the secondary comprising a uniformly slotted deep-bar cage rotor, and yet this has the special feature of being able to operate at speeds below and above synchronism. At subsynchronous speeds the rotor wavelength is such that the induced ASC voltage in the stator is at a pole pitch τ_{p3} smaller than the main pole pitch τ_{p1} as given by

$$\tau_{p3} = \tau_{p1} (1-\sigma) \tag{5.52}$$

It should be emphasized that induced ASC voltage refers to a speed induced voltage rather than a transformer voltage from the main excitation winding, which is always negligible. At high slip values, it is accurate to represent the asynchronous condenser windings as being motionally and magnetically coupled to the rotor. However, at slips of 0.20 per unit and less the motional coupling is dominant and if the number of excitation poles is an even integral number, the motional coupling becomes dominant at slip values larger than 0.20 per unit. It is this motional voltage which gives the designer the freedom to choose exactly the proper phase to operate the ASC in a reactive mode exclusively. To show this cross-coupling of the motional voltage, a three phase equivalent circuit on a pole-by-pole basis is necessary as in

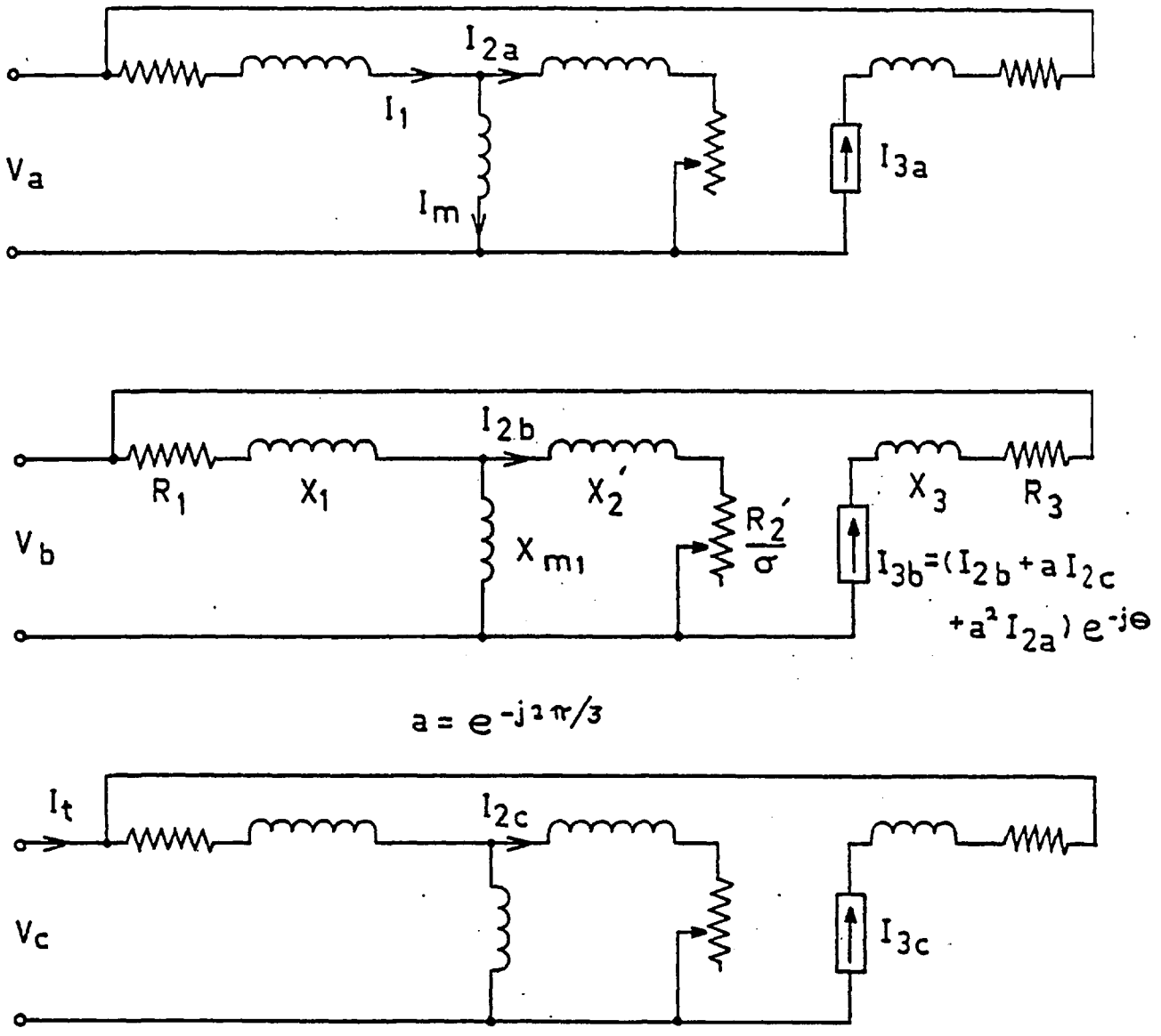

Figure 5.21 Equivalent circuit for 112 kW size SCIM units at high speed showing the tertiary current source as a dependent source on the rotor current in all three phases.

Figure 5.21.

Speed control is attained by extracting small amounts of real power from the rotor via the ASC windings. In essence, if there is a large mismatch between the surface impedance of the ASC winding and the surface impedance of the rotor, then it is impossible to have a balance of rotor and stator currents and the anomaly manifests itself as an adjustable speed mechanism. For example if the magnitude of the ASC current is greatly in excess of the rotor current, the net effect is to shrink the wavelength of the main excitation poles and thus the machine will produce rated torque at significantly less than synchronous speed. In the limit of a very large mismatch in impedances, the machine will run at a slip of $\sigma = 1/(n + 1)$ where n is the number of excitation poles per repeatable section. Conversely if the magnitude of the ASC current is greatly exceeded by the rotor current, then the net effect is a "stretching" of the main excitation poles for the machine produces rated torque at or above synchronous speed based on the formula RPM = 60 x frequency/pole pairs.

This particular modulation of the amplitude of the total radial component of airgap flux density (B_p and B_q) means that the utilization of the machine periphery varies widely but this is a necessary condition to be able to generate sufficient reactive kVA in the ASC windings while experiencing the flux decrement in this section due to the equivalent of armature reaction.

Power factor control demands that difference in the surface impedance between ASC and rotor section be limited to under 35% of the total and if the ASC current circulating

within the excitation winding were to be reversed, then the power factor would become progressively lagging rather than leading.

The subject motor has a total of eight poles and a synchronous speed of 750 R.P.M. Since the ASC winding connections to the main winding are speed dependent, prototype machines have 6 leads brought out per winding so that discrete phase steps of 30^{o} are possible with star and delta combinations. These leads are connected to a 3Ø variac, which controls the amount of current forcing available and thus maximum power factor, and then through synchronization-type switchgear to guard against the ASC current being circulated at the magnitude of a short-circuit or zero-sequence current. Since the effect of this variac will also alter the phase of the circulated current with respect to the main current, the ASC windings can absorb up to about 20 kW or alternately generate 15 kW of power. Speed control is accomplished with approximately the same degree of amplification as would a slip-ring wound-rotor machine with an external pilot exciter or phase advancer.

The primary winding is star connected with two parallel paths per phase and is located in a total of 60 slots. The rotor is entirely conventional and uses rectangular copper bars; giving an apparent increase in surface resistance at starting of 105%. The top portion of the stator slots in the transition region surrounding the θ_1 location in Figure 5.22 contains the primary winding which is directly connected to the ASC winding which occupies the bottom of these slots when the two distinct windings must be overlapped. Figure 5.23 shows a section through a stator slot. With

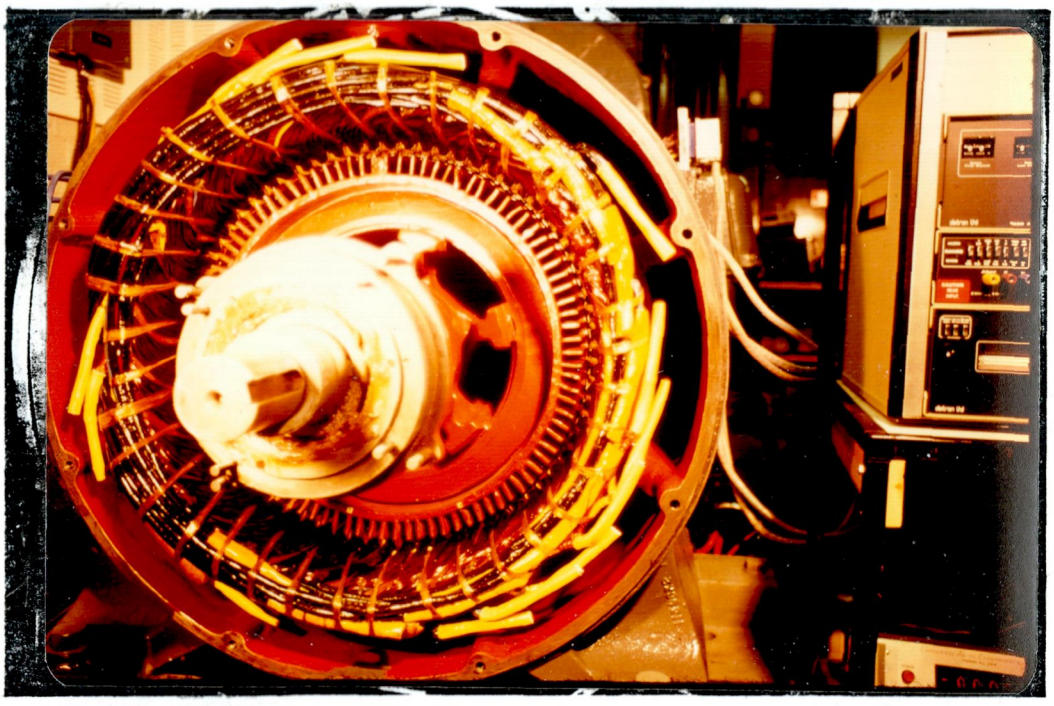

Fig. 5.22 View of the 150 H. P. SCIM unit subsequent to the rewinding operation and prior to the coil instrumentation; the asynchronous condenser sections (Θ_1 locations) are at the two-o'clock and seven-o'clock positions.

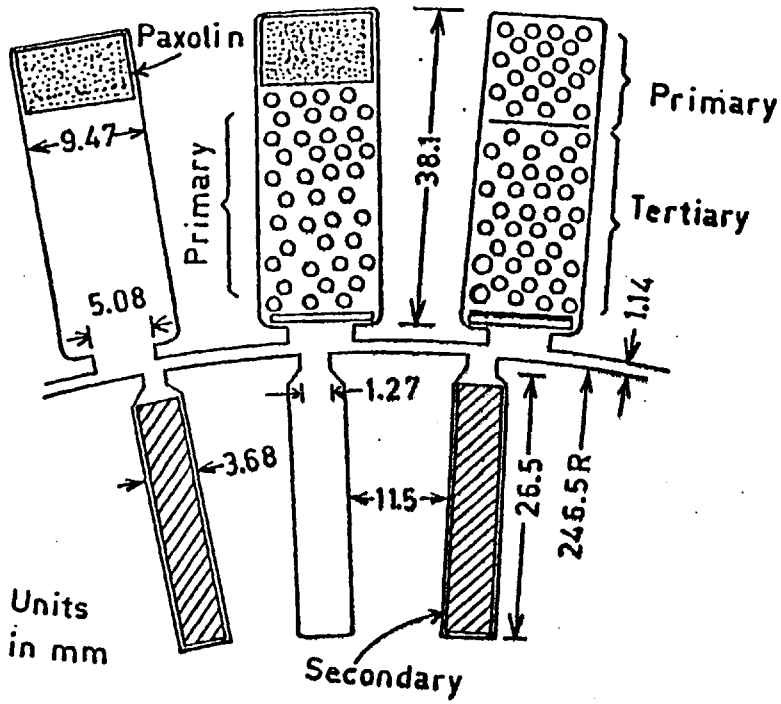

Figure 5.23 Slot geometry for the 112 kW machine at the Θ_1 transition region

respect to this slot the following assumptions are made:

(a) That there is no appreciable leakage between the two separate windings.

(b) That the primary resistance drop is in-phase with the primary current, and

(c) That, since the resultant leakage flux is due to the resultant ampere-turns in only the overlap slots, the primary leakage reactance drop is not always at right angles to the resultant ASC-primary current.

The cage secondary is composed of 94 rotor bars spaced at uniform slot pitches and each slot has an aspect ratio of 7.2:1.

Considering, for the sake of simplicity, a constant stator current loading, two practical operating modes with differing terminal power factors are shown in Figure 5.24 .

Figure 5.24b shows the stator connections corresponding to a no-load speed of about 748 R.P.M. The ASC phases D, E and F are connected in series with primary stator phases A, B and C respectively. The reactive output of the ASC section is at its maximum value for a given terminal voltage, although the machine as a whole is operating at a lagging power factor only a few per cent better than in a conventional machine with a slip approaching zero. In this mode, the flux per pole of the ASC windings is approximately equal to the flux per pole over the motoring sector, and this may be determined from the voltage across the magnetizing reactance.

Figure 5.24b shows the same connections as in Figure

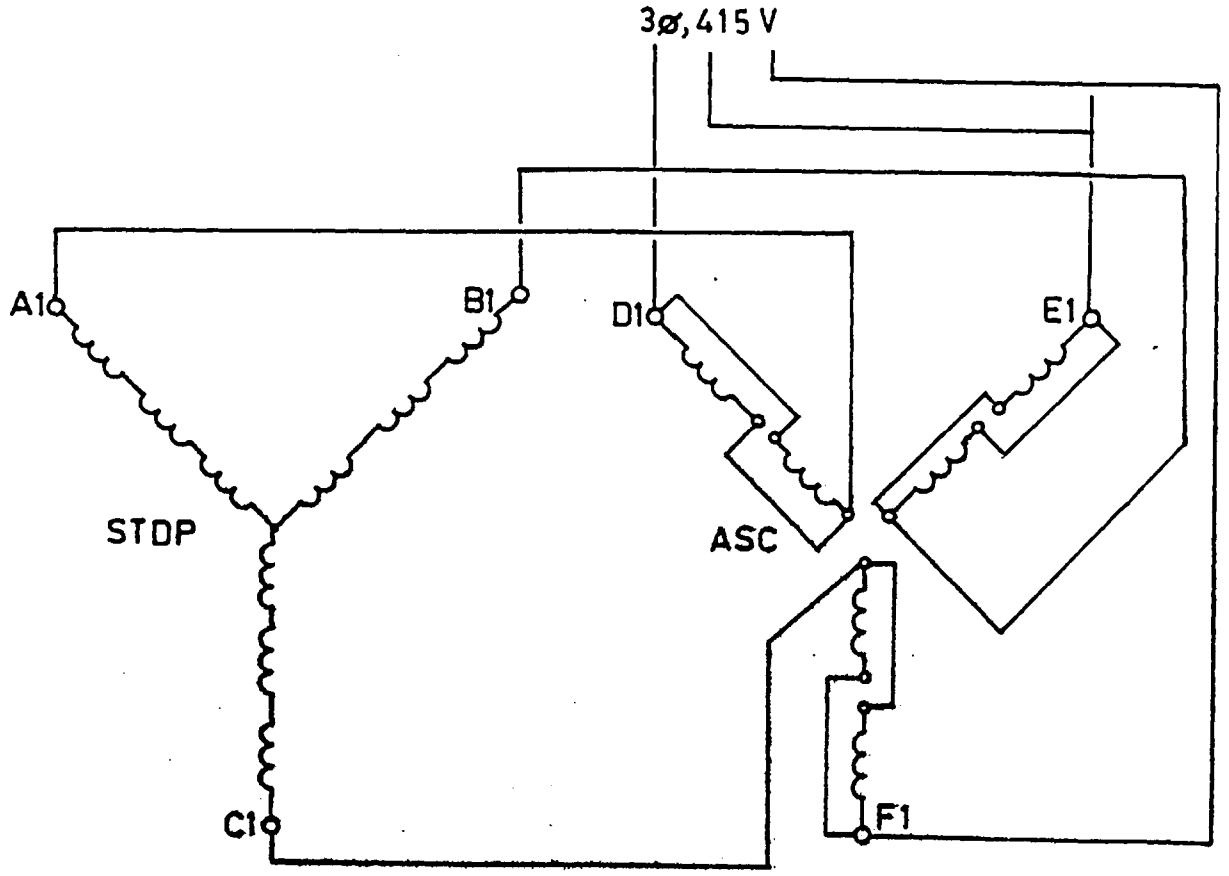

Fig. 5.24a Starting connection to yield full power of conventional machine

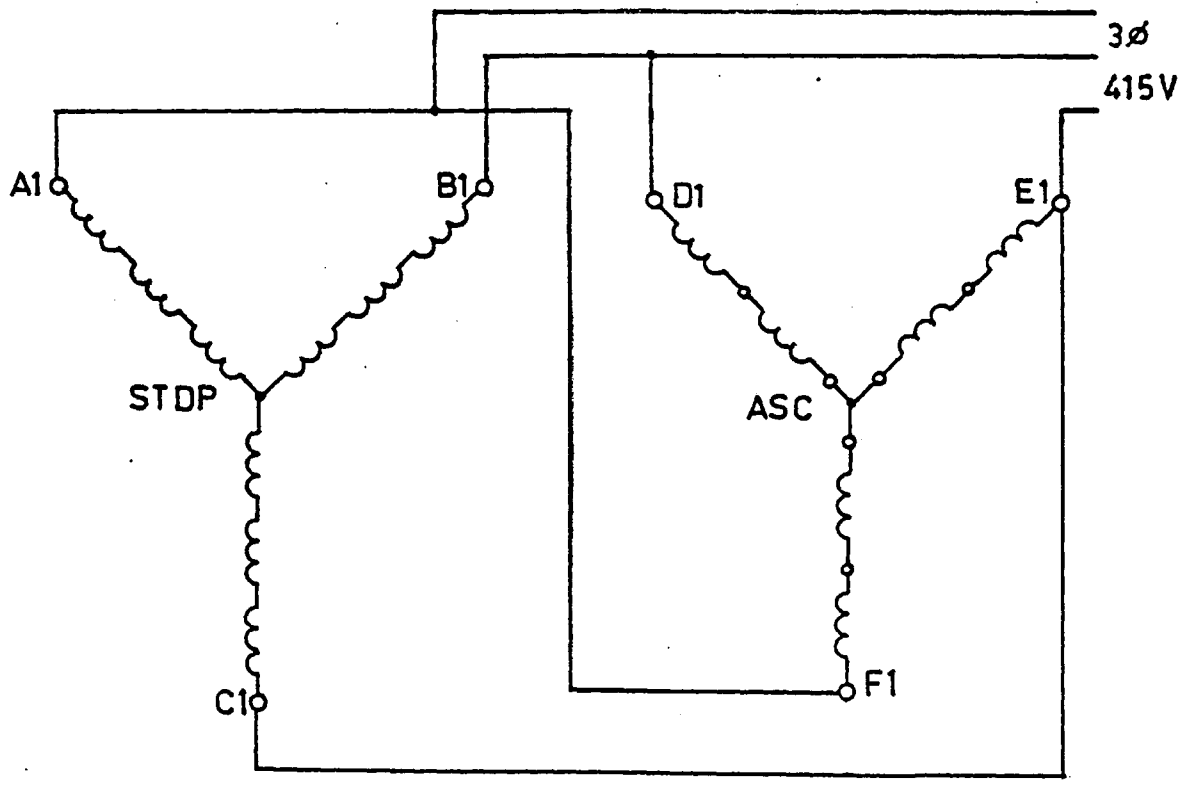

Fig. 5.24b High speed connection to yield unity power factor operation

5.24a but now the machine is loaded to a shaft speed of 725 R.P.M or a 3.3% slip, and is producing 150 H.P. continuously. In this mode, the primary winding alone has a power factor of 87% lagging and the ASC winding alone has a power factor of 0.07 leading; at the terminals the combined power factor of these two windings is exactly 1.00 or slightly leading if the load is increased past the continuously rated value. It is important to note that the flux per pole of the ASC winding exceeds the flux per pole of the primary winding albeit the relative length of the ASC section is 25%.

Also, Figure 5.24a shows the terminal connections corresponding to the preferred arrangement in the start up mode. In order to avoid any MMF harmonic torques occurring at speeds of 500 or 600 R.P.M., the ASC windings are given a phase shift with respect to Figure 5.24a so that they entirely complement the primary winding in producing torque and absorbing reactive power. In the machine under discussion, the torque at locked rotor is 1425 lb.-ft. or 160% of the full load torque. Automatic reswitching to the configuration of Figure 5.24b should occur between speeds of 600 and 650 R.P.M. rather than once full load speed is attained because the phase shifting should occur when the ASC induced voltage is at a minimum which occurs at slips of $\sigma = 1/(n + 1)$ where n is the number of motoring poles per repeatable section.

These conditions were confirmed by using both electrodynamic wattmeters (frequency independent) and a high-precision digital phase meter in conjunction with a data logging system to monitor and record the phase and amplitude of all heavy-current coils in the machine directly at the power level. No potential transformers have been used in the voltage measurements and the data logging system includes

a spectral filter; all voltages presented here are true R.M.S. values of the fundamental unless otherwise stated. All current phase measurements are accomplished using the total phase current through non-inductive shunts; only the electrodynamic wattmeters use current transformers.

The lap winding of the ASC, being located on the stator has a fixed speed with respect to the rotating field, and therefore the magnitude of the E.M.F. between a pair of terminals e.g. A_1 and D_1 is relatively independent of speed variations if $G > 100$ and depends primarily on the relative phase of the rotor flux. If an alternate rotor is substituted with deeper bars than the existing one, it will be necessary to either incorporate an external phase shifter or change the terminals connections (if the number of supply phases is greater than 3) to compensate for the change in the L_2 parameter.

It should be emphasized that despite the reduction in pole-pitch for the ASC, the frequency of the induced voltage is always exactly the main excitation frequency independent of the rotor speed. The primary purpose of the reduction in pole-pitch is to effect maximum utilization of the airgap flux.

If the rotor is driven by an auxiliary motor in a direction opposed to that of the field, then the speed of the transient field in space will depend solely on the speed of the rotor, and when the latter is driven at synchronous speed there is no theoretical advantage to having two distinct pole-pitches.

To confirm this statement the rotor was driven at 97% synchronous speed and an oscillograph record taken of the

ASC induced E.M.F. on open circuit using the supply E.M.F. as a reference. Figure 5.26 shows these two E.M.F. waves and it is seen that, since the fundamental is a 50 Hz wave, the asynchronous condenser E.M.F. is also 50 Hz although high frequency tooth harmonics are superimposed at 1 kHz.

With regard to the secondary circuit located in the rotor slots, the magnitude of the E.M.F. between the two ends of any bars, and also the frequency, depend on the rotational speed of the rotor. However, unlike a conventional machine the magnitude of this E.M.F. has a very wide ranging space dependence and to a first order degree, peaks at the location of the minimum total airgap flux density which is over the first entry pole of the primary winding.

The relative magnitude of airgap permeance harmonics to the fundamental field due to the slotting geometry combined with the rotor leakage time constant determine the total flux pulsation in the airgap over the tertiary windings. For comparison, Figure 5.25 shows the ASC open-circuit E.M.F. of the first prototype machine rated at 35 H.P. which has 90 stator slots, 80 rotor slots and a slot width to airgap width ratio of 6.6. The rotor has shallow copper bars which have a leakage constant of 2.57 ms at 850 Hz, whereas Figure 5.26 refers to a machine with T_2 = 0.49 ms at the tooth frequency. These oscillographs show the only significant time-transients at the power level of the entire stator winding; the fundamental is directly due to the space-modulated distribution of the slowly-decaying dc rotor current for $\theta_1 < \theta < \theta_2$. The magnitude of this dc component may be calculated by the method in [6] .

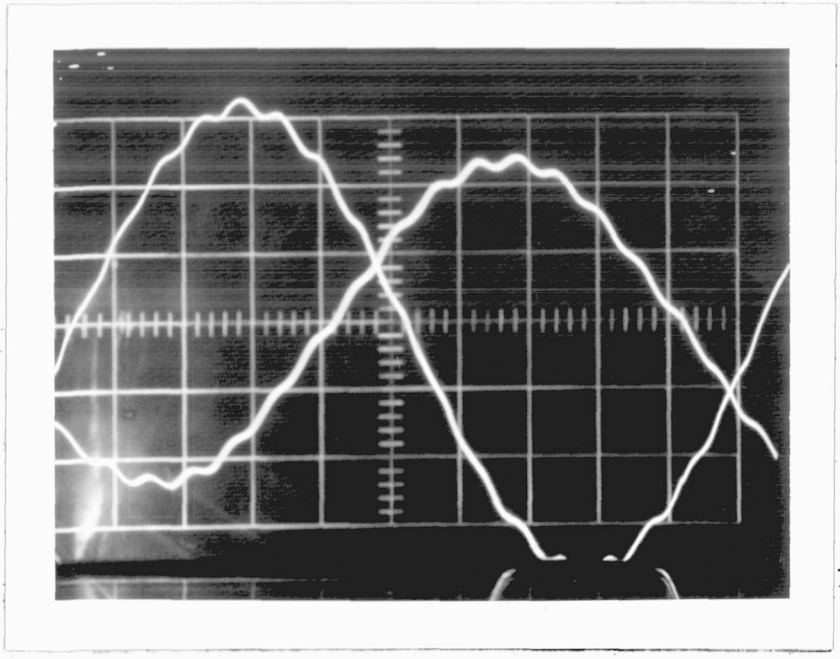

Fig. 5.25 Tertiary induced E.M.F. with gap-permeance harmonics in the 26 kW, 10-pole machine with $J_{s3}=0$ and 75% load, 50 Hz.

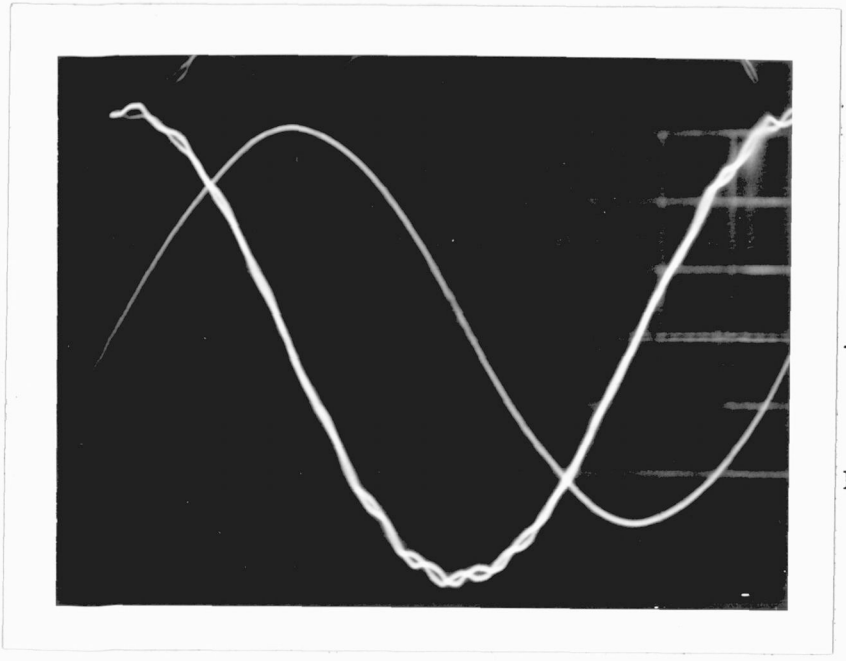

Fig. 5.26 Tertiary E.M.F. and primary input voltage for the 112 kW machine with $J_{s3}=0$ and 25% of rated mechanical load, 50 Hz.

It will be seen that when the machine is operating at unity power factor, the rotor wavelength is exactly matched by the pole-pitch of the ASC winding by design of the stator laminations or by terminal coil connections as in the subject 150 H.P. unit.

With regard to the induced current in the ASC windings, this changes from a low value at subsynchronous speeds to a maximum at about 3% slip, and to a low value again at supersynchronous speeds. Since the field rotates in the same direction to the stator for positive and negative slip values, only the phase of the ASC terminals changes as the rotor passes through synchronism and thus reconnection is necessary to implement P.F. correction for generator operation.

Figures 5.27 and 5.28 show the phase and magnitude of the induced ASC voltage per phase as a function of slip. The primary voltage is used as the reference for the phase plot. For reference, the ASC voltage is shown in conjunction with the voltage across the magnetizing reactance to give an indication of the average flux per pole of the motoring winding. Unlike the inverse relationship between the induced stator E.M.F. and injected-lap E.M.F. of a unity-P.F. commutator motor, the two quantities in Figure 5.28 have approximately the same speed dependence.

One serious disadvantage of the three phase shunt commutator motor is their liability to hunt which is due to the shape of the resultant induced + injected E.M.F. characteristic which has a trough at about 12% slip. However, there is no such equivalent phenomena in the brushless U.P.F. machine once any initial transient overspeeding has passed and the rotor temperature has stabilized.

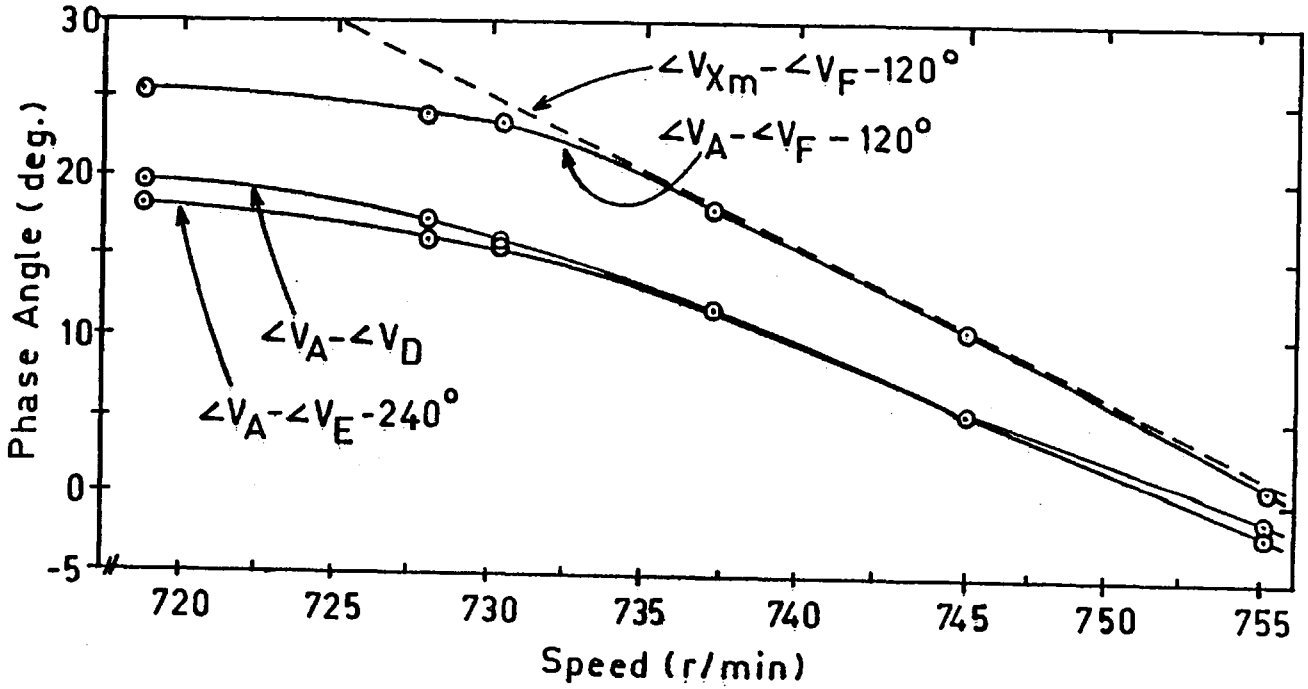

Figure 5.27 Phase angle of tertiary induced voltage with respect to primary input voltage, 50 Hz.

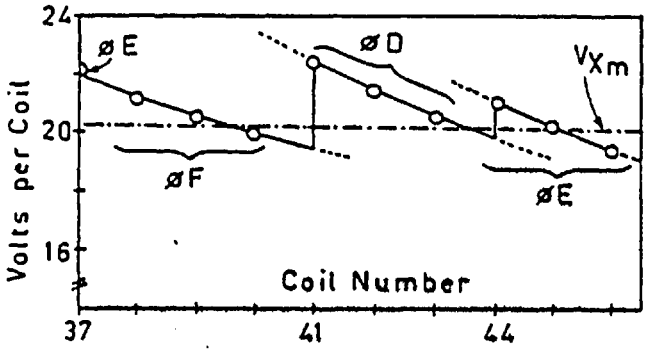

Fig. 5.28 Magnitude of condenser open-circuit voltage and voltage across magnetizing reactance, V_{Xm}.

Cage-machines tend to maintain constant airgap flux despite large peripheral variations in stator MMF. An extreme case of exciting only 130° mechanical per repeatable section at a primary loading of $\hat{J}_{s1}$ = 60 kA/m and leaving the remaining sector open circuit was tried. Figure 5.15 shows line current on reduced voltage and without dynamometer loading, which accentuates variations due to asymmetry. At a harmonic slip of 0.20 the line current dip is 2%; acceleration is constant from locked rotor to slip values of 0.10 per unit.

With the motor working against any given constant torque the speed corresponding to minimum circulating current is fixed; consequently, if the phase shift between the primary and tertiary windings is increased by either a change in connections or a change in leakage reactance values, the speed will generally increase to the point at which the circulating current is a minimum. Assuming no further phase displacement, the speed will remain fixed at this value although the terminal power factor will be no greater than 91%.

Figure 5.29 shows the stator current loading per slot of the combined primary and tertiary windings for the 150 H.P. machine at unity power factor and supplying 112 kW output power. This is not considered the optimum J_s distribution from a thermal consideration, but considering that the original stator laminations were utilized, this does represent the best design to date put into hardware.

Figure 5.30 is a composite plot of the real and reactive powers per group measured at the terminals of the 72 stator coils during the condition that the shaft speed is 725 R.P.M. and the terminal power factor is unity. This plot may be used

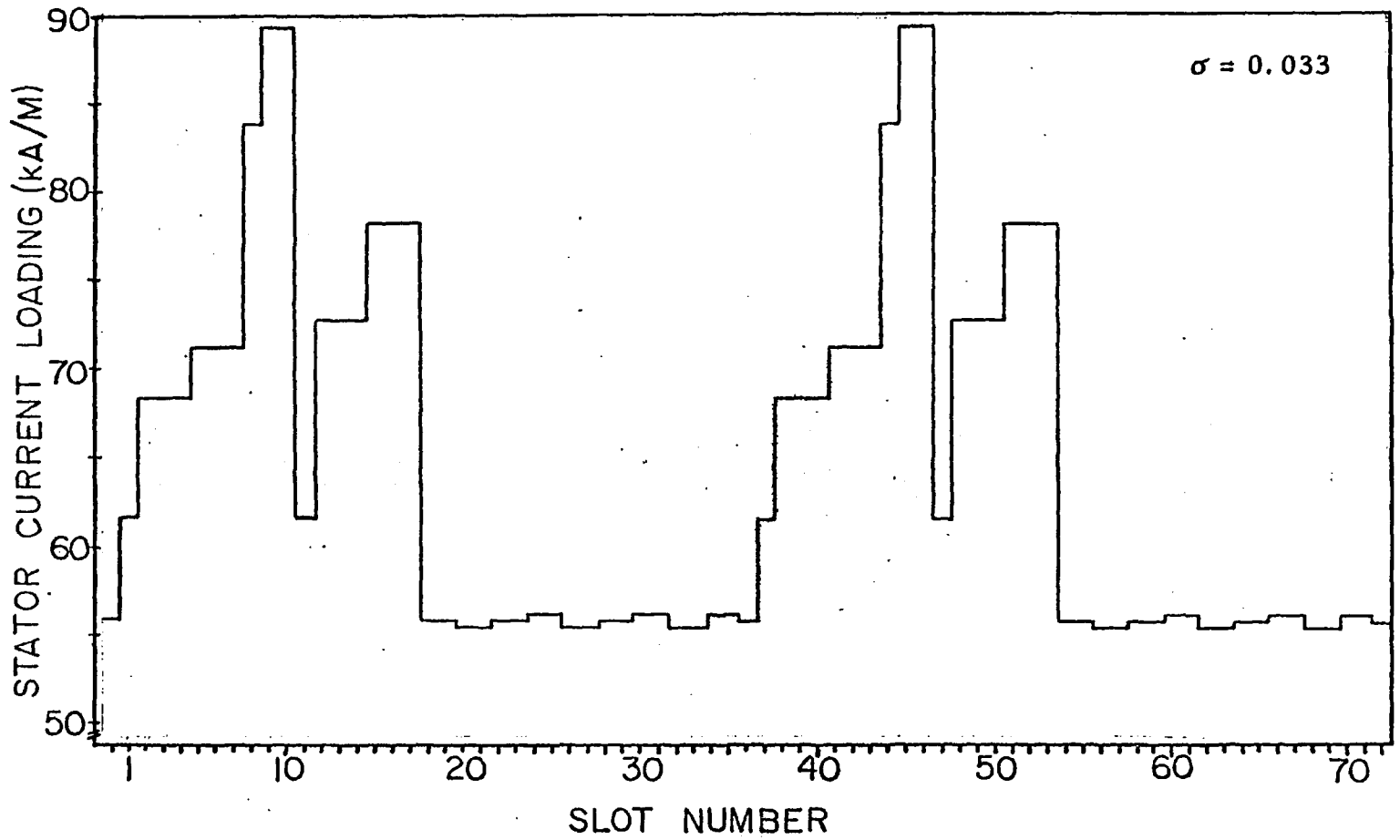

Figure 5.29 Combined primary and tertiary stator current loading at unity power factor.

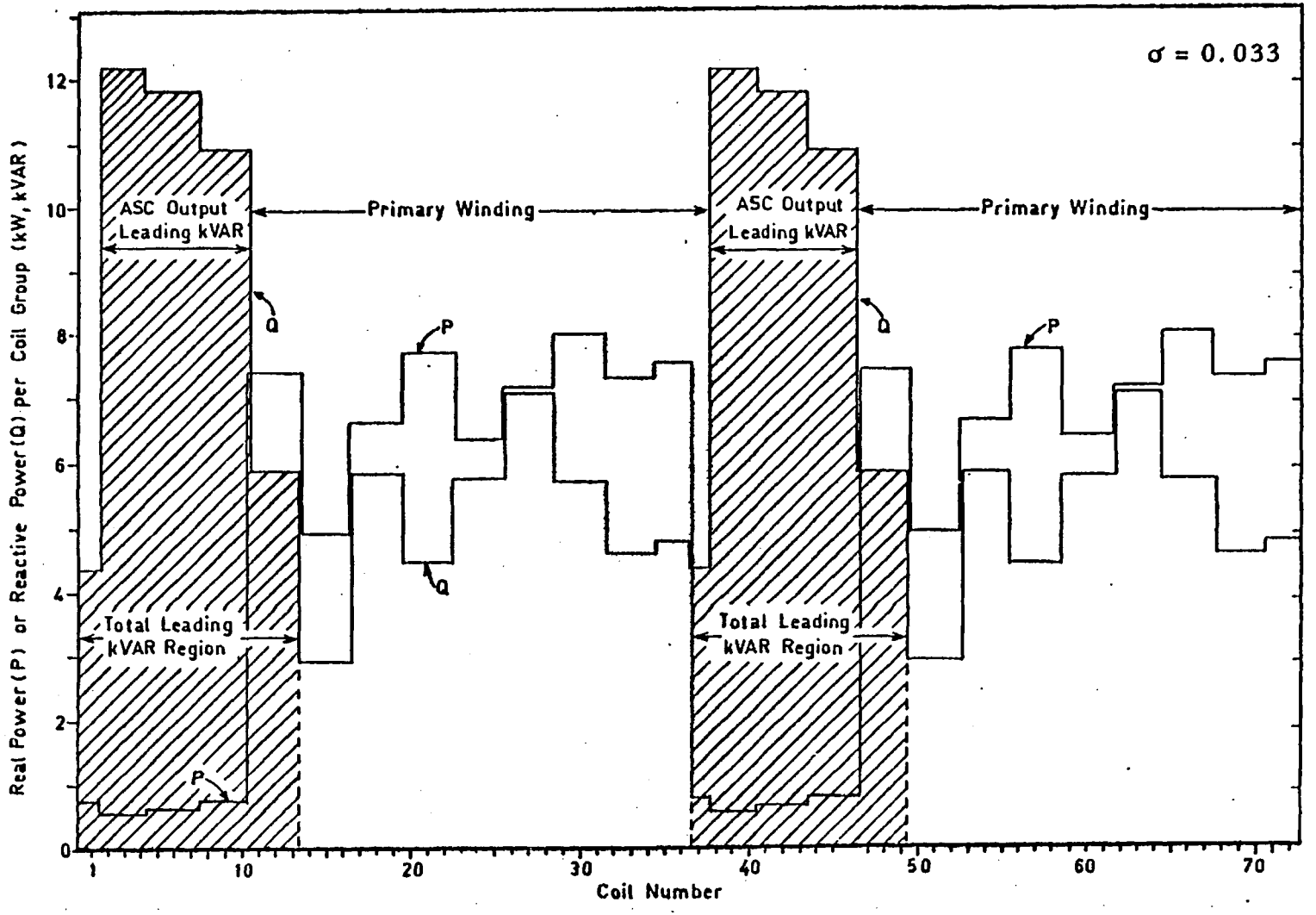

Figure 5.30 Real and reactive powers per coil group of primary and tertiary with cos ϕ=1.0 at input.

to assess the total power input or just the circulating components of power; the stator current loading for this run is given in Figure 5.29 . If this same run would be repeated at 40 Hz instead of at 50 Hz, the slip would increase to about 4% but the terminal power factor would be approximately 0.95 leading.

The most outstanding result of the unity power factor condition is that reactive kVA generation is present in both the asynchronous condenser winding proper as well as in the first three coils of each primary entry pole per repeatable section. In contrast to the Mk. I, 10-pole machine where reactive power generation only occurred in the zone from Θ_1 to Θ_2, here P.F. correction is achieved by both a terminal current feedback loop and a considerable phase shift in the voltage across the magnetizing reactance with respect to the primary current, i.e. voltage reduction. For this latter condition, the "carry-over" flux at Θ_2 is quite significant (ψ < 0.2 per unit) but unlike the Mk.I machine, the phase of this flux has now been used to advantage by giving the entry poles a 60° current phase displacement from the conventional series connection. This design trend will be continued in all future winding layouts, albeit the 60° shift is only exactly perfect at a slip of 4%.

The unity power factor condition is summarized in Table 5.5 .

Typically, early shunt commutator motors with U.P.F. capability were limited in output to under 10 H.P. per pole, and later Schrage motors attained specific outputs as large as 34 H.P./pole. However, the output of the "Θ-Pinch" type brushless motor has no such specific limitation due to a

Table 5.5

Characteristics of the Rewound, 150 HP Motor at Rated Load

Asynchronous Condenser Tertiary Sector	
Phase current (A)	94·5
Reactive power (leading kVAR)	78·48
Real power (input kW)	5·44
Stator I^2R loss (kW)	2·16
Primary Stator Sector at σ = 0·033	
Phase current (A)	191
Real power (input kW)	125·7
Reactive power (lagging kVAR)	70·37
Mechanical power (output kW)	112·5
Stator I^2R loss (kW)	4·05
Conventional rotor I^2R loss (kW)	3·68
Iron loss (kW)	2·10
Stray-load and friction loss (kW)	3·37
Motor efficiency (%)	89·5
Motor power factor (%, lagging)	87·3
Terminal power factor (%, leading)	99·8
Overall efficiency (%)	85·8
Total input apparent power (kVA)	130·8

commutator diameter, but is only dependent on the maximum permissible cage-rotor power dissipation and the minimum number of primary poles which can be a non-integral number but necessarily greater than 2.

The particulars of the lap-tertiary winding are given in Table 5.6 .

Table 5.6

Particulars of the lap-tertiary winding

Number of armature coils	20
Number of coil sides per slot	11-18
Maximum current loading (pk)	90,000 A/m
Maximum slot packing factor	47%
Number of parallels	4
Number of turns per coil	6-9
Maximum temperature rise	90°C
Wire size diameters	2.13 mm, 2.36 mm
Interconnection type	Series
Insulation class	Type F
Mean length of turn	1.2 m
Total length of wire	730 m

5.5 INSTRUMENTATION

All measurements presented here have been carried out in steady-state tests with continuous loading provided by a Type NS (discharge winding) 6-pole commutator dynamometer rated at 150 kW. Torque control is achieved by adjustment of the injected 50 Hz rotor voltage supplied by a moving-coil, double-induction regulator whereas the magnitude of the dynamometer stator voltage is held constant under all conditions. In four quadrant testing of the induction machine, the dynamometer for this type of prototype testing since it is entirely regenerative without the use for 3 machine sets as in a Ward-Leonard system. A diagram of the test facility is provided in Figure 5.32 and the instrumentation of the dynamometer is shown in Figure 5.33 along with the machine instrumentation shown in Figure 5.34.

The data logging system shown in Figure 5.35 is the same system as used with the 26 kW machine and the linear induction condenser experiments with the exception that the number of scanning channels have been increased from 40 to 60. The four digit voltmeter incorporated in this sytem indicates a true root-mean-square value of the waveforms; the specifications for this unit are given in Appendix I. The four digit phase meter has an internal waveform filter but computes phase angles based on zero-crossings of the fundamental component and has been substantiated as being accurate to within ±0.10 degree on 50 Hz. The coil by coil phase measurements have been taken from digital phase readings using the 200 Hz damping and the 50 Hz damping selectors on separate runs immediately following each other. The 200 Hz damping set of results for current and voltage phase angles have proved to be the most reliable over many scans.

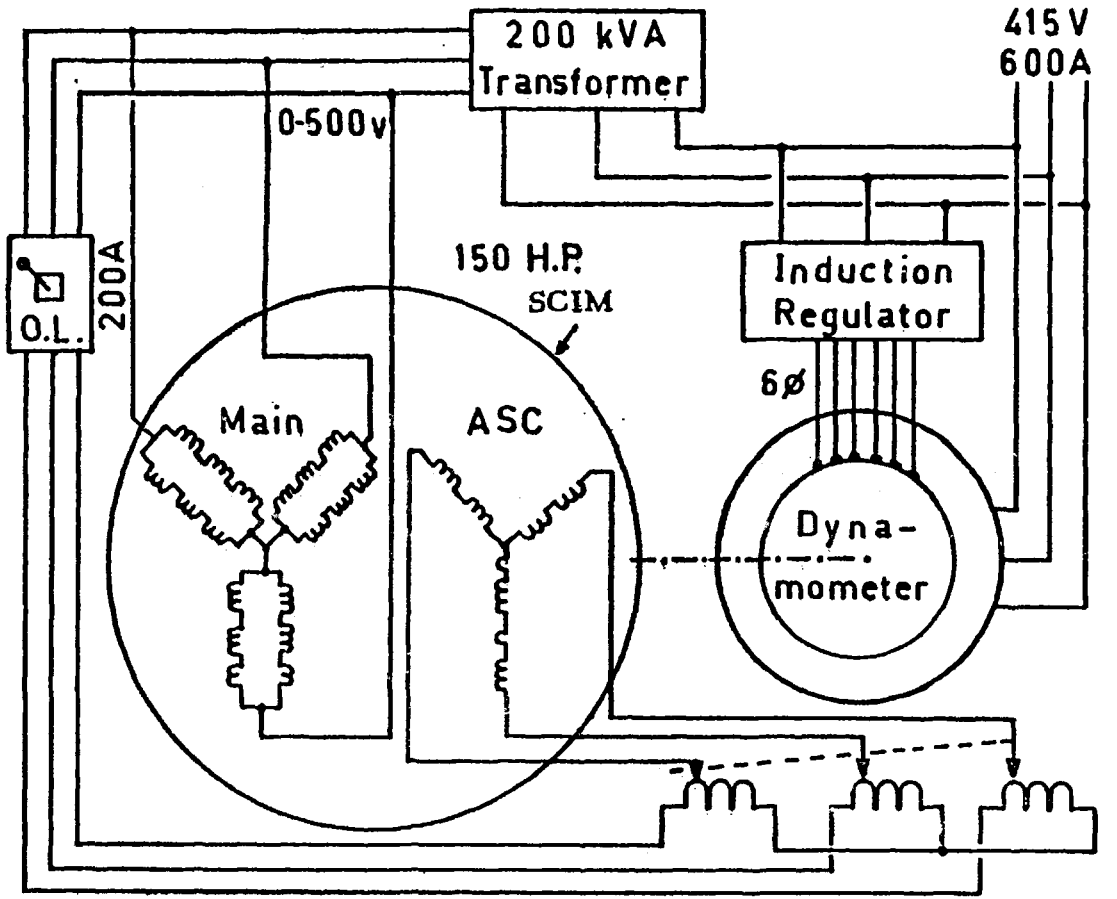

Figure 5.3 2 Regenerative test facility for steady-state loading of the SCIM unit using a Type NS stator-fed AC commutator dynamometer and tap-change transformer.

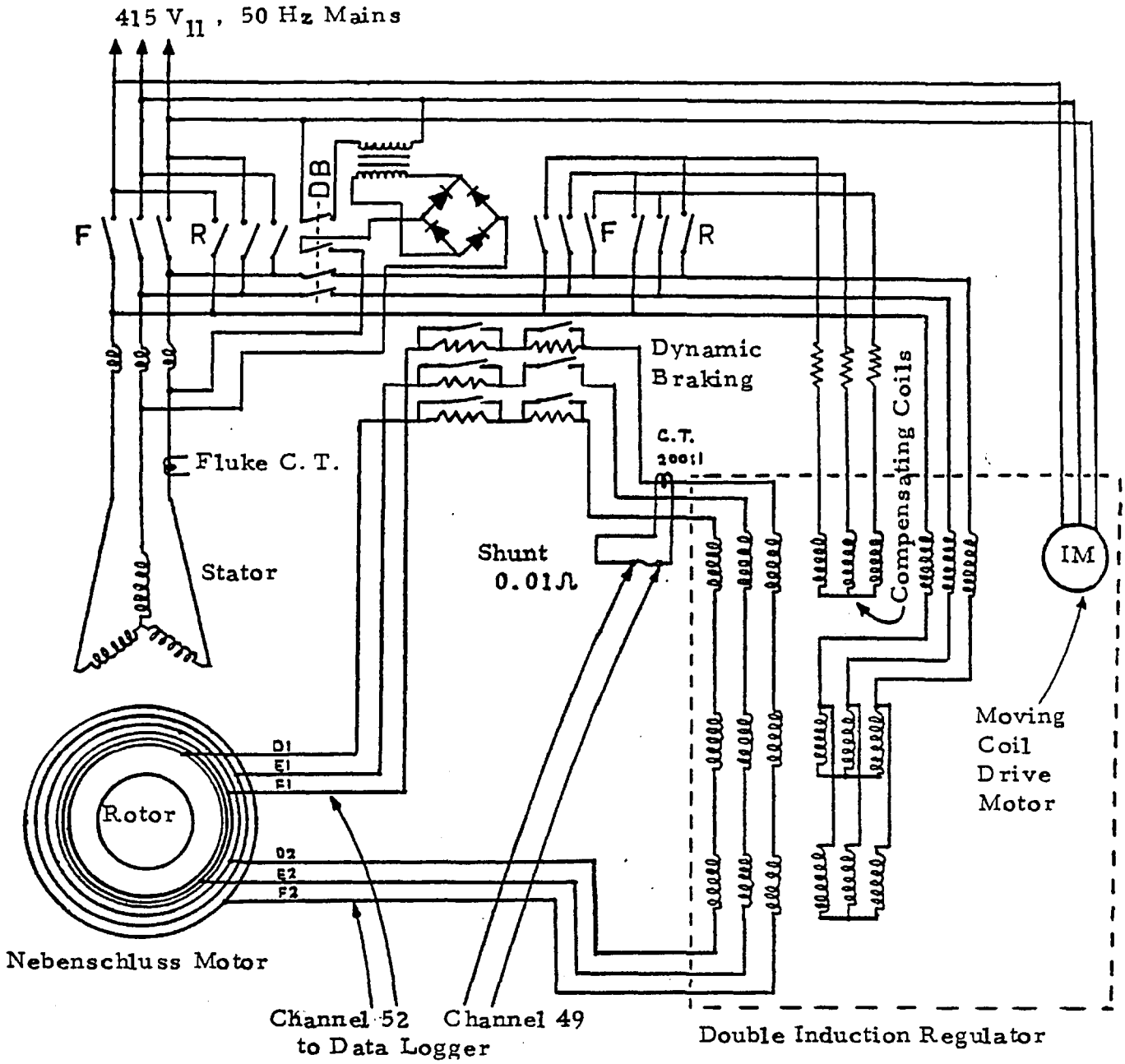

Figure 5.33 Instrumentation of the AC commutator, Type NS dynamometer.

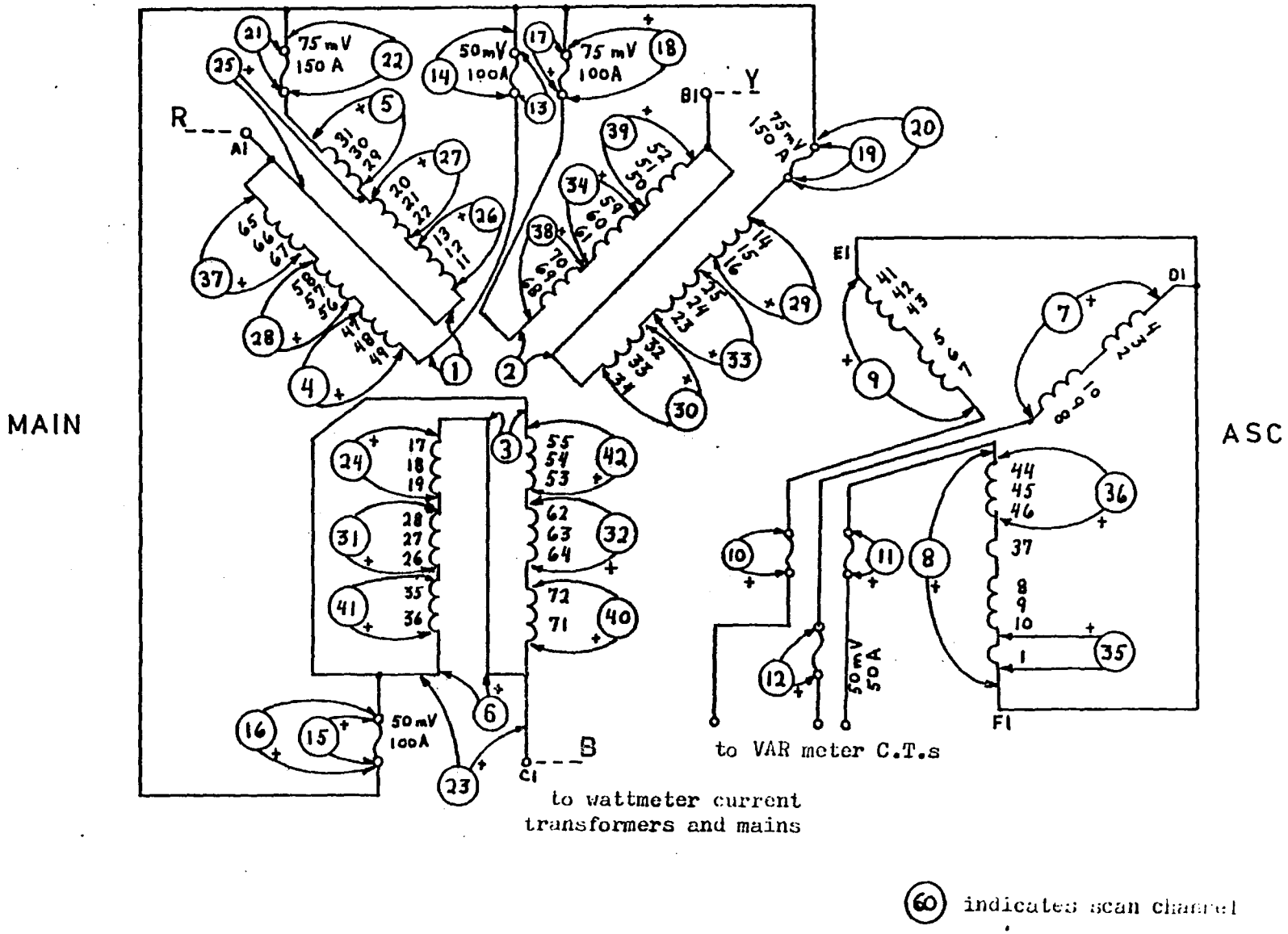

Fig. 5.34 Winding diagram and data logger instrumentation of the 112 kW subsequent to rewind; refer to Figure 4.13 for electronic instruments used in conjunction with data logger and 60 channel scanning system

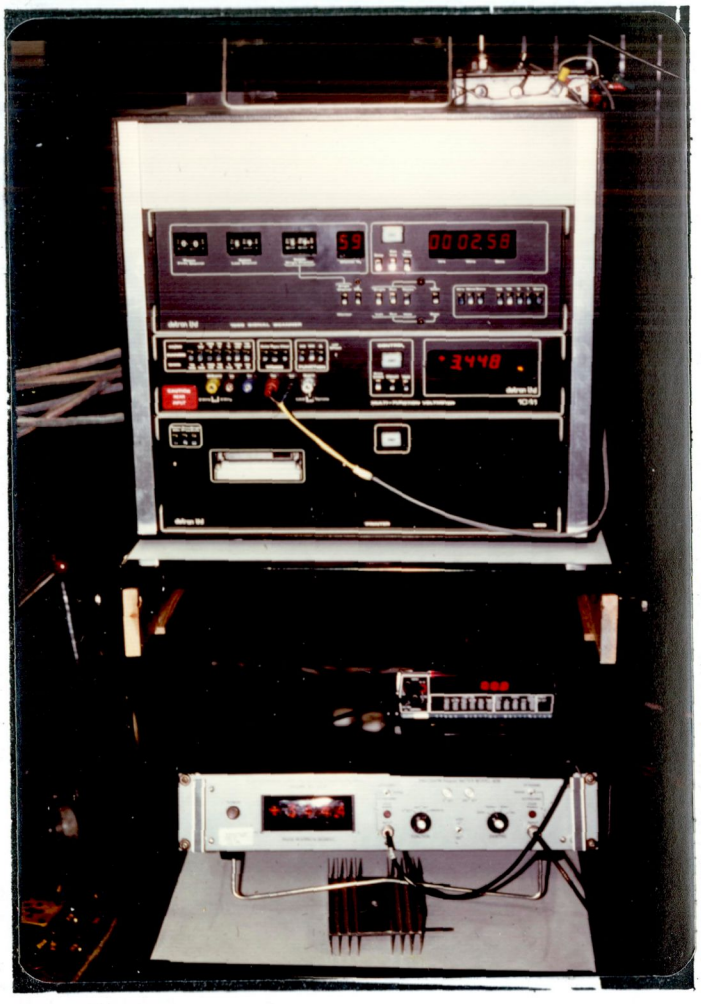

Fig. 5.35 The electronic instrumentation system consisting of a 60 channel scanner, digital voltmeter, printer, digital ammeter and digital precision phase meter.

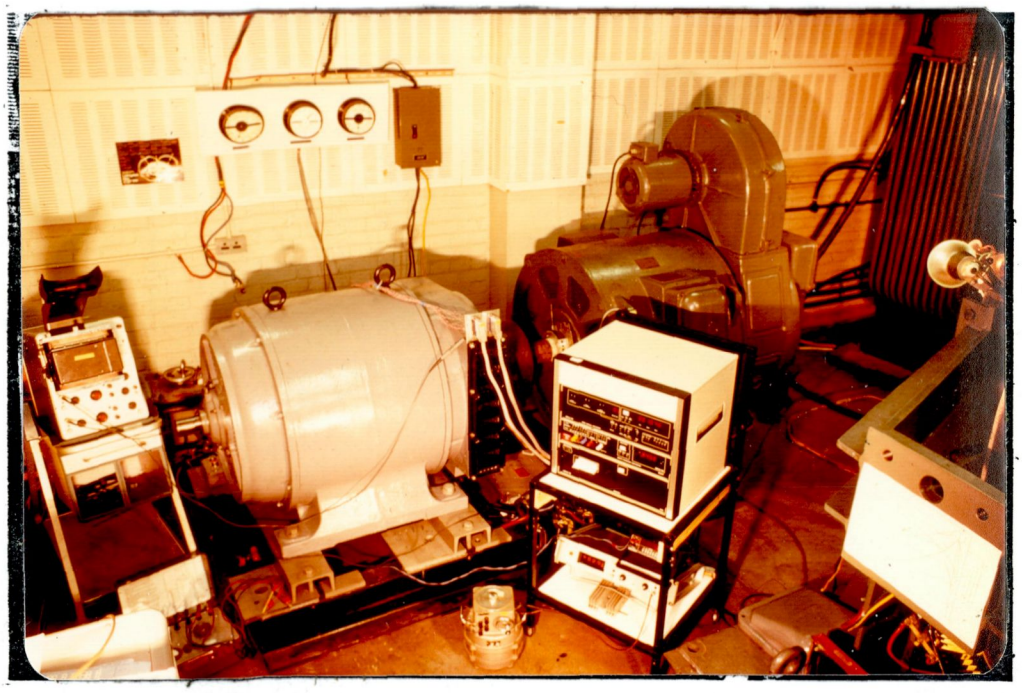

Fig. 5.36 The testing facilities for the 112 kW SCIM unit with the Type NS dynamometer behind the data logging system on the right; the electrodynamic wattmeters and VAR meters are behind the oscilloscope.

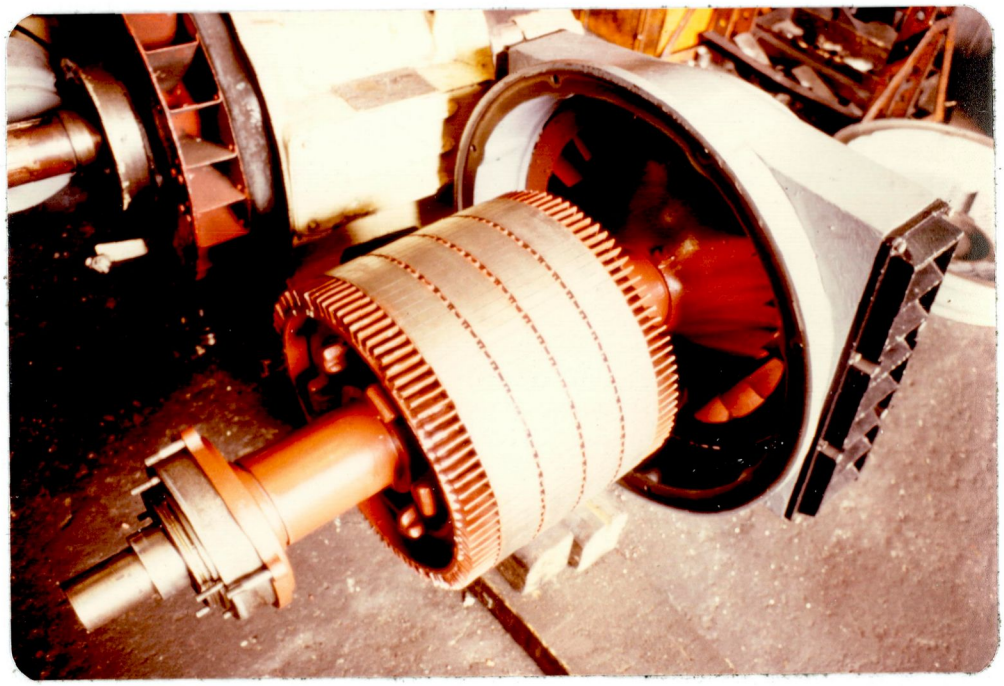

Figure 5.37 The rotor for the 150 H.P. SCIM unit.

5.6. REFERENCES

[1]E.R. Laithwaite and L.L. Freris, Electric Energy: Its Generation, Transmission and Use, McGraw-Hill: England, 1980, p. 124.

[2]E.R. Laithwaite, "The Impossible Dream," Electrical Review, 1975, Vol. 196, No. 13, pp. 717-718.

[3]F.C. Williams, E.R. Laithwaite and J.F. Eastham, "Development and Design of Spherical Induction Motors," Proc. IEE, Vol. 106A, No. 30, 1959, pp. 471-484.

[4]F.J. Teago, "Test Results Obtained from a Three-Phase Shunt Commutator Motor," Journal IEE, 1922, Vol. 60, pp. 328-338.

[5]E.R. Laithwaite and S.B. Kuznetsov, "The Asynchronous Condenser: A Brushless Adjustable Power Factor Induction Machine," IEEE Trans. on Power Apparatus and Systems, Vol. PAS-99, No. 6, Nov./Dec. 1980, pp. 2422-2432.

[6]R.E. Doherty and E.T. Williamson, "Short-Circuit Current of Induction Motors and Generators," Journ. AIEE, Vol. 40, No. 1, Jan. 1921, pp. 1-11.

[7]C.G. Veinott and R.E. Hellmund, "Transformer Ratio and Differential Leakage of Distributed Windings," Trans. AIEE, Vol. 49, July 1930, pp. 1043-1054.

VI. NATURAL THYRISTOR-COMMUTATION

6.1 EXPERIMENTAL OBJECTIVE

A new type of brushless, cage-rotor induction machine has been developed and discussed in Chapter V which is capable of providing enough counter-emf when interfaced with a current-source inverter (CSI) to naturally commutate the thyristor devices in a high-voltage DC-link, adjustable frequency converter. The experimental machine combines the torque characteristics of a conventional cage induction machine with the stable, magnetic commutation capability of an overexcited, DC-field synchronous condenser into one unit using a common cage rotor and a common stator core. For the laboratory 112 kW SCIM and larger units, leading power factor operation of the entire unit, at full load and especially on overloads up to 150%, is compatible with high-speed load commutation of all semi-conductor current-mode devices. The single rotating machine has two distinct airgap wavelengths obtained by the use of two different stator windings which must be necessarily energized from a common CSI unit.

The preferred adjustable speed propulsion arrangement consists of a mains-fed phase delay rectifier (PDR), high-voltage DC link, and a current source thyristor inverter powering an 8 or 10 pole traction motor with constant volts/Hz control. The entire system is entirely free of electrostatic force-commutation capacitors, blocking diodes and flyback semiconductors. The described drive system provides continuously adjustable torque during motoring and regenerative braking modes and specific details are given for the 112 kW

SCIM unit and converter capable of natural commutation up to 200 Hz. The analysis concentrates on determining the magnitude of the cemf available from the asynchronous condenser winding and the consequent operation of the machine in both natural commutation and in a DC-link pulsing mode for start-up.

6.2 STATE OF THE ART

The advances in static, adjustable frequency power conditioning equipment for traction drives has provided new opportunities for DC motors but the evolution of this technology to AC machines has been relatively slow despite the inherent advantages of induction motors as forming inexpensive and robust prime movers in environments that are either prone to contamination or potentially explosive. Generally system studies have concluded that even when motor reliability and maintenance costs clearly place the induction machine ahead of both DC and synchronous drives, the requirements of a typical traction-type torque speed characteristic [1] have necessitated that the inverter equipment is relatively heavy and expensive for the asynchronous drive. Invariably, this is due to the need to force commutate such inverters or else incorporate large capacitor banks on board the traction vehicles. In specialized applications, the synchronous motor drive [2] offers the advantage of a simpler inverter since natural, load commutation is possible but generally the disadvantages are either the need for slip-ring and exciter hardware with a wound field design or else the high cost of a permanent magnet field once units in the several hundreds of horsepower are considered.

Clearly, what was needed is a basic cage-rotor induction motor construction but with the terminal characteristics of an overexcited synchronous machine. In contrast to contemporary traction drive development programs whereby the inverter is the center of attention, the aim of this research work has been concentrated on the machine itself. It was felt that a new look at the internal electromagnetics of the cage-rotor motor could indeed produce a unity or leading power factor

design at the terminals, without the need for any brushgear, slip rings, DC excitation, permanent magnet materials or special laminations. In retrospect, when state of the art inverter schemes for induction motor drives were compared, it was noticed that all types store rather large amounts of commutation energy in capacitor banks, yet it is well known that above a certain kVAR size, the most economical way to store energy is not in a dielectric material but in a magnetic field--not especially in the leakage field of an electrical machine, rather in the same airgap field that produces torque. The commutation energy available from this induction machine scales up as the rotor inertia. The concept of using a DC commutator motor as an electromechanical filter in place of a capacitor was reported in 1972 [3] and now this concept has been extended to the cage rotor induction motor.

The overwhelming criterion for interfacing such a new induction machine with frequency conversion apparatus was that this advance in the machine allows a considerable reduction in the inverter power circuitry in both manufacturing cost and weight. It is important to note that the choice of a square-wave output current-source inverter not only offers a very simple and reliable power path consisting exclusively of 6 thyristor devices, but the particular induction motor electromagnetics prefer being current forced. This is in contrast to the pulse-width modulated (PWM) voltage source inverters commonly employed with lagging power factor induction motors [4]. The only apparent disadvantage with the use of a current fed inverter is that a relatively high DC link voltage must be readily available for natural commutation of high speed traction motors. Thus a mains supply phase-delay-rectifier (PDR) is necessary to control the link voltage with

fast response times. The magnitude of the link voltage necessary for a 1000 H.P. type traction drive is consistent with present working voltages on tap-changer commutator motor schemes.

Recent developments of forced or load commutated schemes for traction drives with induction motors have focused, respectively, on PWM voltage source inverters or the auto-piloted current source inverter incorporating an additional 6 diodes and 6 static capacitors to the basic 6 thyristors. [5] However, the induction machine commutated thyristor drive under discussion, as shown in Figure 6.1 is classified as a true line-commutated scheme in that as far as inverter commutation, overlap, and gating control are concerned, the system behaves nearly identical to state-of-the-art synchronous motor drives as shown in Figure 6.2a.

The use of either permanent magnet or overexcited, wound field synchronous motors to naturally commutate DC-link thyristor inverters has been well advanced. [6-7] Whether the magnitude of the cemf is adjustable at a given shaft speed is not of prime concern because the preferred propulsion arrangements generally allow constant volts/Hz control. Consequently, the ability of the synchronous machine to naturally commutate is fairly constant over large speed ranges. In this arrangement, the high voltage DC-link is adjustable by the use of a mains fed phase-delay-rectifier; the entire converter system comprises a total of 12 thyristor devices and a link smoothing inductor. It is apparent that unlike forced commutation schemes, no power capacitors or diodes are necessary. Synchronous drives provide continuously adjustable torque during motoring and regenerative braking modes and have been built with specific power densities up to 21.7 kW/kg for the basic

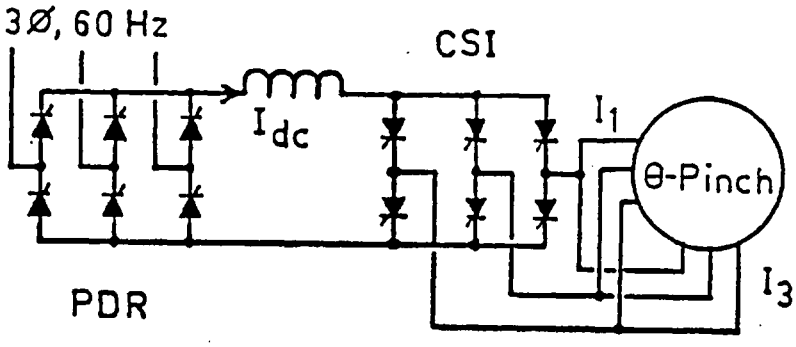

Figure 6.1 Naturally commutated thyristor induction machine drive.

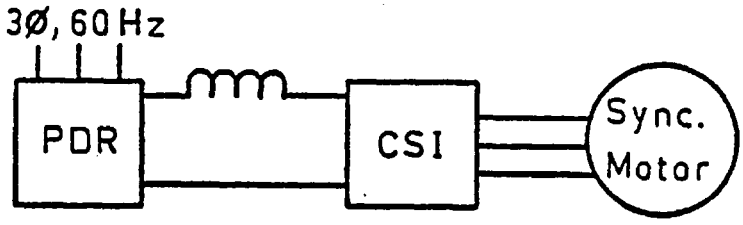

Figure 6.2a State of the art synchronous VVVF drive system.

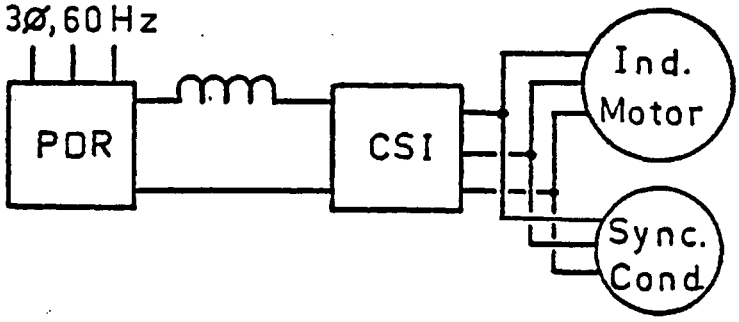

Figure 6.2b State of the art asynchronous VVVF drive system.

machine at 30,000 RPM by using S_mCo_5 magnets. [8] These schemes have been modified to include induction motors as the prime movers but with a synchronous compensator to effect inverter commutation as shown in Figure 6.2b. For this system, overall power densities as high as 0.436 kW/kg have been obtained for the entire 2 machine plus 2 converter unit propulsion system with water cooling of the LIM stator and all other power components. [9]

6.3 INDUCTION COMMUTATION

The development of an induction machine commutated inverter started with assessing state-of-the-art CSI induction motor drives with synchronous compensators. Fundamentally, there was no reason why hitherto technological advances had not combined the most desirable electromagnetic features of a cage-rotor induction motor with the airgap fields of a synchronous condenser to use a common stator core and share the same airgap field, in contrast to present drives which have one machine entirely dedicated to torque production and the second concerned only with VAR generation. Generalized machine theory has always indicated that fundamentally the asynchronous-induction and the synchronous-wound field motor produce torque and consume VARs by exactly the same mechanism. The only major differences between these two are in the shaft speed and in the method by which the rotor currents are established. The advent of the adjustable frequency converter pointed to the fact that not only is the relation between mains frequency and shaft speed entirely arbitrary, but that induction drives would maintain the high efficiency of synchronous drives over a very wide speed range due to the use of constant slip control.

It was subsequently realized that as long as constant per unit slip could be maintained at a stable and low value in an induction machine, these same slip frequency currents could be used to establish the equivalent of a DC field pattern in a synchronous machine. It is not strictly necessary to feed (VAR generating) rotor currents by means of slip rings and brushgear, but that the desired rotor current pattern can be initiated by simple induction motor action.

The major criterion underlying the hardware development was to show that by induction alone, at mains or medium inverter frequencies, the equivalent MMF of an asynchronously operating integral motor/condenser would appear to be overexcited at the terminals of the entire machine once the conventional magnetization and leakage flux requirements were met. This was accomplished by artificially introducing a space-transient magnetic wave travelling at rotor speed into the airgap flux distribution of a conventional induction machine which has a torque producing synchronously travelling magnetic wave. Moreover, it was established that as long as the stator incorporates at least two distinct pole-pitches fed at the same fundamental frequency, the rotor suffices in every respect. Thus the power to weight characteristic of a cage construction can be retained and the overall weight of this leading or unity P.F. machine is 10%-15% less than a large lagging P.F. motor, once the additional weight penalty of either a synchronous condenser or a static capacitor bank is considered. The asynchronous condenser-motor concept permits a CSI drive specific power/weight ratio higher than 0.44 kW/kg without water cooling since only 1 rotating machine is used. This is covered in detail in Section 6.6.

Figure 6.3 shows the thyristor current-source inverter built for the SCIM-II machine; the same unit may also be used as a phase-delay rectifier when the machine is used in the regenerative mode. Figure 6.4 depicts the most important experimental results obtained with this induction drive system for this shows the inverter currents being naturally commutated at high frequency by the SCIM unit at a 4% slip and a 75 Hz fundamental, as well as the filtering action of the ASC windings.

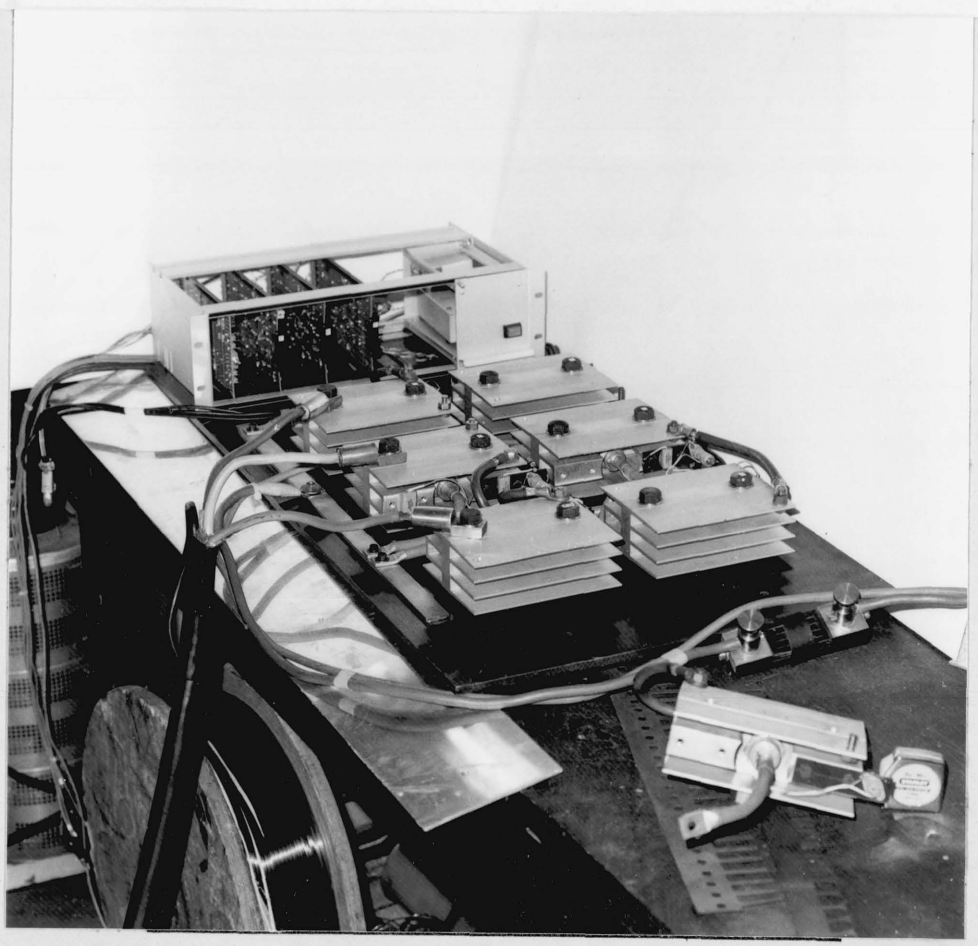

Figure 6.3 The entire current-source inverter with control logic for the 150 H.P. Theta - Pinch Induction Motor. (DC link smoothing inductor not shown in picture.)

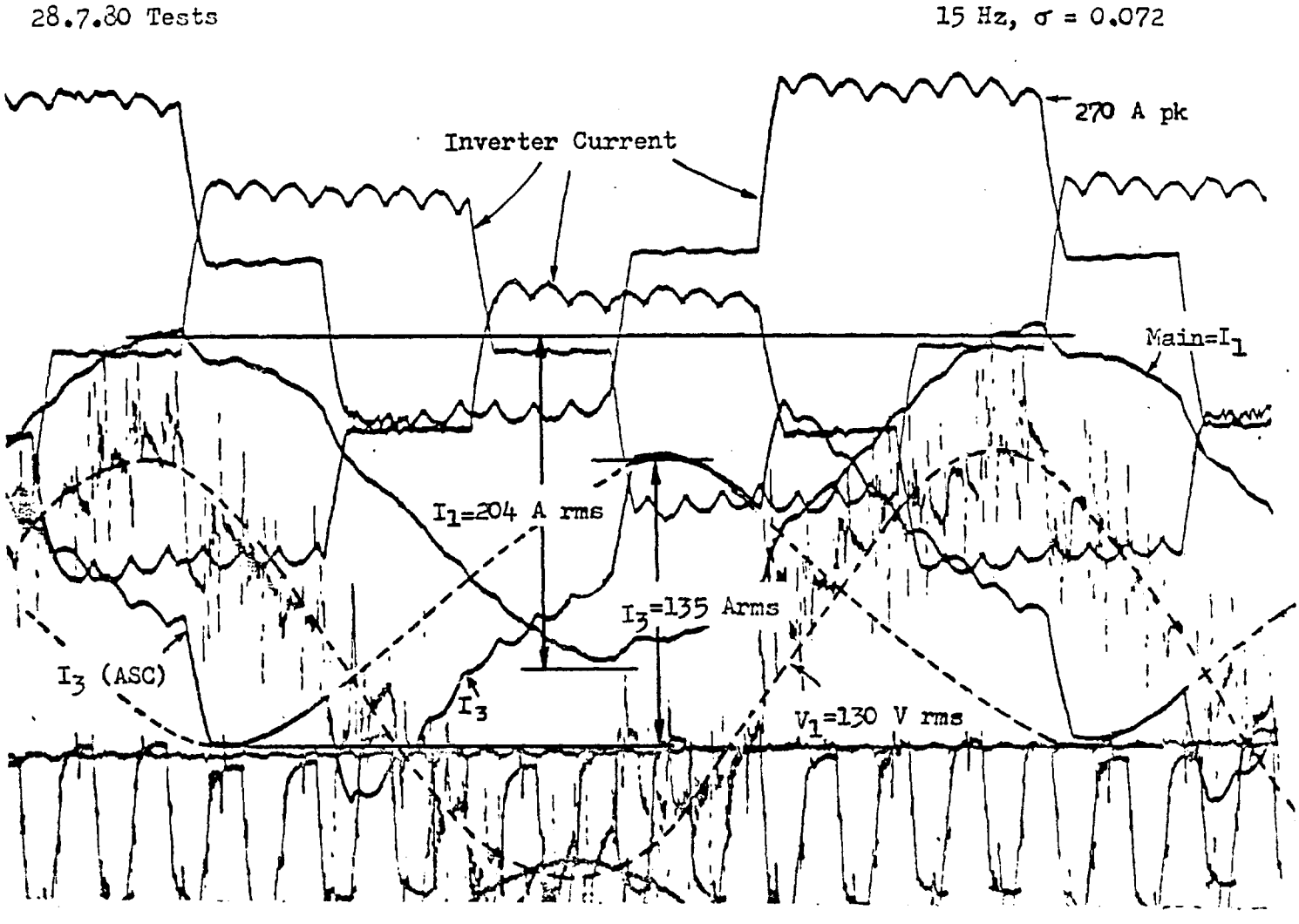

Figure 6.4 Oscillograph traces of the natural commutation mode for the 150 H.P. Theta-Pinch unit at 15 Hz showing machine terminal voltage, primary and tertiary currents along with the fundamental components shown by the dashed curves.

6.4 REACTIVE CEMF MODEL

To establish the limits on the machine commutated inverter, the magnitude of the counter-emf offered by the asynchronous condenser windings will be derived. The machine geometries presently under evaluation using the "θ-Pinch" technique are specific to multipolar stator designs of 8, 10, 12 poles etc. θ-Pinch creates an abrupt transition in the stator MMF at two diametrically opposite positions along the periphery. In essence, the θ-Pinch machine is operating continuously and stably in a space-transient mode and with mains frequency will always have both sinusoidal current and voltage waveforms for every coil. Only when excited by a square wave inverter, will the machine be operating simultaneously in space transient and time transient modes.

The implication of this space-transient mode is that every pole (or slot) around the periphery is subjected to a slightly different airgap flux induction amplitude whereas in a conventional machine the rotating field pattern has a uniform amplitude at all positions. This means that the effective utilization of each tooth is non-uniform but more important from the aspect of calculating terminal performance, each pole has a slightly different magnetizing reactance, X_m, coupled rotor resistance, R_2 and rotor leakage reactance, X_2. The parameters X_1 of stator leakage and R_1 of stator resistance remain constant among the poles.

The conventional induction motor equivalent circuit is strictly a steady-state diagram and it should be emphasized that this representation does not indicate the slip frequency of rotor currents but conveniently interchanges a frequency dependent reactance with a constant resistance; this still permits the output power to be directly calculated from the R_2 parameters but the physical insight is lost. To allow some simplification in modelling space-transient machines, a single frequency equivalent circuit is presented in Figure 6.5 although several reservations are necessary.

a.) The conventional definition of slip, σ as rotor loss/rotor input is not accurate; thus σ only denotes the per unit difference between rotor and synchronous speeds.

b.) The parameters R_2, X_m, and X_2 are average values of all the poles in each section assuming the coils of a particular section are series connected.

c.) The relative magnitudes of the rotational reactance, X_m and X_2 as well as the absolute value of E_q, the counter-emf are only exactly valid over a limited range of low per unit slips at a particular excitation frequency. This frequency dependence of the inductances decreases as the pole pitch or frequency is raised.

The per unit values of Figure 6.5 are specific to a 150 H.P. unit at 200 Hz and $\sigma = 0.016$ p.u.

All of the commutating criteria will be expressed in

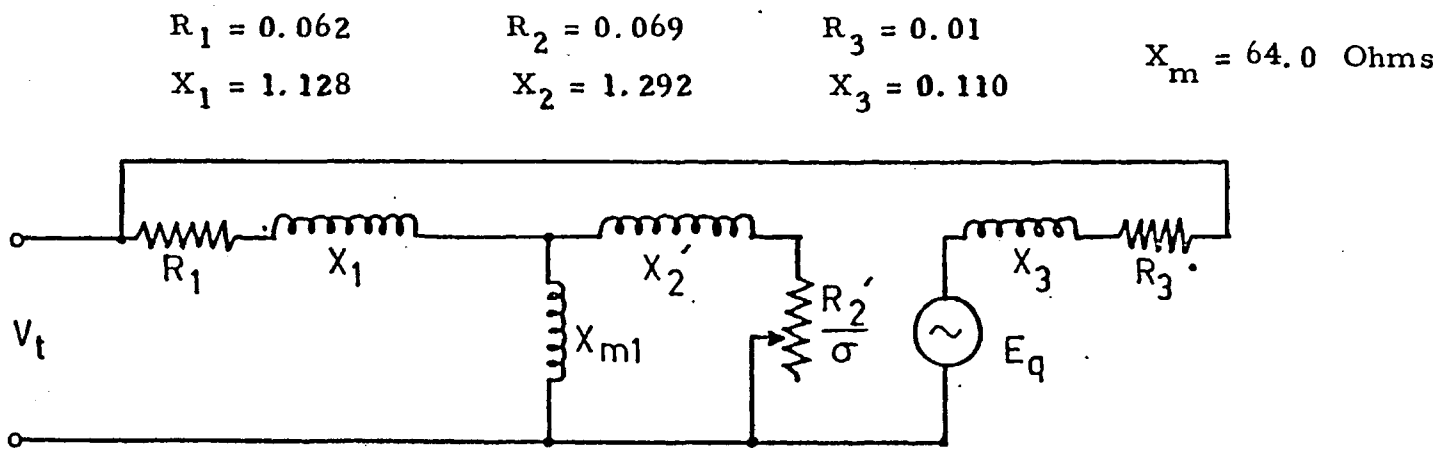

Figure 6.5 Equivalent circuit of integral induction motor-asynchronous condenser with high speed parameters of the 112 kW SCIM unit indicated for 200 Hz.

terms of dimensionless factor

$$G = X_m \; / \; R_2 = \omega T_r \qquad (6.1)$$

where T_r is the rotor coupled time constant of magnetization and this remains substantially constant over the entire slip range. G can be calculated as in equation (3.15) from conventional design formula even with a differing flux amplitude/pole. Although the airgap of the asynchronous condenser contains both a fundamental and subharmonic wave, it is possible to separate their effects and represent this in a closed form solution under the assumption that the rotor leakage is small. The total instantaneous radial flux density crossing the airgap over the motoring winding may be expressed

$$b(\theta,t) = \frac{P_r \hat{J}_s}{\omega\sqrt{\sigma^2+(1/\omega T_r)^2}} \left\{ \sin\left[\omega t-\theta+\tan^{-1}(1/\sigma\,\omega T_r)\right] \right.$$

$$\left. -\exp\left[\frac{-\theta}{(1-\sigma)\,\omega T_r}\right]\cdot\sin\left[\omega t-\frac{\theta}{1-\sigma}+\tan^{-1}(1/\sigma\,\omega T_r)\right]\right\} \qquad (6.2)$$

where θ = angle from transition point of condenser to motoring windings (electrical radians)

$\hat{J}_s$ = stator current line density, peak (A/m)

$$P_r = \frac{\rho \cdot \pi}{\tau_{p1}} = \frac{\text{rotor surface resistivity } (\Omega) \; . \pi}{\text{pole pitch (m)}} \qquad (6.3)$$

The first part of (6.2) is the steady-state component of the B field while the exponentially attenuated terms represent the addition of the transient wave.

As revealed by the second term, to maximize the output of the condenser winding which is magnetized by this total wave, the pole pitch of the motoring section, τ_{p1} must be reduced to $\tau_{p2}=(1-\sigma^*)\tau_{p1}$. The difference between the quantities $(1-\sigma^*)$ and $(1-\sigma)$, where the former is actively controlled by the inverter constant-slip control loop, in effect gives a stator type of field control to compensate for the loss of a rotor exciter with this asynchronous machine.

The Theta-Pinch motor concept departs from convention in that the distribution of the total radial component of airgap flux is no longer a constant level around the periphery but rises and decays over the excitation and condenser sections respectively as shown in Figure 6.6.

With inverter control, constant volts/Hz power may be applied; Figure 6.6 indicates that with increasing frequency the magnitude of the airgap flux increases as

$$\frac{\partial b}{\partial \omega} = \frac{P_r \hat{J}_s \pi}{\tau_{p1} \sigma \omega^2} \left[1-\frac{\theta}{\omega T_r(1-\sigma)} \right] \exp\left[\frac{-\theta}{\omega T_r(1-\sigma)}\right] - 1 \qquad (6.4)$$

due to the increase in the magnetization Goodness factor which is largely what determines the rate of rise of flux (and thus torque) at constant slip. In a conventional machine, constant volts/Hz control generally yields constant airgap flux density.

Figure 6.5 also indicates that the spatial rate of

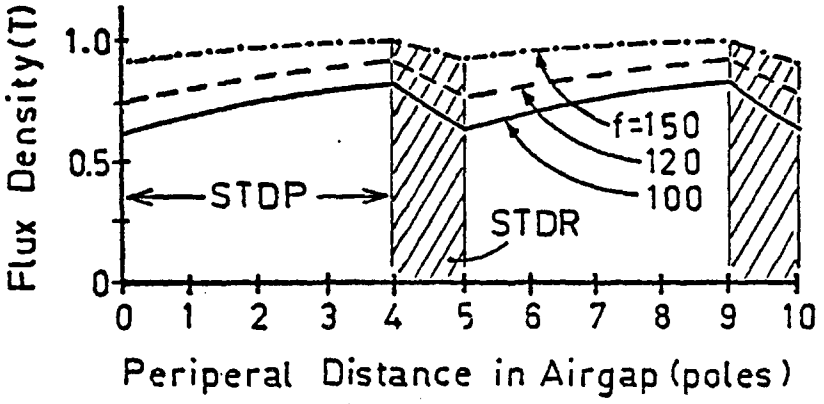

Figure 6.6 General peripheral distribution of the total , normal-component of airgap flux density in a 10-pole SCIM.

change of airgap flux is reduced with higher frequency resulting in a more uniform flux distribution. As long as the machine is wound with a genuine change in pole-pitch winding which necessitates a change in slot pitch stator lamination, no additional stray load losses will be incurred above those for a symmetrical machine.

In the design stages, it is imperative that the space modulation of $b(\theta,t)$ peak at a position θ_1 which initiates the change in pitch from τ_{p1} to τ_{p2}.

$$b(\theta_1,t)=\frac{P_r \hat{J}_s}{\omega\sqrt{\sigma^2+(1/\omega T_r)^2}}\left\{1-\psi\cdot\exp-\left[\frac{\omega t+\tan^{-1}(1/\sigma\,\omega T_r)-\pi/2}{(1-\sigma)G}\right]\right.$$

$$\left.\cdot\sin\left[\frac{2-\sigma}{1-\sigma}\,(\omega t+\tan^{-1}(1/\sigma\,\omega T_r))-\frac{\pi/2}{1-\sigma}\right]\right\} \qquad (6.5)$$

where $\psi \leq 1$ and represents the lower limit on the per unit flux density in the entire machine (at angle θ_2) at high speed. It is specific to a particular winding sequence and its functional relationship is

$$\psi = f\left[(\cos\phi)^{-1},\ G\ ,\ \cos\left(\frac{n\sigma\pi}{1-\sigma}\right)\right] \qquad (6.6)$$

where n is the number of poles in section from θ_2 to θ_1 and ϕ is the power factor angle of the motoring winding alone. From the aspect of maximizing the condenser section cemf, E_q the generated reactive energy maximum occurs at the peak of the transition edge values in the

product $I_q.E_q.u_r$ at a slip given by

$$\cos\left(\frac{n\sigma\pi}{1-\sigma}\right) = 1 \qquad (6.7)$$

The commutation voltage, E_q is the integration of $b(\theta,t)$ over the entire length of the condenser section to yield the volts/turn as

$$E_q = u_r \int_{\theta_1}^{\theta_2} b(\theta,t)\cdot\exp\left[\nu_1(\theta_2-\theta_1)\tau_{p_1}/\pi\right]\, d\theta \qquad (6.8)$$

where ν_1 is the complex attenuation of the space transient wave

$$\nu_1 = -\frac{\pi}{\tau_{p_2}}\left[\frac{1}{\omega T_r'(1-\sigma)^3 + \omega T_2'(1-\sigma)} + j\,\frac{1}{1-\sigma}\right] \qquad (6.9)$$

$$T_r' = T_r(1+x)^2 \qquad (6.10)$$

$$T_2' = T_2(1+x) \qquad (6.11)$$

$$x = \frac{X_2}{X_3 + Q_{asc}/q\cdot I_3^2} \qquad (6.12)$$

for q = number of phases, I_3 = r.m.s. condenser current per phase, and Q_{asc} is the net output of the condenser winding. At the instant of commutation, this reactive power is related to the required inverter reactive power, Q_{inv} as

$$Q_{asc} = Q_{inv} + q(I_m^2 X_m + I_2^2 X_2 + I_1^2 X_1)$$

$$= Q_{inv} + q\left[I_1^2 (X_1 + cX_2)\right] \qquad (6.13)$$

for $c = 1+X_1/X_m$. To find Q_{inv}, the solution for E_q from (6.8) is necessary but this is an iterative process because this voltage is dependent on the effective armature reaction of the asynchronous condenser which is controlled by the surface impedance of the stator. Conversely, the maximum reactive power that can be transmitted across the internal leakage and resistance of the condenser is a strong function of E_q and the terminal voltage of the machine, V_t

$$Q_{asc} = - E_q^2 \frac{X_3}{R_3^2 + X_3^2}$$

$$- \frac{E_q V_t}{\sqrt{R_3^2 + X_3^2}} \sin\left[\gamma + \tan^{-1}(-X_3/R_3)\right] \qquad (6.14)$$

Pertaining to C.S.I. operation, it should be stressed that the Θ-Pinch motor is predominately a slip controlled device rather than being frequency controlled so far as VAR generation by the the ASC winding is concerned. Figure 6.7 emphasizes this point as it is seen that for the specific case of n = 4 excitation poles per repeatable section, VAR generation is insignificant until a slip of 0.166 per unit or less is attained. The ordinate of this figure, Q, the maximum reactive power per unit of condenser section axial edge, is normalized w.r.s.t. the

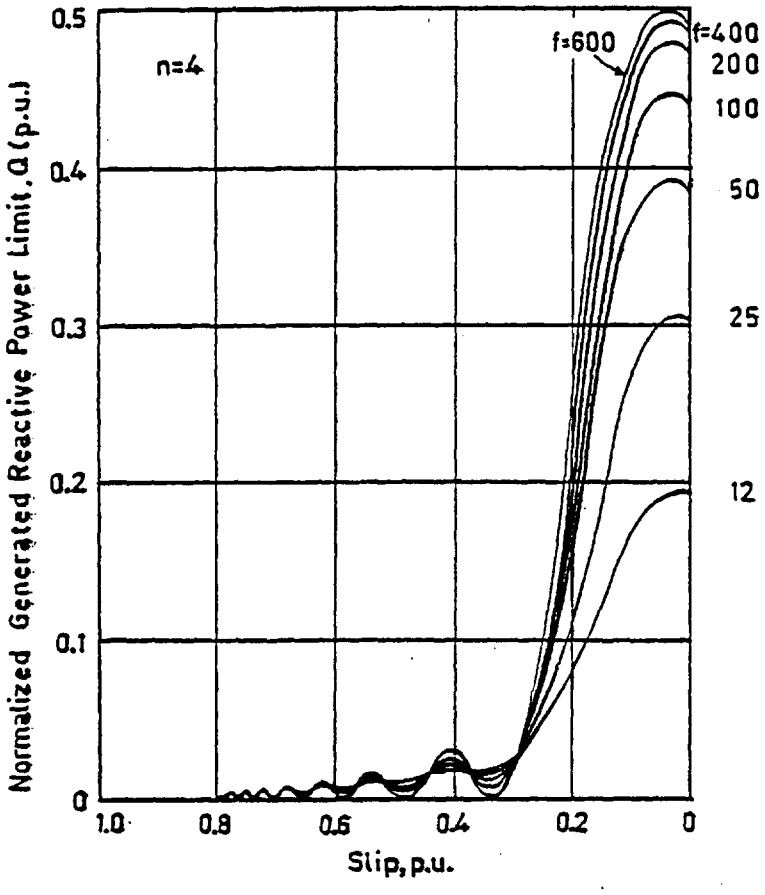

Figure 6.7 Asynchronous condenser winding maximum reactive power generated as a function of frequency for a basic G=200 SCIM unit without carry-over flux compensation and valid for 4 exciting poles/primary section.

rotor copper loss of a conventional cage machine which is

$$P_{base} = \tfrac{1}{2} P_r J_s^2 n \tau_{pl} \qquad (6.15)$$

To generate enough reactive KVA to naturally commutate a thyristor inverter, a slip value less than about 0.075 per unit is necessary. The exact operating slip to allow safe inverter commutating margins, is obviously dependent on the overall machine's leakage and magnetizing flux consumption; noting that these two quantities are basically independent of the amount of kVAR generated by the "exit-edge" transient phenomena at position θ_1.

Concerning variable frequency operation, three characteristics portrayed by Figure 6.7 are vital:

a) The Q_{asc} curves peak around synchronous speed with the higher frequency characteristic actually peaking at just the preferred full load operating slips (in the 1% to 3% range), while low frequency excitation causes the induction machine to peak, reactively, at a super-synchronous speed. The actual shift in optimum slip versus frequency is not crucial. For exciting pole numbers other than n = 4, the buildup of the quantity Q_{asc} at a slip σ^* is given by the general expression

$$\sigma^* = \frac{2}{n + 2} \qquad (6.16)$$

b) While the higher frequencies offer the greatest kVAR output, note that with respect to inverter commutation, it is not the angle margin per say that is crucial

but rather the time available to bias the thyristor devices for natural line commutation. The ASC output characteristic is a natural choice as the net Q output, even with increasing reactance at high frequency, still allows a fairly constant time lead of the current waveform ahead of the voltage waveform. The lowest possible frequency which permits a cage machine to be used in this mode with a C.S.I. traction system at the 150 H.P. level is about 15 Hz. Below this frequency, blanking of the DC link current by the PDR in a pulsing mode from start has been the preferred commutation scheme.

c) The curves of Figure 6.7 are specific to cage rotor induction machines with a Goodness factor of 200 (calculated at 60 Hz) which is appropriate for most modern designs around the 150 H.P. range. These characteristics may be adapted to larger units by changing the frequency notation as fundamentally each curve is the locus of a specific Goodness factor which may be expressed as

$$G = \frac{k\ D^2\ f}{N^2} \qquad (6.17)$$

where D is the diameter of the airgap (m), N is the total number of poles around the periphery assuming a continuous pole pitch of τ_{pl}. The parameter k is nearly constant for all typical cage rotor traction motors around the 100 to 500 H.P. range and if a copper cage is used and operated at about 75°C; for an airgap of 1.25 mm, k will range from about 400 to 500. The exact calculation of G is given in equation (3.15).

For example the curve representing the inverter frequency of 10 Hz for the reference lab machine, G = 200 (60 Hz base) would also be the appropriate curve at 15 Hz for a G = 300 traction motor (assuming the same base.)

6.5 SUBTRANSIENT REACTANCES

One method commonly employed with CSI motor drives to determine the terminal voltage of the synchronous machine is to model the machine's reactance to 120° square wave current as comprising two components. The subtransient reactance, X" carries both fundamental and harmonic currents. The second "adjusted" reactance, in series with the subtransient is the difference between the synchronous and subtransient values or (X_s-X") but the voltage across this is only attributable to fundamental current. The values of X" in the d and q axes are generally assumed to be equal, whereas X_s is allowed to have a rotational variation. [10]

With respect to thyristor commutation, the exact reactance of the synchronous machine at the moment of current transfer is not as important as the time the inverter is in the overlap mode which is in effect a line-to-line short circuit on the machine. The resulting armature reaction MMF initiated every 60° at commutation appears as a large negative sequence reactance and the subtransient reactance are nearly identical and about 10% of the synchronous reactance. In contrast, the stator leakage reactance can be as low as 5% of X_s. In a worst case condition, the synchronous condenser only maintains zero-sequence currents, $\hat{J}_{so} = 1\frac{1}{2}\,\hat{J}_{ss}$ where $\hat{J}_{ss}$ is the stator current loading at rated load. However, the damper cage will have a current loading $\hat{J}_r = \hat{J}_{ss} + \hat{J}_{so} = 2\frac{1}{2}\,\hat{J}_{ss}$.

For the asynchronous condenser, the subtransient response does not closely resemble the characteristics of a cylindrical rotor, DC-field compensator despite the cons-

truction similarities. Although not apparent, the cage rotor condenser is in essence a salient pole machine as viewed from the rotor side due to the non-uniform (stationary) airgap flux distribution; i.e., the airgap reluctance variation of a conventional salient pole machine has been "artificially" created by an asymmetrical MMF design in a uniform gap. Yet even so, to a large extent in machines with G = 100, implying very good rotor to stator coupling, the in-phase and quadrature currents in the main winding of the stator essentially see the same transient reactance since the rotor MMF so closely parallels and opposes any unusual stator MMF distributions. This is characteristic of a cage rotor design with a small airgap where the currents are not series forced as they are in a wound rotor; rather the amplitude of these currents will have a space modulation to satisfy the change in pole pitch boundary conditions that demand semi-abrupt peaks in $J_r(\theta)$ at four positions over the stator periphery.

To a first order degree, the steady-state equivalent circuit of Figure 6.5 and its associated phasor diagram of Figure 6.8 are also valid in a subtransient mode during commutation. The modifications that must be made are:

a.) The 120° square wave current should be seperated into fundamental and harmonic components (h = 5,7,11,13,etc.). The high frequency penetration effects in deep rotor bars can be calculated at each harmonic resulting in a higher R_2 and a lower L_2 parameter than at the slip frequency of the fundamental.

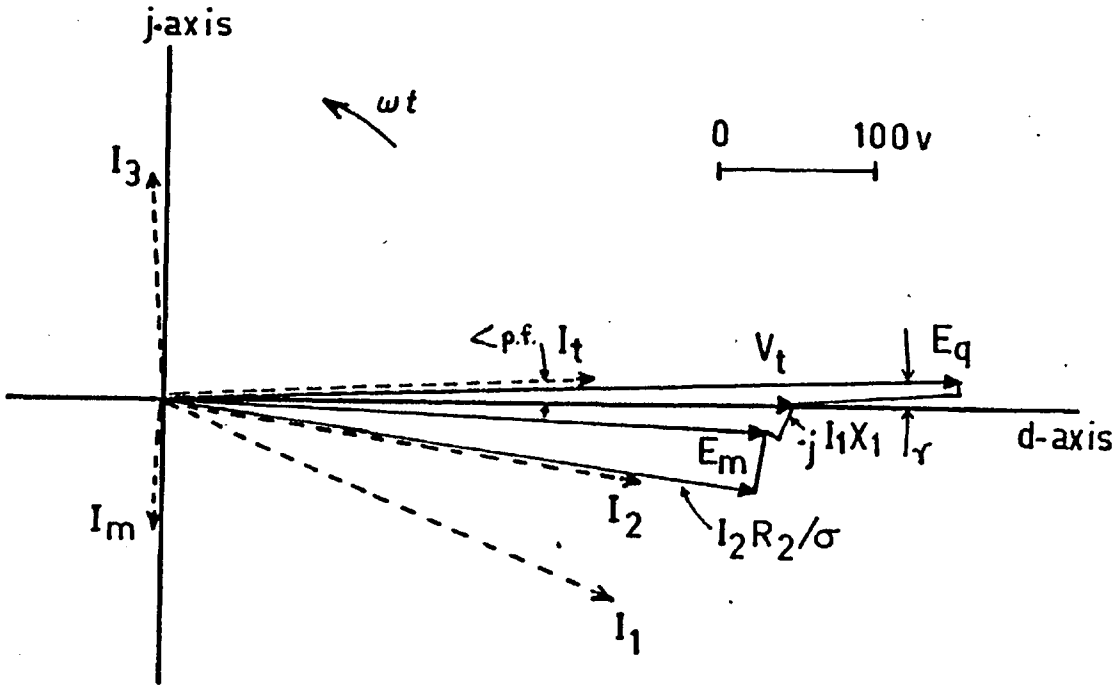

Figure 6.8 Phasor representation of machine voltages at 50 Hz with 112 kW mechanical output and leading power factor mains or terminal current corresponding to Figure 6.5.

$$\frac{L_2(h)''}{L_2} = 1 - 0.00108\ d^2 r(\sigma_h . f_h - 11.4) \qquad (6.18)$$

$$\frac{R_2(h)''}{R_2} = 1 + 0.00381\ d^2 r(\sigma_h . f_h - 9.44) \qquad (6.19)$$

where d = rotor bar depth (cm), r = bar width: rotor slot width and σ_h is the effective per unit slip of the harmonic rotor currents. Formulas 6.18 and 6.19 are specific to rectangular copper rotor bars at 75°C and f_h is in Hz.

b.) The condenser internal voltage must be modelled as a single, fundamental frequency source that is only capable of power transfer at the fundamental frequency.

All of the other reactances X_1, X_3 and X_m scale up linearly with harmonic frequency and in general the change in passive parameters in an asynchronous condenser/induction motor for subtransient operation is a minor effect. The major concern is the harmonic response of E_q; the magnitude of which remains substantially constant during commutation.

Conventional terminology is used in defining the CSI natural commutation interval as shown by Figure 6.9 for a three phase system of quasi-sinusoidal inverter output voltages and finite-rise-time square wave input current. α is the firing delay angle, u is the commutation overlap angle and δ is the commutation margin (or the maximum device-turn-off angle). Under all circumstances

$$\alpha + u + \delta = \pi \text{ radians} \qquad (6.20)$$

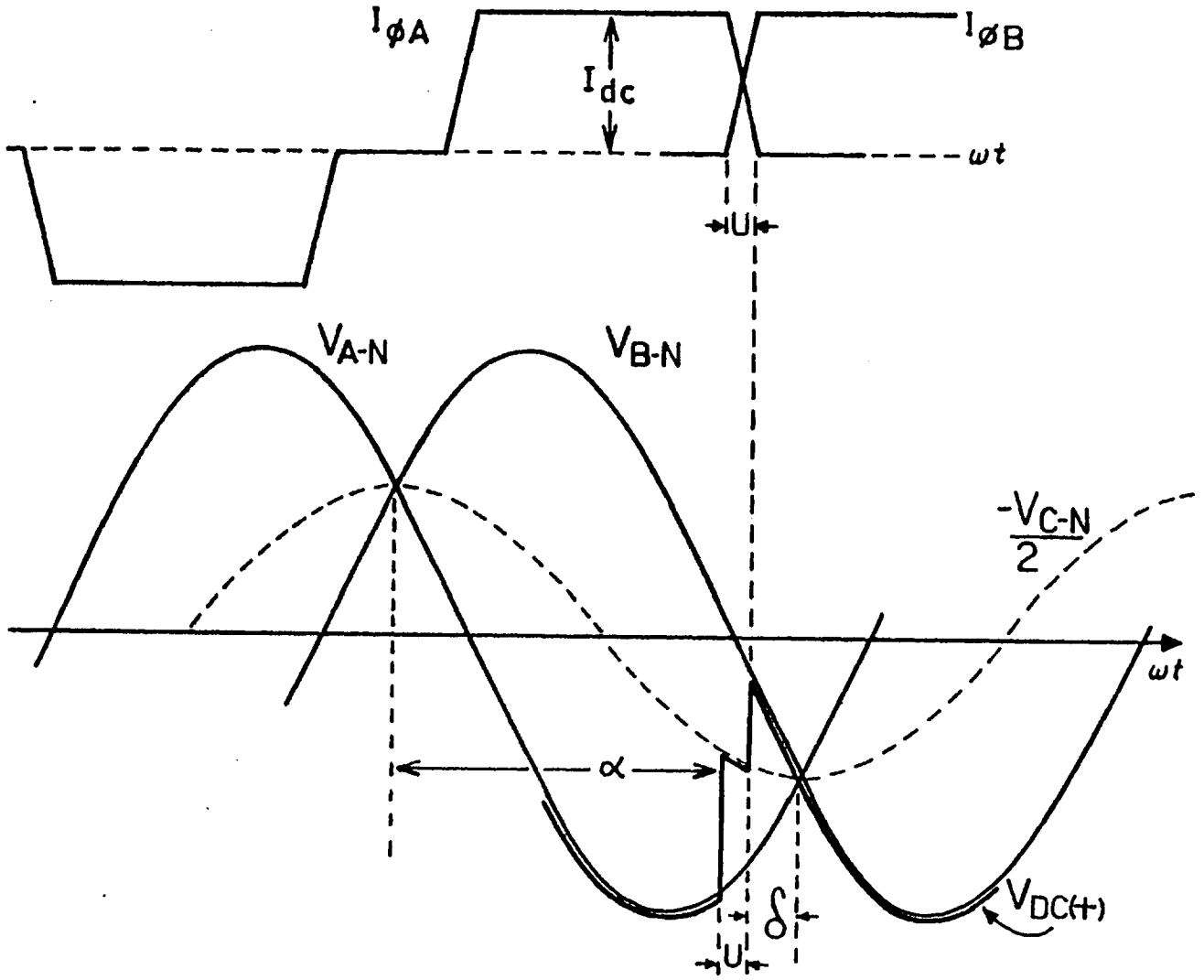

Figure 6.9 Definition of thyristor-commutating terms, DC link current and machine voltages.

To express the commutating margin in terms of the equivalent circuit parameters of the asynchronous condenser, the three path (I_2, I_3, I_m) network of Figure 6.5 can be rearranged into a single Thevenin reactance, X" in front of a single Thevenin source E_q".

$$E_q'' = E_q\left[\frac{R_1 + cR_2 + j(X_1 + cX_2)}{R_1 + R_3 + cR_2 + j(X_1 + X_3 + cX_2)}\right] \tag{6.21}$$

$$X'' = \frac{X_3^2X_t+X_t^2X_3+R_3^2X_t+R_t^2X_3}{(R_3+R_t)^2 + (X_3+X_t)^2} \tag{6.22}$$

$$R'' = \frac{R_3^2R_t+R_t^2R_3+X_3^2R_t+X_t^2R_3}{(R_3 + R_t)^2 + (X_3 + X_t)^2} \tag{6.23}$$

where $$R_t = R_1 + \frac{R_2X_m^2}{R_2^2+(X_2+X_m)^2} \tag{6.24}$$

$$X_t = X_1+ \frac{X_m(R_2^2+X_2^2+X_mX_2)}{R_2^2+(X_2+X_m)^2} \tag{6.25}$$

$$c = 1 + X_1/X_m \tag{6.26}$$

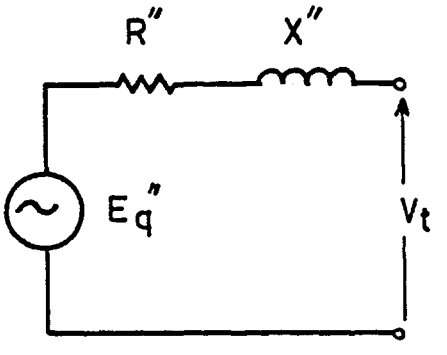

Figure 6.10 Equivalent circuit of the integral asynchronous condenser/motor for commutating calculations.

6.6 INVERTER - MACHINE INTERFACE

In the first experimental machine, the use of pole amplitude modulation windings with just the 10 pole MMF configuration was crucial in that a multi-polar design proved most successful, although the stepped-speed changing capability of the original winding was not a major concern. The creation of the proper transient conditions in the machine must occur at large slip-pole number products, $n\sigma/1-\sigma$ but obviously efficiency considerations demand that the slip be maintained as small as possible by the inverter in addition to constant volts/Hz control. The inverter interfacing has the following constraints:

a) The machine always runs at a N-pole shaft speed characteristic of a conventional cage motor although the actual number of motoring poles is less than N. To determine the exact inverter frequency for a given load, the SCIM air-gap field speed is first determined as $u_s = 2\tau_{pl} f$ and thus the shaft speed is accurately given by

$$\omega_r = \frac{120\tau_{pl}\, f\,(1-\sigma)}{\pi\, D} \qquad \text{R.P.M.} \qquad (6.27)$$

In general, the effect of having not only an unsymmetrical airgap flux distribution but odd or fractional number of motoring poles per repeatable section will not cause any severe differences between the speed calculated in (6.27) and the conventional design equation for shaft speed; i.e., the apparent field speed discrepancy

$$\xi = \omega_r - \frac{120\, f}{N} \qquad (6.28)$$

is negligible for SCIM traction motors in single axle drive systems but this implies that the effective motoring pole

pitch in (6.27) be either measured with airgap flux coils or else numerically calculated using a finite element magnetic field analysis of the airgap region. However, the quantity ξ may be an advantage for SCIM motors employed in a multiple axle drive system.

b) The real and reactive power flow between the inverter and the two stator windings of the SCIM traction motor is only optimum over a narrow range of slip. High speed is depicted in Figure 6.11 a. With the use of a constant-current DC link, obviously only real power is able to flow through the link, yet the inverter has the equivalent of a reactive requirement at the output, Q_{inv} since the current wave must be leading at this point to permit natural commutation with the non-ideal thyristor devices. The novel feature of this system is that the reactive power generated by the ASC windings allows the junction point balance

$$Q_{asc} = Q_{motor} + Q_{inv}$$

in the case of a leading power factor motor. The real power supplied to the ASC is used exclusively for the additional stator I^2-R loss, while P_{motor} accounts for all of the major stator copper loss, all of the rotor copper loss and the mechanical power. However, the designer has a choice over the direction of P_{asc} for this may be zero (or negative if the slip is too high) in which case both the real and reactive ASC losses are entirely rotor supplied. The directions indicated in Figure 6.11a are specific to the motoring mode immediately following the transition to natural commutation at 15 Hz.

The first column of Table 6.1 lists the component real and reactive power flow in the 150 H.P. laboratory traction system at the transition frequency of 15 Hz. In the run mode,

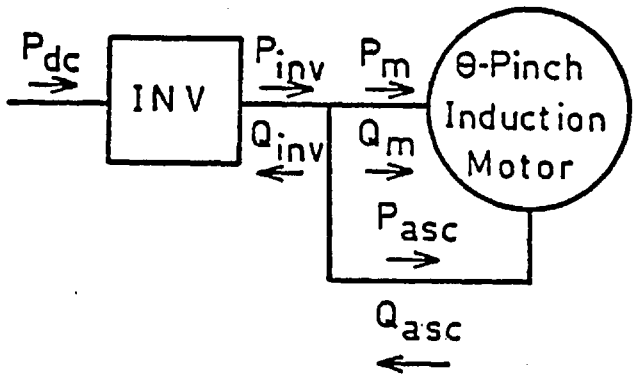

Figure 6.11a Basic power flow directions with natural commutation.

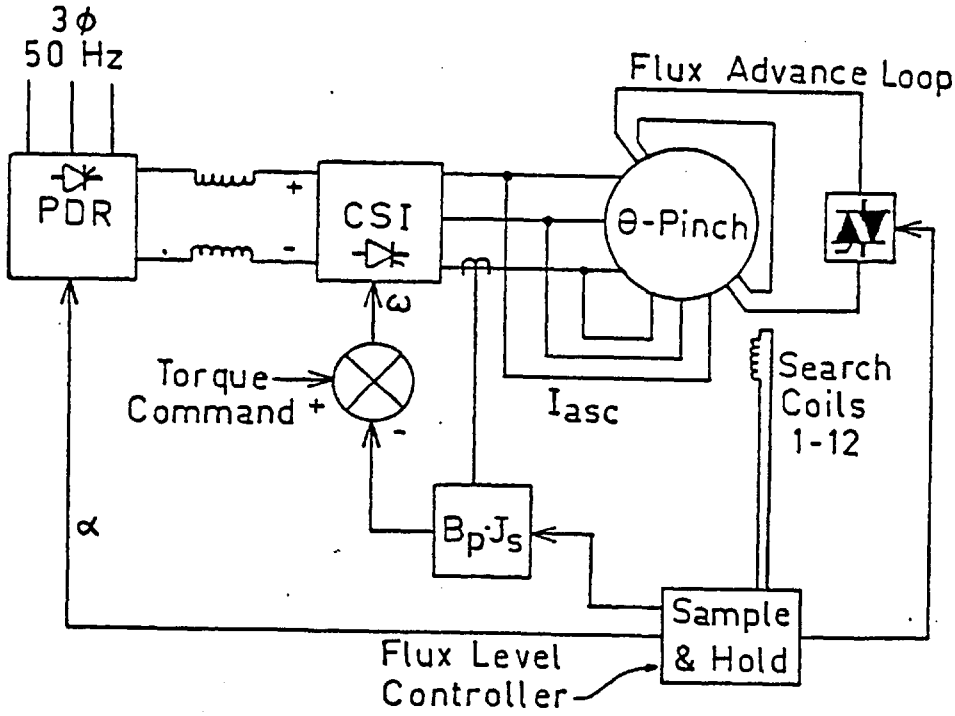

Figure 6.11b Control scheme for the variable speed, constant slip propulsion system with frequency dependent carry-over flux stator short-circuiting coils and closed control loop.

the PDR firing is delayed to an angle $\alpha=170^{\circ}$ and the ripple component of the DC link current is under 15% in the actual system hardware. Most notably, while the induction machine power factor is leading, the use of a 6-6 thyristor device input-PDR, output-CSI conversion equipment has resulted in a 0.18 per unit power factor on the 50 Hz mains due to the input phase chopping action. For comparison, the second column of Table 6.1 lists the 150 H.P. DC rotor field synchronous motor propulsion system with natural commutation to show the differences in efficiency and VAR transfer with the same input conditions and PDR firing angle delay.

Table 6.1

Comparison of Naturally Commutated Single-Machine PDR-CSI 3Ø Drive Systems at Base Frequency 50 Hz

	Asynchronous	Synchronous
Output Power (kW)	112	112
Rotor Power (kW)	2.4	4.2
Direct Axis Reactance (Ω)		3.35
Quadrature Reactance (Ω)		2.21
Subtransient Reactance (Ω)		0.55
Asynchronous Reactance (Ω)	0.025	
Shaft Speed (r/min)	735	750
Rotor Reactive Loss (kVAR)	5.24	
Airgap Magnetization (kVAR)	36.	
Exciter Weight (kg)		200
Machine Weight (kg)	1660	1800
Specific Power/Wt (kW/kg)	0.068	0.056
Inverter Overlap Angle	18°	15°
Machine Efficiency (%)	85	92

6.7 COMMUTATION LIMIT

To express the machine quantities in terms of the DC link current, I_{dc}, the normalized DC current is

$$I^* = \frac{2X'' I_{dc}}{\sqrt{6}\ E_q''} \tag{6.29}$$

From conventional phase controlled rectifier theory, the ratio of the link voltage to the r.m.s. subtransient voltage, E_q'' (line-neutral) is [11]

$$\frac{V_{dc}}{E_q''} = \frac{3\sqrt{6}}{\pi} \left[\cos(u + \delta) + 0.5I^* \right] \tag{6.30}$$

The effect of the commutating overlap u on the voltage regulation may be expressed as

$$\cos u = 1 - I^* \tag{6.31}$$

It can be assumed that the commutating margin will always be small so that the approximation $\sin \delta \approx \delta$ may be used for δ in radians as

$$\delta = \frac{-\sin(u) + \sqrt{1 + \cos(u)\ [1 - 2\pi\ V_{dc}/3\sqrt{6}\ E_q'']}}{\cos(u)} \tag{6.32}$$

Figure 6.12 is a plot of δ versus the ratio V_{dc}/E_q'' for different families of normalized DC-link current, I*. For a value I* = 0.4, it is seen that the converter: machine voltage ratio is 1.75 at a commutating margin of 50μs which corresponds to δ=0.063 radians at 200 Hz. This represents a practical commutation limit for a 150 H.P. SCIM machine with the parameter shown in Figure 6.13 which graphs (6.30).

Figure 6.11 defines the real and reactive power flow directions in the complete propulsion system with a mains feed phase delay rectifier (PDR) and a current source inverter. Until the inverter frequency reaches at least 15 Hz, the magnitude of E_q'' is insufficient to effect natural vol-

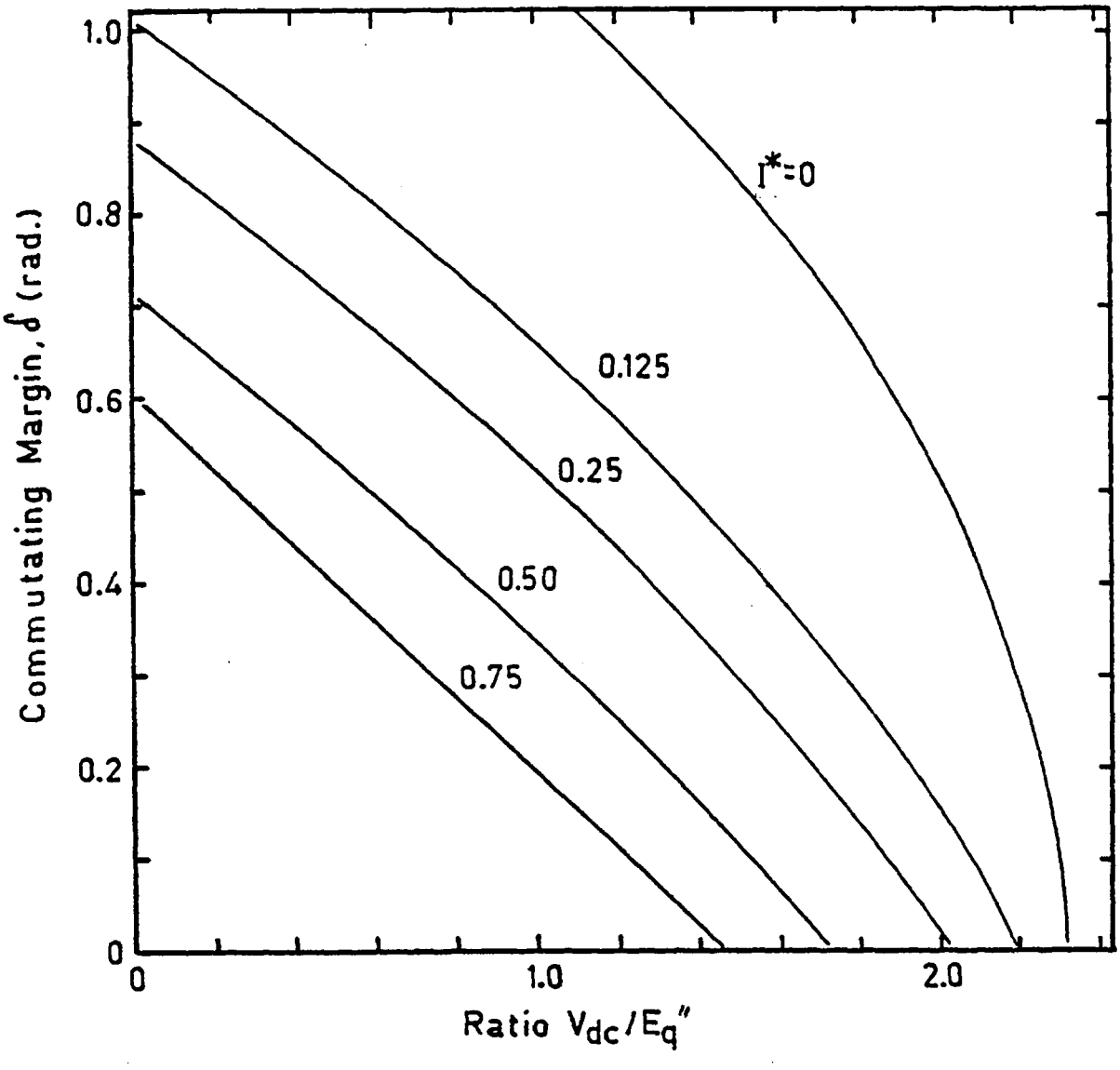

Figure 6.12 Thyristor commutating margin under natural commutation as a function of ASC winding effective counter-emf for different families of normalized DC link current, I^*.

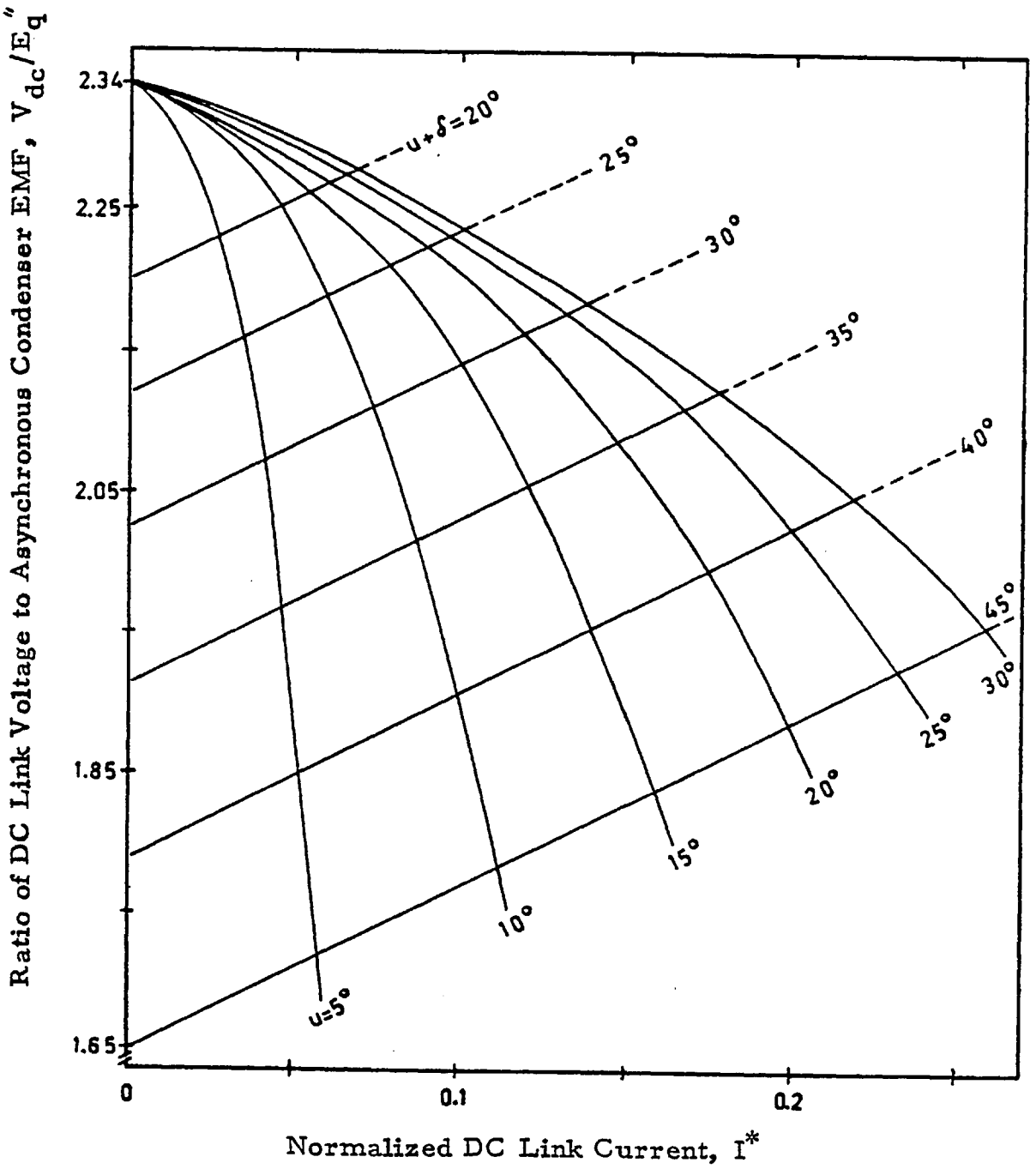

Figure 6.13 Inverter counter-emf requirement as a function of load for different values of overlap and commutating margin.

tage-commutation and consequently the CSI thyristors are current commutated from the input side by allowing the PDR to blank the DC link at 60° intervals on a 6 device CSI. A typical waveform of this sequence is shown in Figure 6.14 for a 150 H.P. cage rotor induction machine in a pulsing mode at 12 Hz. In addition to the increase in E_q'' with frequency, Figures 6.15 and 6.16 depict the phase change in E_q'' as the PDR-CSI- θ -Pinch system transfers from the limit of the startup sequence to the run mode at full rated load and speed. In this latter mode, the inverter reactive requirement is 11% of the component reactive power supplied to just the motoring section of the θ-Pinch machine and this is based on device turn off times of $t_q = 30\,\mu s$.

Since the SCIM drive system prefers units with a large number of poles to satisfy the electromagnetic conditions, the system designer is ultimately concerned with the highest possible frequency that still ensures natural commutation. Obviously a restriction of the motor to say 8, 10, or 12 poles or multiples thereof does not put any specific restriction on the speed capability until the upper limit on the inverter frequency is established. In general, this frequency, f* which occurs when the machine is said to be at exactly unity power factor is not a constant, but in a limited range of traction motor sizes is approximately proportional to the ratio L_m/R_2 where L_m is the magnetizing inductance and R_2 the rotor resistance.

The exact determination of f* is heavily dependent on the stator leakage reactance and to a lesser degree the rotor leakage reactance; these have been taken into account in Figure 6.17 which plots the commutating margin for a CSI using the specific reactances of the 150 H.P. cage rotor

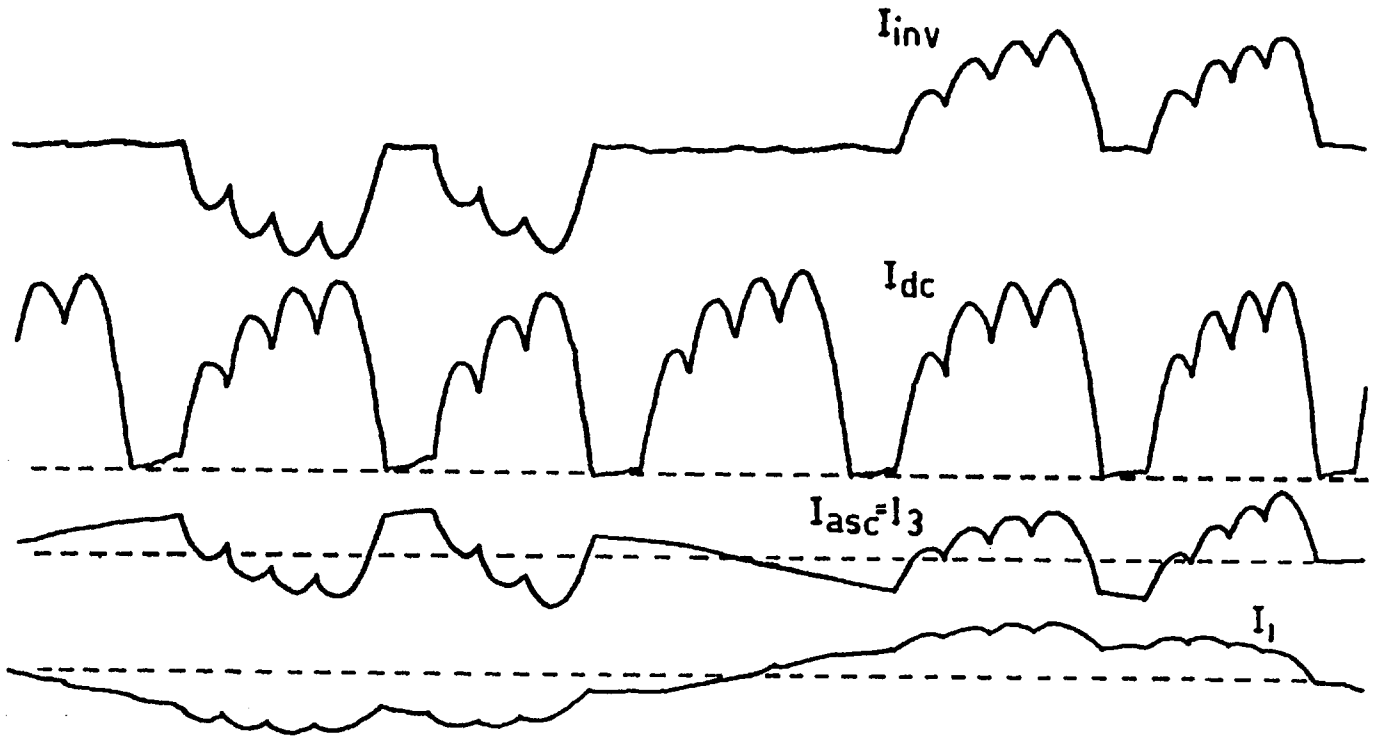

Figure 6.14 Experimentally obtained link, inverter and machine current waveforms during the start-mode current blanking thyristor commutation at 6 Hz with the SCIM-Mk. II.

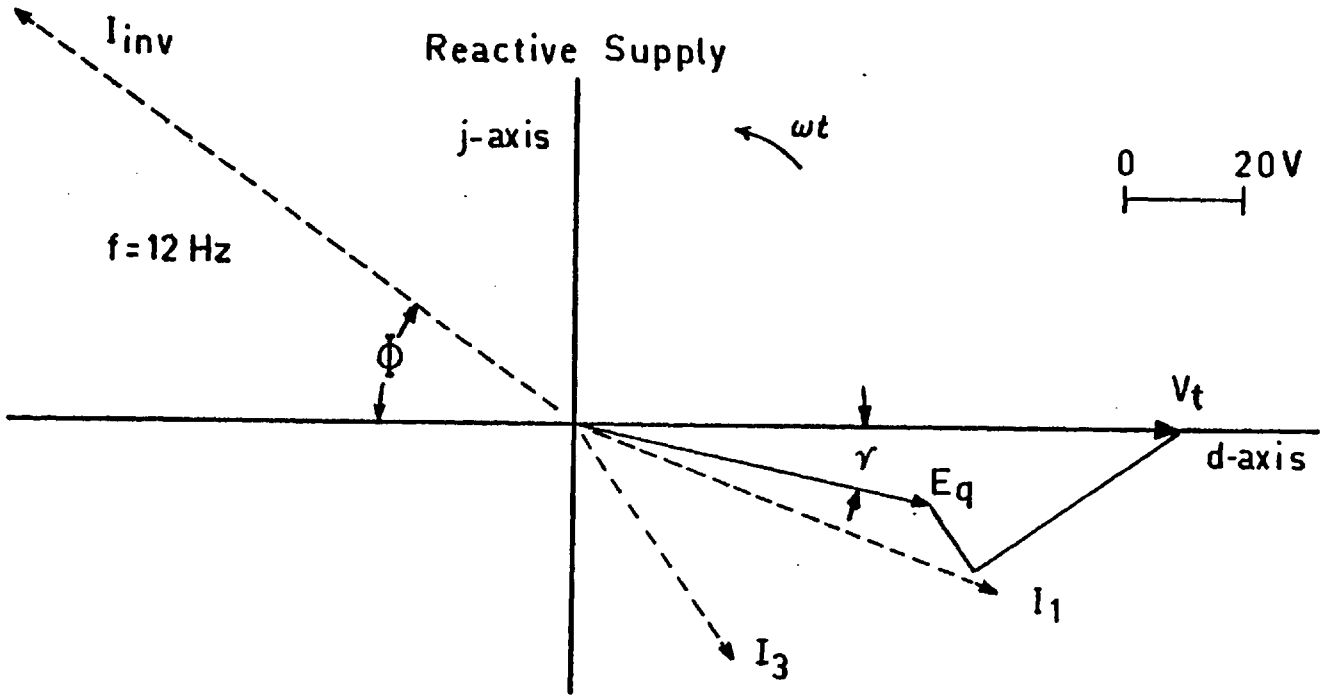

Figure 6.15 Phasor diagram of machine voltages and system currents during start-mode.

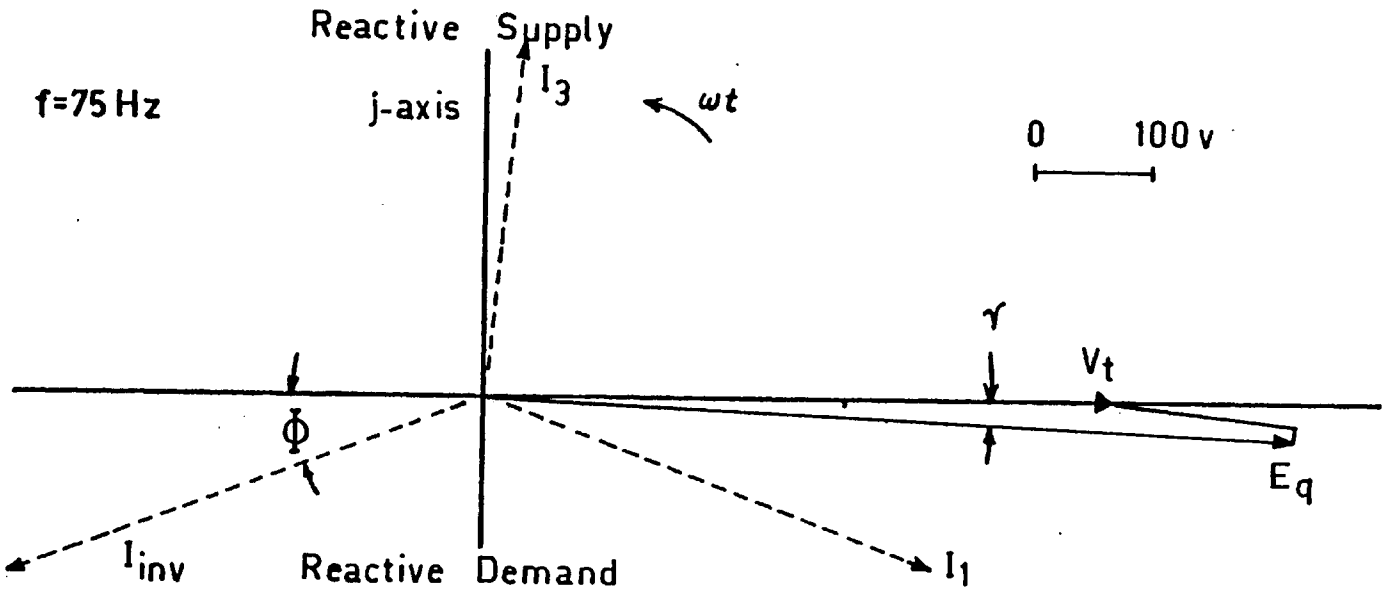

Figure 6.16 Phasor diagram of machine voltages and system currents in high-speed mode.

SCIM detailed in Chapter V. The details of this machine are included in Table 6.2. It is also important to note from Figure 6.17 that the optimum slip is a strong function of the upper inverter frequency, although from efficiency considerations alone the lowest frequency is best as the smallest slip is preferred. These curves are specific for an 8 pole traction motor consisting of about 3½ poles of motoring winding per repeatable section. If the motoring sector were to be extended in the 35 H.P. design with 10 poles, all of the curves would generally be shifted to the right assuming an equivalent G/f ratio.

Table 6.2

Parameters used in Computer Simulation of Figures 6.17 and 6.18
Natural Commutation Mode - Constant Current 8 Pole SCIM Unit.

Maximum Torque Command (N-m)	5000
Full Load Constant-Slip, σ (p.u.)	0.035
Goodness Factor (50 Hz base)	200
ASC Counter-EMF/Rotor Current Ratio, E_q/I_2(V/A)	1.80
Time Increment, Δt (ms)	0.25
Mechanical Output at 100 Hz (kW)	224
Mechanical Speed, $\dot{\theta}$ (rad/sec) at 100 Hz	151.5
Maximum Electrical Frequency, ω_e (Hz)	200
Minimum Electrical Frequency, ω_e (Hz)	25
Primary Resistance (Ω)	0.062
Secondary Resistance (Ω)	0.071
Primary + Secondary Leakage Reactance at 200 Hz (Ω)	2.42
Magnetizing Reactance at 200 Hz (Ω)	64.
Tertiary Reactance (Ω)	0.10
Tertiary Resistance (Ω)	0.015
Max. Gap Flux/Pole (Wb.)	0.026
Max. Terminal Voltage (V_{11} r.m.s.) at 200 Hz	1600
Minimum Commutating Margin, δ (deg)	3.61°
Maximum Overlap Angle, u (deg)	16.4°
Normalized DC Link Current, I*	0.056
Ratio V_{dc}/E_q''	2.265
Commutating Reactance at 200 Hz, X'' (Ω)	0.0922
Effective Commutating Resistance, R'' (Ω)	0.0139
Ratio Commutating Voltage/ASC EMF, E_q''/E_q	$0.959 < 0.22^\circ$
Ratio DC Link Voltage/ASC EMF, V_{dc}/E_q	2.172

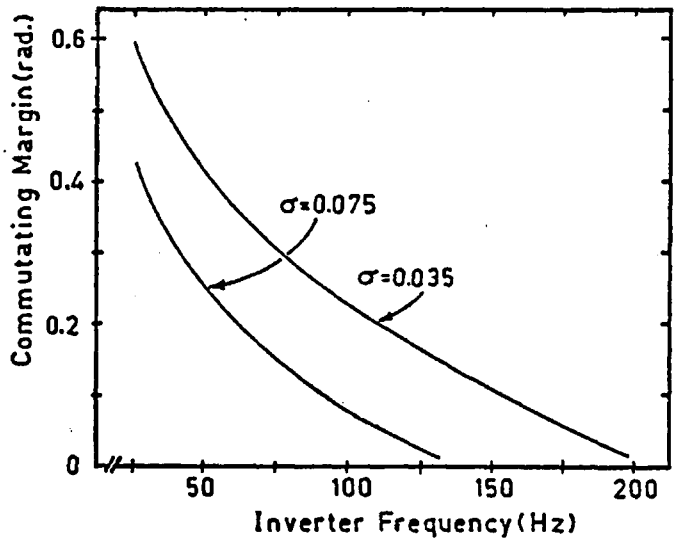

Figure 6.17 Computer simulation summary of SCIM drive system to determine frequency limit on natural commutation.

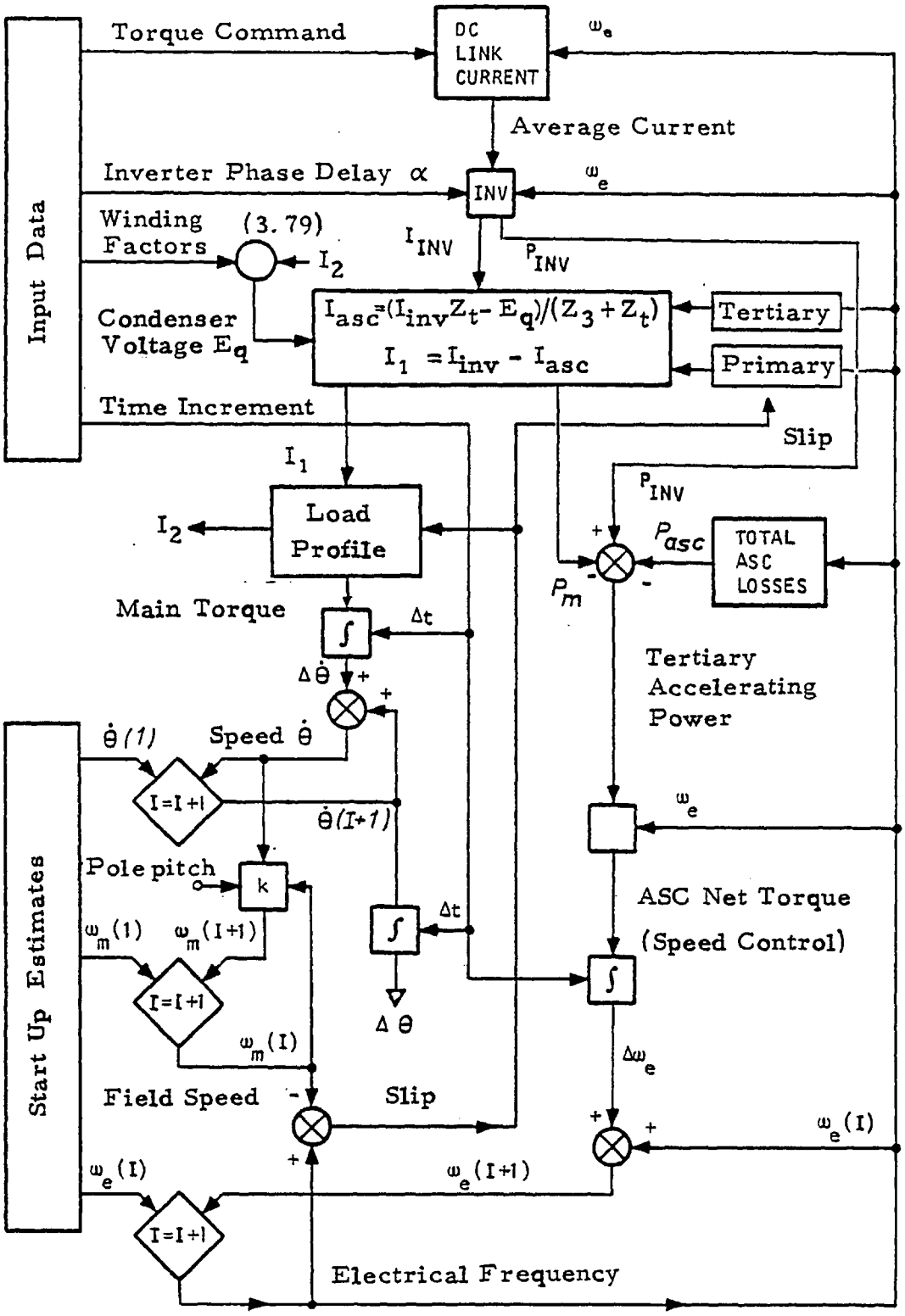

Figure 6.18 Flow Diagram of SCIM Drive System Computer Simulation

6.8 DUPLEX CURRENT SOURCE INTERACTION

Since the major impetus for advocating naturally commutated induction drives is simply based on eliminating the need for any type of electrostatic energy storage elements at very high powers, the only area of concern is the startup mode. The torque pulsations experienced in the pulsing sequence are often objectionable albeit at low speed; however this is only a consequence of controlling the link current in a "digital" fashion rather than limiting the rate of rise and decay of I_{dc} to a value less than e.g. 2 A/ms.

One novel method of entirely eliminating start-up torque pulsations is to incorporate two identical PDR-CSI systems with both the inputs and outputs in parallel. By gating the PDRs in a push-pull type fashion so that the DC-link current of PDR #1 is slowly ramped at a constant + d I_{dc}/dt and PDR #2 is similarly ramped but at - d I_{dc}/dt, the combined CSI output current waveform is nearly a perfect sinusoid at e.g. 10 Hz with the exception of the 120 Hz ripple that amounts to less than 5%. This is a practical configuration, for despite the use of a total of 24 devices, the weight and cost savings still are ahead of a similarly rated drive with static capacitor banks. A duplex CSI arrangement is shown in Figures 6.19 and 6.20 .

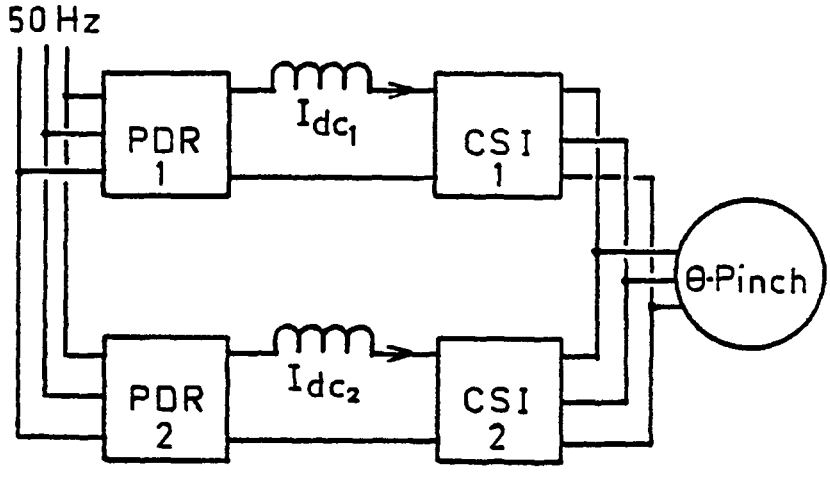

Figure 6.19 A conceptual duplex inverter system for torque smoothing.

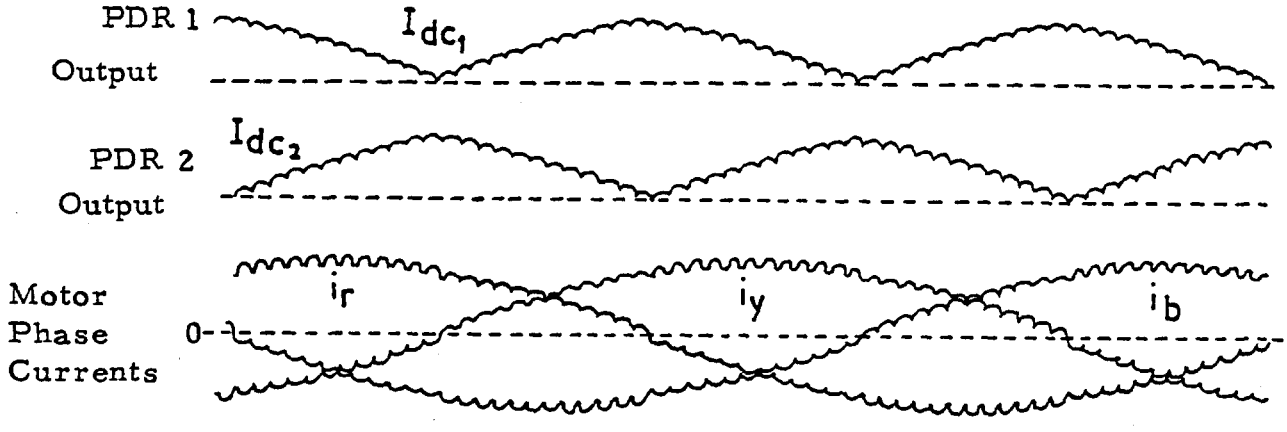

Figure 6.20 Theoretical DC-link and AC-output waveforms for duplex system in the current pulsing start mode at 2 Hz output.

6.9 THE APPLICATION OF CONDENSER WINDINGS AS A HARMONIC CURRENT FILTER

The asynchronous condenser concept may be extended to either propulsion or power generation systems to neutralize the large harmonic waveforms introduced by square wave output thyristor inverters connected to either an isolated machine or an active AC-DC grid network respectively. In the case of the former, this usually takes the form of variable-voltage, variable frequency combination phase delay rectifier-load commutated inverter. Constant volts/Hz control is adhered to but the asynchronous condenser (or separately excited synchronous condenser in conventional systems to date) must be designed for the dual purpose of rejecting fundamental currents from about 25 to 400 Hz and yet absorbing a whole spectrum of frequencies starting with the lowest frequency of 125 to a 2000 Hz fifth harmonic. At first though, this requirement appears to be difficult to implement since there is a broad overlapping of fundamental and harmonic frequencies. The purpose of this section is to give some mathematical proof behind the harmonic filter application and show, with test results, that indeed the active condenser approach (whether synchronous or asynchronous) is superior over the use of static capacitors.

The first area of concern, in reference to adjustable speed drive systems, is how does the machine (or condenser windings) know to either reject or absorb any particular frequency since there is, obviously, no direct line of communication between the control system firing the thy-

ristors (i.e. establishing the systems fundamental frequency) and the electrical machine. Typically, classical propulsion systems have to incorporate either a shaft position sensor on the rotating synchronous condenser or else a zero crossing detector to guard against high current switching, negative sequence operation, etc. Yet this is phase control and not frequency control. The basic concept is that the back e.m.f. of the condenser winding is always a nearly perfect sinusoid (certainly in comparison with the inverter output) and this is what the electrical machine as a whole understands as the system fundamental frequency, whereby it now has a reference by which to reject higher frequencies. This is nothing new to the machines world, but the point to emphasize is that in having the shaft speed of the machine establish the fundamental frequency for filtering purposes, the filtering capacity of the machine is a direct function of the stored rotor inertia, which is obviously independent of speed. Thus, to a large measure, a constant filtering characteristic is obtained, passively, over the range of variable frequency. The only complication to contend with is the effect of the stator leakage inductance which tends to counteract the equivalent capacitance as offered by the emf of the condenser windings, but fortunately, as machines get larger, the ratio of leakage reactance to rotor inertia decreases as the inverse of the fourth power of the rotor diameter. In the example to follow the mathematical analysis, which uses data specific to a 26 KW machine, the filtering effect afforded by the rotor inertia significantly outweighs the VARs consumed by the condenser winding leakage flux.

The initial mathematical treatment of the principle underlying an active harmonic current filter is based on the simplification that the rotary machine may be regarded as a "linear" system, by which the equations of motion are:

$$J \overset{oo}{\theta} + F_r \overset{o}{\theta} = B_p A I \tag{6.33}$$

$$L_1 \overset{oo}{I} + R_1 I + B_q A \overset{o}{\theta} = V_t \tag{6.34}$$

where J = moment of inertia

θ = rotor angular displacement

F_r = friction (speed damping) coefficient

B_p = in-phase airgap flux density

B_q = quadrature flux density

A = coil axial length/turn x winding factors x 2

V_t = harmonic terminal voltage of an ASC coil

I = r.m.s. phase current x number of turns/coil

Z = ASC coil terminal, harmonic impedance

R_1 = ASC coil winding resistance

L_1 = ASC coil leakage inductance

ω_n = angular frequency of natural resonance

ω = angular frequency of fundamental or harmonic voltage

The solution of equations 6.33 and 6.34 for steady state response (still permitting space transients to exist) in terms of an equivalent impedance looking into an ASC coil at the terminals yields

$$Z = \frac{V_t}{I} = R_1 + j\omega L_1 + j\omega \left[\frac{B_p B_q A^2}{j\omega F_r - \omega^2 J} \right] \qquad (6.35)$$

The last term in 6.35 is however, the form of impedance for a parallel RC circuit, i.e. the total impedance can be expressed as

$$Z = R_1 + j\omega L_1 + \frac{R_2}{1 + j\omega R_2 C} \qquad (6.36)$$

and thus the harmonic model of the condenser coil(s) as a current filter is shown in Figure 6.21.

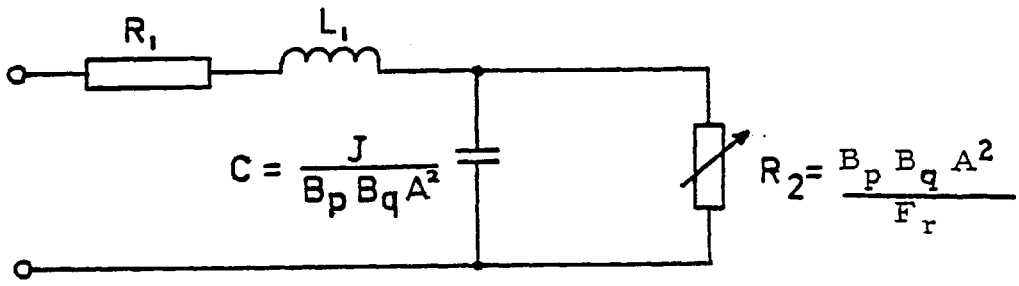

Figure 6.21. Electromechanical filter analogue for either J-Jump or θ-Pinch windings for frequencies not equal to (poles)×(r.p.m.)/120.

The main point is that the quivalent capacitance, C, offered by the windings will be constant over as wide speed range as the airgap flux density remains constant and this is consistent with all modern control schemes responsible for high power-to-weight ratings. This capacitance is

$$C = \frac{J}{B_p B_q A^2} \quad \text{Farads} \qquad (6.37)$$

Conversely, the equivalent resistance, R_2, which will vary with changes in speed due to possible load torque variation, is

$$R = \frac{B_p B_q A^2}{F_r} \quad \text{Ohms} \qquad (6.38)$$

As with any type of tuned circuit, the single most important parameter is the natural frequency, which is given by

$$\omega_n = \omega\sqrt{\frac{R_2^2 C}{L_1[1+(\omega R_2 C)^2]}}$$

$$= \omega\sqrt{\frac{B_p B_q A^2 J}{L_1[F_r^2+(\omega J)^2]}} \qquad (6.39)$$

In general, the electrical machine designer has relatively little freedom in choosing the natural frequency under the assumption, that for economic reasons, variables such as rotor intertia or friction torque should be kept to a minimum. The application of the electromechanical filter is such that it should offer maximum impedance to the fundamental frequency and its lowest impedance (occurring at ω_n) to the strongest higher harmonic, which invariably with thyristor inverters will be the harmonic with the lowest frequency. The waveform considered for example is a standard current-source 6-thyristor bridge, 3 phase square-wave output with a 120^o symmetrical conduction angle

per half cycle. This contains no even harmonics but odd harmonics, n, of order 5, 7, 11, 13, ... and of amplitude 1/n the fundamental. The optimum scheme for using the asynchronous condenser is to have the 5th harmonic coincide with the natural frequency, and the reduced filtering action of the ASC at higher frequencies is nearly perfectly compensated by the fact that the harmonic content drops off linearly with frequency rise. The one critical characteristic to be controlled is the rate of impedance decrement between the fundamental and the natural frequency, and in practice this will establish a limit on the lowest machine speed tolerable for this mode of operation. Fourier analyses of the two modes are given in Figures 6.22 & 6.23.

For harmonic frequency ω, the condenser section will appear capacitive under the criterion that the ASC winding leakage inductance be limited as a value

$$L_1 \leq \frac{B_p B_q A^2 J}{F_r^2 + (\omega J)^2} \tag{6.40}$$

Thus the absolute practical limit on the lower frequency to be filtered is given by

$$\omega_{L.L.} \geq \frac{1}{J} \left[\frac{B_p B_q A^2 J}{L_1} - F_r^2 \right]^{\frac{1}{2}} \tag{6.41}$$

For the 26 kW θ-Pinch lab motor under test, the above variables would have the values (supposing the entire

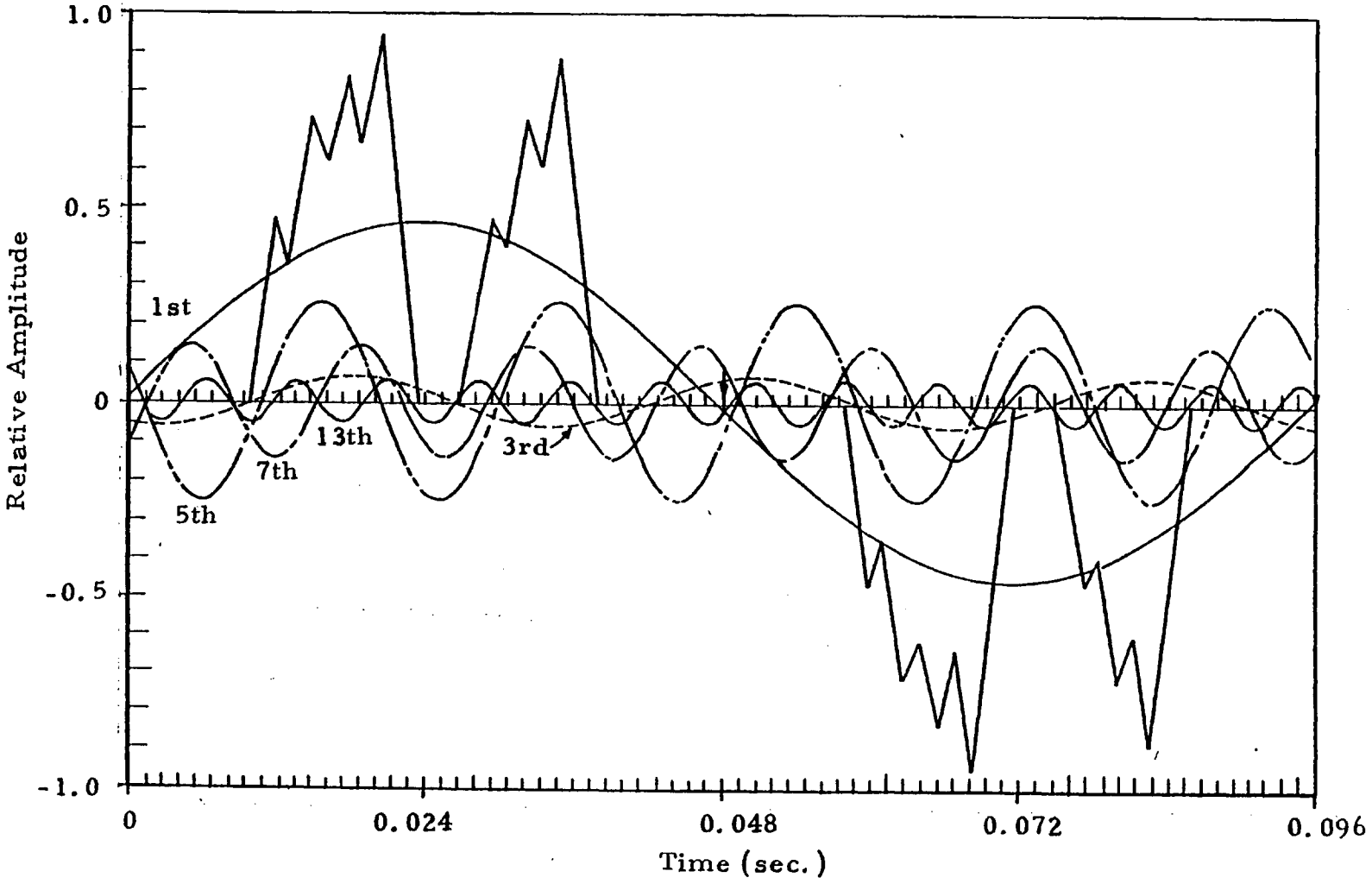

Figure 6.22 Fourier analysis of inverter output current in the low-speed pulsing mode at 10.4 Hz.

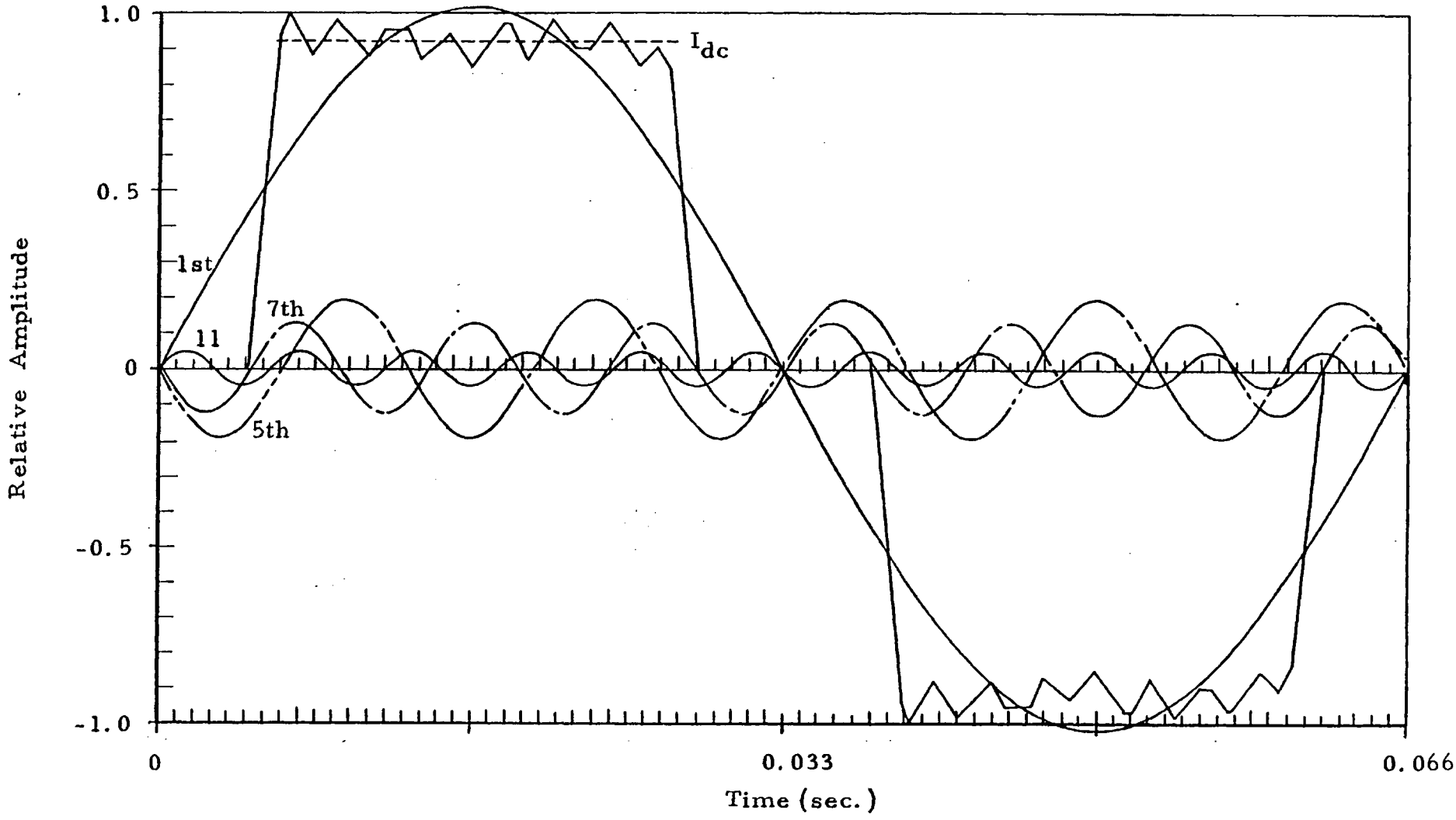

Figure 6.23 Fourier analysis of inverter output current in the high-speed run-mode at 15.0 Hz.

machine was hypothetically wound as an asynchronous condenser)

$$J = 7.98 \text{ N-m-sec}^2$$

$$B_p = 0.6 \text{ T}$$

$$B_q = 0.6 \text{ T}$$

$$A = 90 \times 0.756 \times 2 \times 0.235$$
$$= 31.9 \text{ m for 90 coils}$$

$$L_l = 90 \times 0.238 \text{ mH/coil}$$
$$= 0.0214 \text{ H}$$

The Bode plot of the input impedance versus frequency is given in Figure 6.24 for the case that the load torque damping, F_r is zero; corresponding to the assymptotically best performance attainable for the lab motor. With the above constants, the lower limit on the frequency of the fifth harmonic to be filtered as a function of load torque damping is, by evaluating (6.41),

$$\omega_{L.L.} \geq 0.1253 \sqrt{1.366 \times 10^5 - F_r^2}\Big|_{F_r=0} = 46.3 \text{ rad/sec.} \qquad (6.42)$$

It should be emphasized that the lower limit frequency of 46.3 rad/sec (or 7.38 Hz) for absorbing harmonic currents, is by no means definite because, for example, the values of B_p and B_q were rather arbitrarily chosen. For an actual CSI-rotating machine application, $\omega_{L.L.}$ would have to be larger than 125 Hz for say, operation of a 4 pole propulsion motor to commence at 75 r.p.m. and increase in speed. The

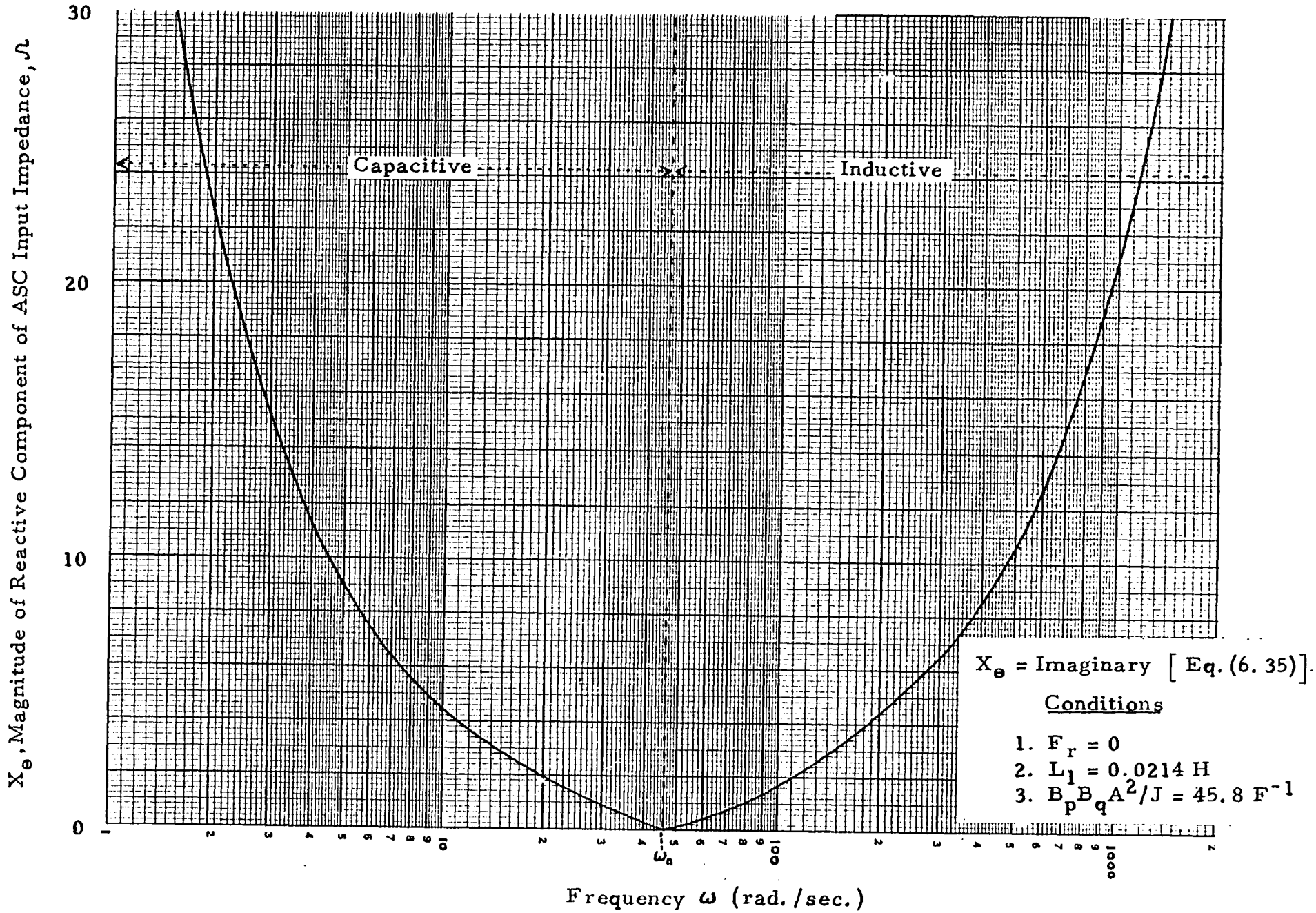

Figure 6.24 Equivalent reactance of asynchronous condenser windings for limiting condition of zero damping.

point is that, at this time the harmonic current filtering principle appears feasible for medium size machines such as 35 H.P. with enough design margin to allow an integral motor and asynchronous condenser windings on one frame (without recourse to demonstrating the concept on 500 H.P. size machines).

An interesting electromechanical filter used to suppress harmonics generated in AC-DC power transmission systems and to supply the reactive demand of the converter stations has been under investigation since 1973 in the power systems lab of Imperial College, but this is a moving coil actuator rather than a rotating machine. [15]

6.10 REFERENCES

[1]A.B. Plunkett and D.L. Plette, "Inverter Induction Motor Drives for Transit Cars," IEEE Trans. Ind. Appl., Vol. IA-13, No. 1, pp. 26-37, Jan./Feb. 1977.

[2]F.J. Bourbeau, "Synchronous Motor Railcar Propulsion," IEEE Trans. Ind. Appl., Vol. IA-13, No. 1, pp. 8-17, Jan./Feb. 1977.

[3]N.V. Hurley and H.R. Bolton, "High Performance Low Pass Filter Utilizing a Mechanical Energy Store," Proc. IEE, Vol. 124, No. 1, pp. 61-66, Jan. 1977.

[4]A.B. Plunkett, "Direct Flux and Torque Regulation in a PWM Inverter Induction Motor Drive," IEEE Trans. Ind. Appl., Vol. IA-13, No. 2, pp. 139-146, Mar./April 1977.

[5]K.P. Phillips, "Current Source Converter for AC Motor Drives," IEEE Trans. Ind. Appl., Vol. IA-8. pp. 679-683, Nov./Dec. 1972.

[6]R. Weakley and S.B. Kuntz, "Static Testing Report - Tracked Levitated Research Vehicle Propulsion System," U.S. Dept of Transportation, NTIS Document FRA-74-10650, August 1974.

[7]T.E. Brown and R.F. Grahl, "Design, Development, Fabrication and Testing of a Synchronous Condenser for the Tracked Levitated Research Vehicle," U.S. Dept of Transportation, NTIS Document FRA-76-266, June 1976.

[8]K.M. Chirgwin, Chief Scientist, Industrial Power Systems Division, Garrett-AiResearch Corporation, Los Angles, California, private discussion, December 1977.

[9]"Development and Manufacture of a Linear Induction Motor Propulsion System for the Tracked Air Cushion Research Vehicle," U.S. Dept. of Transportation, NTIS document FRA-RT-72-35, 1971.

[10]J. Rosa, "Utilization and Rating of Machine Commutated Inverter Synchronous Motor Drives," IEEE Trans. Ind. Appl., Vol. IA-15, No. 2 March/April 1979, pp. 155-164.

[11]B.D. Bedford and R.G. Hoft, Principles of Inverter Circuits, Wiley: New York, 1964, p. 72.

[12]E.R. Laithwaite and S.B. Kuznetsov, "Development of an Induction Machine Commutated Thyristor Inverter for Traction Drives," Proc. IEEE Ind. Appl. Society Annual Meeting, September 30, 1980, pp. 580-585.

[13]E.R. Laithwaite and S.B. Kuznetsov, "Natural Commutation of Current-Source Thyristor Inverters by Cage-Rotor Induction Machines," Proc. IEEE Ind. Appl. Society Annual Meeting, October 2, 1980, pp. 897-902.

[14]G.W. McLean, G.F. Nix and S.R. Alwash, "Performance and Design of Induction Motors with Square-Wave Excitation," Proc. IEE, Vol. 116, No. 8, pp. 1405-1411, 1969.

[15]E. Saraiva and L.L. Freris, "Development of Electro-mechanical Filter and Performance Evaluation in DC Link," Proc. I.E.E., Vol. 126, No. 12, Dec. 1979, pp. 1282-1286.

VII. TRANSIENT SIMULATION

7.1 A DERIVATION FROM PARK'S SYNCHRONOUS MACHINE

Without considering saturation or hysterisis effects, suppose that both the secondary and primary machine windings have only one circuit in each axis of the two-axis system and that the per-unit total flux linkages will depend linearly on their respective currents as

$$\Psi = I_f - b \cdot i_d \qquad (7.1)$$

where i_d is the per unit instantaneous direct-axis, primary current for which the term b can be evaluated by initiating a primary terminal linkage ψ_d with zero initial current and an open-circuited secondary

$$i_d = - \frac{\psi_d}{X_d'} \qquad (7.2)$$

where the negative sign indicates an armature reaction flux and X_d' is defined to be the transient reactance. In the steady-state it is clear that b is the direct-axis synchronous reactance, under the condition that the only component of Ψ which is represented is ψ_d the primary terminal flux linkage and therefore

$$I_d = \psi_d + X_d \cdot \left[\frac{-\psi_d}{X_d'} \right] \qquad (7.3)$$

The initial conditions demand that the total flux linkage is zero but $\psi_d \neq 0$

$$\psi = 0 = \psi_d \left[\left(1 - \frac{X_d}{X_d'}\right) - b\left(\frac{-1}{X_d'}\right) \right] \qquad (7.4)$$

$$\therefore\ b = X_d - X_d' \qquad (7.5)$$

The normalized secondary EMF must be

$$E_2 = K_2 p \psi + I_2 \qquad (7.6)$$

for which K_2 may be evaluated by opening the primary circuit ($i_d = 0$) and short-circuiting the secondary

$$0 = K_2 p \psi + I_2 \qquad (7.7)$$

and by (7.1)

$$0 = K_2 p I_2 + I_2 \qquad (7.8)$$

and constant K_2, referred to in the literature as the open-circuit field time constant, T_o is with respect to the polyphase induction machine equivalent circuit

$$T_o = \frac{X_3 - X_m}{R_2 \omega} \triangleq \frac{G''}{\omega} \qquad (7.9)$$

which is henceforth referred to as the modified Goodness factor since $G'' \approx G = X_m/R_2$ in all practical applications. These concepts were well established before the advent of generalized machine theory, but in 1929 Park introduced the convenience of operational terms which greatly simplified the understanding of the synchronous machine in a two-axis representation and made the analysis applicable to asynchronous electromagnetic machinery. A basic advance of this approach was that the direct axis MMF could

be expressed in the form [1]

$$I_d = F_{(p)} E_2 + H(p) \cdot i_d \qquad (7.10)$$

where $F_{(p)}$ and H(p) are laplacian operators, for which three of the four boundary conditions at initiation (p=d/dt=∞) and steady-state (p = 0) are obvious

$$F(o) = 1$$
$$H(o) = 0$$
$$F(\infty) = 0$$
$$H(\infty) = X_d - X_d''$$

X_d'' is the subtransient reactance. For the analytic expressions, Park assumed that the primary reactance operator will always take the form of

$$H(p) = X_d - X_d(p) \qquad (7.11)$$

In the most basic case of only one d-axis secondary circuit, using (7.1), (7.5) and (7.6)

$$E_2 = T_o \cdot p \left[I_d - (X_d - X_d') \cdot i_d \right] + I_d \qquad (7.12)$$

by (7.10)

$$I_d = F_{(p)} \left[I_2 [T_o p + 1] - (X_d - X_d') T_o p \, i_d \right] + \left[X_d - X_d(p) \right] \cdot i_d \qquad (7.13)$$

To evaluate $F(p)$, $i_d = 0$ and therefore $I_d = I_2$

$$\therefore \quad F_{(p)} = \frac{1}{T_o p + 1} \tag{7.14}$$

To derive $H_{(p)}$, I_2 and I_d are set to zero leaving

$$\frac{(X_d - X_d')T_o\, p}{T_o\, p + 1} - [X_d - X_{d(p)}] = 0 \tag{7.15}$$

$$\therefore \quad H_{(p)} = X_d - X_{d(p)} = X_d - \frac{X_d'\, T_o\, p + X_d}{T_o\, p + 1} \tag{7.16}$$

Equation (7.16) is universal because it is still general enough to represent induction machines as

$$H_{(p)} = L_1 + M - \frac{L_1\, G''\, p + \omega(L_1 + M)}{G''\, p + \omega} \tag{7.17}$$

where L_1 and M are the per unit primary leakage and magnetizing reactances.

Park's original equations may be summarized as

$$\begin{aligned} e_d &= p\, \psi_d - r\, i_d - \psi_q\, p\, \theta \\ e_q &= p\, \psi_q - r\, i_q + \psi_d\, p\, \theta \\ e_o &= p\, \psi_o - r\, i_o \end{aligned} \tag{7.18}$$

$$\psi_d = G(p)\cdot E_2 - X_d(p)\cdot i_d$$

$$\psi_q = I_q - X_q\cdot i_q = - X_q(p)\cdot i_q \qquad (7.19)$$

$$\psi_o = - X_o\cdot i_o$$

where Θ is the electrical space angle in radians between the secondary direct axis and the axis of phase a of the primary. Consequently, the per unit instantaneous electrical torque is

$$T = \frac{e_d\, i_d + e_q\, i_q + e_o\, i_o + r\,[i_d^2 + i_q^2 + i_o^2]}{p\Theta} \qquad (7.20)$$

But suppose that the machine is fed at constant current for the mains two-axis currents as well as the total currents I_d and I_q. Consequently (7.20) may be reduced by assuming that the rate of change of magnetic energy in each axis is negligible or $p\cdot\psi_d$, $p\cdot\psi_q$ and $p\cdot\psi_o = o$ which allows by modification of (7.18)

$$T = i_q\cdot\psi_d - i_d\cdot\psi_q \qquad (7.21)$$

which is simply the phasor product of the flux linkages with primary MMF.

The analysis readily handles the transient starting of a cage machine from locked rotor with symmetrical three phase closing which results in the transformation

$$e_d = -V \cdot \sin(\omega t - \phi_o) \qquad t > o \qquad (7.22)$$

$$e_q = V \cdot \cos(\omega t - \phi_o) \qquad t > o$$

$$X_d(p) = X_q(p) \qquad (7.23)$$

$$p \cdot \theta = 0 \qquad (7.24)$$

where ϕ_o is the initial phase angle of switch-on and (7.22) is zero for $t \leq 0$. In addition to (7.21) the system of equations is

$$\begin{aligned} e_d &= p \cdot \psi_d - r \cdot i_d \\ e_q &= p \cdot \psi_q - r \cdot i_q \end{aligned} \qquad (7.25)$$

$$\begin{aligned} \psi_d &= -[L_1 + M]_{(p)} \cdot i_d \\ \psi_q &= -[L_1 + M]_{(p)} \cdot i_q \end{aligned} \qquad (7.26)$$

where it is assumed that $L_1 + M$ is the same in both direct and quadrature axes. The simultaneous solution of the above nine equations yields the instantaneous torque as

$$T = -\frac{\omega V^2}{[(L_1 + M)'] \cdot G''(\lambda_1^2 + 1)\cdot(\lambda_2^2 + 1)} \left\{ \left[1 + e^{-\lambda_1 t} e^{-\lambda_2 t} \right] \right.$$

$$\left. - \left[e^{-\lambda_1 t} + e^{-\lambda_2 t} \right] \cdot \cos(\omega t) - \frac{\lambda_1 \lambda_2 + 1}{\lambda_2 - \lambda_1} \left[e^{-\lambda_1 t} - e^{-\lambda_2 t} \right] \sin(\omega t) \right\}$$

where

$$\lambda_1 = \frac{1}{2(L_1 + M)(L_2 - M)} \left[(L_1 + M)r_2 + (L_2 - M)r_1 - \sqrt{\left[(L_1 + M)r_2 + (L_2 - M)r_1\right]^2 - 4(L_2 - M)(L_1 + M)r_1 r_2} \right]$$

$$\lambda_2 = \frac{1}{2(L_1 + M)(L_2 - M)} \left[(L_1 + M)r_2 + (L_2 - M)r_1 + \sqrt{\left[(L_1 + M)r_2 + (L_2 - M)r_1\right]^2 - 4(L_2 - M)(L_1 + M)r_1 r_2} \right] \qquad (7.27)$$

As can be expected from the particular set of differential equations initially chosen, the solution contains two complimentary decay rates the most prominent being the λ_2 term while the λ_1 term is only significant with low Goodness factor machines for which the term M is relatively small. In an analysis performed by Kilgore on the same subject and using the same initial conditions, only one decay rate is indicated, the λ_2. [2]

A. Induction Simulation During Start-Up Sequence

Three different types of variations have been simulated on the digital computer according to:

1. Load torque which is specifically assumed to be linearly proportional to rotor speed

   a) No-load
   b) Light-load
   c) Abnormally heavy load

2. Excitation closing sequence three-phase

   a) Synchronous closing of contactor
   b) Non-synchronous closing, two-phase at voltage zero (3Ø, 90° later).
   c) Non-synchronous closing, two-phase at voltage maximum (3Ø, 90° later).

3. A range of inertia constants from H=1 sec. to H=10 sec. are used to model different classes of induction motor design. The bulk of the programming utilizes a standard industrial design value of inertia constant equal to 2 sec.

The simulation is divided into two major sections for analysis purposes.

1. The machine matrix equations are derived in terms of the stator and rotor direct and quadrature-axis currents. It has been necessary to include the speed-torque relationship with respect to these currents to fully simulate the machine. It is essential that all machine phenomenon is linearized.

A modified unified-machine theory approach is used to linearize the SCIM unit. As shown, the output indicates cases where the machine torque at start-up will approach 5 per unit. In a real machine, such torques can be expected but in practice the inductances are a function of current, which is not accounted for in the unified theory. Physically, this one effect is best explained by the larger stator and rotor currents than predicted with constant inductances and

no saturation of stator teeth.

2. The machine equations are arranged in the form

$$x = A\,x + B\,u \tag{7.28}$$

where "x" is a column matrix of D-Q currents and rotor speed, "u" is the colum matrix describing the three different types of voltage inputs for synchronous and non-synchronous on-line connection.

The "B" matrix, a 5x2, is constant. The "A" matrix, 5x5, must be continually updated at each time step because it contains speed terms and also current terms (due to relationship between the time derivative of rotor speed and current products). Also, the frictional load torque relationship is included in "A".

A numerical solution of the "state" equation for linear systems is developed and adapted to fit the peculiar requirements of transient overspeeding phenomena.

B. A Derivation From Generalized Machine Theory

By applying the C_1 phase transformation and the C_2 commutator transformation to a symmetrical 3Ø induction motor, and the familiar impedance matrix is obtained [3].

$$Z^1 = \begin{bmatrix} R_s + L_s p & 0 & 0 & Mp \\ 0 & R_s + L_s p & Mp & 0 \\ -M\omega_r & Mp & R_r + L_r p & -L_r\omega_r \\ Mp & M\omega_r & L_r\omega_r & R_r + L_r p \end{bmatrix} \tag{7.29}$$

in the system

$$[v''] = \begin{bmatrix} v_{as} \\ v_{bs} \\ v_{qr} \\ v_{dr} \end{bmatrix} = [Z^1] \begin{bmatrix} i_{as} \\ i_{bs} \\ i_{qr} \\ i_{dr} \end{bmatrix} = [Z^1]\,[i'] \tag{7.30}$$

Specifically, $[Z^1]$ can be broken down into

$$[Z^1] = [R] + [L]p + \omega_r[G] \tag{7.31}$$

$$[R] = \begin{bmatrix} R_s & 0 & 0 & 0 \\ 0 & R_s & 0 & 0 \\ 0 & 0 & R_r & 0 \\ 0 & 0 & 0 & R_r \end{bmatrix} \tag{7.32}$$

$$[L] = \begin{bmatrix} L_s & & & M \\ & L_s & M & \\ & M & L_r & \\ M & & & L_r \end{bmatrix} \tag{7.33}$$

$$[G] = \begin{bmatrix} 0 & 0 & 0 & 0 \\ 0 & 0 & 0 & 0 \\ -M & 0 & 0 & -L_r \\ 0 & -M & L_r & 0 \end{bmatrix} \tag{7.34}$$

The inverse inductance matrix is

$$[L^{-1}] = \frac{1}{L_s L_r - M} \begin{bmatrix} L_r & & & -M \\ & L_r & -M & \\ & -M & L_s & \\ -M & & & L_s \end{bmatrix} \tag{7.35}$$

To simulate transient phenomena, it is necessary to solve the system equation:

$$\frac{d\,[i'']}{dt} = [L^{-1}][v''] - L^{-1}\left[[R] + \omega_r [G]\right][i''] \tag{7.36}$$

This may be accomplished in two-stages, the first representing the applied excitation. Since only cage rotors are considered rather than wound or commutator rotors, an important simplication is allowed even in the transient mode in that the d and q-axis voltages are short-circuited or

$$v_{qr} = 0$$

and

$$v_{dr} = 0$$

$$[L^{-1}][v''] = \begin{bmatrix} L_r \cdot Y & 0 \\ 0 & L_r\ Y \\ 0 & -M \cdot Y \\ -M \cdot Y & 0 \end{bmatrix} \begin{bmatrix} v_{as} \\ \\ v_{bs} \end{bmatrix} \qquad (7.37)$$

where $Y = \dfrac{1}{L_r L_s - M}$

The power transfer matrix may now be expressed although no special modifications for cage rotors are included

$$[L^{-1}][R+\omega_r G] = \frac{1}{L_s L_r - M} \begin{bmatrix} L_r & 0 & 0 & -M \\ 0 & L_r & -M & 0 \\ 0 & -M & L_s & 0 \\ -M & 0 & 0 & L_s \end{bmatrix} \begin{bmatrix} R_s & 0 & 0 & 0 \\ 0 & R_s & 0 & 0 \\ -\omega_r M & 0 & R_r & -\omega_r L_r \\ 0 & \omega_r M & \omega_r L_r & R_r \end{bmatrix}$$

(7.38)

$$= \frac{1}{L_s L_r - M} \begin{bmatrix} L_s R_s & -\omega_r M^2 & -\omega_r M L_r & -R_r M \\ \omega_r M^2 & L_r R_s & -M R_r & -\omega_r L_r M \\ -\omega_r L_s M & -M R_s & L_s R_r & -\omega_r L_r L_s \\ -M R_s & \omega_r M L_s & \omega_r L_r L_s & L_s R_r \end{bmatrix}$$

Before combining (7.37) and (7.38) into one state-equation, the torque formulation is now included as

Electrical Torque = Frictional-Load Torque + Accelerating Torque

$$T_{elec} = T_l + J \frac{d\omega_r}{dt} \qquad (7.39)$$

In the interests of maintaining a linear systems model, the load torque is simulated as

$$T_l = f_t \, \omega_r$$

Where f_t is a viscous friction constant in N-m-sec/rad and ranges from zero through 0.10, indicated as

Case a) No-load, $f_t = 0$

b) Light load, $f_t = 0.01$

c) Normal load, $f_t = 0.033$

d) Heavy load, $f_t = 0.10$

The moment of inertia is represented as

$$J = \frac{8 \cdot H \cdot S \cdot N_p^2}{\omega_b^2 \quad (9.807 \text{ kg-m}^2)} \qquad \text{N-m-sec}^2 \quad (7.40)$$

where S is the machine VA rating, N_p the number of pole-pairs, ω_b the base excitation frequency in radians and the standard inertia constant is for

Case a) Aircraft type, H = 1.0s

b) High-speed industrial design, H = 2.0s

c) Multipolar design (e.g. 0.02 kW/kg power-weight), H = 10.0s

Fundamentally, the electric torque is always related to the current and mutual coupling matrices as

$$\begin{aligned} T_{elec} &= [i_t''][G][i''] \\ &= [i_{as} \; i_{bs} \; i_{qr} \; i_{dr}] \begin{bmatrix} 0 & 0 & 0 & 0 \\ 0 & 0 & 0 & 0 \\ -M & 0 & 0 & -L_r \\ 0 & -M & L_r & 0 \end{bmatrix} \begin{bmatrix} i_{as} \\ i_{bs} \\ i_{qr} \\ i_{dr} \end{bmatrix} \\ &= M[i_{dr} i_{bs} - i_{qr} i_{as}] \end{aligned} \qquad (7.41)$$

Therefore, assuming a speed dependent load torque completely, we have in the form $\dot{x} = B\,u + A\,x$

$$\begin{bmatrix} \dot{i}_{as} \\ \dot{i}_{bs} \\ \dot{i}_{qr} \\ \dot{i}_{dr} \\ \dot{\omega}_r \end{bmatrix} = \begin{bmatrix} L_r Y & 0 \\ 0 & L_r Y \\ 0 & -M Y \\ -M Y & 0 \\ 0 & 0 \end{bmatrix} x \begin{bmatrix} \mathcal{V}_{as} \\ \mathcal{V}_{bs} \end{bmatrix} +$$

$$\begin{bmatrix} -L_r R_s Y & \omega_r M^2 Y & \omega_r M L_r Y & R_r M Y & 0 \\ -\omega_r M^2 Y & -L_r R_s Y & M R_r Y & -\omega_r L_r M Y & 0 \\ \omega_r L_s M Y & M R_s Y & -L_s R_r Y & \omega_r L_r L_s Y & 0 \\ M R_s Y & -\omega_r M L_s Y & -\omega_r L_s L_r Y & -L_s R_r Y & 0 \\ 0 & 0 & -M i_{as} / J & -M i_{bs} / J & -f_t/J \end{bmatrix} x \begin{bmatrix} i_{as} \\ i_{bs} \\ i_{qr} \\ i_{dr} \\ \omega_r \end{bmatrix}$$

(7.42)

The terms containing ω_r must be updated for each time step. Note that two terms in the "A" matrix contain currents. This poses no special problem for the currents from the previous time-step are used; the change in currents between successive time-steps is always small enough to allow this.

C. Solution of the State Equation

The matrix system will be converted to discrete mechanics with the input excitation represented by a linear approximation. The exact solution of

$$\dot{X} = AX + BU$$

is known to be [4]

$$X(t) = e^{At} \int_{t_o}^{t} e^{-At} BU(\tau)d\tau + e^{A(t-t_o)}X(to) \qquad (7.43)$$

where the gothic terms are matrices.

For use in the computer, a difference equation similar to the exact solution can be utilized, as it is only possible to calculate $X(t)$ for some discrete values of time.

Let k = integer, T = Δt = time interval

The equivalent difference equation is

$$X[(k+1)T] = e^{AT}(kT) + e^{A(k+1)T} \int_{kT}^{(k+1)T} e^{-A\tau} BU(\tau)d\tau \qquad (7.44)$$

The above integral can be evaluated <u>exactly</u> if the input can be exactly matched to a discrete representation. However, even if a sinusoidal input is approximated by a piecewise-linear function, the integral is still evaluated quite accurately.

The stator voltages are approximated as

$$[\upsilon''] \triangleq U(t) = U(kT) + \frac{U[(k+1)T] - U(kT)}{T}(t-kT) \qquad (7.45)$$

The piece-wise linear input difference equation solution is

$$X[(k+1)T] = F \cdot X(kT) + E \cdot U(kT) + D \cdot U(k+1)T \tag{7.46}$$

where $$F = e^{At} = \sum_{n=0}^{\infty} \frac{1}{n!} (AT)^n \tag{7.47}$$

$$E = [e^{AT}(-1+AT)+1](A^2T^2)^{-1}BT$$

$$= \sum_{n=0}^{\infty} \frac{1}{n!(n+2)} (AT)^n \, BT \tag{7.48}$$

$$D = [e^{AT}-1-AT](A^2T^2)^{-1}BT$$

$$= \sum_{n=0}^{\infty} \frac{1}{(n+2)!} (AT)^n BT \tag{7.49}$$

D. Phase Transformation

A conventional three-phase to two-phase tranformation is necessary for the preferred state-variable solution but symmetrical and two types of asymmetrical mains excitation are exactly simulated.

case i.) Symmetrical closing assumes positive sequence phasor rotation with zero voltage crossing arbitrarily established at t=o for phase number 1 represented by α=o. Since this is a balanced excitation system

$$v_{os} = 0$$

and

$$\upsilon_1 = \sqrt{2}\, V \cos(\omega t)$$
$$\upsilon_2 = \sqrt{2}\, V \cos(\omega t - 2\pi/3)$$
$$\upsilon_3 = \sqrt{2}\, V \cos(\omega t + 2\pi/3)$$

Applying the C_1 transformation

$$\upsilon_{as} = \sqrt{2/3}\left[\upsilon_1 - \frac{\upsilon_2 + \upsilon_3}{2}\right] \qquad (7.50)$$

$$= \frac{2V}{\sqrt{3}}\left[\cos(\omega t) - (\cos\omega t \cos 2\pi/3)\right]$$

$$= \sqrt{3}\_V\_\underline{\cos}(\omega\underline{t})$$

$$\upsilon_{bs} = \sqrt{2/3}\left[\frac{\sqrt{3}}{2}(\upsilon_2 - \upsilon_3)\right] \qquad (7.51)$$

$$= \sqrt{3}\, V \sin(\omega t)$$

case ii.) Asymmetrical closing represented by $\alpha=\pi/2$ and $\beta=\pi/2$.

The $\alpha=\pi/2$ implies that the phase voltages will be sinusoidal rather than co-sinusoidal as above, i.e. the mains excitation is initiated when phase number 1 is at its maximum. The $\beta=\pi/2$ condition means that only two phases are connected at t=o, but $\pi/2$ radians later, the third phase is connected.

In this condition, the three-phase currents are defined as

$$I_r = 0, \quad I_y = +I, \quad I_b=-I$$

which after applying the C_{13}, combination phase and symmetrical components, tranformation

$$I_o = 0, \quad I_+ = jI, \quad I_- = -jI$$

The sequence voltages are

$$V_o = 0, \quad V_+ = jZ_+ I, \quad V_- = -jZ_- I$$

With application of the C_{13} matrix again, the phase voltages are

$$V_r = \frac{1}{\sqrt{3}} j(Z_+-Z_-)I \tag{7.52}$$

$$V_y = \frac{1}{\sqrt{3}} j(a^2Z_+-aZ_-)I \tag{7.53}$$

$$V_b = \frac{1}{\sqrt{3}} j(aZ_+-a^2Z_-)I \tag{7.54}$$

where $a = -\frac{1}{2} + j\frac{\sqrt{3}}{2}$ (7.55)

$a^2 = -\frac{1}{2} - j\frac{\sqrt{3}}{2}$ (7.56)

Surprisingly enough, the voltage of the unexcited phase is almost equal to that (with a phase shift) of an excited phase.

$$aV_y = \frac{1}{\sqrt{3}} j(a^3Z_+ - a^2Z_-)I$$
$$= V_r + \frac{1}{\sqrt{3}} jZ_-I - \frac{1}{\sqrt{3}} ja^2Z_-I$$
$$= V_r + \frac{1}{\sqrt{3}} jZ_-(1\tfrac{1}{2} + j\frac{\sqrt{3}}{2})I \quad (7.57)$$

However, in both symmetrical and Theta-Pinch type machines, it can be assumed that $Z_+ >> Z_-$

$$\therefore \quad |V_r| \approx |V_y|$$

Reverting to the standard C_1 transformation

$$\upsilon_{as} = \sqrt{2/3}\left[\upsilon_1 - \left(\frac{\upsilon_2+\upsilon_3}{2}\right)\right]$$

and using a standard balanced positive sequence system

$$\upsilon_1 = \sqrt{2}\,V \sin(\omega t), \quad \upsilon_2 = \sqrt{2}\,V \sin(\omega t - 2\pi/3), \quad \upsilon_3 = \sqrt{2}\,V \sin(\omega t + 2\pi/3)$$

$$\therefore \upsilon_{as} = \sqrt{3}\,V \sin(\omega t) \quad (7.58)$$

$$\upsilon_{bs} = \frac{\sqrt{2}}{2}(\upsilon_2 - \upsilon_3)$$

$$= -2\,V \sin(2\pi/3) \cos(\omega t)$$

$$\therefore \upsilon_{bs} = -V\sqrt{3} \cos(\omega t) \quad (7.59)$$

However, to consider the effect of zero stator current in one phase it is necessary to give explicit expressions for the

transformed currents, since the input voltages, υ_{as} and υ_{bs} are unchanged.

$$i_1 = \frac{\upsilon_1}{\vec{Z}}$$

$$= \frac{\sqrt{2}V}{\vec{Z}} \sin(\omega t) \qquad (7.60)$$

where

$$\vec{Z} = R_s + j\omega L_{ss}$$

and L_{ss} is a three-phase coupled inductance value.

$$i_2 = \frac{\sqrt{2}V}{\vec{Z}} \sin(\omega t - 2\pi/3)$$

$i_3 = 0$ due to the $\beta = \pi/2$ condition

$$i_{as} = \sqrt{2/3}\left[i_1 - \left(\frac{i_2+i_3}{2}\right) \right]$$

$$= \frac{2V}{\sqrt{3}|Z|}\left[1.25 \sin(\omega t - \emptyset) + \frac{\sqrt{3}}{4} \cos(\omega t - \emptyset) \right] \qquad (7.61)$$

$$\emptyset = \tan^{-1}(\omega L_{ss}/R_s)$$

$$i_{bs} = \frac{\sqrt{2}}{2}(i_2+i_3)$$

$$= \frac{V}{|Z|} \sin(\omega t - 2\pi/3 - \emptyset) \qquad (7.62)$$

The rotor currents at very low speeds (for example in the first 90^o degrees of operation) are dependent just on transformer terms rather than both transformer and speed terms, i.e.

$$i_{qr} \approx - i_{bs}/K_b \qquad (7.63)$$

$$i_{dr} \approx - i_{as}/K_a \qquad (7.64)$$

where K_a and K_b are coupling coefficients found from previous programs on synchronous closing.

where $\psi = \tan^{-1}(\frac{\sqrt{3}}{5})$.

These values are imputed to the [X] matrix to calculate $\dot{\omega}_r$ during the interval (5 ms) of two-phase excitation. For $\omega t > \pi/2$, the numerical solution of the state equation is used to simulate i_{qr} and i_{dr} independent of i_{bs} and i_{as} from the relationship shown above.

E. Machine Simulation Parameters

The 112 kW cage rotor induction machine is first used to illustrate the state variable solution of the transient rotor and stator currents during the start-up mode with a symmetrical stator winding in all 90 slots. The Theta-Pinch mechanism is not simulated directly in this example because the primary interest is in the transient DC component of conventional induction machinery which exists at switch-on, both asymmetrical and symmetrical, as well as during run-up and possible transient overspeeding above synchronous speed. The parameters used in the digital simulation are given in Table 7.1.

Table 7.1

Characteristics of the 112 kW Rotary Machine Prior to Modification

Base Quantities (Delta Connected)

Apparent Power (kVA)	134
Voltage (V r.m.s.)	420.
Current (A r.m.s.)	202.
Frequency (Hz)	50.
Time (ms)	20.
Inertia Constant with dynamometer, H (sec)	3.68
Torque (N-m)	1425.

Three-Phase Parameters (Locked Rotor)

Stator Resistance, R_s (p.u.)	0.0172
Stator Reactance, X_1 (p.u.)	0.0783
Rotor Resistance, R_2 (p.u.)	0.0383
Rotor Reactance, X_2 (p.u.)	0.0752
Magnetizing Reactance, X_m (p.u.)	3.6670
Base Impedance, Z (Ω)	3.6012

Two-Phase Parameters

Stator Resistance, R_s (p.u.)	0.0172
Positive-Sequence Stator Reactance, ωL_s (p.u.)	5.5788
Rotor Resistance, R_r (p.u.)	0.0383
Positive-Sequence Rotor Reactance, ωL_r (p.u.)	5.5757
Mutual Coupling, ωM (p.u.)	5.5005
Coupling Factor, K_c (%)	98.6

Table 7.2

Characteristics of the 26 kW Rotary Machine Prior to Modification

Base Quantities (Y-Connected)

Apparent Power (kVA)	37.76
Voltage (V_{11} r.m.s.)	400
Current (A r.m.s.)	54.5
Frequency (Hz)	50.
Time (ms)	20.
Inertia Constant with dynamometer, H (sec)	4.08
Torque (N-m)	416.

Three-Phase Parameters

Stator Resistance, R_s (p.u.)	0.0566
Stator Reactance, X_1 (p.u.)	0.2590
Rotor Resistance, R_r (p.u.)	0.0307
Rotor Reactance, X_2 (p.u.)	0.1320
Magnetizing Reactance, X_m (p.u.)	3.3960
Base Impedance Z (Ω)	4.2400

Two-Phase Parameters

Stator Resistance, R_s (p.u.)	0.0566
Positive-Sequence Stator Reactance, ωL_s (p.u.)	5.3530
Rotor Resistance, R_r (p.u.)	0.0307
Positive-Sequence Rotor Reactance, ωL_r (p.u.)	5.2260
Mutual Coupling, ωM (p.u.)	5.0940
Coupling Factor, K_c (%)	96.3

Table 7.3

Characteristics of a Commercial Cage-Rotor Induction Machine for Transient Overspeeding Simulation.

Base Quantities (Y-Connected)	
Apparent Power (kVA)	2.52
Voltage (V_{11} r.m.s.)	208
Current (A r.m.s.)	7.0
Frequency (Hz)	60
Time (ms)	16.6
Inertia Constant (sec)	2.0
Torque (N-m)	20
Three-Phase Parameters	
Stator Resistance, R_s (p.u.)	0.0642
Stator Reactance, X_1 (p.u.)	0.095
Rotor Resistance, R_r (p.u.)	0.0637
Rotor Reactance, X_2 (p.u.)	0.095
Magnetizing Reactance, X_m (p.u.)	1.65
Base Impedance Z (Ω)	17.2
Two -Phase Parameters	
Stator Resistance, R_s (p.u.)	0.0642
Pos.-Seq. Stator Reactance, ωL_s (p.u.)	2.57
Rotor Resistance, R_r (p.u.)	0.0637
Pos.-Seq. Rotor Reactance, ωL_r (p.u.)	2.57
Mutual Coupling, ωM (p.u.)	2.475
Coupling Factor, K_c (%)	96.2

F. Simulation Results

To depict the nature of torque oscullations on start-up, the parameters of the 112 kW laboratory machine have been used in Figure 7.1 without the pole-amplitude modulation feature. The purpose of this series of simulations is the evaluation of the constant components of d and q axis rotor currents rather than harmonic phenomena. As predicted by the analytic expression (7.21) or the matrix approach (7.41), the torque is seen to peak at 0.013 seconds after the initiation of the transient at a 3-phase symmetrical breaker closing at locked-rotor. The only unusual parameter is that a very low friction constant ($f_t = 0.001$) is used so that the speed increase is noticeable. The torque peaks at the same instant that the positive d-axis rotor current and negative d-axis stator current (i_a) peaks but note that this is not coincident with the zero crossing of the i_q and i_b currents for clearly then the instantaneous torque is zero. Rather, a significant phase shift less than 90^o exists between axis currents and for example, before the first cycle is complete, the q axis currents are lagging the d-axis currents by 77^o based on zero crossing measurements (or this may be calculated by the rotor phase angle $\emptyset = \tan^{-1}(0.079/0.0194) = 76.2^o$). Despite this time-varying phase shift, rotor and stator currents will always be mirror images since the manetization current is negligible in the first simulations. In Figure 7.1 the Goodness factor is 206 due to a high mutual coupling, M. The important conclusion to be drawn from this figure is that rotor leakage inductance must not be excessively large or else the q-axis phase-shift so described will approach 90^o with zero instantaneous torque. Second, the most prominent transient phenomena will always occur in the q-axis current since switching

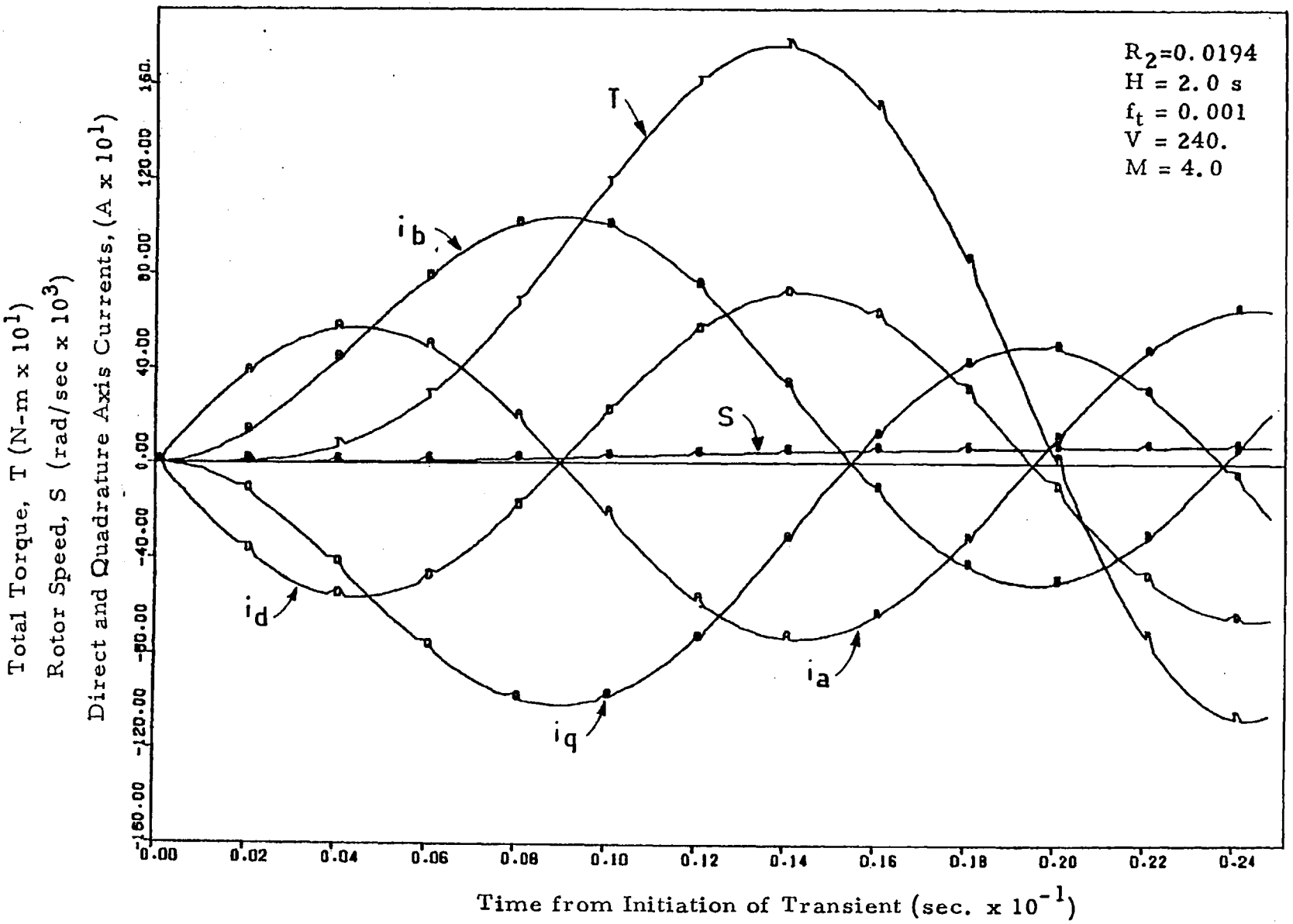

Figure 7.1 Transient performance of a 112 kW, 8-pole induction machine with symmetrical three-phase, 50 Hz excitation and breaker closing; two axis numerical simulation.

demands $i_q(t=0)=0$ whereas the d-axis transient is much less severe. In the first cycle, the i_q and i_b responses exhibit a $\pm$ 35% deviation in peak values, while the i_d and i_a types show $\pm$ 13%. This is a direct representation of the dc-component in the rotor, which decays at equal rates for both d and q axis due to the use of a cylindrical rotor model, e.g. $L_{rq} = L_{rd}$. Figure 7.2 shows a machine for similar parameters (except G = 160) as in the Figure 7.1 simulation and five complete cycles are simulated using time increments of 0.8 ms. The q-axis oscillations in magnitude have reduced to $\pm$ 17.6% after 0.10 seconds indicating an exponential decay time constant of approximately $[-Ln\ (17.6/35)]^{-1}\ (0.1s) = 0.145$ seconds. This time constant may also be calculated by the inverse of the decay rate, λ_2 given in (7.27).

In Figures 7.2 and 7.3, the friction constant has been changed to $f_t = 0.01$, the latter plot extending the simulation to ten cycles and removing the i_d and i_q traces. This clearly shows that:

(i) damping of the torque oscillations demands at least ten cycles in the 112 kW machine,

(ii) peak torques during the first or second cycle after breaker closing will exceed the steady-state torque by over 200% of the steady-state value,

(iii) the transition from an oscillation-dominated torque characteristic to a steady value is entirely explained by the decay of the dc-component in the i_q and i_b currents (and to a smaller extent the i_d and i_a dc-component decay) rather than a significant change in the phase angle of the i_q alternating component.

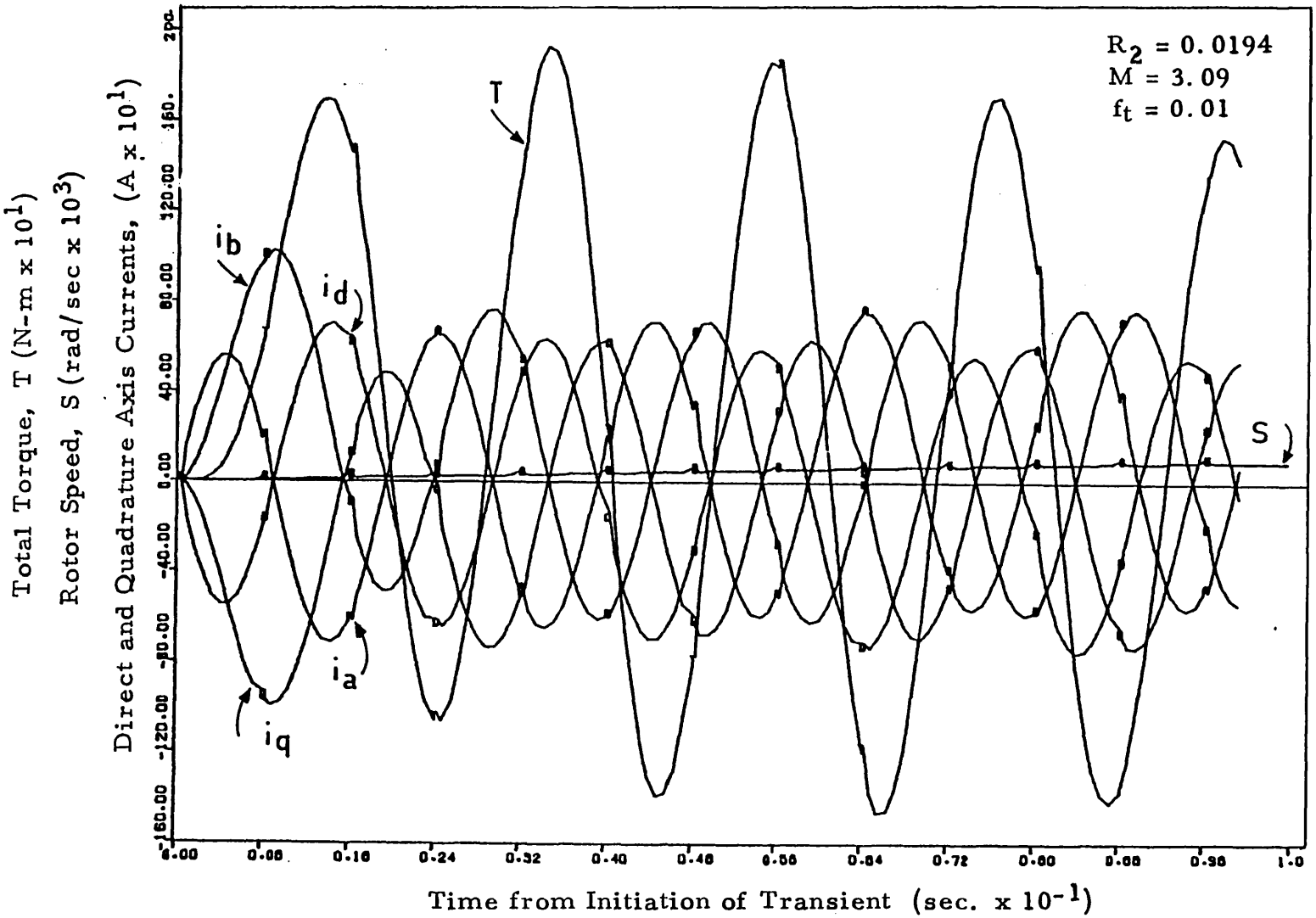

Figure 7.2 Transient performance, stator and rotor currents of an 8-pole induction machine with symmetrical three-phase 50 Hz excitation during torque oscillation region.

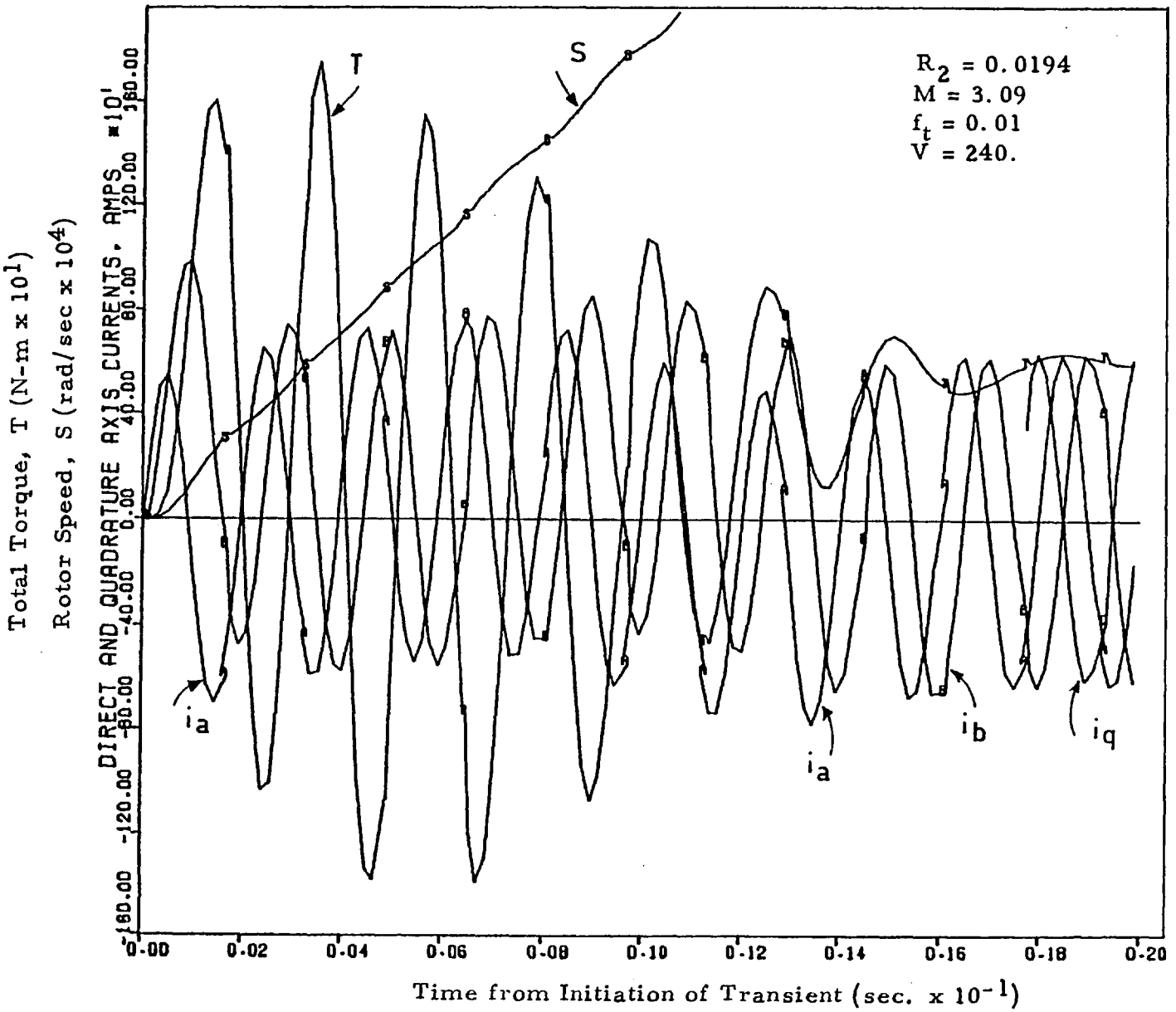

Figure 7.3 Transient performance, stator-reference two-axis currents of 8-pole machine with symmetrical excitation; same conditions as in Fig. 7.2, larger time steps.

In Figure 7.3 this transition region is from t = 0.12 to t = 0.18. The sharp peaks on the current and torques are a result of having a time increment of 0.0016 s or larger. Figure 7.4 considers the same basic 112 kW cage machine design but with twice the rotor resistance as used for the Figure 7.3 simulation. In comparison, the peak torques are higher by 49% using 174 N-m/pole as a base and retaining the X_2 = 0.0907 value.

To show the effects of magnetization, the original 112 kW parameters are used in the Figure 7.5 simulation with the exception that the mutual coupling is reduced by a factor of ten with a consequent G = 16 characteristic. The reduction in magnitude between i_d and i_a or between i_q and i_b is apparent but note that the overall effect is to reduce the variations in peak torque as well as causing the constant-component of torque to increase at a faster rate, at least during the first five cycles, This plot should be compared with Figure 7.2 as both use the same time steps and an unusually low constant f_t = 0.001s. Figure 7.6 goes one stage further by reducing the coupling to M = 0.301 Ω (or G = 1.6) and as seen, secondary currents are typically only 32.8% of the primary currents. The net result is the effective phase shift so introduced among all four currents damps the torque to the extent that four cycles after an α = 0, β = 0 mains closing, oscillations are clearly less than 50% of the steady-state value; after two cycles the instantaneous torque does not exhibit any negative excursions. It is worth noting the slight phase shift (7^{o}) present between similar-axis primary and secondary currents which was not apparent in Figures 7.1-7.5

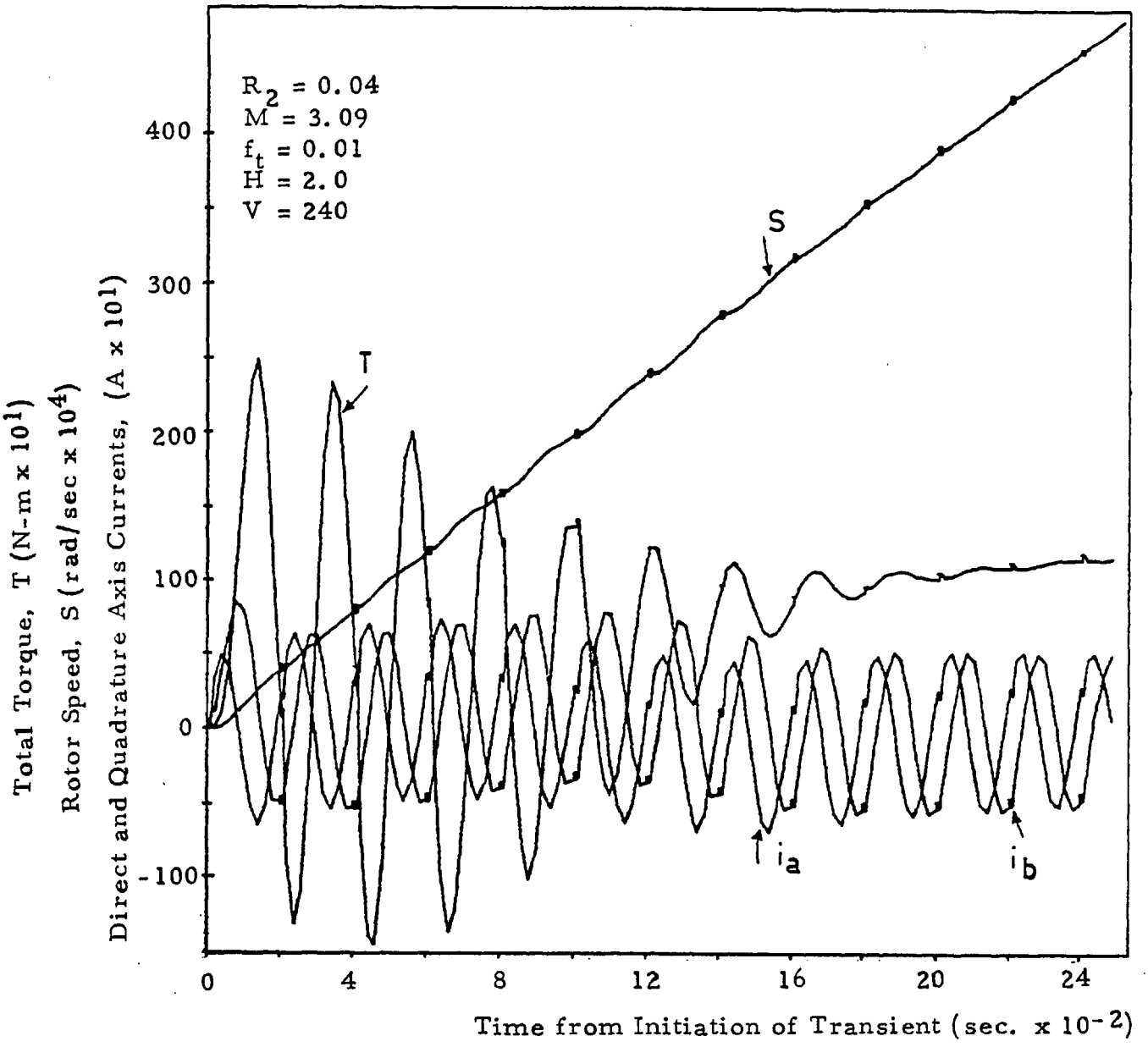

Figure 7.4 Transient characteristics of 8-pole machine with high rotor resistance, average magnetization requirement (G=77.25) and symmetrical three-phase excitation.

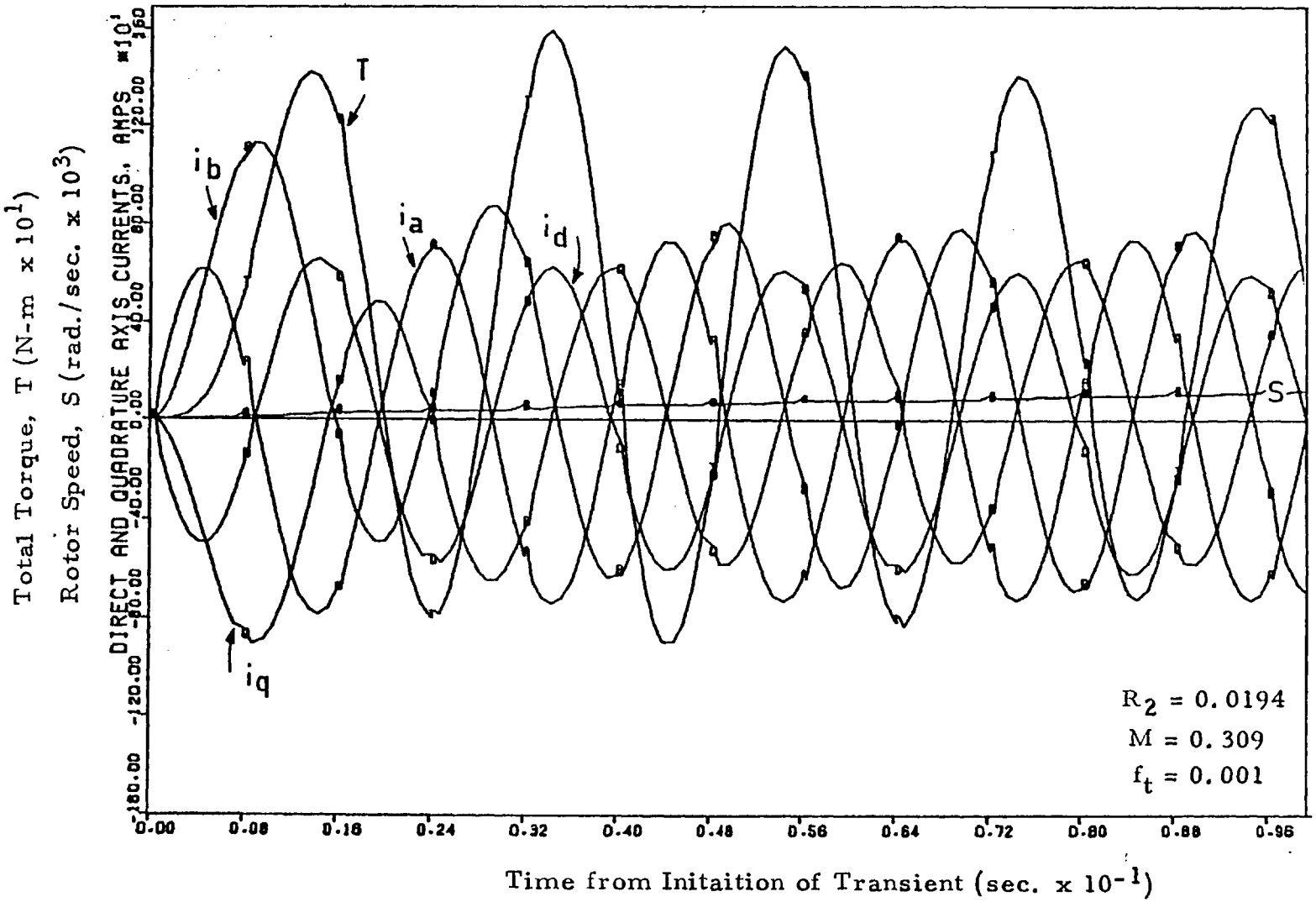

Figure 7.5 Transient characteristics of 8-pole machine with large magnetization requirement (G=16) and below average friction torque loading, symmetrical closing.

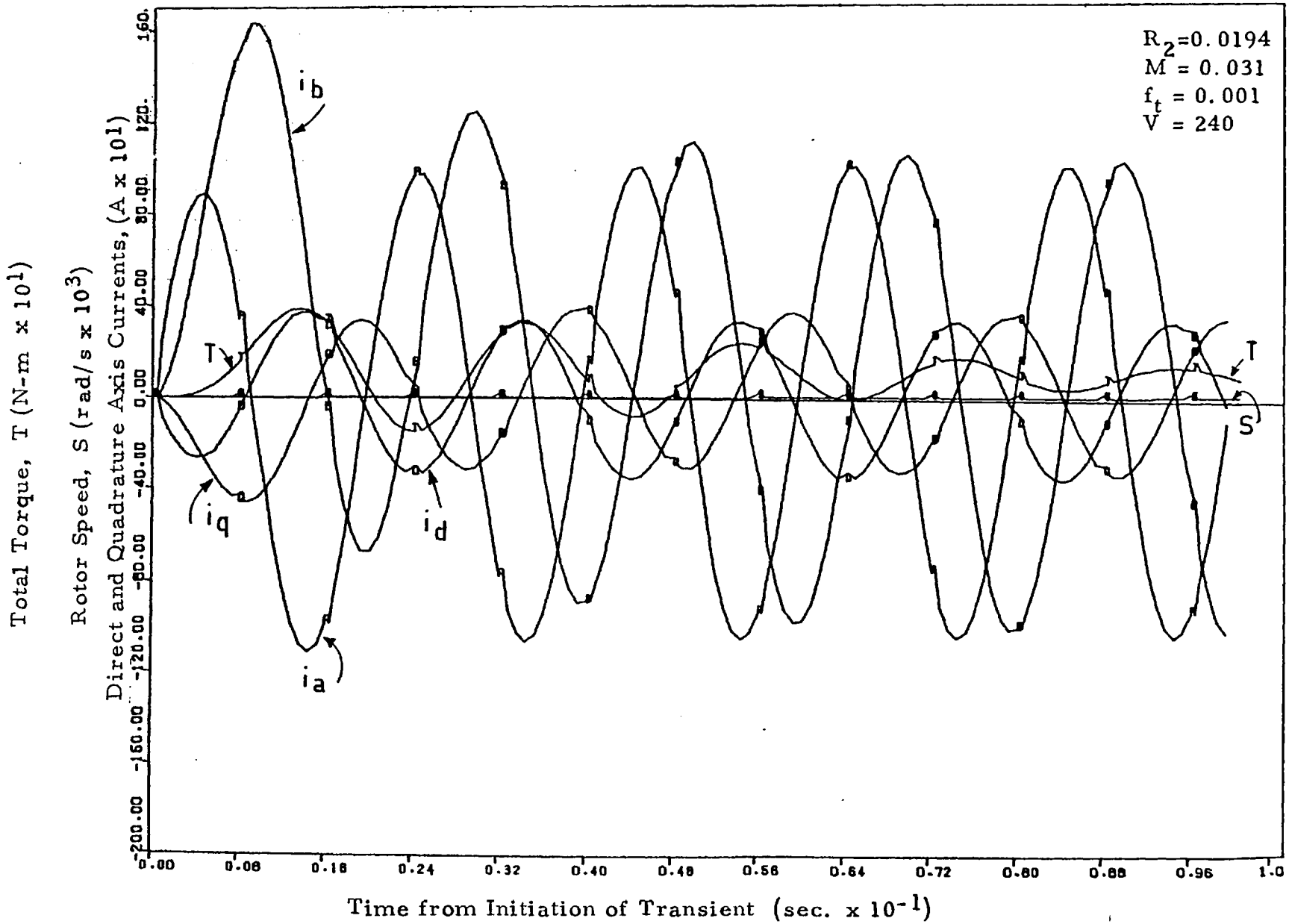

Figure 7.6 Transient characteristics of an 8-pole induction machine with excessive magnetization (G= 1.6) and below average friction torque loading with symmetrical three-phase excitation.

7.3 TRANSIENT OVERSPEEDING SIMULATION

The speed locus of lightly-loaded induction machines when subject to sudden full excitation and a low rotor inertia has been explained graphically [5] by showing that supersynchronous operation can be estimated by superimposing a series of steady-state torque-speed curves, each shifted along the speed axis by a particular speed (or time) lag. The basis of this technique is that in short it simulates some of the physical phenomena underlying transient overspeeding on fixed frequency supplies for it is clear that with considerable rotor inductance, rapid accelerations in rotor speed do not allow enough time for the transient (or dc) component of rotor current to decay and consequently the total rotor current pattern is only appropriate to that which would exist in steady-state but at a lower speed. The same phenomena persists in both the normal inductance limited and resistance-limited regions of operation; it is this latter mode which is responsible for the supersynchronous operation.

This phenomena may be explained analytically by either the adaptation of Park's equations for the generalized machine as presented in section 7.1 or by a simpler analysis by Ager [6] which was verified by some in-depth experimental work with a 4-pole, 11 kW cage motor. However, modern analysis explains transient overspeeding by a different mechanism than Ager, for in his particular experimental apparatus, there was apparently some frequency modulation of the power supply caused by the rapid variation of the power taken from the line. In summary, the machine was instrumented with a digital, stroboscopic tachometer (with 500 pulses per revolution) and the first

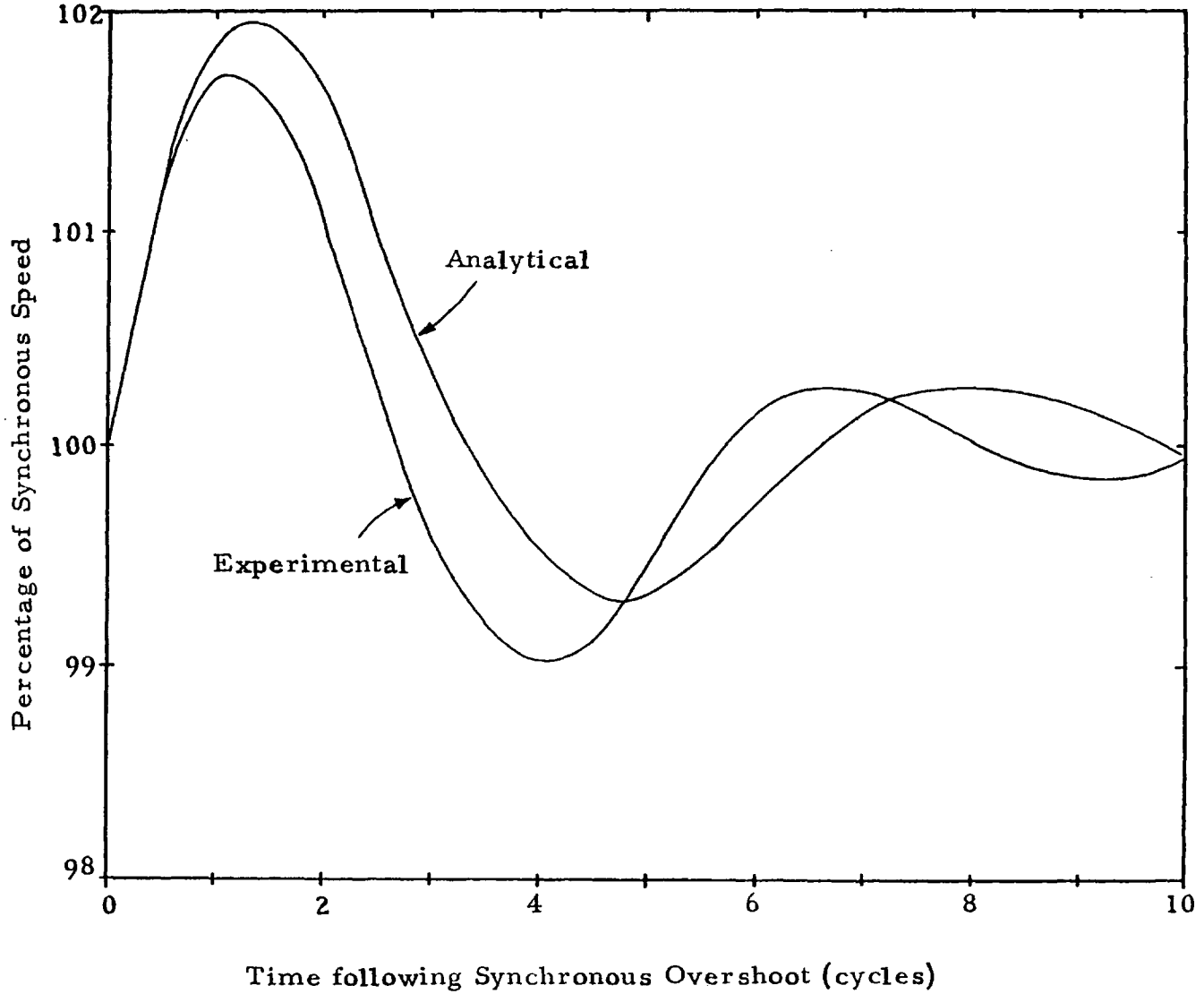

Figure 7.7 Comparison of experimentally-obtained transient overspeeding phenomena in a four-pole induction machine as originally reported by Ager and analytic solution given by equation (7.3) for the case of 60 Hz excitation and no load.

supersynchronous oscillation occurred 35.5 cycles after mains closing. This overswing rose to two per cent above synchronism followed by two more swings; the first swing developing full load torque at ω_s.

The test results are summarized in Figure 7.7 for the Ager machine as well as his analytical solution which was derived from the second-order ordinary linear differential equation in terms of the slip,

$$K_2 \frac{d^2\sigma}{dt^2} + \omega_s \frac{d\sigma}{dt} + \frac{K_1 n}{2\ WR^2}\ \sigma = 0 \qquad (7.65)$$

where $K_1 = \frac{WR^2}{\sigma}\ \dot{\omega}_r$ evaluated at full-load steady-state

$$K_2 = \alpha/\sigma$$

for WR^2 = moment of inertia

α = electrical angle between an infinite-bus voltage and the voltage across the magnetizing reactance.

n = number of poles

Unfortunately, these K_1 and K_2 constants were not derived from general principles but had to be taken from experimental evidence; the values used by Ager were $K_1 = 2{,}250$ and $K_2 = 10$. The solution of (7.65) is

$$\sigma' = -\ 0.0315\ e^{-18.8t}\ \sin\ (57.2\ t) \qquad (7.66)$$

which shows a damped oscillation of 9.1 Hz with t = o chosen at the instant the machine passes through synchronism. Figure 7.7. plots the quantity 100 $(1 - \sigma')$. In general, oscillations

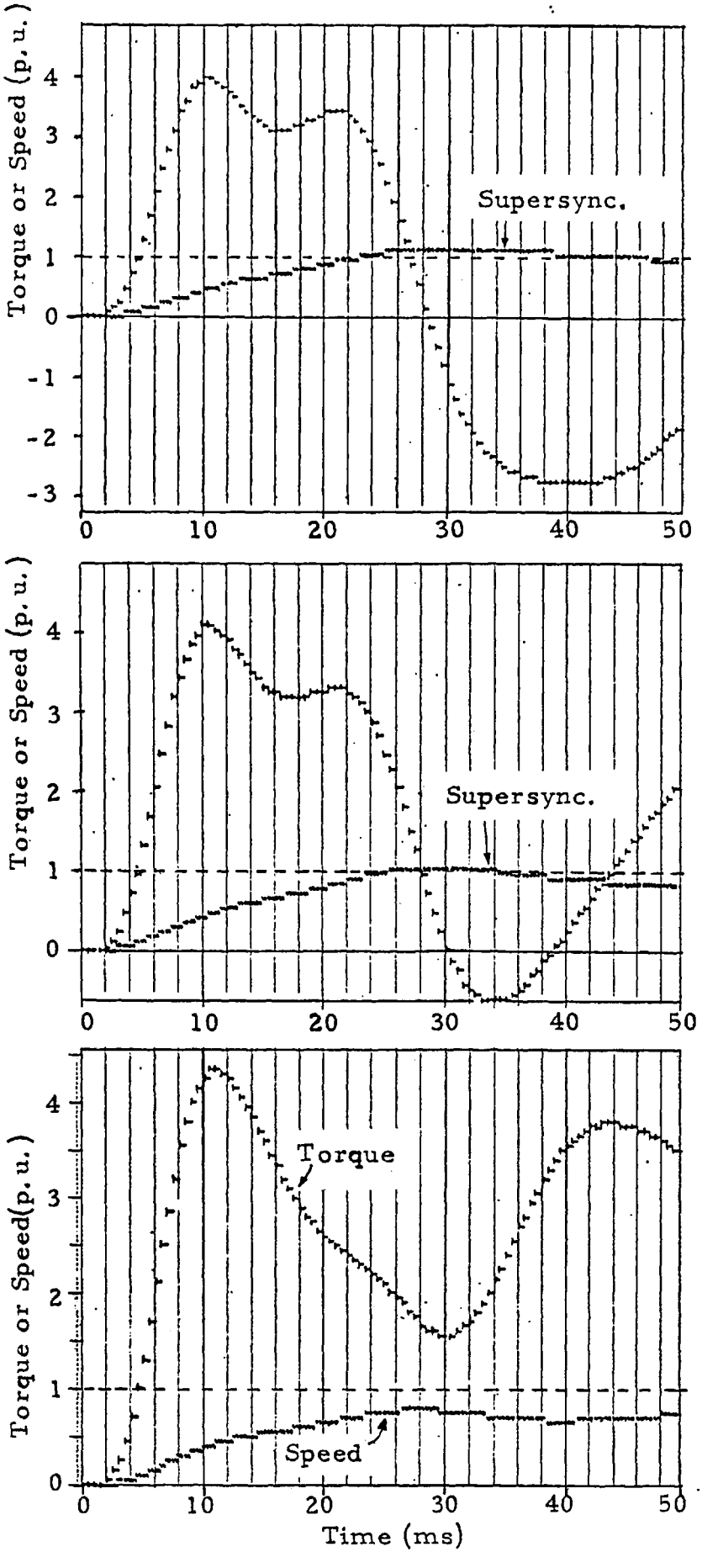

Figure 7.8 Transient performance of 6-pole induction machine with H=1.0 second, sudden synchronous breaker closing and differing values of friction torque.

will occur when

$$\frac{T_{fl}\,\alpha\, n}{WR^2\,\sigma_{fl}^2} > \frac{\omega_s^2}{2} \tag{7.67}$$

where T_{fl} and σ_{fl} are the full load torque and slip. From this one concludes that machines with small full-load slips (high Goodness) are more prone to supersynchronous operation than high-slip types.

Rather than improve upon Ager's combination analytical and experimental approach, the method undertaken in this section has been to extend the numerical state-variable solution of d- and q-axis rotor currents up to synchronous speed. It is felt that this is one area for which general closed-form analytic solutions are impractical to obtain considering that a "time-hysterisis" effect is evident. Considerable computational experience with the parameters of the 112 kW SCIM unit revealed that due to a combination of an 8 pole design and the large inertia, transient overspeeding would not occur on light-load. However, a 2 kW, 6 pole, 3-phase cage machine design was found which transiently oversped on a 60 Hz sudden excitation. The parameters of this machine are listed in Table 7.3; unlike the previous simulations, these numerical simulations will only be changing the load torque and the inertia constant rather than the magnetization requirement or R_2. Additionally, three different starting sequences (as fully described in section 7.2-D) are simulated;
(i) $\alpha=0$, $\beta=0$; (ii) $\alpha=\pi/2$, $\beta=\pi/2$; (iii) $\alpha=0$, $\beta=\pi/2$. It is seen that the differences between non-synchronous and synchronous breaker closing are noticeable even at high speed.

Figure 7.8 shows synchronous closing for values of fric-

tion load ranging from f_t=0.01 to 0.10 N-m-sec/rad., for which it is seen that f_t=0.01 and f_t=0.033 yield transient overspeeding starting around 25 ms and then reverting back to subsynchronous operation at t=47 ms and 37 ms respectively. Figure 7.9 plots torque and speed for the case of zero load torque and synchronous closing for different values of inertia constant ranging from H=1.5 through H=10 seconds. In particular, the H=1.5 case yields two overspeeds, the first up to 1260 RPM (105%) and the second to 1240 RPM (103%). Yet, even near synchronism, the torque has a negative slope and then a negative value after the first swing; a peculiarity that only exists for a f_t=0 condition. Figure 7.10 is similar to Figure 7.8 except that an H constant of 2.0 sec. is used and now it is seen that at 60 ms after a synchronous closing, a zero load-torque case causes overspeeding up to 1220 RPM to occur whereas this was not evident in the traces of Figure 7.9 up to 50 ms. Two non-synchronous closing conditions are simulated in Figure 7.11 and compared against a symmetrical excitation; all three cases utilizing the same inertia (H=2) and load torque constant (f_t = 0.033).

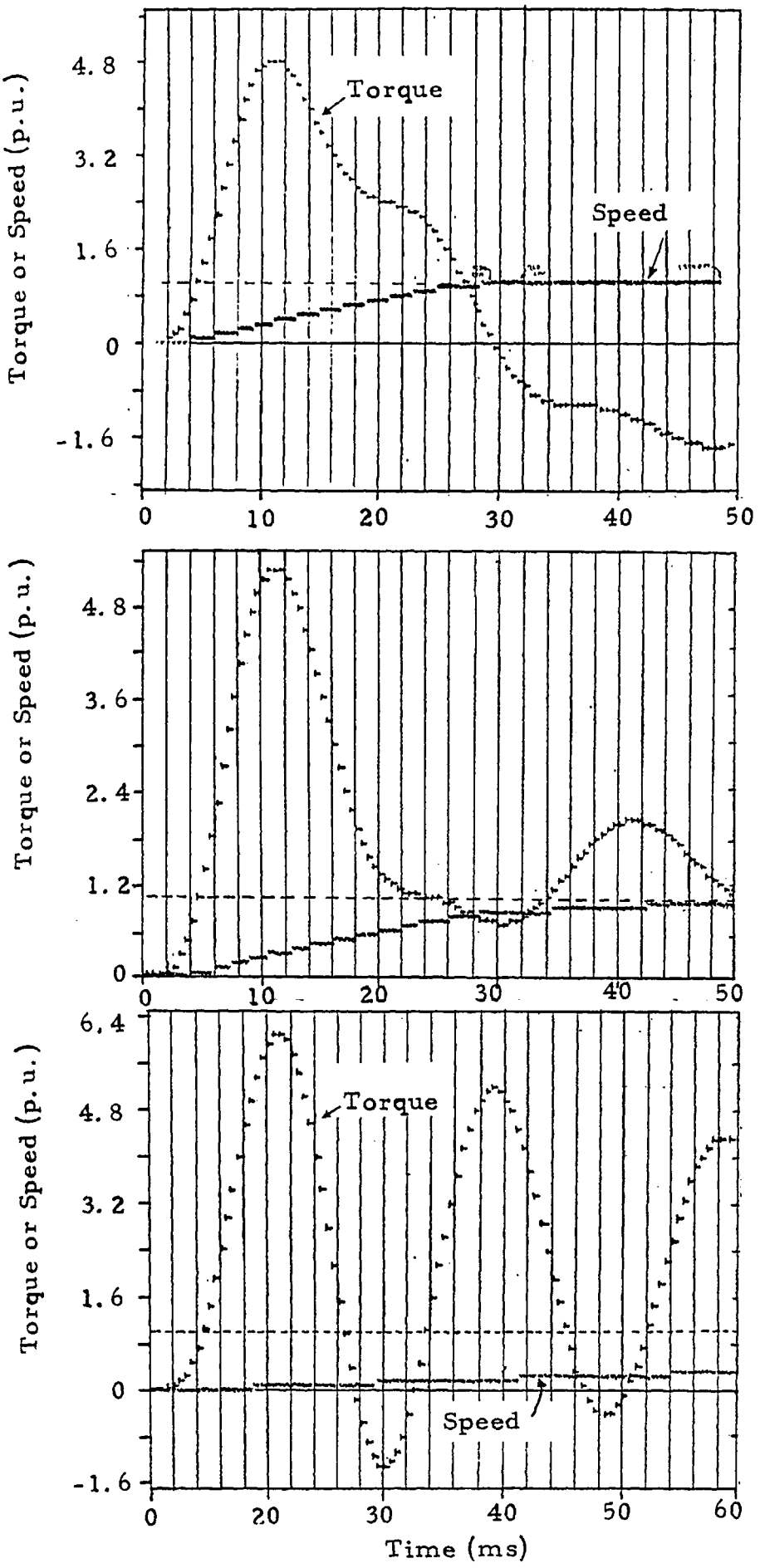

Fig. 7.9 Transient performance with symmetrical closing and zero load torque for different inertia constants, H.

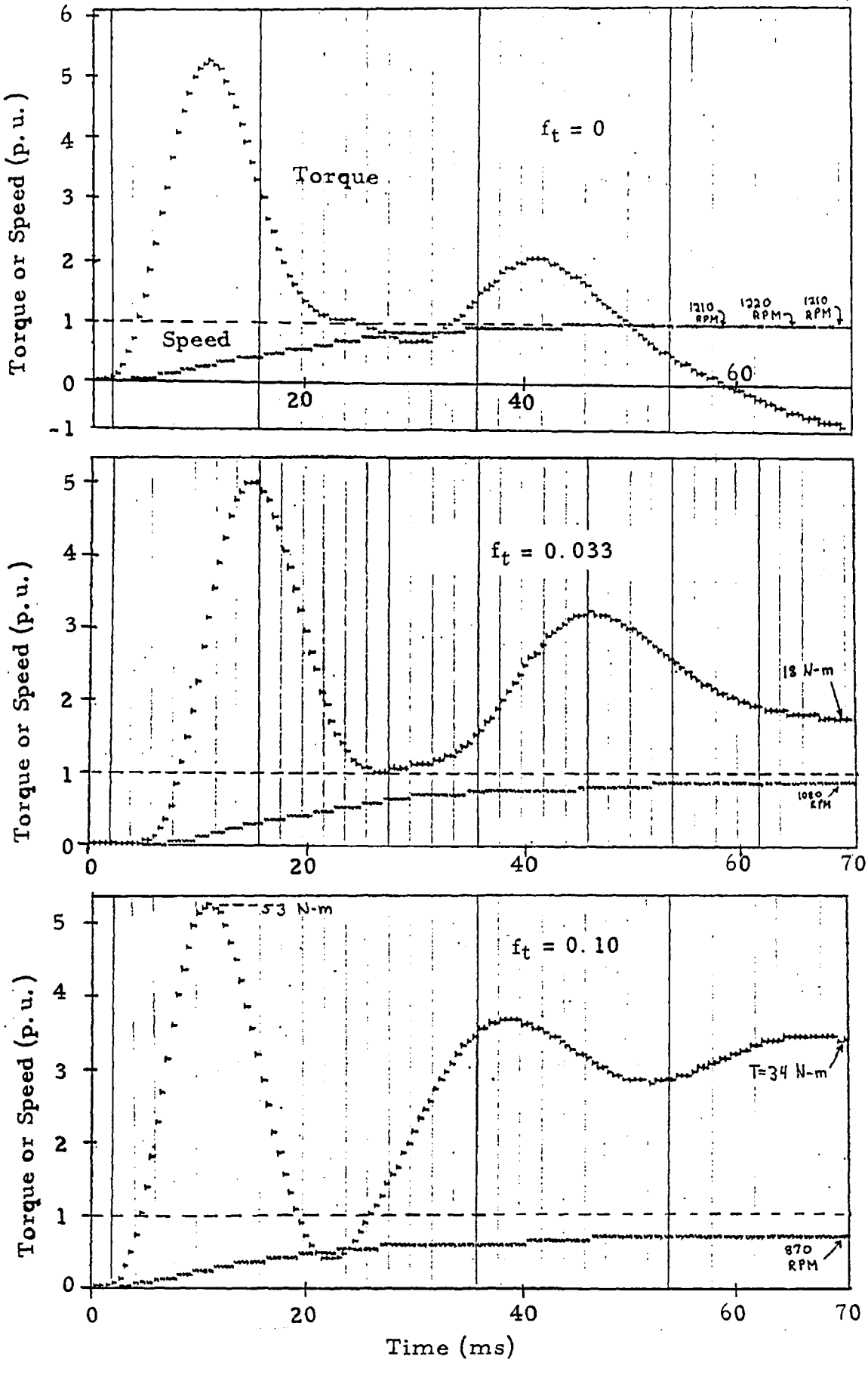

Figure 7.10 Transient performance of 6-pole machine with H=2.0 seconds inertia constant, sudden synchronous breaker closing and differing values of friction torque.

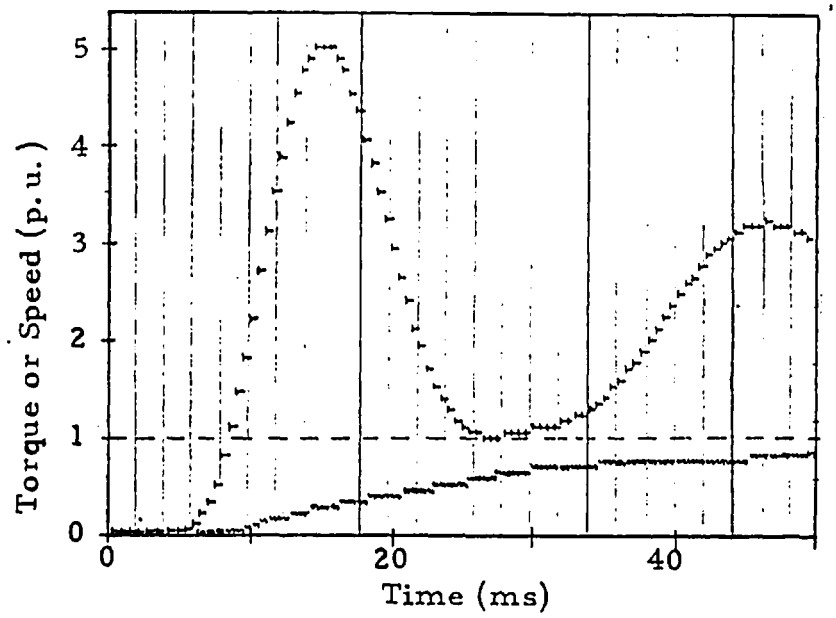

$\alpha = 0$
$\beta = 0$

a. Synchronous Closing

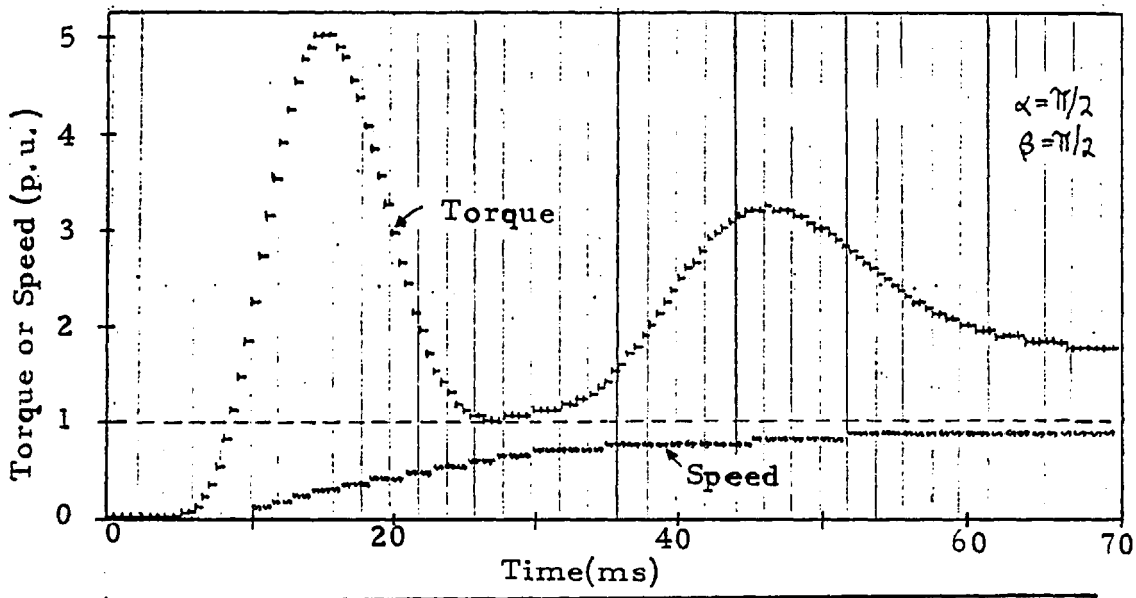

b. Asvnchro-nous Closing

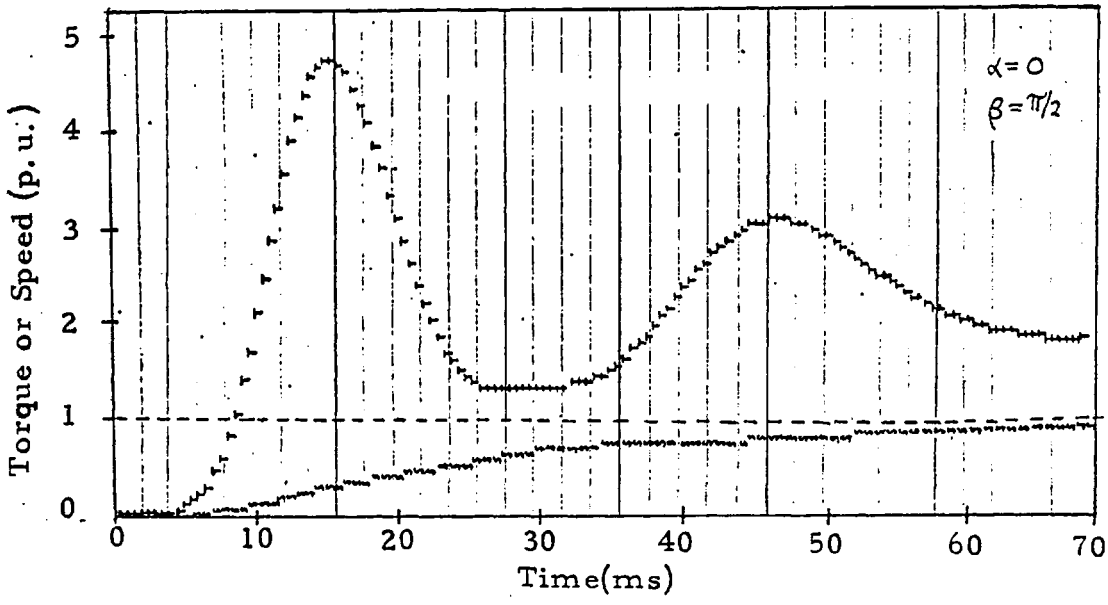

c. Asynchro-nous Closing

Figure 7.11 Instantaneous torque during synchronous and non-synchronous mains closing for f_t=0.033 friction constant and H=2.0 seconds.

7.4 REFERENCES

[1] Park, R.H., "Two-Reaction Theory of Synchronous Machines: Generalized Method of Analysis - Part I," Trans. A.I.E.E., Vol. 48, July 1929, pp. 716-730.

[2] Wahl, A.M. and Kilgore, L.A., "Transient Starting Torques in Induction Motors," Trans. AIEE, Vol. 59, November 1940, pp. 603-607.

[3] Jones, C.V., The Unified Theory of Electrical Machines, Butterworths: London, 1967, pp. 147-212.

[4] Chua, L.O., Lin, P.M., Computer Aided Analysis of Electronic Circuits: Algorithms and Computational Techniques, Prentice-Hall: New Jersey, 1975, pp. 368-372.

[5] Laithwaite, E.R. and Freris, L.L., Electric Energy: Its Generation, Transmission and Use, McGraw-Hill: England, 1980, p. 233-235.

[6] Ager, R.W., "Transient Overspeeding of Induction Motors," Trans. AIEE, Vol. 60, December 1941, pp. 1030-1032.

VIII. CONCLUSIONS

The introduction of space-transients in the primary excitation of brushless induction machines with cage or sheet secondaries has demonstrated several characteristics common to both rotary and linear types which are as follows.

1. Two general mechanisms of generating reactive VA exist.

a. The first and most adaptable to distributed VAR generation schemes is based on the natural oscillation of the airgap flux waves that occurs for a relatively large number of primary poles or else for unusually large slip values. In general, this accrues relatively small reduction in torque/thrust capacity but the capability to produce a leading power factor design for the entire machine is very heavily dependent on having unusually low magnetization and leakage flux losses since the negative quadrature flux is not maximized with this scheme. This approach does not require any specific amount of rotor leakage.

b. The second type and most adaptable to lumped VAR generation exclusively designates various peripheral regions of the airgap to distinct roles of either torque (primary) or VAR (tertiary) functions and is the approach pursued throughout the bulk of the thesis. This necessarily prefers a significant value of rotor leakage inductance and most important is able to generate a larger amount of reactive VA than the first scheme since the negative quadrature flux is based on the phasor sum of the in-phase and quadrature flux components at the distinct transition boundary. This effect more than compensates for the extra rotor leakage flux reactive loss and the leading power factor capability of the machine is less dependent on having unusually low magnetization or primary leakage requirements. This particular arrangement is considered advantageous because the tertiary also

comprises a harmonic current filter (which is not generally possible with the distributed winding approach) especially suited for state-of-the-art semiconductor frequency conversion equipment with quasi-square wave output current characteristics.

2. The exit-edge real power loss characteristic of a short-primary machine has been reproduced in a continuous primary member with a uniform airgap but with the benefit that the power transfer has manifested itself as a reactive power generation rather than as a loss.

3. In comparison with experimental evidence on two large linear machines and two large rotary machines exhibiting the second reactive generation scheme, the classical analytical theory explaining the short-stator exit-edge effect very accurately predicts the principal slip at which this loss or transfer characteristic (proportional to B_t^2) starts to occur and moderately well predicts the general shape of the reactive power versus slip curve. The major discrepancies occur in the exact location of the peak reactive power point near zero slip. It should be stressed that the previous analytical work on the short-stator effect explained a single exit-edge phenomenon whereas the machines under discussion have a multitude of edges as for example under one complete pole-pitch surface.

4. The second reactive scheme is self-compensating and necessarily prefers as large a rotor power dissipation as possible in that the greater the torque-producing rotor current, the greater the reactive compensation current on a linear basis for the machine may be described simply as a rotating, variable-phase polyphase current transformer. It exhibits excess rotor loss for leading power factor operation (above that for an overexcited synchronous motor) but this excess rotor loss is entirely a rotor slip loss rather than a stray loss. In the developments to follow

this thesis it is expected that this rotor loss will progressively diminish to the point where the SCIM unit will have exactly the same losses as an overexcited synchronous motor of the same size.

With respect to rotating self-compensating induction machines (SCIM) incorporating the second generation scheme the following conclusions are relavent.

1. Based upon the test results of the 26 kW unit, the power to weight and efficiency are too adversely effected for total power factor correction even if new stator laminations with the requisite change in pole-pitch are specified.

2. Based upon the test results of the 112 kW unit, the power to weight ratio and efficiency have not been adversely effected at high or unity power factors and if new laminations of reduced slot depth and change in slot-pitch would be incorporated, then this basic lumped winding scheme could represent a viable commercial machine design.

3. Even with magnetic power factor correction at the 112 kW level and efficiencies in excess of 90%, modern electrostatic power factor control is very competitive in terms of power to weight ratio and total capital expenditure at a unity power factor base, assuming that a single frequency is specified.

4. However,between 100 kW and 1000 kW, design studies clearly indicate that magnetic power factor correction integral to the SCIM unit is far advantageous over the conventional electrostatic capacitor control methods in power to weight and capital expenditure on a 50 or 60 Hz base frequency and no external switchgear.

5. The main advantage of the SCIM design in the range from 100 kW to 1000 kW is in adjustable-frequency propulsion systems for which the alternative induction, brushless drives must rely on the use of high-power electrostatic capacitors in parallel to

the power semiconductor conversion apparatus, whereas the described one-machine system avoids the frequency impedance-matching problem due to its magnetic self-compensation characteristic which is slip dependent rather than frequency dependent.

6. Since both reactive generation schemes rely on maintaining a very small band of slip values over all frequency excursions, power conversion apparatus must incorporate a constant-slip controller and it is concluded this is most effectively implemented in the "current-source" thyristor inverter without any type of pulse-width modulation control. Natural commutation has been shown to be a viable and preferred method of operating current-controlled devices such as thyristors far beyond the power range feasible for dissipative semiconductor devices such as field-effect or bipolar junction transistors. It is concluded that the most general approach to interfacing the SCIM unit with state-of-the-art power conditioning equipment for use in widely varying loads and variable speeds is to always maintain constant fundamental slip to the SCIM unit by virtue of the inverter or cycloconverter controller scheme. It is in this respect that the brushless SCIM technology is seen to be far advantageous over existing electronic armature-controlled direct-current commutator drive systems in efficiency, power-to-weight and capital investment at the 112 kW level and above.

Appendix I

Table A1

Specifications of the Datron Electronic Scanning Unit

General

Power Supply 205-255 or 105-127 volts, 48-440 Hz.
Consumption approximately 12VA.

Operating Temperature 0°C to 50°C.

Storage Temperature –25°C to +70°C.

Dimensions	1200 Scanner	Height	132mm (5.2")
		Width	433mm (17")
		Depth	327mm (12.9")
	1210 Extension – as above.		

Weight	1200 Mainframe (unloaded)	6kg (13 lb)
	1201 Relay Module	850gm (30oz)
	1219 Extension (unloaded)	4.5kg (10 lb)

Rack Mounting "Ears" mounted on side of instrument.

Clock Accuracy 10ppm @ 23°C.
Temperature Coefficient 10ppm/°C.

Inputs

Channel Capacity 1200 Scanner Up to 3 modules (2 or 4 pole switching)
1210 Extension Up to 7 modules (2 or 4 pole switching)

4.1.2.1 **1201 Relay Modules**

Capability 20 x 2 pole channels) + guard
or 10 x 4 pole channels) per module

Channel Switching Time < 20mS

Thermal emf error < 2μV

Maximum voltages:

Between any 2 poles of one channel or between channels	250V rms
Between any signal input and guard	250V rms
Between guard and earth (case)	250V rms

Minimum switching operations 10^8

Cold Junction Compensation : See 1241/1251 Operating Manual.

Appendix I

Table A2

Specifications of the Digital Voltmeter and Filter

General			
Power Supply	205 – 255 or 105 – 127 volts, 48 – 440Hz. Specify line frequency and voltage when ordering. Consumption is approximately 12 VA.		
Operating Temperature	0°C to 50°C.		
Storage Temperature	–25°C to +70°C.		
Dimensions	H = 90mm (3.5"), W = 440mm (17.25"), D = 343mm (13.5").		
Weight	5.5kg (12 lbs).		
Rack Mounting	"Ears" mounted on side of instrument.		
Specification Validity	For 6 months over 18 – 28°C or as described.		
1041 only			
DC Voltage measurement			
Ranges	10.000 mV, 100.00 mV, 1.0000 V, 10.000 V, 100.00 V, 1000.0 V Automatic.		
Overrange	100% i.e. 19999 full scale (FS) on all ranges except 1000.0 V.		
Accuracy	After mV offset adjustment, all ranges. ± 0.01% reading ± 0.005% FS ± 1 microvolt. N.B. Use of SF1 option adds 0.05% to full scale accuracy.		
Temperature Coefficient	± 1/10 (of above accuracy rating)/°C ± 0.2 microvolts/°C.		
Stability	After six months use better than above accuracy rating per year plus microvolt offset of typically less than 2 microvolts per month.		
Common Mode Rejection (1 kΩ Source Unbalance)	DC > 140 dB AC > 80 dB + SERIES MODE up to 174 dB (1 Hz to 60Hz).		
Series Mode Rejection	**FILTER OUT**	> 20 dB @ 50 Hz increasing at 30 dB per octave + NOTCH REJECTION	
	FILTER IN	> 57 dB @ 50 Hz increasing at 18 dB per octave + NOTCH REJECTION	
	NOTCH REJECTION	> 50 dB @ Line Frequency ± 0.15% 36 dB @ Line Frequency ± 1%	
	FILTER OUT – (OPTION F01)	NOTCH REJECTION alone.	
Settling Time (to 0.01%)	**FILTER OUT**	78 milliseconds)	ADD 30 milliseconds
	FILTER OUT (F01)	5 milliseconds)	if changing into or out
	FILTER IN	350 milliseconds)	of 100 V, 1 kV ranges.
Read Rate	Normal internally triggered read rate ~ 2.5 readings/sec. Maximum externally triggered read rates:		
	FILTER OUT	10 readings/sec.	
	FILTER OUT (F01)	20 readings/sec.	
	FILTER OUT (SF1)	150 readings/sec. (at full range), 120 readings/sec (at full scale).	
	FILTER IN	2.5 readings/sec.	

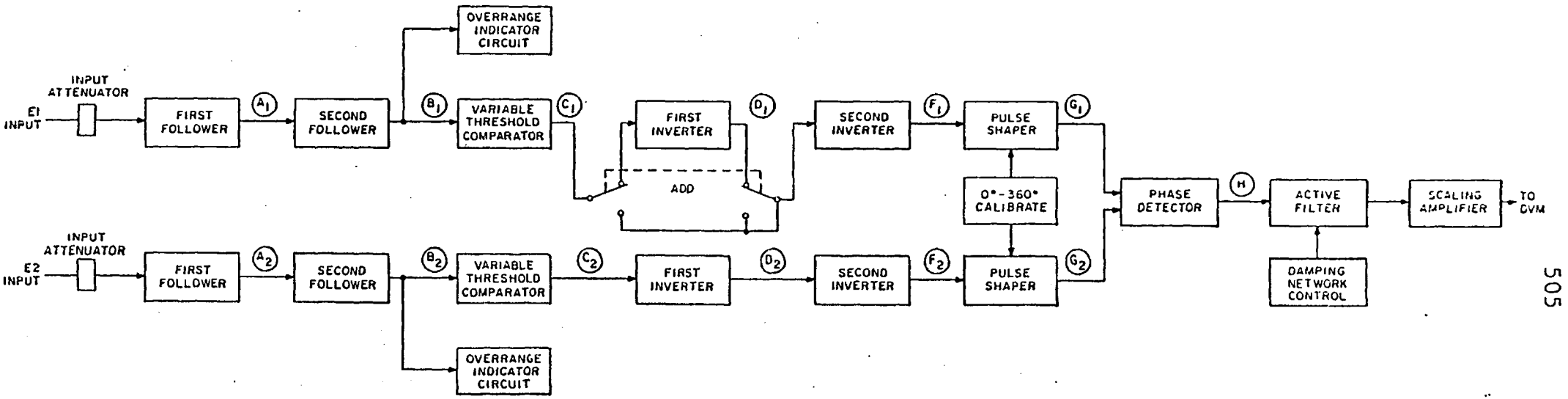

Figure A. 1 Block diagram of the digital electronic phase meter used for both linear and rotary unit measurements.

Appendix I

Appendix I

Table A3

Specifications of the Electronic Digital Phase Meter

<table>
<tr><td>Frequency Range:</td><td>1 Hz - 100 kHz</td></tr>
<tr><td>Input Signal Range:</td><td>Two overlapping ranges:
10 mv-10 v rms
100 mv-100 v rms
(front panel selectable)</td></tr>
<tr><td>Accuracy:</td><td><table><tr><th>1 kHz</th><th>10 kHz</th><th>100 kHz</th></tr></table></td></tr>
<tr><td>With equal inputs:</td><td><table><tr><td>±0.3°</td><td>±0.7°</td><td>±1.5°</td></tr></table></td></tr>
<tr><td>With 60 dB ratio between inputs:</td><td><table><tr><td>±0.5°</td><td>±1.5°</td><td>±3°</td></tr></table></td></tr>
<tr><td>DC Output:</td><td>0-3.6 v (10 mv/degree)</td></tr>
<tr><td>Input Impedance:</td><td>1 Megohm shunted by 30 pf</td></tr>
<tr><td>Output Impedance:</td><td>1 ohm max (5 ma drive capability)</td></tr>
<tr><td>Resolution:</td><td>0.1°</td></tr>
<tr><td>Input Power:</td><td>115 or 230 v ac, 50-60 Hz, 20 watts</td></tr>
<tr><td>Size:</td><td>19" wide x 3-1/2" high x 11" deep</td></tr>
<tr><td>Weight:</td><td>13 lbs.</td></tr>
</table>

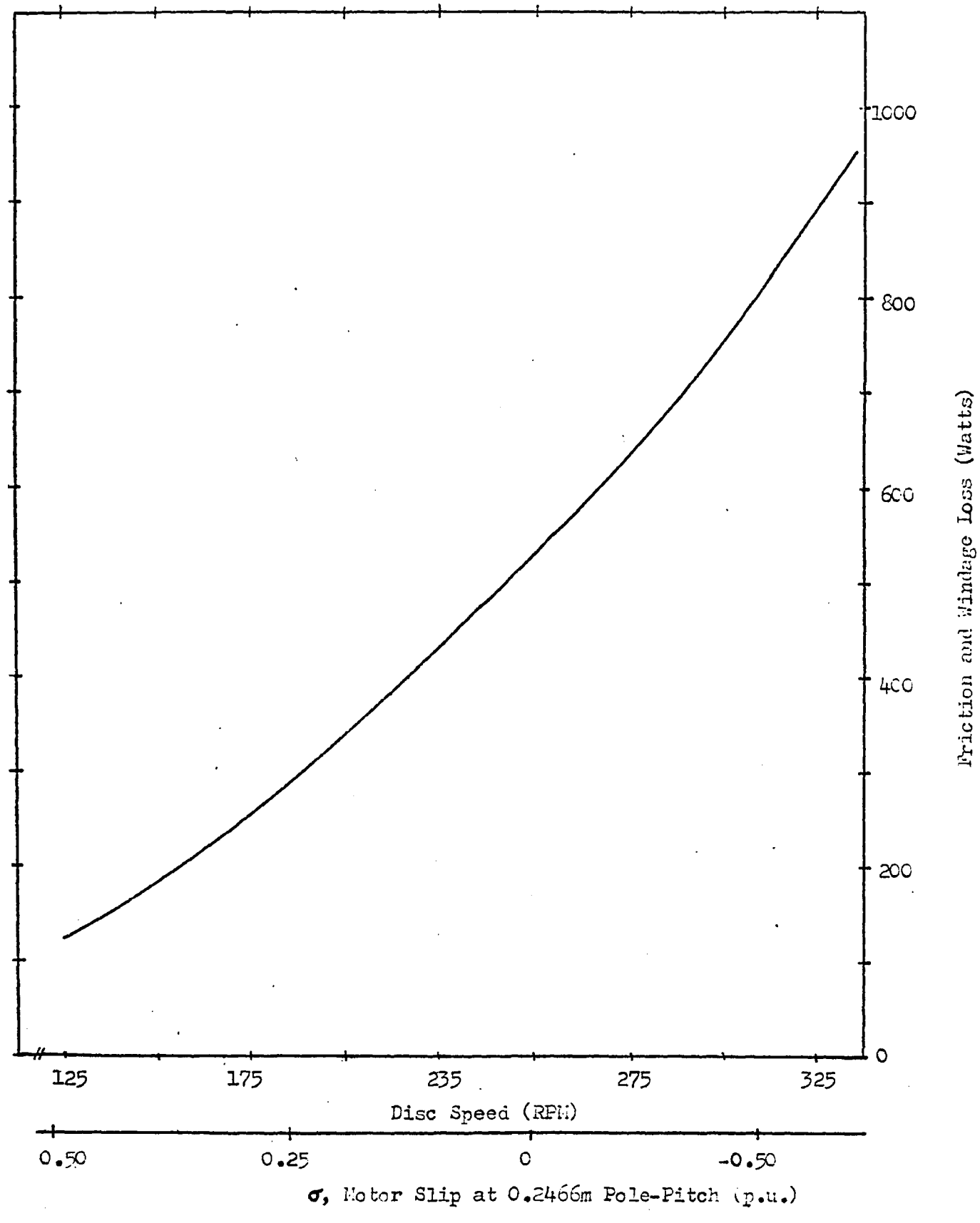

Appendix II

Figure A.2 LIM test-rig high-speed friction and windage losses

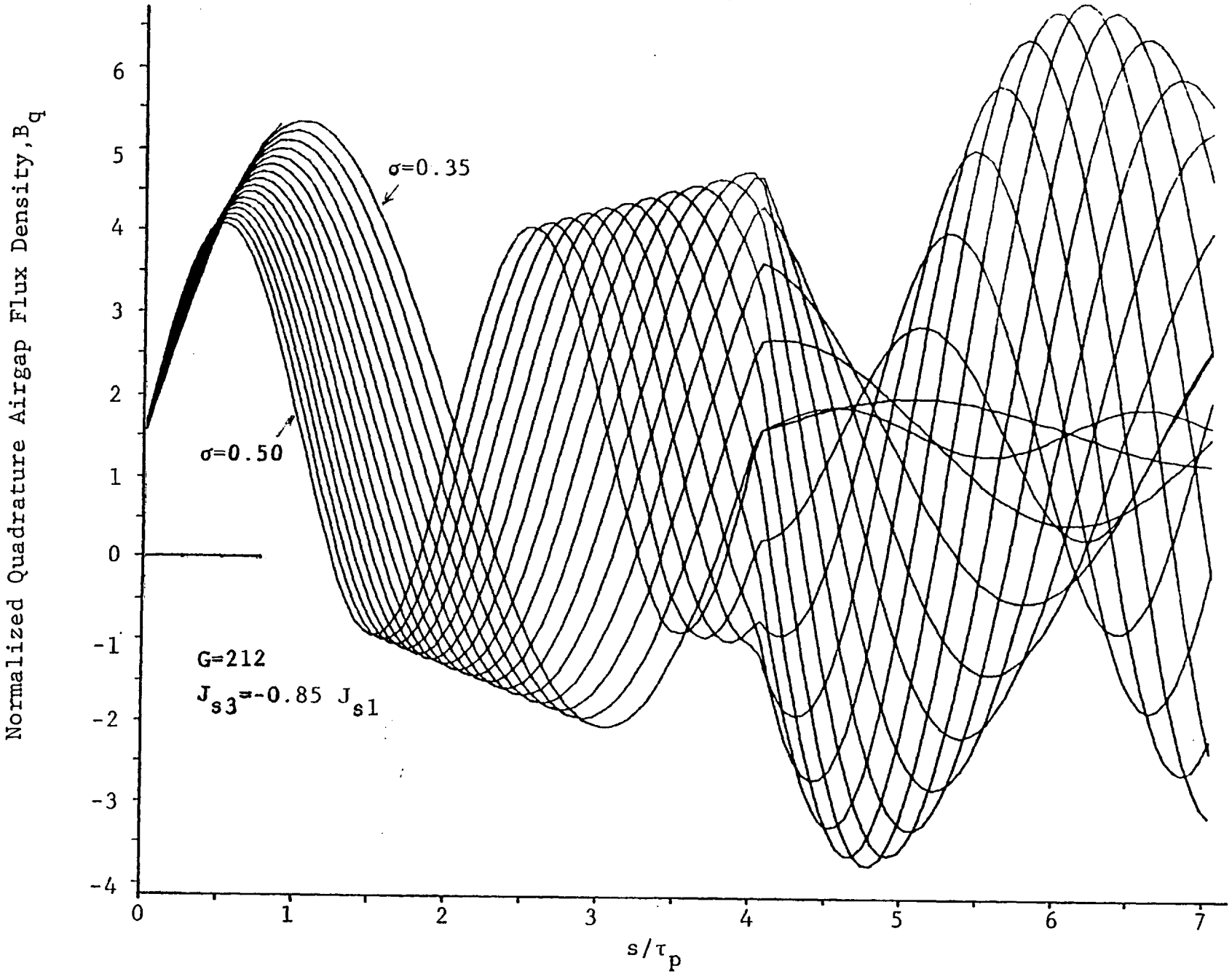

Figure A.3 Quadrature Flux Density for primary from 0 to 7 poles and tertiary from 4 to 7 poles

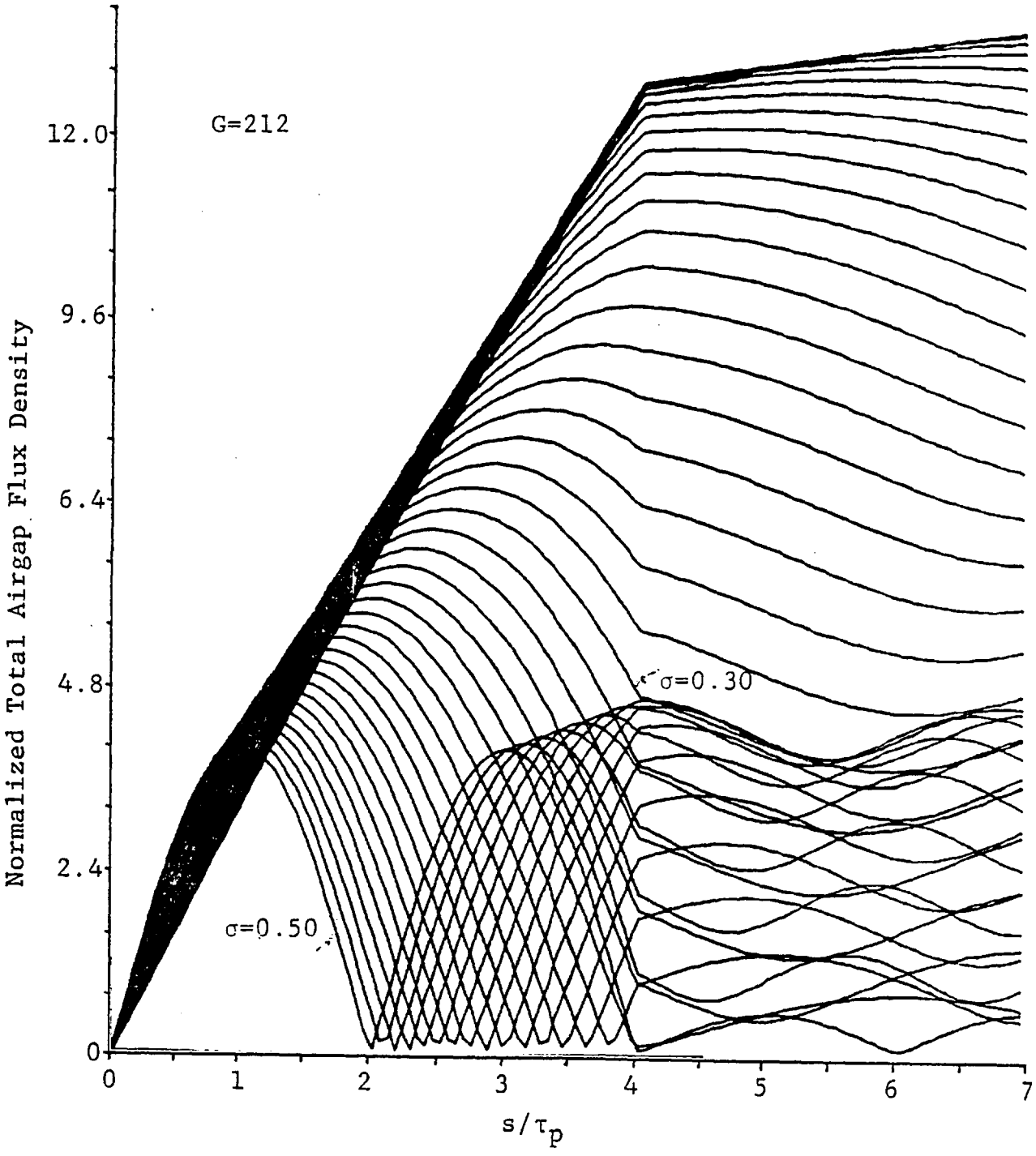

Figure A.4 Total airgap flux density for primary winding from 0 to 7 poles and tertiary from 4 to 7 poles with current loading J_{s3}=-0.85 J_{s1}.

Appendix IV

Determination of the Attenuation Coefficients of the Airgap Flux Density for the Surface Layer Rotor Model

The characteristic equation for the excitation section airgap magnetic field density was derived in Section 3.1 as

$$\omega T_2 \lambda^3(1-\sigma)\dddot{B}_g + \lambda^2(1+j\omega T_2)\ddot{B}_g - G\lambda(1-\sigma)\dot{B}_g - jG B_g = -jG \frac{\rho_r \hat{J}_s}{u_s}(1 + j\sigma\omega T_2)e^{-j\theta} \quad (A.1)$$

where $\lambda=\tau_p/\pi$ and B_g is the radial airgap field density represented by a complex function in time and varies in space with respect to θ only. The roots of this system may be found by solving the auxiliary equation

$$\omega T_2\lambda^3(1-\sigma)\alpha^3 + \lambda^2(1+j\omega T_2)\alpha^2 - G\lambda(1-\sigma)\alpha - jG = 0 \quad (A.2)$$

and for the case of $1+j\omega T_2 \simeq j\omega T_2$ the principal root is determined from the one factor of

$$(1-\sigma)\alpha_1' + j = 0$$

$$\alpha_1' = \frac{1}{j(1-\sigma)} \quad (A.3)$$

and the minor roots from the other factor

$$\alpha_{2,3}'^2 \frac{\omega T_2}{G} - 1 = 0$$

$$\alpha_2' = -\{G/\omega T_2\}^{\frac{1}{2}} \quad (A.4)$$

$$\alpha_3' = \{G/\omega T_2\}^{\frac{1}{2}} \quad (A.5)$$

To consider the most general case for which the rotor leakage time constant, T_2 may approach the value $1/\omega$, it is convenient to express the roots as a first-order series function based on the upper val-

ues of the roots expressed in (A.3),(A.4), and (A.5), where the term γ is now introduced and will be negative and less than one in magnitude.

Let $$\alpha_1 = \alpha_1'\{1+\gamma_1\} \tag{A.6}$$

by substituting this into (A.2) and retaining a linear systems model by ignoring second and third order terms of γ, we have

$$0 = \alpha_1'^3\lambda^3\{1+3\gamma_1\}\omega T_2(1-\sigma)/G + \alpha_1'^2\lambda^2\{1+2\gamma_1\}\left[\frac{1}{G} + j\frac{\omega T_2}{G}\right] - \alpha_1'\lambda\{1+\gamma_1\}(1-\sigma) - j$$

$$0 = \gamma_1\lambda\{ j\omega T_2 - 2 + j(1-\sigma)^2 G \} - 1$$

$$\gamma = \frac{1}{\lambda\{-2 + j[\omega T_2 + (1-\sigma)^2 G]\}}$$

$$\alpha_1 = \frac{1}{\lambda}\left[\frac{1}{j(1-\sigma)} - \frac{1}{-2j(1-\sigma) - \{\omega T_2(1-\sigma) + (1-\sigma)^3 G\}}\right] \tag{A.7}$$

and this may be compared to equation (3.49) which neglects the the $-2j(1-\sigma)$ term. The tertiary (or secondary) solution may be found as

$$\alpha_3 = \alpha_3'\{1+\gamma_3\}$$

and substituting this into (A.2) with the use of (A.5) yields

$$0=\{G/\omega T_2\}^{3/2}\lambda^3\{1+3\gamma_3\}\omega T_2\cdot(1-\sigma)/G + \lambda^2\{1+2\gamma_3\}\{\frac{1}{\omega T_2} + j\}$$

$$-\lambda\left[G/\omega T_2\right]^{\frac{1}{2}}\{1+\gamma_3\}(1-\sigma) - j \tag{A.8}$$

This reduces to

$$0= \gamma_3\lambda\{G/\omega T_2\}^{\frac{1}{2}}\left\{2(1-\sigma) + 2\{1/\omega T_2 + j\}\right\} + 1/\omega T_2$$

The tertiary attenuation coefficient is thus

$$\alpha_3= \frac{1}{\lambda}\{G/\omega T_2\}^{\frac{1}{2}}\left\{1 - \frac{1}{2\{\sqrt{G\omega T_2}\cdot(1-\sigma) + 1 + j\omega T_2\}}\right\} \tag{A.9}$$

Appendix V

Table A4

Characteristics of the Prototype Lintrol SLIM with Power Factor Correction

Motoring Section

Number of slots	36
Pole-pitch, mm	120
Core length, cm	72
Core depth, mm	16
Overall depth, mm	56
Core width, cm	14
Tooth top-surface length, mm	11.9
Slot opening, mm	8.1
Total slot cross section incl. wedge space, mm^2	494
Slots/pole/phase	2
Number of coils	36
Number of poles	6
Lamination thickness, mm	1.626

Asynchronous Condenser Section (ASC)

Number of slots	12
Pole-pitch, mm	112
Core length, cm	24.3
Overall depth, mm	56
Core depth, mm	29
Core width, cm	14
Tooth top surface length, mm	6
Slot opening, mm	13
Slot cross section incl. wedge space, mm^2	345
Slots/pole/phase	2
Number of coils	12
Number of poles	2
Lamination thickness, mm	0.762

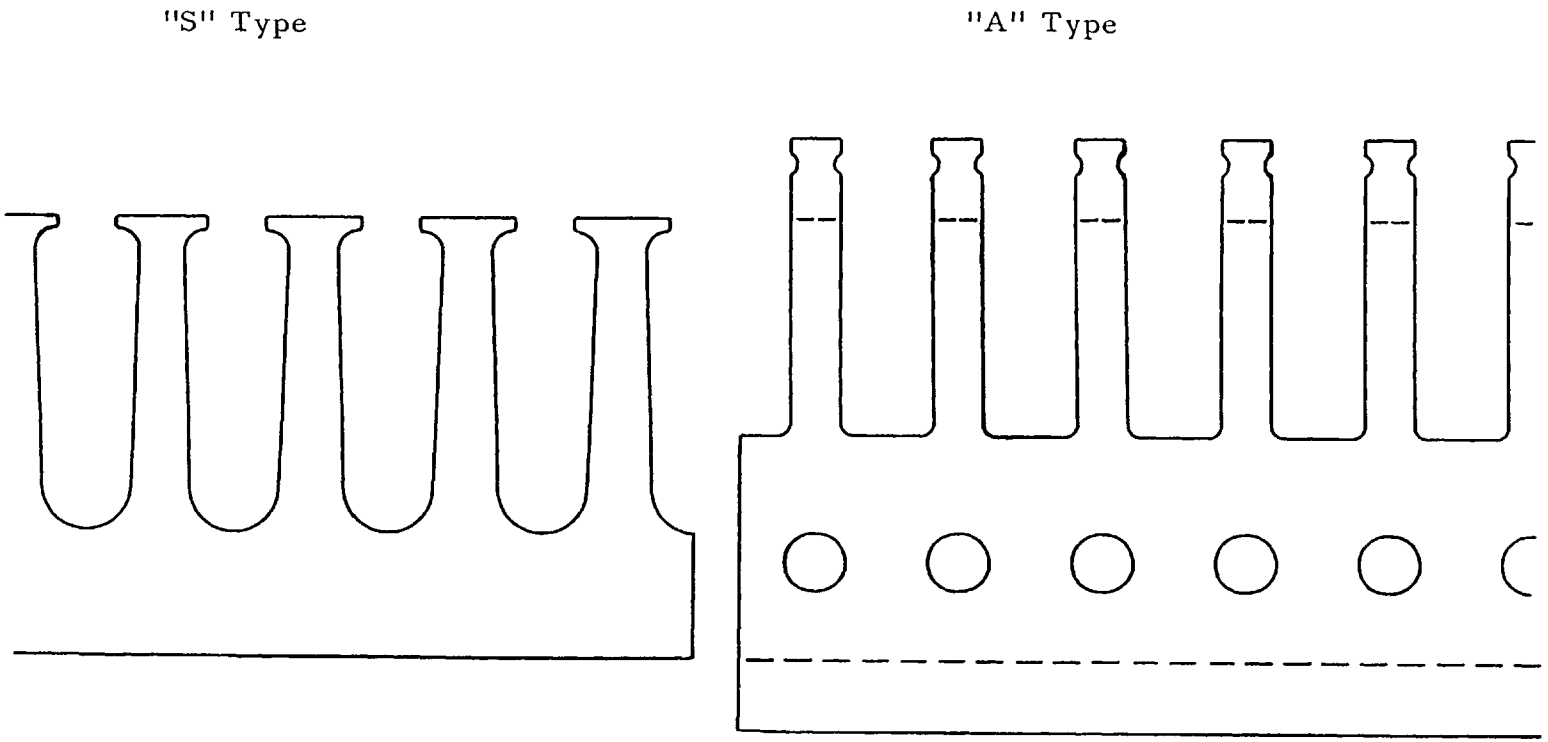

Fig.A5 Profiles of the two Lintrol laminations to be used for the prototype LIM-ASC machine with depth modifications to the "A" type as indicated by dashed lines.

Appendix V

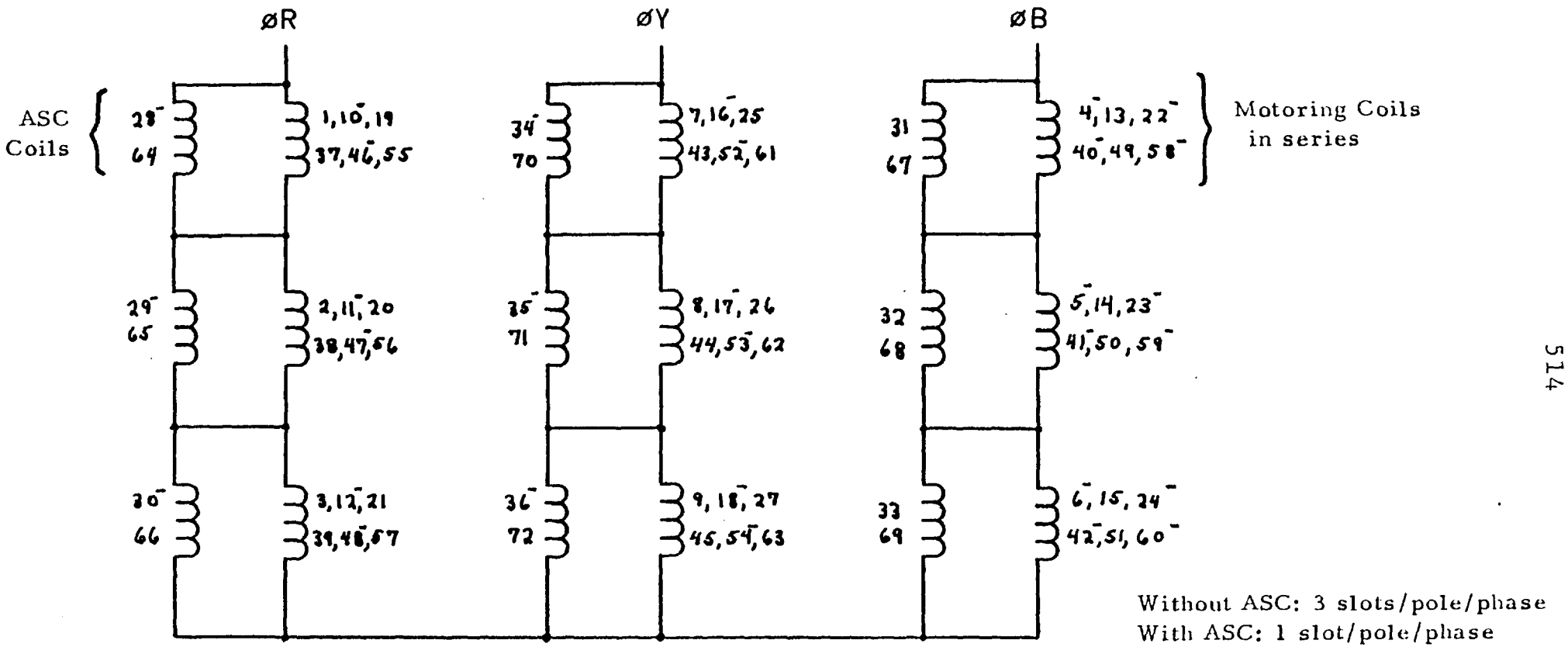

Figure A.6 Suggested Coil Arrangement for Near Unity Power Factor Operation of 20 H.P. Induction Machine to run at an 8 Pole Speed, 415 V_{l-l}, 50 Hz.

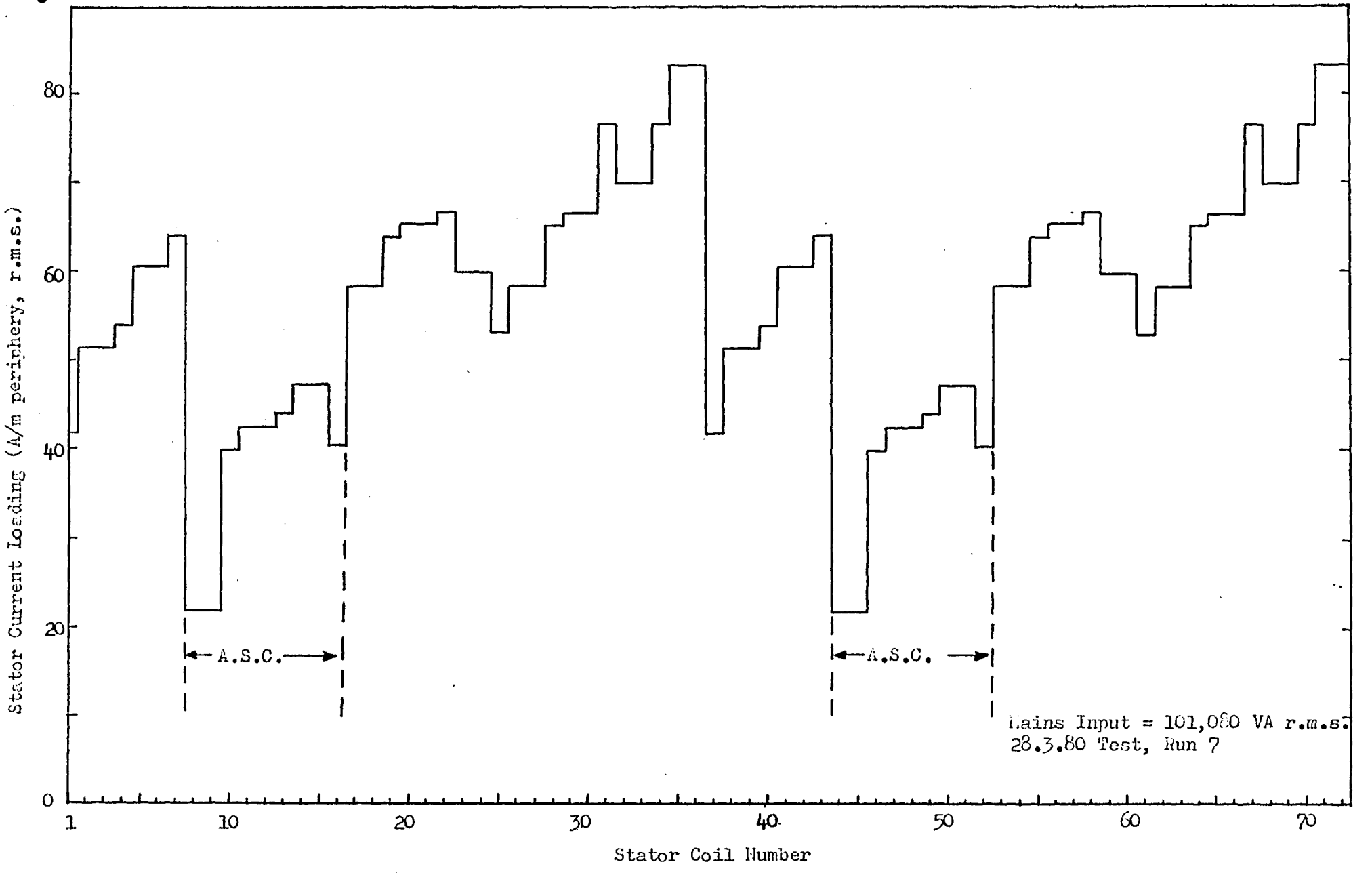

Appendix VII

Figure A. 7 Stator current loading of 150 H.P. Machine in reconnection testing at full rated voltage and current.

Appendix VIII. AC Dynamometer Loss Characteristics

LAURENCE, SCOTT & ELECTROMOTORS LTD

P.O. Box No.25, NORWICH, NR1 1JD

Mr. S.B. Kuznetsov,
Research Assistant,
Dept. of Electrical Engineering,
Imperial College of Science &
Technology,
Exhibition Road,
LONDON. SW7 2BT

KEG/RM

8th August, 1980.

Dear Mr. Kuznetsov,

Thank you for your letter of 14th July from which I was grateful to note that one of our equipments manufactured about 30 years ago is still giving useful service. Regarding the efficiency determination of NS motors, we always use the summation of losses method based on BS4999 Pt. 33 1977. The fixed loss and most of the copper loss for various speeds and loads can be obtained in the normal manner by operating the equipment on no load and load , but there are three losses which cannot be obtained from normal tests. These are the brush contact loss, the rotor copper loss and the load dependent stray losses. These are calculated as follows:-

Brush Contact Loss

We always use the value of one volt specified in BS for D.C. machines and multiply by the secondary current and the number of secondary phase ends.

Rotor Copper Loss

Owing to the configuration of the rotor winding its effective resistance cannot be obtained from direct measurements and a calculated value of resistance per phase is used based on the known copper area and the known length of turn.

Stray Losses

Again we use the values given in BS4999 i.e. .5% of the input to the equipment at full load.

In our experience this gives reasonably accurate values of total losses and in general we would expect the loss obtained in this way to be within 10% accuracy.

If you would like further information regarding NS equipment or indeed other equipments of our manufacture, we would be pleased to help you, but suggest that it would be better for you to pay us a visit at a mutually convenient time.

Yours sincerely

R. Mederer
Chief Electrical Engineer

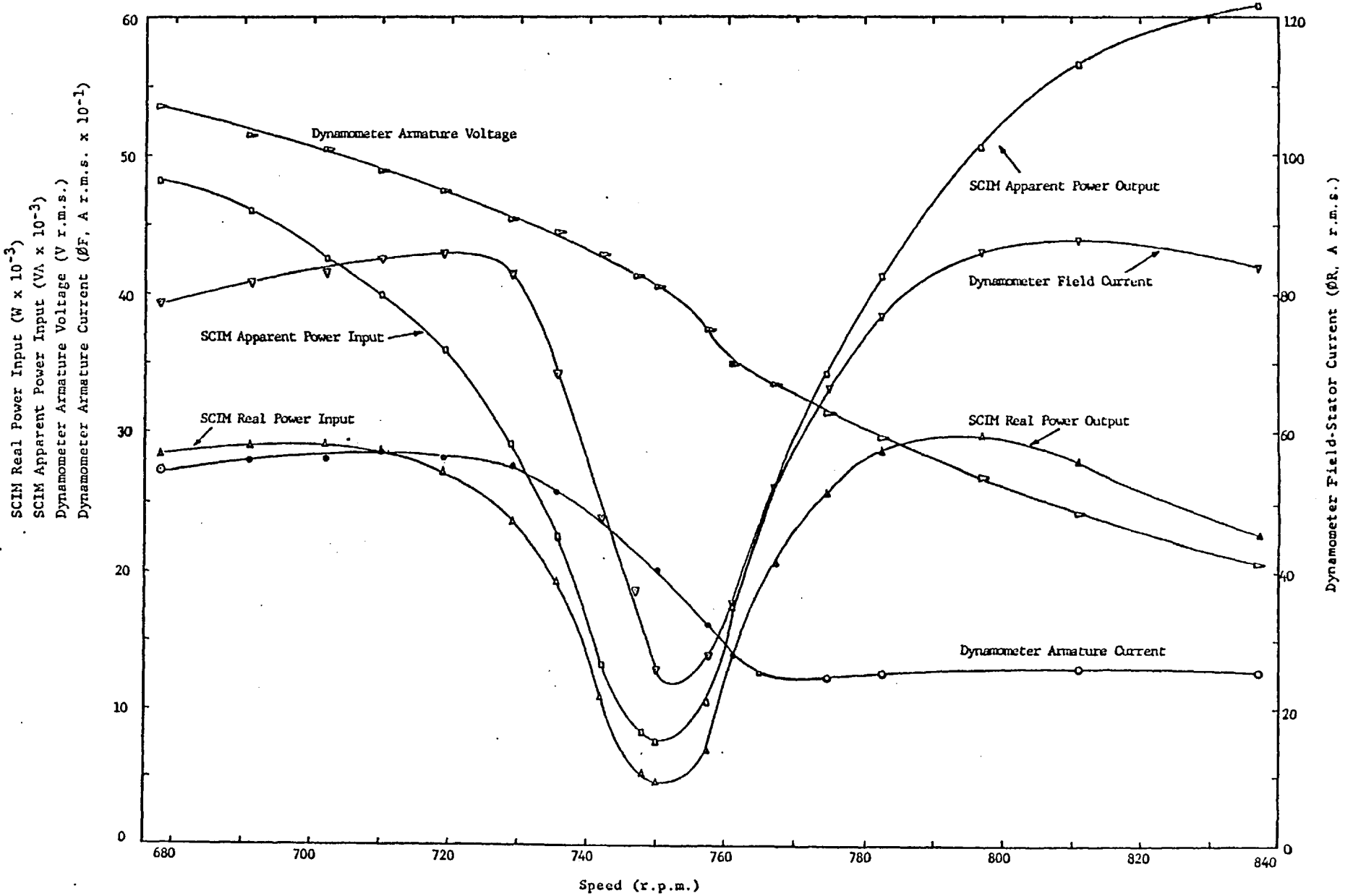

Appendix VIII

Fig. A.8 Characteristics of the AC Commutator dynamometer with SCIM unit-motoring winding on 80 V_{ln}, 50 Hz.

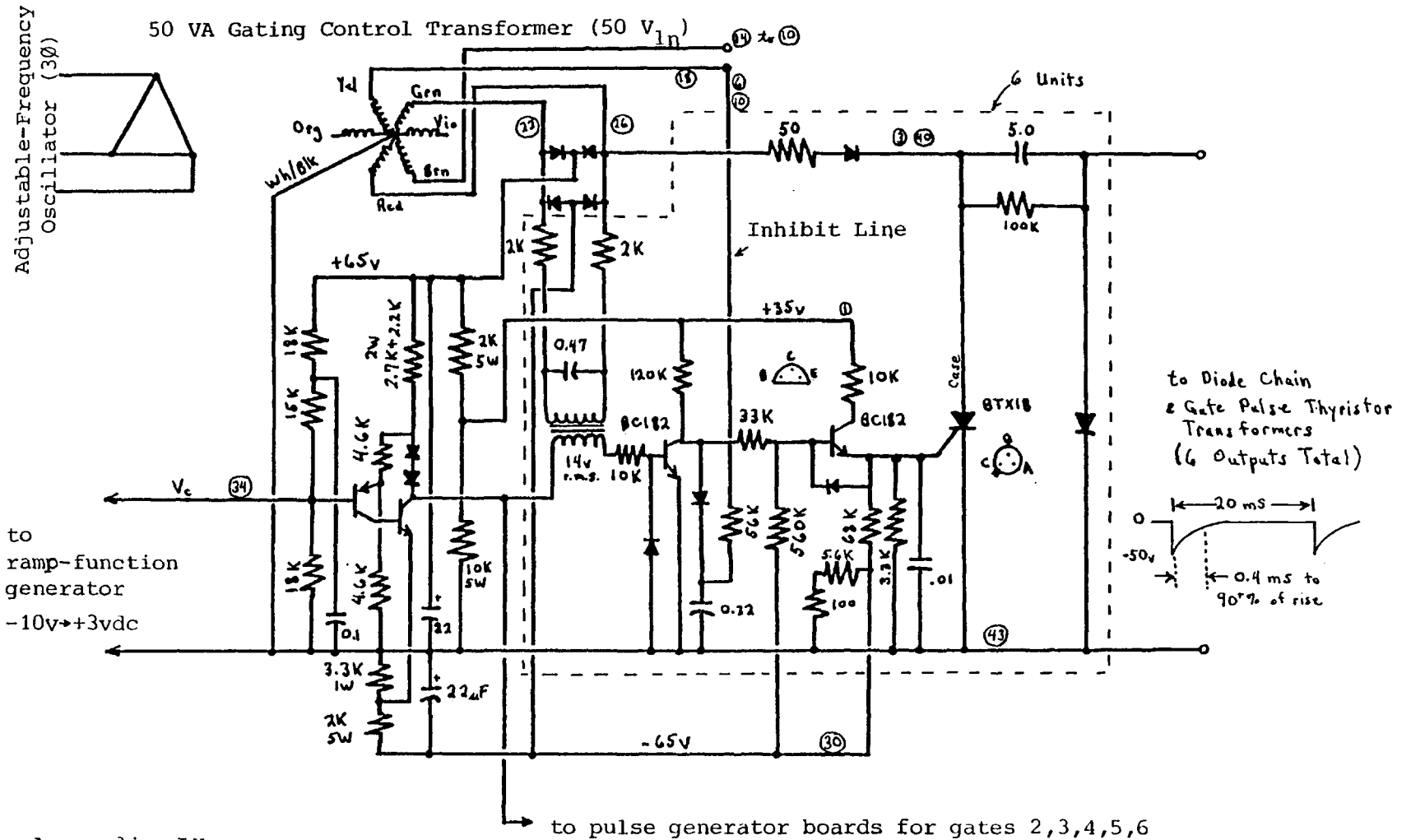

Appendix IX

Figure A.9 Gate Pulse Control Schematic for 2-Quadrant Variable Frequency Inverter

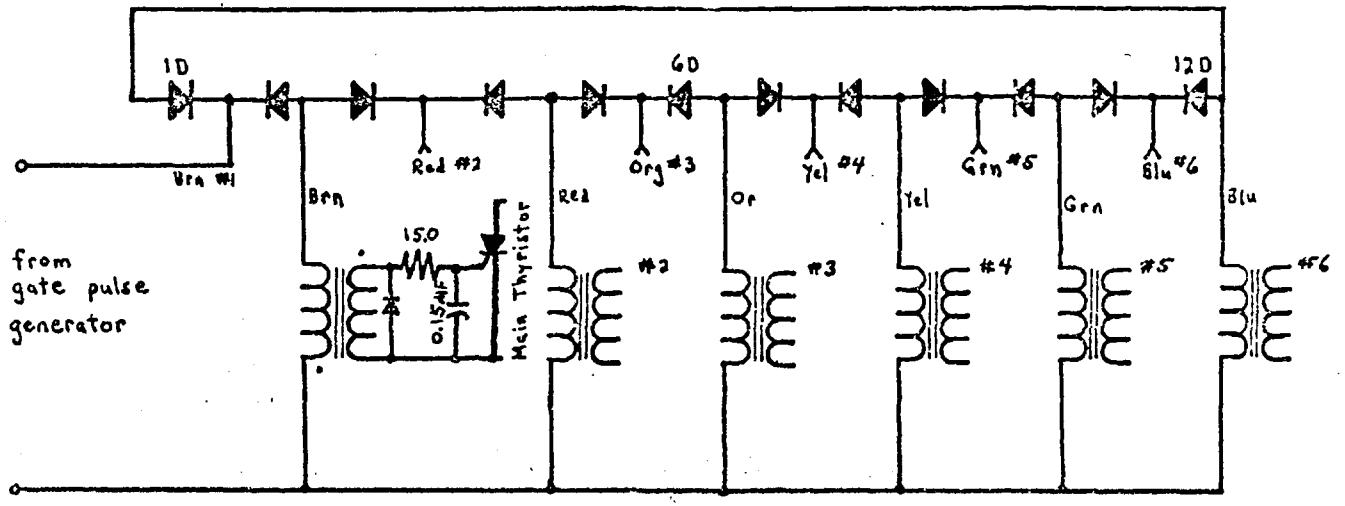

$$V_{11(max)} = \frac{V_{dc}\,\pi}{3\sqrt{2}}$$

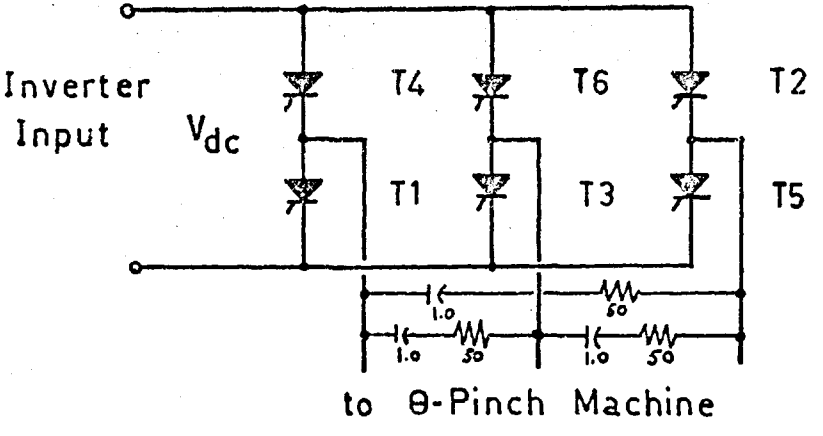

Appendix IX

Figure A.10 Gate Sequencing and Main Thyristor Circuit for Current Source Inverter supplying Leading P.F. Induction Machine in Natural Commutation Mode.

APPENDIX X

Set up an arbitrary reference frame to decouple induction machine equations for a 3Ø, 3 wire symmetrical winding.

Objective: Transform, by the C_1 and C_2 matrices, the voltages and currents of both the rotor and stator to a common and arbitrary frame of reference - the D-Q set. In particular to make the D-Q reference arbitrary, set it rotating at a velocity, ω_e, with respect to the stationary frame of the stator winding; this justifies applying the C_2-commutator matrix to the stator.

$$\frac{d\theta_r}{dt} = \omega_e - \omega_r$$

$$\frac{d\theta_s}{dt} = \omega_e$$

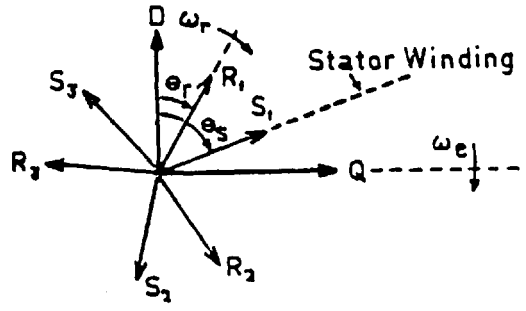

$$\alpha_1 = \theta_s - \theta_r$$

$$\alpha_2 = \alpha_1 + 120^\circ$$

$$\alpha_3 = \alpha_1 - 120^\circ$$

Initially $[v] = [Z][i]$ where $[Z] = [R] + [L]\,p$

Inductance Matrix

$$[L] = \begin{bmatrix} L_s & M_s & M_s & L_{sr}\cos\alpha_1 & L_{sr}\cos\alpha_2 & L_{sr}\cos\alpha_3 \\ M_s & L_s & M_s & L_{sr}\cos\alpha_3 & L_{sr}\cos\alpha_1 & L_{sr}\cos\alpha_2 \\ M_s & M_s & L_s & L_{sr}\cos\alpha_2 & L_{sr}\cos\alpha_3 & L_{sr}\cos\alpha_1 \\ L_{sr}\cos\alpha_1 & L_{sr}\cos\alpha_3 & L_{sr}\cos\alpha_2 & L_r & M_r & M_r \\ L_{sr}\cos\alpha_2 & L_{sr}\cos\alpha_1 & L_{sr}\cos\alpha_3 & M_r & L_r & M_r \\ L_{sr}\cos\alpha_3 & L_{sr}\cos\alpha_2 & L_{sr}\cos\alpha_1 & M_r & M_r & L_r \end{bmatrix}$$

$$[\upsilon] = \begin{bmatrix} \upsilon_{1s} \\ \upsilon_{2s} \\ \upsilon_{3s} \\ \upsilon_{1r} \\ \upsilon_{2r} \\ \upsilon_{3r} \end{bmatrix} \qquad [i] = \begin{bmatrix} i_{1s} \\ i_{2s} \\ i_{3s} \\ i_{1r} \\ i_{2r} \\ i_{3r} \end{bmatrix}$$

Instead of applying the C_1 transformation to the stator and Rotor impedances to find the 6 x 6 matrix Z' , since both the stator and rotor are transformed into the D-Q axis, there is only interest in $[Z'']$, $[\upsilon'']$ and $[i'']$.

1) $[\upsilon''] = [C_{2t}]^* [\upsilon'] = [C_{2t}]^* [C_{1t}]^* [\upsilon]$

$$[C_{1t}]^* [\upsilon] = \sqrt{\frac{2}{3}} \begin{bmatrix} 1/\sqrt{2} & 1/\sqrt{2} & 1/\sqrt{2} & 0 & 0 & 0 \\ 1 & -\frac{1}{2} & -\frac{1}{2} & 0 & 0 & 0 \\ 0 & \sqrt{3}/2 & -\sqrt{3}/2 & 0 & 0 & 0 \\ 0 & 0 & 0 & 1/\sqrt{2} & 1/\sqrt{2} & 1/\sqrt{2} \\ 0 & 0 & 0 & 1 & -\frac{1}{2} & -\frac{1}{2} \\ 0 & 0 & 0 & 0 & \sqrt{3}/2 & -\sqrt{3}/2 \end{bmatrix} \begin{bmatrix} \upsilon_{1s} \\ \upsilon_{2s} \\ \upsilon_{3s} \\ \upsilon_{1r} \\ \upsilon_{2r} \\ \upsilon_{3r} \end{bmatrix}$$

$$= \begin{bmatrix} 1/\sqrt{3}(\upsilon_{1s} + \upsilon_{2s} + \upsilon_{3s}) \\ \sqrt{2}/\sqrt{3}(\upsilon_{1s} - \frac{1}{2}(\upsilon_{2s} + \upsilon_{3s})) \\ 1/\sqrt{2}(\upsilon_{2s} - \upsilon_{3s}) \\ 1/\sqrt{3}(\upsilon_{1r} + \upsilon_{2r} + \upsilon_{3r}) \\ \sqrt{2/3}(\upsilon_{1r} - \frac{1}{2}(\upsilon_{2r} + \upsilon_{3r})) \\ 1/\sqrt{2}(\upsilon_{2r} - \upsilon_{3r}) \end{bmatrix}$$

$$[C_{2t}]^{*}[C_{1t}]^{*}[\upsilon] = \begin{bmatrix} 1 & 0 & 0 & 0 & 0 & 0 \\ 0 & \sin\theta_s & \cos\theta_s & 0 & 0 & 0 \\ 0 & \cos\theta_s & -\sin\theta_s & 0 & 0 & 0 \\ 0 & 0 & 0 & 1 & & \\ 0 & 0 & 0 & 0 & \sin\theta_r & \cos\theta_r \\ 0 & 0 & 0 & 0 & \cos\theta_r & -\sin\theta_r \end{bmatrix} \times$$

$$\begin{bmatrix} \sqrt{1/3}(\upsilon_{1s} + \upsilon_{2s} + \upsilon_{3s}) \\ \sqrt{2/3}(\upsilon_{1s} - \tfrac{1}{2}(\upsilon_{2s} + \upsilon_{3s})) \\ \sqrt{1/2}(\upsilon_{2s} - \upsilon_{3s}) \\ \sqrt{1/3}(\upsilon_{1r} + \upsilon_{2r} + \upsilon_{3r}) \\ \sqrt{2/3}(\upsilon_{1r} - \tfrac{1}{2}(\upsilon_{2r} + \upsilon_{3r})) \\ \sqrt{1/2}(\upsilon_{2r} - \upsilon_{3r}) \end{bmatrix}$$

$$= \begin{bmatrix} 1/\sqrt{3}(\upsilon_{1s} + \upsilon_{2s} + \upsilon_{3s}) \\ \upsilon_{1s}(\frac{\sqrt{2}}{\sqrt{3}}\sin\theta_s) + \upsilon_{2s}(\frac{1}{\sqrt{2}}\cos\theta_s - \frac{1}{\sqrt{6}}\sin\theta_s) + \upsilon_{3s}(-\frac{1}{\sqrt{2}}\cos\theta_s - \frac{1}{\sqrt{6}}\sin\theta_s) \\ \upsilon_{1s}(\sqrt{2/3}\cos\theta_s) + \upsilon_{2s}(-\frac{1}{\sqrt{2}}\sin\theta_s - \frac{1}{\sqrt{6}}\cos\theta_s) + \upsilon_{3s}(\frac{1}{\sqrt{2}}\sin\theta_s - 1/\sqrt{6}\cos\theta_s) \\ 1/\sqrt{3}(\upsilon_{1r} + \upsilon_{2r} + \upsilon_{3r}) \\ \upsilon_{1r}(\sqrt{2/3}\sin\theta_r) + \upsilon_{2r}(1/\sqrt{2}\cos\theta_r - 1/\sqrt{6}\sin\theta_r) + \upsilon_{3r}(-\frac{1}{\sqrt{2}}\cos\theta_r - 1/\sqrt{6}\sin\theta_r) \\ \upsilon_{1r}(\sqrt{2/3}\cos\theta_r) + \upsilon_{2r}(-1/\sqrt{2}\sin\theta_r - 1/\sqrt{6}\cos\theta_r) + \upsilon_{3r}(1/\sqrt{2}\sin\theta_r - 1/\sqrt{6}\cos\theta_r) \end{bmatrix}$$

$$\therefore [\upsilon''] = \begin{bmatrix} 1/\sqrt{3}(\upsilon_{1s} + \upsilon_{2s} + \upsilon_{3s}) \\ \sqrt{2/3}(\upsilon_{1s}\sin\theta_s + \upsilon_{2s}\sin(\theta_s + 120^{o}) + \upsilon_{3s}\sin(\theta_s - 120^{o})) \\ \sqrt{2/3}(\upsilon_{1s}\cos\theta_s + \upsilon_{2s}\cos(\theta_s + 120^{o}) + \upsilon_{3s}\cos(\theta_s - 120^{o})) \\ 1/\sqrt{3}(\upsilon_{1r} + \upsilon_{2r} + \upsilon_{3r}) \\ \sqrt{2/3}(\upsilon_{1r}\sin\theta_r + \upsilon_{2r}\sin(\theta_r + 120^{o}) + \upsilon_{3r}\sin(\theta_r - 120^{o})) \\ \sqrt{2/3}(\upsilon_{1r}\cos\theta_r + \upsilon_{2r}\cos(\theta_r + 120^{o}) + \upsilon_{3r}\cos(\theta_r - 120^{o})) \end{bmatrix}$$

Similarly, [i''] is exactly the same form as [υ''].

Since the zero sequence voltages only are dependent on one voltage, they are decoupled and are not utilized any further in the analysis.

2) To find [Z''] first use the [Z'] result found from applying the C_1 transformation to both stator and rotor impedances, $M \triangleq 3/2\, M_{sr}$

$$\begin{bmatrix} \upsilon_{as} \\ \upsilon_{bs} \\ \upsilon_{ar} \\ \upsilon_{br} \end{bmatrix} = \begin{bmatrix} Z'_{11} & Z'_{12} \\ Z'_{21} & Z'_{22} \end{bmatrix} \begin{bmatrix} i_{as} \\ i_{bs} \\ i_{ar} \\ i_{br} \end{bmatrix} \begin{bmatrix} R_s + pL_{ls} & 0 & pM\cos\alpha_1 & -pM\sin\alpha_1 \\ 0 & R_s + pL_{ls} & pM\sin\alpha_1 & pM\cos\alpha_1 \\ pM\cos\alpha_1 & pM\sin\alpha_1 & R_r + pL_{lr} & 0 \\ -pM\sin\alpha_1 & pM\cos\alpha_1 & 0 & R_r + pL_{lr} \end{bmatrix}$$

Note that $\alpha_1 = \theta_s - \theta_r$ is used exclusively in the [Z'] matrix alone.

$$[Z''] = \begin{bmatrix} C_{4t}^{*}{}_{\theta_s} & 0 \\ 0 & C_{4t}^{*}{}_{\theta_r} \end{bmatrix} \begin{bmatrix} Z'_{11} & Z'_{12} \\ Z'_{21} & Z'_{22} \end{bmatrix} \begin{bmatrix} C_{4\theta_s} & 0 \\ 0 & C_{4\theta_r} \end{bmatrix} = \begin{bmatrix} C_{4t}^{*} Z'_{11} C_4 & C_{4t}^{*} Z'_{12} C_4 \\ C_{4t}^{*} Z'_{21} C_4 & C_{4t}^{*} Z'_{22} C_4 \end{bmatrix}$$

Note positions of θ_s and θ_r

where the C_4 matrix is used instead of the C_2 matrix

$$C_4 = C_{4t}^{*} \triangleq \begin{bmatrix} -\sin\theta & \cos\theta \\ \cos\theta & \sin\theta \end{bmatrix}$$

$$[Z'_{11}][C_{4_{\theta_s}}] = \begin{bmatrix} R_s + pL_{1s} & 0 \\ 0 & R_s + pL_{1s} \end{bmatrix} \begin{bmatrix} -\sin\theta_s & \cos\theta_s \\ \cos\theta_s & \sin\theta_s \end{bmatrix}$$

$$= \begin{bmatrix} -(R_s + pL_{1s})\cdot\sin\theta_s & (R_s + pL_{1s})\cdot\cos\theta_s \\ (R_s + pL_{1s})\cdot\cos\theta_s & (R_s + pL_{1s})\cdot\sin\theta_s \end{bmatrix}$$

$$[C_{4_t}]^* [Z'_{11}][C_4] = \begin{bmatrix} -\sin\theta_s & \cos\theta_s \\ \cos\theta_s & \sin\theta_s \end{bmatrix} x$$

$$\begin{bmatrix} -\sin\theta_s(R_s + pL_{1s}) - \dot{\theta}_s L_{1s}\cos\theta_s & \cos\theta_s(R_s + pL_{1s}) - \dot{\theta}_s L_{1s}\sin\theta_s \\ \cos\theta_s(R_s + pL_{1s}) - \dot{\theta}_s L_{1s}\sin\theta_s & \sin\theta_s(R_s + pL_{1s}) + \dot{\theta}_s L_{1s}\cos\theta_s \end{bmatrix}$$

$$= \begin{bmatrix} R_s + pL_{1s} & \omega_e L_{1s} \\ -\omega_e L_{1s} & R_s + pL_{1s} \end{bmatrix}$$

$$[Z'_{12}][C_{4_{\theta_r}}] = pM \begin{bmatrix} \cos\alpha_1 & -\sin\alpha_1 \\ \sin\alpha_1 & \cos\alpha_1 \end{bmatrix} \begin{bmatrix} -\sin\theta_r & \cos\theta_r \\ \cos\theta_r & \sin\theta_r \end{bmatrix}$$

$$= M \begin{bmatrix} -\sin\theta_s p - \dot{\theta}_s\cos\theta_s & \cos\theta_s p - \dot{\theta}_s\sin\theta_s \\ \cos\theta_s p - \dot{\theta}_s\sin\theta_s & \sin\theta_s p + \dot{\theta}_s\cos\theta_s \end{bmatrix}$$

$$[C_{4t_{\theta_s}}]^* [Z'_{12}][C_{4_{\theta_r}}] = M \begin{bmatrix} (\sin^2\theta_s + \cos^2\theta_s)\,p & \dot{\theta}_s(\sin^2\theta_s + \cos^2\theta_s) \\ -\dot{\theta}_s(\sin^2\theta_s + \cos^2\theta_s) & (\sin^2\theta_s + \cos^2\theta_s)\,p \end{bmatrix} = \begin{bmatrix} Mp & \omega_e M \\ -\omega_e M & Mp \end{bmatrix}$$

$$[Z'_{21}][C_{4_{\theta_s}}] = pM\begin{bmatrix}\cos\alpha_1 & \sin\alpha_1\\ -\sin\alpha_1 & \cos\alpha_1\end{bmatrix}\begin{bmatrix}-\sin\theta_s & \cos\theta_s\\ \cos\theta_s & \sin\theta_s\end{bmatrix}$$

$$= M\begin{bmatrix}-\sin\theta_r\, p - \dot{\theta}_r\cos\theta_r & \cos\theta_r\, p - \dot{\theta}_r\sin\theta_r\\ \cos\theta_r\, p - \dot{\theta}_r\sin\theta_r & \sin\theta_r\, p - \dot{\theta}_r\cos\theta_r\end{bmatrix}$$

$$[C_{4t_{\theta_r}}]^* [Z'_{21}][C_{4_{\theta_s}}] = \begin{bmatrix}Mp & (\omega_e - \omega_r)\, M\\ -(\omega_e - \omega_r)\, M & Mp\end{bmatrix}$$

$$[Z'_{22}][C_{4_{\theta_r}}] = \begin{bmatrix}R_r + pL_{1r} & \theta\\ \theta & R_r + pL_{1r}\end{bmatrix}\begin{bmatrix}-\sin\theta_r & \cos\theta_r\\ \cos\theta_r & \sin\theta_r\end{bmatrix}$$

$$[C_{4t_{\theta_r}}]^* \quad [Z'_{22}][C_4]_{\theta_r} = \begin{bmatrix}-\sin\theta_r & \cos\theta_r\\ \cos\theta_r & \sin\theta_r\end{bmatrix} x$$

$$\begin{bmatrix}-\sin\theta_r(R_r + pL_{1r}) - \dot{\theta}_r L_{1r}\cos\theta_r & \cos\theta_r(R_r + pL_{1r}) - \dot{\theta}_r L_{1r}\sin\theta_r\\ \cos\theta_r(R_r + pL_{1r}) - \dot{\theta}_r L_{1r}\sin\theta_r & \sin\theta_r(R_r + pL_{1r}) + \dot{\theta}_s L_{1r}\cos\theta_r\end{bmatrix}$$

$$= \begin{bmatrix}R_r + pL_{1r} & (\omega_e - \omega_r)\, L_{1r}\\ -(\omega_e - \omega_r)L_{1r} & R_r + pL_{1r}\end{bmatrix}$$

Collecting the 4 impedences, the complete transformation to d-q variables is:

$$\begin{bmatrix} \upsilon_{qs} \\ \upsilon_{ds} \\ \upsilon_{qr} \\ \upsilon_{dr} \end{bmatrix} = \begin{bmatrix} R_s + pL_{ls} & \omega_e L_{ls} & Mp & \omega_e M \\ -\omega_e L_{ls} & R_s + pL_{ls} & -\omega_e M & Mp \\ Mp & (\omega_e - \omega_r)M & R_r + pL_{lr} & (\omega_e - \omega_r)L_{lr} \\ -(\omega_e - \omega_r)M & Mp & -(\omega_e - \omega_r)L_{lr} & R_r + pL_{lr} \end{bmatrix} \begin{bmatrix} i_{qs} \\ i_{ds} \\ i_{qr} \\ i_{dr} \end{bmatrix}$$

which defines $[\upsilon''] = [Z''][i'']$

Note that ω_e in the above equations is completely arbitrary and can be replaced by any frequency other than supply frequency including $\omega_e = 0$.

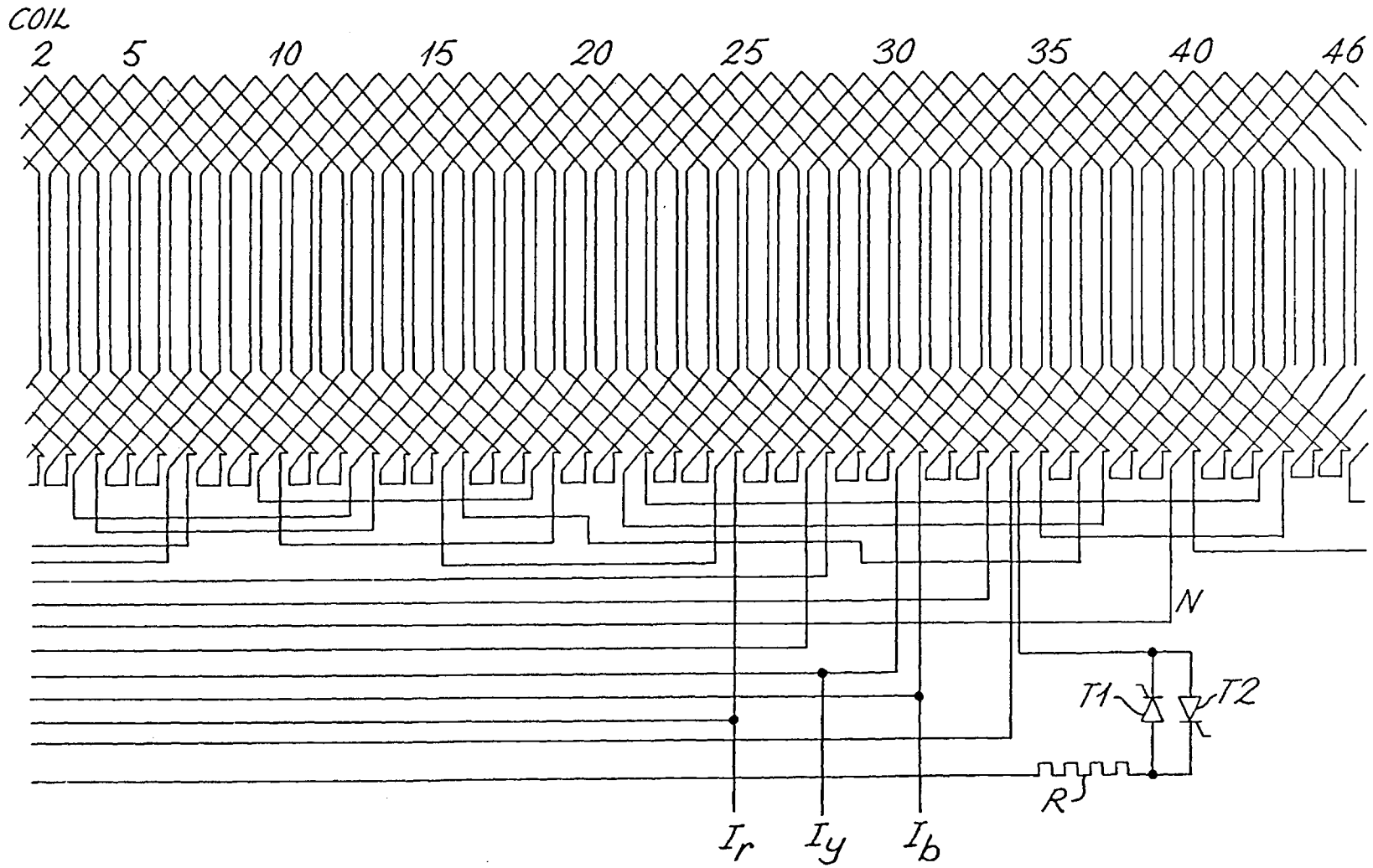

Appendix XI.

Figure A.11 Winding layout for a 26 kW rotary machine with thyrsitor control of the re-entry flux between motoring and condenser sections.

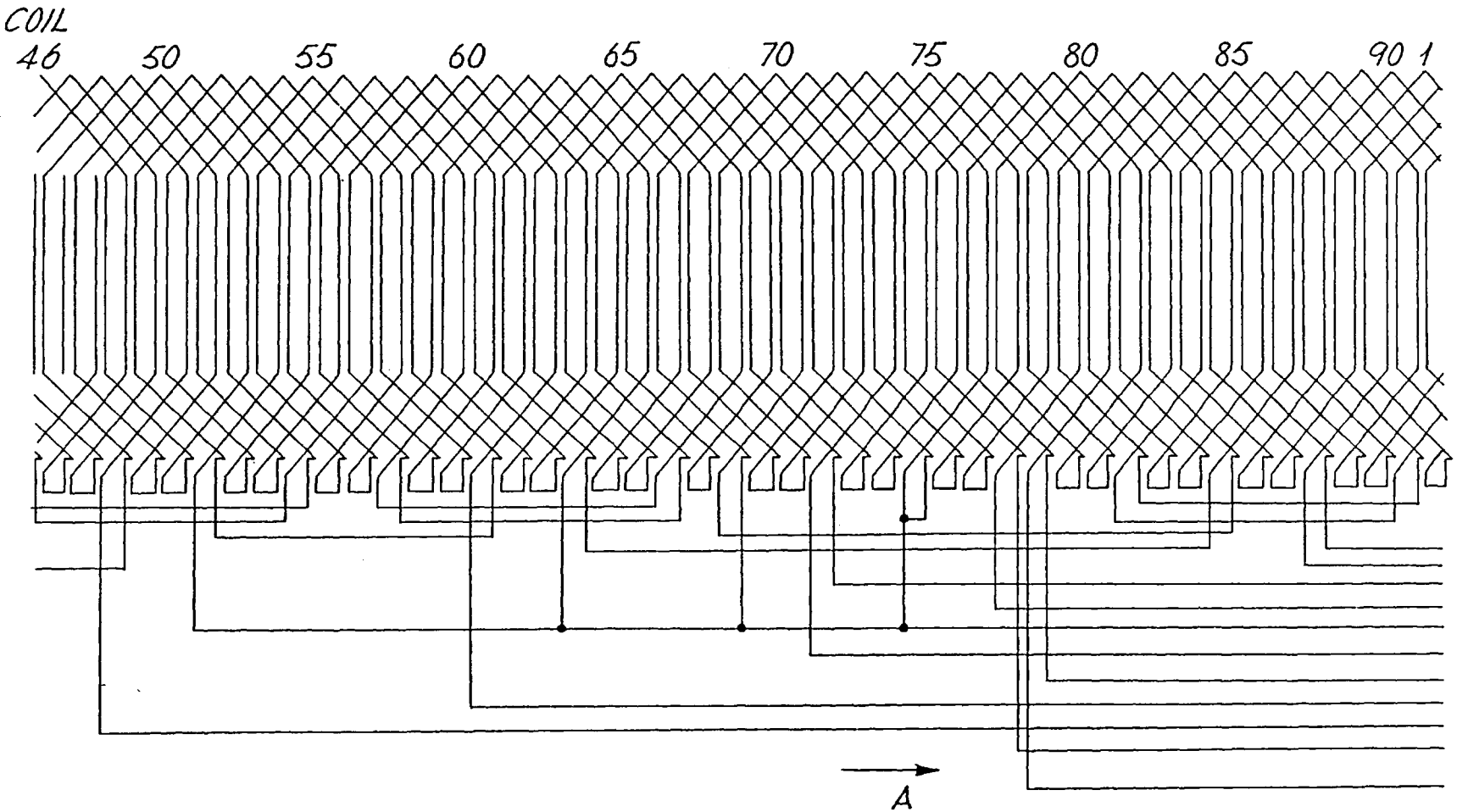

Figure A.11 Continued

THE ASYNCHRONOUS CONDENSER: A BRUSHLESS, ADJUSTABLE POWER FACTOR INDUCTION MACHINE

Professor E.R. Laithwaite, Fellow IEEE Stephen B. Kuznetsov, Member IEEE

Department of Electrical Engineering
Imperial College of Science and Technology
Exhibition Road, London SW7 England

Abstract- A new mechanism of continuously generating reactive kVA from the stator of a brushless induction machine is formulated and tested on 10 kW and 35 H.P. laboratory machines. A space-transient magnetic wave, travelling at rotor speed must be artificially created and at least two distinct windings of different pole-pitch must be incorporated. The per unit kvar generation effect increases with machine rating, and leading power factor operation of the entire machine is viable for large industrial motors and power system induction generators.

INTRODUCTION

In 1957 Williams et al [1] made a simple analysis of an induction motor in which the primary (stator) was not continuous around the periphery of a cage rotor but consisted of a sector covering a limited arc of the rotor. In such a situation unmagnetized rotor teeth, each surrounded by its own short-circuited loop consisting of a pair of rotor bars and their appropriate bits of end conductor, enter the active zone of the stator at high speed. The teeth are unable to accept full flux density instantaneously because such a change would demand an infinite emf and current in the rotor bars.

When the coils of the sector of stator are series-connected (as they invariably are in most rotary induction machines) rotor current tends to oppose the stator mmf at the entry point, reducing the flux density just inside that end of the stator virtually to zero. The effect is entirely due to the high speed entry of rotor bars and to the ability of the rotor to "remember" the pattern of current printed on to it by the entry edge transient. In this context, a long "memory" is easily identified as corresponding with a machine of high Goodness Factor [2].

Williams' analysis treated the phenomenon as being comparable with the "beats" effect of two sound waves of nearly the same frequency. He saw a transient rotor current pattern, printed by the stator coils at the entry edge, travelling at rotor speed $\omega_r = \omega_s(1-\sigma)$ where σ is the fractional slip and ω_s is the stator field speed or synchronous speed. This wave therefore drifts in and out of phase repeatedly with the stator mmf wave proper and the resulting modulation of the airgap flux density can be represented as Fig. 1 shows.

On this graph the flux wave has been resolved into two components, B_p and B_q. The first of these is a flux wave in phase with the stator current loading wave $j_s = J_s \sin(\omega t - \pi s/\tau)$ whilst the second is in quadrature with it. The convenience of such a resolution is that the integral $\int B_p J_s$ is the mechanical power developed, and $\int B_q J_s$ represents the reactive power circulating in the machine. The total length of the machine can be measured along the abscissa of Fig. 1, and the number of waves under the active zone depends on the relationship between the fractional slip σ, and the number of stator poles in the sector, n. Thus for $\sigma = \frac{1}{2}/(n+\frac{1}{2})$ the stator ends at A. For $\sigma = 1/(n+1)$ the end of the block is at B. The points C and D correspond to slip values of $1\frac{1}{2}/(n+1\frac{1}{2})$ and $2/(n+2)$, respectively, and so on.

Now a conventional rotary machine recognizes no such behavior. If its performance were to be shown on a diagram such as Fig. 1, it is understood that such a comparison is made between machines of the same pole pitch, active length of periphery, fed with the same current loading J_s. (Such a machine is referred to as an 'equivalent conventional machine'.) In such a comparison the straight line PQ represents the B_p curve, and the baseline OR is the B_q curve. This comparison also assumes that neither machine requires magnetizing current (infinite Goodness) and neither has magnetic leakage

Several interesting points emerge from this analysis.

(i) For values of σ and n such that $\sigma < 1/(n+1)$ $\int B_p ds$ is less for the arc machine than the rectangle PB'BO, i.e. rotor losses above those in the equivalent conventional machine will occur. At precisely $\sigma = 1/(n+1)$ there will be no difference in output.

(ii) For values such that $1/(n+1) < \sigma < 1\frac{1}{2}/(n+1\frac{1}{2})$ more output per unit current will be obtainable from the transient-ridden arc motor than in the equivalent conventional machine. This is not a false claim for efficiency exceeding 100%. Rather, in the transient mode an induction motor may have a higher efficiency than predicted by the relation σ = rotor loss/rotor input.

(iii) At $\sigma = 2/(n+2)$ the two machines are externally indistinguishable, but internally the arc machine incurs a penalty (as it does for all values of slip between $\sigma = \frac{1}{2}/(n+\frac{1}{2})$ and $1\frac{1}{2}/(n+1\frac{1}{2})$) in that both the core flux and the tooth flux in the central regions of the arc exceed those in the equivalent conventional machine.

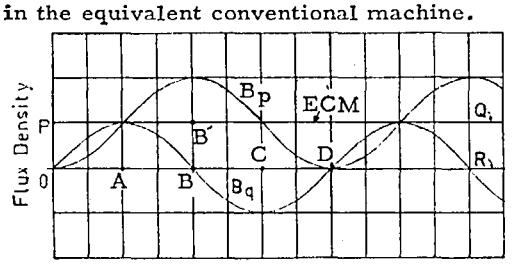

Fig. 1 Theoretical flux distribution in an arc machine.

F 80 273-3 A paper recommended and approved by the IEEE Rotating Machinery Committee of the IEEE Power Engineering Society for presentation at the IEEE PES Winter Meeting, New York, NY, February 3-8, 1980. Manuscript submitted September 4, 1979; made available for printing November 20, 1979.

(iv) For all values of slip other than $\sigma = 2/(n+2)$, $4/(n+4)$, $6/(n+6)$ etc, the value of $\int B_q \, ds > 0$.

It is this last phenomenon that gives rise to the technique that is the subject matter of this paper. For what is implied by (iv) above is that there is a third source of reactive VA that can be identified (the first two being conventional magnetizing current and leakage flux). This third method is seen to operate when every part of the machine is working under transient conditions, as if each bit had just been switched on.

Now it is rare in machines, indeed in the whole of science, that a positive effect occurs without the possibility of a similiar negative effect. In this case what would be required for a negative effect would be a mechanism to hold the flux values at point C in Figure 1, and to continue supplying B_p at the conventional rate yet to accumulate simultaneously an ever increasing amount of negative B_q.

The birth of Generalized Machine theory is recognized as being contained in classic papers by R.H. Park in 1929 and 1933 [3]. It was subsequently realized that there was basically no difference between the synchronous machines and the asynchronous machines (induction motor, a.c. commutator motor, etc). It is impossible to know, from measurements made at the primary terminals of an a.c. machine, whether what spins inside it and delivers mechanical power from its shaft is a cage rotor, a set of d.c. energized magnets, a set of permanent magnets, a commutated winding, a solid iron rotor with saliency or a thin cylinder of high hysteretic material (although one could often hazard a shrewd guess, based on the size of the machine so tested). Every phenomenon of the synchronous machine, e.g. hunting, can be identified in the induction machine (in this example, transient overspeeding). There is therefore no reason why the equivalent effect to that obtained by over-exciting a synchronous motor (unity or leading power factor) should not be possible in an induction machine. The mental block that tended to preclude it was that nothing physical (as opposed to things like flux that are creations of the mind) rotated at synchronism in the induction motor.

It is now seen however that there is such a physical thing - the rotor current pattern - "printed" on to the rotor from the stator, and we shall show how this can be augmented so as to cause it to act (over a part of the arc) in the manner of a second primary inductively fed from the first, capable, when the phase is correct, of delivering magnetizing current from the rotor side. In this it resembles the action of the moving-coil regulator, whose action was described in precisely these terms by Rawcliffe and Smith in 1957 [4].

EXPERIMENTAL INDUCTION CONDENSER

The first machine built to demonstrate the concept of reactive power generation is a 10 kW size, axial flux induction motor with 8 poles, but of the short-primary type in which the stator core is only a 90° arc segment rather than being continuous. In contrast to a rotor cage construction, the secondary is an aluminium disc 2.1 m in diameter, 9.5 mm thick supported by a solid magnetic steel disc 19 mm thick. The aluminium is a continuous disc to prevent rotor induced transients and the air gap can be adjusted from 1 mm to 5 mm. The stator block has an arc length of 1.46 m with 54 slots, 14 mm wide by 38.1 mm deep on a 27 mm pitch. Forty-eight coils with 12 turns/coil are wound on to the stator and connected as shown in Figure 2. The connections provide three different field speeds when energized with a single frequency, 3 phase supply. In the winding, coils 1 to 22, section 1 provide three poles at pole pitch τ_{p1} =0.2025 m, coils 23 through 40, section2 also provide three poles but at a pitch τ_{p2} of 0.162 m, and coils 41 to 48 provide two poles at a pitch τ_{p3} = 0.108 m.

As the slip varies, the effect of sections 2 and 3 changes. For example, at a slip of 0.5 per unit for section 1, this construction produces a slip of 0.375 for section 2 and 0.062 for section 3, all three sections giving some forward thrust to the rotor. However, at high speed, sections 2 and 3 can be considered as forming a generator of reactive VA which operates without significant braking thrust, while section 1 provides the propulsive thrust, drawing power from the supply at a lagging power factor typical of a short primary induction motor. At a slip of 0.25 for section 1, the slip of section 2 is apparently +0.062 and for section 3 is apparently -0.406. It must be remembered that the whole of the pole surface is operating under transient conditions, and provided that sections 2 and 3 are phase advanced with respect to section 1 either by winding layout or by the use of an external phase shifter, both the last two sections are reactive generators in both the negative and positive slip modes of operation. The single most important operational aspect of this VAR generation is that the slip for the propulsion section must be smaller than about 0.25 per unit.

To confirm that the output performance can be correlated with the precise electromagnetic conditions in the airgap, each stator tooth is fitted with a search coil to permit tooth flux measurements to be made at slot pitch resolution without a noticeable contribution of slot leakage flux. The transverse running search coil wires are mounted in 0.5 mm deep groves machined in the center of each tooth face; with such instrumentation

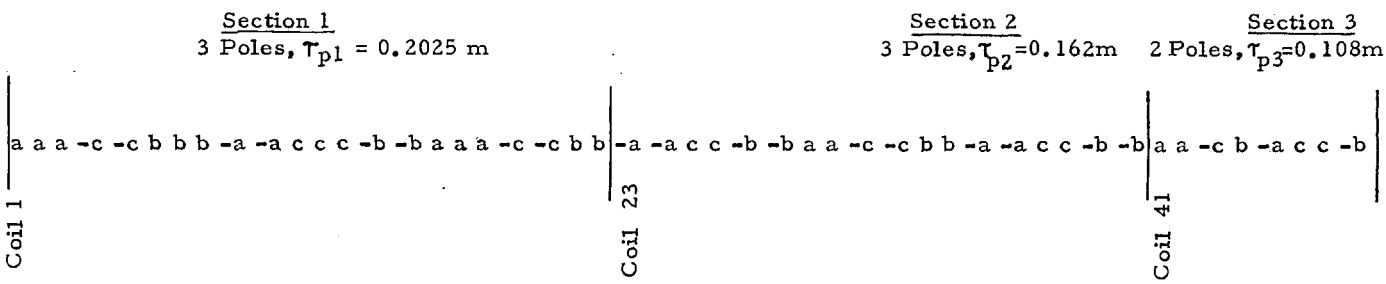

Fig. 2 Stator winding layout for the first experimental integral induction motor-asynchronous condenser.

it is possible to determine the Maxwell stress vector at any point in the airgap for use in calculating rotor torques. A magnitude plot of the total, normal component of airgap flux density, B_t in the experimental machine is given in Figure 3 for high speed and supersynchronous operation (with respect to the section 1 winding). In this machine, the tangential component of airgap flux is insignificant. The figure depicts two sets of plots whereby the asynchronous condenser (ASC) windings are either open-circuited or on line. The current loading of the stator has been established at 34,600 A/m periphery throughout these runs and the ASC section current loading is maintained at 14,500 A/m. The important conclusion is that the flux build-up of section 1 is nil affected by the loading of the ASC as long as the latter is operated in phase-quadrature. This has been confirmed by the output characteristics which have shown that power factor control takes place with the propulsion windings remaining at constant efficiency; the I^2R losses for the ASC stator windings being supplied by the mains rather than rotor supplied.

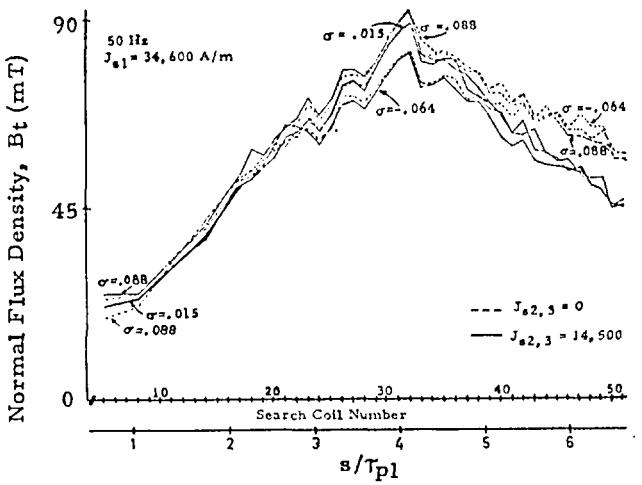

Fig. 3. Total airgap flux density as a function of block location at high speed and supersynchronous.

Secondly, from Figure 3, the demagnetizing effect of the ASC loading on the airgap flux, equivalent to the armature reaction in a conventional synchronous condenser, is apparent and this is independent of the rotor current decrement which will be described by a single exponential decay in the analysis.

Initially the ASC sections 2 and 3 were isolated from the propulsion windings and connected to a bank of high-Q, air core inductors. Individual phase measurements of the ASC section coils indicated that nearly all of the section 2 coils were operating as anticipated along the quadrature axis but the last 1/3 pole of section 2 and the two poles of section 3 were absorbing reactive power. Most important, independent of the sections 2/3 slip, the rotor current decrement was partially responsible for this loss in output although Figure 3 indicates that the rotor current time constant was long enough to maintain sufficient excitation over 5 poles of the stator surface. In effect, the solution is to initiate a second current jump in the ASC section; subsequently the last 9 coils of the first machine were rewound with 36 turns/coil.

Although a graduated change in the ASC current loading is preferable, further tests confirmed that the step change in coil reactance so described proved to

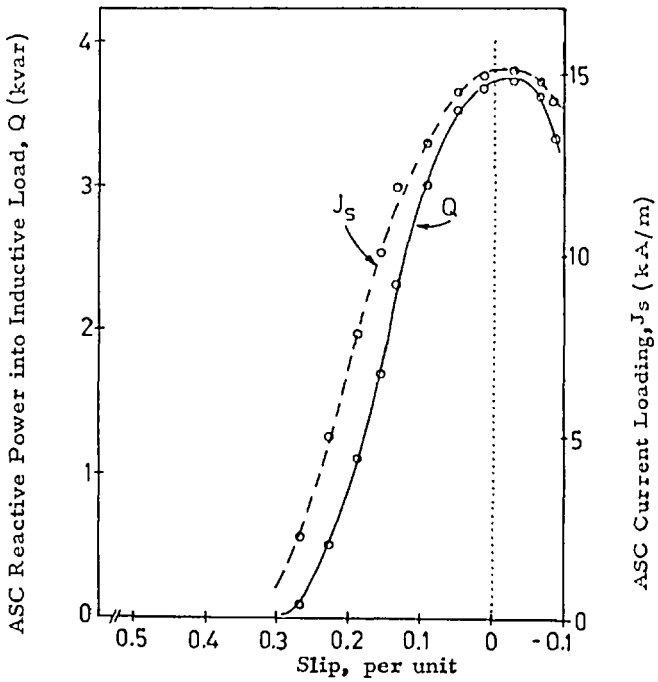

Fig. 4. Asynchronous condenser terminal output and current loading.

yield an asynchronous condenser section with all coils operating at phase angles between 78° and 110° when connected on-line. The output performance of this "two-stage j-jump" asynchronous condenser is shown in Figure 4.

ANALYSIS

Over a limited range of high speed conditions, it is possible to represent the combination induction motor -var generator by the simplified equivalent circuit of Figure 5. However, the first reservation that must be noted is that while stator parameters X_1, R_1, X_3 and R_3 are the same from pole to pole, the main magnetizing reactance X_{m1} or the quadrature magnetizing reance as seen by the rotor X_{m3}, are not the same on a per pole basis. Rather, these magnetizing reactances range from being nearly a short-circuit at the first pole to a value at the last pole of the main winding well above the overall magnetizing reactance measured at the terminals; a similiar condition holds for the R_2 parameter in trying to make a conventional-type steady state equivalent circuit adaptable for a machine with a continuously occuring space transient. The ratio of the magnetizing reactance to rotor resistance has been found to be essentially constant over the entire machine. Therefore as a matter of convenience to avoid specifying different

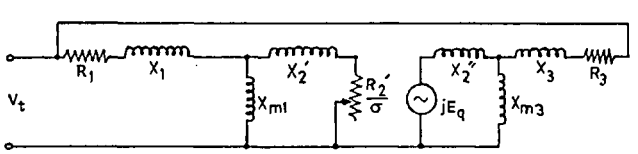

Fig. 5. Equivalent circuit of integral induction-motor/ asynchronous condenser machine.

circuit parameters for each pole or coil, this ratio is assumed to be constant and expressable as [2]

$$G = \frac{2\tau_p^2 \mu_o f \delta}{\rho_r \pi g} = 2\pi f T_r \quad (1)$$

where T_r is defined as the rotor-magnetization time constant and G is referred to as the machine "Goodness Factor". The major advantage of using a figure of merit such as G is that analytical expressions for both the transient and steady-state flux density at any point along the airgap, or real and reactive power thereof, can be expressed in a closed-form solution.

The total instantaneous flux density in the air-gap of a short-stator machine may be represented as

$$b_s = B_p \sin\omega t + B_q \cos\omega t \quad (2)$$

where B_p and B_q are the normal-flux density components at position s from the entry-edge of the stator, in time-phase and quadrature with the stator current, j_s at s in the case of zero entry edge flux. Their basic relationship is shown in Figure 1 but to include the air-gap magnetization these components are [5]

$$B_p = \frac{J_s \rho_r u_s \sigma}{(\sigma u_s)^2 + (u_s/G)^2} \{1 - \exp[-s\pi / \tau_p(1-\sigma)G] \cdot \left[\cos\frac{s\pi\sigma}{\tau_p(1-\sigma)} + \frac{1}{\sigma G}\sin\frac{s\pi\sigma}{\tau_p(1-\sigma)}\right]\} \quad (3)$$

$$B_q = \frac{J_s \rho_r u_s/G}{(\sigma u_s)^2 + (u_s/G)^2} \{1 - \exp[-s\pi/\tau_p(1-\sigma)\ G] \cdot \left[\cos\frac{s\pi\sigma}{\tau_p(1-\sigma)} - \sigma G \sin\frac{s\pi\sigma}{\tau_p(1-\sigma)}\right]\} \quad (4)$$

The resultant travelling wave attributable to the B_p and B_q components may be regarded as due to separate steady-state and transient phenomena, for in the case of the former both the phase and quadrature components are due to stator current interacting with the component of rotor current that is maintained indefinately by the agency of slip. This is the final steady state flux at points distant from the entry-edge and corresponds to the flux in a conventional machine of equal construction labeled the ECM level in Figure 1 for B_p. The small element of B_q is attributable only to the excitation winding magnetizing current and the large value B_p corresponds with the real power load current.

The transient component of the total flux is equal and opposite to the steady-state value at the entry point but is due to the excess currents induced in the rotor which decay with the time constant T_r. Moreover, the transient airgap flux wave not only differs from the first component in terms of a decay in magnitude, but travels at rotor speed u_r whereas the steady state component travels at u_s. The basis of effecting reactive power generation is centered on exploiting this slightly slower rotor transient wave, which by itself is a harmonic-free sinusoid. Consequently, the reduced pole-pitch for the special asynchronous condenser windings is theoretically linearly proportional to the rotor speed.

To utilize the transient traveling wave effectively, the two most basic considerations are that:

a) the ratio of the asynchronous condenser pole pitch to the motoring pole-pitch follows the ratio of rotor speed: synchronous speed rather than being related by the factor $(1-\sigma)/\sigma$ as might be deduced from (3).

b) the electrical frequency induced in the condenser windings is always at the same frequency that excites the motoring winding independent of rotor speed.

To appreciate these two guidelines, (3) and (4) must be substituted in (2) to yield the total instantaneous flux density

$$b(s,t) = \frac{\rho_r J_s}{u_s\sqrt{\sigma^2 + (1/G)^2}} \{\sin\omega t - \frac{s\pi}{\tau_p} + \tan^{-1}(\frac{1}{\sigma G})\} - \exp\left[\frac{-s\pi}{\tau_p(1-\sigma)G}\right] \{\sin\omega t - \frac{s\pi}{\tau_p(1-\sigma)} + \tan^{-1}(\frac{1}{\sigma G})\} \quad (5)$$

The total peak value of b(s,t) at any location is $B_t = (B_p^2 + B_q^2)^{\frac{1}{2}}$. Therefore, to maximize the utilization of the condenser windings the pole-pitch of section 2 or 3 must be

$$\tau_{p2,3} = \tau_{p1}(1-\sigma) \quad (6)$$

In the first experimental machine, the section (3) pole-pitch was further reduced from that of the first in the interest that possibly the electromagnetic interaction between the two asynchronous condenser sections would require a two-stage pole reduction since the section 2 might initiate a strong and new rotor transient. However, it was found that the rotor current pattern initiated by section 1 was stiff enough to dominate any subsequent demagnetization occuring at a smaller wavelength. Thus in general, if both sections 2 and 3 are used exclusively as reactive power generators, then they must be the same pole-pitch but of different reactance levels. In the event that an application would call for section 2 to be a var generator while section 3 might be used in isolation as a real power machine then there would be an advantage to using three distinct wavelengths on the stator. Alternatively, the experimental machine in lieu of including pole-changing windings in the ASC section, has two maxima of reactive performance in terms of coil utilization.

For the section 3 condenser winding, the reactive energy maximum occurs near a slip corresponding to the first discernible peak of the exit-edge product VA $*u_r$ energy which corresponds to the case of m=1 in the general expression

$$\sigma = \frac{2m+1}{n+2m+1} = 0.50 \quad (7)$$

where m is an integer value and n is the number of poles of the motoring winding. The section 2 utilization peaks at $\sigma = 0.20$ which is significantly less than the experimentally obtained kVAR-build-up slip of 0.25 as per Figure 4 but exactly at the theoretical maximum airgap-efficiency slip. In commercial applications, either the ASC would consist of a single pole-pitch distinct from the main pole-pitch, or in the case of two frequently used machine speeds, two pole pitches closer in wavelength than the "two-stage, j-jump" laboratory machine.

The upper limit on the reactive power available per unit of exit-edge stator width beyond the main winding section 1 for recovery is

$$Q = \frac{g\, B_q(s^*)^2\, u_r}{4\,\mu_o} \int_0^{n_2 \tau_{p2}} e^{-\frac{(s-s^*)}{\tau_{p1}(1-\sigma)G}}\, d(s-s^*) \qquad (8)$$

where the value of B_q is obtained by evaluating (4) at $s^* = n_1 \tau_{p1}$. The rotor current decrement in the asynchronous condenser sections are included by the integration in (8) for the case of zero armature reaction. To include this demagnetizing effect, under the constraint that the ASC is supplying a purely reactive load and that the rotor leakage flux is negligible, the peak value of the quadrature flux density for values of stator position $s>s^*$, is

$$B_q = \frac{X_{asc}\; J_{s1}\left[1 - \exp(-s^*\pi/\tau_{p1}(1-\sigma)\,G)\right]}{\sigma\, u_s \cot\left[(s-s^*)\pi/\tau_{p2}\right] - X_{asc}\; g/4\,\tau_{p2}\,\mu_o} \qquad (9)$$

where X_{asc} is the total reactance of the winding leakage flux and the equivalent reactance offered by the mains when referred to the airgap and is given by

$$X_{asc} = \frac{X_{leakage}}{\text{series turns/phase}} + \frac{Q_{output}/3}{J_{s2}^2} \qquad (10)$$

Figure 6 shows the general shape of the generated reactive VA characteristic normalized with respect to the real power absorbed as rotor loss in a conventional machine (which is $\frac{1}{2}\rho_r J_s^2 n_1 \tau_{p1}$) as a function of slip and ignoring the effects of the natural rotor decrement and ASC armature reaction, for the specific case of 4 poles of motoring winding.

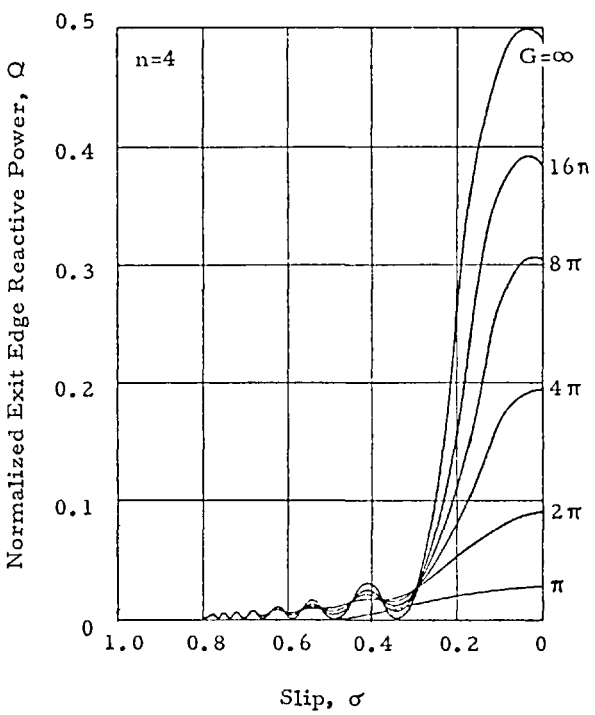

Fig. 6. Effect of magnetizing current on exit-edge reactive power.

THE THETA-PINCH ROTARY MACHINE

With a view towards extending the induction condenser principle to large squirrel-cage induction motors, a commercial 35 H.P. 10/12-pole machine with pole-amplitude-modulation (PAM) windings was chosen for modification. The speed changing capability itself is not a major concern, however the choice of a multipolar is crucial. The creation of the proper transient conditions in the machine must occur at large slip-pole number products but obviously efficiency considerations demand that the slip be small. In contrast to the discontinuous core of the two-stage, j-jump axial flux machine, the new design constraints on the cylindrical motor are as follows.

a) To minimize the effects of unbalanced magnetic pull on the rotor, the stator must have at least 2 repeatable sections (i.e. 180° mechanical magnetic symmetry) or multiples thereof.

b) Since the Goodness Factor, G is nearly an order of magnitude better than for the first experimental machine (due primarily to the cage construction), the effects of the rotor current natural decrement are negligible in comparison to the armature reaction.

c) A continuous, conventional stator core with uniform slot-pitch is permissible and the rewound machine runs at a 10-pole speed although the actual number of poles is less than 10.

d) It is convenient for manufacturing reasons to have a form of lumped ASC winding although a distributed reactive winding mixed with the main winding along the entire periphery has some theoretical advantages. The former approach necessitating that specific segments of the stator be allocated exclusively to power factor correction is henceforth referred to as the "Theta-Pinch" technique.

Figure 7 shows a possible distribution of the winding portions in a cylindrical machine with symmetrically-spaced slots of equal width. Stator and rotor

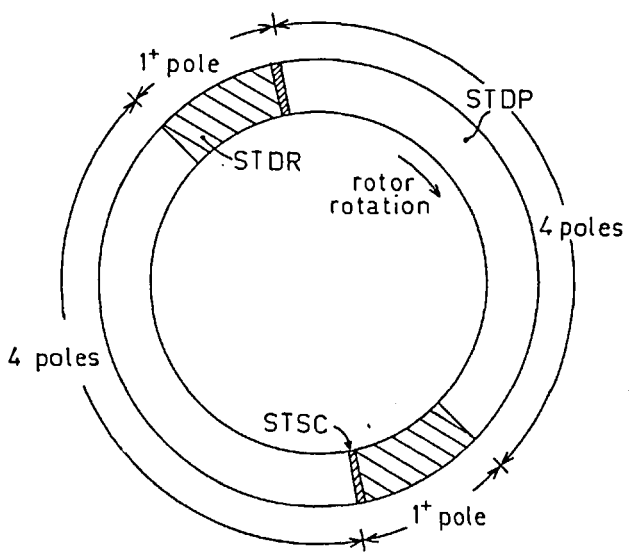

Fig. 7. General location of stator winding sectors in the Θ-Pinch machine with two repeatable sections.

details are given in Table I. Each repeatable section of the power winding, STDP is (without pole amplitude modulation) a conventional 4-pole, 3-phase winding of 3 slots/pole/phase. The reactive recovery stator winding, STDR has "1 plus" poles of high impedance, i.e. 28 turns/coil instead of 6 for the power winding. The total pole layout is $4\text{-}1^{+}\text{-}4\text{-}1^{+}$. The "1 plus" indicates that there is greater than 1 ASC pole in the original one pole space due to the reduced wavelength of the ASC. These windings are connected directly to the power winding without the use of an external phase shifter.

Table I

Characteristics of the Θ-Pinch Rotary Machine

Stator	
Bore diameter, mm	316
Number of slots	90
Copper cross section, mm^2	5.25
Coil throw slots	1-11 incl.
Core length, mm	235
Slot depth, mm	34
Slot width, mm	6.0
Slot pitch, mm	11.1
Coil span, m	0.111
Pole-pitch, m	0.0989
Turns per coil	variable
Pole-pitch: airgap ratio	>150
Winding factor	0.756
Airgap flux density on load, T	0.62
Maximum current loading, A/m	29,700
Rotor	
Number of bronze bars	80
Bar width, mm	5.0
Bar depth, mm	8.0
Copper end ring, mm	6.5 x 25.4
Slot pitch at bottom of slot, mm	10.9
Tooth top width, mm	10.0
Ratio slot opening: airgap	1.5

The appropriate phase offset between power and condenser windings has been built into the machine by winding design. This means that a particular layout is only exactly appropriate for one supply frequency, one voltage, one load and one slip value at which nil braking torque exists despite recovery of reactive power. Semiconductor devices could be included in selected windings to extend the passive operating mode by providing automatic variation of phase to maximize reactive output during load changes.

The one simplification introduced in the first experimental Θ-Pinch machine was that all of the original coils with uniform span were utilized in both power and condenser windings. This was permissible in the first lab machine because the full load slip was less than 5%. However, if there is a phase error of rotor induced voltage in the first stator coil at the entry-edge of the ASC section, successive coils have progressively larger phase errors, unlike conventional machinery which have a constant value of phase error/coil. Techniques such as fractional slot windings for the ASC only, or greater than two ASC arcs along the stator may be incorporated so that the accumulative phase error is always small, but in general two distinct wavelengths are vital.

The major advantage of the Θ-Pinch method over the two-stage, j-jump type is that the space distribution of the airgap flux at the entry-edge of the power winding in the former will never start at zero. The time that any rotor bar passes under the transition region between power windings of adjacent repeatable sections is relatively small in comparison to the time spent under the power winding proper. Consequently, for all practical Θ-Pinch machines with N poles of condenser winding, the maximum deviation of the total air gap flux is approximately

$$\Delta B_t \approx \tfrac{1}{2}\left\{1 - \exp\left[-N\pi/(1-\sigma)G\right]\right\} \qquad (11)$$

Thus when running light at 50 Hz, the experimental machine has about a $2\frac{1}{4}\%$ variation in B_t based on a Goodness Factor of 70 or greater. Under optimal experimental conditions, the current loading of the ASC has been operated up to the value

$$J_{s(asc)} = J_{s1} - 2\,J_{s(magnetization)} \qquad (12)$$

for which it was found that the maximum value of ΔB_t is under 8%.

Figure 8 depicts the distribution envelope of total airgap flux density for the Θ-Pinch machine of Figure 7. τ_r is the notional pitch of a recovery pole which is less than that of a propulsive pole τ_p. Line $B_{t(ecm)}$ is the total nominal level of flux in the airgap for a conventional induction motor using the same rotor and core size. The range of slip for which the plot is valid is from zero to 0.20 per unit.

The asynchronous condenser so described can be operated in an adjustable power factor mode either by thyristor switching of winding connections to effect a different phase shift, or alternatively, a continuously variable method can be used whereby the phase of the rotor flux can be advanced. The latter is accomplished by including one or more short-cicuiting coils in the stator slots between the exit-end of the recovery winding and the start of the propulsive winding, labeled STSC in Figure 7. With this arrangement, phase control is simply performed by regulating the magnitude of the short-circuiting-loop current according a specific load/slip profile; additionally the connection of these loops from diametrically opposite poles in series aiding then allows superior compensation of fluxes initiating an unbalanced magnetic pull condition.

For reference purposes, the in-phase and quadrature flux densities for the two-stage, j-jump machine are shown in Figures 9a and 9b for an extended motor sector of 9 poles.

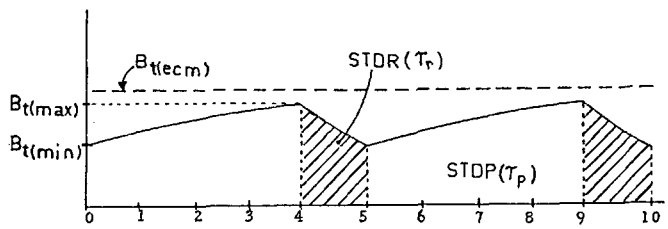

Fig. 8 Distribution envelope of total airgap flux density for a general Θ-Pinch machine.

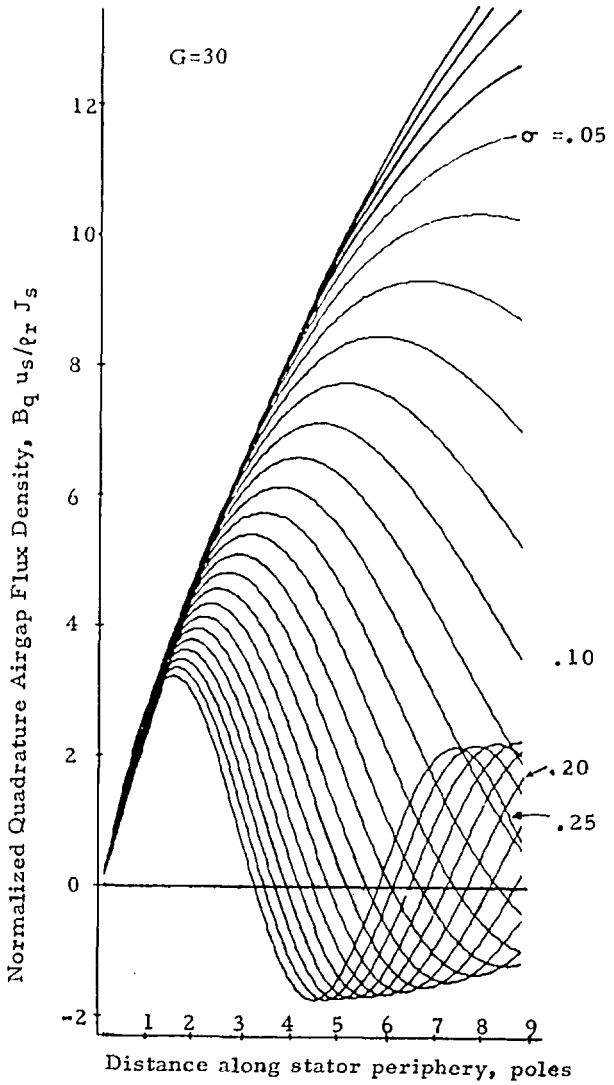

Fig.9a Quadrature airgap flux density in motoring sector of the two-stage, j-jump arc machine.

These two plots represent the minimum condition for which the rotor-current decrement is no longer characterised as being prominent, i.e. the value of $G(1-\sigma)/n > \pi$ at the transition point between motoring and condenser sections for the near-optimum, full-power slip of 5%.

HARMONIC CURRENT FILTER

As an alternative to power factor improvement, the Θ-Pinch concept may be applied as a harmonic current filter to suppress incoming line transients. By winding design only, the pitch of the ASC section can be so designated that the reactance it offers to any one specific line harmonic is equivalent on a per-unit basis to the transient reactance of a synchronous machine thereby allowing the propulsive winding to receive a substantially-sinusoidal current waveform. As with conventional synchronous condensers, the ASC winding in absorbing a whole spectrum of line-transients imposes additional thermal loading on the rotor cage. The scheme is generally valid for rotors of high inertia and thus again the multipolar machine is favorable.

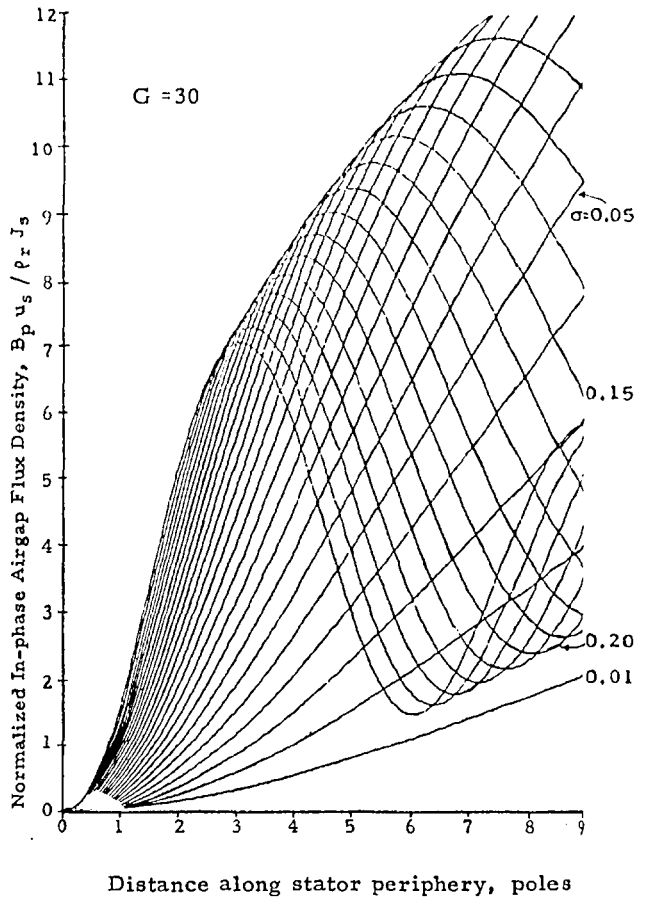

Fig. 9b. In-phase flux density in motoring sector of the two-stage, j-jump machine at high speed.

In context to variable-speed propulsion systems whereby variable frequency is generated by a square wave, current-source inverter and fed to a Θ-Pinch cage motor, the ASC winding in addition to providing the commutation margin for the inverter, also can be designed to have its reactance minimum at the 5th harmonic of the main travelling wave in order to best suppress the dominant harmonic of the inverter.

Implicit in the Θ-Pinch propulsion system, the inverter firing angle is advanced in response to the value of the B_p decrement directly sensed by airgap coils, in addition to the conventional method of torque control in a closed-loop regulator with slip and mains current feedback. As has been suggested by Lipo [6], the proper regulation of brushless induction drives under time-transient conditions should be accomplished by the use of flux coils (typically 3 per axis) along the stator slots; a similiar case applies to the space-transient ASC system. However, the classical "field orientor" method of separating the magnetizing flux from the B_p flux in a symmetrical machine has to be modified in accordance with (3) and (4), since the d- and q-axes of the Θ-Pinch machine are always changing during run-up. Undoubtedly, two practical requirements are that the stator search coils must have at least slot-pitch-resolution and, further, these coils must be centered directly over the slot rather than surrounding a tooth [1]. Fundamentally, this latter approach reduces the third harmonic saturation problem mentioned in [6] and considerably simplifies the case for a series of interconnected

electronic integrators. Slot harmonics are invariably the major source of concern when using flux coils for closed-loop control, but fortunately in the two-stage j-jump machine, there are no prominent slot harmonics due to the use of an inductanced-limited, sheet rotor.

Figure 12 shows the Θ-Pinch propulsion system presently under construction, where both the phase delay rectifier (PDR) and current source inverter (CSI) are rated at 20 kVA. The three basic quantities being controlled are the DC link current, the inverter-firing angle and the short-circuiting loop current internal to the induction machine for advancing the phase of the rotor flux. The control scheme, anticipating line-commutation of the inverter by the ASC winding at very high speed, incorporates the PDR for zero-blanking of the DC link current until the transition to self-commutation occurs at about $\sigma = 0.08$ p.u.

The field-decomposition circuitry utilizes 12 air-gap search coils spaced at distances of

$$s = \left[1.5 + \frac{m(1-2\sigma^*)}{12\sigma^*} \pm \frac{1}{18} \right] \tau_{p1} \qquad (13)$$

where m=0 through 5 and σ^* is the operating slip.

FUTURE DEVELOPMENTS

Based on the most promising correlation between the space-transient theory of brushless, induction machines and the two laboratory machines built to date, it is anticipated that leading power factor operation will be attained on a slightly larger Θ-Pinch unit which will incorporate two distinct wavelengths. Since the key to attaining unity power factor operation at the terminals is primarily a matter of neutralizing the generated kvar against the stator slot and zig-zag leakage reactive requirements, it is felt that in a 200 B.H.P. cage machine, these reactances are low enough on a per unit basis to demonstrate the full potential of the Θ-Pinch mechanism. For this purpose, a 200 H.P., 8 pole unit is to be rewound in early 1980 using the principles underlying the first Θ-Pinch machine, tested on full load and results presented detailing the maximum power/weight ratio available with this technology.

CONCLUSIONS

A new mechanism of continuously generating reactive kVA from the stator of a brushless induction machine has been described and tested on a 10 kW and a 35 H.P. laboratory machine. The concept is independent of the usual magnetizing or leakage flux reactive power requirements common to all induction machines. Fundamentally, a space-transient magnetic wave, travelling at rotor speed must be artificially created and at least two distinct windings of different pole-pitch must be incorporated for full utilization. Calculations and experimental results seem to confirm that the per-unit kvar generation effect increases with machine size and rating, and that leading power factor operation of the entire machine is viable for large industrial motors and power system induction generators.

ACKNOWLEDGEMENTS

The authors would like to express their gratitude to Dr. C. J. Carpenter of Imperial College and to Professor M.G. Say of Heriot-Watt University for their helpful discussions, and to the National Research Development Corporation for financial support.

REFERENCES

(1) F. C. Williams, E.R. Laithwaite and L. Piggott, "Brushless variable-speed induction motors," Proc. IEE, vol. 104A, pp. 102-118, April 1957.

(2) E.R. Laithwaite, "The goodness of a machine," Proc. IEE, vol. 112, pp. 538-541, March 1965.

(3) R.H. Park, "Two-reaction theory of synchronous machines," Part I, Trans. AIEE, vol. 48, pp. 716-730, 1929 and Part II, Trans. AIEE, vol. 52, pp. 352-354, 1933.

(4) G.H. Rawcliffe and I.R. Smith, "The moving-coil regulator: a treatment from first principles", Proc. IEE, vol. 104A, pp. 68-76, February 1957.

(5) E.R. Laithwaite, Induction Machines for Special Purposes, Chemical Publishing Co., New York, 1966, pp. 39-92.

(6) T.A. Lipo, "Flux sensing and control of static AC drives by the use of flux coils", IEEE Transactions on Magnetics, vol. MAG-13, No. 5, September 1977, pp. 1403-1408.

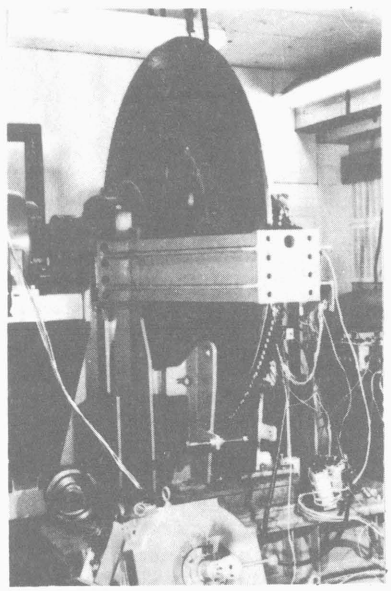

Figure 10. The axial-flux, j-jump ASC motor test rig.

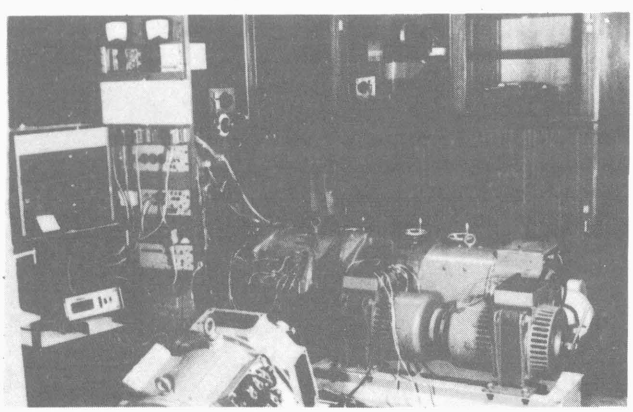

Figure 11. The Θ-Pinch machine test facility.

NOMENCLATURE

B = airgap flux density, peak
E_q = rotor induced transient voltage in stator winding
f = mains frequency
g = iron-iron electrical airgap
G = Goodness Factor
n = number of poles
m = mode number
R_3 = condenser winding phase resistance of stator
s = distance along airgap periphery from entry-edge
t = time
T_r = rotor magnetization time constant
u_s = synchronous field speed (m/s)
u_r = rotor speed
X_{asc} = reflected surface reactance of condenser wdg.
X_2 = rotor leakage reactance referred to stator
X_3 = stator leakage reactance of condenser winding
J_s = stator current loading, peak (A/m)

δ = rotor conducting-sheet thickness
ω_s = radian frequency
ρ_r = rotor conductor resistivity
σ = per unit slip
τ_p = pole-pitch
μ_0 = free-space permeability

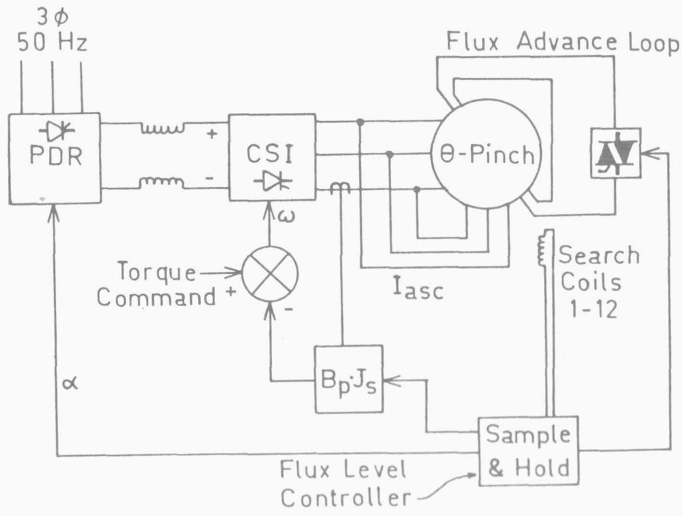

Fig. 12 Variable-voltage, variable-frequency AC drive system with Θ-Pinch motor used for inverter line-commutation and slip compensation of the rotor-flux phase angle.

Eric Laithwaite was born in Atherton Lancashire, England in 1921. He joined the RAF in 1941 and worked on automatic pilots at the Royal Aircraft Establishment, Farnborough. After the war he graduated at Manchester University, subsequently being appointed Lecturer, then Senior Lecturer. He received the Ph.D. and D.Sc. degrees in 1957 and 1964 respectively. In 1964 he became Professor of Heavy Electrical Engineering at Imperial College of Science and Technology, London, and also held the post of Professor of Applied Electricity at the Royal Institution from 1967 to 1976. A Director of Landspeed Ltd and Linear Motors Ltd, he also consults for Brian Colquhoun and Partners.

In 1966 he was awarded the Royal Society S.G. Brown Gold Medal for inventions relating to linear induction motors. He has written over 200 papers and 8 books on electrical engineering and allied subjects.

Stephen Kuznetsov was born in Pittsburgh, Pennsylvania on July 10, 1956. He received the B.S.E.E. degree from Carnegie-Mellon University in 1976 and completed the graduate training program in electrical machinery with Westinghouse Electric the same year. In 1974, he became involved with linear induction motor design while working for Garrett-AiResearch, Los Angeles on the 300 mph tracked-levitated research vehicle.

In 1977, Mr. Kuznetsov received the M.A.Sc. degree from the University of Toronto where he continued the research on the design of superconducting synchronous motors. Subsequently he was employed by Brown Boveri & Company, Switzerland as a designer in the large turbine generator division. Presently, he is a Ph.D. candidate in Heavy Electrical Engineering at Imperial College of Science and Technology where he specializes in research on self-excited induction machines and magnetic field analysis of superconducting generators.

Discussion

L. T. Rosenberg (Turbogenerator Consultant, Wauwatosa, WI): Elimination of collector rings and brushes from the motor or generator that operates at unity or a leading power factor, is indeed a worthwhile development. The Consolidated Edison Co. of New York could have saved several million dollars on the million kilowatt Ravenswood unit 3, had it not been necessary to rate it at 80% power factor in order to supply the reactive kVA taken by the thousands of induction motors on the Con Ed system. The energy savings through the years since 1965 involved in transmitting all that reactive current would have been worth even more than the initial cost saving.

Apparently two or more sets of windings are required in the stator and 8, 10, or 12-pole arrangements are possible, judging from the 10 kW and 35 hp examples described. Establishing a rotating flux pattern that remains at rotor speed, evidently permits separating the direct and quadrature axis currents in the normal driving circuit into direct and quadrature axis components, thus producing the output curves of Fig. 4.

I would like to ask the authors whether the design could be applied to two or four-pole, 60 Hz machines, and whether the fields created by the respective windings would not induce unwanted voltages and currents in eachother? Also, how does the torque vary with speed? Is the usual speed-torque curve of the cage motor still applicable? In other words, will the motor be suitable for widely varying load service?

Manuscript receved February 19, 1980.

S. B. Kuznetsov and **E. R. Laithwaite**: In agreement with Mr. Rosenberg's concern about the savings in energy and capital investment at the generator site, the proper application of the asynchronous condenser concept is as an integral winding with the main induction motor winding as it solves the high reactive current problem at the source, whereas present central power-factor correction using synchronous compensators or static capacitor banks still have to contend with the additional transmission losses associated with low power factor loads. It should be emphasized that in normal applications, two operating modes for the asynchronous condenser windings are apparent. First, the machine's terminal power factor may be raised to unity at the rated load and slightly above since the motoring section power factor alone is usually above 90% in large machines. Alternately, the ASC winding may be designed to peak at a slip value very close to or at zero, whereby the motor is running lightly loaded and the motoring winding power factor could be as low as 30%. Although it would be impractical to raise the terminal power factor to unity in the latter case, the option of maintaining a reasonable power factor such as 80% under light load is very attractive on a systems basis considering the extraordinary number of lightly loaded machines on the grid at any one time.

The rotary machine with 10 poles (denoted 4−1+−4−1+) followed as a natural development of the first linear machine of 8 poles with power factor correction windings. The choice of the number of motoring poles/repeatable section is a crucial parameter because the rate of rise or demagnetization of the airgap magnetic field for a given rotor time constant, is dependent on the combination of slip, σ and the exciting pole numbers. The concept of using space transients to affect appreciable reactive power generation at the exit-edge of the excited section is restricted to pole number-slip value products lying in the range

$$n^* R_2' < \frac{n^* \sigma}{1-\sigma} < 1.0 \qquad (14)$$

where R_2' is the per unit referred rotor resistance. The basis of this general guideline is that appreciable reactive power generation, Q denotes that the exit-edge power is greater than 0.25 per unit of the equivalent conventional machine rotor copper loss, $\frac{1}{2}P_r J_s 2 n \tau_p$. This value of Q will have a limiting value of 0.50 per unit for machines with a large Goodness factor when the rotor speed is at or near synchronous, as exemplified in Figure 6. However, prior to building up the maximum exit-edge energy, efficiency constraints demand that such a small slip never be used and hence, the inclusion of R_2' in (14). If the total number of poles around the periphery in the equivalent rotary machine is n, the effective number of motoring poles n^* never exceeds n/k since an even number of repeatable sections, k are mandatory so as to neutralize the effects of unbalanced magnetic pull. Therefore, it would be possible to produce an efficient unity-power-factor 4 pole machine at a low slip if only one repeatable section is attempted, but should two repeatable sections be used in practice, then the high-power-factor slip would have to be greater than 33% for which excess rotor losses would be incurred. Conversely, if the total number of poles is greater than 8, then operating slip values can always be between 20% (the latter being a typical per unit value of R_2) because of the greater freedom in choosing repeatable section lengths.

Should the question of the lowest feasible number of poles be readdressed to asking if shaft speeds in the region of 3600 RPM are practical at unity power factor, the answer is yes. For example, the use of the 10-pole "Θ-Pinch" machine in combination with a current source inverter operating at ideally 312 Hz would give an exact shaft speed of 3600 RPM. It should be emphasized that while this approach uses 6 power thyristors, it does not require any capacitor or forced commutation circuits since the induction machine naturally commutates the 6-component inverter; the rotor efficiency of this machine is 96%. The extent to which the inverter can operate below 312 Hz in this mode is dependent on the combination of leakage and magnetizing reactance requirements versus the thyristor turn-off time; in general the changes in Goodness factor with frequency are more crucial than the associated reactance changes. At this time, the theoretical problems involved with extending the asynchronous condenser concept to 2 pole and 4 pole machines are being investigated, although it is clear that the "Θ-Pinch," lumped ASC layout will not be used.

The fields created by the two sets of stator windings do not induce any significant transformer voltages in each other by virtue of their particular space separation. These windings are ideally, exclusively rotor motion coupled (as evidenced by the $J_{s(asc)}$ curve in Figure 4) and thus no stray voltages will be induced provided that the ASC winding comprises a speed-dependent pole-pitch which obviously has to be fixed depending on whether power factor correction is to be employed at either full load or running light.

The torque varies with speed as in a conventional cage rotor machine with low resistance bars. Using the conventional steady-state equivalent circuit and neglecting the stator resistance and the magnetizing reactance, the torque of the "Θ-Pinch" machine may be described under constant voltage excitation, V_t as

$$T \approx \frac{3 V_t^2}{X_1 + X_2} \frac{(\sigma - \sigma_o)\alpha}{\alpha^2 + (\sigma - \sigma_o)^2} \qquad (15)$$

where $\alpha = R_2/(X_1 + X_2)$. The only departure of this from an equivalent machine is the introduction of the quantity σ_0 which is the per unit difference in slip from zero at which zero torque occurs. The effect of producing torque either above or below synchronism has been well documented for linear and spherical induction machines [7, 8] and with respect to the Θ-Pinch machine the functional relationship of this slip offset is

$$\sigma_o = f\left(G, J_s / J_{s(asc)}\right)$$

In general if the Goodness is low or if the ratio of the main stator current loading to the ASC stator loading is near unity, the magnitude of σ_0 will be negligible and zero torque occurs at synchronism.

The only important consideration during startup under constant voltage is that asynchronous crawling can occur and this is dependent on the exact division between motoring and ASC poles. There is one significant harmonic synchronous speed in the Θ-Pinch configuration which can occur at a slip

$$\sigma = 1 - \frac{k n^* + (n - k n^*)/1 - \sigma^*}{n + 2} \qquad (16)$$

This is usually a problem in small machines unless pole-amplitude-modulation is used on just the motoring winding. Nevertheless, in the 150 H.P., 8 pole cage machine currently under test in a Θ-Pinch reconnection, no torque pulsations are evident which is due in part to the use of deep rotor bars.

Subsequent to submitting the main paper, the 35 H.P. laboratory machine was reconnected internally to extend the number of ASC coils from 18 to 24 at the expense of the motoring section length. A 50 Hz test was conducted with the recovery winding feeding an isolated inductive load (due to the low coil impedance) and the same cage rotor as before, with a rotor coupled time constant of 250 ms, was used. A stable slip value near 1% was maintained such that the reactive power

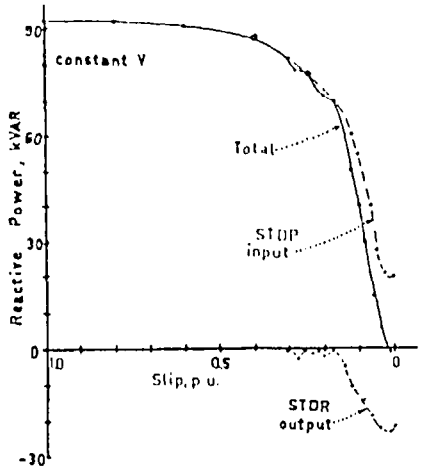

Fig. 13. Experimentally obtained reactive power generated and absorbed by machine sections.

generated by the recovery windings exceeded the reactive power supplied by the mains to the motoring winding, i.e. the machine consumed a net negative kVAR as shown in Figure 13. The total power input to the machine was 17.2 kW and the shaft was loaded to 12.6 kW, thus indicating an overall efficiency at unity power factor of 73%. The drop in efficiency from that of a standard cage motor is attributed to the use of an overchorded winding by 11/9 for all coils and a uniform slot-pitch around the entire periphery. The core loss of this machine is 0.34 kW and the stray load loss is 0.19 kW; other details of construction and analysis are give in [9].

REFERENCES

[7] F.C. Williams, E. R. Laithwaite and J. F. Eastham, "Development and Design of Spherical Induction Motors," *Proc. I.E.E.*, vol. 106A pp. 471-484, December 1959.

[8] K. Oberretl, "Three Dimensional Analysis of the Linear Motor," *Transport Without Wheels*, London: E.R. Laithwaite, Elek Science, 1977, pp. 217-247.

[9] E. R. Laithwaite and S. B. Kuznetsov, "Reactive Power Generation in High Speed Induction Machines by Continuously Occurring Space Transients," Paper No. 0090-09-03, *International Magnetics Conference*, Boston, April 21, 1980, and *Magnetics*, Sept. 1980, Vol. MAG-16, No. 5, pp. 716-718.

Manuscript received April 4, 1980.

REACTIVE POWER GENERATION IN HIGH SPEED INDUCTION MACHINES BY CONTINUOUSLY OCCURRING SPACE-TRANSIENTS

Professor E.R. Laithwaite and S.B. Kuznetsov

Abstract - A new technique of continuously generating reactive power from the stator of a brushless induction machine is conceived and tested on a 10 kW linear machine and on 35 H.P. and 150 H.P. rotary cage motors. An auxiliary magnetic wave, travelling at rotor speed is artificially created by the space-transient attributable to the asymmetrical stator winding. At least two distinct windings of different pole-pitch must be incorporated. This rotor wave drifts in and out of phase repeatedly with the stator MMF wave proper and the resulting modulation of the airgap flux is used to generate reactive VA apart from that required for magnetization or leakage flux. The VAR generation effect increases with machine size, and leading power factor operation of the entire machine is viable for large industrial motors and power system induction generators.

EXPERIMENTAL INDUCTION CONDENSER

Figure 1 shows the distribution of the windings in the 35 H.P. rotary machine with symmetrically spaced slots of a conventional 10-pole frame. Each repeatable section of power winding, STDP is a 4-pole, 3-phase, overchorded winding with pole-amplitude-modulation coil connections. The reactive recovery stator section, STDR has "1+" poles of high impedance coils with respect to STDP to effect changes in current loading and phase. The "1+" indicates that there is greater than 1 asynchronous condenser pole in the original one-pole space due to the former's reduced wavelength, which is proportional to rotor speed. Thus a particular stator layout is only exactly appropriate for one load and slip value at which nil braking torque exists despite recovery of reactive power. The details are included in Table 1.

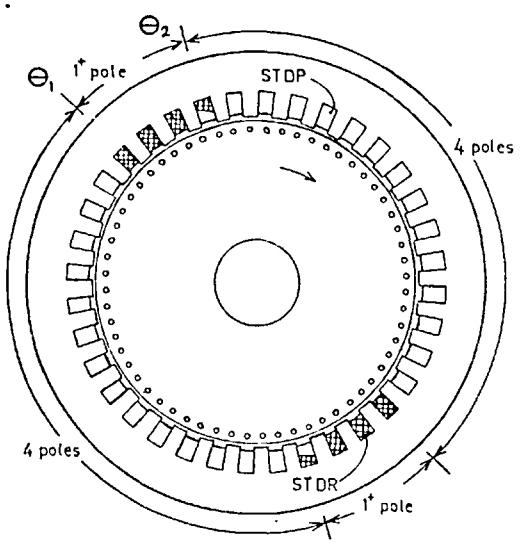

Fig. 1. Layout of the integral motor/induction condenser.

RESULTS

The first 50 Hz tests of this rotary induction condenser were conducted with the recovery windings feeding an isolated inductive load, and with a rotor magnetization time constant of 250 ms. A slip value near 1% was found such that the reactive power generated by the recovery winding exceeded the reactive power supplied by the mains to the motoring section, i.e. the machine consumed a net negative kVAR as indicated in Fig. 2. This was substantiated on both an electronic phase meter and an electrodynamic VAR meter on all three phases.

Table 1

Characteristics of the θ-Pinch Mk I Rotary Machine

Motoring Section (66 coils)		Condenser Section (24 coils)	
Pole-pitch, τ_p (m)	0.0989	Induced pole-pitch (m)	0.097
Core length (m)	0.222	Slot depth (mm)	34
Airgap (mm)	0.65	Airgap (mm)	0.65
Current loading, $\hat{J}_s$ (A/m)	33,400	Current loading (A/m)	29,750
Airgap flux density (T)	0.62	Slot pitch (mm)	11.1
Winding Factor	0.756	Chording Factor	0.95
Core loss (kW)	0.34	Total rotor bars	80
Copper loss (kW)	2.76	ASC copper loss (kW)	0.78
Stray load loss (kW)	0.19	Turns/coil	6
Reactive input, 1% slip (kVAR)	22	Reactive output (kVAR)	23
Power input, total (kW)	17.2	Core outer diameter (m)	0.42
Shaft output power (kW)	12.6	Overall efficiency at U.P.F.	73%

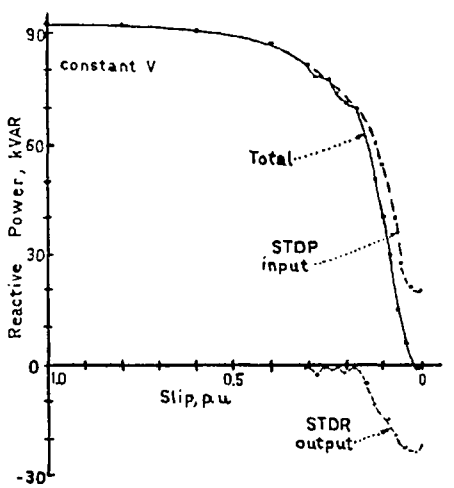

Fig. 2. Experimentally obtained reactive power generated and absorbed by machine sections.

ANALYSIS

The approach is one-dimensional in that only the radial component of airgap magnetic flux is considered. The cage rotor is modelled as having an equivalent sheet layer of conducting material of surface resistivity, ρ_r/t sandwiched between the rotor magnetic core and a magnetically anisotropic outer shell of thickness δ with an infinite radial permeability and a finite permeability, μ_r in the tangential direction to establish the rotor leakage flux path. This allows the useful nature of the rotor leakage flux to be represented as in rotary machines with small airgaps, g_e while the analysis presented in [1] on the linear version of the induction condenser assumed no rotor leakage flux.

The rotor flux is separated into two radial components, the main airgap flux and the rotor leakage flux; the other independent variable is the rotor current density. These apply to the excitation region, but

Manuscript received March 8, 1980.
Department of Electrical Engineering,
Imperial College of Science and Technology,
Exhibition Road, London SW7 2BT, ENGLAND.

when the ASC field is determined, the induced stator current density $J_{s(asc)}$ as well as its stator leakage flux are included. The stator leakage path of the excitation winding is not considered basic to the electromagnetics of VAR generation.

The characteristic equation for the excitation section airgap magnetic field density is

$$\omega T_2 \lambda^3 (1-\sigma)\dddot{B}_g + \lambda^2(1+j\omega T_2)\ddot{B}_g - G\lambda(1-\sigma)\dot{B}_g - jG B_g = -jG\frac{\rho_r \hat{J}_s}{u_s}(1 + j\sigma\omega T_2)e^{-j\theta} \quad (1)$$

where λ is the principal pole-pitch/π of region STDP and B_g is the airgap field density represented by a complex function in time and varies in space with respect to θ only. The rate of rise of the airgap field with peripheral distance is controlled by the product of the rotor magnetization time constant and the supply frequency ($\omega = 2\pi f$) which yields a non-dimensional

$$G = \frac{2\tau_p^2 \mu_o f t}{\rho_r g_e \pi} \quad (2)$$

The ratio of the leakage inductance in an axial-tangential cross-section of the magnetic shell to the surface resistivity of the conducting layer is termed the rotor leakage time constant

$$T_2 = \frac{\mu_r \delta}{\rho_r/t} \quad (3)$$

The general solution of (1) is, for B_g separated into the in-phase and time-quadrature components

$$B_p = \frac{\rho_r \hat{J}_s}{\sigma u_s \varepsilon}\left\{\cos(\theta) + \left[\sigma\omega T_2 + \frac{\sigma(\omega T_2)^2}{G} + \frac{1}{\sigma G}\right]\sin(\theta)\right\} + \mathrm{Re}\left[\sum_{n=1}^{2} A_n e^{\alpha_n \theta}\right] \quad (4)$$

$$B_q = \frac{\rho_r \hat{J}_s}{\sigma u_s \varepsilon}\left\{\left[\sigma\omega T_2 + \frac{\sigma(\omega T_2)^2}{G} + \frac{1}{\sigma G}\right]\cos(\theta) - \sin(\theta)\right\} + \mathrm{Im}\left[\sum_{n=1}^{2} A_n e^{\alpha_n \theta}\right] \quad (5)$$

where $\varepsilon = (1+\omega T_2/G)^2 + (1/\sigma G)^2$ and u_s is the synchronous speed.

The expressions to the L.H.S. of (4) and (5) represent the airgap for an equivalent conventional machine with 360° of excitation in the steady-state. However, the introduction of the abrupt edge in the excitation has introduced the two transients in the airgap flux as well as in rotor current and leakage flux.

For these space transients to be of use, their attenuation must be in the same direction as the main travelling field. Physically, the α_1 type follows this criterion and is attributable to the entry edge of the excitation section, i.e. the transition from the ASC to the STDP regions as located by θ_2 in Fig. 1. The α_2 type occurs here and also as rotor bars exit from the excitation region to the condenser region as located by θ_1. Fundamentally, both components of the α_2 are equal in magnitude but they propagate in opposing directions at much greater than rotor speed (e.g. 30 times for rotary machines). Since this type is attenuated quickly it is of minor importance, but the α_1 transient has a wavelength longer than any conceivable peripheral length of the condenser region, $(\theta_2 - \theta_1)\tau_p/\pi$. It travels at exactly rotor speed in the hypothetical case of zero airgap and slightly slower (2%) than rotor speed, u_r in the case of airgaps typical of rotary induction machines.

The α_1 is the subject of exploitation. If

$$\frac{1}{G(1-\sigma)^2 + \omega T_2} = \frac{R_2}{X_m(1-\sigma)^2 + X_2} \ll 1 \quad (6)$$

holds, which is generally true when close to synchronous speed, the α_1 transient may be approximated as [2]

$$\alpha_1 = -\frac{1}{\lambda}\left[\frac{1}{G(1-\sigma)^3 + \omega T_2(1-\sigma)} + j\frac{1}{1-\sigma}\right] \approx -j\omega/u_r \quad (7)$$

Under these conditions, such that $G \gg 1$ and $G > \omega T_2$, the α_2 effective wavelength is too large at normal operating speeds to affect the power or var transfer across the airgap or the induced condenser voltage. Rather, they are confined to the 4 transition regions of the machine (with 2 repeatable sections) and thus only function to match boundary requirements.

The condenser winding as seen by the rotor current is acting in a similar manner as the rotor is seen to behave by the main stator excitation. Thus, over a limited airgap angle, the rotor is acting as a second primary, inductively fed from the first (STDP). To complete the analogy, the equivalent of the rotor leakage layer as applied to the condenser winding is merely the sum of the internal leakage fluxes (due to slot, end-winding and zig-zag components) with the external reactive load placed on the ASC winding (as referred to the airgap). Similarly, the equivalent surface resistivity of the ASC section is the total of the windings and the real component of the ASC load; this also allows ρ_3' to be a negative resistance. Consequently, the condenser leakage time constant has been defined as

$$T_3 = \frac{\mu_3 \delta_3 + Q_{asc}/3J_s^2\omega}{\rho_3/t_3 + P_{in}/3J_s^2} = \frac{L_3}{\rho_3'} \quad (8)$$

Since the stator is the reference frame, no speed term is introduced in describing the induced voltage in the condenser winding. The ASC current is represented as

$$\lambda^3 \omega T_2(1-\sigma)\dddot{J}_{s(asc)} + \lambda^2(1+j\omega T_2)\ddot{J}_{s(asc)} - G\lambda(1-\sigma)\left(1+j\frac{G/\rho_r}{\rho_3'+j\omega L_3}\right)\ddot{J}_{s(asc)} - jG\left(1+\frac{\rho_r}{\rho_3'+j\omega L_3}\right)\dot{J}_{s(asc)} = 0 \quad (9)$$

The result is that the airgap flux over the ASC section may be expressed (neglecting the α_2 transient):

$$B_g = \frac{\rho_3'\pi(1-\sigma)}{\omega\tau_p}\left\{\left[\frac{1}{\omega T_2'} - \omega T_3\right]\sin(\alpha_\theta) - \left[1 + T_3/T_2'\right]\cos(\alpha_\theta) + j\left(\left[1+T_3/T_2'\right]\sin(\alpha_\theta) + \left[\frac{1}{\omega T_2'} - \omega T_3\right]\cos(\alpha_\theta)\right)\right\} K_1 \quad (10)$$

where K_1 is a complex number, a function of the phase and loading of the ASC electric circuit and on the relative length of the ASC winding in terms of main wave-lengths. To determine K_1, six independent boundary values and one integral condition must be satisfied for each repeatable section. At both the θ_1 and θ_2 transitions, the rotor current density, J_r, the airgap flux density, B_g and the total rotor sheet flux density must be continuous. The excitation field is

described by a third-order system while the ASC requires a fourth-order representation as in (9); a total of 7 integration constants are necessary. The last integration constant can be met by the integral of the induced ASC current which is always finite, and assuming a balanced polyphase load on the ASC

$$\int_{\theta_1}^{\theta_2} J_{s(asc)}\, d\theta = \left[1 - \cos\left(\frac{\theta_2 - \theta_1}{1-\sigma}\right)\right] \hat{J}_s \qquad (11)$$

This implies that the constants of integration for all airgap and rotor field parameters are jointly dependent on the proportion of a rotor wavelength(s) occupied by one condenser winding, as obviously odd or fractional number of poles are possible.

Irrespective of the value obtained in (11), the integral of B_q or J_r around the entire machine must always be zero based on a 1-dimensional analysis. Normally, a double layer polyphase excitation winding with balanced currents will have a zero net surface current around the periphery, however should the value of (11) be significant then the result is that while $\int J_r\, d\theta$ will remain zero, the condenser section will initiate a large zero-sequence component of current in the other stator winding STDP by way of the coupled rotor currents.

For machines with a high Goodness factor, G but not necessarily a small slip, it is generally true that when rotor current experiences an increase in amplitude (without large phase changes) this occurs in inverse-proportion to the ratio of the inductances into which the rotor currents must establish flux in the regions surrounding the "artificial" edges of the stator. Moreover, if the amplitude of J_r is increased at the boundary, then it follows that its decay rate will be similarly increased. The converse is also valid, and this was demonstrated on the first linear version of the induction condenser principle as described in [1] whereby an abrupt change in stator current loading between motoring and condenser sections was practical because of the low G value.

VAR GENERATION

To characterize the rotor current when it is being maintained by the agency of slip, it is only marginally "stiff" despite its inductance-limited impedance; J_r will exhibit sharp changes in both the in-phase and quadrature components so as to maintain gradual phase and magnitude changes in the airgap flux. However, over the ASC section, the added stator-inductance coupled to the rotor circuit as well as a possible reduction in the apparent rotor resistance mean that the rotor current is less susceptible to sharp changes.

In contrast, the airgap flux has a strong dependence on rotor velocity; principally the in-phase component will tend toward zero as synchronous speed is approached while the quadrature component rises in concert with the rotor speed for the excitation section. The exact division between B_p and B_q in the condenser section is strictly dependent on the ASC load phase angle rather than on speed. Fig. 3 is a contour plot of the B_q distribution in the condenser section airgap for different values of rotor plus ASC-coupled leakage time constant.

The single most important criterion for the generation of reactive volt-amps by maintaining a large value of negative B_q, is to ensure that at the transition from excitation to ASC windings, the total airgap flux density, $B_t = (B_p^2 + B_q^2)^{\frac{1}{2}}$ is as large as possible. The maximum volt-amps available at the "exit edge" is

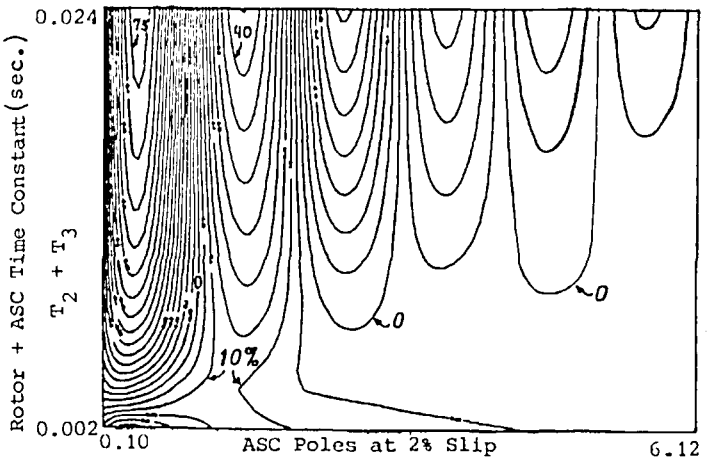

Fig.3 Lines of Constant $B_q(\theta_2)/B_q(\theta_1)$ Ratio in 5% steps.

$$S_{max} = \frac{g_e B_t^2 u_r}{4 \mu_o} \qquad (12)$$

If there are no sharp changes in airgap length at this boundary, then in practice the maximum reactive power available at this edge is $Q_{max} \approx S_{max}$ assuming the phase angle of the ASC load current is $\geq 80^{\circ}$.

Commensurate with the desired VAR characteristics of both stator windings in a high speed mode of operation, the quadrature flux density is always decreasing gradually from its peak at θ_1. Should B_q peak at a location other than this, such as midway along the excitation section, it is clear that the slip-excitation-pole-number product is above the value

$$\frac{n\sigma}{1-\sigma} = 2 \qquad (13)$$

Conversely, if B_q peaks at a location greater than θ_1 (in the direction of rotor travel), then clearly the ASC winding is consuming positive reactive power beyond that required for the leakage flux field.

FUTURE DEVELOPMENTS

Based on this theory of the space-transient effects in brushless induction machines and the two laboratory machines built to date, leading power factor operation of the entire machine will be attained over a less restricted range of slip and load for units which have a lower per unit slot and zig-zag leakage flux requirement. For this purpose a 150 H.P., 8 pole squirrel-cage machine is currently being retrofitted with two distinct wavelength windings, tested on full load and results will be available detailing the maximum power-to-weight characterizing this technology.

ACKNOWLEDGEMENTS

The authors would like to express their gratitude to Dr. H.R. Bolton of Imperial College for his many suggestions and to the National Research Development Corporation of the United Kingdom for financial support.

REFERENCES

[1] E.R. Laithwaite and S.B. Kuznetsov, "The asynchronous condenser: a brushless, adjustable power factor induction machine," Paper No. F-80-273-3 presented at the IEEE Winter Power Meeting, New York, February 5, 1980.

[2] E.R. Laithwaite, Induction Machines for Special Purposes. London: Newnes, 1966, p.86.

NATURAL COMMUTATION OF CURRENT-SOURCE THYRISTOR INVERTERS BY CAGE-ROTOR INDUCTION MACHINES

Professor E.R. Laithwaite, Fellow IEEE and S.B. Kuznetsov, Member IEEE

Imperial College of Science and Technology

London SW7 2BT ENGLAND

Abstract-A new type of brushless, cage-rotor induction machine has recently been developed [1-3] which is capable of providing enough counter-emf when interfaced with a current-source inverter (CSI) to naturally commutate the thyristors in a high-voltage DC-link, adjustable frequency converter. The basis of this system is that by stator electromagnetic design the induction motor may have the terminal characteristics of a DC-field synchronous machine yet still retain the torque and constructional features of a conventional induction machine. Four quadrant operation has been demonstrated on 35 and 150 H.P. cage motors and most important, leading power factor operation of the entire unit at full load is compatible with high power natural commutation of thyristor inverters. The single rotating machine has two distinct and different stator pole-pitches which must be excited from a common CSI. The analysis determines the magnitude of the cemf available from the asynchronous condenser winding and the consequent operation of the machine in both natural commutation and in a DC-link current pulsing mode for startup.

I. INTRODUCTION

In the art of variable speed ac drive systems, the use of either permanent magnet or overexcited, wound field synchronous motors to naturally commutate DC-link thyristor inverters has been well advanced. [4-5] Whether the magnitude of the cemf is adjustable at a given shaft speed is not of prime concern because the preferred propulsion arrangements generally allow constant volts/Hz control. Consequently, the ability of the synchronous machine to naturally commutate is fairly constant over large speed ranges. In this arrangement, the high voltage DC-link is adjustable by the use of a mains fed phase-delay-rectifier (PDR); the entire converter system comprises a total of 12 thyristor devices and a link smoothing inductor. It is apparent that unlike forced commutation schemes, no power capacitors or diodes are necessary. Synchronous drives provide continuously adjustable torque during motoring and braking modes; these schemes have been modified to include induction motors as the prime movers but with a synchronous compensator to effect inverter commutation. For the latter system, specific power densities as high as 0.436 kW/kg have been obtained for the entire 2 machine plus 2 converter unit propulsion system with water cooling [6].

The development of an induction machine commutated inverter started with assessing state-of-the-art CSI induction motor drives with synchronous compensators. Fundamentally, there is no reason why it is not possible to combine the most desirable electromagnetic features of a cage-rotor induction motor with the airgap fields of a synchronous condenser to use a common stator core and share the same airgap field, in contrast to present drives which have one machine entirely dedicated to torque production and the second concerned only with VAR generation. Generalized machine theory has always indicated that fundamentally the asynchronous-induction and the synchronous-wound field motor produce torque and consume VARs by exactly the same mechanism. The only major differences between these two are in the shaft speed and in the method by which the rotor currents are established. The advent of the adjustable frequency converter pointed to the fact that not only is the relation between mains frequency and shaft speed entirely arbitrary, but that induction drives would maintain the high efficiency of synchronous drives over a very wide speed range due to the use of constant slip control.

It was subsequently realized that as long as constant per unit slip could be maintained at a stable and low value in an induction machine, these same slip frequency currents could be used to establish the equivalent of a DC field pattern in a synchronous machine. It is not strictly necessary to feed (VAR generating) rotor currents by means of slip rings and brushgear, but that the desired rotor current pattern can be initiated by simple induction motor action.

The major criterion underlying the hardware development was to show that by induction alone, at mains or medium inverter frequencies, the equivalent MMF of an asynchronously operating integral motor/condenser would appear to be overexcited at the terminals of the entire machine once the conventional magnetization and leakage flux requirements were met. This was accomplished by artificially introducing a space-transient magnetic wave travelling at rotor speed into the airgap flux distribution of a conventional induction machine which has a torque producing synchronously travelling magnetic wave. Moreover, it was established that as long as the stator incorporates at least two distinct pole-pitches fed at the same fundamental frequency, the rotor suffices in every respect. Thus the power to weight characteristic of a cage construction can be

Reprinted from IAS CONFERENCE RECORD, September 1980

retained and while the overall weight of this leading or unity P.F. machine is 10%-15% less than a large lagging P.F. motor, once the additional weight penalty of either a synchronous condenser or a static capacitor bank is considered, the asynchronous condenser-motor concept permits a CSI drive specific power/weight ratio higher than 0.44 kW/kg without water cooling since only 1 rotating machine is used. Specific details are given in [7] for a 150 H.P. cage rotor traction system currently under development with natural commutation.

II. REACTIVE EMF

To establish the limits on the machine commutated inverter, the magnitude of the counter-emf offered by the asynchronous condenser windings will be derived. The machine geometries presently under evaluation using the "θ-Pinch" technique are specific to multipolar stator designs of 8, 10, 12 poles etc. θ-Pinch creates an abrupt transition in the stator MMF at two diametrically opposite positions along the periphery. The constructional features of this machine are similar to those in the single-winding, two-speed pole-amplitude-modulation induction motor in that the desired characteristics are achieved exclusively by stator winding design alone without the need for special laminations, auxiliary excitation or reluctance effects. In essence, the θ-Pinch machine is operating continuously and stably in a space-transient mode and with mains frequency will always have both sinusoidal current and voltage waveforms for every coil. Only when excited by a square wave inverter, will the machine be operating simultaneously in space transient and time transient modes.

The implication of this space-transient mode is that every pole (or slot) around the periphery is subjected to a slightly different airgap flux induction amplitude whereas in a conventional machine the rotating field pattern has a uniform amplitude at all positions. This means that the effective utilization of each tooth is non-uniform but more important from the aspect of calculating terminal performance, each pole has a slightly different magnetizing reactance, X_m, coupled rotor resistance, R_2 and rotor leakage reactance, X_2. The parameters X_1 of stator leakage and R_1 of stator resistance remain constant among the poles.

The conventional induction motor equivalent circuit is strictly a steady-state diagram and it should be emphasized that this representation does not indicate the slip frequency of rotor currents but conveniently interchanges a frequency dependent reactance with a constant resistance; this still permits the output power to be directly calculated from the R_2 parameters but the physical insight is lost. To allow some simplification in modelling space-transient machines, a single frequency equivalent circuit is presented in Figure 2 although several reservations are necessary.

a.) The conventional definition of slip, σ as rotor loss/rotor input is not accurate; thus σ only denotes the per unit difference between rotor and synchronous speeds.

b.) The parameters R_2, X_m, and X_2 are average values of all the poles in each section assuming the coils of a particular section are series connected.

c.) The relative magnitudes of the rotational reactances, X_m and X_2 as well as the absolute value of E_q, the counter-emf are only exactly valid over a limited range of low per unit slips at a particular excitation frequency. This frequency dependence of the inductances decreases as the pole pitch or frequency is raised.

The per unit values of Figure 2 are specific to a 150 H.P. unit at 60 Hz and σ=0.016 p.u.

All of the commutating criteria will be expressed in terms of a dimensionless factor

$$G = X_m / R_2 = \omega T_r \qquad (1)$$

where T_r is the rotor coupled time constant of magnetization and this remains substantially constant over the entire slip range. G can be calculated from conventional design formula even with a differing flux amplitude/pole. Although the airgap of the asynchronous condenser contains both a fundamental and subharmonic wave, it is possible to separate their effects and represent this in a closed form solution under the assumption that the rotor leakage is small. The total instantaneous radial flux density crossing the airgap over the motoring winding may be expressed

$$b(\theta,t) = \frac{P_1 \hat{J}_S}{\omega\sqrt{\sigma^2+(1/\omega T_r)^2}}\left\{\sin[\omega t-\theta+\tan^{-1}(1/\sigma\omega T_r)]\right.$$
$$\left.-\exp[\frac{-\theta}{(1-\sigma)\omega T_r}]\cdot\sin[\omega t-\frac{\theta}{1-\sigma}+\tan^{-1}(1/\sigma\omega T_r)]\right\} \qquad (2)$$

where θ= angle from transition point of condenser to motoring windings (electrical radians)

$\hat{J}_S$= stator current line density, peak (A/m)

$$P_1 = \frac{\rho\cdot\pi}{\tau_{p1}} = \frac{\text{rotor surface resistivity}(\Omega)\cdot\pi}{\text{pole pitch (m)}}$$

The first part of (2) is the steady-state component of the B field while the exponentially attenuated terms represent the addition of the transient wave.

As revealed by the second term, to maximize the output of the condenser winding which is magnetized by this total wave, the pole pitch of the motoring section, τ_{p1} must be reduced to $\tau_{p2}=(1-\sigma^*)\tau_{p1}$. The difference between the quantities $(1-\sigma^*)$ and $(1-\sigma)$, where the former is actively controlled by the inverter constant slip control loop, in effect gives a stator type of field control to compensate for the loss of a rotor exciter with this asynchronous machine.

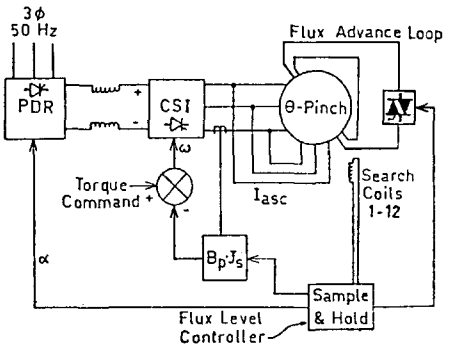

Fig. 1 Naturally-commutated induction drive system.

R_1=0.062 R_2=0.069 R_3=0.01

X_1=0.282 X_2=0.323 X_3=0.025 X_m=16.0 Ω

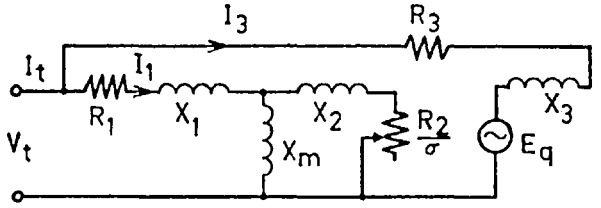

Fig. 2 Equivalent circuit of integral induction motor asynchronous condenser at high speed.

In the design stages, it is imperative that the space modulation of $b(\theta,t)$ peak at a position θ_1 which initiates the change in pitch from τ_{p1} to τ_{p2}.

$$b(\theta,t)=\frac{P_1 \hat{J}_s}{\omega\sqrt{\sigma^2+(1/\omega T_r)^2}}\left\{1-\psi\exp-\left[\frac{\omega t+\tan^{-1}(1/\sigma\omega T_r)-\pi/2}{(1-\sigma)G}\right]\right.$$

$$\left.\sin\left[\frac{2-\sigma}{1-\sigma}\left(\omega t+\tan^{-1}(1/\sigma\omega T_r)\right)-\frac{\pi/2}{1-\sigma}\right]\right\} \quad (3)$$

where $\psi \leq 1$ and represents the lower limit on the per unit flux density in the entire machine (at angle θ_2) at high speed. It is specific to a particular winding sequence and its functional relationship is

$$\psi = f\left[\cos\phi^{-1},\ G\ ,\ \cos\left(\frac{n\sigma\pi}{1-\sigma}\right)\right] \quad (4)$$

where n is the number of poles in section from θ_2 to θ_1 and ϕ is the power factor angle of the motoring winding alone. From the aspect of maximizing the condenser section cemf, E_q the generated reactive energy maximum occurs at the peak of the transition edge values in the product $I_q \cdot E_q \cdot u_r$ at a slip given by

$$\cos\left(\frac{n\sigma\pi}{1-\sigma}\right) = 1 \quad (5)$$

The commutation voltage, E_q is the integration of $b(\theta,t)$ over the entire length of the condenser section to yield the volts/turn as

$$E_q = u_r \int_{\theta_1}^{\theta_2} b(\theta,t)\cdot\exp[\nu_1(\theta_2-\theta_1)\tau_{p_1}/\pi]\, d\theta \quad (6)$$

where ν_1 is the complex attenuation of the space transient wave

$$\nu_1 = -\frac{\pi}{\tau_{p_2}}\left[\frac{1}{\omega T_r'(1-\sigma)^3+\omega T_2'(1-\sigma)}+j\frac{1}{1-\sigma}\right] \quad (7)$$

$$T_r' = T_r(1+\chi)^2 \quad (8)$$

$$T_2' = T_2(1+\chi) \quad (9)$$

$$\chi = \frac{X_2}{X_3 + Q_{asc}/q\cdot I_3^2} \quad (10)$$

for q=number of phases, I_3 = r.m.s. condenser current per phase, and Q_{asc} is the net output of the condenser winding. At the instant of commutation, this reactive power is related to the required inverter reactive power, Q_{inv} as

$$Q_{asc} = Q_{inv} + q(I_m^2 X_m + I_2^2 X_2 + I_1^2 X_1) \quad (11)$$

$$= Q_{inv} + q[I_1^2(X_1 + cX_2)] \quad (12)$$

for $c=1+X_1/X_m$. To find Q_{inv}, the solution for E_q from (6) is necessary but this is an iterative process because this voltage is dependent on the effective armature reaction of the asynchronous condenser which is controlled by the surface impedance of the stator. Conversely, the maximum reactive power that can be transmitted across the internal leakage and resistance of the condenser is a strong function of E_q and the terminal voltage of the machine, V_t

$$Q_{asc} = -E_q^2\frac{X_3}{R_3^2+X_3^2} - \frac{E_q V_t}{\sqrt{R_3^2+X_3^2}}\sin[\gamma+\tan^{-1}(-X_3/R_3)] \quad (13)$$

III. SUBTRANSIENT REACTANCES

One method commonly employed with CSI motor drives to determine the terminal voltage of the synchronous machine is to model the machine's reactance to 120° square wave current as comprising two components. The subtansient reactance, X" carries both fundamental and harmonic currents. The second "adjusted" reactance, in series with the subtransient is the difference between the synchronous and subtransient values or (X_S-X") but the voltage across this is only attributable to fundamental current. The values of X" in the d and q axes are generally assumed to be equal, whereas X_S is allowed to have a rotational variation. [5]

With respect to thyristor commutation, the exact reactance of the synchronous machine at the moment of current transfer is not as important as the time the inverter is in the overlap mode which is in effect a line-to-line short circuit on the machine. The resulting armature reaction MMF initiated every 60° at commutation appears as a large negative sequence current and the damper windings compensate for this. In large machines, the per unit negative sequence reactance and the subtransient reactance are nearly identical and about 10% of the synchronous reactance. In contrast, the stator leakage reactance can be as low as 5% of X_S. In a worst case condition, the synchronous condenser only maintains zero-sequence currents, $\hat{J}_{so} = 1\frac{1}{2}\,\hat{J}_{ss}$ where $\hat{J}_{ss}$ is the stator current loading at rated load. However, the damper cage will have a current loading $\hat{J}_r = \hat{J}_{ss} + \hat{J}_{so} = 2\frac{1}{2}\,\hat{J}_{ss}$.

For the asynchronous condenser, the subtransient response does not closely resemble the characteristics of a cylindrical rotor, DC-field compensator despite the construction similarities. Although not apparent, the cage rotor condenser is in essence a salient pole machine as viewed from the rotor side

due to the non-uniform (stationary) airgap flux distribution; i.e., the airgap reluctance variation of a conventional salient pole has been "artificially" created by an asymmetrical MMF design in a uniform gap. Yet even so, to a large extent in machines with G≥100, implying very good rotor to stator coupling, the in-phase and quadrature currents in the main winding of the stator essentially see the same transient reactance since the rotor MMF so closely parallels and opposes any unusual stator MMF distributions. This is characteristic of a cage rotor design with a small airgap where the currents are not series forced as they are in a wound rotor; rather the amplitude of these currents will have a space modulation to satisfy the change in pole pitch boundary conditions that demand semi-abrupt peaks in $J_r(\theta)$ at four positions over the stator periphery.

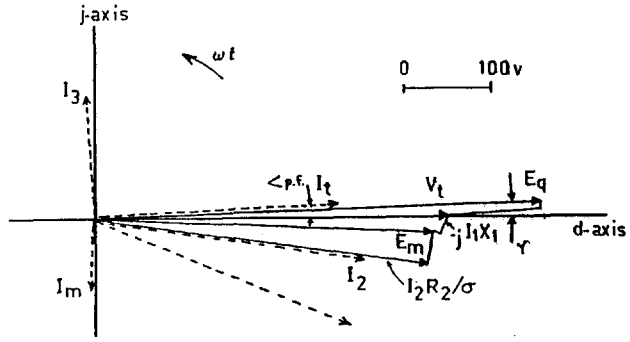

Fig. 3 Phasor representation of machine voltages.

To a first order degree, the steady-state equivalent circuit of Figure 2 and its associated phasor diagram of Figure 3 are also valid in a subtransient mode during commutation. The modifications that must be made are:

a.) The 120° square wave current should be separated into fundamental and harmonic components (h=5,7,11,13,etc.). The high frequency penetration effects in deep rotor bars can be calculated at each harmonic resulting in a higher R_2 and a lower L_2 parameter than at the slip frequency of the fundamental.

$$\frac{L_2(h)''}{L_2} \approx 1 - 0.00108\ d^2 r(\sigma_h \cdot f_h - 11.4) \qquad (14)$$

$$\frac{R_2(h)''}{R_2} \approx 1 + 0.00381\ d^2 r(\sigma_h \cdot f_h - 9.44) \qquad (15)$$

where d = rotor bar depth(cm), r = bar width:rotor slot width and σ_h is the effective per unit slip of the harmonic rotor currents. Formulas (14) and (15) are specific to rectangular copper rotor bars at 75°C and f_h is in Hz.

b.) The condenser internal voltage must be modelled as a single, fundamental frequency source that is only capable of power transfer at the fundamental frequency.

All of the other reactances X_1, X_3 and X_m scale up linearly with harmonic frequency and in general the change in passive parameters in an synchronous condenser/induction motor for subtransient operation is a minor effect. The major concern is the harmonic response of E_q; the magnitude of which remains substantially constant during commutation.

IV. COMMUTATION MARGIN

Conventional terminology is used in defining the CSI natural commutation interval as shown by Figure 4 for a three phase system of quasi-sinusoidal inverter output voltages and finite-rise-time square wave input current. α is the firing delay angle, u is the commutation overlap angle and δ is the commutation margin (or the maximum device-turn-off angle). Under all circumstances

$$\alpha + u + \delta = \pi \quad \text{radians} \qquad (16)$$

To express the commutating margin in terms of the equivalent circuit parameters of the asynchronous condenser, the three path (I_2,I_3,I_m) network of Figure 2 can be rearranged into a single Thevenin impedance, X" in front of a single Thevenin source E_q".

$$E_q'' = E_q\left[\frac{R_1 + cR_2 + j(X_1 + cX_2)}{R_1 + R_3 + cR_2 + j(X_1 + X_3 + cX_2)}\right] \qquad (17)$$

$$X'' = \frac{2[R_1X_1+R_1cX_2+cR_2X_1+c^2R_2X_2]+X_3(R_1+cR_2)+R_3(X_1+cX_2)}{(R_1+R_3+cR_2)^2 + (X_1+X_3+cX_2)^2}$$

To express the machine quantities in terms of the DC link current, I_{dc}, the normalized DC current is

$$I^* = \frac{2\ X''\ I_{dc}}{\sqrt{6}\ |E_q''|} \qquad (19)$$

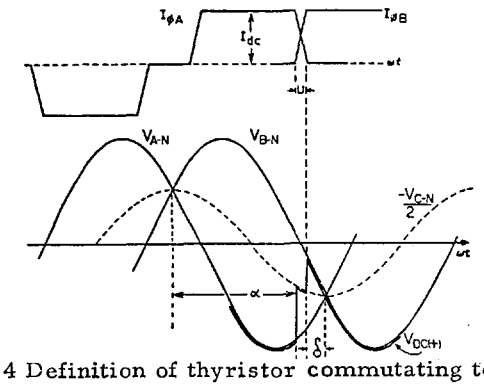

Fig. 4 Definition of thyristor commutating terms.

From conventional phase controlled rectifier theory, the ratio of the link voltage to the r.m.s. subtransient voltage, E_q''(line-neutral) is

$$\frac{V_{dc}}{|E_q''|} = \frac{3\sqrt{6}}{\pi}\left[\cos(u+\delta) + 0.5\,I^*\right] \qquad (20)$$

The effect of the commutating overlap u on the voltage regulation may be expressed as [8]

$$\cos u = 1 - I^* \qquad (21)$$

It can be assumed that the commutating margin will

always be small so that the approximation $\sin\delta \approx \delta$ may be used for δ in radians as

$$\delta = \frac{-\sin(u) + \sqrt{1 + \cos(u)\,[\,1 - 2\pi V_{dc}/3\sqrt{6}\ E_q"\,]}}{\cos(u)} \qquad (22)$$

Figure 5 is a plot of δ versus the ratio $V_{dc}/E_q"$ for different families of normalized DC-link current, I*. For a value I* = 0.4, it is seen that the converter: machine voltage ratio is 1.75at a commutating margin of 50μs which corresponds to δ=0.063 radians at 200 Hz. This represents a practical commutation limit for a 150 H.P. θ-Pinch machine with the parameter shown in Figure 2.

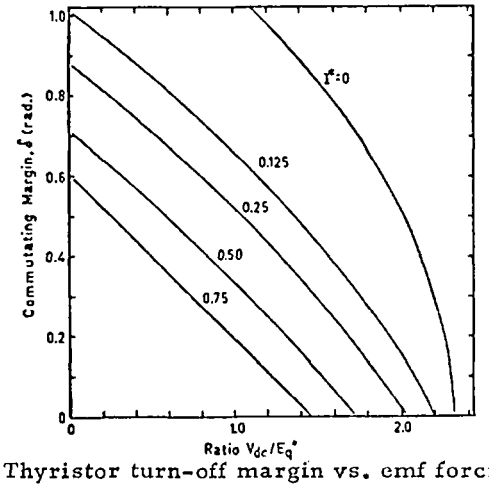

Fig. 5 Thyristor turn-off margin vs. emf forcing.

V. LINK COMMUTATION

Figure 6 defines the real and reactive power flow directions in the complete propulsion system with a mains feed phase delay rectifier (PDR) and a current source inverter. Until the inverter frequency reaches at least 15 Hz, the magnitude of $E_q"$ is insufficient to effect natural voltage-commutation and consequently the CSI thyristors are current commutated from the input side by allowing the PDR to blank the DC link at 60° intervals on a 6 device CSI. A typical waveform of this sequence is shown in Figure 7 for a 150 H.P. cage rotor induction machine in a pulsing mode at 12 Hz.

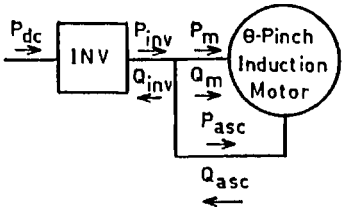

Fig. 6 Power flow in machine-inverter system.

In addition to the increase in $E_q"$ with frequency, Figures 8a and 8b depict the phase change in $E_q"$ as the PDR-CSI- θ -Pinch system transfers from the limit of the startup sequence to the run mode at full rated load and speed. In this latter mode, the inverter reactive requirement is 11% of the component reactive power supplied to just the motoring section of the θ-Pinch machine and this is based on device turn off times of t_q = 30μs.

VI. DUPLEX CSI SYSTEM

Since the major impetus for advocating naturally commutated induction drives is simply based on eliminating the need for any type of electrostatic energy storage elements at very high powers, the only area of concern is the startup mode. The torque pulsations experienced in the pulsing sequence are often objectionable albeit at low speed; however this is only a consequence of controlling the link current in a "digital" fashion rather than limiting the rate of rise and decay of I_{dc} to a value less than e.g. 2 A/ms.

One novel method of entirely eliminating startup torque pulsations is to incorporate two identical PDR-CSI systems with both the inputs and outputs in parallel. [9] By gating the PDRs in a push-pull type fashion so that the DC-link current of PDR #1 is slowly ramped at a constant + d I_{dc}/dt and PDR #2 is similarly ramped but at - d I_{dc}/dt, the combined CSI output current waveform is nearly a perfect sinusoid at e.g. 10 Hz with the exception of the 120 Hz ripple that amounts to less than 5%. This is a practical configuration, for despite the use of a total of 24 devices, the weight and cost savings still are ahead of a similarly rated drive with static capacitor banks. A duplex CSI arrangement is shown in Figure 9.

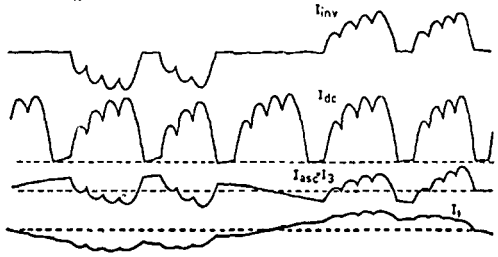

Fig. 7 Machine current waveform in start-mode.

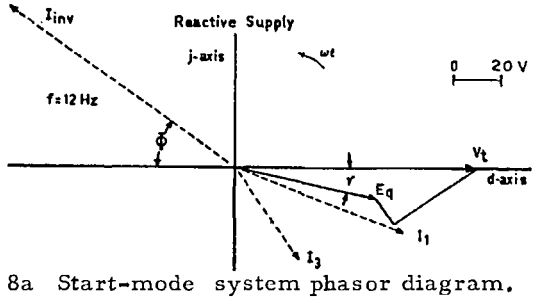

Fig. 8a Start-mode system phasor diagram.

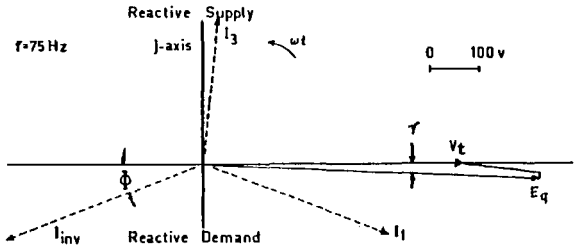

Fig. 8b Run-mode, natural commutation phasors.

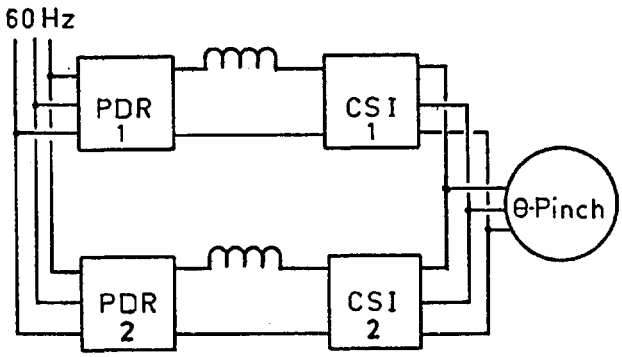

Fig. 9 Duplex CSI system for torque smoothing.

VII. SPECTRAL CURRENT FILTER

If the θ-Pinch machine is wound such that the condenser and motoring windings are connected in parallel, then the condenser winding(ASC) additionally serves as an electromechanical filter to suppress undesired current harmonics or incoming line transients;permitting the motoring winding proper to receive substantially fundamental current. For example, the ASC can be designated to have its reactance minimum at the fifth harmonic of the main travelling wave in order to best suppress the dominant harmonic of the CSI; this energy is absorbed by the rotor and due to the cage construction the thermal overloading is acceptable. The ASC input impedance versus frequency is plotted in Figure 10 for the 150 H.P. machine. The response is similar to resonant,ac-moving coil EM filters.[10]

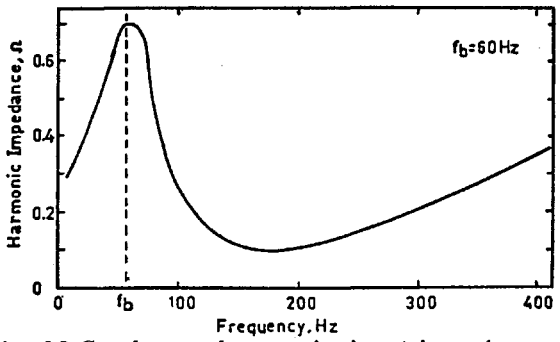

Fig. 10 Condenser harmonic-input impedance.

VIII. CONCLUSION

As an alternative to mains power factor improvement, the mechanism of continuously generating reactive kVA from the stator of a brushless induction machine has been applied to static power converters;specifically where adjustable frequency is generated by a square-wave current-source thyristor inverter. By winding design alone, the integral asynchronous condenser/induction motor terminal power factor remains in the leading region for slip values between 0.075 per unit and zero, whereby the machine provides the commutation margin for the inverter(analogous to synchronous machine applications). This natural voltage-commutation capability of the described induction machine is only present at high speed and for machines with rotor magnetization time constants in excess of about 200 ms.Until the commutating speed is reached,the inverter is commutated by pulsing the input current. Development of this system beyond the 150 H.P. level is fully anticipated.

IX. ACKNOWLEDGEMENTS

The authors would like to express their gratitude to Dr. H.R. Bolton and Dr. L.L.Freris of Imperial College for their many discussions and to the National Research Development Corporation of the U.K. for financial support.

REFERENCES

(1) E.R. Laithwaite and S.B. Kuznetsov, "The Asynchronous Condenser:A Brushless Adjustable Power Factor Induction Machine,"Paper No. F80-273-3, IEEE Winter Power Meeting, New York, Feb. 1980.

(2) E.R. Laithwaite and S.B. Kuznetsov, "Reactive Power Generation in High Speed Induction Machines by Continuously Occuring Space Transients," Paper No. 0090-09-3, International Magnetics Conference, Boston, April 21, 1980. See also IEEE Magnetics, Sept. 1980, Vol. MAG-17.

(3) E.R. Laithwaite and S.B. Kuznetsov, "The Development of Unity Power Factor Brushless Induction Machines, "International Conference on Electrical Machines, Athens, Sept. 16, 1980.

(4) "Development and Manufacture of a Linear Induction Motor Propulsion System for the Tracked Air Cushion Research Vehicle," U.S. Dept. of Transportation, NTIS document FRA-RT-72-35, 1971.

(5) J. Rosa, "Utilization and Rating of Machine Commutated Inverter Synchronous Motor Drives," IEEE Trans. Ind. Appl., Vol. IA-15, No.2. March/April 1979, pp. 155-164.

(6) T.E.Brown and R.F.Grahl, "Design, Development, Fabrication and Testing of a Synchronous Condenser for the Tracked Levitated Research Vehicle," U.S. Dept. of Transportation, NTIS Document FRA-76-266, June 1976.

(7) E.R. Laithwaite and S.B. Kuznetsov, "Development of an Induction Machine Commutated Thyristor Inverter for Traction Drives," IEEE Ind. Appl. Society Annual Meeting, September 30, 1980.

(8) B.D. Bedford and R.G. Hoft, Principles of Inverter Circuits, Wiley:New York, 1964, p. 72.

(9) A. Nabae, et.al., "A New Multiple Current Source Inverter," Paper 77CH1183, Semiconductor Power Converter Conf., Orlando, Florida, 1977.

(10) E. Saraiva and L.L. Freris, "Development of Electromechanical Filter and Performance Evaluation in DC Link," Proc. IEE, Vol. 126,No. 12, Dec. 1979, pp. 1282-1286.